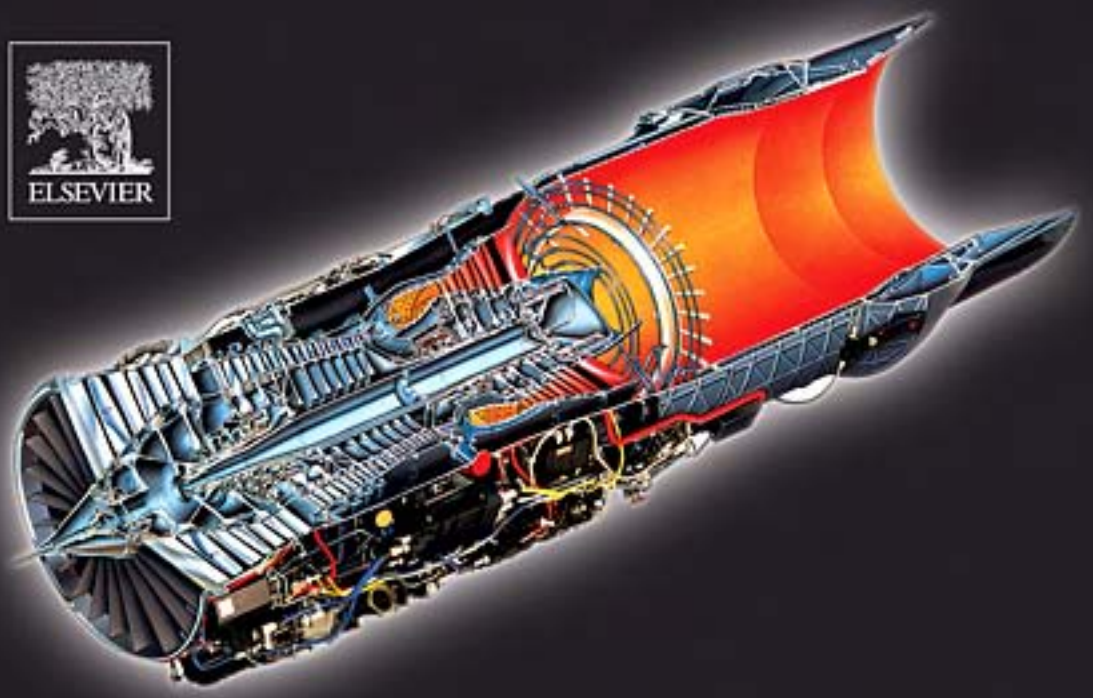
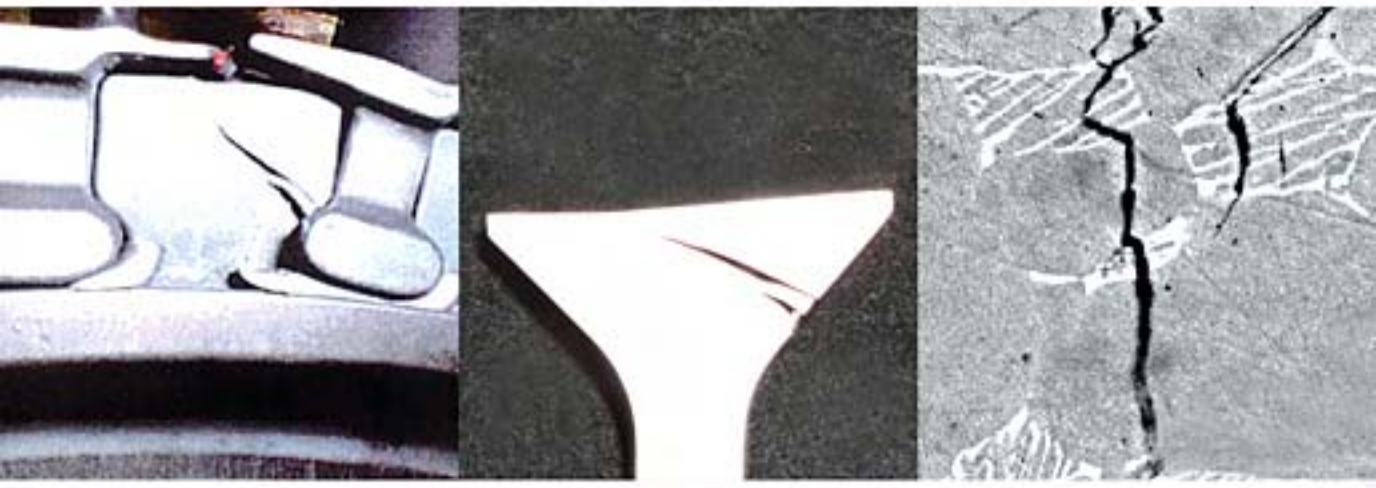


HIGH CYCLE FATIGUE

A MECHANICS OF MATERIALS PERSPECTIVE



THEODORE NICHOLAS

High Cycle Fatigue

A Mechanics of Materials Perspective

This page intentionally left blank

High Cycle Fatigue

A Mechanics of Materials Perspective

Theodore Nicholas

Air Force Institute of Technology
Department of Aeronautics and Astronautics
Wright Patterson AFB, Ohio, USA



ELSEVIER

AMSTERDAM • BOSTON • HEIDELBERG • LONDON • NEW YORK • OXFORD
PARIS • SAN DIEGO • SAN FRANCISCO • SINGAPORE • SYDNEY • TOKYO

Elsevier Ltd.
The Boulevard, Langford Lane
Kidlington, Oxford
OX5 1GB
UK

Elsevier B.V.
Radarweg 29
P.O. Box 211, 1000 AE
Amsterdam
The Netherlands

Elsevier Inc.,
525 B Street, Suite 1900
San Diego,
CA 92101-4495
USA

Elsevier Ltd.
84 Theobalds Road
London
WC1Z 8RR
UK

© 2006 Elsevier Ltd. All rights reserved.

This work is protected under copyright by Elsevier Ltd, and the following terms and conditions apply to its use:

Photocopying
Single photocopies of single chapters may be made for personal use as allowed by national copyright laws. Permission of the Publisher and payment of a fee is required for all other photocopying, including multiple or systematic copying, copying for advertising or promotional purposes, resale, and all forms of document delivery. Special rates are available for educational institutions that wish to make photocopies for non-profit educational classroom use.

Permissions may be sought directly from Elsevier's Rights Department in Oxford, UK: phone (+44) (0) 1865 843830; fax (+44) (0) 1865 853333, e-mail: permissions@elsevier.com. Requests may also be completed on-line via the Elsevier homepage (http://www.elsevier.com/locate/permissions).

In the USA, users may clear permissions and make payments through the Copyright Clearance Center, Inc., 222 Rosewood Drive, Danvers, MA 01923, USA; phone: (+1)(978) 7508400, fax: (+1)(978) 7504744, and in the UK through the Copyright Licensing Agency Rapid Clearance Service (CLARCS), 90 Tottenham Court Road, London W1P 0LP, UK; phone: (+44) 20 7631 5555; fax: (+44) 20 7631 5500. Other countries may have a local reprographic rights agency for payments.

Derivative Works
Tables of contents may be reproduced for internal circulation, but permission of the Publisher is required for external resale or distribution of such material. Permission of the Publisher is required for all other derivative works, including compilations and translations.

Electronic Storage or Usage
Permission of the Publisher is required to store or use electronically any material contained in this work, including any chapter or part of a chapter.

Except as outlined above, no part of this work may be reproduced, stored in a retrieval system or transmitted in any form or by any means, electronic, mechanical, photocopying, recording or otherwise, without prior written permission of the Publisher.

Address permissions requests to: Elsevier's Rights Department, at the fax and e-mail addresses noted above.

Notice
No responsibility is assumed by the Publisher for any injury and/or damage to persons or property as a matter of products liability, negligence or otherwise, or from any use or operation of any methods, products, instructions or ideas contained in the material herein. Because of rapid advances in the medical sciences, in particular, independent verification of diagnoses and drug dosages should be made.

First edition 2006

ISBN–13: 978-0-08-044691-2
ISBN–10: 0-08-044691-4

♾ The paper used in this publication meets the requirements of ANSI/NISO Z39.48-1992 (Permanence of Paper).

Printed in Great Britain

06 07 08 09 10 10 9 8 7 6 5 4 3 2 1

Working together to grow
libraries in developing countries

www.elsevier.com | www.bookaid.org | www.sabre.org

ELSEVIER BOOK AID International Sabre Foundation

Contents

Preface **x**

Part One Introduction and Background **1**

1 Introduction **3**
1.1 Historical background 3
1.2 What is High Cycle Fatigue? 4
1.3 HCF design considerations 5
1.4 HCF design requirements 9
1.5 Root causes of HCF 11
1.5.1 Field failures 13
1.6 Damage tolerance 16
1.6.1 Application to HCF 20
1.7 Current status 23
1.8 Field experience 25

2 Characterizing Fatigue Limits **27**
2.1 Constant life diagrams 27
2.2 Gigacycle fatigue 27
2.3 Characterizing fatigue cycles 34
2.4 Fatigue limit stresses 35
2.5 Equations for constant life diagrams 41
2.6 Haigh diagram at elevated temperature 47
2.7 Role of mean stress in constant life diagrams 51
2.8 Jasper equation 56
2.9 Observations on step tests at negative R 65

3 Accelerated Test Techniques **70**
3.1 Historical background 70
3.1.1 Coaxing 70
3.2 Early test methods 72
3.3 Step test procedures 75
3.3.1 Statistical considerations 76
3.3.2 Influence of number of steps 78
3.3.3 Validation of the step-test procedure 80
3.3.4 Observations from the last loading block 85
3.3.5 Comments on step testing 89
3.4 Staircase testing 90
3.4.1 Probability plots 91

3.4.2 Statistical analysis 95
3.4.2.1 Dixon and Mood method 95
3.4.2.2 Numerical simulations 99
3.4.2.3 Sample size considerations 104
3.4.2.4 Construction of an "artificial" staircase 105
3.5 Other methods 106
3.6 Random fatigue limit (RFL) model 109
3.6.1 Data analysis 113
3.7 Summary comments on FLS statistics 120
3.8 Constant stress tests 123
3.8.1 Run-outs and maximum likelihood (ML) methods 126
3.9 Resonance testing techniques 129
3.10 Frequency effects 134

Part Two Effects of Damage on HCF Properties 143

4 LCF–HCF Interactions 145
4.1 Small cracks and the Kitagawa diagram 145
4.1.1 Behavior of notched specimens 149
4.2 Effects of LCF loading on HCF limit stress 153
4.2.1 Studies of naturally initiated LCF cracks 170
4.3 Crack-propagation thresholds 170
4.3.1 Overloads and load-history effects 172
4.3.1.1 An overload model 180
4.3.1.2 Analysis using an overload model 182
4.3.2 Examples of LCF–HCF interactions 183
4.4 Design considerations 193
4.4.1 LCF–HCF nomenclature 196
4.4.2 Example of anomalous behavior 197
4.4.3 Another example of anomalous behavior 200
4.5 Combined cycle fatigue case studies 204

5 Notch Fatigue 213
5.1 Introduction 213
5.2 Stress concentration factor 213
5.3 What is k_t? 215
5.4 Fatigue notch factor 216
5.4.1 k_f versus k_t relations 217
5.4.2 Equations for k_f 218
5.5 Fracture mechanics approaches for sharp notches 222
5.6 Cracks versus notches 225
5.7 Mean stress considerations 228
5.8 Plasticity considerations 232
5.8.1 Negative mean stresses 238

5.9 Fatigue limit strength of notched components 239
5.9.1 Non-damaging notches 241
5.10 Size effects and stress gradients 242
5.10.1 Critical distance approaches 242
5.11 Analysis methods 246
5.12 Effects of defects on fatigue strength 251
5.13 Notch fatigue at elevated temperature 254

6 Fretting Fatigue 261
6.1 Introduction 261
6.2 Observations of fretting fatigue 263
6.3 Representing total contact loads, Q and P 267
6.4 Load and stress distributions 271
6.5 Effects of local and bulk stresses on stress intensity 272
6.6 Mechanisms of fretting fatigue 277
6.7 Mechanics of fretting fatigue 279
6.8 Stress analysis of contact regions 281
6.8.1 Multiple crack considerations 283
6.8.2 Analytical solutions 284
6.9 Role of slip amplitude 292
6.10 Stress-at-a-point approaches 295
6.11 Fracture mechanics approaches 300
6.12 A combined stress and K approach 306
6.13 Comparison of fretting-fatigue fixtures 309
6.14 Role of coefficient of friction 312
6.14.1 Average versus local coefficient of friction 317
6.15 Summary comments 317

7 Foreign Object Damage 322
7.1 Introduction 322
7.2 Field experience and observations 324
7.3 Repair by blending 325
7.4 Background 326
7.5 FOD data mining and investigation 326
7.6 Definition of FOD 328
7.7 Types of damage 329
7.8 Scope of the FOD problem 336
7.8.1 Laboratory simulation methods 338
7.8.1.1 Solenoid gun 338
7.8.1.2 Pendulum 338
7.8.1.3 Quasi-static 339
7.8.2 Simulations using a leading edge geometry 339
7.8.3 Role of residual stresses 344
7.8.4 Energy considerations 345

7.9 Fatigue limit strength 347
7.9.1 Simulations using a flat plate 352
7.9.2 Other laboratory FOD simulations 359
7.10 Analytical modeling of FOD 368
7.10.1 Perturbation study 371
7.11 Summary comments 374

Part Three Applications 377

8 HCF Design Considerations 379
8.1 Factors of safety 379
8.1.1 Modeling errors 381
8.1.2 Material variability 384
8.2 Fracture mechanics considerations 386
8.2.1 Effects of defects 390
8.2.2 Application to LCF–HCF 396
8.3 Damage tolerance for HCF 398
8.3.1 Material allowables 400
8.4 Threshold concept for HCF 403
8.4.1 Representing fatigue limit data 405
8.4.2 Threshold considerations 408
8.4.3 Experimental threshold measurements 409
8.4.3.1 "Jump-in" method 409
8.4.4 Mechanisms in threshold testing 412
8.4.5 Load-history effects 414
8.4.5.1 Compression precracking 416
8.4.5.2 Load-shed rates 416
8.4.6 Crack closure 418
8.4.6.1 $K_{max}-\Delta K$ concept 419
8.4.6.2 Crack propagation stress intensity factor 422
8.4.7 An engineering approach to thresholds 423
8.4.8 Observations from field failures 424
8.5 Probabilistic approach to HCF/FOD design 425
8.6 Residual stresses in HCF design 430
8.6.1 Application to notches 436
8.6.2 Shot peening 441
8.6.3 Deep residual stresses 447
8.6.3.1 Application to an airfoil geometry 449
8.6.3.2 Crack arrest 458
8.6.3.3 Crack growth retardation 461
8.6.3.4 A numerical example 462
8.6.4 Autofrettage 464

Appendices

A. Early Railroad Accidents and the Origins of Research on Fatigue of Metals **472**
George P. Sendeckyj

B. Final Report for the USAF High Cycle Fatigue Program **493**
Otha Davenport

C. HCF in ENSIP **499**

D. Evaluation of the Staircase Test Method using Numerical Simulation **517**
Major Randall Pollak

E. Estimation of HCF Threshold Stress Levels in Notched Components **531**
Alan Kallmeyer

F. Analytical Modeling of Contact Stresses **542**
Bence B. Bartha, Narayan K. Sundaram and Thomas N. Farris

G. Experimental and Analytical Simulation of FOD **558**
Jeffrey Calcaterra

H. FOD in JSSG **600**

I. Computation of High Cycle Fatigue Design Limits under Combined High and Low Cycle Fatigue **617**
Joseph R. Zuiker

Index **639**

Preface

The first question a prospective reader or purchaser of this book may ask is, "Why another book on fatigue?" This is a very legitimate question because there are many books and hundreds of journal articles dealing with various aspects of fatigue, including high cycle fatigue (HCF). In fact, in researching various aspects of HCF, the author was drawn back in history to works like those of Wöhler in the late 1800s as well as many related articles on fatigue of railroad wheels and bridges. Hopefully, what makes this book both unique and of technical interest is the background and history of recent HCF failures within the US Air Force, and the program that evolved from the concerns raised by those failures. This book should be of value to students, scientists, engineers, and researchers who deal with HCF. However, the main audience for this book is the practicing engineer who has to deal with HCF from design or analysis point of view. The book can also serve as a supplement to graduate level courses that delve into almost any aspect of HCF or as the basis for continuing education short courses. The book has been put together in the form of a series of review articles on the various aspects of HCF, which are both of importance and which have not been covered extensively in one place in the open literature. From this perspective, it should be of use to researchers and scientists dealing with any of a wide variety of topics associated with HCF.

It is assumed that the reader has a basic knowledge of fracture mechanics, a background that includes mechanics of materials, and some knowledge of general fatigue concepts. Where appropriate, the reader is referred to some general references for more complete coverage of certain topics that cannot be covered completely in this book. The book is written at a slightly higher level and with more detail than many books on mechanical behavior, fatigue, design, or materials. There is no intent to duplicate the existing literature but rather to expand the coverage at a somewhat more advanced level. For basic coverage of some of the material contained herein, the reader is referred to, for example, the chapter on HCF in the book by Collins.[*] The present book addresses HCF issues from a mechanics of materials point of view. There is no attempt in this book to deal with fatigue mechanisms. Books such as those of Suresh and Hertzberg address fatigue mechanisms quite extensively and are recommended to those who wish to pursue that aspect of HCF.[†]

High Cycle Fatigue has been a serious engineering problem in many industries since the 1800s. Around 1995 there were a series of gas turbine engine failures on US Air

[*] Collins, J.A., *Failure of Materials in Mechanical Design: Analysis, Prediction, Prevention*, Second Edition, John Wiley & Sons, New York, 1993.

[†] Suresh, S., *Fatigue of Materials*, 2nd ed., Cambridge University Press, New York, 1998. Hertzberg, R.W., *Deformation and Fracture Mechanics of Engineering Materials*, 3rd ed., Wiley, New York, 1989.

Force fighter jets that caused great concern because of excessive maintenance costs and potential costs of redesigns, but mostly because of the threat to operational readiness. While the cause of these failures was widely attributed to HCF– the specific causes were not known and the risk of continued operation was even less known. It is interesting to note that, over the years, failure investigations and detailed fault tree analyses have shown that, beyond reasonable doubt, many of these HCF failures should or could not have occurred! Because of the concern about HCF, and even though HCF has been studied extensively for many years, the Air Force initiated a program to deal with the technological issues associated with HCF in gas turbine engines. The primary goal was to reduce the incidence of HCF-related failures and to reduce the associated maintenance and replacement costs. Another goal was to produce more damage tolerant design approaches for HCF and apply these procedures to the next generation of engines, namely the engine for the Joint Strike Fighter. The team that put together the HCF program included the author and other experts from both industry and government. The program was broken down into a number of technical areas, most dealing with propulsion. One aspect of the program that ended up accounting for nearly a third of the overall effort was materials; particularly the damage tolerant aspects as related to HCF. What came out early in the program planning stages was that design for HCF is actually quite straightforward, given the actual loading (which is an entire problem in itself). However, the HCF capability of a material in a real environment, where it is simultaneously subjected to "damage" from other operational conditions, is a subject that has received little or no attention historically. HCF – in conjunction with three real-world conditions, low cycle fatigue, contact fatigue, and foreign object damage – was defined as the major problem and formed the basis of a research and development program that was originally forecast to last for 5 years or more. It is largely the works associated with that program that is the theme of this book. As with many other authors, the present book relies heavily on the author's own publications. The background notes and studies, many of which did not get included in published papers for reasons of length limitations, are included along with works from many colleagues and other authors who have contributed so much to this field. Finally, the author has to look back and give credit to a group of individuals, universities, and companies, that made up the team which worked on the HCF program. Like a mini-Manhattan project, one of the finest and most talented teams in history was formed and worked together to advance the state of the art in HCF and provide the technology which has advanced our capability to deal with the perplexing problem of materials damage tolerance under HCF in gas turbine engine environments. The present book documents some of those advancements and expands the problem to include materials and applications beyond turbine engines, which involve rotating machinery or any structural components subjected to high frequency vibratory loading.

While much of this book deals with HCF of turbine engine components, it was the intent to make the application of the relevant technologies much broader to include all

applications where cyclic loading at high frequencies for a large number of cycles is involved. Thus, rotating machinery in general produces conditions where HCF can be a problem and the technologies addressed in this book are applicable. Interaction of low cycle fatigue (LCF) with HCF, for example, is a condition that occurs under almost any simple spectrum loading in a rotating component. Just bringing a component up to a steady rotational speed and occasionally shutting it down constitutes a condition where LCF–HCF interactions have to be evaluated. As pointed out in the beginning of Chapter 6, whenever two bodies in contact undergo relative motions with superimposed contact loading, conditions are favorable for fretting fatigue, a type of HCF, to occur.

Another aspect of this book is the extensive reference to Ti-6AI-4V as a material for HCF data. In the Air Force HCF program, a decision was made to use a single material as a "model" material to study various features of HCF behavior. The choice of a single material was made so that everyone working on the program would have access to the same material as well as the database accumulated by all participants in the program. A very large number of forgings were produced from the same heat under nominally identical and carefully controlled and monitored conditions. The data obtained and trends in HCF behavior were felt to be rather generic and applicable to other materials. The advantage of the use of a single model material was the ability to generate a large database from which comparisons could be made on any aspect of HCF behavior by anyone conducting research on the program. For this reason, the reader will come across many examples that use Ti-6AI-4V forged plate as the reference material to point out specific behavior. Similar to the use of aluminum to study crack closure, steels to study gigacyle fatigue, or aluminum to study overload effects in crack growth, the use of titanium to study HCF is felt to be representative of the generic behavior of other materials. To apply the findings to another material, however, a database for that material would have to be established. That is not a small task when dealing with long life or very high cycle counts that are typical of HCF.

A comment is in order regarding the length and detail contained in Chapter 7 and the accompanying Appendix G on the subject of foreign object damage (FOD). While the original intent was not to write a book or even have a detailed discussion of FOD as an issue in HCF, it became obvious as this book was being written that the discussion of FOD in the open literature is extremely sparse. That, combined with the many questions and issues that were raised during the Air Force HCF program (and are still being raised), led to the detailed discussion of the subject presented in this book. Similar comments are in order regarding the extensive coverage of statistics. With increased emphasis on statistics of HCF data and use of a probabilistic type of approach in HCF design, extensive coverage has been given to statistical aspects of HCF data since such details are not commonly found in the fatigue literature.

While some topics such as FOD and statistics are given extensive coverage in this book, other topics such as HCF under multiaxial stresses are neglected completely. For

this topic, experimental data into the long life (HCF) regime are essentially non-existent. Thus, much of the limited work in this area is somewhat speculative and is an extension of work dealing with LCF that is covered extensively in the open literature.

The nomenclature used in this book may differ somewhat from what is considered standard or common usage. In such instances, this has been noted in a footnote. Additionally, units of measurement are not standard in many cases. While technical publications typically adhere to SI units these days, much of the work published by the engine manufacturers in the United States is presented using English units (pounds, inches, for example), because these are the units used as standard practice in that industry. The graphs and calculations came in those units and no attempt was made to convert to SI units. A similar situation arises when dealing with data from older publications. In most of the cases, the absolute numbers are not important but rather the concepts conveyed are what matters.

It will become apparent in reading this book that the references are not as complete as they would be in a comprehensive review article. Rather, references have been chosen, in many cases from the authors' own works, to illustrate certain points. Many appropriate and relevant references are not included. For this the author apologizes with no intent to slight anyone who has contributed to the HCF field and whose work is not referenced.

The book is arranged into three Parts consisting of eight Chapters. Part one deals with the background related to HCF and includes chapters on the history of the subject, methods for presenting data, and test techniques. Part two covers damage states that affect HCF behavior, namely LCF and its influence, notches, fretting, and FOD. The final chapter addresses a number of issues related to HCF design and includes discussion of crack growth thresholds and effects of residual stresses among other topics. The text is supplemented by nine Appendices.

I would like to acknowledge the support of many that contributed to this book. The reviewers for Elsevier helped and encouraged me to get this book into a presentable form. My greatest appreciation goes to the authors of the various appendices that supplement the contents of the book. These appendices were not just taken from existing documents. Rather, they were put together by the individual authors to provide insight into specific subjects that could not be easily incorporated directly as part of the text. To these authors – Otha Davenport, George Sendeckyj, Major Randall Pollak, Alan Kallmeyer, Bence Bartha, Narayan Sundaram, Thomas Farris, Jeffrey Calcaterra, and Joseph Zuiker – go my sincerest thanks. I would also like to thank the following individuals who read different sections of the book and provided suggestions that led to improvements in the text in the specific areas indicated: Prof. Skip Grandt of Purdue University (Chapters 1–3), Mr Steve Thompson of the Air Force Research Laboratory (FOD), Dr Michele Ciavarella, CNRITC, Bari, Italy (fretting and notches), Prof. Tom Farris of Purdue University (fretting), Mr Rick Wade formerly in the Air Force Research Laboratory Propulsion Directorate (FOD), Mr Patrick Conor of the New Zealand Defence Technology Agency (FOD), Dr Pat

Golden of the Air Force Research Laboratory (fretting), Mr Charles Annis of Statistical Engineering, Mr Jerry Griffiths of General Electric Corp., and Mr Al Berens of University of Dayton Research Institute (accelerated test techniques and statistics). The support of the US Air Force in my positions at the Air Force Materials Lab and, more recently, at the Air Force Institute of Technology (AFIT) is gratefully acknowledged. This last assignment was through my employment at the University of Dayton Research Institute under the US Government IPA program, which allowed me to accomplish a substantial part of the writing of this book while at AFIT. Finally, I would like to thank Mr Ted Fecke, Director of Engineering, Propulsion Product Group, Wright Patterson AFB, and his predecessor, Mr Otha Davenport for their support in establishing and guiding the Air Force HCF program and for the many opportunities they have given me to be involved in Air Force HCF problems and to learn about the real world of HCF in turbine engines.

Part One
Introduction and Background

In the first three Chapters we present some of the historical background on high cycle fatigue (HCF) to introduce the reader to some of the concepts and approaches that were developed over a century ago. The primary reason for presenting this material is to illustrate the many concepts that formed the basis for what now constitutes the basis of modern-day procedures that have not changed, or are very similar, to what was introduced when HCF was first developed. Moreover, it is important to recognize the limitations and intended applications of some of these technologies as pointed out by the original developers. With the exceptions of modern-day experimental methods and instrumentation as well as today's powerful computational tools, HCF has not seen what could be labeled tremendous advancements over many years.

In Chapter 1, the reader is exposed to the history of development of HCF as well as some of the more recent trends based on experience within the US Air Force which precipitated a major program on HCF to improve the damage tolerance of aircraft engines to HCF. In Chapter 2, the methods for representing data from HCF tests are presented, again with a strong historical perspective. In Chapter 3 methods for obtaining HCF data are reviewed. Here, both traditional methods and, some recent developments are presented.

This page intentionally left blank

Chapter 1
Introduction

1.1. HISTORICAL BACKGROUND

Fatigue has not always been a technical subject or consideration in the disciplines of solid mechanics or strength of materials. In fact, one of the earliest researchers to address the topic was Wöhler [1], who, in 1870, gave a general law which may be stated as:

> Rupture may be caused, not only by a steady load which exceeds the carrying strength, but also by repeated application of stresses, none of which are equal to this carrying strength. The differences of these stresses are measures of the disturbance of the continuity, in so far as by their increase the minimum stress which is still necessary for rupture diminishes.

Wöhler performed many experiments that eventually were used as the basis for much of the fatigue modeling that was carried out in the late 1800s and beyond. In researching the contributions of August Wöhler, one should not be confused with Friedrich Wöhler, a distinguished and well-published German chemist, nor with Karen Wöhler who wrote extensively about preventing pain and fatigue in people, both of whom were active in the same time period as August Wöhler.

This book deals with a specific portion of the general problem of fatigue, namely high cycle fatigue (HCF). Any book on HCF should begin with a short introduction to the history of fatigue. Fatigue is not a technical subject that has been around hundreds of years. In fact, it came into being in the 1800s because of numerous accidents associated with railroad axles and railroad bridges, both of which were subjected to repeated loading. Although the terminology "high cycle fatigue" (HCF) was not used in connection with these accidents and the subsequent investigations, the high cycle counts associated with some of these incidents put them in the high cycle category. Most of the early papers on fatigue (see, for example, the works of Wöhler cited in Appendix A) dealt with tests to failure and an attempt to establish an endurance limit, a term now associated with HCF. The British work (in the commission report discussed in Appendix A) dealt with shorter life comparative tests of rails, that is which rail design was best based on shorter life tests. The railroad industry had adopted a definition of service life and used it for scheduling replacement or repair of axles and wheels. This was a modern concept used quite early by the railroad people.

The origins of the history of fatigue, particularly with respect to railroad accidents, have been documented in a heretofore unpublished article by Dr George Sendeckyj, a former colleague of mine at the Air Force Research Laboratory. This article, with his

permission, appears as Appendix A in this book and provides the reader with some very interesting documentation of the history of the subject of this book. Additionally, the history of fatigue, particularly the efforts in Germany, is presented in an extensive review article by Schütz [2]. There, the enormous and significant contributions of Wöhler are reviewed. Wöhler, who is often cited in discussing the beginnings of fatigue, was the Royal "Obermaschinenmeister" of the "Niederschlesisch-Mährische" Railways in Frankfurt an der Oder. Also included in that review are the details of the contributions of Thum, who, with coworkers, authored no less than 574 publications on the subject of fatigue [2]. The extensive review by Schütz is recommended reading for anyone with an interest in the history of the subject.

1.2. WHAT IS HIGH CYCLE FATIGUE?

A number of years ago I was preparing to give a briefing to some high-level managers at Air Force headquarters. It was for the purpose of informing them of the program that was being put together to address issues related to HCF in turbine engines, particularly with respect to material behavior. Since this was a high-level briefing, the charts had to be reviewed by the appropriate staff members to make sure it had the proper length, format, and content. My briefing charts were all found to be satisfactory, with no changes, except for one additional chart that they felt I needed at the beginning. I was asked to define HCF. I was partially stumped because I had never seen a good formal definition of HCF. I don't remember what I put together for the briefing, but it centered around the premise that HCF involved longer lives than low cycle fatigue (LCF), which I also had to explain, and it generally involved high frequencies in excess of around 1000 Hz (cycles per second, which I also had to explain!). Perhaps a better definition would be a fatigue condition where the number of cycles between possible inspections is too large to be able to do anything about it in a practical sense. I avoided a popular definition where purely elastic behavior is associated with HCF while LCF involves cyclic plasticity. What if someone asked "How much plasticity?" LCF is usually conducted under strain-controlled conditions while HCF generally involves load control, but this also is a rather vague way to define the difference between the two. There is no formal definition in my mind, but HCF generally involves high frequencies, low amplitudes, nominally elastic cyclic behavior, and large numbers of cycles. On a conventional stress-life curve, commonly called a *S–N* curve or a Wöhler diagram, HCF occurs at the right end of the curve where the number of cycles is usually too large to be able to obtain sufficient statistically significant data to be able to characterize the material behavior with a very high degree of confidence. It is this hard to define subject that will be discussed in this book, specifically from a material's behavior point of view.

1.3. HCF DESIGN CONSIDERATIONS

Before discussing design for HCF, it is instructional to review general design procedures for turbine engines in general with specific emphasis on structural durability and issues dealing with fatigue. While design procedures differ from industry to industry, the specific concern with HCF in US Air Force turbine engines makes this background relevant to many of the subjects addressed in this book. One of the features in design which has received increased attention in recent years is a trend away from deterministic design to one involving probabilistics to insure reliability of the resulting product. To address the reliability aspects of design along with a review of general design practices, the following is cited from a presentation given by Crouch [3] in 2000. The quoted portions of the presentation by Crouch contain many details that might be excessive for the beginning of an introductory chapter. Rather than relegate these quotations, which are not the entire presentation, to an appendix, the important features and main points of the article are highlighted in bold below.

Aircraft turbine engine reliability and its growth are important parameters to manage and control during development, production, fielding and sustainment. It can influence system safety, aircraft readiness, and operational support costs. Its roots are early in the development phase with the operational requirements. Operational requirements flow down to weapon system, air vehicle and propulsion system requirements. Next there occurs a functional requirements allocation, the engine manufacturer's design synthesis, analysis, and the development of a failure modes and criticality effects analysis. In the past, engine reliability requirements are spelled out in a table in the specification. **There have been goals for the in-flight shutdown rate; shop visit rate and line replaceable unit rate per 1000 engine flight hours**. Although all problems occurring during the Engineering and Manufacturing Development (EMD) activity are corrected, they are also tracked and categorized in one of these three categories. In this way the demonstrated reliability of the development engine can be monitored. After hardware and software are produced; component tests, bench tests, rig tests and finally ground and altitude engine tests are performed to assure the engine meets performance, operability, functionality and durability requirements.

The general basis for aircraft turbine engine design requirement and verification processes is resident in the Joint Service Specification Guide for Aircraft Turbine Engines (JSSG-2007 dated 30 October 1998). In the course of EMD, distress and/or failures occur which indicate potential reliability problems. These are corrected iteratively and are verified to eliminate the problems. **The analysis and tests feature both loading and operating environments representative of the projected usage and in some cases severe loading and environment beyond the expected level of usage to evaluate robustness**. The tests and analyses include compressed usage cycles such that one hour of tests might equal 4–10 hours of usage. In this way test time is minimized to reduce the development cycle time and the development cost. We refer to such full-scale engine tests as accelerated mission tests (AMT). These are usually accomplished in sea level and altitude engine test cells. In addition product variability is studied analytically with the limited test components and engines.

The Engine Structural Integrity Program (ENSIP) handbook (MIL-HDBK-1783A dated 22 Mar 99)* **is used as a guide to design, develop, produce and sustain engines to assure their structure eliminates or minimizes safety, reliability and durability problems**. Many mechanical, electronic and software problems are identified and corrected in the EMD program. At the end of the EMD program, a review of the analyses and test reports validates the functional requirements.

Two of the challenges of the development program, which affect reliability of the field engine, are engine to engine tolerances and variations and the required operational usage of the engine. Test time and test hardware are expensive. The limited number of test assets limits the tested tolerances and variations whose characteristics can account for some problems in field operation with the hundreds of engines produced. Secondly, the original usage projection of the engine in terms of throttle cycles, altitude profiles influences the design. The projected usage is compiled for the engine as a set of component and engine test cycles used to evaluate the product design. **Sometimes the pilots fly the system different than the original projection of the usage. This can result in a more severe operation of the engine and affect different component failure modes in the engine**. Modeling, simulation and analysis improvements and application throughout the weapon system life cycle will hopefully limit these two problems.

Once the engine goes into production for a production aircraft installation or as a spare engine, it is released for field service evaluation. Sometimes a field service evaluation is performed on the aircraft/engine combination in which case it is an initial operational test and evaluation. Usually a small group of aircraft and spare engines are used, perhaps 6 aircraft/engines and 2 spare engines. The length of the evaluation might be 1–2 years. In this time the engines might each accrue some 300–600 flight hours or 600–1200 cycles. This represents but 15–30% of the typical engine hot section 2000 flight hour (4000 cycle life). Oftentimes it's the engine's hot section i.e. combustor and turbines that deteriorate and drive maintenance inspection rejects. Infant mortality, manufacturing/quality, software and electronic problems are usually the type of problems to surface in the field service evaluation. The field service evaluation is also employed for design changes prior to approval of the engineering change proposal for software changes to the engine control, diagnostic system or ground support equipment. It is effective because it employs the software for several different engines. Sometimes software problems with engine-to-engine variability surface during these tests.

Crouch [3] goes on to point out how changes are made in design based on field problems through a Component Improvement Program (CIP), which the Air Force, Navy and Army all have, which funds redesigns and verification tests to correct fielded engine safety, reliability and operational support cost problems. He notes:

"**Reliability analyses are also used to manage field problems. Statistical distributions are used to predict component failure rates**. These are used to perform risk management

* The version referenced here has been superceded by a more recent version [4] cited elsewhere in this book. These, in turn, supercede the original version [5] adapted and published in 1984.

on our aircraft engines to judge the needed frequency of part replacement, safety inspection or retrofit of a redesign. Usually we use the Weibull distribution but sometimes other distributions better fit the data. Also we must plan for engine support through spare part and engine provisioning. Once again the field data for part failure or the engine shop visit rate data and projections are used as inputs to models to estimate the number of spare parts or spare engines needed.

One reliability limitation occurring during the operational use of the engines is the lack of accurate and timely failure data. The Air Force has a deficiency reporting system to identify component or system failures. Oftentimes this system is also used to report warranty claims. After the warranty runs out often the maintenance personnel fail to use it to report failures. Thus the engine program office may be surprised with a new failure mode. Other factors which influence the reporting system include: reduced number of maintenance personnel to report the faults, frustration with the shipment and transportation of the failure exhibits, and frustration with the engine program office, repair center and engine contractor with the length of time it takes to perform the investigation and complete the report. Sometimes the time from initial report of failure to a report analyzing the problem and recommending a corrective action takes well over a year. A video made on the deficiency reporting system will hopefully raise awareness of the importance of the system and address the problem.

Other data systems are used to report aircraft and engine problems as well. Lack of complete reports with proper malfunction codes result in both over and under reporting of field problems. Correlation with engine contractor reports from their service representatives with data from their daily reports has produced variance in engine shop visit and line replaceable unit rates of about 50%. Thus the engine problems histories and reliability trends can be suspect.

Secondly many high cycle fatigue problems have affected engine safety, reliability, readiness and support cost problems over the recent decade. We do not understand the phenomena well nor have the design tools to analyze it nor the test equipment to measure it. With the help of the National High Cycle Fatigue Initiative these deficiencies will be eliminated."

The diagram used most commonly in LCF is generally referred to as an S–N curve which is a plot of maximum stress (S) as a function of number of cycles to failure (N) as depicted in Figure 1.1(a). This diagram is also referred to as a stress-life curve or a Wöhler diagram, after the famous scientist August Wöhler who conducted the first extensive series of fatigue tests and is often referred to as the father of fatigue. The diagram is drawn for test data obtained at a constant value of stress ratio, R. For each value of R, a different curve is drawn. Many attempts have been made and models developed to consolidate data at different values of R with a single parameter based on combinations of stress amplitude and maximum stress or other functions of stress. In this book, we will deal with such models only as they pertain to the values of stress at or near the fatigue limit corresponding to a large number of cycles in the HCF regime, typically 10^7 cycles or greater.

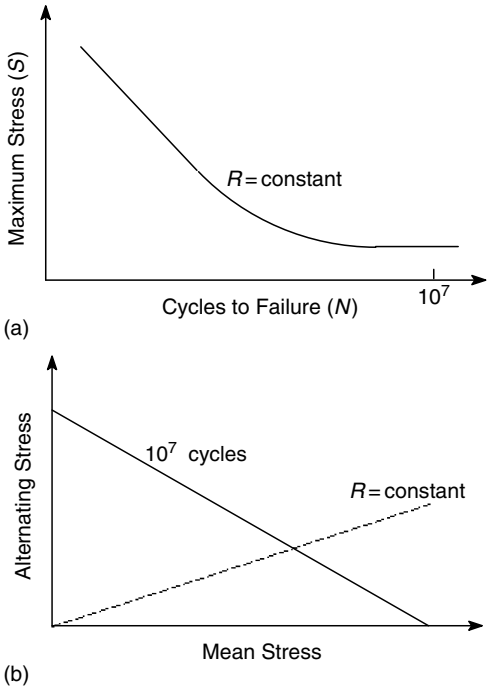


Figure 1.1. Schematic of fatigue diagrams: (a) *S–N* curve for LCF and (b) Goodman diagram for HCF.

For HCF, the emphasis is on the value of stress at the fatigue limit and the data are represented on a Goodman diagram which is a plot of alternating stress against mean stress as shown in Figure 1.1(b). Each value of R is represented as a straight line drawn radially outward from the origin and the plot is the locus of points having a constant life in the HCF such as 10^7 cycles. The Goodman diagram, which should correctly be called a Haigh diagram, is discussed in Chapter 2.

With this as a background for engine design practices, we focus on aspects of design specifically for HCF and the associated problems that arose based on field experience. Design for constant amplitude HCF loading can be rather straightforward when there are no other factors involved. The procedure involves the generation of fatigue limit data at different values of stress ratio, R, and plotting them on, for example, a Goodman diagram as shown above. This plot of alternating stress against mean stress is a constant life diagram and can be made for any number of cycles (Constant life diagrams are discussed in detail in Chapter 2). Typically 10^7 cycles or higher is used, which is the traditional maximum number of cycles that a component may be subjected to in its design life. It may be more of a convenience in balancing testing time and expense with what a component actually may see in service (see the discussion on gigacycle fatigue in Chapter 2). It is

normally difficult to produce sufficient data at these long lives to be statistically significant, even with some of the newer high frequency machines being used. If the product form, machining technique, and surface finish are identical for the laboratory samples and the component for which the data are to be used, the behavior should be identical. However, there are many instances where the component validation uses a geometry or surface finish that does not conform to the laboratory test conditions. Many components are shot peened or subjected to surface treatments (see Chapter 8) that are different than those used on laboratory specimens. This is representative of the potential problems that face designers involving transferring data from laboratory size samples to components, especially if the components experience a multi-axial stress state [2]. A primary issue in HCF design, one that has not been commonly addressed adequately, is the material capability after it has been subjected to service conditions. For rotating components in gas turbine engines, damage due to ingestion of foreign objects, fretting fatigue or wear, and LCF can reduce the HCF capability of the material and must be considered in design. These are some of the issues discussed in Part III (Chapters 4–7) of this book.

The stress corresponding to HCF design life is defined in various manners throughout the literature. For cycle counts that are below the region that we classify as HCF, the term "fatigue strength" is generally used. This is best defined as the stress that causes failure in a set number of cycles, usually in the LCF regime. It is sometimes used for higher number of cycles. We prefer the terminology fatigue limit or fatigue limit stress (or strength) to indicate stress to cause failure at a fixed (large) number of cycles, typically 10^6 or 10^7. This implies that it is not quite an endurance limit because of either material behavior (a non-horizontal S–N curve), or limitations on either testing or expected number of usage cycles. More recent work in the field called gigacycle fatigue extends conventional testing and material characterization into the regime encompassing 10^9 cycles. This subject is addressed in Chapter 2. The terminology endurance limit, therefore, is reserved for the case of "infinite life," referring to a stress level at which the material will never fatigue. Since such experiments are never conducted, it is an engineering approximation to the fatigue limit and the two terms are commonly used interchangeably. Thus, the term endurance limit can be used for cases where the expected number of cycles in service does not exceed the number of cycles applied in laboratory testing.

1.4. HCF DESIGN REQUIREMENTS

High cycle fatigue was identified as a primary cause of a number of failures in USAF fighter engines in the 1990s. While the number of failures has been reduced since then, they have not been eliminated. Failure due to HCF is not unique to USAF engines but, rather, has been encountered in commercial engines in this country as well as abroad. The concern over HCF failures led the Air Force to convene a team of government and

industry experts to determine the root cause of these failures and to review the entire design process for HCF in order to identify potential weaknesses. At the same time, several independent review teams composed of experts from government and academia were evaluating causes of individual HCF failures.

The combined findings of these teams centered around many aspects of the design, field usage, and materials and their characterization. In particular, the use of the Goodman diagram* in the design process was evaluated extensively. Because of the number and type of failures, it was generally concluded that the design process is flawed, and that the usage of the Goodman diagram had to be modified or replaced by a more robust and damage tolerant design methodology.

These conclusions further strengthened the findings of separate studies by two Air Force Scientific Advisory Board (SAB) teams. In 1992, an SAB team evaluating failures in titanium components in turbine engines recommended that the Air Force should expand its ENSIP to extend the application of fracture mechanics to structural problems arising from HCF. Further, they recommended that the Air Force should initiate a substantial research program to increase the understanding of HCF in gas turbine engines because they felt that this was essential to decrease the frequency of such in-service failures. In 1995, another SAB team reviewing the design process and failures in propulsion systems found that although basic technology work cannot be expected to provide near-term solutions to current field problems, the critical questions that must be answered before HCF can be dealt with systematically have been identified. Most of these questions centered around the ability of a Goodman diagram to account for in-service damage and the ability to use damage tolerance in HCF design. Among other components of a program, this team strongly favored the development of prediction methods for the HCF of titanium parts in the belief that they must be included in any rational HCF program.

The Air Force, therefore, committed to developing a damage tolerant approach to design for HCF, although the definition of damage is broader than an inspectable crack, and the use of conventional fracture mechanics principles and approaches may not be the final approach adapted. The situation with HCF is analogous, in some ways, to the scenario in the 1960s when structural failures in USAF aircraft were occurring and in the 1970s when LCF failures were much too common in USAF turbine engine components to be acceptable. Both of these scenarios led to the development and adaptation of damage tolerant design procedures for airframe and engine components which are now required through the USAF Aircraft Structural Integrity Program (ASIP) specifications and the ENSIP specifications, respectively. In both cases, design is based on the assumption of the existence of defects, and a combination of the ability to calculate remaining life and to

* The Goodman diagram should correctly be called a Haigh diagram. This will be explained in the next chapter. For the present, this chapter will use (misuse) the "Goodman diagram" terminology.

inspect for defects. Whether or not such an approach is applicable to HCF because of the long initiation and short crack propagation lives under HCF remains to be determined but is highly doubtful (see Chapter 2). Nonetheless, an approach which is an improvement over the existing use of Goodman diagrams was needed. The applicability of a new approach for HCF design to other industries dealing with rotating machinery and vibratory problems for very long lives (large number of cycles) is apparent.

1.5. ROOT CAUSES OF HCF

At the start of the Air Force National Turbine Engine High Cycle Fatigue program around 1995, each of the major engine manufacturers in the United States was queried about what they felt had been the root causes of HCF. Their responses were based on both observed and suspected causes of specific field incidents as well as some general speculation about the closeness of operating conditions to the "edge of the cliff" as well as areas where data and information were quite limited. In addition, government engineers summarized these inputs and speculated on their own experience with HCF as a pervasive problem. The following is a summary of the root causes of HCF at that time, before the major HCF program was initiated. Many of the root causes led to research and developments in HCF that is discussed in subsequent chapters. While the findings below are specific to gas turbine engines, they appear to be generally applicable to any type of rotating machinery where vibratory and cyclic loading and response occur.

HCF–LCF interactions: There was great concern for the scenario where LCF could cause damage or fatigue cracking that, in turn, would alter the HCF capability of a material. If the sizes of such cracks were sufficiently small, then the applicability of long crack fracture mechanics and thresholds to a propagating LCF crack was questionable. Crack orientation and mixed mode loading, particularly for small cracks and in anisotropic materials such as single crystals, were also a concern. It was also not clear if LCF or HCF could be the primary cause of crack initiation or whether there was a synergistic effect between them. Debit in LCF life due to HCF was also a concern.

Fretting Fatigue: Fretting fatigue had been experienced in dovetail slots and was considered to be the cause of several HCF failure incidents. There was little understanding of contact mechanics or tribological effects in these contact regions, let alone any systematic design procedure beyond taking some empirical debit for fatigue strength in these regions. While fretting fatigue was recognized as an extremely important issue, it was also anticipated to be a very complicated issue. Solutions to this problem were acknowledged to require a good understanding of how LCF–HCF interaction and residual stresses affect HCF capability as well as an understanding of how the state of stress (normal, shear, combined, etc.) in the contact region affects HCF capability.

Foreign object damage (FOD): FOD was a common occurrence in fan and compressor blades. While bird ingestion was treated empirically through actual bird ingestion testing in engines, the effects of hard objects such as sand or stones was not treated in design much beyond the establishment of an empirical value of stress concentration factor, k_t, to account for the potential debit in fatigue strength. Empirical rules for blending out damage or removing components from service have been in use for a very long time, but the basis for these rules was not very scientific. It was recognized by the engine community that the effect of notches on fatigue strength was an important first step toward treating FOD, but that FOD was far beyond a simple notch problem because of residual stresses and material damage resulting from the FOD event.

Manufacturing/handling damage: Concern was expressed on how damage in the form of manufacturing defects such as machining marks, inclusions, pores, surface hardening, or hard alpha particles (in titanium) effect the HCF strength of materials and how these could be taken into account in the design phase. Handling damage as well as unfavorable residual stresses can aggravate the situation as well.

Reliability of threshold and fatigue limit properties: One of the greatest concerns in trying to establish a design methodology for HCF was the general lack of sufficient data with which to establish material capability including the reliability (scatter) of such data. In addition, data in the high mean stress regime were found to be severely lacking, partially because of the difficulty of conducting smooth bar tests in that region without introducing net-section plasticity or ratcheting. There was also a general feeling that fatigue limits up to 10^7 cycles, common in some databases, was not sufficient for HCF resulting from resonant vibrations that could produce far more than 10^7 cycles in service.

Overloads and spectrum loading: Recognition was given to the fact that engine usage is different than what is anticipated in the design phase and spectrum loading including surge levels are not well known. While this is not specifically a materials problem, accounting for such loads in material capability assessments is necessary.

No book on HCF, particularly from a USAF perspective, would be complete without a quote from or acknowledgement of Otha Davenport who was responsible for leading the USAF National Turbine Engine High Cycle Fatigue program. His work included formulation as well as implementation of the program. The results of that program are quoted throughout this book. In a short document, the genesis of the program and some summary statements about accomplishments as of 1994 are presented as a draft final report. That report appears as Appendix B and, although some of the material duplicates what appears elsewhere in this book, the document serves to summarize the events that led to one of the most challenging and exciting technology programs in history.

1.5.1. Field failures

HCF failures in USAF fighter engines are probably no more common today than they have been over many years. In the 1950s, creep in turbine components was a primary cause of failure, and the associated design stresses were relatively low, so LCF failure was not a concern. With the introduction of creep-resistant superalloys, operating stresses were increased and LCF soon became a major cause of failure. The introduction of retirement-for-cause as a life management philosophy, utilizing fracture mechanics, and the adaptation of a damage tolerant design requirement through ENSIP [5] have led to a significantly reduced incidence of LCF failures. The result has been that HCF is left as the last remaining major mode of failure. With the commonality of parts in engines on many different aircraft, combined with a draw down in the number of field assets, the existence of HCF failures becomes a problem of immediate and critical concern. It is certainly difficult to describe and document the exact scenario under which HCF failures have occurred in USAF assets because of the proprietary nature of the design and usage specifications and, in many instances, insufficient information to pinpoint root causes. While there is no single general theme that is common to all failures, some aspects share a degree of commonality. Additionally, failures have not been confined to one type of component, one class of material, one particular engine, or one specific manufacturer. The widespread nature of HCF failures is what has raised the question of the adequacy of the design process.

Consider the following instances of field failures due to HCF. In one case, a single crystal turbine blade failed below the platform in a contact area near a stress concentration, with the failure initiating slightly subsurface at very small pores which are characteristic of this class of materials. The crack propagated as a stage I crack along a crystallographic plane before changing to stage II and propagating along a plane normal to the loading direction. In addition to the very high vibratory amplitudes that are assumed to have occurred, an unusual aspect of this class of failures was the apparently small number of HCF cycles within any given mission. This indicates that the resonance, whatever the cause, is not a steady-state phenomenon but, rather, a transient phenomenon which occurs only under specific operating conditions and which does not persist very long. The hypothesis of this scenario was developed partly through fractographic examination of failed blades. What is of significance from a material's characterization point of view is that failure was not caused by an unusually large number of HCF cycles, but a smaller number of high frequency, low amplitude cycles. It is of importance to point out that little is known about the Mode II crack initiation and crack growth characteristics of single crystal alloys, particularly along crystallographic planes. Work at the time by John et al. [6] showed that growth rates are higher and thresholds are significantly lower in Mode II and mixed mode I and II compared to pure Mode I in certain crystallographic directions in a single crystal nickel-base superalloy at room temperature. Certainly, design methodology such as the Goodman diagram

does not consider all possible combinations of mode mixity and crystallographic plane orientation.

Another source of field failures attributed to HCF is related to FOD through the ingestion of debris into engines. Titanium fan and compressor blades with thin leading edges have been shown to be especially susceptible to FOD along the leading edge and, in some newer engines, along very thin trailing edges. This service-induced type of damage, combined with vibratory loading from forced response resonances, has led to HCF failures in several components and engines. The vibratory stresses, as in the previous example, were transient rather than steady state and occurred only during specific conditions in the flight and operational envelope. The design of such a component for HCF in the presence of FOD was based, in part, on the use of a Goodman diagram which had been modified to account for FOD through the use of an equivalent stress concentration factor (k_t) or through the use of a limiting level of vibratory stress. The various types and levels of FOD, which includes a surrounding region of residual stresses, is not handled well in a Goodman diagram combined with an equivalent k_t in terms of its total HCF life. In analysis of field failures, it is still not apparent whether the failures were due to extremely high stresses due to excessive vibrations, or that the FOD on the components severely degraded the HCF capability of the material. This is particularly true in several instances where the fracture surface indicated a fatigue initiation site that was in the form of a dent or ding, but of an unusually small size. Such incidents have been classified as involving "micro FOD" because of the extremely small size of the initiation site that is too small to measure or detect in the field. Other incidents, involving small FOD, have led to the use of techniques such as dental floss being rubbed along the leading edge to detect damage of the order of 0.5 mm or less in depth. These are not small enough to classify as micro FOD, but they are very difficult to detect. Various aspects of FOD and related analysis and design issues are discussed in Chapter 7.

In other instances, titanium fan and compressor blades, and the disk lugs which support them, have experienced HCF failures due, in part, to fretting which occurs in service under vibratory loading from a steady state or transient resonance or from a forced response. These types of failures, where the HCF resistance of the material is degraded significantly due to fretting, are not confined solely to the contact region. In some instances, failure occurs just outside the fretted region and may be due to the redistribution of stresses because of the uneven wear due to fretting. Here, again, the vibratory stresses causing failure are not necessarily steady-state stresses but, rather, the result of transient phenomena which occur only under certain engine operating conditions. The use of the Goodman diagram under conditions of fretting fatigue is based, traditionally, on knockdown factors to account for the reduction in HCF resistance and is based, almost exclusively, on empirical data. Developments in this area are contained in Chapter 6.

A most unusual failure scenario developed in the HCF of a rotating seal which experienced resonances causing bending stresses superimposed on high centrifugal stresses from

the very high engine speeds. In a series of these types of failures, there were no failed parts recovered from which to deduce the failure scenario in terms of number of cycles, HCF or LCF, or initial defects, the type of information which might be available from fractographic analysis. It was only on the chance discovery of cracks in an identical part during an overhaul inspection that the cause of these failures became more apparent. It now appears that during the initial break-in operation, some of these rotating seals experienced transient resonances which led to excessive rubbing, heating, and the development of very small cracks on the outer edge of the seal. When subjected to normal service, these slightly damaged seals were again subjected to vibratory loading through bending resonances and the cracks propagated. It appears from limited data that the amount of crack extension per flight was slight and that the resonances were transient rather than steady state in nature. Although the operating conditions, including the fatigue loading, were within the design envelope of the Goodman diagram, the damaged material had HCF resistance substantially below that determined from a Goodman diagram which is based on tests of undamaged material.

Another example of failures in engines involved what appeared to be LCF. Yet testing and analysis showed no defect in the material taken from the region around the cracked part, and LCF analysis showed stress levels that were nowhere near the level to produce failure in the number of cycles to which the engine was exposed. Assuming that a vibratory component had to be present, extensive testing and fractography led to the conclusion that some HCF vibratory stresses had to be present. Questions as to the HCF capability of the material at very high mean stresses, the effect of dwell times (hold at constant stress) on the fatigue behavior of titanium alloys, or the interaction of LCF and HCF still have not been adequately answered in order to adequately explain the failures.

While no one common thread connects all these failures with one another, a common feature of many of them is the presence or development of damage from sources such as fretting, FOD, LCF, and others. These types of damage are not all handled adequately with a Goodman diagram, or they are handled in a highly empirical fashion. Another point of commonality among many of the failures is that the number of HCF cycles is not extremely large, but rather that a limited number may occur within a given mission due to transient phenomena which occur for short durations. Thus, concern over a run-out stress equivalent to 10^8 or 10^9 cycles in an S–N plot may not be justified for some cases. Finally, two aspects of field failures seem to be common among the many cases involved. First, many of the failures involved new designs, materials, and operating conditions (steady stress, temperature, geometries), which are somewhat new and slightly outside of the envelope of operating experience. The second is that many of the failures appear to be occurring at high mean stresses associated with high engine speeds.

What operational experience shows, in summary, is that pure HCF is generally not the primary problem and that the use of a Goodman diagram, given appropriate data as well

as a knowledge of the vibratory loading, is a viable and reliable method for designing for pure HCF. The failures encountered also indicate that the problem is typically not one of long-life degradation or a high number of accumulated cycles, but rather one of shorter life including infant mortality and conditions which were not anticipated in design or detected in developmental engine testing. The problem appears to be the synergistic combination of HCF with other modes of initial or service-induced damage, something that is not addressed in a Goodman diagram. As noted earlier, the HCF problem in turbine engines provides an example of how HCF capability can be degraded by service usage which also has to be considered in a robust design process. Although the examples cited in this book come largely from experience with turbine engines, the problem and approaches are felt to be quite generic and applicable to other applications where HCF is a design consideration.

A final aspect of HCF design has to be related to the statistical distribution of fatigue strengths. There are a number of scenarios surrounding field failures where analysis indicates that failures should not have taken place under the assumed circumstances. On the one hand, the circumstances may not have been properly categorized and vibratory loading, for example, may have been greater than that determined from detailed analysis or actual component or engine testing. On the other hand, the fatigue strength could be shown to be adequate to prevent failure. Under both circumstances, there is little known about the tail end of the distribution function that describes either the applied loading or the material capability. In an attempt to shed some light on this subject, specifically in regard to material capability, some aspects of the statistics of fatigue limit strength are presented in Chapter 3.

1.6. DAMAGE TOLERANCE

Before discussing damage tolerance, the distinction between durability and damage tolerance should be established. From the original version of ENSIP [5], the following definitions are established. Section 3.1.3 defines damage tolerance as “the ability of the engine to resist failure due to the presence of flaws, cracks or other damage for a specified period of unrepaired usage.” Section 3.1.7 defines durability as “the ability of the engine to resist cracking (including vibration, corrosion and hydrogen induced cracking), corrosion, deterioration, thermal degradation, delamination, wear and the effects of foreign and domestic object damage for a specified period of time.” It is Noteworthy that damage tolerance is applied to critical structural components whose failure would cause major damage or total failure. Durability, on the other hand, eliminates the task of excessive and unscheduled maintenance involving part replacement or added inspections. The remainder of this section is concerned with the concept of damage tolerance and its potential application to HCF.

While damage tolerance as applied to LCF has a limited role in HCF, the concepts and philosophical aspects are important to grasp in understanding how HCF problems can be addressed. Damage tolerance is a design philosophy that was adapted by the US Air Force for both airframe structures in the 1970s and for turbine engines in the 1980s. It evolved from experience with field failures attributable to either initial or service-induced damage or flaws that were not accounted for initial design. It involves the assumption of the existence of initial defects (flaws) in critical structural components combined with inspection methods to assure flaws of a size larger than those assumed do not exist when the structure enters service. For a comprehensive discussion of all of the aspects of damage tolerance as well as the associated nondestructive evaluation techniques, the reader is referred to the book by Grandt [7]. It is the intent of this section only to provide an overview of some of the concepts involved in damage tolerant design and how they relate to problems in HCF.

The Air Force defines damage tolerance in engines in the latest version of ENSIP [4] in the same manner as in the original version [5] as cited above, namely "the ability of the engine to resist failure due to the presence of flaws, cracks, or other damage. . . ." Among the other guidance provided in ENSIP, the scope of the applicability of damage tolerance is established as:

> Damage tolerance requirements should not, in general, be applied to components in which structural cracking will result in a maintenance burden but not cause inability to sustain flight or complete the mission; i.e., durability-critical parts. However, damage tolerance requirements should be applied to durability-critical parts to: (1) identify components sensitive to manufacturing variables and pre-damage which could cause noneconomical maintenance (e.g., blades), or (2) aid in the establishment of economic repair time or other maintenance actions.

Damage tolerance is the only one method used in design to assure structural integrity. Other methods include safe-life design or fail-safe design (see [7], for example). One of the reasons that damage tolerance is not used universally for critical structural components is the maintenance burden and associated cost for the required inspections. Nonetheless, the requirement by the US Air Force provides details on how to achieve a damage tolerant design. In ENSIP [4] it states

> Damage tolerance will be achieved by proper material selection and control, control of stress levels, use of fracture-resistant design concepts, manufacturing and processing controls, and the use of reliable inspection methods. The design objective will be to qualify components as in-service noninspectable to eliminate the need for depot inspections prior to achievement of one design lifetime. As a minimum, components will be qualified as depot- or base-level inspectable structure for the minimum interval. Damage tolerance can be achieved by performing crack growth evaluation as an integral part of detail design of fracture-critical engine components. Initial flaws (sharp cracks) should be assumed in highly-stressed locations such as edges, fillets, holes, and blade slots. Imbedded defects

(sharp cracks) should also be assumed at large volume locations such as live rim and bore. Growth of these assumed initial flaws as a function of imposed stress cycles should be calculated. Total growth period from initial flaw size to component failure (i.e., the safety limit) is thus derived. Trade studies on: (1) inspection methods and assumed initial flaw size, (2) stress levels, (3) material choice, and (4) structural geometry can be made until the safety limit is sufficiently large such that the need for in-service inspection is eliminated or minimized. Damage tolerance design procedures which account for distribution of variables that affect growth of imbedded defects are permitted (e.g., probability of imbedded defects associated with the specific material and manufacturing processes). Specific requirements on initial flaw sizes, residual strength, critical stress intensities, inspection intervals, damage growth limits, and verification are contained elsewhere in this document. Damage tolerance requirements may be applied to durability-critical parts to: (1) identify components sensitive to manufacturing variables and pre-damage which could cause non-economical maintenance (e.g., blades), or (2) aid in the establishment of economic repair time or other maintenance actions.

The concepts embodied within a damage tolerant approach to structural integrity can be illustrated with the aid of several figures. In Figure 1.2, the traditional design approach to LCF is illustrated schematically and shows that fatigue life, being a statistical variable in life for a given stress level, has to be treated with enough of a factor of safety (or uncertainty) to account for a worst case scenario in terms of material capability. The shape of the *S–N* curves depicted in Figure 1.2 has no physical meaning and is used merely to illustrate the concept of having both an average and a design curve. Since these curves are different, the resultant design allowables can then severely underestimate the average behavior of the material. Because of the conservative nature of this design

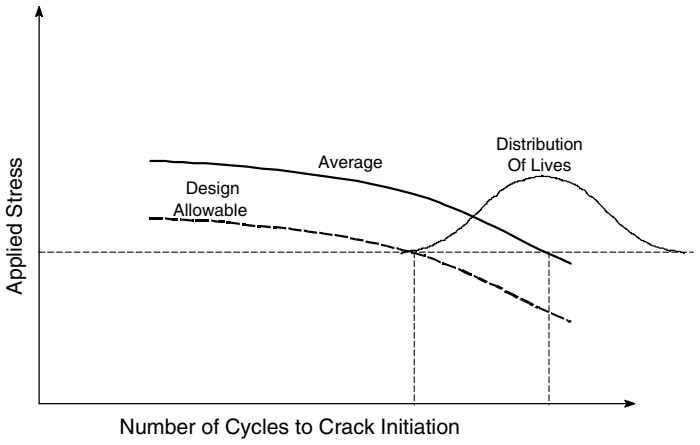


Figure 1.2. Schematic of *S–N* curve with illustration of scatter.

approach, the US Air Force implemented a program called "Retirement for Cause (RFC)" on some of their engines that had not been designed using damage tolerance procedures. RFC was actually an early application of damage tolerance to an existing design. The RFC approach allowed the Air Force to keep in service components that had reached their design life (see Figure 1.2) but had not developed any signs of fatigue cracking. Since only a small fraction of components would be expected to show signs of failure at the design lifetime because of the conservatism in the design, inspection procedures coupled with crack growth analyses based on fracture mechanics were implemented on the remaining components. The procedure is shown schematically in Figure 1.3, which incorporates the fundamental philosophy of damage tolerant design. If the inspection capability to reliably detect a flaw of a given size is available, then all inspected parts will have flaws no larger than those shown as "inspection capability" in the figure. The worst case, shown as curve "A," would then have the crack growth behavior shown and would fail after two inspection intervals if the interval was chosen as half of the predicted crack growth life as shown. The interval could be chosen as one-third to be more conservative. For the worst case, A, the crack would be found at the first inspection and the part removed from service. All remaining parts where no crack was found could be kept in service for another inspection interval and the new worst case component would follow curve "C" as shown. The procedure could be repeated for curve "D" as many times as practical. Note that as the life increases, the probability of a crack developing increases as the average life is approached (see Figure 1.2). Note also that an average part, denoted by curve "B," would be retired when a crack above the inspection limit was detected and that, in the example

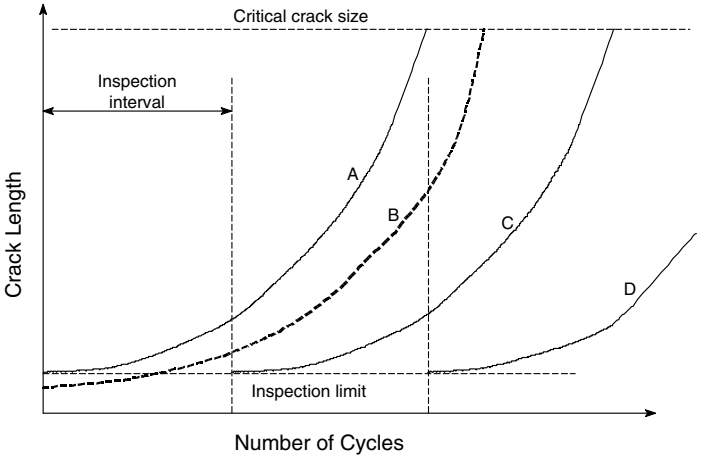


Figure 1.3. Schematic of crack growth in damage tolerant design.

cited, there would be two inspections available to find the crack if it was missed at the first inspection.*

The applicability of damage tolerance to HCF, discussed in Chapter 8, is severely limited because of the rapid growth of cracks under HCF where large numbers of cycles can be accumulated in a short period of time. This would require unacceptably short inspection periods, some of which could be shorter than a single mission. Another aspect of damage tolerance applied to HCF is illustrated in Figure 1.4 where, as an example, a single event such as FOD can cause a level of damage that is severe compared to an inspection level and can occur at any time. It is the possibility of such damage occurring and the concurrent rapid rate of crack growth under HCF that precludes the applicability of damage tolerance to HCF in many cases as discussed below.

1.6.1. Application to HCF

A damage tolerant design approach for HCF must take into account both potential initial (manufacturing) and service-induced damage in order to be successful. Further, the margin of safety must be determined for any operating condition in order to know how close to the "edge of the cliff" one is operating. The types of damage that must be addressed, if relevant, include fretting, galling, FOD, combined LCF–HCF, corrosion pitting, thermomechanical fatigue, creep, and their combinations. It is of interest to note the limited scope of requirements, especially details, for HCF that were contained within the original ENSIP [5], the document which governs the design and development of US

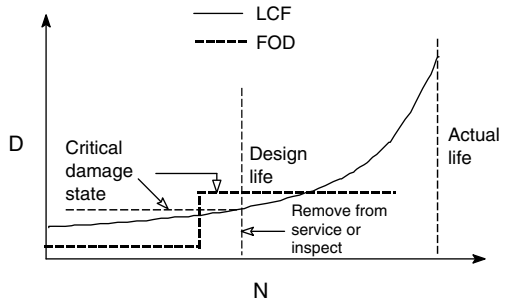


Figure 1.4. Schematic of damage accumulation applicable to HCF.

* Figures 1.2 and 1.3, and many variations thereof, were used numerous times as an illustration of how a damage tolerant approach could save costs in not having to replace engine components when they reached their design lifetimes. These schematic plots were created and used by Dr Walter Reimann of the Air Force Materials Laboratory many times to champion the Retirement for Cause (RFC) program that was eventually adopted by the US Air Force and produced cost savings approaching a billion dollars.

Air Force engines. The following sections are extracted from that original version of ENSIP and deal specifically with, or are applicable to, HCF:

Section 4.6.2 defines initial flaw size: "Initial flaws shall be assumed to exist as a result of material, manufacturing and processing operations. Assumed initial flaw sizes shall be based on the intrinsic material defect distribution, manufacturing process and the NDI methods to be used during manufacture of the component."

Section 4.7.4 addresses HCF design requirements: "Engine components shall be capable of withstanding combined steady and high cycle fatigue stresses, including vibratory stresses that occur at sustained power conditions, for the required design service life."

Section 5.7.4 requires: "The HCF life of engine components shall be evaluated by analysis and measurement of vibratory stresses during the engine tests. . . . "

Appendix Section 5.6b "Certain levels of vibratory stress, e.g., 10 ksi, should be assumed to exist on each fracture critical part to identify sensitive components."

Appendix Section 4.7.4 . . . "it is recommended that vibratory or high cycle stress be restricted to a value of 40% of that allowed by the minimum value material property allowable due to the sensitivity of high cycle stresses to damping variability, part to part resonance variation, unknown excitations, etc. An alternative design approach to achieve margin is to limit the steady stress such that a significant level of vibratory stress (e.g., 30 ksi peak-peak) will not exceed the minimum value material allowable."

It is important to recognize that ENSIP was written and implemented at a time when LCF failures were the major concern of the US Air Force. While ENSIP was establishing a damage tolerant approach to LCF, it was also recognized that HCF is another problem of great concern, but no approach as detailed as that developed for LCF was suggested for addressing HCF design at that time. It is of interest, therefore, to examine a more recent approach to HCF through the use of a Goodman diagram in the light of the requirements and intent specified in the ENSIP document.* The approach to HCF in a more recent version of ENSIP is documented in Appendix B.

It can be seen from the above requirements and specifications that HCF design does not address some of the aspects of field service–induced damage and does not present any methodology for doing so. The requirements, like a 40% allowable of

* Subsequent to the original ENSIP document in 1984 [5], several revisions have taken place. Many of these revisions deal with HCF and are the result of the Air Force National Turbine Engine High Cycle Fatigue program. Appendix C presents some of the sections that were revised or added to deal specifically with HCF issues.

the Goodman vibratory stress or an absolute limit on allowable alternating stress, are based on experience and may have little applicability to newer designs, materials, or operating conditions. In particular, one can note that the guidelines proposed in the original ENSIP become less conservative at higher mean stresses because the fractional approach is based on lower vibratory stress allowables at high mean stress (see Chapter 2) or an absolute vibratory level which eventually intersects the Goodman allowable if mean stress is allowed to increase. What is not specified or accounted for in design is any in-service damage including that caused by loading such as LCF. Most components that are subjected to HCF are not designed based on HCF considerations alone. In general, they are checked for tolerance to HCF, or an allowable vibratory stress level is specified. What governs the design, for example LCF, is addressed separately and then the HCF resistance is evaluated by itself. There does not appear to be any systematic approach to designing for the combination of HCF and another damage mechanism. If interactions occur, the synergism might cause failure even though failure is not predicted by any one mode individually. This is particularly true for combined LCF–HCF loading which is discussed below and in Chapter 4 in greater detail.

One of the key parameters which must be considered in damage tolerant design for HCF is mean stress. Mean stress, resulting primarily from the rotational speed of an engine in the form of centrifugal loading, has a very significant influence on the fatigue limit of a material. For example, Greenfield and Suhr [8] show data for a low alloy steel which has a tensile strength of 840 MPa and a yield strength of 700 MPa. For this material, which exhibits a true run-out stress, the increase in mean stress from zero up to 775 MPa reduces the fatigue strength by greater than a factor of four. They observe that, for design purposes, "a reduction in the level of mean stress may be regarded as almost as important as a reduction in the level of fatigue stress in reducing the risks of failure by fatigue." Similarly, in fracture mechanics, the threshold stress intensity, which is the value below which cracks will not propagate at a very low chosen value of growth rate (10^{-10} m/cycle in some standards), is a decreasing function of stress ratio or mean stress. Under combined LCF–HCF loading, for example, it has been shown that the threshold at which HCF influences the growth rate under LCF, denoted by ΔK_{onset}, is not a material constant, but rather it is a function of stress ratio, R [9]. In one specific example, the value of ΔK_{onset} was found to decrease by over a factor of two in Ti-6Al-4V when R increases from 0.1 to 0.7 whereas it remains nearly constant for $R > 0.7$ [9] (HCF crack growth thresholds are discussed in Chapter 8). From the preceding, it appears that a margin of safety which is either a fixed fraction of the allowable alternating or vibratory stress or a fixed value of vibratory stress, independent of mean stress, becomes smaller as mean stresses become higher. This is true whether a total life criterion, such as the Goodman diagram, or a damage tolerant approach based on an initial flaw size is being used. Given this observation, in an Air Force review of root causes of HCF failures,

it was not surprising to find that designers from the major engine companies identified components with high mean stresses to be the most likely candidates for potential HCF problems.

1.7. CURRENT STATUS

The Goodman diagram is still considered to be an acceptable design tool for HCF provided it is applied correctly. Two aspects which may not yet be handled adequately are the presence of initial damage and the accumulation of service-induced damage. Initial damage, such as rogue flaws or inclusions, for example, would have to be found in laboratory or component testing and taken into account in establishment of the minimum design allowables. An alternate approach would be to characterize initial damage in terms of an expected statistical distribution of defects, a process now employed for internal defects in LCF design. One could question how many organizations or laboratories use data from a specimen or component which was clearly defective as part of their database, even though the defect is discovered only after performing the test! It is this situation, where defects appear only occasionally, that has led the USAF to adapt the damage tolerant approach to engine structures because defects are not always found in baseline testing for LCF. Good statistics on the presence of defects from specimen testing would require an inordinate number of tests. Thus, the assumption of the presence of initial damage is a logical approach to avoid potential failure due to the occasional defect.[*] A similar approach based on damage tolerant concepts could also be warranted for HCF. The second aspect, service-induced damage, is not addressed in a Goodman diagram. Illustrative calculations for combined LCF–HCF clearly indicate that service life and safe design space under pure HCF is affected by the superimposed presence of LCF loading, and a potential methodology for considering this damage is presented in Chapter 4. It remains to be seen if a similar approach can be developed for constructing a damage tolerant Goodman diagram for other types of field-induced damage such as fretting, FOD, corrosion pitting, and others. Certainly this would appear to be a more rational approach than limiting allowable vibratory stresses to some percentage of the Goodman diagram or

[*] It should be noted that in LCF design, the assumption of initial flaws in a damage tolerant design did not add weight to components. In the latest version of ENSIP [4], referring to historical experience with engines designed using damage tolerance, it states: "These design configurations have shown that damage tolerance requirements can be met with small or modest increases in overall engine weight, will have little impact on engine performance, and will provide greatly-improved engine durability while weapon system life cycle cost is significantly reduced." In pure LCF design assuming no initial flaws, the use of design allowables based on extensive testing which provides data representing the lower bound on a distribution curve, similar lives are predicted. In other words, the lower bound on the LCF database reflects the existence of the same type of flaws that are assumed in damage tolerant design. It was cases where the occasional flaws or defects were not discovered in specimen testing that led to problems when such flaws appeared in component hardware.

some absolute magnitude. For both cases where the Goodman diagram does not handle design adequately, the requirement in the 1984 ENSIP document [5] defining initial flaw size should be noted again. Section 4.6.2 of that document states that initial flaw size can be based on inherent material defect distribution. This indicates that perhaps inspection for initial or in-service damage may not be necessary but, rather, calculations or statistical data on damage accumulation could be substituted in an HCF design life methodology.

In these summary observations, it should be noted that a Goodman diagram is a total life diagram even though most of the life under HCF is attributed to the initiation phase. Initiation, or nucleation, in fatigue is defined in various manners in the technical literature. One of the more common engineering definitions is the time (number of cycles) it takes for a crack to form and grow to a detectable or observable size. Dependent upon the inspection capability, this crack size can become large and initiation can then become a dominant portion of the entire fatigue life. The second part of total life is the crack propagation portion which can be determined using fracture mechanics principles (which are not addressed to any significant extent in this book). If crack initiation is defined as the formation of a crack-like defect at the microstructural level, then crack-propagation life can become a larger fraction of total life. This latter interpretation of crack initiation is more commonly referred to a crack nucleation. In this book, we lean more toward an engineering definition for initiation and find, in general, that very long-life fatigue tests have a minimal fraction of their lives associated with crack propagation. For this reason, the Goodman diagram is often used interchangeably as a total or infinite life criterion as well as an initiation criterion. The fraction of life that is initiation to a specific crack size, however, may differ with change in mean stress. Crack propagation life from the defined initiation crack size to failure would have to be subtracted from total life to come up with a true initiation diagram. The addition of fracture mechanics principles to the construction and use of Goodman diagrams, discussed in Chapter 8, would help separate the initiation and propagation stages in the plot and provide a better indication of the inherent damage tolerance of the material to HCF. This is shown clearly in the calculations for HCF loading only where there are regions where a crack will not grow if initiated (damage tolerant) and other regions where the crack will grow at stresses below those needed for initiation (damage intolerant). It is possible that a true initiation diagram combined with a superimposed fracture mechanics–based plot will give better insight into the stress states where such behavior can be expected. Analyses, such as that by Barenblatt [10] which deals with crack propagation within the grain and between grains in a material, can then be interpreted better from a design point of view when they demonstrate the potential for cracks to initiate but subsequently either slow down or arrest, a phenomenon commonly associated with small crack behavior [11, 12]. It is possible, for example, that the propensity for this phenomenon to occur may be constrained to certain combinations of mean and alternating stresses, based on the information contained in a combination of a Goodman diagram and fracture mechanics–based analysis.

From the analysis of the conditions under which initiation and propagation under HCF, LCF, or combined HCF/LCF can occur, it appears that a very important design consideration for any component is a realistic estimate of the number of LCF as well as HCF cycles to which it will be subjected in service. This could result in drastic changes in the allowable design space, for example, if the component is potentially subjected to some type of steady state or resonant vibratory loading as opposed to transient vibratory conditions which may only produce a limited number of HCF cycles per mission or per LCF cycle.

Any component designed for anything other than HCF alone will generally undergo some degree of damage from that design consideration (e.g., LCF, TMF, creep). Even though the condition on which design is based will not cause component failure during the design life, some degree of subcritical damage or degradation may occur and that, in turn, can result in less resistance to HCF. Thus, the Goodman diagram may not be a valid indicator of HCF resistance if these other damage modes exist. Further, the HCF resistance will decay with life and this decay should be taken into account by combining the effects of HCF with any other mechanism which is the basis for design. The use of a damage tolerant Goodman diagram, therefore, is recommended.

1.8. FIELD EXPERIENCE

In HCF, as in other modes of failure, field experience tends to improve our knowledge base. "Lessons learned" are often the basis of new approaches, and many of these are documented in guide specifications such as ENSIP. On the other hand, I have had experience in several investigations where closure cannot be reached on the root cause or exact scenario under which an HCF failure occurred. We still have much to learn about HCF material behavior and design.[*] I can recall many meetings where, as a group of technical experts, we went through a systematic analysis of the conditions leading to an HCF failure and can prove, through existing data, knowledge, and analysis, that a failure could not have occurred. Only the failed parts in our hands were able to convince us of our inability to completely describe the event accurately. Eventually, we arrive at an unlikely

[*] In a recent revision, dated 22 September 2004, to ENSIP [4], under **VERIFICATION LESSONS LEARNED (A.5.13.3.2),** the following appears: "The most significant lessons learned for this requirement is that, for almost every field failure experienced by the USAF over the last decade, the test data showed the failure should not have occurred. This experience conclusively demonstrates that a deterministic approach to verification of HCF capability cannot succeed. One statistical study by a major engine manufacturer estimated that a deterministic process (analysis and testing) could at best discover less than forty percent of the HCF failures that would occur over the life of the program." The document goes on to recommend that a new approach must recognize "the stochastic nature of the material strength, the component behavior and the operational usage." The statistical aspect of HCF design is discussed briefly in Chapter 8.

scenario to explain the events that occurred, however unlikely it might seem. Incidents such as these bring to mind the words of the famous detective Sherlock Holmes who said "when you have eliminated the impossible, whatever remains, however improbable, must be the truth" [13]. Hopefully, the information contained within this book will add to the understanding of many of the aspects of high cycle fatigue material behavior.

REFERENCES

1. Wöhler, A., "Über die FestigkeitsVersuche mit Eisen und Stahl" [On Strength Tests of Iron and Steel]. *Zeitschrift für Bauwesen*, **20**, 1870, pp. 73–106.
2. Schütz, W., "A History of Fatigue", *Engng Fract. Mech*., **54**, 1996, pp. 263–300.
3. Crouch, J.O., "Air Force Turbine Engine Reliability", presented at the NAS Committee of National Statistics Sponsored Reliability Workshop, Washington, DC, 9–10 June 2000.
4. Engine Structural Integrity Program (ENSIP), MIL-HDBK-1783B (USAF), 15 February 2002.
5. Engine Structural Integrity Program (ENSIP), MIL-STD-1783 (USAF), 30 November 1984.
6. John, R., Nicholas, T., Lackey, A.F., and Porter, W.J., "Mixed Mode Crack Growth in a Single Crystal Ni-Base Superalloy", *Fatigue 96, Vol. I*, G. Lütjering and H. Nowack, eds, Elsevier Science Ltd, Oxford, 1996, pp. 399–404.
7. Grandt, A.F., Jr., *Fundamentals of Structural Integrity*, John Wiley & Sons, Inc., Hoboken, NJ, 2004.
8. Greenfield, P., and Suhr, R.W., "The Factors Affecting the High Cycle Fatigue Strength of Low Pressure Turbine and Generator Rotors", *GEC Review*, 3, No. 3, 1987, pp. 171–179.
9. Hawkyard, M., Powell, B.E., Husey, I., and Grabowski, L., "Fatigue Crack Growth under Conjoint Action of Major and Minor Stress", *Fatigue Fract. Eng. Mater. Struct*., **19**, 1996, pp. 217–227.
10. Barenblatt, G.I., "On a Model of Small Fatigue Cracks", *Eng. Fract. Mech*., **28**, 1987, pp. 623–626.
11. Miller, K.J., "The Short Crack Problem", *Fatigue Engng Mater. Struct*., **5**, 1982, pp. 223–232.
12. Lankford, J., "The Influence of Microstructure on the Growth of Small Fatigue Cracks", *Fatigue Engng Mater. Struct*., **8**, 1985, pp. 161–175.
13. Sir Arthur Conan Doyle, *The Sign of Four*, 1890.

Chapter 2
Characterizing Fatigue Limits

2.1. CONSTANT LIFE DIAGRAMS

Unlike in LCF where life is a function of applied stress or strain, and stress ratio is a parameter, HCF tries to deal with infinite life, endurance limits, or FLSs. In the long-life regime, then, the issue is whether HCF failure will occur under a stress level that is exceeded, or infinite (or very long) life can be achieved if the stresses are below that level. If, in the ideal world, *S–N* curves had a horizontal asymptote at some reasonably achievable number of cycles, then the terminology infinite life, endurance limit, or FLS corresponding to some large number of cycles would all refer to the same information. In the early days of fatigue, it was generally felt that such an endurance limit existed and that the information on the stresses corresponding to this limit could and should be represented by some simple equation or plot. Material capability of this type is often called the run-out stress, but it is more correct to refer to it as the FLS corresponding to a given number of cycles, typically 10^7 or greater.

In the 1850s, Wöhler [1] introduced the fatigue limit at 10^6 cycles because that was considered the useful engineering life for many HCF applications such as steam engine components. Further, it would appear that it was also a practical limitation based on available test techniques. While 10^6 and 10^7 have been used widely as the fatigue limit for many years in many applications, recent data indicate that FLSs for some materials may continue to decrease at cycle counts up to and beyond 10^{10} cycles [2, 3]. Today, high speed rotating machinery can achieve service lives approaching and perhaps exceeding cycle counts of 10^9–10^{10}. Thus testing must include large numbers of cycles representative of potential service exposures. This, in turn, requires high frequency testing capability or extremely long testing times.

2.2. GIGACYCLE FATIGUE

In the field of "gigacycle fatigue," indicating lives of the order of 10^9 cycles or higher, data have been generated indicating that some materials do not have a fatigue limit within the range of cycles tested using ultrasonic test machines. For many materials, the behavior is as depicted in Figure 2.1 where a dual behavior is noted. For example, the observed fatigue behavior in the region between 10^7 and 10^9 cycles has shown that the *S–N* curve still has a slightly negative slope [4]. The duality of the *S–N* curves has been linked in many cases with fractographic observations that partition the behavior

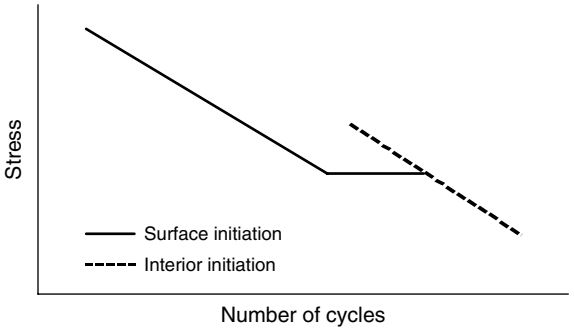


Figure 2.1. Schematic of observed behavior in gigacycle fatigue.

into failures that initiate at or near the surface, and failures that initiate subsurface. In the latter case, longer lives are observed as depicted in the figure. An example of such observed behavior is illustrated in Figure 2.2 for 2024 T3 aluminum [5]. In this case, two mechanisms are observed from fracture surfaces. Mode A denotes specimens that failed from broken inclusions in the material. These events occurred for tests that lasted less than 10^6 cycles. Mode B refers to longer life specimens where failure is believed to have been initiated by persistent slip bands. If all of the data are taken together, the scatter in life is extremely large, especially at stress levels corresponding to average lives around 10^6 cycles. However, if the data are segregated according to the two observed mechanisms, the scatter for each mode is much less and the duality of the S–N curve is more easily distinguished. The authors attribute the scatter in lives about 10^6 cycles to the competition between these two mechanisms of crack initiation. In this particular material,

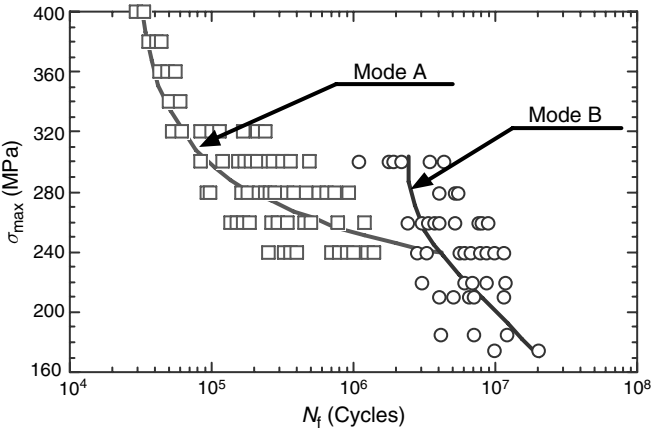


Figure 2.2. S–N curve for 2024/T3 aluminum alloy ($R = 0.1$) from [5].

the two mechanisms of crack initiation are not distinguished by being on or away from the surface.

Data on two materials from another source [6] illustrate the more common demarcation between surface and subsurface initiation as depicted schematically in Figure 2.1. In Figure 2.3, data on Ti-6Al-4V are shown that were obtained with an ultrasonic test apparatus operating at 20 kHz as well as with a conventional machine operating at 150 Hz. The two frequencies produced data that could not be distinguished from each other and are not separated in Figure 2.3. The first part of the curve up to 10^7 cycles appears to have a fatigue limit above 600 MPa below which infinite life could be expected to occur. It is only with the addition of the longer life data that the drop in the S–N curve is noted and a fatigue limit of approximately 340 MPa is observed corresponding to 10^{10} cycles. The sharp drop in fatigue strength between 10^7 and 10^{10} cycles is attributed to a change in failure mechanism whereby fatigue changes from surface to subsurface initiation as identified in the figure. The authors also point out the possibility that mean stress (these experiments were conducted at $R = 0$) plays an important role in the decrease in fatigue strength at very high fatigue lives.

Data from the same investigation [6] on a martensitic stainless steel produced results that have some similarities but some differences from that on titanium. The results, shown in Figure 2.4, show no indication of a drop in fatigue strength as longer lives are reached. This tends to validate the test procedure involving ultrasonic excitation of the specimen. On the other hand, the change from surface to subsurface initiation at very long lives is also observed in the stainless steel.

The concept of material behavior at the surface of a specimen compared to that at the subsurface is discussed in Chapter 5 in conjunction with shot peening. However, the behavior at the surface being different from that at the subsurface has been a common

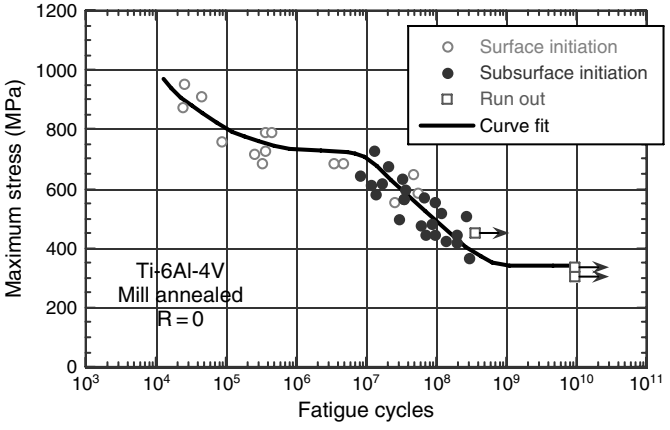


Figure 2.3. Fatigue data for Ti-6Al-4V from tests up to 20 kHz.

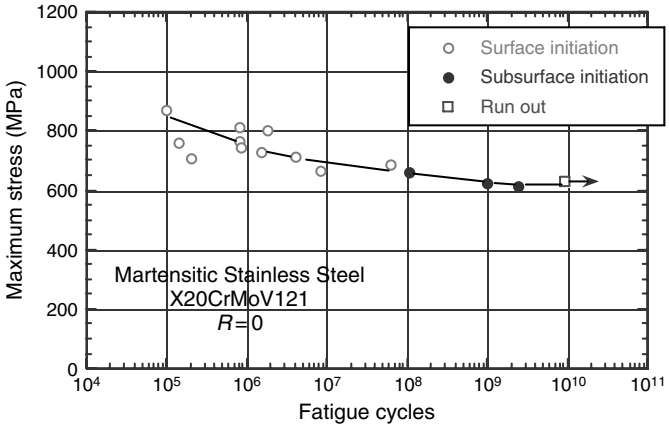


Figure 2.4. Fatigue data for tempered martensitic steel from tests up to 20 kHz.

observation in many works dealing with gigacycle fatigue where the duality of *S–N* curves has been observed in some cases, as noted in Figure 2.4. Shiozawa et al. [7] point out that the fracture mode is different in steels in the gigacycle regime and can be characterized, in general, as being either surface initiation or subsurface initiation. In the latter case, while they do not specifically distinguish the internal material being different than the material on the surface as was done by [8], they distinguish the mechanisms of crack initiation as being different. Internal initiations, characterized by the presence of defects which lead to what is termed a "fish-eye" pattern, are deemed to constitute a different fracture mechanism. The two different modes are deemed to have different *S–N* curves, each one having its own characteristic curve based on stress level and cycle count, dependent on the probability of the dominant mode being present. Figure 2.5, after [7], illustrates the concept of each mode having a different probability of occurrence at

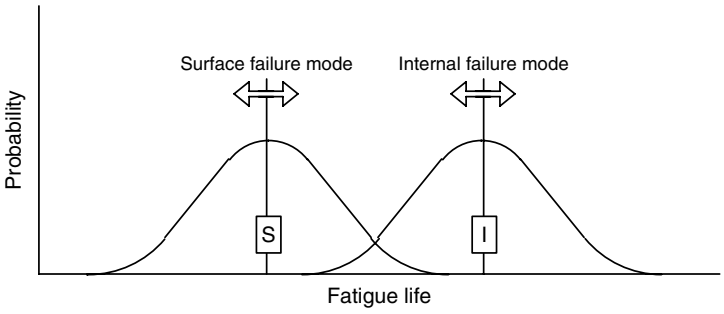


Figure 2.5. Schematic of probabilities for surface and internal failure modes [7].

different fatigue lives. From these concepts, the authors [7] propose that four different types of *S–N* behavior in steels can take place as illustrated conceptually in Figure 2.6. Each *S–N* curve corresponds to the relative position of the probability distributions of the internal and surface initiation modes illustrated in Figure 2.5. Type A is the common *S–N* curve governed by the surface fracture mode with the internal fracture mode occurring (speculatively) at very long or infinite lives as illustrated in Figure 2.4 for martensitic steel. Data on another material, forged titanium plate (Figure 2.7), also illustrate such behavior as shown by Morrissey and Nicholas for Ti-6Al-4V [9]. In this figure, the 20 kHz

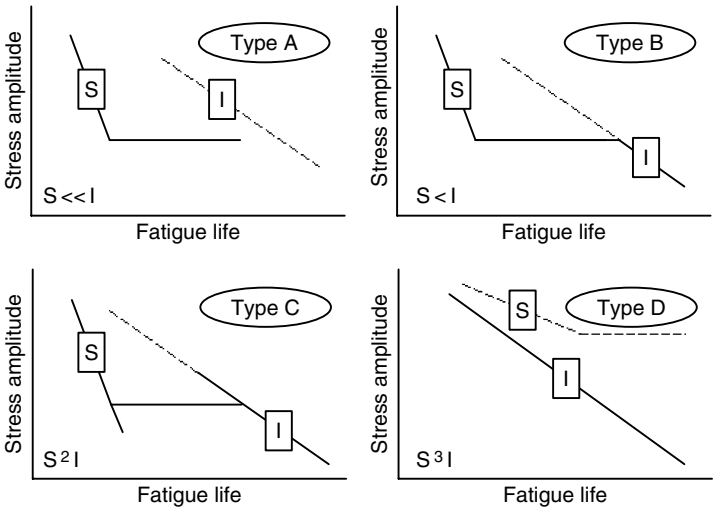


Figure 2.6. Classification of *S–N* curves using the concept of duplex *S–N* curves [7].

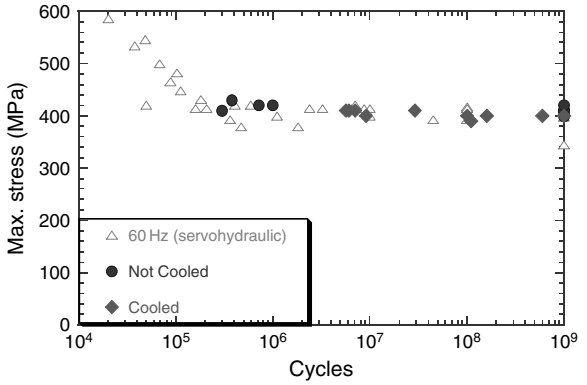


Figure 2.7. *S–N* fatigue data obtained at 20 kHz on Ti-6Al-4V forged plate [9].

data were obtained with and without cooling applied to the specimen. The temperature rise of under 100 °C and the data show that temperature effects had no effect on the fatigue behavior. The data obtained at 20 kHz are also compared with 60 Hz data obtained on a conventional test machine and again show no difference. In this figure, the data at both frequencies at cycle counts of exactly 10^7, 10^8, and 10^9 are all run-outs. Further, the staircase test results provide an FLS of 510 MPa at both 10^8 and 10^9 cycles, but these points are not shown in the figure.

In this case, long-life data points at 10^8 and 10^9 cycles, not shown, were obtained using statistical methods to establish the mean of the long-life fatigue strength at specified cycle counts (see Chapter 3 for a discussion of these methods). Type B is the well-known step-wise *S–N* curve for which the probability distributions for the surface and subsurface modes are separated. Type C is called a duplex *S–N* curve and occurs when the probability distributions of Figure 2.5 are close to each other. Type D is the *S–N* curve governed only by the internal fracture mode because the probability distribution for the internal mode is at a shorter lifetime than that for the surface mode. In these figures, the dashed lines represent the hypothetical curves that are never obtained experimentally because failure is dominated by another mode present at a lower cycle count for the given stress level. Whether the duality of the *S–N* curves is attributed to different mechanisms or internal versus surface behavior, the observations and proposed explanations available in the literature point to a conclusion that there are two different *S–N* curves. Further, the data in hand seem to indicate that there is no general relationship between the two curves. One of the main distinctions between internal versus surface initiation, particularly in the long-life HCF regime where initiation constitutes a major portion of life, is the often overlooked role of environment. While surface initiation occurs in the laboratory or operational test environment, subsurface initiation is representative of vacuum or an inert environment that can have a major role in extending the fatigue life compared to behavior in air.

Gigacycle fatigue, often conducted using ultrasonic test machines, has also been performed rather extensively on rotating bending apparatus operating at nominal frequencies under 60 Hz, thereby taking much longer times to reach the very high cycle regime. Compared to axial resonance testing where uniform stresses are achieved, under rotating bending the maximum stress occurs at the surface. For subsurface initiations, the stress is lower than at the surface but can be corrected for the actual stress at the location of the fatigue origin. This is not always done in the literature. Nonetheless, comparison of short- and long-life behavior and mechanisms can be performed using this technique. *S–N* curves from rotating bending tests, demonstrating the dual mechanism behavior of surface versus subsurface initiation, are shown in Figures 2.8 and 2.9 for two high-strength steels [10]. SUJ2 is a high-carbon-chromium-bearing steel while SNCM439 is a nickel chrome molybdenum steel. The data shown are for specimens that were ground during the machining process and contained surface residual stresses. The lines are those of the authors whereas the actual data may or may not really demonstrate a plateau in

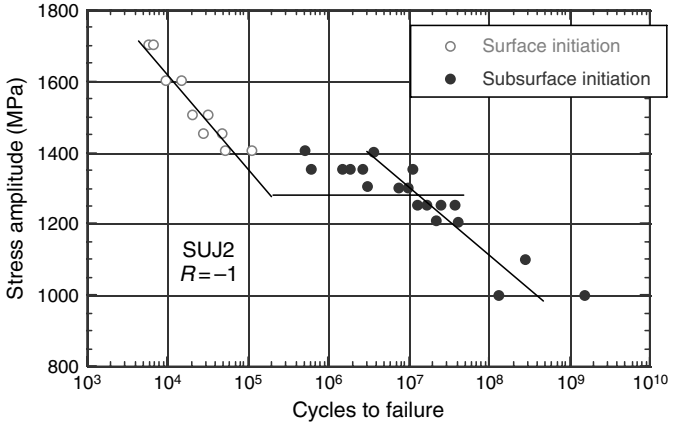


Figure 2.8. Fatigue behavior of SUJ2 steel under rotating bending.

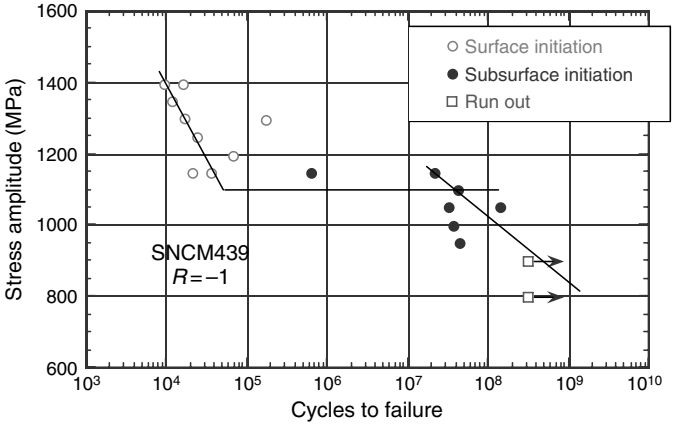


Figure 2.9. Fatigue behavior of SNCM439 steel under rotating bending.

the 10^6–10^7 life regime after which the curve drops. A single continuous curve without a plateau could easily be drawn to fit the data. However, the data show the dual behavior where surface initiation occurs at shorter lives whereas subsurface initiation from an inclusion occurs for longer lives in both materials. This seems to contradict the notion that a mean stress contributes to the observed decrease in fatigue strength, certainly not for all materials. Further, the behavior under bending fatigue is similar to that observed under axial loading though the values for fatigue strength are generally different. Based on these observations, when presenting data in the form of *S*–*N* curves into the gigacycle regime, it is important to note the conditions under which the tests were conducted including the

maximum number of cycles attempted (definition of run out). Additionally, for failed specimens, information about the mechanism such as surface versus subsurface initiation should be provided.

The general subject of gigacycle fatigue has been addressed in the Euromech Colloquium 382, held in Paris in June 1998, the papers of which were published in a special issue of a journal [11]. A second conference was held in Vienna in July 2001. Papers from the International Conference on Fatigue in the Very High Cycle Regime were published in another special issue [12]. A third conference was in Japan in September 2004. A summary of a large amount of experimental data on gigacycle fatigue as well as a description of the test apparatus used in such studies can be found in the book by Bathias and Paris [13]. To date, there have been numerous attempts made to understand the very long-life of materials and the apparent lack of a fatigue limit using ultrasonic test machines [5]. They show that in higher strength materials such as spring steel and martensitic stainless steel there is no fatigue limit up to 10^9 cycles whereas in carbon steel and cast iron a fatigue limit may exist somewhere beyond 10^8 cycles. While the lack of a fatigue limit is seen in many of the reported tests in the literature, materials such as cast 319 aluminum show a definite fatigue limit beyond 10^8 to 10^9 cycles [14]. The data of Morrissey and Nicholas [9] shown earlier in Figure 2.7 for a forged titanium alloy also show evidence of a definite fatigue limit beyond 10^9 cycles.

Ultrasonic test devices are not yet common laboratory equipment and require skill and experience for their proper use. There are not a large number in existence, so the generation of data in the long-life regime is still fairly limited. As an engineering compromise, cycle counts of the order of 10^7 using conventional testing machines operating at their maximum frequencies are often used as the definition of run-out or an endurance limit. The gigacycle fatigue community certainly takes issue with such a low number based on data that continue to be generated on many structural materials in the longer-life regime.

2.3. CHARACTERIZING FATIGUE CYCLES

Before the twentieth century was very old, there were already several methods for representing endurance limit data. Under constant stress-controlled conditions, there are five variables that can be used to characterize the fatigue cycle that is shown schematically in Figure 2.10, only two of which are independent parameters:

σ_{max}, the maximum stress,
σ_{min}, the minimum stress,
$\sigma_{mean} = (\sigma_{max} + \sigma_{min})/2$, the average or mean stress,
$\sigma_{alt} = (\sigma_{max} - \sigma_{min})/2$, the alternating stress or half of the stress range, and
$R = \sigma_{min}/\sigma_{max}$, the stress ratio.

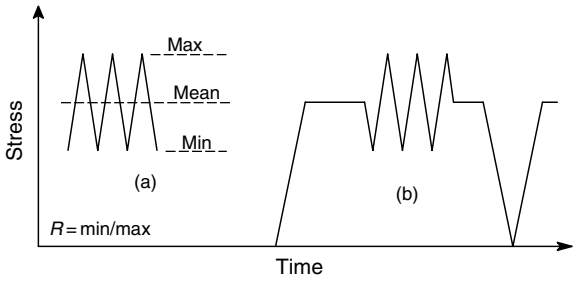


Figure 2.10. Schematic of (a) portion of a fatigue cycle included within (b) portion of a more complicated combined LCF–HCF cycle.

The stress range is defined as the difference between $\sigma_{\max}$ and $\sigma_{\min}$. An alternate nomenclature, used at times in industry, is the amplitude ratio defined as

$$\mathrm{A} = \frac{\sigma_{\mathrm{alt}}}{\sigma_{\mathrm{mean}}} = \frac{1-\mathrm{R}}{1+R}$$

It is somewhat disappointing that, to this day, no general agreement has been reached in the technical community regarding which pair of parameters should be used to characterize a fatigue cycle. The reason for this is that each parameter has some physical or mathematical significance, or is convenient to the user. For example, stress ratio, R, may have no real physical significance, but many tests are conducted where R is the parameter that is varied from one test to another and appears in the resultant database as the constant under which the test was conducted. It was probably this type of thinking and the number of available parameters that led the pioneers of HCF research to adopt many different methods for representing endurance limit data. The diagrams on which the data are represented can be classified as constant life diagrams, even though the intent may have been for them to represent endurance limits. For practical purposes, tests were often carried out to some reasonably long life, depending on the machines available, the required number of tests or parameters to be varied, or the patience or available resources of the investigator.

2.4. FATIGUE LIMIT STRESSES

The terminology "fatigue limit stress" or "strength" refers to the stress at a constant (long) life that is normally used in place of the endurance limit (infinite life) in a constant life diagram. Methods, particularly accelerated methods, for obtaining such stress values are commonly obtained from S–N plots either by having data at the desired life or

extrapolating data to the required life, often 10^7 cycles. A schematic diagram of *S–N* data, obtained at different values of $R =$ constant, is presented as Figure 2.11. Here, points A, B, and C represent the FLS either directly from the data or by extrapolation to 10^7 cycles in this case. In Figure 2.11, the stress is plotted as the maximum stress although the stress range or alternating stress could also be used. Each of the data points can then be used in a constant life plot such as a Haigh diagram as depicted in Figure 2.12. For each data point, the mean stress and alternating stress have to be computed for the given value of *R*.

The Haigh diagram, Figure 2.12, represents the locus of points having a specified number of cycles to failure, for example 10^7 as illustrated in the example. The number of cycles is typically taken to be those corresponding to a "run-out" condition, perhaps 10^8 or even 10^9, but there are few data available to demonstrate that a true run-out condition ever exists for a material. Rather, the cycles chosen can be either in a region where the *S–N* curves of Figure 2.11 become nearly flat with increasing number of cycles, or where the number exceeds the number of cycles that might be encountered in service. In some

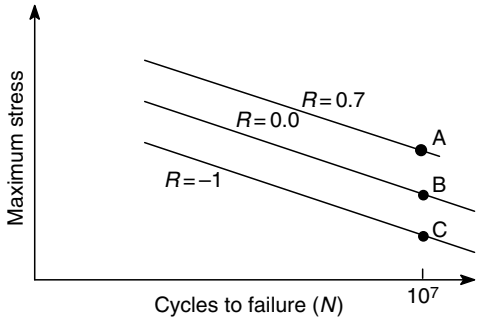


Figure 2.11. Schematic of *S–N* curves obtained at constant values of *R*.

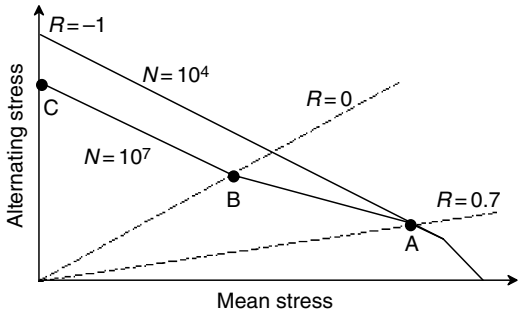


Figure 2.12. Schematic of Haigh diagram constructed from *S–N* data obtained at constant values of *R* and extrapolated to 10^7 cycles.

cases, neither condition may be satisfied. The points A, B, and C from Figure 2.11 are shown in the Haigh diagram, Figure 2.12, corresponding to stress ratios, R, of 0.7, 0.0, and -1, respectively. In this plot, alternating stress (half of the stress range) is plotted against mean stress. Lines corresponding to these stress ratios are also shown, with the vertical axis being the $R = -1$ line for fully reversed cycling. Although the Haigh diagram is often presented or used with a straight line to represent data over a wide range of mean stresses, there is no physical mechanism which requires the diagram to be linear over any region. The straight line is often associated with the terminology "Goodman diagram," as discussed later in this chapter. The diagram is a locus of points obtained from a series of experiments conducted under a range of values of R, and cases exist where it is highly nonlinear. The Haigh diagram,* a constant life diagram, could also represent the locus of points at a lower life as depicted in Figure 2.12 for an arbitrary life of 10^4 cycles. This usage, however, is not very common for establishing LCF limits.

The term "mean stress" is used in a Haigh diagram, although "average stress" or "steady stress" is also commonly used. The steady stress is the stress level upon which the vibratory stresses are superimposed, but the Haigh diagram represents only constant amplitude loading, and does not represent a condition where variable amplitude or LCF loading is superimposed. Further, the conventional Haigh diagram is valid only for the frequency at which the data were obtained, which is typically less than that for which it is applied in design. It is also not valid to use the Haigh diagram for random vibratory loading without the existence of a validated cumulative damage model for HCF.

Although the majority of S–N data and curves are obtained under conditions at constant values of R, some experiments, particularly on rotating components, are conducted under conditions of constant mean stress. The difference between constant R and constant mean stress is illustrated schematically in Figure 2.13. Recall that R is the ratio of minimum to maximum stress. For constant mean stress cycles, each one will have a different value of R. Conversely, cycles at constant R will have different mean stresses for different values of stress range or maximum stress. Consider a material whose S–N behavior is described by an equation of the form

$$\log N = \beta_0 + \beta_1 \log(S - \beta_2) \tag{2.1}$$

where β_0 and β_1 are fitting parameters, assumed for illustrative purposes, to be independent of R. Note that this is a deterministic model and β_2 represents the endurance limit.

* The constant life or fatigue limit diagram that we refer to as the Haigh diagram, often incorrectly called the Goodman diagram, has been referred to in early literature as an R–M diagram [15] or, alternately, as a R/M diagram [16]. There, R refers to the range of stress (twice the alternating stress) while M refers to the mean stress. The obvious confusion with stress ratio, R, probably led to other nomenclatures such as the (incorrect) Goodman diagram, Haigh diagram, or alternating versus mean stress diagram.

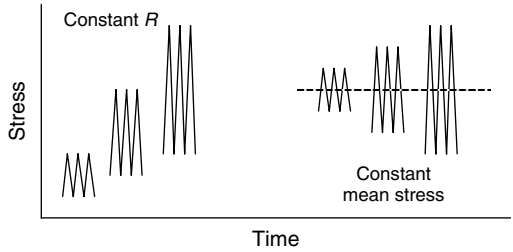


Figure 2.13. Schematic illustrating constant R and constant mean stress cycles.

To be consistent with fatigue thresholds typically being linearly decreasing functions of R, we arbitrarily choose the following relationship to represent the endurance limit:

$$\beta_2 = 150 - 100R \tag{2.2}$$

In this numerical simulation, S is taken as the stress amplitude in arbitrary units. Using constants $\beta_0 = 10$ and $\beta_1 = -2$, S–N curves are constructed as shown in Figure 2.14.

If the same equation is used to construct S–N curves at constant values of mean stress, the resulting curves are as shown in Figure 2.15. The numerical values were taken only for values of R between 0 and 1. Thus the range of mean stresses where a complete S–N curve over the range of log N between 5 and 10 for this numerical exercise, is somewhat limited. For this particular illustration, the constant mean stress curves have the same general shape as the constant R curves but seem to be bunched together more. However, this aspect of presenting the curves is highly dependent on the shape of the S–N curves for the particular material.

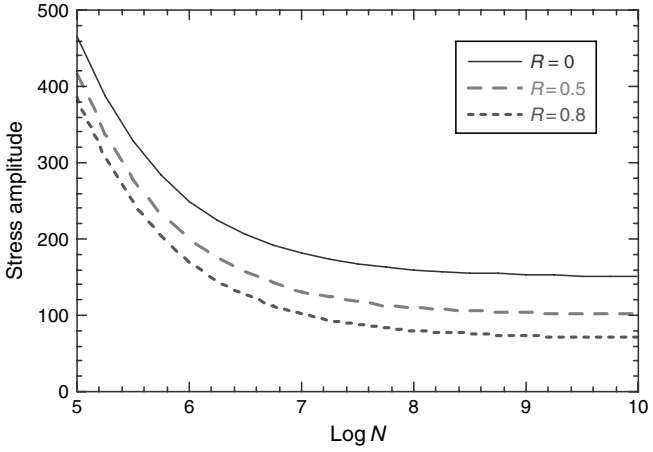


Figure 2.14. S–N curves for a hypothetical material at constant R.

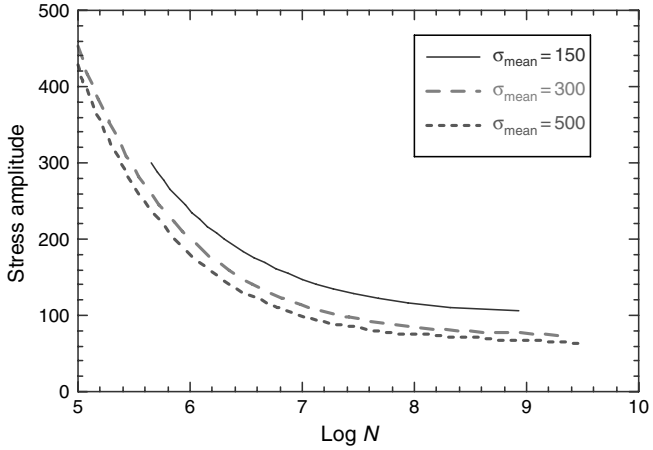


Figure 2.15. *S–N* curves at constant values of mean stress.

An example of data obtained at several values of mean stress is presented in Figure 2.16 for a SKH51 tool steel [17]. While extrapolation and interpolation of data sets are often necessary, the data in Figure 2.16 illustrate that single parameters with which to consolidate data sets are not always viable because the individual groupings of data, at constant mean stress in this case, do not follow well-behaved trends. In this case, the slopes on the *S–N* curves do not change continuously with increase or decrease in mean stress. Further, the cycles to failure where the curves become horizontal, indicating a fatigue limit, also do not follow a consistent trend. Converting this data set to one where stress ratios, *R*, are constant, is not very practical if formulae exist for interpolating or extrapolating constant *R* data. This subject is discussed further in Chapter 8.

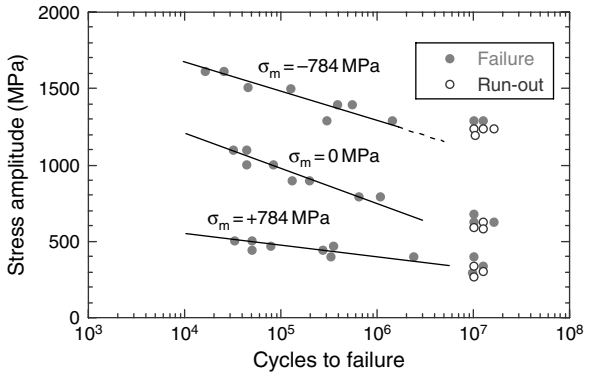


Figure 2.16. *S–N* data on SKH51 tool steel obtained at constant mean stresses [17].

While most of the data in many cases are obtained at $R = -1$, representing fully reversed loading with no mean stress, the application of the Haigh diagram to HCF often involves conditions at high values of R such as 0.7–0.9. These conditions represent high mean stresses with small, superimposed vibratory stresses. There are often very few data available in this region, and the extrapolation of data from low values of R and the assumption that statistical distributions of data are the same at high R as they are at low R are questionable.

Material quality is another parameter which has to be considered when using the Haigh diagram in the design process. If the data are obtained in the laboratory on smooth specimens, heat treatment, processing, microstructure, surface finish, and specimen size must all be considered when applying the data to structural components. Perhaps, the single most critical issue in the use of a Haigh diagram is the degree of initial or service-induced damage which the material in the component may contain when such damage is not present in the material used for the database. If, for example, microcracks or other damage develops in service, then the High diagram has no meaning for this material because it represents "good" or undamaged material. A design methodology which considers the development of damage from any other source than the constant amplitude HCF loading must be used to account for the different state of the material. For example, if cracks develop due to LCF, then the tolerance of the material might be evaluated using fracture mechanics and the concept of threshold stress intensity factor. The Haigh diagram has no validity under this situation. It is these type of issues that are addressed in the remainder of this book.

One method of developing a Haigh diagram which represents material in a component is to develop the data on actual hardware. In this case, a combination of LCF and HCF loading, or general spectrum loading, could be used to obtain a single point on the diagram. Connecting this point to any other point on a Haigh plot has no physical basis and no meaning, and most probably will be misleading. Unless the data are obtained under purely HCF loading, with no other contributing damage mechanisms, the Haigh diagram has no basis for use in design and the data would be better used in tabular fashion for specific design conditions. It is relevant to note that trying to mix LCF and HCF data on a single diagram is dangerous because the physical processes are different. LCF usually involves high amplitude, low frequency loading, which leads to crack initiation early in life and a considerable fraction of life under crack propagation. It is this aspect that has allowed for the successful application of damage tolerance using fracture mechanics in design. HCF, on the other hand, generally involves low amplitude, high frequency loading, with a considerable portion of life spent in crack initiation. Interaction of the two types of loading, therefore, can involve a process of crack initiation and growth under LCF, and subsequent propagation under HCF. The Haigh diagram only represents the HCF initiation portion in the absence of initial cracks and, therefore, has no meaning under combined LCF–HCF loading. This topic is discussed in detail later in Chapter 4.

2.5. EQUATIONS FOR CONSTANT LIFE DIAGRAMS

To illustrate the different methods of representing data graphically, we consider several models or equations that have been used traditionally for constant life diagrams [18]. The first and probably most popular is the Goodman line or equation, more commonly referred to as the straight line in the modified Goodman diagram. It was actually proposed by Haigh [19] in 1917 as a method for representing constant life, so the diagram that plots alternating stress as a function of mean stress is not really a Goodman diagram but a Haigh diagram and is thus referred to as such throughout this book. While some of the equations to be discussed later are used to represent FLS data in Haigh diagram plots, many have generally been established from empirical fits to data and have no scientific basis. However, some of the earliest works tried to establish physical principals for fatigue [18]. Goodman [20] proposed use of the "dynamic theory," which is explained in detail by Fidler [21], where it is assumed that vibratory loads produce the same effect on a material as a suddenly applied load. Thus, vibratory loads are considered to instantaneously produce stresses that are double those as if they were applied slowly. The consequence of this is that the sum of the mean load and twice the alternating load should not exceed the static ultimate strength of a material in order to have infinite fatigue life. This results in a straight line on a Haigh diagram when the allowable alternating stress is taken equal to half the ultimate stress (see Figure 2.17). Of interest is that Goodman proposed such an equation as one that is "very easy of application and is, moreover, simple to remember" [20]. He also noted that "whether the assumptions of the theory are justifiable or not is quite an open question." While the dynamic theory was simple, it was observed that experimental data on all materials did not agree with the theory. To better

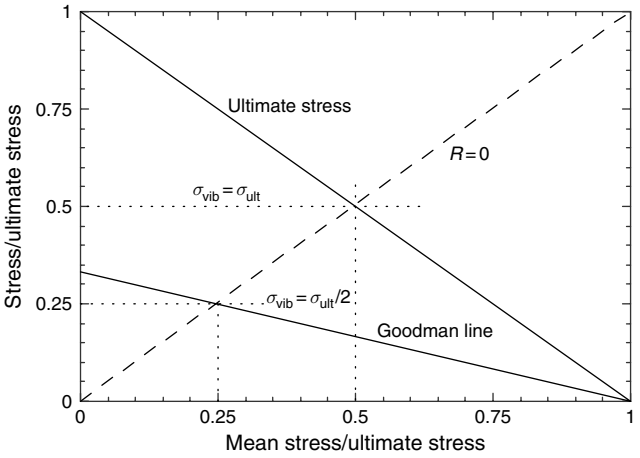


Figure 2.17. Schematic of Goodman diagram showing allowable vibratory stress.

address true material behavior, the fully reversed alternating stress was adopted as an empirical constant rather than half of the ultimate strength. What was originally termed the "modified Goodman diagram" involved using straight line fit on a Haigh diagram based on the experimentally determined fully reversed loading data point(s). The so-called Goodman equation (or Modified Goodman equation) represented in the following plots is of the form

$$\sigma_a = \sigma_{-1}\left(1 - \frac{\sigma_m}{\sigma_u}\right) \tag{2.3}$$

where subscripts a, m, and u refer to the alternating, mean, and ultimate stresses, respectively, and σ_{-1} represents the experimental value of the alternating stress under fully reversed cyclic loading ($R = -1$). An alternate form of the Goodman equation is a straight line that intersects the mean stress axis at the yield stress, σ_y, as opposed to the ultimate stress. Such a representation of a fatigue limit constant life diagram was suggested by Soderberg [22] and the equation is named after him in the literature.

$$\sigma_a = \sigma_{-1}\left(1 - \frac{\sigma_m}{\sigma_y}\right) \tag{2.4}$$

To possibly better represent experimental data, a parabolic equation attributed to Gerber [23] has been used which is of the form

$$\sigma_a = \sigma_{-1}\left[1 - \left(\frac{\sigma_m}{\sigma_u}\right)^2\right] \tag{2.5}$$

Summarizing available fatigue limit data on a Haigh diagram, Forrest [15] observed from a large body of data on ductile metals that 90% lie above the Goodman line and two-thirds between the Goodman line and the Gerber parabola. He concluded that "although not 100% safe, the Goodman line can therefore be recommended as a useful working rule in design, when the fluctuating stress fatigue data are not available." He cautioned, however, that these conclusions do not necessarily apply to parts containing stress raisers.

There are a number of other representations of constant life data points [18], but one more that achieved some popularity in the 1870s is known as the Launhardt–Weyrauch (L–W) formula, developed by Launhardt [24] for positive values of R and extended by Weyrauch [25] for negative values of R. Using σ_u as the ultimate stress, the equations are

$$\sigma_{max} = \sigma_0 + (\sigma_u - \sigma_0)R \quad R > 0 \tag{2.6}$$

$$\sigma_{max} = \sigma_0 + (\sigma_0 - \sigma_{-1})R \quad R < 0 \tag{2.7}$$

where subscript max refers to the maximum stress and σ_0 and σ_{-1} refer to the maximum stress at $R = 0$ and $R = -1$, respectively. For the three formulas, the Modified Goodman

equation, the Gerber equation, and the L–W formulas, experimental data of Wöhler on Krupp steel were used to establish a best-fit curve.

The first method of representing data is the diagram where maximum stress is plotted against minimum stress, as shown in Figure 2.18. It can be seen that the Launhardt–Weyrauch (L–W) formula and the Gerber parabola are almost identical in their representation of the data (not shown). The straight line attributed to Goodman does a lesser job of fitting data. The line representing minimum stress was often drawn to indicate the lower stress boundary for admissible stress. The distance between the minimum and maximum curves is then the allowable vibratory stress. In this and subsequent plots, the curves are shown in terms of normalized stresses with respect to the ultimate stress. It was Goodman [20] who stated that fatigue behavior should depend on the ultimate stress, not the elastic limit.

Another way of representing constant life data is a plot of maximum and minimum stress against stress ratio, as shown in Figure 2.19. Note that the Gerber and L–W equations look almost identical again while the Goodman line is somewhat different. In this particular plot, the linearity of the Goodman line disappears because of the particular axes being used. This may be one reason why this type of plot has never retained any popularity in the fatigue community.

A third type of plot, where maximum and minimum stresses are plotted against mean stress, is shown in Figure 2.20. This plot probably contains the most information of use to a designer of rotating machinery because mean stresses are not only well determined from calculations based on centrifugal loads, but can also be well controlled in usage. Alternating stresses that result from the vibration characteristics of the machinery are much less controllable and not as well known in most cases. At high mean stresses (high

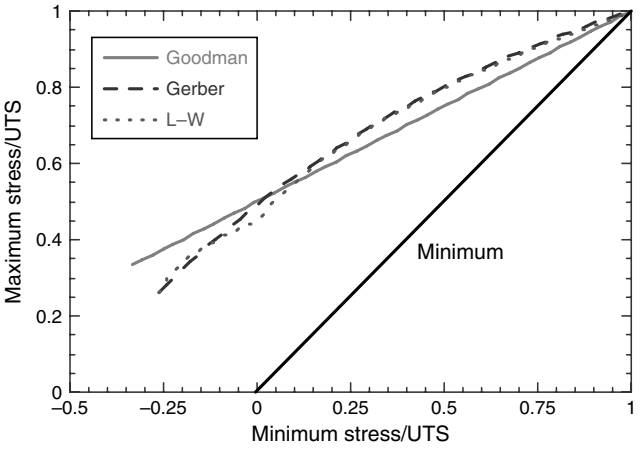


Figure 2.18. Maximum and minimum stress as a function of minimum stress.

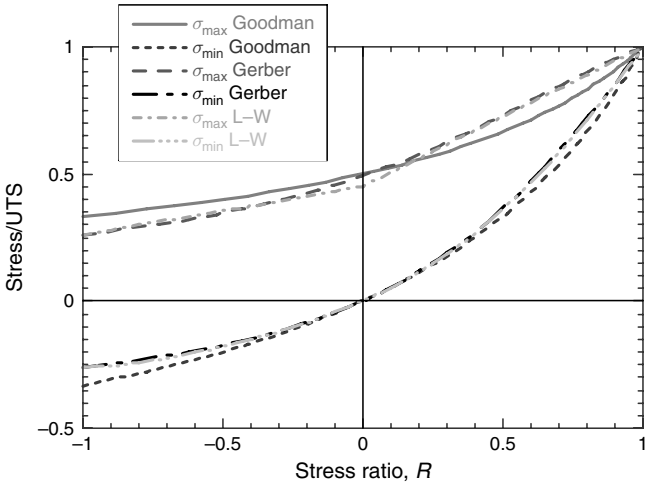


Figure 2.19. Maximum and minimum stress as a function of stress ratio, R.

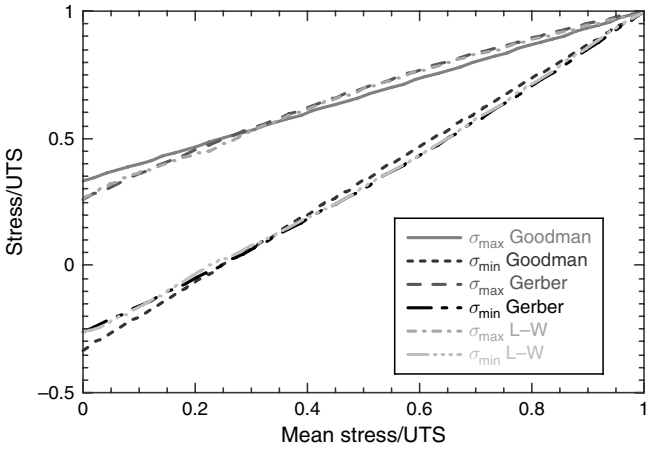


Figure 2.20. Maximum and minimum stress as a function of mean stress.

values of R), the maximum stress can become the governing stress for design because it can approach the yield or ultimate strength of the material. The difference between the two curves is the stress range, or twice the alternating stress. In this as in the previous plots, the Gerber and L–W equations look nearly identical while the Goodman line, which is now straight, differs a little from the other two equations.

The final method of plotting data is a plot of alternating stress against mean stress, commonly but incorrectly referred to as the Goodman diagram, Figure 2.21. What should

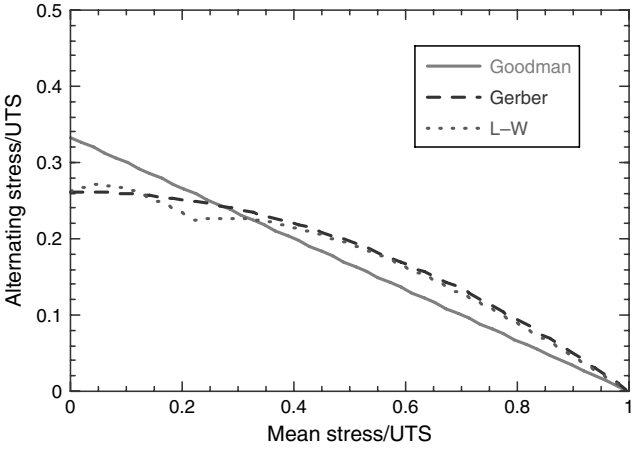


Figure 2.21. Alternating stress as a function of mean stress.

be properly called a Haigh diagram has evolved into the most commonly used method of plotting FLS or endurance limit stress data, but the use of a straight line fit to the data still seems to be popular.

The diagram most closely related to these methods of representing fatigue limit or constant life data is the actual Goodman diagram shown in Figure 2.22, taken directly from Goodman's book [20]. The two curves shown in the figure are labeled maximum and minimum stress. They are apparently plotted against minimum stress, as shown in Figure 2.18, although there is no label on that plot or on the y axis. Regions of tension and compression are shown above and below a zero stress line. Of greatest significance in this plot, closest to what may be called a true Goodman diagram, is that the lines used to represent the fatigue limit are straight lines on this particular plot. This is consistent with the straight line formulation of Goodman shown in Figure 2.18 by comparison.

The L–W equations, shown in previous plots, can also be examined on a Haigh diagram. For positive values of R, Equation (2.6) the shape of the curve depends on the value of σ_0, the maximum stress at $R = 0$. In a non-dimensional plot, where stresses are divided by σ_u, the curves obtained for several values of σ_0/σ_u are plotted in Figure 2.23. The label "σ_0" refers to the normalized value of σ_{max} at $R = 0$. When $\sigma_0 = 1$, the Haigh diagram represents the points where $\sigma_{max} = \sigma_u$ for all values of R and is a straight line as shown. For other values of σ_0, the lines are curved. Only the equation for positive values of R is plotted in the figure. The line representing $R = 0$ is shown, so the curves are valid only to the right of that line. It is now obvious why the equation, valid now for positive R, was modified to fit data at $-1 < R < 0$ as given in Equation (2.7). For this range of R, the points representing $R = 0$ and $R = -1$ are connected by a smooth curve with slight curvature (not shown here). The curve in Figure 2.23 for $\sigma_0 = 0.5$ goes through the point

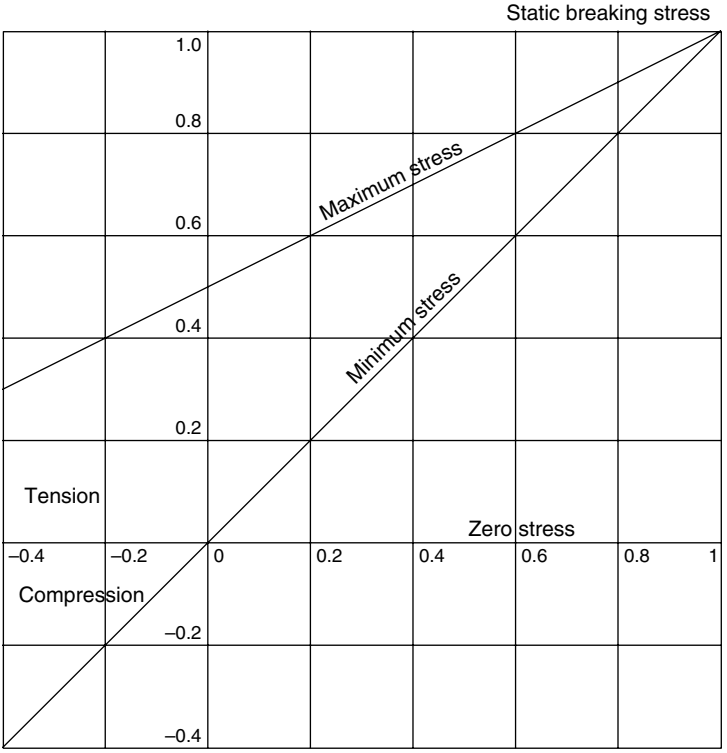


Figure 2.22. Goodman diagram as shown in Goodman, 1899 [20] on p. 455.

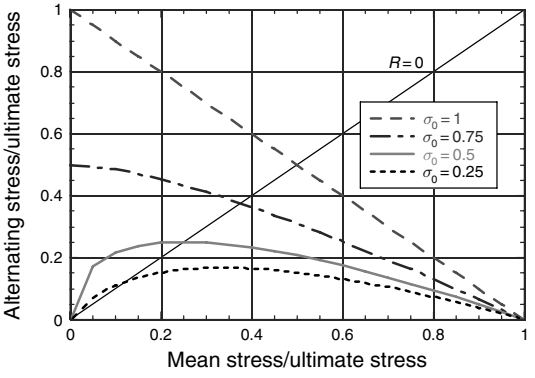


Figure 2.23. L–W equation for $R > 0$ plotted on a Haigh diagram.

from the original Goodman equation at $R = 0$ where $\sigma_{max} = 0.5\sigma_u$. The curve is closer to a Gerber parabola than a straight line in that region but may not have any more physical significance than the other two representations of experimental data.

It can be seen that the development of methods to represent fatigue limit data was based on a combination of mathematically simple forms as well as graphical representations. While there seemed to be a physical basis of some sort for all of the approaches, combined with simplicity, it should be pointed out that the choices of methods of representing data were scrutinized throughout their development. A particularly insightful example of such a critique was made in 1880 [26], although similar words would be equally valid today. Commenting on the W–L formula, used to fit Wöhler's data, Smith writes, "In fact, the formula seems to be more the product of pure imagination than to be based on the experiments." He further points out that "the formula can, of course, be made to agree with the *extreme* results of any particular set of experiments. What I, and I dare say some others, would like to know, is whether this formula agrees with even a rough degree of approximation with the *intermediate* results." He goes on to question "whether the parabolic curve . . . . is the correct curve . . . " and sums up: "I submit that the proper thing to do is not to coin rules out of imagination, but to persevere in careful and patient experiments, and to watch narrowly and to study and analyze closely the results until the true intimate laws of the stress and fatigue of metals are revealed."

2.6. HAIGH DIAGRAM AT ELEVATED TEMPERATURE

In the final program on HCF material behavior [27], a Haigh diagram was constructed for a single crystal alloy, PWA 1484 at a life of 10^7 cycles based on 1900 °F *S–N* test data. The stress-life behavior was characterized for each stress ratio, *R*, in terms of the alternating stress σ_{alt} using a power law relationship:

$$N_f = k\sigma_{alt}^m \tag{2.8}$$

Data were used only from <001> oriented specimens with the exception of eight specimens oriented at <001 + 15> that were tested at $R = 0.8$. The <001 + 15> oriented data fall on top of the <001> data and consequently were included in the data set to characterize the $R = 0.8$ stress-life behavior. Values for the constants *k* and *m* for each tested value of *R* are shown in Table 2.1.

Using the empirical *S–N* relationships, the curve was extrapolated to longer lives and a Haigh Diagram was constructed corresponding to a life of 10^7 cycles, as shown in Figure 2.24.

The Haigh diagram shows the HCF capability of PWA 1484 at 1900 °F. The shape of the diagram is fairly conventional for low values of mean stress. A gradual decrease

Table 2.1. Constants for *S–N* empirical fits at 1900 °F

R	*m*	*k*
−1	−12.4	2.0E + 27
−0.333	−3.0	1.9E + 11
0.1	−5.9	5.6E + 14
0.5	−4.9	1.0E + 12
0.8	−7.5	1.9E + 11

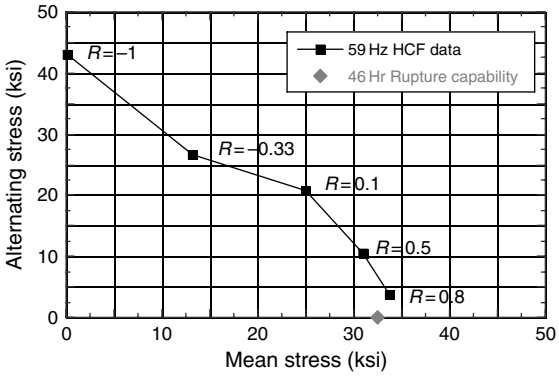


Figure 2.24. 1900 °F Haigh diagram for PWA 1484, 10^7 cycles.

in alternating stress capability is accompanied by an increase in allowable mean stress. However, above $R = 0.5$, the alternating stress capability drops off rapidly as the stress rupture capability is approached. The stress rupture capability can be represented as an asymptote at $R = 1$ at 46 hours, the time for 10^7 cycles at 60 Hz (which was the original planned frequency). For this material, there are both cycle-dependent and time-dependent modes of failure, the former normally associated with the value of the alternating stress and the latter associated primarily with the mean stress.

To account for this more complex fatigue behavior, a Walker model was used to represent the behavior of the material. In the Walker model, an equivalent alternating stress is defined to take into account different mean stress conditions. This equivalent alternating stress, $\sigma_{\text{equivalent\_alt}}$, is then used in the stress-life power law relationship as shown below:

$$N_f = k\sigma_{\text{equivalent\_alt}^m} \tag{2.9}$$

where the equivalent alternating stress is given by:

$$\sigma_{\text{equivalent\_alt}} = \sigma_{\text{alt}}(1 - R)^{(W-1)} \tag{2.10}$$

The Walker exponent, w, was determined by taking data from several values of R and iterating until the standard error in predicted life was minimized. The Walker model collapsed the S–N response over a range of stress ratios. While the Walker exponent is normally determined over the full range of stress ratio data that are available, in this case $R = -1$ to $R = 0.8$, the goal here was to capture only those specimens failing in a pure fatigue mode. Fractography showed that failure was dominated by fatigue only at low stress ratios or low mean stress loading conditions.

Two approaches were considered for fitting the Walker model. The first (termed "Walker model A" in what follows) used 59 Hz HCF data at all $R \leq 0.1$. A second approach (Walker model C) was examined because despite the fatigue-based appearance of specimens at $R = 0.1$ tested at 59 Hz, previous work showed that a time-dependent process is also present at this test condition [27]. At a constant stress level at $R = 0.1$, fatigue life in cycles increased as the frequency was increased from 59 to 900 Hz. A linear line with a slope of 1:1 approximated the data fairly well indicating a fully time-dependent process up to the highest frequency that was tested, 900 Hz. A transition to time-independent behavior with cycles to failure maintaining a constant level may exist just beyond 900 Hz or could occur well beyond that frequency. As a result, the estimate of the Walker exponent for pure HCF may be affected by using the lower 59 Hz data. Therefore the second approach used only high frequency data (370–400 Hz) at $R = 0.1$ in combination with 59 Hz data at $R = -1$ and $R = -0.333$ to represent time-independent behavior. Walker model constants for each subset of HCF data are shown in Table 2.2.

In Figure 2.25, Walker model A approximates the 59 Hz HCF data fairly well up to a value of $R = 0.1$. Walker model C shows a benefit in alternating stress capability at $R = -0.333$ and $R = 0.1$ compared to the other models. Both Walker models deviate from the 59 Hz Haigh diagram above $R = 0.1$ since the mean stress increases and time-dependent failure mechanisms reduce the cyclic capability of the material.

To account for the time-dependent behavior of the material, two approaches were used in modeling the rupture behavior of PWA 1484 at 1900 °F. The first approach, the simpler of the two, assumes that only the applied mean stress contributes to rupture damage. This approach is referred to as the Mean Stress Rupture Model. The second method, the Cumulative Rupture Model considers the summation of rupture damage from applied stress over the entire fatigue cycle.

Table 2.2. Constants for 1900 °F Walker models

Walker model	*HCF Data subset*	*Number of tests*	*k*	*m*	*Walker exponent, w*
A	$R \leq -0.1$ @ 59 Hz	24	5.83E16	−7.17	0.165
C	$R \leq -0.333$ @ 59 Hz, $R = 0.1$ @ 370–400 Hz	20	7.63E16	−6.98	0.3817

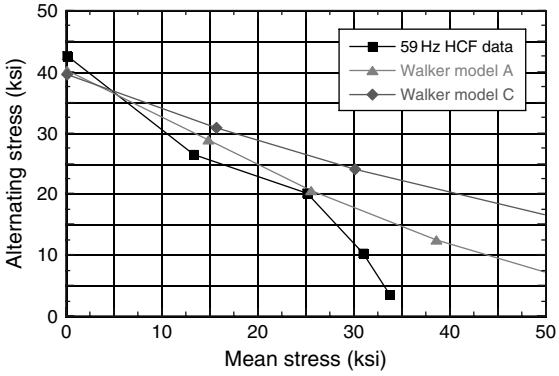


Figure 2.25. Walker models A and C with 59 Hz 10^7 cycles Haigh diagram.

The Mean Stress Rupture Model is represented by the expression in Equation (2.11) that relates mean stress to time to rupture. The expression was derived by fitting a power law relationship to four tests that were conducted until rupture. The resulting equation is

$$t_f = 2.19 \times 10^9 \ \sigma_{mean}^{-5.069} \tag{2.11}$$

where σ_{mean} is the applied mean stress in ksi and t_f is the time to failure in hours.

In the Cumulative Rupture Model, the rupture damage due to the applied stress is integrated over the cyclic load and the applied stress is expressed as a sinusoidal function using τ as the period of the cycle in hours. To do this, the load cycle is divided into small time increments, Δt. At each time increment, the applied stress is calculated and the corresponding rupture life is determined using Equation (2.10). The rupture damage for the time increment is calculated and damage fractions for Δt are summed over the loading cycle. The number of cycles to failure can be calculated using the assumption that failure occurs when the rupture damage equals one.

When R is less than zero, a portion of the loading cycle is compressive. Two scenarios were considered when applying the Cumulative Rupture Model: (a) compressive stress is neither damaging nor beneficial to life, and (b) compressive stress is damaging to life. Thus, in total, three rupture models were considered: Mean Stress Rupture Model, Cumulative Rupture without compressive damage, and Cumulative Rupture with compressive damage.

Figure 2.26 shows the rupture model predictions for a constant life of 10^7 cycles at 59 Hz compared to the HCF test data. Both cumulative rupture models approximate the shape of the Haigh diagram based on the experimental data. The mean stress model predicts a mean stress of 32.5 ksi independent of R for 10^7 cycles at 59 Hz since the model is purely time-dependent and does not consider any cyclic contribution to the damage process. It is worth noting that the cyclic models, Figure 2.25, seem to do a good job

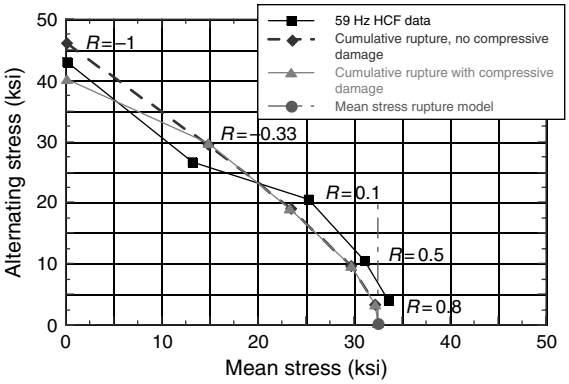


Figure 2.26. 1900 °F 10^7 cycle Haigh diagram at 59 Hz with rupture model predictions.

of fitting the data at low values of mean stress. They are derived, however, from fitting those very same data. The rupture model predictions, on the other hand, are derived strictly from rupture data with no cyclic content. The ability of the rupture models to represent data over the entire range of mean stresses, Figure 2.26, seems to indicate that the behavior of PWA 1484 at 1900 °F is purely time-dependent, or, at least for modeling purposes, can be treated as such.

The example cited above points out some of the considerations that are encountered when plotting data on a Haigh diagram and then trying to interpret the data or model the material fatigue limit when the material behavior includes time dependence. Factors such as cyclic frequency become important considerations and, at a minimum, should be indicated in Haigh diagram plots.

2.7. ROLE OF MEAN STRESS IN CONSTANT LIFE DIAGRAMS

In dealing with data on FLSs, it is common to plot these stresses as a function of stress ratio (R = ratio of minimum to maximum stress), or, more commonly, of mean stress. The Haigh diagram, incorrectly referred to as a Goodman diagram, is a common method of representing the fatigue limit or endurance limit stress of a material in terms of alternating stress, defined as half of the vibratory stress amplitude. Thus, the maximum dynamic stress is the sum of the mean and alternating stresses. For many rotating components, the mean stress is known fairly accurately, but the alternating stress is less well defined because it depends on the vibratory characteristics of the component. Thus a Haigh diagram represents the allowable vibratory stress as the vertical axis as a function of mean or steady stress as the x axis. While attempts have been made to define the equation which best represents the data on a Haigh diagram, as described earlier in this chapter,

variability from material to material, scatter in the data, and lack of sufficient data in many cases prevent the fitting of an equation to such data.

When mean stress values are negative, or for values of R less than minus one, there are very few data and no general guidelines for extrapolating equations which were meant to represent data on a Haigh diagram only for positive values of mean stress. In cases such as contact fatigue, very high compressive stresses can be present, necessitating knowledge of fatigue behavior or fatigue limits for negative mean stresses. One of the most important areas where negative mean stresses can occur is in the case of the introduction of compressive residual stresses into a material or component. Shot peening, for example, is commonly used as a surface treatment to improve the fatigue properties of a material by introducing residual compressive stresses into the material up to depths typically no greater than 0.1 mm. While compressive stresses in the vicinity of the surface reduce the maximum stress from vibratory loading at the surface, they do not reduce the vibratory amplitude. Thus, in effect, they drive the mean stress lower, often into the compressive regime. While these residual compressive stresses are known to improve the fatigue characteristics in many materials and geometries, they are generally not taken into account in design and are used, instead, to improve the margin of safety. If such a condition is to be taken into account in design, a thorough understanding of material behavior and fatigue limits under negative mean stresses is required. The subject of residual stresses and accounting for them in design is discussed in Chapter 8.

Forrest [15] has assembled a large body of fatigue limit strength data on ductile metals and plotted them in dimensionless form as indicated in Figure 2.27. The thick straight

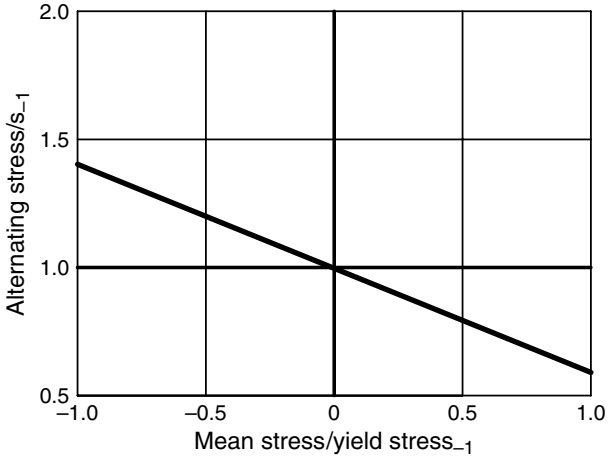


Figure 2.27. Schematic of observed behavior at negative mean stress.

line represents the data (not shown) quite well and illustrates that extending the fit into the mean stress regime produces alternating stress values that continue to increase with decreasing mean stress. The data chosen by Forrest [15] for this type of plot were filtered from available data to meet a criterion to accept only those results where special precautions were taken to insure axiality of loading. The data covered a range of aluminum and steel alloys. As noted earlier, when discussing the effects of compressive residual stress on fatigue limit strength, Forrest [15], in 1962, already recognized the importance of the shape of the curve fit to the data by stating that the "behaviour is particularly significant with regard to the effect of residual stresses on fatigue strength."

Representing compressive mean stress data on Haigh or other types of diagrams described above was never much of a consideration because data obtained at mean stresses below zero, corresponding to fully reversed loading or $R = -1$, essentially did not exist. We now examine the capability of equations to represent negative mean stress data.

In addition to the modified Goodman equation and the others described above, there have been many variations of straight lines and other curves to try to represent fatigue limit data for HCF design. Additionally, there are fatigue equations that are used mainly to fit data in the LCF regime, which try to account for the effects of mean stress or stress ratio by introducing a single parameter to consolidate such data. Two such equations are the one due to Smith, Watson, and Topper (SWT) [28] and the commonly used Walker equation. For the SWT equation, an effective stress is given in terms of maximum stress and strain range. In HCF, elastic behavior is assumed, thus strain range and stress range can be used interchangeably when dealing with FLS conditions. The SWT equation for elastic behavior is in the form

$$\Delta\sigma_{\text{eff}} = \sigma_{-1} = \left(\frac{\sigma_{\max}\Delta\sigma}{2}\right)^{1/2} = (\sigma_{\max}\sigma_{\text{a}})^{1/2} \tag{2.12}$$

where $\Delta\sigma_{\text{eff}}$ can be treated as a constant, $\Delta\sigma$ is the stress range, $\Delta\sigma = 2\sigma_{\text{a}}$, and $\sigma_{\max}$ is the maximum stress. The fully reversed ($R = -1$) stress, both the maximum and alternating value, is denoted by σ_{-1}. This equation is plotted in the form of a Haigh diagram in Figure 2.28 using a value of $\Delta\sigma_{\text{eff}} = 200$ MPa which is representative of data on a forged titanium bar material [29]. The exponent in Equation (2.12) is taken as the one used most commonly, namely 0.5. For reference purposes, the Jasper equation, discussed later, is plotted because it is found to describe the shape of the Haigh diagram for positive mean stress quite well. Of greatest interest in Figure 2.28 is the shape of the curve for the SWT equation for negative mean stress, which shows an ever increasing alternating stress as mean stress becomes further negative. As an alternative, if we choose to take half the strain range (or half the stress range) as that corresponding to positive stresses only ($\Delta\sigma = +$ in the figure), this changes the curve only slightly in the negative mean stress regime. Note, finally, the symmetric shape of the Jasper equation about zero mean stress. This also will be discussed later.

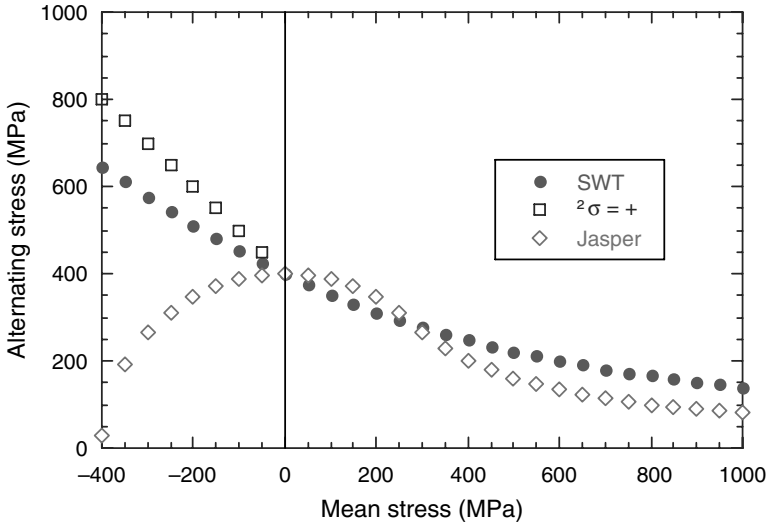


Figure 2.28. Haigh diagram representation of SWT and Jasper equations.

A similar treatment can be given to the Walker equation which, as for the SWT equation, is commonly used to consolidate LCF data obtained at different stress ratios, R. The equation is similar to the SWT equation, but adds a degree of flexibility through the exponent w. It has the form

$$\sigma_{\text{eq}} = 2^{w}\sigma_{-1} = (\Delta\sigma)^{w}(\sigma_{\max})^{(1-w)} \tag{2.13}$$

where w is the Walker exponent. With the exception of the value of the coefficient in Equation (2.13), it is identical in form to the SWT equation when $w = 0.5$. Figure 2.29 is a plot of the Walker equation for various values of the exponent w, including extension of the equation to account for negative mean stress or values of $R < -1$. The curves are all forced to go through the same point at zero mean stress. While some data are handled by changing the value of w for negative values of R, it can be seen that the Walker equation has the same general characteristics as the SWT equation for negative mean stress, namely that alternating stress continues to increase as mean stress goes further negative. Further, for both equations, the shape of the curves for positive mean stress is concave up over the entire region.

Several attempts were made in the early days of fatigue modeling to account for the observed behavior of the FLS when the mean stress was negative. In 1930, Haigh [30] pointed out that experimental data indicate that the constant life diagram is not symmetric

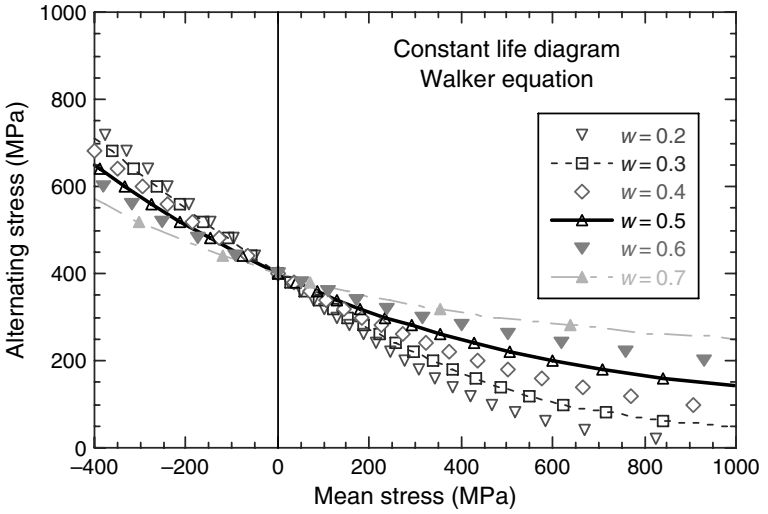


Figure 2.29. Haigh diagram representation of Walker equation.

with respect to σ_m as required by the Gerber and generalized Goodman formulas.* He suggested that the data can be represented by the generalized parabolic relation

$$\sigma_a = \sigma_{-1}\left[1 - k_1\left(\frac{\sigma_m}{\sigma_u}\right) - k_2\left(\frac{\sigma_m}{\sigma_u}\right)^2\right] \tag{2.14}$$

where the constants k_1 and k_2 are selected to give the best fit of the data. A plot of this equation is presented in Figure 2.30 for several combinations of k_1 and k_2 while constraining the curves to go through the ultimate stress point on the x axis and the alternating stress value at $R = -1$ on the y axis. The case where $k_1 = 0, k_2 = 1$ represents the Gerber parabola, Equation (2.5), symmetric about the y axis. When $k_1 = 1$ and $k_2 = 0$, the modified Goodman line is obtained, extrapolated for negative mean stress.

More complex equations have been proposed, such as that by Heywood [31], who used an empirical cubic equation for representing constant life data. His equation has the form

$$\sigma_a = \left[1 - \left(\frac{\sigma_m}{\sigma_u}\right)\right]\left[\sigma_{-1} + \gamma(\sigma_u - \sigma_{-1})\right] \tag{2.15a}$$

* While the generalized Goodman equation [3] does not indicate symmetry with respect to σ_m, the formulation in the first Edition of Goodman's book [20] presents equations for the static load capability in terms of the dynamic theory. If it is assumed that the strength is equal in tension and compression, the equations indicate that there is symmetry with respect to mean stress. The lack of data for negative mean stresses prevented any substantial debate on this issue of symmetry. The symmetry of the Goodman equation and its history are discussed in [18].

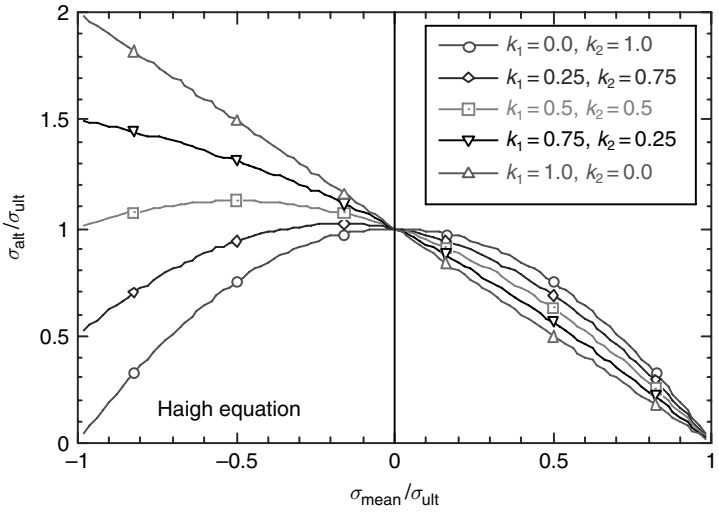


Figure 2.30. Constant life diagram for parabolic equation of Haigh.

$$\gamma = \left(\frac{\sigma_m}{\sigma_u}\right)\left[e + g\left(\frac{\sigma_m}{\sigma_u}\right)\right] \tag{2.15b}$$

where e and g are either positive or negative constants. Because of the large number of terms, most experimentally determined constant life data may be represented by proper selection of the constants.

2.8. JASPER EQUATION

Of both practical and historical significance is the observation that Jasper [32], in 1923, proposed that fatigue life is related to the stored energy density range per cycle in a material when evaluating data obtained earlier by Haigh. Applying this concept to HCF conditions, it can be assumed that all stresses and strains are elastic, thus all equations represent purely elastic behavior. For purely uniaxial loading, the shaded area in Figure 2.31 illustrates schematically the stored energy for the cases where loading is purely tensile ($R > 0$). The energy for the case where $R < 0$, which involves tension and compression in a single cycle, is illustrated in Figure 2.32 by the shaded area. The stored energy density range per cycle is then given for uniaxial loading by

$$U = \int_{\sigma_{min}}^{\sigma_{max}} \sigma \, d\varepsilon = \frac{1}{E}\int_{\sigma_{min}}^{\sigma_{max}} \sigma \, d\sigma \tag{2.16}$$

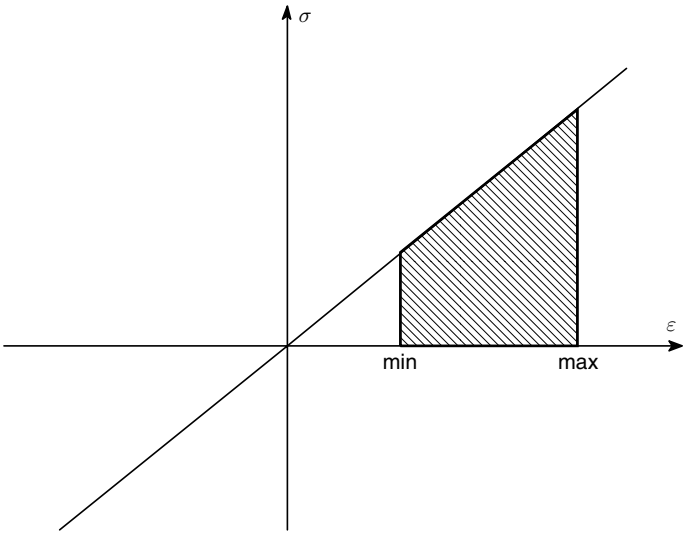


Figure 2.31. Stored energy (shaded) for elastic loading under tension fatigue ($R > 0$).

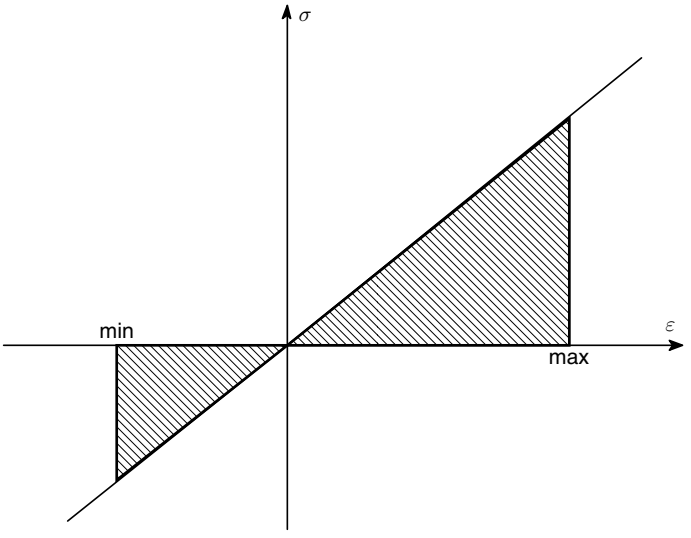


Figure 2.32. Stored energy (shaded) for elastic loading under reversed fatigue ($R < 0$).

since $\sigma = E\varepsilon$, E is Young's modulus. The energy can then be written as

$$U = \frac{1}{2E}\left(\sigma_{\max}^2 \pm \sigma_{\min}^2\right) \tag{2.17}$$

where the plus sign is for $R < 0$ and the minus sign for $R > 0$ (see Figures 2.31 and 2.32). For purposes of presenting the equation in the form of a Haigh diagram, the stress limits are written in terms of mean and alternating stresses

$$\sigma_{\max} = \sigma_{\mathrm{m}} + \sigma_{\mathrm{a}} \tag{2.18a}$$

$$\sigma_{\min} = \sigma_{\mathrm{m}} - \sigma_{\mathrm{a}} \tag{2.18b}$$

where σ_{m} and σ_{a} represent the mean and alternating stresses, respectively.

For the specific case of fully reversed loading, $R = -1$, the energy is written as

$$U = \frac{1}{2E}(2\sigma_{-1}^2) \tag{2.19}$$

where σ_{-1} represents the alternating stress (= maximum stress) at $R = -1$. For any other case of uniaxial loading, the following equation is easily derived and can be used to obtain the value of the alternating stress on a Haigh diagram in terms of stress ratio, R:

$$\sigma_{\mathrm{a}} = \frac{\sigma_{-1}}{\sqrt{2}}\sqrt{\frac{(1-R)^2}{1-R|R|}} \tag{2.20}$$

where $|R|$ is used to denote the absolute value of R. It follows that the alternating stress when $R = 0$, defined as σ_0, is

$$\sigma_0 = \sqrt{\frac{{\sigma_{-1}}^2}{2}} \tag{2.21}$$

Of interest is the shape of the Haigh diagram corresponding to a constant energy density range for any positive mean stress value. Such a diagram is shown in Figure 2.33 which has the same general shape as that for Ti-6Al-4V bar material (Figure 2.34) obtained by Maxwell and Nicholas [33]. It should be noted that only a single parameter, σ_{-1}, is required to describe the values on both the x and y axes. This plot (Figure 2.33) is the same type as shown previously as the Jasper equation in Figure 2.28, using typical numbers for titanium plate, where the alternating stresses corresponding to negative mean stresses are also included.

Data on another high strength titanium alloy, Ti-6-2-4-6, that extend into the negative mean stress regime are shown in Figure 2.35. These data show the same general trend as the Jasper equation curve of Figure 2.33 for positive mean stresses and have a shape

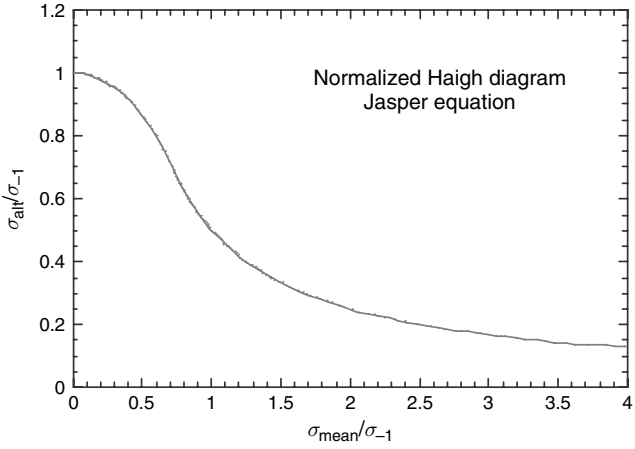


Figure 2.33. Normalized Haigh diagram representing Jasper equation for positive mean stresses.

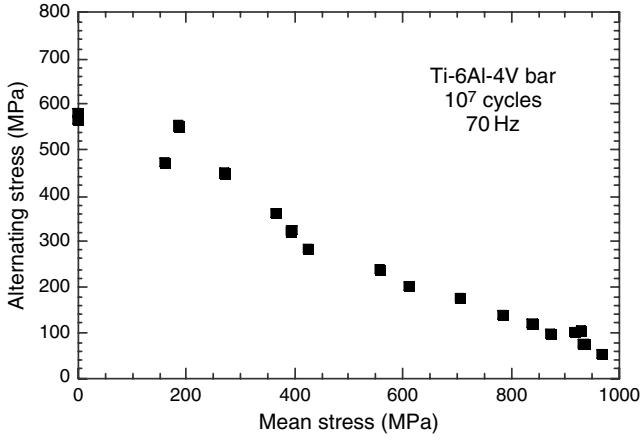


Figure 2.34. Haigh diagram for Ti-6Al-4V bar [33].

similar to that shown subsequently in Figure 2.36 when extended into the negative mean stress regime. The representation of data for negative mean stresses is discussed in the following paragraphs.

Experimental data for negative mean stress were obtained by Nicholas and Maxwell [29] that showed they neither followed the Jasper equation nor the SWT or Walker equations (see Figure 2.28). For that reason, they proposed a modification to the Jasper equation that treats the stored energy due to tension differently than that due to compression stresses. Haigh [30], in 1929, in referring to Bauschinger's results from 1915

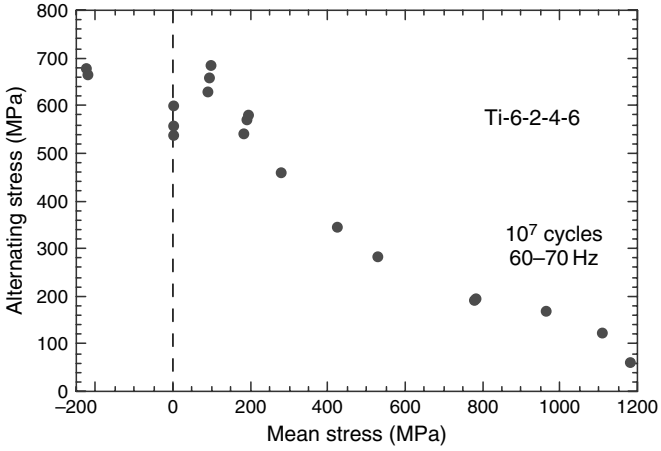


Figure 2.35. Haigh diagram for Ti-6-2-4-6.

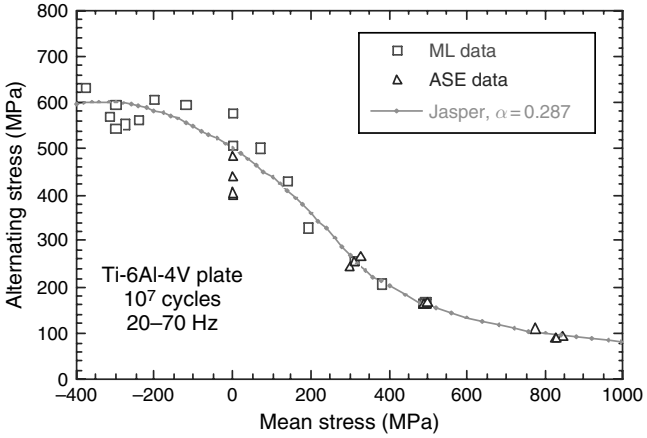


Figure 2.36. Haigh diagram for Ti-6Al-4V plate including modified Jasper equation fit.

and 1917, noted that "this series of tests . . . was probably the first that ever revealed any difference between the actions of pull and push in relation to fatigue."* Referring to data on naval brass, he indicated, "In this metal, as in many others, pull tends to reduce the fatigue limit while push increases the resistance to fatigue." Following this idea, Nicholas and Maxwell postulated that stored energy density per cycle does not contribute

*"Push" and "pull" was the common nomenclature for tension and compression, respectively, in that time period.

towards the fatigue process as much when the stresses are compressive as when they are in tension. Taking the simplest approach, where compressive stress energy contributes a fraction, α, compared to comparable energy in tension, then the total effective energy was formulated in the following manner, where $\alpha < 1$:

$$U_{\text{tot}} = U_{\text{tens}} + \alpha U_{\text{comp}} = \text{constant} \tag{2.22}$$

In the use of this equation, energy terms corresponding to negative stresses have to be modified by the coefficient α. The introduction of the constant α has the effect of modifying the shape of the Jasper equation as shown in Figure 2.37 for several values of the constant α. The stresses on both axes are the same as those used in Figure 2.28. The constant α was then used to fit actual experimental data obtained at values of $R < -1$ corresponding to negative mean stresses.

Using the Ti-6Al-4V forged plate material, fatigue tests were conducted under constant amplitude stress conditions over a wide range of stress ratios from 0.8 to −3.5. The minimum stress ratio value at which tests could be conducted was limited by the compressive yield strength of the material. To establish the fatigue limit strength corresponding to 10^7 cycles, samples were fatigue tested using the step-loading procedure of Maxwell and Nicholas [33] that is discussed in the next chapter.

The experimental values for the FLS obtained for a broad range of values of R are plotted in the form of a Haigh diagram in Figure 2.36. The data are shown as ML in the figure, and are combined with previously unpublished data from Allied Signal Engines (ASE), now Honeywell, on the same material. A best fit of the data using the modified Jasper equation is also shown in the figure. The constant, α, in the modified Jasper equation (2.22) was obtained as 0.287 by fitting to the experimental data obtained from

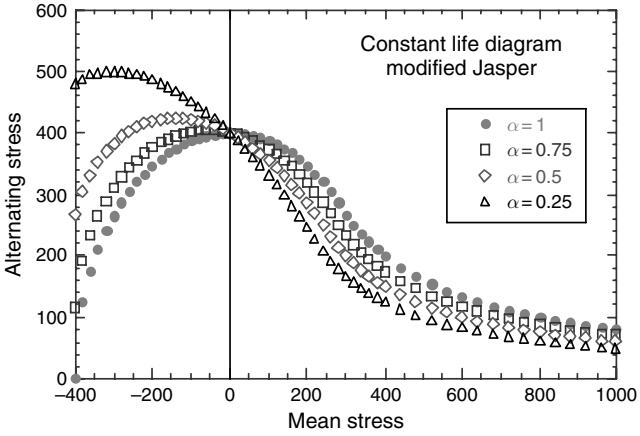


Figure 2.37. Haigh diagram for modified Jasper equation for various values of α.

$R = 0.8$ to $R = -3.5$. The weighted energy was obtained for each data point as a function of the variable α in Equation (2.22) and the percent least squares error between the average energy of all the data points and the individual energy values was minimized. To plot the resulting modified Jasper equation, the stress corresponding to the average energy at $R = -1$ had to be obtained and was found to be 500 MPa.

In reviewing the methods for representing fatigue limit data on constant life diagrams, Maxwell and Nicholas [33] noted that the Haigh diagram is the one that has achieved the most popularity. In a review of these diagrams, the authors suggested that the most important information for design was not only the alternating stress, but also the maximum stress, as represented in a plot against mean stress (see Figures 2.20 and 2.21 above). To this end, a diagram called the Nicholas–Haigh diagram was proposed [33] which, as history would note, received absolutely no acceptance or recognition from the technical community and was short-lived, never to be mentioned again until here. For the sake of posterity, the reasoning behind the proposed diagram, and more importantly, the importance of maximum stress in constant life diagrams is discussed next.

The plot of both alternating stress and maximum stress against mean stress, initially referred to as a Nicholas–Haigh diagram [33] is presented at the possible expense of duplicating past efforts as well as confusing future historians. This plot can be used to present data for engineering design in two fashions. For low values of mean stress or low R ($R < 0.5$), the alternating stress is the crucial allowable quantity, particularly for rotating machinery applications where mean stresses are relatively predictable and normally are well defined. For high values of mean stress or high R ($R > 0.5$), maximum stress becomes the more critical parameter in design. It is suggested here that margins of safety be imposed on both parameters (alternating stress and maximum stress) in order to insure a safe design. The Nicholas–Haigh diagram was an attempt to present data in a form that would allow a designer to recognize the importance of both quantities. Such a plot may not be totally new, but the following features were incorporated in it:

a. It is a method of representing experimental data. There is no equation or formula intended or implied to represent the data.
b. There is no specific value of an y-axis intercept (zero mean stress or $R = -1$) which is related to any material property such as yield or ultimate stress.
c. There is no value, experimental or theoretical, associated with an x-axis intercept ($R = 0$).

This last condition differs from most previous diagrams or laws that attempt to pin the data to the ultimate strength for theoretical reasons, or to yield stress for engineering purposes. One of the main reasons for avoiding an intercept such as the ultimate strength is that ultimate strength depends on the strain rate at which a test is conducted, and since most metals exhibit some degree of strain-rate hardening [34]. Data plotted on a

Nicholas-Haigh diagram are normally conducted at a single frequency which produces a different strain rate for each different amplitude of alternating stress. For increasing values of mean stress, as R approaches 1, the strain rate approaches zero since the alternating stress amplitude is normally found to decrease in this region. This is equivalent to having a cyclic stress–strain curve near the ultimate stress at an arbitrarily slow rate of loading. Thus, a fourth condition can be suggested for a completely defined Nicholas–Haigh diagram, namely, that the frequency of loading for all data points be specified on the diagram.

It should be noted that data for Haigh or other constant life diagrams for large cycle counts, generally in excess of 10^7 for HCF applications, are obtained at high frequencies. Thus, the strain rates associated with such tests are not quasi static. For this reason, maximum stress values obtained under fatigue testing at high values of R and high frequency can often be above the quasi-static ultimate strength of the material. This, in turn, will not produce a smooth plot on a Haigh diagram if a quasi-static ultimate strength is used to anchor the plot to the x-axis.

As a further consideration, it is recommended that all data points be included, particularly those obtained at high values of R ($R \rightarrow 1$). In this region, many materials tend to exhibit creep behavior which may lead to a creep rather than a fatigue failure (see the discussion in Chapter 3 on testing at high stress ratios as well as the earlier discussion on Haigh diagrams at elevated temperature). Nonetheless, if the frequency is specified, the time to failure can be easily deduced. Data of this type should be appended with a footnote if necessary, but they are still valid design data, even though the mode of failure is not pure fatigue.

In the limit, a "fatigue" test at very high values of R becomes a creep or sustained load test. Any strain hardening which occurs due to strain rate effects, therefore, is influenced by the rate of loading which is used in going from zero to mean stress during the first half cycle at the start of the test. This rate of loading should be recorded, particularly if data are to be compared with an ultimate stress value. The ultimate stress, consequently, should be obtained from a test at the same rate of loading for consistency.

An example of a Nicholas–Haigh diagram is presented in Figure 2.38 for titanium alloy Ti-6Al-4V. The data are those presented previously in Figure 2.36 and are represented by the modified Jasper equation for both maximum and alternating stress. Note that the maximum stress approaches and then exceeds the yield stress of the material (930 MPa) at high values of mean stress.

It is of importance to note that the Haigh diagram, especially when extended into the negative mean stress regime, provides useful information on the potential beneficial effects of residual stresses. (Residual stresses and their role in endurance limits are discussed in detail in Chapter 8.) Notwithstanding the fact that stress gradients play an important role in fatigue, comparing allowable alternating stresses as a function of mean stress can give guidance on the role that residual stress can play in altering the fatigue

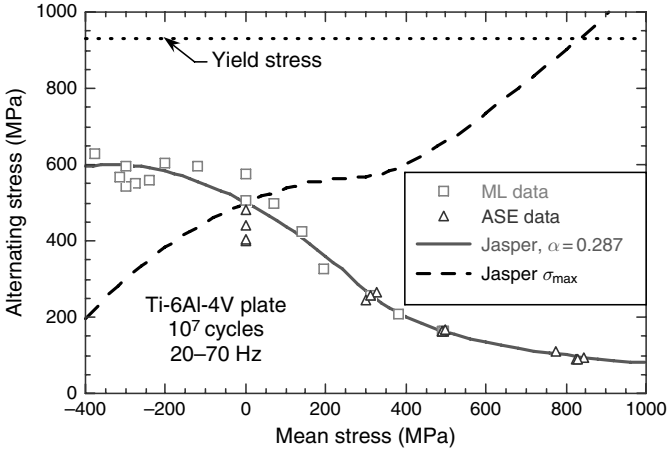


Figure 2.38. Nicholas–Haigh diagram for Ti-6Al-4V plate with modified Jasper equation fit shown for alternating stress (solid line) and maximum stress (dashed line).

limit strength. Noting again that compressive residual stresses do not alter the range of stress or alternating stress applied to a material or structure but, rather, reduce the mean stress, the Haigh diagram provides data on the reduction of the allowable alternating stress as a function of mean stress. Using the Jasper equation as a measure of the allowable alternating stress, if a material is subjected to a vibratory stress at $R = 0$, with an alternating stress magnitude denoted by σ_0, then the mean stress is also σ_0. Addition of a compressive residual stress of an equal magnitude σ_0 will then result in a mean stress of zero which, in turn, will increase the allowable alternating stress by a factor of $\sqrt{2}$, as seen from Equation (2.21). Yet if the original stress state is at $R = -1$, and a compressive residual stress is added, then the modified Jasper diagram representing Ti-6Al-4V plate material, Figure 2.36 shows that the benefit of compressive residual stress is somewhat limited. In going from a mean stress of zero to a mean stress of -400 MPa, for example, Figure 2.36 indicates a benefit in allowable alternating stress of only approximately 20% since the alternating stress of approximately 500 MPa only increases to approximately 600 MPa. This type of information can be easily seen in a plot of maximum stress against mean stress, Figure 2.38, where the maximum stress corresponding to the fatigue limit is seen to decrease as mean stress decreases in the negative mean stress regime. Thus, it has to be ascertained where the mean stress is without residual stress and where the mean stress will be after a compressive residual stress is developed. From that information, the allowable alternating stress for the material can be determined and the benefit of the residual stress ascertained. The subject of residual stresses and their effect on fatigue behavior in conjunction with other considerations evolving from surface treatments is discussed further in Chapter 8.

2.9. OBSERVATIONS ON STEP TESTS AT NEGATIVE *R*

Data obtained in [29] have been examined for implications on the initiation and subsequent propagation of cracks in smooth bars cycled at negative stress ratios. The data, shown above in a Haigh diagram in Figure 2.38, cover a range of stress ratios, R, from a high value of 0.8 down to -3.5. They were fit to a modified form of the Jasper equation which accounts for the different behavior in initiation in compression compared to that in tension using the constant α. In addition to the alternating stress normally provided in a Haigh diagram, the maximum stress is also shown by a dashed line in the figure. The data were obtained using the step-loading procedure, described in the next chapter, with blocks of 10^7 cycles. Of significance is the number of cycles to failure in the last loading block as a function of R shown in Figure 2.39. The relatively low number of cycles in the last block leads to speculation that these specimens, at low values of R, had already developed cracks in earlier cycle blocks and that these cracks did not propagate until some higher stress level was reached in the final block. If, according to this speculation, the crack propagates only due to positive stresses (positive K), then the cracks formed at lower values of R must be larger than those at higher R because the maximum stress (positive portion of cycle) decreases with decreasing R (see Figure 2.38). The indirect evidence of small numbers of cycles in the last loading block is discussed further in Chapter 3 when dealing with specimens that are deliberately precracked before endurance limits are determined using step loading.

The speculation about crack initiation and subsequent propagation at negative R can be explained with the aid of Figure 2.40, where the conditions for initiation compared to propagation are shown schematically. The initiation of a crack, if associated with the

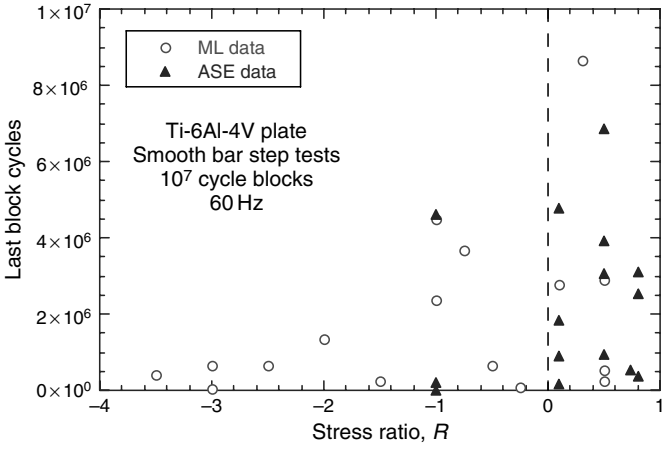


Figure 2.39. Cycles to failure in last cycle block for smooth bar specimens.

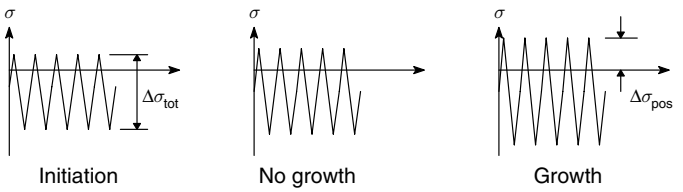


Figure 2.40. Schematic of initiation/growth dilemma for fatigue under negative R.

total stress or strain range,* will occur at some critical value of $\Delta\sigma_{tot}$ as shown. At those same stresses, the positive stress range may be below the threshold for crack propagation. It is only when the crack driving force due to positive stresses only, $\Delta\sigma_{pos}$, exceeds the threshold that the crack will continue to grow. Thus, there may be a condition where cracks initiate but do not propagate if the loading applied is incrementally increased such as in a step-loading sequence.

An alternate and more plausible explanation, without any direct evidence, is that the stress intensity needed to propagate an existing crack becomes smaller as the amount of compression increases. Of some relevance is the observation by Moshier et al. [35] that LCF cycling at $R = 0.1$ produced an overload type effect on the subsequent HCF threshold when the HCF peak stress was lower than that in the LCF precracking, but under similar conditions there was no overload effect using $R = -1$ for the LCF. Stephens et al. [36] found compression overloads to be either detrimental or have no effect on fatigue life, meaning that lower loads would be necessary to produce the same crack growth rate after a compression overload. Although this deals with growth rates, Lang and Huang [37] found that K_{PR}, the crack propagation stress intensity factor, decreases with increasing level of compression overload. For the same maximum K, this means that a lower stress range is needed to propagate the crack. Another similar finding is that of Lenets [38] who showed that a compressive overload allows resumption of crack growth under compression cycling of a previously arrested crack in an aluminum alloy. With these various observations and the present data, it seems reasonable to deduce the reasons behind the shape of the Haigh diagram at negative R (Figure 2.38), namely the relatively flat alternating stress which produces initiation, and the maximum stress or positive stress that decreases with mean stress which leads to threshold crack propagation.

Similar observations on the non-propagation of cracks from sharp notches, while mostly attributed to the complex stress and K fields ahead of the notch, can be interpreted as being due to the use of fully reversed loading where the crack initiates at a lower load than the one at which it propagates. This subject of notches and notch stress fields is discussed in Chapter 4. Data obtained in [39] under notch fatigue, for example, show

* In the Jasper formulation of Nicholas and Maxwell [29], the fatigue limit used the positive stress range plus a fraction of the negative range to fit experimental data.

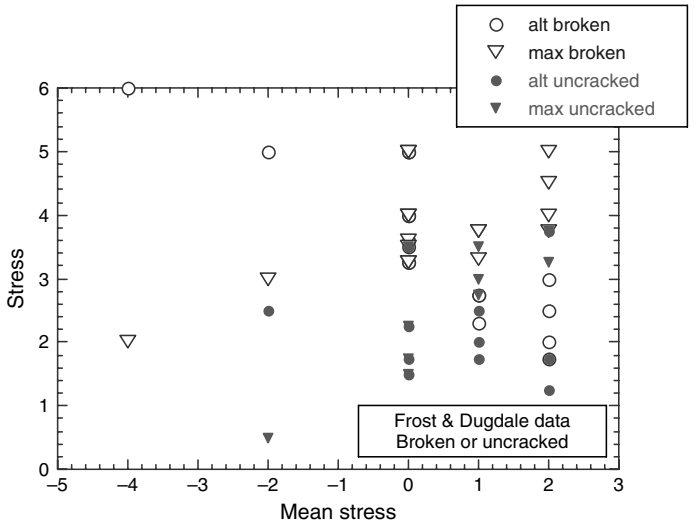


Figure 2.41. Data from Frost and Dugdale [39] showing boundary between cracked and uncracked specimens as function of mean stress.

that for the case where several mean stresses were used in notch fatigue, the only cases where arrested cracks were observed were under cycling at negative values of R. Those data are plotted as a function of mean stress (dimensionless) in Figure 2.41. Individual data points show both the alternating as well as the maximum stress where specimens were found to be either cracked or uncracked. The maximum stress can be interpreted as the quantity needed to propagate a crack when R is negative whereas the alternating stress (or twice the alternating stress for $R > 0.5$) governs both crack initiation and crack propagation. For the right side of the diagram, corresponding to positive mean stress, the boundary between broken and unbroken for alternating or mean stress follows the trends seen in a typical Haigh diagram such as that in Figure 2.38. For negative mean stress, the maximum stress for the broken specimens decreases slightly with decreasing mean stress. This could indicate that there is a nearly constant value of positive stress that is needed to fracture a specimen or cause an existing crack to continue to propagate. This observation bears some consistency with the observation of the number of cycles in the last block for smooth specimens, Figure 2.39, where the implication of the existence of a precrack for negative R can be made.

REFERENCES

1. Wöhler, A., "Bericht über die Versuche, welche auf der Königl. Niederschlesisch-Märkischen Eisenbahn mit Apparaten zum Messen der Biegung und Verdrehung von Eisenbahn-wagen-Achsen während der Fahrt, angestellt wurden", *Zeitschrift fur Bauwwesen*, **8**, 1858, pp. 642–651.

2. Bathias, C., Drouillac, L., and Le Francois, P., "How and Why the Fatigue S–N Curve does not Approach a Horizontal Asymptote", *Int. J. Fatigue*, **23**, Supp. 1, 2001, pp. S143–S151.
3. Bathias, C., "There is no Infinite Fatigue Life in Metallic Materials", *Fatigue & Fracture of Engineering Materials & Structures*, **22**, 1999, pp. 559–565.
4. Bathias, C., "Relation Between Endurance Limits and Thresholds in the Field of Gigacycle Fatigue", *Fatigue Crack Growth Thresholds, Endurance Limits, and Design, ASTM STP 1372*, American Society for Testing and Materials, West Conshohocken, PA, 2000, pp. 135–154.
5. Marines, I., Bin, X., and Bathias, C., "An Understanding of Very High Cycle Fatigue of Metals", *Int. J. Fatigue*, **25**, 2003, pp. 1101–1107.
6. Atrens, A., Hoffelner, W., Duerig, T.W., and Allison, J.E., "Subsurface Crack Initiation in High Cycle fatigue in Ti6Al4V and in a Typical Martensitic Stainless Steel", *Scripta Met.*, **17**, 1983, pp. 601–606.
7. Shiozawa, K., Lu, L., and Ishihara, S., "S-N Curve Characteristics and Subsurface Crack Initiation Behaviour in Ultra-Long Life Fatigue of a High Carbon-Chromium Bearing Steel", *Fatigue Fract. Engng Mater. Struct.*, **24**, 2001, pp. 781–790.
8. Li, J., Yao, M., and Wang, R.-Z., "A New Concept for Fatigue Strength Evaluation of Shot Peened Specimens", *Proceedings of the ICSP4, 4th International Conference on Shot Peening*, Tokyo, 1990, pp. 255–262.
9. Morrissey, R.J. and Nicholas, T., "Staircase Testing of Titanium in the Gigacycle Regime", presented at *3rd International Conference on Very High Cycle Fatigue (VHCF-3)*, Ritsumeikan University, Shiga, Japan, September 16–19, 2004 (to be published in *Int. J. Fatigue*).
10. Ochi, Y., Matsumura, T., Masaki, K., and Yoshida, S., "High-Cycle Rotating Bending Fatigue Property in Very Long-Life Regime of High-Strength Steels", *Fatigue Fract. Engng. Mater. Struct.*, **25**, 2002, pp. 823–830.
11. *Fatigue and Fracture of Engineering Materials and Structures*, **22**, No. 7, 1999.
12. *Fatigue and Fracture of Engineering Materials and Structures*, **25**, No. 8/9, 2002.
13. Bathias, C. and Paris, P.C., *Gigacycle Fatigue in Mechanical Practice*, Marcel Dekker, New York, 2005.
14. Caton, M.J., Jones, J.W., Mayer, H., Stanzl-Tschegg, S., and Allison, J.E., "Demonstration of an Endurance Limit in Cast 319 Aluminum", *Metal. Mater. Trans.*, **34A**, 2003, pp. 33–41.
15. Forrest, P.G., *Fatigue of Metals*, Pergamon Press, Oxford, 1962 (U.S.A. Edition distributed by Addison-Wesley Publishing Co., Reading, MA).
16. Gunn, K., "Effect of Yielding on the Fatigue Properties of Test Pieces Containing Stress Concentrations", *Aeronautical Quarterly*, **6**, 1955, pp. 277–294.
17. Murakami, Y., *Metal Fatigue: Effects of Small Defects and Nonmetallic Inclusions*, Elsevier Science, Ltd, Kidlington, Oxford, 2002.
18. Sendeckyj, G.P., "Constant Life Diagrams – A Historical Review", *Int. J. Fatigue*, **23**, 2001, pp. 347–353.
19. Haigh, B.P., "Experiments on the Fatigue of Brasses", *Journal of the Institute of Metals*, **18**, 1917, pp. 55–86.
20. Goodman, J., *Mechanics Applied to Engineering*, Vol. 1, 9th edn, Longmans, Green & Co., Inc., New York, 1930, p. 634; see also 1st edn, 1899, p. 455.
21. Fidler, T.C., *A Practical Treatise on Bridge-Construction*, Charles Griffin and Company, London, 1887.
22. Soderberg, C.R., "Factor of Safety and Working Stress", *Trans., American Society of Mechanical Engineers*, **52**, 1939, pp. 13–28.

23. Gerber, W.Z., "Relation Between the Superior and Inferior Stresses of a Cycle of Limiting Stress (in German)", *Zeitschrift des Bayerischen Architekten-und Ingenieur-Vereins*, **6**, 1874, pp. 101–110.
24. Launhardt, W., "The Stressing of Iron (in German)", *Zeitschrift des Architekten-und Ingenieur-Vereins zu Hannover*, **19**, 1873, pp. 139–144.
25. Weyrauch, J.J., "Strength and Determination of the Dimensions of Structures of Iron and Steel with Reference to the Latest Investigations" (English translation by A.J. DuBois) John Wiley and Sons, New York, 1877.
26. Smith, R.H., "The Strength of Railway Bridges", *Engineering, London*, **29**, 1880, pp. 262–263.
27. Gallagher, J. et al., "Advanced High Cycle Fatigue (HCF) Life Assurance Methodologies", Report # AFRL-ML-WP-TR-2005-4102, Air Force Research Laboratory, Wright-Patterson AFB, OH, July 2004.
28. Smith, K.N., Watson, R., and Topper, T.H., "A Stress-Strain Function for the Fatigue of Metals", *Journal of Materials*, **5**, 1970, pp. 767–778.
29. Nicholas, T. and Maxwell, D.C., "Mean Stress Effects on the High Cycle Fatigue Limit Stress in Ti-6Al-4V", *Fatigue and Fracture Mechanics: 33rd Volume, ASTM STP 1417*, W.G. Reuter, and R.S. Piascik, eds, American Society for Testing and Materials, West Conshohocken, PA, 2002, pp. 476–492.
30. Haigh, B.P., "The Relative Safety of Mild and High-Tensile Alloy Steels Under Alternating and Pulsating Stresses", *Proceedings of the Institution of Automotive Engineers*, **24**, 1930, pp. 320–347.
31. Heywood, R.B., *Designing Against Fatigue of Metals*, Reinhold Publishing Corp., New York, 1962.
32. Jasper, T.M., "The Value of the Energy Relation in the Testing of Ferrous Metals at Varying Ranges of Stress and at Intermediate and High Temperatures", *Philosophical Magazine*, Series. 6, **46**, October 1923, pp. 609–627.
33. Maxwell, D.C. and Nicholas, T., "A Rapid Method for Generation of a Haigh Diagram for High Cycle Fatigue", *Fatigue and Fracture Mechanics: 29th Volume, ASTM STP 1321*, T.L. Panontin, and S.D. Sheppard, eds, American Society for Testing and Materials, West Conshohocken, PA, 1999, pp. 626–641.
34. Nicholas, T., "Material Behavior at High Strain Rates", *Impact Dynamics*, Chap. 8, J. Zukas et al. eds, Wiley, New York, 1982, pp. 277–332.
35. Moshier, M.A., Nicholas, T., and Hillberry, B.M., "High Cycle Fatigue Threshold in the Presence of Naturally Initiated Small Surface Cracks", *Fatigue and Fracture Mechanics: 33rd Volume, ASTM STP 1417*, W.G. Reuter and R.S. Piascik, eds, American Society for Testing and Materials, West Conshohocken, PA, 2002, pp. 129–146.
36. Stephens, R.I., Chen, D.K., and Hom, B.W., "Fatigue Crack Growth with Negative Stress Ratio Following Single Overloads in 2024–T3 and 7075–T6 Aluminum Alloys", *Fatigue Crack Growth Under Spectrum Loads, ASTM STP 595*, American Society for Testing and Materials, Philadelphia, 1976, pp. 27–40.
37. Lang, M. and Huang, X., "The Influence of Compressive Loads on Fatigue Crack Propagation in Metals", *Fatigue Fract. Engng. Mater. Struct*., **21**, 1998, pp. 65–83.
38. Lenets, Y.N., "Compression Fatigue Crack Growth Behaviour of an Aluminium Alloy: Effect of Overloading", *Fatigue Fract. Engng. Mater. Struct*., **20**, 1997, pp. 229–256.
39. Frost, N.E. and Dugdale, D.S., "Fatigue Tests on Notched Mild Steel Plates with Measurements of Fatigue Cracks", *J. Mech. Phys. Solids*, **5**, 1957, pp. 182–192.

Chapter 3
Accelerated Test Techniques

3.1. HISTORICAL BACKGROUND

Since the beginning of fatigue research in the 1800s, the problems associated with long life or HCF have produced an obvious need to generate data at very high numbers of cycles. Turbine engine components undergoing high frequency resonances, reciprocating automotive engines travelling hundreds of thousands of miles at several thousand rpm, railroad wheels making contact with the rails on every revolution over hundreds of thousands of miles, bridges carrying thousands of moving axle loads every day, and rotating machine components that operate on a continuous basis are just some of the examples where materials can be subjected to large numbers of cycles. While 10^6, 10^7, and 10^8 may be typical design lives for some applications, even larger numbers are now recognized as the actual cycle counts to which some materials and components may be exposed in service. These large numbers of cycles may take many years to accumulate in service whereas in design, data are needed in a much shorter period of time.

Historically, researchers have devoted considerable effort to developing both equipment that can operate at high frequencies and test procedures to accelerate the manner in which the long-life fatigue limit can be determined. Lacking either, obtaining data at long cycle counts could take weeks, months, or even years. Testing machine frequencies have been improved in response to the need for longer life testing. Laboratory testing with servo-hydraulic machines up to frequencies approaching 1 kHz is becoming state of the art [1].

The field of "gigacycle fatigue" has seen great interest in recent years because of the need to obtain material fatigue strength data at exceedingly high cycle counts. The subject was discussed in the previous chapter. Regarding the testing technique, piezoelectric test devices have been developed that operate with an axial specimen in a longitudinal first mode resonance condition at the driving frequency of 20 kHz [2]. The frequency of the driving force has been extended to 30 kHz [3] using the same excitement principle.

3.1.1. Coaxing

These new test techniques and other advances in electronics, instrumentation, computers, and other technical fields have provided the capability to evaluate the long life fatigue behavior of materials far beyond what was envisioned in the late nineteenth and early twentieth centuries. Yet, in that time period, concerns were expressed by early fatigue

researchers over the needs for accelerated test methods and the possible existence of load-history effects such as coaxing. Noting that endurance testing is very time consuming, Gough [4] identified a critical need for rapidly determining fatigue endurance limits. He noted that the requirements of such a test are:

1. It must be expeditious.
2. It should be simple, not requiring elaborate apparatus, or particularly skilled personnel.
3. It should require the minimum number of specimens, which should be of a simple form.
4. It must be accurate.

Gough [4], however, noted that by subjecting a material to periods of cycling in steps of increasing magnitude, it can be made to withstand stresses considerably above the primitive fatigue limit. This phenomenon is referred to as coaxing.

Coaxing refers to the subjecting of a material to stresses below those to which it may be subjected in a long-life fatigue test. This phenomenon, also called "understressing," was investigated early by Smith [5] who first drew attention to the fact that understressing might have an effect on the endurance limit of a material. In particular, he found that many metals are permanently strengthened by under stressing them before fatigue testing in the endurance limit stress regime. Similar examples of raising the fatigue limit by understressing were also reported by Moore and Jasper [6].

Perhaps the most revealing statement regarding the coaxing phenomenon is that of Walter Schütz [7], who, in writing about the history of fatigue, commented on whether research results published in the fatigue literature were useful for the coming generations. He cites as a negative example works on understressing, "which uselessly haunted people's minds for decades." He notes that Ransom and Mehl [8] and others "proved by fatigue tests on a statistical basis that effects that had been claimed for decades, like coaxing by understressing, did not exist." In an extensive study of statistics of fatigue involving numerous tests, Epremian and Mehl [9] showed that, in most cases, understressed specimens have longer fatigue life than virgin specimens at a given stress in the fracture range. While this type of conclusion is often noted in the literature, it has to be pointed out that in the same paper they wrote that "the understressing effect may be interpreted, in part, as a statistical phenomenon based on selectivity. Note that the specimens used to demonstrate coaxing were taken from the population of unfailed specimens tested using the staircase testing procedure. Therefore, they were in the upper range of fatigue strengths because of the selectivity in choosing them and were not representative of the general population of fatigue strengths."

It has been noted over the years that coaxing occurs only in detectable form in ferrous materials, is commonly associated with the phenomenon of strain ageing, and that the final fracture stress after coaxing was greater if the stress was built up slowly [10]. Two

possible phenomena were suggested by Forsyth [11]. One is that understressing may subject a material to less time at stress than in a conventional test and may reduce the amount of environmental degradation. Such an accelerated step test may not be able to simulate the time-dependent effects of atmospheric corrosion and strength-reducing effects which might depend on corrosion. Another phenomenon may be the development and arrest of microcracks at low stresses which would have propagated at higher stress levels. One can only speculate that it may be more difficult to propagate an arrested crack than to start one fresh in an untested material. While Forsyth noted that the coaxing phenomenon had been associated with strain ageing, he concluded that "it is very likely that the strain-ageing phenomenon is peculiarly effective in prohibiting the formation of brittle-component growth, perhaps by plastically deforming the root of the crack and upsetting what is a purely crystallographic cleavage process."

When all is said and done, coaxing, if it exists at all, provides a beneficial effect to a materials' fatigue resistance. Any increase in FLS due to coaxing, however, seems to depend on unknown combinations of material, loading history, and statistics of FLS (discussed later in this chapter in Section 3.5.2). For these reasons, coaxing cannot and should not be considered in design or in the development of a material database for use in HCF design. Ignoring coaxing, however, can only be conservative because of the improvements in FLS that have to, as yet, be demonstrated.

3.2. EARLY TEST METHODS

Standard methods for determination of the fatigue or endurance limit require not only a large number of fatigue tests but also statistical analysis to establish their reliability [12]. Fatigue data corresponding to a given life or what is termed the greatest number of cycles, N_g, e.g. 10^7, can be grouped into three categories according to applied stress level. At high stresses, all specimens fracture before N_g is reached. These stresses correspond to the range of finite life. Over a range of lower stresses, at least one but not all of the specimens fails before N_g: this region is called the transition region. Finally, at some lower stress level and below, no failures are obtained before N_g: this is called the range of infinite endurance. Testing is usually performed to identify the boundary between the transition and infinite endurance regions. For each stress level, a minimum of ten specimens are usually required, and four stress levels are recommended [12]. The data are treated statistically to identify the endurance limit corresponding to a probability of failure of less than some small amount like 1%, depending on the scatter in the data and the width of the transition region. This approach, while both scientifically based and statistically sound, requires an extensive amount of testing which is prohibitive for many investigations, particularly when N_g is a large number like 10^7 or greater. While other non-standard or accelerated methods are available for determining the endurance

limit, the number of specimens and testing time are generally too large for practical engineering applications. An example that requires a large database is a Haigh diagram, which requires data at a number of mean stress or stress ratio conditions.

By early in the 1900s, numerous accelerated tests for endurance limit had been proposed and rejected because they did not prove to be reliable. Among these early accelerated tests was that of Moore and Wishart [13], who developed an "overnight" test based on application of a fixed number of HCF cycles followed by determination of tensile strength. The basis of this test was that fatigue testing below the endurance limit increases the tensile strength and endurance limit, while above the endurance limit, cracks form and ultimately degrade the tensile strength. Commenting on this paper, Gough stated, "I have arrived definitely at the conclusion that no reliable form of short-time test known has yet been devised" and he saw "no fundamental reason why any short-time test can be expected to prove reliable."

Later, Prot [14] developed a rapid test for determining the fatigue limit without using conventional tests under constant stress conditions. His technique involved starting at a stress below the estimated fatigue limit and increasing the stress at a constant rate until failure occurs. Each successive test is conducted at a reduced rate of increase, thereby producing a series of stress values associated with each rate of stress increase. In his approach, one test specimen is required for each rate of increase in stress. Still, it was claimed that this method reduces testing time by nine-tenths. The Prot method, though not widely used today, is considered to be the standard of reference for accelerated testing methods.

An illustrative example of the *S–N* behavior that is inherently assumed in the Prot method is presented in Figure 3.1. Under the assumption used by Prot that the stress

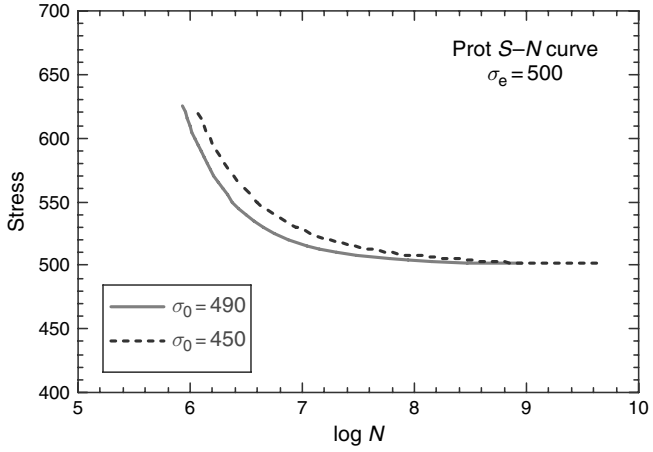


Figure 3.1. Illustrative numerical example of assumed *S–N* behavior for Prot method.

is proportional to the square root of the rate of stress increase, a numerical example is calculated assuming that the endurance limit stress is 500 (arbitrary units). For initial starting values of 490 and 450, the expected *S–N* behavior based on the Prot assumption is shown in the figure. While the method assumes that the starting stress in the constant rate of stress increase is near the endurance limit, the calculations show that there is very little difference when the two different values of initial stress are used. On the other hand, any other shape of an *S–N* curve, particularly at large numbers of cycles near the endurance limit, will not produce a straight line plot and thus makes it difficult to extrapolate to a zero rate of increase of stress from which the endurance limit is determined in the Prot method.

While concerns over coaxing persisted in accelerated test development, the Prot method was validated by Ward et al. [15] on welded SAE 4340 steel and found to be applicable to ferrous metals with a well-defined endurance limit [16]. However, Corten et al. [16] noted that for ferrous metals that are susceptible to coaxing, the Prot procedure appreciably raises the endurance limit compared to that obtained by conventional methods. In a discussion of their paper, they pointed out the following: "Only if coaxing is absent and the number of cycles in each step is sufficiently large (possibly 10^7 cycles), does it appear reasonable to expect that the fracture stress data obtained from the step-up method will agree with the endurance limit obtained from conventional tests." Other work by Dolan et al. [17] showed that improvement in the fatigue life by under-stressing depended a great deal on the relative difference between the under-stress level and the endurance limit. Re-testing with a small increase in stress level resulted in abnormally long life, but re-testing with a large difference in stress level showed no apparent coaxing effect. In structural steels, Hempel [18] observed that fully reversed bending fatigue at a stress level 22% below the endurance limit did not lead to development of slip lines, even at stress numbers in excess of 10^7. At higher stress amplitudes, but still below the endurance limit, slip traces occur only in individual crystallites. At stresses above the endurance limit, slip markings were far more conspicuous and were present in a large number of crystallites. But slip markings do not necessarily lead in every case to the formation of micro- and macro-cracks or to fatigue failure.

The existence of a coaxing effect, while important in establishing the validity of an accelerated test procedure of the type according to Prot, does not appear to have an established scientific basis. One possible explanation of the coaxing effect is one which is purely statistical in nature. Epremian and Mehl [19] point out that elimination of the weaker specimens during fatigue testing below the fatigue limit biases the population of specimens tested at higher stress levels. Because of the statistical selectivity, specimens subsequently tested above the fatigue limit tend to show longer lives. For any of the proposed explanations of the existence of a coaxing phenomenon, it is not felt that coaxing is a real phenomenon in titanium alloys and, therefore, the step-loading test procedure described in the next section is valid for determination of the fatigue limit. The

Prot approach has been found to be reasonably reliable for a titanium alloy [20] and an alternate step-test method was validated in several investigations using Ti-6Al-4V as the test alloy [21].

3.3. STEP TEST PROCEDURES

In addition to the Prot method described above, another form of accelerated test involving step loading was developed by Maxwell and Nicholas [22]. At a fixed stress ratio, a specimen is fatigued to a limit of typically 10^7 cycles at a stress level lower than the expected fatigue limit. After each block of 10^7 cycles, the stress is increased by some small amount (approximately 5% in their tests) until failure occurs at less than 10^7 cycles. The FLS is then determined using a linear interpolation scheme as described in the following equation:

$$\sigma_e = \sigma_0 + \Delta\sigma \left(\frac{N_{fail}}{N_{life}} \right) \tag{3.1}$$

where σ_e is the maximum fatigue strength corresponding to N_{life} cycles, σ_0 is the previous maximum fatigue stress that did not result in failure, $\Delta\sigma$ is the step increase in maximum fatigue stress, N_{fail} are the cycles to failure at the fatigue stress $(\sigma_0 + \Delta\sigma)$, and N_{life} the defined cyclic fatigue life (i.e., 10^6, 10^7, etc.). The linear interpolation concept embodied in Equation (3.1) was developed from the idea that damage accumulation might be a linear function of cycles. While no data were obtained to demonstrate that concept, use of a similar formula to Equation (3.1) based on log N rather than N did not seem to produce values that were as consistent as those with the linear formula when comparing results to interpolated S–N data. For small step sizes, the differences did not appear to be significant.

In much of the work under the National Turbine Engine High Cycle Fatigue Program [23, 24], the step-loading procedure was used to obtain FLS data. Typical steps of 10^7 cycles are used, while $\Delta\sigma$ is taken typically at 5% of the initial load block. The step-loading procedure is shown schematically in Figure 3.2 for blocks of 10^7 cycles. The size of the step depends on the degree of accuracy desired in determining the FLS. Steps as high as 20% of the first block stress have been used to assess effects of FOD on the fatigue limit [25]. In cases such as those, the degree of damage due to FOD is very variable, so accurate determination of the FLS is not warranted. Further, the starting stress for the first block is not very predictable, so small increments could result in a very large number of steps and, consequently, long testing times.

There are some advantages to the use of the proposed technique other than the considerable savings in testing time. The proposed technique results in failure in each specimen, contrary to conventional fatigue testing where some fraction of specimens tested fail and

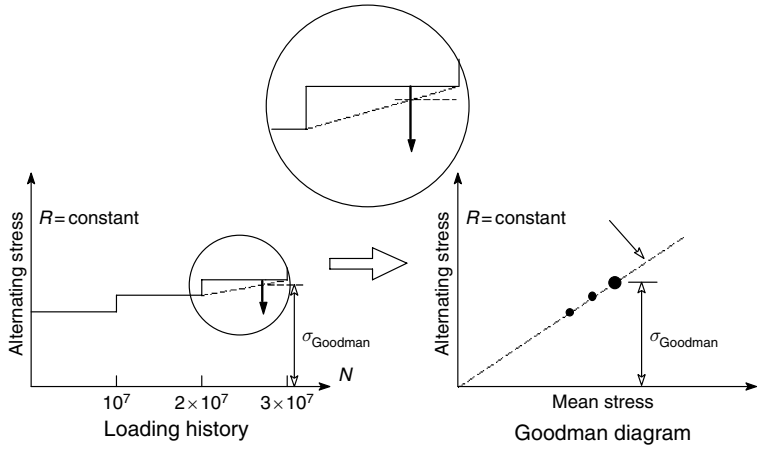


Figure 3.2. Schematic of step-loading procedure.

others do not because the test is terminated after a large number of cycles (run-out). This results in two populations of specimens, one failed and the other unfailed, which are difficult to analyze statistically. Another justification for a non-constant load to determine the fatigue limit is, as Prot [14] points out, "in practice, fatigue loads are not regularly variable, but they are not uniform amplitude loads."

One of the main concerns in establishing material allowables for HCF is the sparse amount of data available and the time necessary to establish data points for fatigue limits at 10^7 cycles or beyond. The conventional method for establishing a fatigue limit is to obtain *S–N* data over a range of stresses and to fit the data with some type of curve or straight-line approximation. For a fatigue limit at 10^7 cycles, for example, this requires a number of fatigue tests, some of which will be in excess of 10^7 cycles. This is both time consuming and costly. One method for reducing the time is to use a high frequency test machine such as one of those that have appeared on the market within the last several years. In addition, the use of a rapid test technique such as one developed by Maxwell and Nicholas [22] involving step loading, described above, can save considerable testing time. It has been demonstrated that such a technique provides data for the fatigue limit of a titanium alloy which are consistent with those obtained in the conventional *S–N* manner [22, 26].

3.3.1. Statistical Considerations

To examine the expected outcome using the step-loading technique, consider the schematic of Figure 3.3. One can define a fatigue limit on an *S–N* curve arbitrarily as N_f, even though there is no assurance that this is a true endurance limit corresponding to "infinite" life. At N_f, there will exist an unknown cumulative distribution function (CDF) which

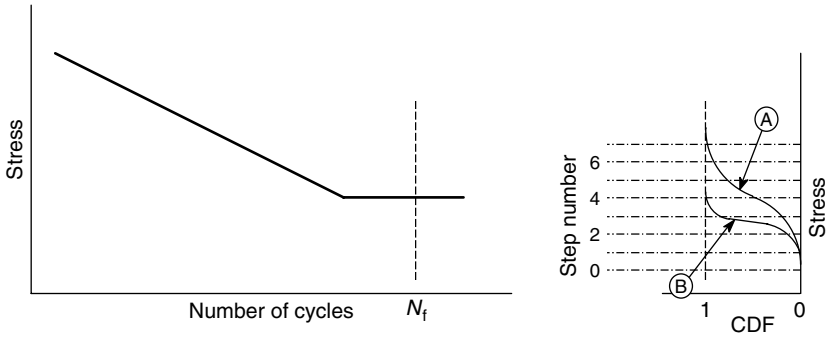


Figure 3.3. Schematic of *S–N* curve and CDF for two different degrees of scatter.

will define the failure function at that number of cycles over some range of stresses. The stress corresponding to CDF = 0 defines the stress level below which there are no failures within N_f cycles. When CDF = 1, the corresponding stress defines the condition under which all specimens fail at or below N_f cycles.* If there is a large amount of scatter as in curve "A," which may occur if the *S–N* curve is very flat, then a larger number of steps in the step-loading technique will be required to cover all of the possible values of stress where failure may occur below the cycle count being considered, N_f. If, however, there is less scatter as in curve "B" or the *S–N* curve is steeper, which will essentially cut off the higher values of stress which cause failure at lower numbers of cycles, then the number of steps is fewer. In either case, the larger the number of steps in a test, the higher is the expected stress. Thus, what might appear to be a "coaxing" effect is no more than the statistics of the distribution of material fatigue strength. The actual number of steps in a step-loading experiment depends on the starting stress, the distribution function or range in stress levels, and the size of the step.

An alternate to the step-loading approach for determining the fatigue limit is to conduct tests at various values of stress up to the number of cycles corresponding to the fatigue limit. Two types of data are obtained. First, some specimens will fail before N_f is reached, and these will provide data for a *S–N* curve which can be fit and extrapolated to N_f. The second type of data will be stress levels for which no failure was obtained within N_f cycles. These stress levels will be denoted as run-outs or lower bounds on the fatigue limit. In conducting tests under constant stress, consider the case where the *S–N* curve is relatively flat such as when the number of cycles, N_f, is very large. As a hypothetical example, consider the fatigue behavior in the region between 10^7 and 10^9 cycles, where it

* It should be noted here that some mathematical representations of distribution functions can go from zero to infinity, such as a normal distribution. In those cases, we have to deal with a situation where the CDF approaches 0 or 1 within some very small probability.

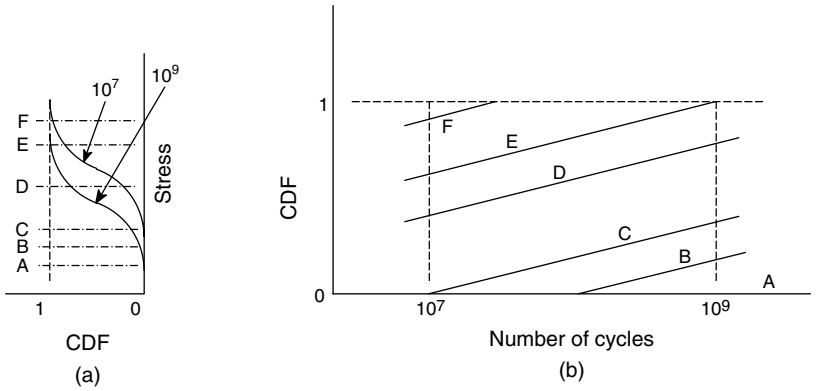


Figure 3.4. Schematic of CDF (a) for two different values of N_f, (b) as a function of N.

has been shown that the S–N curve still has a slightly negative slope for some materials [27]. For illustrative purposes, the CDF for failure within a given number of cycles is shown schematically in Figure 3.4(a) for either 10^7 or 10^9 cycles. At 10^7 cycles, there is no failure for stresses below level "C" and all samples will fail at or above "F." Similarly, at 10^9 cycles, no failure occurs below "A" and all samples will fail at "E" or above. Clearly, "A" corresponds to the fatigue limit at 10^9 cycles. Consider, however, what happens in a typical experimental investigation. The CDF is shown as a function of number of cycles in Figure 3.4(b) for several stress levels depicted in Figure 3.4(a). As shown, there are no failures at "A" while at "F" most samples will have failed below 10^7 and none will reach 10^9. At "E" there is a higher probability of survival beyond 10^7 but all fail by 10^9. At some intermediate level "D," some will fail by 10^7 and most will have failed by 10^9, but as the stress level decreases to "C" or "B," the likelihood of failure before 10^9 decreases. Considering the time and cost of conducting such long life tests, the likelihood of determining the probability density functions for a number of stress levels and, in turn, defining the fatigue limit, is poor. In this situation, the step-loading procedure may provide an equally good answer with fewer tests. Tests conducted at constant levels of stress, separated by equal increments, are discussed later in this chapter (see Section 3.6) along with the statistics for determining fatigue limits and the corresponding scatter.

3.3.2. Influence of number of steps

Experimental data using Ti-6Al-4V forged plate material and employing the step-loading procedure [28] are shown in Figure 3.5. In that investigation, the values of the fatigue limit for four different values of R were not known *a priori*. Thus, the initial stress value in the step-loading procedure was highly variable. The results, plotted against the number of steps, show no indication of a systematic increase with number of steps and, therefore,

no evidence of coaxing. On the other hand, experimental results which show an increase in stress with number of steps are shown in Figure 3.6 where the starting stress for any of the four conditions was either the same or very similar. The tests are on a notched sample with $k_t = 2.2$ with one batch untested and the other subjected to LCF cycling as indicated on the plot [21]. The plots of stress versus number of steps show a linear increase. Since the starting stresses are the same for each condition, the slope is related to the size of the step. Thus, this increase with number of steps is not necessarily coaxing, it is probably no more than the scatter in material behavior as described above.

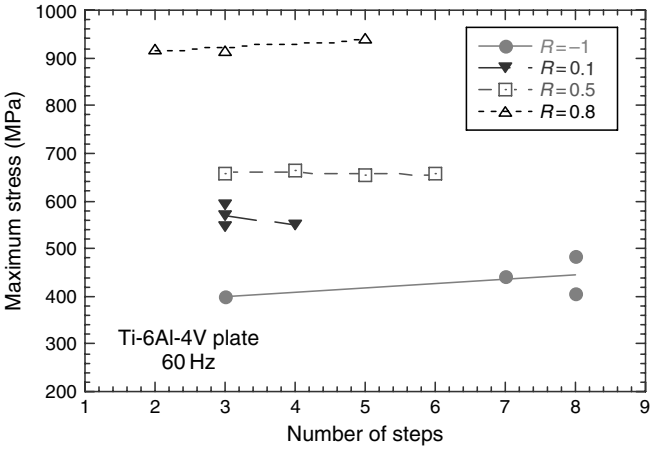


Figure 3.5. Fatigue limit stress vs. number of steps.

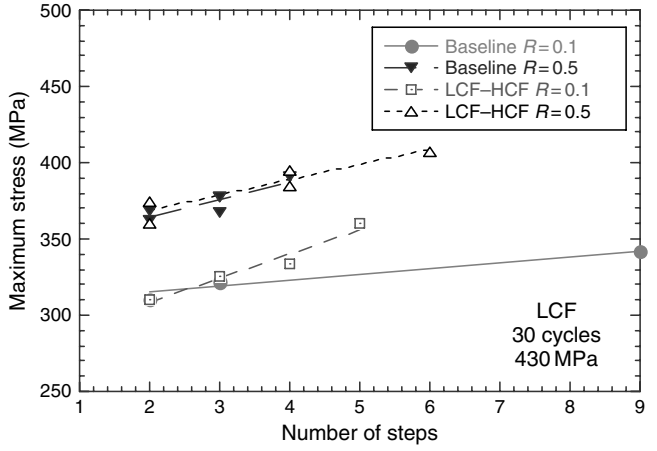


Figure 3.6. Fatigue limit stress vs. number of steps.

3.3.3. Validation of the step-test procedure

Data for a Haigh diagram were obtained using the step-loading procedure for both the bar and plate forms of Ti-6Al-4V [21]. The data are shown in Figures 3.7 and 3.8. In each of the figures, the number of steps that were used for each specimen is indicated in the legend. All steps within an individual step-loading test were conducted with a constant value of R. Careful study of the data shows that there does not appear to be any systematic trend which would lead one to believe that the number of steps has any

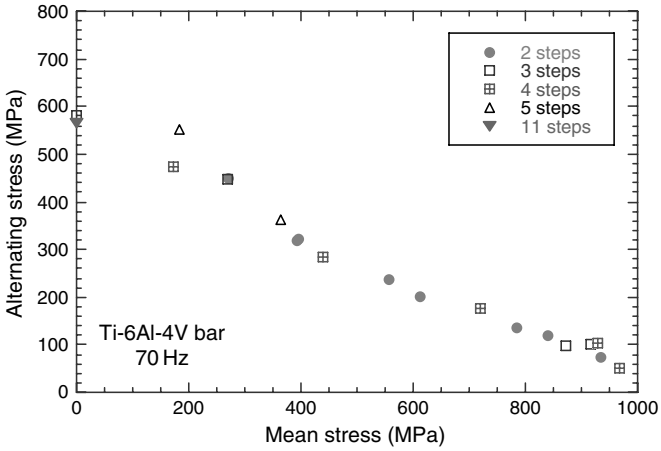


Figure 3.7. Haigh diagram for bar material.

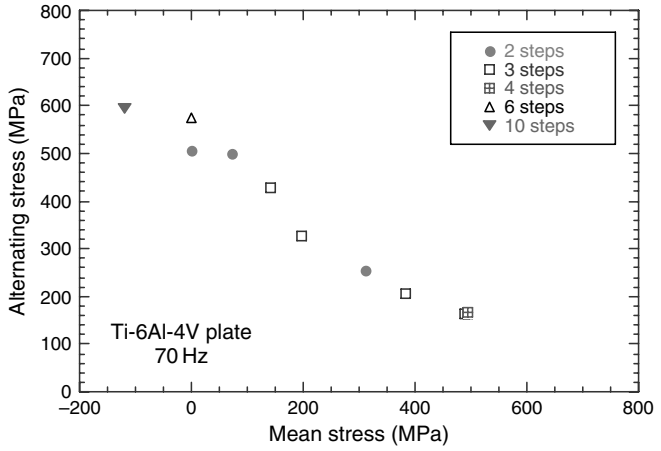


Figure 3.8. Haigh diagram for plate material.

influence on the results. In fact, it is rather remarkable that the expected trend of higher strength versus number of steps from a purely statistical point of view is not observed. This is probably due to the choice of starting stress for each test which was very variable because each test covered a different value of R compared to the prior test.

Conventional S–N tests conducted at 420 Hz on plate material were used to determine the fatigue strength corresponding to 10^7 cycles by least squares fit to the S–N data obtained at lives close to 10^7 cycles. The results are shown in Figure 3.9 for tests conducted at a number of values of stress ratio, R, from 0.5 to 0.8. It can be seen that the data lie right on top of the data from step-loading tests in the same range of R. Further, there seems to be no effect of frequency in going from 70 Hz in earlier tests to 420 Hz in the present tests.

Data were also obtained at $R = 0.5$ and $R = 0.8$ using the step-loading procedure to compare with the interpolated S–N data (horizontal line) as shown in Figure 3.10. Different values of stress in the first loading block, shown on the x-axis, were used to evaluate the effect of number of blocks for the two values of R. Numbers in parenthesis in the figure indicate the number of load blocks used to determine the stress corresponding to 10^7 cycles. In both the plate material used here and the bar material used elsewhere, the failure at $R = 0.5$ is purely fatigue, while at $R = 0.8$, it is observed that the fracture surface shows no indication of fatigue, but rather, ductile dimpling [29]. This issue is discussed later. In both cases, however, Figure 3.10 shows no indication of a trend with number of blocks or starting stress for the step-loading procedure.

Data obtained at 1.8 kHz are presented in Figure 3.11. Three types of tests are represented, conventional S–N to failure, terminated S–N producing run-outs, and step loading at either 10^7 or 10^8 cycles. While the vertical scale is blown up significantly, it can be

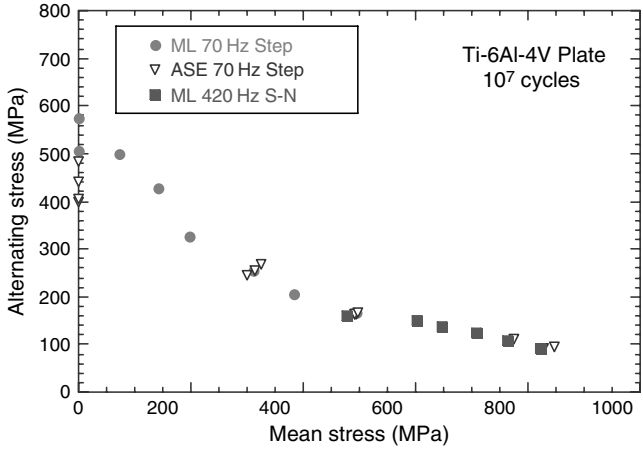


Figure 3.9. Haigh diagram for plate material comparing step test and S–N data.

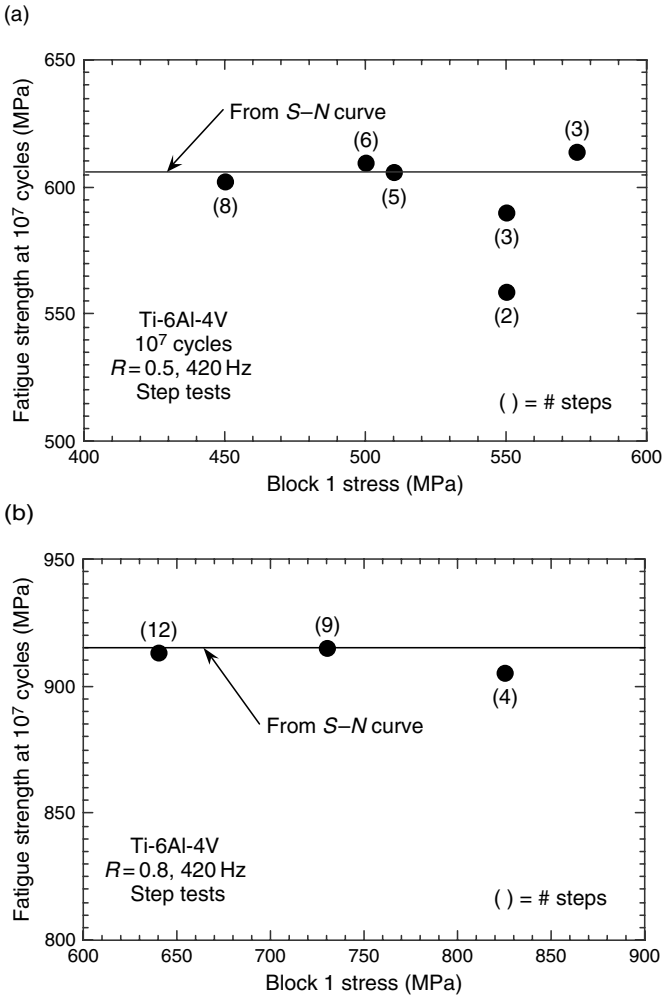


Figure 3.10. Influence of block 1 stress on FLS at 10^7 cycles in step-loading fatigue limit strtess; (a) $R = 0.5$, (b) $R = 0.8$.

noted that there is very little scatter at $R = 0.8$ where all the tests were conducted, and no influence of a history effect due to the step-loading procedure. The lower step-test data point at 10^8 cycles represents two independent tests which had a maximum stress within 1 MPa of each other.

The data obtained at $R = 0.8$ are of particular interest in the evaluation of the validity of the step-loading procedure. In an investigation on the bar material, Morrissey et al. [29] noted that at high values of R, the material accumulated strain under fatigue loading.

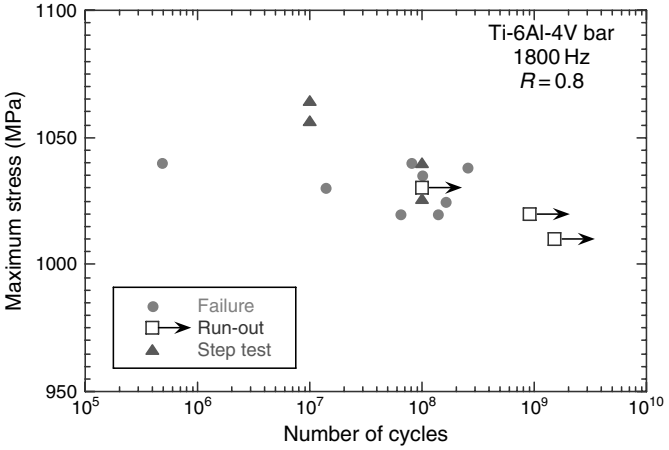


Figure 3.11. Fatigue limit stress results at $R = 0.8$, 1800 Hz.

Tests conducted at different frequencies showed that the strain accumulation was dependent primarily on number of cycles, not on time, so that the phenomenon could not be considered to be cyclic creep. Rather, the strain accumulation is due to ratcheting. A similar phenomenon has been observed in the Ti-6Al-4V plate material, where cycling at stress ratios higher than approximately 0.7 leads to strain accumulation. Micrographs of the fracture surface at various magnifications taken with a scanning electron microscope (SEM) are presented in Figures 3.12 and 3.13 for stress ratios, R, of 0.7 and 0.8,

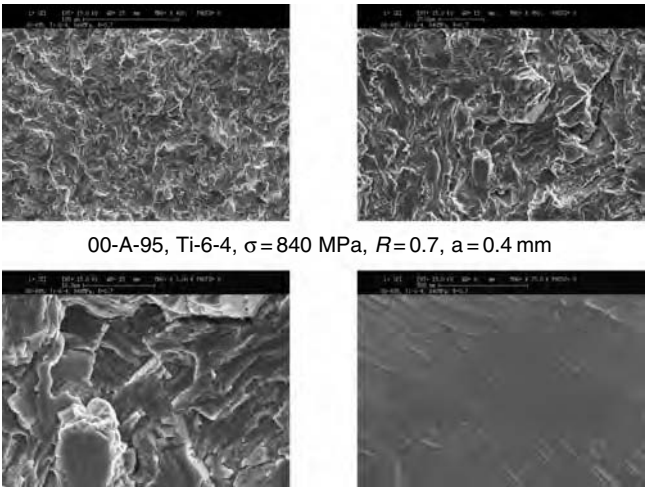


Figure 3.12. Fractographs at $R = 0.7$.

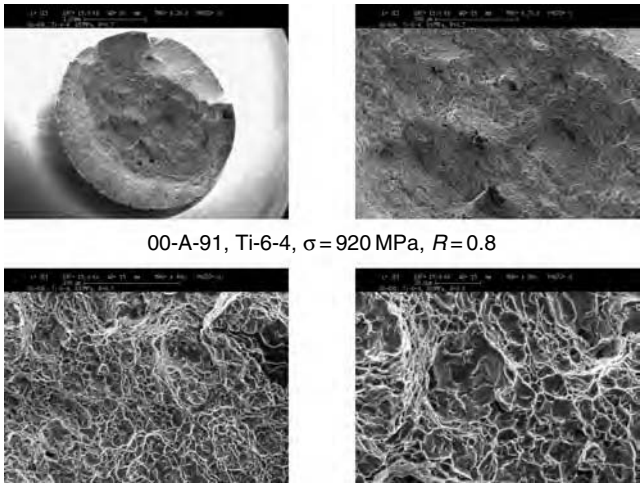


Figure 3.13. Fractographs at $R = 0.8$.

respectively. It can be observed that at $R = 0.7$ (Figure 3.12), the fracture surface looks like fatigue with well-defined faceted features and evidence of striations. At $R = 0.8$ (Figure 3.13), the features are those of a tensile test with ductile dimpling in evidence and no indications of cleavage or striations. The crossover point, at about $R = 0.75$, is nominally the same as in the bar material as reported by Morrissey et al. [29].

Data obtained over a range of frequencies from 30 to 1000 Hz under the Air Force HCF program at various laboratories are presented in Figure 3.14 for $R = 0.8$. Including

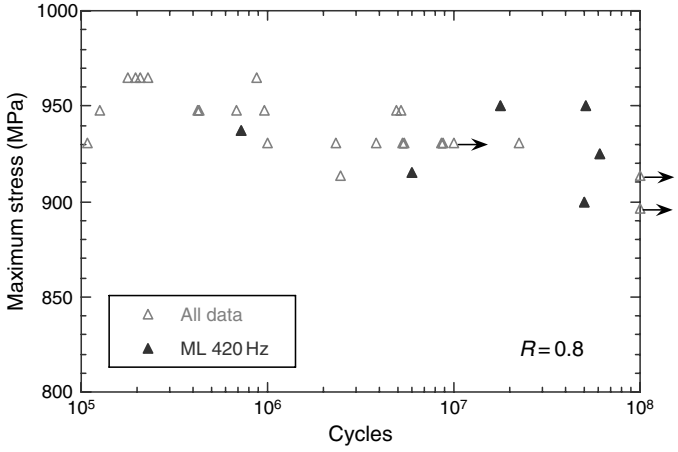


Figure 3.14. *S–N* data obtained from 30 to 1000 Hz.

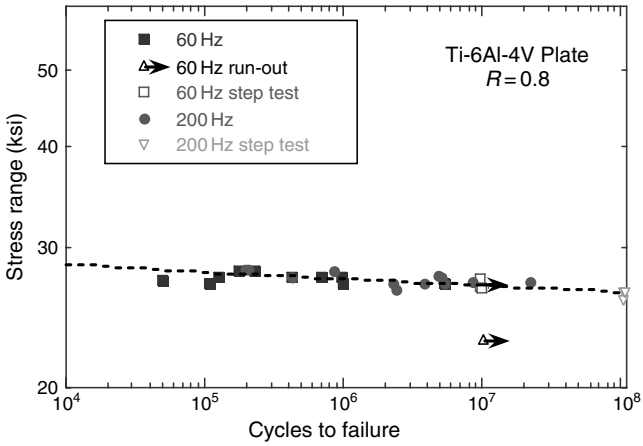


Figure 3.15. Honeywell data at 60 and 200 Hz.

the Materials Laboratory (ML) data at 420 Hz, there is very little scatter over the fatigue cycle range from 10^5 to 10^8 cycles, and no effect of frequency although frequencies of each data point are not shown. Additional data from Honeywell are shown in Figure 3.15 at $R = 0.8$ at both 60 and 200 Hz. No frequency effect is apparent, the scatter is minimal, and data using the step-test procedure at 10^7 cycles fall right on top of the other data. From these results, as well as from the data in Figure 3.11 at 1800 Hz, it is concluded that step testing produces an accurate estimate of FLS in the 10^7–10^8 life regime for $R = 0.8$ in the titanium plate where strain ratcheting is the dominant fatigue failure mechanism.

3.3.4. Observations from the last loading block

An interesting observation was made by Moshier et al. [30] when evaluating the data from the step-test method on specimens with LCF cracks compared to data on specimens with no cracks. The last loading block, defined as the block of 10^7 cycles during which failure occurred, can have a cycle count anywhere from 1 to 10^7. The data for number of cycles to failure in this block are normalized with respect to 10^7 to show at what fraction of the block failure occurred. The results, presented in Figure 3.16, show that for specimens with no prior cracks, the failure can occur anywhere in the block. When cracks are present, however, failure always occurred early in the loading block. These data show that there appears to be a very well defined HCF threshold for a cracked specimen for which failure occurs within a short time, typically under one million cycles, or does not occur at all for a given applied stress (or K). Alternately, these data show that when a crack is present, we are dealing only with the propagation phase of fatigue which is small compared to the nucleation phase which dominates the HCF life in an

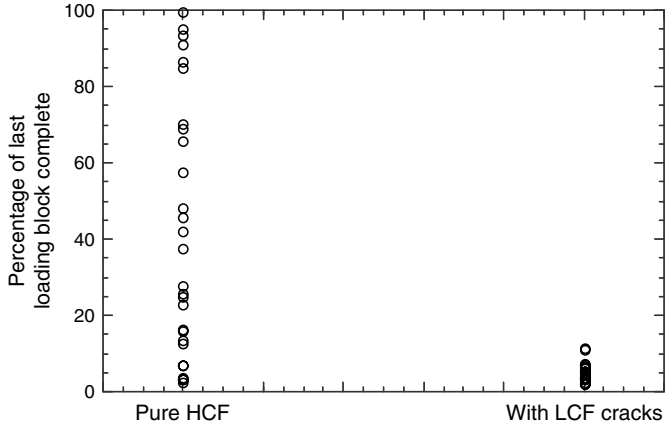


Figure 3.16. Comparison of number of cycles in last loading block of step test for HCF with and without LCF precrack.

uncracked specimen. This observation is similar to the speculation in Chapter 2 where tests at negative R are thought to initiate cracks at stresses below the failure stress when using step loading.

Additional data are available on the number of cycles on the last loading block in the step-loading tests when a crack is present. The data of Figure 3.16 are supplemented with additional data on precracked notch specimens and replotted in Figure 3.17 as a function of crack size. While very small crack lengths did not show a very well

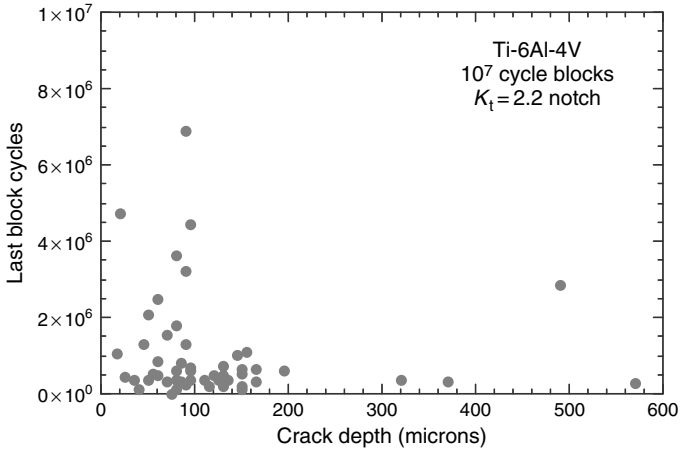


Figure 3.17. Number of cycles in last block for notched bars with LCF cracks.

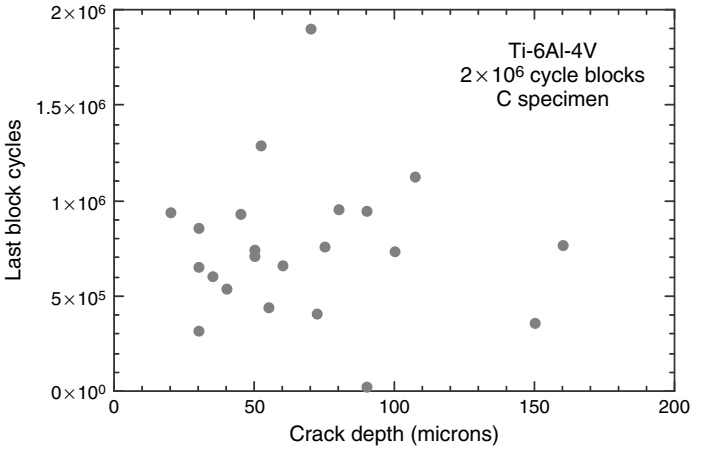


Figure 3.18. Number of cycles in last block for C-specimens with LCF cracks.

defined threshold, the longer crack lengths showed that specimens typically failed early in the block, within a million cycles, indicating that the precrack eliminated some of the initiation life. A similar observation can be made for the data in Figure 3.18 which are obtained on a C-shaped specimen which was originally a pad in a fretting fatigue experiment where cracks were formed on the pad in the contact region [31]. From earlier observations, the HCF load block was reduced from 10^7 to 2×10^6 cycles. Here, again, most of the failures occur within a million cycles, indicating that initiation life in the step tests is reduced or eliminated. Of significance is the observation that in both series of tests, uncracked specimens failed at a random number of cycles up to 10^7, which was the loading block used in the step tests in both cases for uncracked specimens.

Another example of the small number of cycles in the last block of step testing can be seen in the work by Caton [32] on commercially cast aluminum alloy W319. In this material, porosity plays the role of initial defects and, in that work, is treated as an initial crack. Experiments were performed on three solidification conditions referring to average secondary dendrite arm spacing (SDAS) of approximately 23 μm, 70 μm and 100 μm denoted by low, medium, and high, respectively. The step-loading technique to determine the FLS involved increments that were typically under 10% of the previous step stress and each step was carried out to 10^8 cycles or until failure occurred. The number of cycles in the last block is plotted in Figure 3.19 for the three material solidification conditions. With the exception of one data point, the results show that the failure occurs early in the last step, indicating that the threshold for crack extension is quite well defined in this material and that the initiation phase occurred at lower stresses than the final block. For a material with initial defects, there may be little

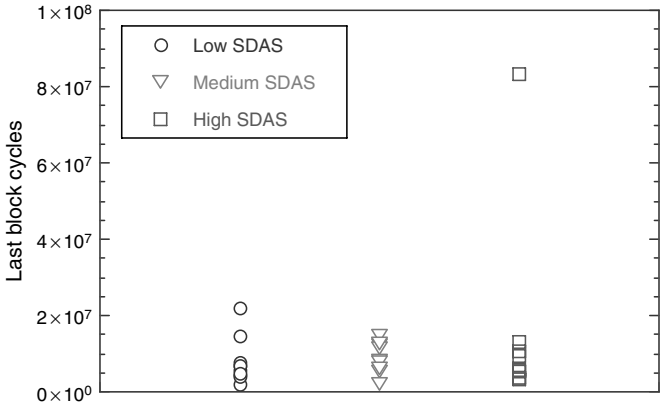


Figure 3.19. Number of cycles in last block for cast aluminum step-tested at 20 kHz to 10^8 cycles (data from [32]).

or no initiation phase because defects that act like cracks are already present in the material.

Finally, we examine the results of fatigue limit testing using conventional constant-stress testing. Exploring the fatigue limit corresponding to 10^9 cycles in a 1.8 kHz testing machine, fatigue life and run-out data [33] are shown in Figure 3.20. It appears that there is a small degree of scatter in the data, but the fatigue limit at 10^9 cycles can be established as approximately 1020 MPa. It remains to be shown if a similar number can be obtained using the step-test method using fewer specimens.

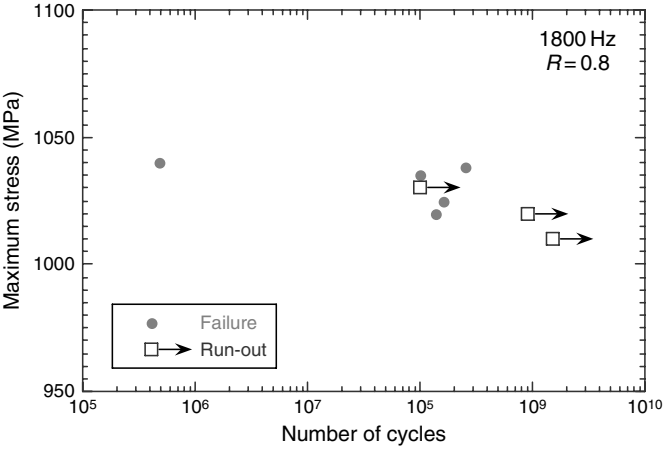


Figure 3.20. S–N data for establishing N_f at 10^9 cycles.

3.3.5. *Comments on step testing*

The results obtained on Ti-6Al-4V do not provide any conclusive evidence of a coaxing effect. On smooth bar specimens and ones with carefully machined notches, the fatigue limit is expected to have a small amount of scatter. The experimental data show this in general, but the occasional data point which is higher than expected can either be attributed to scatter or to coaxing. A systematic study of coaxing has not been conducted, but up to this point the step-loading procedure appears to be a valid method which saves considerable testing time. For specimens which have damage from FOD or fretting fatigue, the statistical scatter is expected to be much larger. Whether or not high values of a FLS are due to scatter or coaxing remains a question that may never be answered. Fortunately, in design, an engineer does not have to worry too much about the occasional high value of the fatigue limit, but rather the low ones and the range of experimental scatter. For these purposes, a step-loading technique appears adequate for use on Ti-6Al-4V in both bar and plate form. Its validity for use on other materials is yet to be established.

Another way to present data from step testing is illustrated in Figure 3.21 where, in the test series, most of the tests had failures during the first step. Thus, what started out as a planned step test series to evaluate the fatigue limit became largely an S–N test program. Nonetheless, four tests reached the second loading block of 10^7 cycles and the run-out data are shown with horizontal arrows. The data points for cycles on the last block are also plotted. In this test series, the step sizes for the four step tests ranged from 11 to 19%, somewhat higher than what has been recommended. The first set of data points, labeled "No step data" are conventional S–N data that could be extrapolated to longer lives to estimate a FLS corresponding to 10^7 cycles. Such a value would appear to be somewhat below 110 ksi as seen in the figure. No attempt was made to obtain a specific

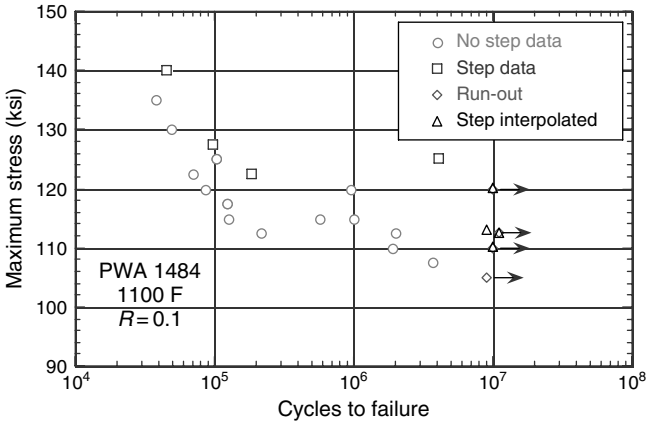


Figure 3.21. Experimental data on PWA 1484 from step test series.

value because of the limited amount of data, particularly in the longer life region. The next set of data points, denoted as "Step data," are experimental values of the cycles to failure in the last loading block of the step tests plotted against the stress that was used in that block. In all four cases, the number of cycles represents that obtained in the second block. Because of the large step sizes, one might be tempted to use these values under the assumption that no history effect is present from the first loading block. This turns out to be a very questionable assumption since failures occurred in other samples tested at the same stress level as in the first loading block. These stress levels can be seen from the data plotted as run-outs. These represent the first loading block of the step tests and, in a conventional *S–N* testing program, would be the censored run-out data. Arrows have been added to help identify the points which all correspond to a fatigue limit of 10^7 cycles. Looking at these data combined with the "No step data" leads one to revise the estimate for the FLS because there are now 3 run-out points at or above 110 ksi. Dealing with such limited data sets, the conclusion that there is a lot of scatter in the FLS of this material starts to become more of a reality. Finally, we look at the four interpolated points as computed from the step-testing procedure described earlier. These seem to show that the fatigue limit is in the range 110–120 ksi. The above data set, albeit quite limited, also shows some aspects of what has been interpreted as a coaxing effect. The data points from the last cycle block in the step tests seem to lie above the remaining *S–N* data, assuming that the first block of loading did no damage. A better way to interpret these points is that they are from a censored set of samples, those that did not fail during the first loading block. This simple data set and the various methods of estimating the FLS serve to illustrate some of the complex issues that arise in trying to determine FLSs from experimental data, especially when the number of available samples or tests is quite limited and run-out data are involved. This subject is discussed in more detail later in this chapter.

3.4. STAIRCASE TESTING

In addition to their statistical studies of number of cycles to fracture at each of a number of stress levels, Ransom and Mehl [8] introduced a new abbreviated statistical method known as "staircase testing." which is still widely used today. In a series of tests, the stress level for the next test is determined by whether the previous specimen failed or ran unbroken for 10^7 cycles (survived). If the specimen failed, the stress on the next test is reduced by one step. If the specimen survived, the stress on the subsequent specimen is raised by one step, and so on. Statistical methods, described below, are then used to determine the average endurance limit as well as the standard deviation. The results of such tests on an SAE 4340 steel are shown in Figure 3.22 which includes the values of the mean stress, σ_0, and the range $\pm 2\sigma$ where 95% of the values would fall.

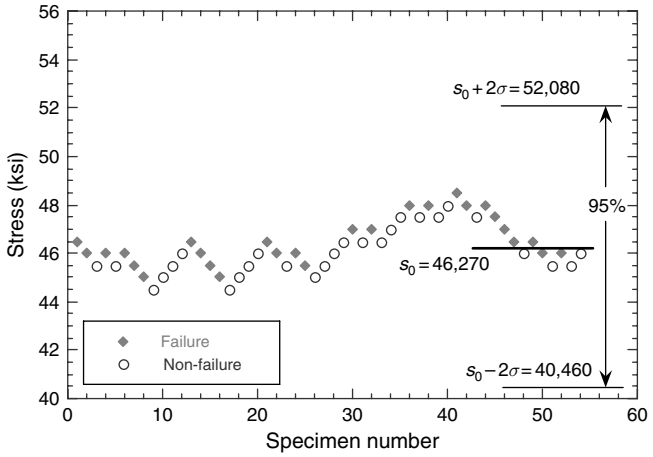


Figure 3.22. Results of staircase testing on an SAE 4340 steel. Data are taken from [8].

The staircase method involves conducting a series of tests to a predetermined number of cycles corresponding to what is defined as the FLS. The cycle count (often 10^7 cycles or less) is assumed to be large enough to produce an endurance limit, but data show that an endurance limit may not exist for most materials. Nonetheless, the FLS is a useful number for many applications, particularly when the cycle count exceeds the number of cycles that may be reasonably expected in the lifetime of a given application. In the staircase method, the stress increment from one test to another is kept a constant.*

3.4.1. Probability plots

At the end of the up-and-down method, there are data at each stress level that was reached which contain either failures or run-outs. Thus, for each stress level, the test data can be used to calculate the percent of tests in which failure occurred. These data are used, in turn, to compute a mean stress level at which 50% fail, 50% survive (run-out) and a standard deviation about the mean. Some of the earliest data on the statistical nature of FLSs, or endurance limits, were presented by Epremian and Mehl [9]. Based on a limited number of staircase tests, the data shown in Figure 3.23 were obtained. They are plotted on a linear scale as percent failures against stress for SAE 1050 steel. This type of plot shows the cumulative distribution of percent failures for discrete values of stress level as used in the staircase tests. If, as was done at the time, a normal distribution is assumed, then a probability plot will produce a straight line as is illustrated for the same data in

* The staircase method was referred to as the "up-and-down" method in the early days of its development and usage.

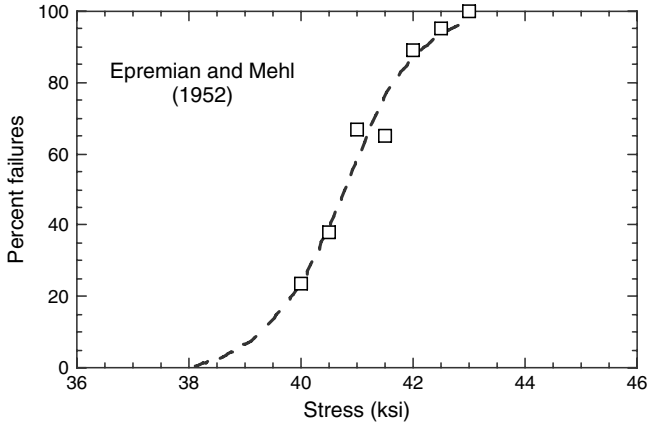


Figure 3.23. Experimental data of Epremian and Mehl on SAE 1050 steel [9].

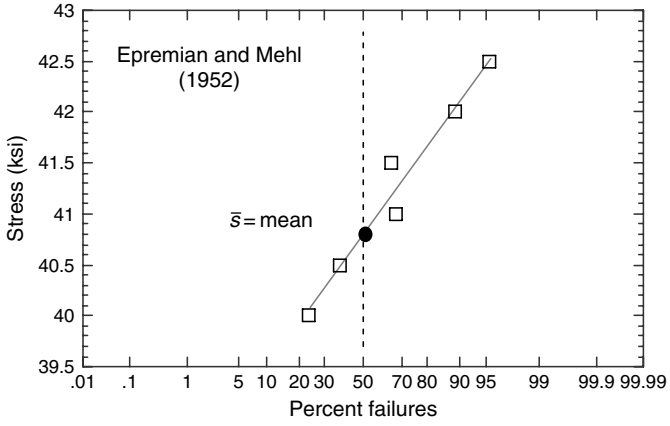


Figure 3.24. Probability plot of data from Epremian and Mehl [9].

Figure 3.24. On the probability plot, the mean value, $\bar{s}$ corresponds to the intersection at 50% failures (40.8 ksi), and the slope of the line is a measure of the standard deviation. If $\bar{s}$ is the mean endurance limit and σ is the standard deviation ($\sigma = 1.028$ ksi), then $\bar{s} \pm 2\sigma$ includes 95% of the endurance stress range.

Other examples of data from staircase tests can be used to illustrate the nature of the probability plot used to estimate the mean of the distribution function and the ability of a normal distribution function to represent the data. The results from Ransom and Mehl [8] are plotted on a linear scale in Figure 3.25 and on probability paper in Figure 3.26. These results are derived from a total of 54 tests, where equal numbers of failed and surviving

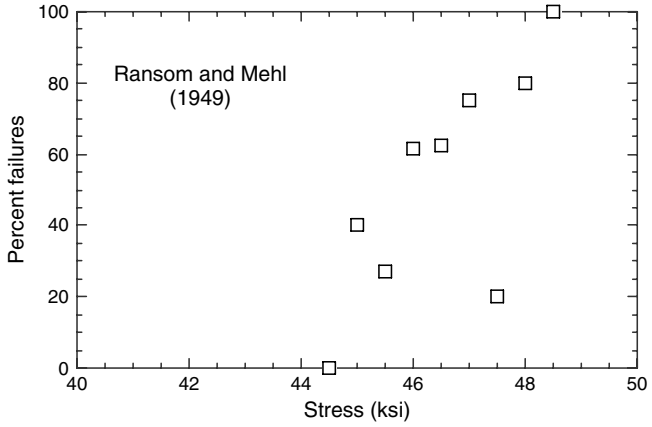


Figure 3.25. Experimental data of Ransom and Mehl [8].

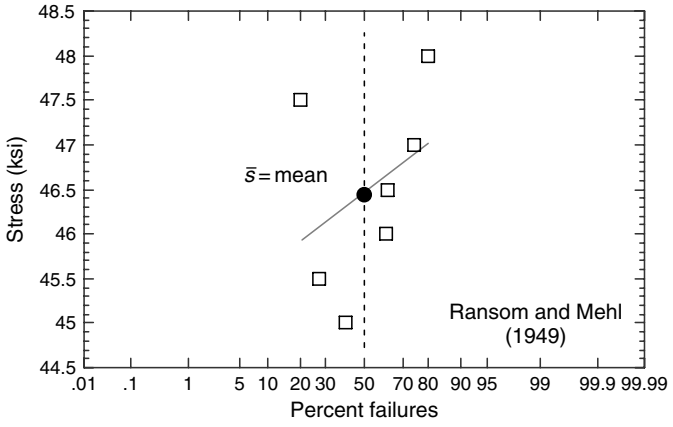


Figure 3.26. Probability plot of data from Ransom and Mehl [8].

specimens were obtained (27 each). Figure 3.25 shows that a simple distribution function would not be able to represent these data to any reasonable extent. The plot includes the stress level at which all of the specimens failed in the staircase testing, even though this number is of little statistical significance. Continuing, however, with a probability plot, Figure 3.26, an estimate of the mean is obtained as the intersection of the best-fit curve (linear) with the 50% probability of failure line.

Similar plots are made from the results of 26 staircase tests on Ti-6Al-4V at a frequency of 900 Hz and a stress ratio $R = 0.1$ [24]. The linear plot, Figure 3.27, shows that a distribution function might represent this data set. Included in the plot, as done above

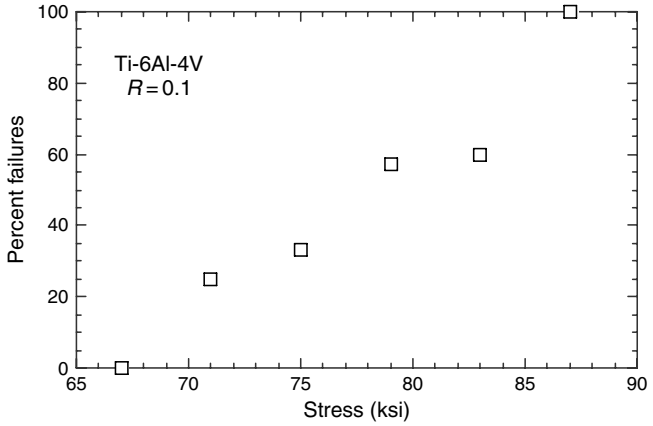


Figure 3.27. Experimental data on Ti-6Al-4V from National HCF program.

for the Ransom and Mehl data, are the stress levels where either none or all of the samples failed. The probability plot for the titanium data is presented in Figure 3.28. The limited data show that a straight line, representing a normal distribution, fits data at the four stress levels where both failures and survivals occurred reasonably well. Two additional data points, shown as circles, represent stress levels where either all or none of the specimens failed. Assigning a probability of 99.9 and 0.1 to these stress levels shows that these would not correspond to a normal distribution. Because there are so few data at the extremes of stresses used in the staircase method, trying to estimate the tails of a normal distribution curve is nearly impossible.

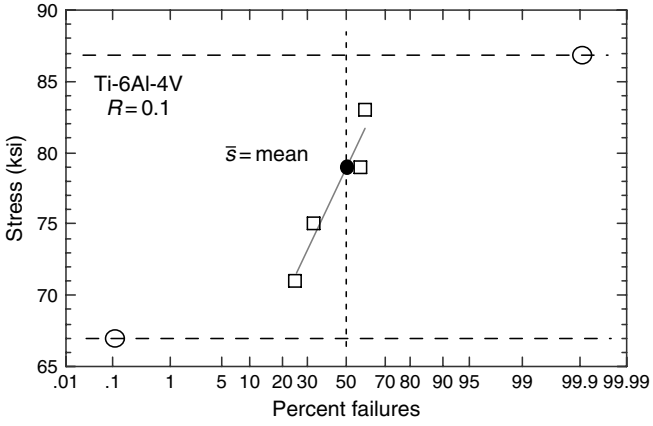


Figure 3.28. Probability plot of data on Ti-6Al-4V from National HCF program.

3.4.2. Statistical analysis

Data from staircase tests can be analyzed statistically by assuming any type of statistical distribution for the percent failure data. Normal and Weibull distributions are the most commonly used, but lognormal and smallest extreme value (SEV) distributions are also found to be useful. If the stress increments are not constant, or data are obtained at lives beyond the defined life used for the endurance limit definition (10^7, for example) then statistical analysis of the data becomes more complicated and other methods have to be introduced [34]. An example of such data can be found in the final report on the National HCF Program [24] where staircase tests, using 10^7 as the reference, often continued beyond that cycle count because there was no automatic shutoff at 10^7 cycles if failure did not occur when tests ran over a weekend or holiday.

For a limited set of data, the staircase method provides nearly the same value of the endurance limit as regular *S–N* tests at constant stress levels. For a very large number of tests, however, at many different stress levels in *S–N* testing, the *S–N* approach provides more information about the dispersion of the endurance limit than the staircase test method because fewer tests are conducted at the extremes of stress in the staircase method. In the staircase method, it is assumed that the endurance limit is a statistical variable. What is quite surprising is that, over the years, the endurance limit has often been treated as a material constant. Epremian and Mehl [19], in 1952, noted, "It has been known for some time that the fatigue life of a metal at a given stress varies statistically and more recently it was discovered, in this laboratory,* that the endurance limit is also a statistical quantity and not an exact value."

3.4.2.1. Dixon and Mood method

The statistics of the staircase method can be found in the paper by Dixon and Mood [35]. The staircase method, or the "up-and-down" method, is sometimes referred to as the Dixon and Mood method and was developed for explosives research where an explosive is dropped from a certain height and it either explodes or survives. This is an example of an "all or none" philosophy that has been applied to the determination of fatigue limits corresponding to a fixed number of cycles, 10^7, for example. The primary advantage of this method is that it automatically concentrates all of the testing near the mean. As opposed to testing equal numbers of specimens at various levels, the up-and-down method may save of the order of 30–40% in the number of observations [35]. Another great advantage to the method is that the statistical analysis is quite simple under certain conditions.

Many advances in statistical analysis of data come from the field of biology. In the book by Finney [36], for example, the statistics dealing with the effectiveness of insecticides

* Carnegie Institute of Technology.

is discussed based on experimental observations of the type that are classified as all-or-nothing or quantal. While it is generally desirable to have quantitative measurements, many cases can be expressed only as "occurring" or "not-occurring." The obvious example with insects is death. The analogous situation with FLSs, especially those obtained from staircase type testing, is failure or survival (run-outs) after a certain number of cycles. Not only is it important to analyze the data, but the planning of the experiments is equally important. The type of fatigue testing carried out, for example, the number of tests at each of several stress levels, can influence the results. In the application of statistical methods to biological data, Fisher [37] suggested that the statistician should be consulted during the planning of an experiment and not only when statistical analysis of the results is required. His advice on experimental design may greatly increase the value of the results eventually obtained, whether they be biological experiments or FLS experiments.

For the staircase method, we can determine the average fatigue limit, μ_{sc}, and its standard deviation, σ_{sc}, from the equations of Dixon and Mood [35], which are also presented in an ASTM publication [38].* The method is based on a maximum-likelihood estimation (MLE) and provides approximate formulas to calculate the mean and standard deviation, assuming that the FLS follows a Gaussian (normal) distribution. The equations for the mean and standard deviation are

$$\mu_{sc} = S_{i=0} + s\left(\frac{\sum_{i=0}^{i_{max}} i m_i}{\sum_{i=0}^{i_{max}} m_i} \pm 0.5\right) \tag{3.2}$$

$$\sigma_{sc} = 1.62\, s\left(\frac{\sum_{i=0}^{i_{max}} m_i \sum_{i=0}^{i_{max}} i^2 m_i - \left(\sum_{i=0}^{i_{max}} i m_i\right)^2}{\left(\sum_{i=0}^{i_{max}} m_i\right)^2} + 0.029\right) \tag{3.3}$$

$$\text{provided} \quad \frac{\sum_{i=0}^{i_{max}} m_i \sum_{i=0}^{i_{max}} i^2 m_i - \left(\sum_{i=0}^{i_{max}} i m_i\right)^2}{\left(\sum_{i=0}^{i_{max}} m_i\right)^2} > 0.3 \tag{3.4}$$

When the quantity above is ≤ 0.3, the mathematics becomes very complicated and a rough approximation can be made using $\sigma_{sc} = 0.53\, s$ [35]. In the above equations, s is the step size, the parameter "i" is an integer that denotes the stress level and i_{max} is the

* The subscript "sc" refers to staircase tests. In statistics, μ and σ are commonly used to represent the mean and standard deviation, respectively. The latter often causes confusion because σ is used to represent stress in the field of solid mechanics.

highest level in the staircase, while m_i is the number of broken or non-broken specimens at level i, depending upon whether or not most of the specimens are non-broken or broken, respectively. If most of the specimens have broken, $i = 0$ corresponds to the lowest step at which a specimen survives. On the other hand, if most of the specimens survive, $i = 0$ is the lowest stress at which a specimen fails. The plus sign in Equation (3.2) is used when the analysis is based on the survivals, and the minus sign when it is based on the failures. This rule is often stated incorrectly in the literature (see [34, 35], for example) or not addressed at all (see [39], for example). It is somewhat confusing because if failure is the more common event, then the analysis is based on the number of survivals. Thus, it should be stated (correctly) that the plus sign is used when the more frequent event is failure, and the minus sign is used when the more frequent event is survival. In the case where equal numbers of specimens fail or survive, either calculation provides the same result as would be expected. Of significance is the observation that the computations are based on the incidence and values of the *less* frequent event, failure or survival.

Some examples of the application of the analysis of the distribution function for some specific data sets are given here. The data of Epremian and Mehl, Figures 3.23 and 3.24, Ransom and Mehl, Figures 3.25 and 3.26, and titanium from the National High Cycle Fatigue program, Figures 3.27 and 3.28, are summarized in Table 3.1.

The calculated values for the mean stress, shown in the table, agree reasonably well with those shown in the probability plots, Figures 3.24, 3.26, and 3.28, since both are based on an assumption of a normal distribution function for the FLS. The first series of tests, those of Epremian and Mehl, represent the largest number of tests of the three being evaluated, and show the best fit to a normal distribution curve in Figures 3.23 and 3.24, and the lowest ratio of the standard deviation, s, to the mean as shown in the last column of Table 3.1. The data of Ransom and Mehl, on the other hand, show little resemblance to a normal distribution function, Figures 3.25 and 3.26, yet the calculation for the ratio of the standard deviation to the mean shows this ratio not to be that large. The third set of data on titanium represents the fewest number of staircase tests, shows a reasonable fit to a standard deviation, but indicates a very high degree of dispersion. The dispersion appears to be more a function of the number of tests than the true inherent dispersion of the material property (FLS) being evaluated.

Another application of the staircase method is illustrated in [40] where, for each of 3 mean shear stresses, the alternating shear stress for a fatigue limit corresponding

Table 3.1. Summary of statistical evaluations using Dixon and Mood method

Reference	*# fail*	*# survive*	μ_{sc} (ksi)	σ_{sc} (ksi)	*σ/mean*
Epremian and Mehl	93	43	40.96	1.43	1.15
Ransom and Mehl	27	27	46.27	2.93	1.29
National HCF Ti	12	14	78.0	8.95	1.60

to 5×10^6 cycles (run-out) was desired. Thirteen specimens were tested at each mean stress (0, 45, and 90 MPa) using a shear stress increment of 15 MPa. With the limited number of specimens (13) tested at each mean stress level, the calculated standard deviation was determined to not be statistically significant because of the small number of tests. It is of significance to note that the standard deviation was found to be less than the stress increment of 15 MPa. Using the assumption that the fatigue limit follows a normal distribution, the authors concluded that there were not enough samples tested to compare the fatigue limit as a function of mean stress in a statistically significant manner.

Data from fatigue strength tests, where the result of any single test is either fail or survive before a specific number of cycles at the given stress level (S) of the test, can be plotted in terms of the proportions failed (P), the number failed divided by the total number tested at that stress level. The fatigue strength data can be obtained from either testing equal numbers of specimens at equally spaced stress levels (P–S tests) or from up-and-down (staircase) testing, described above, where the majority of tests end up at stresses near the median fatigue strength at the specific number of cycles. The up-and-down testing can be used to precede the P–S tests, or to generate design data. But it has been pointed out that the insoluble problem in strength analyses is to establish the true shape of the underlying strength distribution function [41]. If only the median strength is desired, then it makes little difference which distribution function is used in analysis of the data. On the other hand, if the tails or the spread of the distribution function are needed for design, for example, then the results are very sensitive to the form of the actual distribution function. Another advantage of the up-and-down method is that small sample numbers can be used to accurately determine the median strength [41]. Regardless of the analysis involved, there are basically two forms of plots which display quantal response data (fail or survive), one having a linear scale for P and one where P is plotted on probability paper. Such plots were shown, for example, in Figures 3.23 and 3.24, above.

The primary requirement for the use of the simple statistical analysis of the results from staircase testing is that the variate under analysis be normally (Gaussian) distributed. If not, the natural variate can be transformed to one that does have a normal distribution. The logarithm of the natural variate is often used. While the staircase method is particularly effective in estimating the mean, it is not a good method for estimating the extremes of the distribution unless normality of the distribution can be assured. A second condition is that the sample size be large if the analysis is to be applicable since it is based on large sample theory. A third condition requires that the standard deviation must be larger than the interval of the variate in the staircase testing procedure, a condition that is not generally known before the testing begins. A more desirable situation is if the interval used is less than twice the standard deviation [35]. Lin et al. [34] recommend that the fixed stress increment should be in the range from half to twice the standard deviation.

3.4.2.2. Numerical simulations

To further demonstrate some of the statistical aspects of the staircase test procedure, numerical simulations have been conducted. The FLS is assumed to be distributed normally. A hypothetical material having a median FLS of 50 and a standard deviation of 5 was chosen. The mean value is an arbitrary unit for this material, only the standard deviation, s, is of importance in the numerical examples.

The first numerical exercise consisted of simulating a series of staircase tests using different numbers of samples, ranging from 10 to 50, and different step sizes, ranging from $0.1s$ to $1.0s$, where s is the standard deviation (5 in this case). For each test simulation, a random number for the FLS was generated from EXCEL corresponding to a normal distribution with the mean of 50 and $s = 5$. The protocol for the staircase test was followed numerically, but the first test of each series was started at the mean value of 50. For each different value of the stress increment, the same set of random numbers for the FLS was used for each set of numbers of tests. The results are summarized in Table 3.2. The results are not statistically very significant since only one simulation was conducted for each condition. Nonetheless, the values for the standard deviation obtained from the formulas of Dixon and Mood [35] show no trend or relationship to the "true" distribution where a value of $s = 5$ was chosen. On the other hand, the values for the mean FLS, which was chosen as 50 in the simulation, are reasonably close for all of the conditions simulated. While little can be stated about the significance of these results, the trend for a better value (closer to 50) with larger number of tests and decreasing size of the increment between each successive test simulation in the staircase procedure seems to be established, although very weakly. From these results, it would be recommended that the fixed stress increment would ideally be less than half of the standard deviation which is a much tighter guideline that either those of Dixon and Mood [35] or, more recently, Lin et al. [34].

To further explore the trend with number of tests, the numerical exercises were repeated 10 times each for numbers of tests of 10, 30, and 50. The random numbers for each value of the FLS were chosen corresponding to the same normal distribution as above, with

Table 3.2. Normal distribution, mean = 50, s = standard deviation

Increment	0.1 s		0.25 s		0.5 s		1.0 s	
# *trials*	*Mean*	s	*Mean*	s	*Mean*	s	*Mean*	s
10	51.58	5.60	51.50	3.29	52.25	2.71	52.50	6.71
20	50.86	2.50	50.50	1.67	51.25	4.17	53.50	4.77
30	50.68	0.70	51.03	1.53	50.92	1.67	51.50	2.61
40	50.39	5.23	48.50	10.62	47.75	5.95	49.00	7.61
50	50.83	6.48	50.71	3.82	50.55	3.53	50.70	5.34

Table 3.3. Mean = 50, increment = 0.5 (0.1s) mean = 50

# *Tests*	10		30		50	
Trial #	*Mean*	*s*	*Mean*	*s*	*Mean*	*s*
1	49.85	0.48	49.79	1.23	50.61	0.77
2	48.13	0.58	51.63	2.20	51.82	2.70
3	49.35	0.48	49.04	1.15	51.92	6.53
4	48.75	1.64	49.32	1.28	49.81	2.25
5	50.42	0.74	49.65	0.59	51.23	4.92
6	51.92	0.74	51.13	1.54	49.94	1.97
7	49.35	0.48	50.75	0.49	50.48	3.33
8	50.05	0.54	50.12	0.83	49.73	2.97
9	48.85	1.13	48.93	2.06	50.97	1.49
10	50.00	0.23	49.46	1.84	50.57	6.37
Mean	49.67	0.70	49.98	1.32	50.71	3.33
Std Dev	1.05		0.91		0.78	

mean = 50 and $s = 5$. All of the simulations corresponded to staircase tests that started with a value of 50 for the first test and used a FLS increment of 0.5 which corresponds to 0.1s. The results of each test series simulation are summarized in Table 3.3. For the 10 test series simulated for totals of 10, 30, or 50 tests in each series, the mean value and the standard deviation is computed at the bottom of the table. Statisticians will recommend that up to 100 trials should be performed before the results start to be statistically significant, but the results of 10 trials show the trends adequately. For FLS increments corresponding to 0.1s, reasonably accurate values of the mean value can be obtained from as few as 10 tests in a staircase sequence, and more consistency is noted as the number of tests is increased to 30 and to 50. In fact, looking at the numbers from these randomly generated values of FLS for the simulations, the series of 50 tests provides numerical values of the FLS that appear to be no better than those obtained from test series where only 10 tests were simulated. From this, it appears that very large numbers of tests are not needed to get a good approximation for the mean value when the increment between tests is small and the starting value is near the correct value. Values for the standard deviation of the distribution function of the value of FLS, however, do not provide any consistent numbers related to the real distribution, even for as many as 50 tests in a test sequence. As pointed out often in the literature, the staircase method concentrates testing near the mean value and provides very little information about behavior at values of FLS away from the mean.

The last part of these numerical simulations explored the consequences of starting the simulated test series at values of FLS that were not at the "correct" value. For additional simulations, the series of 50 tests shown in Table 3.3 was duplicated, using the same statistical distribution of values for FLS, but the starting values for the first test were

Table 3.4. All tests at inc = 0.5 (0.1s), Mean = 50, 50 tests

Start value	45		55		50	
Trial #	*Mean*	*s*	*Mean*	*s*	*Mean*	*s*
1	49.98	1.52	50.75	3.01	50.61	0.77
2	48.53	5.44	52.66	1.90	51.82	2.70
3	50.56	14.19	52.75	1.31	51.92	6.53
4	49.73	5.81	50.38	2.77	49.81	2.25
5	50.47	14.80	52.55	3.53	51.23	4.92
6	49.63	4.03	51.01	6.19	49.94	1.97
7	49.18	6.06	51.38	10.58	50.48	3.33
8	49.60	6.43	50.60	4.32	49.73	2.97
9	49.61	6.59	52.72	2.20	50.97	1.49
10	50.08	8.15	51.13	9.98	50.57	6.37
Mean	49.74	7.30	51.59	4.58	50.71	3.33
Std Dev	0.60		0.97		0.78	

chosen as either 45 or 55. These values are an amount "s" away from the true value of 50. Computed values for the mean and standard deviation for these starting values in each test series simulation, along with the baseline using a starting value of 50, are shown in Table 3.4. The simulation for a starting value of 50 is repeated from Table 3.3, and the same 50 random numbers for FLS were used for each starting value. The results are summarized in Table 3.4 which shows that values for the mean FLS do not appear to be dependent on the starting value of the test series. To further illustrate what happens in a series of staircase tests such as these, the results for the last trial (#10) are presented graphically in Figure 3.29. In this figure, the sequence of testing is illustrated on a test-by-test basis for each of the 3 starting values of FLS, 45, 55, and 50. What the figure illustrates is that starting low or high with respect to the mean requires a number of tests before the tests start oscillating about the mean as the staircase method proceeds. In the series of 50 tests, the data from a single simulation show that between 10 and 20 tests are required before the staircase method approaches equilibrium. What this produces, in essence, is a smaller test sequence. So although 50 tests are conducted, the results correspond to a test sequence of only 30 to 40 tests. In the particular case illustrated, it is not before the 19th test that the stresses at which the tests are conducted are within one unit of each other, and at the 28th test the tests are identical. Recall that the randomly generated numerical values for each of the three simulations are identical and occur in the same order. Thus, after the 28th test in each simulation, the three plots in Figure 3.29 are identical.

Further work on numerical simulations of the staircase method has been conducted as part of a PhD dissertation by Major Randall Pollak at the Air Force Institute of Technology. The results of these extensive simulations as well as some suggestions for

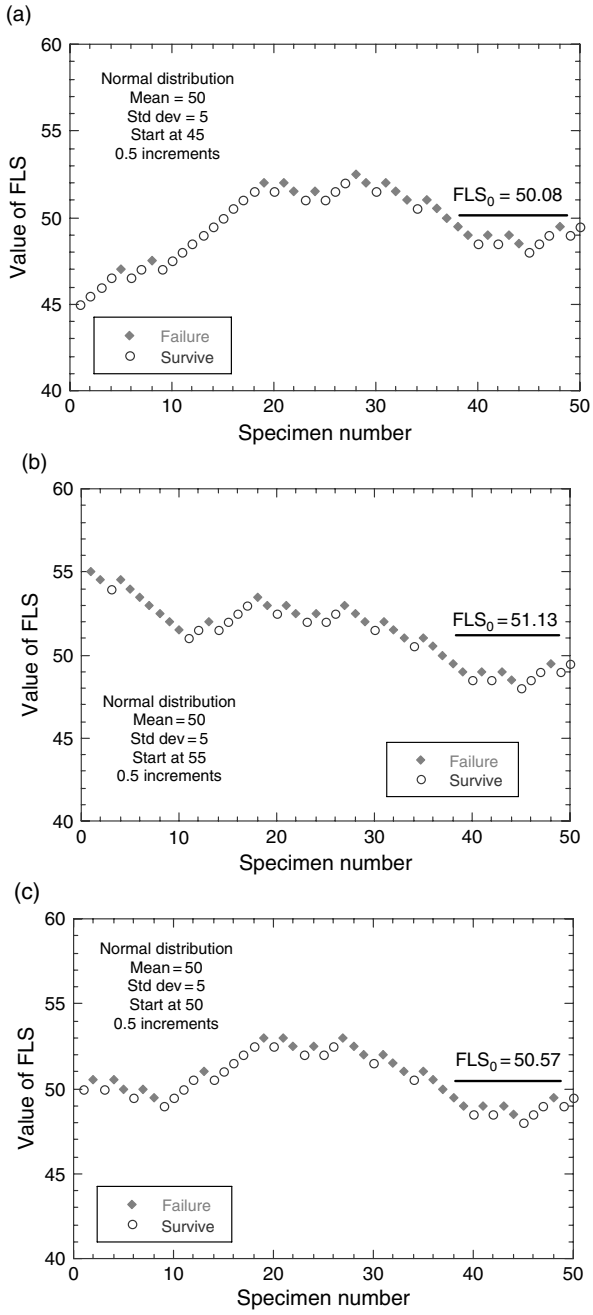


Figure 3.29. Illustration of numerical simulation of staircase tests for different starting values of FLS. (a) FLS = 45; (b) FLS = 55; (c) FLS = 50.

optimizing the test procedure to determine the FLS at a large number of cycles are presented in Appendix D. These simulations produce somewhat different guidance than that reported previously in the literature as described above. Of greatest significance is the finding that step sizes of the order of 1.7σ are best for reducing standard deviation bias, in contrast to the generally accepted guidance of using steps from $2\sigma/3$ to $3\sigma/2$.

The numerical simulations presented herein serve to illustrate the inherent weakness of the staircase method, namely that good results can be very dependent on a knowledge of the answer first, both for the mean value of FLS as well as the variance. Having this information available in advance, such as from extrapolated LCF test data, will help in choosing a starting value as well as a stress increment. If the starting value is low, many tests will produce survival (run-out), so equilibrium about the mean value will not be achieved right away. For such a sequence, the number of survivals will generally exceed the number of failures. In the analysis, however, only the failed tests are counted. This, in turn, has the net effect of having conducted fewer tests. The opposite is true when the starting value is high compared to the actual mean. In either case, fewer effective tests are performed, but the simulations shown above indicate that this does not seriously hamper the ability to determine the mean value of the FLS from staircase tests.

For comparison to the statistical aspects of staircase testing, numerical simulations were carried out to evaluate the statistical aspects of step testing. In this case, the assumption will be made that a step test will provide a true value of the FLS and that no history effects such as coaxing are present. This assumption has certainly not been proven in the general case for all test conditions like number of steps and step sizes and for all materials. Nonetheless, the numerical simulations are carried out assuming the FLS corresponding to a specified number of cycles such as 10^7 follows a normal (Gaussian) distribution. As in the above simulations for the staircase tests, the mean $= 50$ and the standard deviation $= 5$. These simulations amount to nothing more than a numerical evaluation of how many samples have to be obtained to recover the properties of the normal distribution if each sample follows that distribution function statistically. This type of information is widely available in the statistics literature but is repeated here for comparison of test methods for determining the FLS. The simulations were carried out assuming that the number of step-test experiments conducted was either 10, 20, 30, 40, or 50. In the first series of simulations, the procedure was repeated 10 times. This is essentially a test of the randomness of a random number generator when the number of tests is finite. The results of the simulations are presented in Table 3.5. For each number of experiments, the mean and standard deviation of the 10 simulations are shown in columns 2 and 3. The standard deviation of these quantities is shown in columns 4 and 5, respectively. This provides a measure of the repeatability of the results of a single simulation. To get a better feel for how random the numbers are, the same simulations were carried out 100 times and the results are presented in Table 3.6. The simulations appear to be quite similar, but these results give a slightly better feel for how accurately a normal distribution of values for

Table 3.5. Summary of numerical simulations of step tests repeated 10 times

# of Experiments	*Mean*	*Std dev*	*Std dev of mean*	*Std dev of std dev*
10	49.18	4.78	2.20	0.89
20	50.14	4.93	2.15	0.59
30	49.82	4.72	0.77	0.52
40	49.96	4.98	0.73	0.41
50	50.09	5.05	1.00	0.45

Table 3.6. Summary of numerical simulations of step tests repeated 100 times

# of Experiments	*Mean*	*Std dev*	*Std dev of mean*	*Std dev of std dev*
10	49.93	4.82	1.70	1.18
20	50.01	4.87	1.20	0.76
30	49.93	4.92	0.91	0.60
40	50.02	4.89	0.79	0.53
50	50.02	4.97	0.79	0.46

FLS can be expected to be reproduced from a finite number of test results. It can be seen from the table that even for as few step tests as 10, the mean and standard deviation for the FLS are close to the actual values, unlike the results shown earlier for the staircase method. Thus, the type of information required from a test series (mean or scatter) should help govern the type of test chosen.

3.4.2.3. Sample size considerations

The staircase method, or up-and-down method, was not originally explored for small sample sizes in terms of the efficiency of the test method. In their original work, Dixon and Mood [35] were concerned that "measures of reliability may well be very misleading if the sample size is less than forty." The numerical examples above seem to validate that fear if looking for the standard deviation as well as the mean using the estimating formulas from the original paper. Subsequent to their original work, the use of small sample sizes was investigated by Brownlee et al. [42] and again by Dixon [43], among others. Brownlee et al. [42] determined actual performance estimates for the mean based on series of length 10 or less. They found that the Dixon and Mood formula for the (asymptotic) variance is reasonably reliable even in samples as small as 5–10. They also showed that the up-and-down method does not necessarily have to be run sequentially, but might be run in a number of parallel short series without much loss of accuracy. Dixon [43] developed a modified version of the original up-and-down method for small sample sizes using sequentially determined test levels and sequentially determined sample sizes. He provided tables from which estimates of the mean square error could be obtained and

showed that the error for the mean was relatively independent of the starting level of the test sequence and the spacing between test levels. The procedure allows a design of experiments approach where very small sample sizes can be achieved without sacrificing accuracy.

The staircase method is the commonly used method for determining the statistical characteristics of the fatigue strength at any specified life and is used in standards of the British, Japanese, and French.

Staircase testing can be very expensive because of the large sample sizes and the lengthy time at least for the survival tests which can be 10^7 cycles or longer, and comprise approximately half of the staircase tests. Because of this, accelerated tests have been proposed [34] where the HCF strength (e.g. at 10^7 cycles) is extrapolated from small numbers of LCF (e.g. 10^3–10^6 cycles). Doing this, however, requires an assumption of the shape of the *S–N* curve over the LCF range and up to the HCF limit. In their work, Lin et al. [34] assume an expression of the form

$$S_a = S'_f(N_f)^b \tag{3.5}$$

where S_a and N_f represent the stress amplitude and number of cycles to failure, respectively, and S'_f (fatigue strength coefficient) and b (fatigue strength exponent) are material parameters fit to the data. In the methods used in [34], assumptions are made regarding the statistical nature of the LCF data and its relation to the statistical fatigue limit strength distribution.

3.4.2.4. Construction of an "artificial" staircase

There are times when conducting an entire staircase sequence is impractical and overly time consuming. Perhaps it was not the initial objective when planning the experiments, or some data already exist on *S–N* behavior at equal stress increments near the fatigue limit. Rather than throwing out existing data, these data may be used and supplemented by additional data to construct what will be called an "artificial" staircase. Recall that for a "true" staircase, each subsequent test is conducted at a fixed stress increment either above or below the previous stress level depending on whether the previous test resulted in a survival or a failure, respectively, within the targeted number of cycles. If a batch of data have been obtained at equally spaced stress levels, these data can be pooled together and drawn from the pool in a random fashion, a method that is referred to as the bootstrap method [44]. All of the data should be used, and no single data point may be used more than once in constructing an artificial staircase sequence. Additional test data may be required, at lower stresses if the majority of the data are failures, or at higher stresses if most of the data are survivals. The mathematics of constructing such an artificial sequence has not been developed, not is any analysis available to demonstrate

that random construction of a staircase sequence will provide similar results, particularly for the mean value of the FLS.

In preparing data for a publication, Morrissey and Nicholas [45] used the bootstrap method to determine the FLS of Ti-6Al-4V for a cyclic life of 10^9 cycles based on available test data, some of which were obtained from tests to only 10^8 cycles or even less. In this artificial staircase procedure using the bootstrap method, every data point was treated in one of the following three manners and every data point was used once:

1. If a specimen failed at a given stress level in less than 10^8 cycles, for example, then that data point provided a failure point for 10^9 cycles at the same stress level.
2. If a specimen failed within 10^9 cycles at a given stress level, then that specimen provided a failure point at any of the higher stress levels used in the staircase sequence, that is, at any number of stress increments (fixed) above the stress level at which the original test was performed.
3. If a specimen survived for 10^9 cycles at a given stress level, then that specimen provides a survival point for any stress level lower than the one at which it was actually conducted.

Using this logic, and using all of approximately 20 data points, several different "artificial" staircase test sequences were constructed from the available data pool. Surprisingly, the mean value of the FLS from each sequence used was reproducible to within 1 MPa for a FLS of approximately 510 MPa. There is no rigorous mathematical basis for applying the bootstrap method to the construction of an "artificial" staircase test sequence using the three rules stated above, but the consistency of the values for the mean suggests that the method is both viable and reliable when testing time, machine availability, or limitation in number of specimens available becomes a practical limitation in conducting a real staircase test sequence.

3.5. OTHER METHODS

In addition to step and staircase testing, another method for determining the fatigue limit or fatigue limit strength is referred to as the $\mathrm{ArcSin}\sqrt{P}$ method, where a pre-selected number of stress levels are used to test a fixed number of specimens at each level [38, 39]. Similar to what is used for the staircase tests, the FLS and the associated statistics are determined from the probability of fracture at each stress level. Whereas the staircase method tends to test near the mean stress, the $\mathrm{ArcSin}\sqrt{\mathrm{P}}$ method deliberately spreads out the stress levels to hopefully encompass a wider range of stresses with which to determine the scatter in the distribution function that is used to describe the FLS. Both methods provide an accurate estimate of the mean, even for small numbers of tests, but

neither method can provide an accurate estimate of the standard deviation unless large numbers of tests are conducted. When small numbers of specimens are used, both the staircase and the ArcSin$\sqrt{\mathrm{P}}$ method underestimate the standard deviation of the FLS [39]. From observations of a number of numerical simulations, Braam and van der Zwaag [39] developed a method for evaluating the statistical properties of the FLS as determined from the ArcSin$\sqrt{\mathrm{P}}$ method and provided insight into the planning and conducting of such tests.

For the ArcSin$\sqrt{\mathrm{P}}$ method, a fixed number of equidistant stress levels (m) are used and at each stress level a fixed number of specimens (n) is tested. For these data, a sinusoidal distribution function is used to represent the FLS. The probability density function (pdf) is

$$f_{\mathrm{P}}(x) = \frac{\pi}{2b} \sin\left(\pi \frac{x-a}{b}\right) \quad a \le x \le a+b \tag{3.6}$$

The probability of failure at each stress level is fitted to this distribution function using a least-squares routine, this providing the values of the parameters a and b as

$$b = \frac{2}{\pi}\left(\frac{\sum_{i=1}^{m} z_i S_i - \sum_{i=1}^{m} S_i \dfrac{\sum_{i=1}^{m} z_i}{m}}{\sum_{i=1}^{m} z_i^2 - \dfrac{\left(\sum_{i=1}^{m} z_i\right)^2}{m}}\right) \tag{3.7}$$

$$a = \frac{\sum_{i=1}^{m} \mathrm{S}_i - \mathrm{b}\dfrac{\pi}{2}\sum_{i=1}^{m} z_i}{m} \tag{3.8}$$

Here, S_i is the stress at level i, where $i = 1$ is the lowest stress in the test series, and m represents the number of stress levels used. The quantity z_i is the ArcSin$\sqrt{P_i}$, with P_i being the probability of fracture at stress level i. The probability of fracture equals the ratio of the number of specimens broken to the total number of specimens tested at a given stress level. The quantity $a + b\pi/4$ is the average value of the sinusoidal distribution and b is the interval between the two points where the pdf becomes 0.

The sinusoidal pdf, unlike a normal (Gaussian) pdf, has the feature of covering a finite limit for values of the FLS. This implies that failures will not occur below some finite stress and, further, that all samples will fail above another value of stress. The Gaussian probability density function is of the form

$$f_{\mathrm{G}}(x) = \frac{1}{\sqrt{2\pi\sigma}} \exp\left(-\frac{(x-\mu)^2}{2\sigma^2}\right) \tag{3.9}$$

The two distribution functions are very similar and can be compared for the same value of the function at the mean value, μ. For the averages of each function to be equal,

$$\mu = a + b/2 \tag{3.10}$$

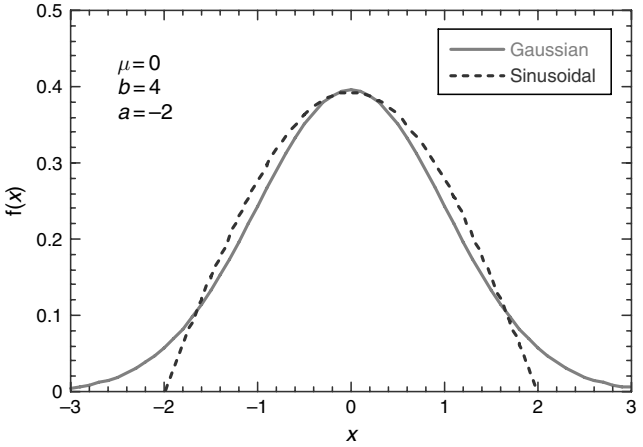


Figure 3.30. Comparison of Sinusoidal and Gaussian pdf's.

and the two functions are compared for a mean value $m = 0$ [39]. The resulting curve is shown in Figure 3.30, where the similarities are demonstrated. For the numbers chosen, $\sigma = 1.016$ for the Gaussian distribution.

Braam and van der Zwaag [39] performed a number of simulations for staircase and ArcSin$\sqrt{P}$ methods of testing to evaluate the effects of the numbers of tests on the ability of the methods to produce the correct distribution function inherently assumed in the simulation. Note that the staircase method has two parameters that can be varied in the test sequence, namely the total number of tests and the step size. In all the simulations, the starting value was at the mean value, similar to what was shown above. For the ArcSin$\sqrt{P}$ method, three parameters can be varied in the test simulation: the number of steps, the step size, and the number of tests per stress level. For the staircase test simulations, total numbers of tests (N) of 20, 50, and 100 were used. In each case, the mean was well predicted and the distribution function became more narrow as N increased. As N decreased, the standard deviation was underestimated since for small numbers of tests, the probability of a failure at a low stress level is small. Their simulations for the staircase test method also showed that the influence of the step size on the mean is only significant if N is very small (<30). However, the step size was found to have a large influence on the standard deviation. A similar observation can be made from the results of the numerical simulations summarized in Table 3.3 where the "true" normal distribution of FLS has a standard deviation of 5. For 10 numerical simulations of a series of 10, 30, or 50 tests, the average value of the computed standard deviation is 0.70, 1.32, and 3.33, respectively. Worse yet, the individual values for the standard deviation have a significant amount of variability from one test series to another, even when a total of 50 specimens is used in a staircase test series (see Table 3.3).

For the ArcSin$\sqrt{P}$ simulations in [39], results showed that a larger number of total tests leads to a narrower distribution function, as expected, while the conclusion that the mean is well predicted for most cases was verified. From simulations of both methods, it was concluded that the error in standard deviation depends on the ratio of s, the step size, to σ, and the standard deviation (which is never really known!). The difficulty of this problem can be summarized in the following conclusion drawn by Schütz [7] in his review article on the history of fatigue: "A probably unsolvable problem is the scientifically and practically correct calculation of fatigue life at very low probabilities of failure, because the type of distribution would have to be known."

3.6. RANDOM FATIGUE LIMIT (RFL) MODEL

Berens and Annis [24 (Appendix B)] point out that it has been common procedure to determine FLSs of a Haigh diagram corresponding to some HCF life from fits to constant amplitude *S–N* data. At a constant value of *R*, for example, fatigue strength at *N* cycles can be defined statistically in terms of the stress level for which *p* percent of a population of specimens will survive for at least *N* cycles. This definition, however, does not provide for the characterization of the fatigue limit in terms of an observable stress property since the result of a fatigue test is the random number of cycles to failure for the fixed stress level that was used in the test. As a result, the distribution properties of fatigue strengths at a fixed, large *N* have generally been inferred from the distribution of cyclic lives from specimens that have failed or have reached some defined run-out life at a fixed stress level.

There are at least three practical problems in this traditional approach to estimating fatigue limits: First, at the stress levels of interest, *S–N* curves are relatively flat. While accurate mean values can be determined from step or staircase methods as pointed out earlier in this Chapter, extremes of the distribution curve are hard to obtain. It is the extremes that are important for design. A second problem is the large variation in fatigue lives near the endurance limit. Third, there are requirements to determine fatigue limit strengths at longer and longer lives, making the testing even more time consuming.

In addition to step and staircase testing, an innovative approach to estimating the FLS distribution was proposed by Pascual and Meeker [46]. A random fatigue limit (RFL) model is postulated in which each specimen has its own fatigue limit strength in much the same way that each specimen has its own finite fatigue lifetime if tested at a sufficiently high stress above the endurance limit. This random fatigue limit is explicitly included in the *S–N* model.

Past attempts at modeling the stress-life (*S–N*) behavior of cyclic fatigue and extending it into the long life regime often used an equation of the form:

$$\ln N_i = \beta_0 + \beta_1 \ln(S_i - \beta_2) + \varepsilon_i \tag{3.11}$$

where, for specimen i, N_i represents cycles to failure, S_i is the applied stress parameter, β_2 is a constant fatigue limit ($S_i > \beta_2$), and ε_i is a random variable representing the scatter in cycles to failure about the predicted life [47]. The parameters of the median life prediction, β_0, β_1, and β_2 are estimated from test data and β_2 is interpreted as the FLS condition. Since β_2 is an asymptote, the *S–N* curve flattens as S approaches the fatigue limit. This model may be adequate for the median behavior in the long life regime but it is not consistent with the commonly observed increase in the standard deviation of lives as S approaches the constant fatigue limit where the *S–N* curve becomes nearly horizontal. But its main shortcoming is that it does not work. Since the single-valued, constant, fatigue limit, β_2, must be less than the lowest stress tested (so that the logarithm of $(S_i - \beta_2)$ is defined) it must be less than even the lowest run-out stress tested. This causes the β_2 asymptote to be so low as to produce an unrealistic material model.

The RFL model [46] is a generalization of Equation (3.11) in which the fatigue limit term is modeled as a random variable that can be considered to result from inherent, but unknown, quality characteristics of each specimen in the population. Thus, the fatigue limit is not a single constant, but rather an individual characteristic of each specimen, namely, a statistical variable. The RFL model for test specimen i is given by:

$$\ln N_i = \beta_0 + \beta_1 \ln(S_i - \gamma_i) + \varepsilon_i \tag{3.12}$$

where γ_i is the random fatigue limit for specimen $i(S_i > \gamma_i)$ and is expressed in units of the stress parameter. In this model, ε is the random life variable associated with scatter from specimens that have the same fatigue limit.

The RFL model produces probabilistic *S–N* curves that have the characteristics commonly seen in fatigue data. An example of this can be found in [48] and is illustrated in Figure 3.31 which presents the 1st, 25th, 50th, 75th and 99th percentile *S–N* curves as would be determined from the distribution of fatigue limits. The percentile *S–N* curves display the commonly observed shape in the HCF regime even though the majority of the data were obtained in the lower life regime. Further, it is easily seen in Figure 3.31 that a difference in test lives from two specimens with slightly different fatigue limits could be quite large. The increased scatter in fatigue lives is explained by different specimens having different fatigue limits and this is true regardless of the scatter in life at higher stresses. Thus, the RFL model accommodates not only the flattening of the *S–N* curve but also the increased scatter that is typical of HCF lives.

The two random variables in the RFL model require probability distributions. In [48], the conditional distribution of cycles to failure, given γ, was assumed to have a lognormal distribution while the random fatigue limit, γ, was assumed to have an SEV distribution. The equations for the cumulative distribution and probability density function of the SEV distribution are

$$F(z) = 1 - \exp[-\exp(z)] \tag{3.13}$$

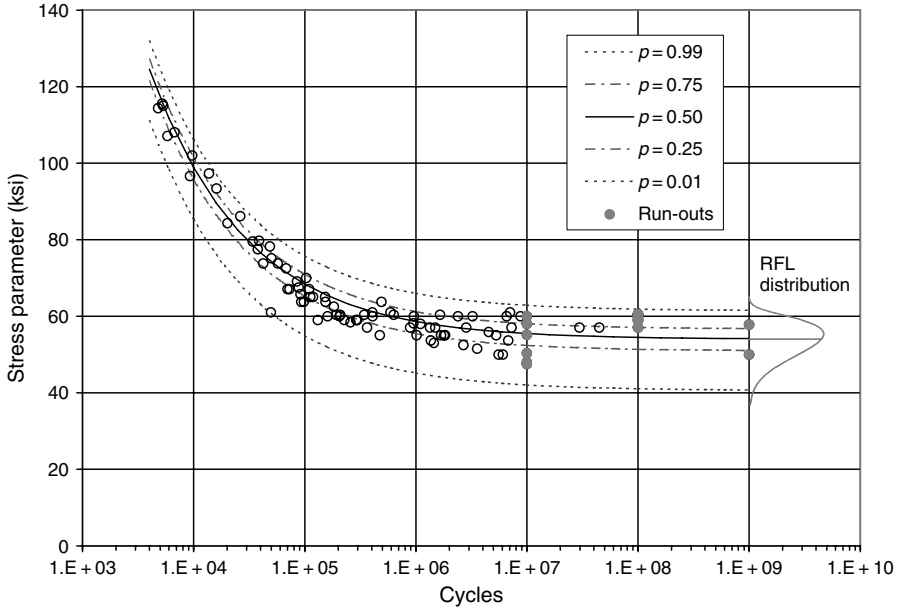


Figure 3.31. Example *S–N* curves calculated from percentiles of the random fatigue limit distribution.

$$f(z) = \left(\frac{1}{\sigma_\gamma}\right) \exp\,[z - \exp(z)] \tag{3.14}$$

$$\text{where } z = \frac{(\gamma - \mu_\gamma)}{\sigma_\gamma} \tag{3.15}$$

The SEV distribution was selected as a model for fatigue limits because it has a basis in extreme value theory and it is skewed to the left, that is, to values smaller than the median. Berens and Annis [48] note that if the random variable Y has a Weibull distribution then log Y will have an SEV distribution – the SEV is to the Weibull as the lognormal is to the normal.

From a set of *S–N* data including run-outs, the five parameters of the RFL model can be estimated using maximum likelihood methods [46]. Maximum likelihood estimates have known, desirable statistical properties and confidence bounds can be calculated when wanted [49], but these calculations require sophisticated software.*

An example application of the RFL model approach is presented in [48] that demonstrates that the model can produce a valid description of *S–N* data in the HCF regime. It also demonstrates one use for the model by investigating the necessity of having long

* Computer software that works with the S-PLUS statistical analysis program can be obtained from Dr. Meeker (wqmeeker@iastate.edu or http://www.public.iastate.edu/~wqmeeker/other_pages/wqm_software.html).

run-out lives in the analysis. The data for this application, shown in Figure 3.31, consisted of 95 *S–N* test results on Ti-6Al-4V plate with 15 of these being run-outs at 10^7, 10^8, or 10^9 cycles and two that failed between 10^7 and 10^8 cycles; the others had shorter lives.

Results showed that the scatter in life of the smooth bar specimens was adequately described by the distribution of the fatigue limit parameter. Further, it was shown that the added information from testing to lives greater than a run-out life of 10^7 did not significantly change the fatigue limit distribution. However, it was illustrated that using only lives less than 10^7 in the analysis produced a significantly lower and unreasonable fatigue limit distribution. Thus, the assumption that shorter life data provide useful information about the HCF limit strength distribution can be seriously questioned.

Annis and Griffiths [50] used the results from the RFL model to generate sample staircase results for the FLS with a Monte Carlo simulation. Unlike the normal distribution used in much of the earlier work on scatter in staircase test results, a Weibull distribution was used for the scatter in the RFL (stress axis), while a lognormal distribution was used to represent the scatter in lives (cycles axis). Their preliminary results, using a Bayesian-based likelihood estimation technique to analyze the randomly generated staircase data, showed that the mean value of the RFL was well predicted for small numbers of tests ranging from a total of 10 to a total of 31. The scatter, as observed previously for staircase testing, was not as well represented from such a small population. Their results are summarized in Table 3.7 which provides computed values for the mean, where the probability of failure is $p = 0.5$, and $p = 0.01$ which is near the tail end of the distribution where the probability of failure is only 1%.

While the scatter is not well represented, the values at $p = 0.01$ seem to be better than those obtained using a normal distribution for such small sample sizes and where only scatter in FLS is considered. In the RFL model, scatter in lives as well as stress is considered. As noted by Annis and Griffiths [50], the centering nature of the staircase method results in a limited range of stress levels with a corresponding clustering of run-out life within 1–2 orders of magnitude. The RFL model, which contains 5 parameters, requires substantial data over a range of stress levels and lives to accurately estimate the parameters. Using Bayesian methods, the analysis of the parameters makes use of prior knowledge of the behavior. A further advantage of this method, where Weibull statistics are used to represent fatigue strength, is that in the HCF regime the upper limit of the

Table 3.7. Numerical simulations of staircase tests using RFL model [50]

Number of tests	*FLS* ($p = 0.5$)	*FLS* ($p = 0.01$)
"Truth"	53.84	40.31
10	53.98	42.08
20	54.28	42.98
31	53.38	40.54

fatigue strength is more restrictive than the lower limit. The Weibull distribution reflects this behavior where very low quality specimens are sometimes, although infrequently, observed, but extremely high run-out stresses are never observed. The infrequent low run-out stresses are the crux of the problem in determining lower bound stresses for design purposes and the RFL model is felt to provide a means to measure the propensity for this life-limiting behavior [50].

3.6.1. Data analysis

In addition to the staircase data obtained on titanium under the National HCF program, step testing was used to determine the FLS at a life of 10^7 cycles [24]. In the staircase testing, the results of which are shown in Figures 3.27 and 3.28 above, the number of cycles to failure for the tests that failed before 10^7 cycles were also recorded. These additional data can be used to evaluate statistical approaches for representing *S–N* data and different methods for experimentally determining the fatigue limit strength as well as minimum HCF capability. The additional step tests were conducted because they result in a failure point for each specimen tested. This can be an advantage when material is costly and test failures are required for needed assessments. A summary of the step-test matrix in this evaluation is provided in Table 3.8. The step tests were run with 10^7 fatigue blocks and 4 ksi maximum stress steps. The average number of cycles/specimen was $\sim 5.2 \times 10^7$ cycles for a total of 260×10^6 cycles for the step test program. The average of the five step tests gave a FLS of 79.8 ksi whereas the analysis of the staircase tests totaling 26 specimens resulted in a mean value of 79.4 ksi (see Table 3.1). For comparison purposes, the RFL model (see Table 3.7), which is based on a combination of LCF and HCF data as well as an empirical fit to the *S–N* curve, provided a value for the SWT parameter of 53.84 which, in turn, for $R = 0.1$ provides a FLS mean value of 80.3 ksi. In that application of the RFL model, neither the staircase-test nor the step-test results had been used.

Unlike in the step tests, a single load level on each specimen is used for the staircase approach. The first staircase test was run at $S_{max} = 67$ ksi without failure. Stresses were increased on additional specimens until failure occurred within 10^7 cycles. Stresses on

Table 3.8. Ti-6Al-4V Step test matrix at 900 Hz, $R = 0.1$, and 75 °F

Spec ID	*Starting* s_{max} (ksi)	*Final* s_{max} *at failure* (ksi)	*# steps*	*Last step* N_f	*Interpolated* s_{max} (ksi)
121-2	61.5	77.5	4	8202785	76.78
124-4	61.5	89.5	7	1125814	85.95
47-10	61.5	81.5	5	5617819	79.75
173-2	65.5	77.5	3	5627646	75.75
47-9	65.5	81.5	4	8252952	80.80

subsequent tests were continually increased or decreased based on N_f of the last tests versus 10^7 target life. Roughly 1/2 of the specimens (12 out of 26, see Table 3.1) failed within the targeted life regime. Six of the staircase tests were long-life failures that continued overnight or through the weekend awaiting setup of the next test specimen. Given that over-night or weekend test time is run without additional costs, the staircase matrix of 26 tests was similar in cost to the step matrix (Table 3.8). More staircase tests can be run at similar costs to step tests which are conducted using multiple steps/specimen.

While fail/no fail methods can be used to evaluate the statistics of the FLS, additional information is available in the form of number of cycles for each failed specimen, as well as cycle counts for specimens that were not terminated when they reached the number of cycles for survival. For the Ti-6Al-4V material whose results from staircase testing are shown in Figures 3.27 and 3.28 and in Table 3.1, the data involving cycles to failure can be presented in the form of an *S–N* curve, as shown in Figure 3.32. The step test results, Table 3.8, as well as the staircase run-outs, are also shown on a log–log plot. The results are qualitatively very similar. The fatigue capability of only the staircase tests where failure occurred is analyzed in Figures 3.33 and 3.34. A 1D scatter in the stress direction is assumed in Figure 3.33. A 1D scatter in life is assumed in Figure 3.34. The scatter assumption in life is similar to the approach typically used in analyzing LCF results. Because the tests involve failures in the long life regime, the statistics using scatter in life, Figure 3.34 show much more scatter than that in Figure 3.33 where scatter in stress was used. At a fatigue life of 10^7 cycles, both methods produce a mean value of log S_{max} of about 1.9 (about 79 ksi), but the -3σ value of log S_{max} goes from about 1.83 (67.6 ksi) when scatter in stress is used to about 1.7 (50.1 ksi) when scatter in life is used. In the

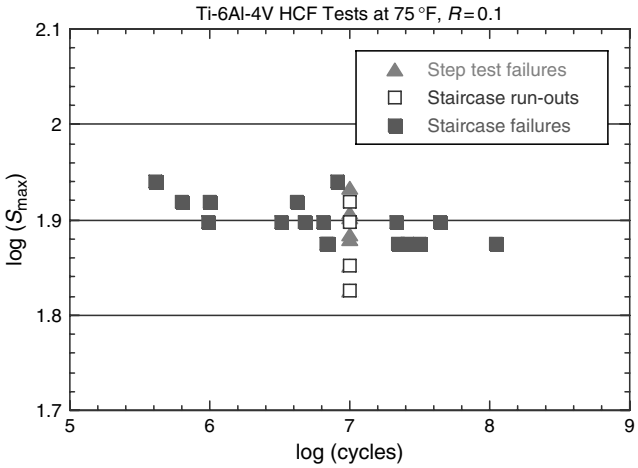


Figure 3.32. Step and staircase test results for Ti-6Al-4V at 75 °F and $R = 0.1$ (step at interpolated S_{max} using the step interpolation approach).

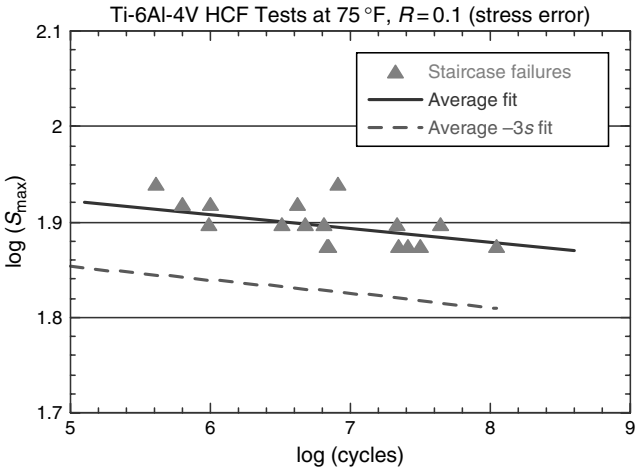


Figure 3.33. Staircase failures for Ti-6Al-4V at 75 °F and $R = 0.1$ with average and $-3s$ predictions assuming a 1D stress scatter.

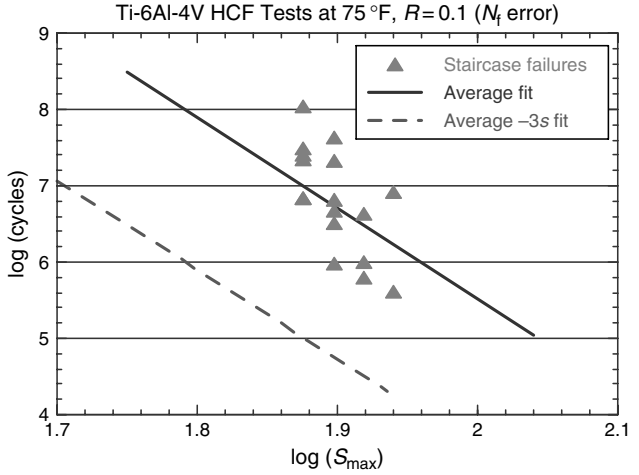


Figure 3.34. Staircase failures for Ti-6Al-4V at 75 °F and $R = 0.1$ with average and $-3s$ predictions assuming 1D life scatter.

latter case, the statistics are almost meaningless because they are trying to fit an almost horizontal *S–N* curve (Figure 3.32) based on scatter in the life direction only.

To further evaluate the statistics of the *S–N* behavior of this material, predictions were made with a combination of the step and staircase tests with baseline tests from an earlier program ($N_f < 10^6$ cycles) previously analyzed as shown in Figure 3.31. For these

predictions, the RFL model, described above, was used. The baseline tests with $N_f < 10^6$ cycles were selected as LCF tests that would typically be available from test programs in addition to HCF properties. The RFL model treats run-out and failure tests with 2D scatter in both life (LCF regime) and the endurance stress (HCF regime). An advantage of the RFL model is that the 1D scatter assumptions are not required. The RFL model predictions with the baseline + step or staircase results are given in Figure 3.35.

If only the step tests are used in combination with the LCF tests, a tighter fatigue limit variation is obtained with more error in life than for the staircase plus LCF tests where fatigue limit variation dominates the life error term. In Figure 3.36, the average and lower bound HCF limits for all approaches are summarized. If a 1D scatter in stress (s) is used, similar lower bound predictions are obtained for the step and staircase tests. However, a 1D scatter in life results in a different lower bound as noted before. For the cases using

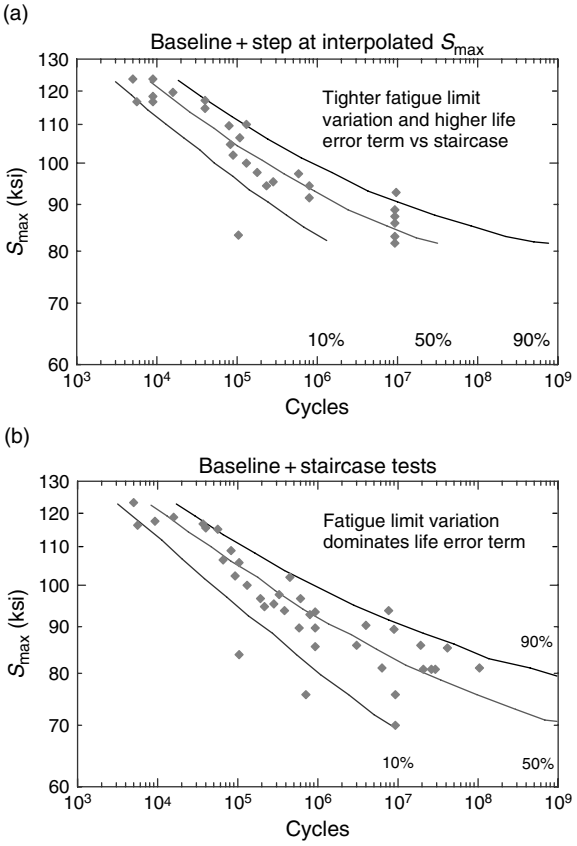


Figure 3.35. Random fatigue limit model predictions using baseline tests ($N_f < 10^6$ cycles) + step or staircase approaches.

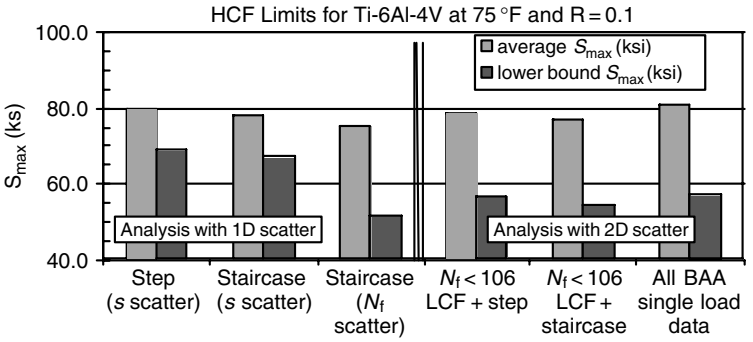


Figure 3.36. Summary of predicted average and lower bound HCF limits for Ti-6Al-4V at 75 °F and $R = 0.1$.

the 2D scatter, a similar lower bound is observed for either step, staircase, or all data, when combined with the baseline LCF data. These predictions are seen to be different than those obtained with the 1D scatter assumptions.

Another important feature that distinguishes the RFL model from conventional least squares fitting (LSF) is the manner in which run-out tests are handled. As pointed out in [50], the RFL model deals with the probabilities of an observation being above or below some value whereas in ordinary LSF routines, the behavior is addressed as an average. In the RFL model, each specimen has its own FLS. Least squares cannot deal with run-outs because there is no specific data point to evaluate, but the RFL type model can deal with the life exceeding some number at a given stress. These "censored" observations, where a specimen could fail at any unknown time after the test was suspended, cannot be included in any least squares calculations of the sum of the errors, so the LSF method breaks down if these observations are to be included. For the RFL model, on the other hand, these observations can be included if exceedance is the criterion being evaluated. In the estimation of the parameters for the RFL model, a maximum likelihood approach is used. As Annis and Griffiths [50] point out, if there are no censored observations, the maximum likelihood method produces the exact same results as the least squares error method.

As observed in all of the statistical approaches discussed above, and illustrated for specific cases in Figure 3.36, the average HCF limits are relatively insensitive to the assumptions. However, predicted lower bound limits are highly dependent on the assumed scatter direction for the 1D scatter approaches (stress versus life scatter). Lower bound limits are also highly dependent on the assumed scatter type (1D versus 2D scatter). In the final report [24], the authors who represent the turbine engine industry conclude that "the best approach needs to be assessed within the current design systems. Additional work establishing confidence limits for the RFL model also is needed for use in design."

The RFL assessment for all single load Ti-6Al-4V tests is also included as a final assessment [24]. Load control tests with maximum stresses above the material yield stress were not used in the final analysis. The model was fit with strain and load control tests at different values of R with the σ_{equiv} damage parameter defined in Equation (3.20) below as the alternating Walker equivalent stress and $\Delta\varepsilon$ is the total strain range for the cases where inelastic behavior was encountered. $\sigma_{\max}$ is the maximum stress as measured on test specimens or calculated with elastic-plastic analyses, and w is a material constant. Strain control tests were used to establish the baseline half-life stress-strain properties. The values of maximum stresses and strain were taken from strain control measurements near the specimen half-life. The constant $w = 0.42$ was obtained with a non-linear regression of the strain and load control tests. The average and $-3s$ RFL fits are given in Figure 3.37. The equations for the average and lower bound fit to the RFL model are:

$$\text{Average fit: } \log\,(N_{\text{f}}) = -2.39472\ \log(\sigma_{\text{equiv}} - 36.199) + 7.629937 \tag{3.16}$$

$$-3\sigma \text{ fit: } \log\,(N_{\text{f}}) = -2.39472\ \log(\sigma_{\text{equiv}} - 23.758) + 7.629937 \tag{3.17}$$

In the RFL model development and analysis described in the section above, a SWT and a σ_{equiv} parameter are used to consolidate data obtained at various stress ratios in order to provide a larger database. The vertical axis in Figure 3.31 is the SWT parameter while Figure 3.37 uses the σ_{equiv} parameter. The Smith–Watson–Topper [51] parameter is defined as

$$\text{SWT} = \left(\sigma_{\max}\frac{E\Delta\varepsilon}{2}\right)^{0.5} \tag{3.18}$$

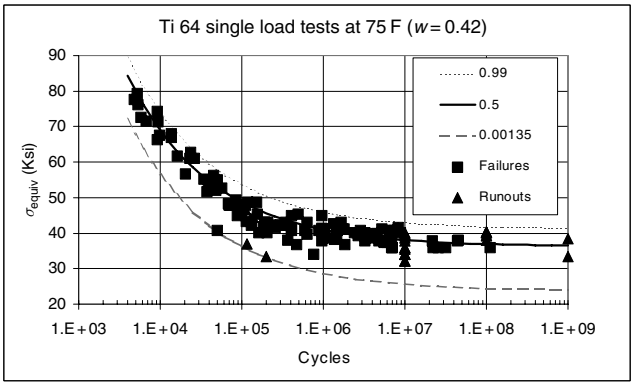


Figure 3.37. Single load test results and random fatigue limit fits for Ti-6Al-4V.

where σ_{max} is the maximum value of stress, $\Delta\varepsilon$ is the strain range, and E is Young's modulus. For purely elastic behavior, typical of the HCF regime, the formula becomes

$$\text{SWT} = \left(\sigma_{max}\frac{\Delta\sigma}{2}\right)^{0.5} = \sigma_{max}\left(\frac{1-R}{2}\right)^{0.5} \tag{3.19}$$

where R is the stress ratio. A modified version of the SWT parameter, used in industry [52], has additional flexibility to consolidate data at different values of R. One form of this modified parameter, which will be denoted as SWT_{MOD} is

$$\text{SWT}_{\text{MOD}} = 0.5(\Delta\sigma)^{w}(\sigma_{max})^{(1-w)} \tag{3.20}$$

where w is a fitting parameter. This modified version of the SWT parameter is often referred to as an equivalent stress, σ_{equiv}. Equation (3.20) is written for purely elastic behavior using $\Delta\sigma$ instead of $E\Delta\varepsilon$ for the more general inelastic case. For the case where $w = 0.5$, SWT and SWT_{MOD} differ by a constant factor of $\sqrt{2}$ for all values of R. For other values of w, the difference depends on stress ratio, R. Figure 3.38 shows values of SWT and SWT_{MOD} as a function of R for values of $w = 0.75$, 0.5 and 0.25 to illustrate the differences between the parameters. The values of the SWT and SWT_{MOD} parameters are normalized with respect to σ_{max} in the plots.

Step tests at the interpolated failure stresses were not used in the final baseline fits. Yet for all of the other data, one observation still puzzles those involved in analyzing the data obtained on Ti-6Al-4V. Though step and single load tests produced equivalent results for $R = 0.1$, step tests potentially produced unrealistically high allowable HCF limits at $R = -1$, leading some to speculate whether coaxing actually exists in this material. In their final report [24], the researchers recommended that "possible issues with step tests at negative R should be assessed in future work."

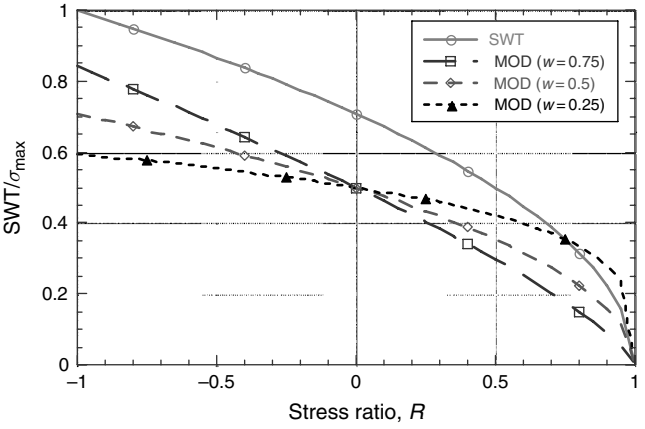


Figure 3.38. Normalized SWT and modified SWT parameter as function of stress ratio.

3.7. SUMMARY COMMENTS ON FLS STATISTICS

In summary, determination of the FLS and the corresponding statistics of scatter can be accomplished in a number of ways. For the Ti-6Al-4V used in the National HCF program, a number of methods and combinations thereof were used. The simplest case was the use of step tests to determine the FLS by averaging the results of 5 tests. Next, 26 staircase tests were conducted and the results analyzed using the Dixon and Mood method assuming a Gaussian distribution for the FLS. Third, results of a large number of LCF tests including run-outs as well as a few long life tests beyond 10^7 cycles were used in an assessment of the RFL model which considers scatter in both stress and life. Finally, the RFL model was applied to a combination of the LCF data and the staircase test data, where cycles to failure in the failed staircase tests were used as part of the database. A summary of the results from the four procedures is presented in Table 3.9. All data are presented for the FLS at 10^7 cycles and $R = 0.1$. For the normal distribution function, the -3σ value is calculated. For the RFL model using the SEV distribution, the value corresponding to a probability of failure of $p = 0.01$ at 10^7 cycles is used. The results demonstrate that from four different combinations of databases and statistical procedures that a mean value is obtained that has little variability among the procedures. However, a design value at the tail end of a distribution function corresponding to -3σ or $p = 0.001$* can have a large amount of scatter among the various techniques. It is certainly not apparent what is the appropriate value of a FLS for design if the design criterion is a probability of failure of one in a hundred or one in a thousand. It is not even apparent what is the appropriate distribution function with which to represent FLS based on sample sizes that do not exceed approximately 100. Another point to consider in looking at the results presented in Table 3.9 is that the database used in the evaluations with the RFL model contain data obtained at several values of stress ratio, R, while the step tests and staircase tests were all performed at a single value of R. The RFL results

Table 3.9. Summary of statistical representation of FLS at 10^7 cycles, $R = 0.1$

Data source	*Parameter*	*Distribution function*	*Mean stress* (ksi)	-3σ *value* (ksi)
Step tests	FLS	Normal	79.8	N/A
Staircase	FLS	Normal	78.0	51.1
LCF + HCF	SWT	SEV	80.3	60.1*
All (no step)	σ_{equiv}	SEV	79.5	53.5*

* Represents $p = 0.01$ value in distribution function.

* For a normal distribution, a probability of failure of 0.001 corresponds to -3.090σ. Conversely, -3σ corresponds to $p = 0.00135$. Similarly, $p = 0.01$ equates to -2.326σ while -2σ equates to $p = 0.0227$.

are interpolated for $R = 0.1$ using the SWT or σ_{equiv} parameters. The scatter in the results reflects both the inherent material variability as well as any inability of the models to consolidate data at various values of R into a single parameter.

Another example of the possible problems that may be encountered in step testing, in addition to those mentioned above for Ti-6Al-4V at $R = -1$, are associated with data obtained on Ti-17 under the National High Cycle Fatigue program [24]. A limited number of tests were conducted on this alloy at two stress ratios, $R = 0.1$ and $R = -1$. Both conventional S–N tests, using single specimens at fixed stress levels, and step tests where the specimen is reused until it fails, were conducted. The test matrix did not constitute a statistically designed experiment, but the data obtained revealed some interesting features. At $R = 0.1$, Figure 3.39, S–N tests showed failures at stresses above approximately 105 ksi and run-outs at stresses below that. Yet step tests produced slightly higher values of the FLS at 10^7 cycles, with one test starting at 110 ksi and not failing on the first block at that stress level where other samples had failed at cycle counts below 10^5 cycles. This anomalous behavior was attributed to a combination of material scatter, possible variances in batches of material preparation/machining, and the possibility of a coaxing phenomenon in this material. Even more perplexing are the results obtained at $R = -1$ shown in Figure 3.40. Here, a similar phenomenon is observed as in the tests at $R = 0.1$, but the number of specimens and the extent of the phenomenon seems to be more prominent. While speculation abounded about the specimens coming from two distinct batches that were prepared differently, no such conclusion could be drawn based on incomplete records of the history of the individual specimens. The data, however, seem to imply that there are two populations of specimens producing two distinct sets of behavior. While the duality in S–N curves has been observed in gigacycle fatigue and

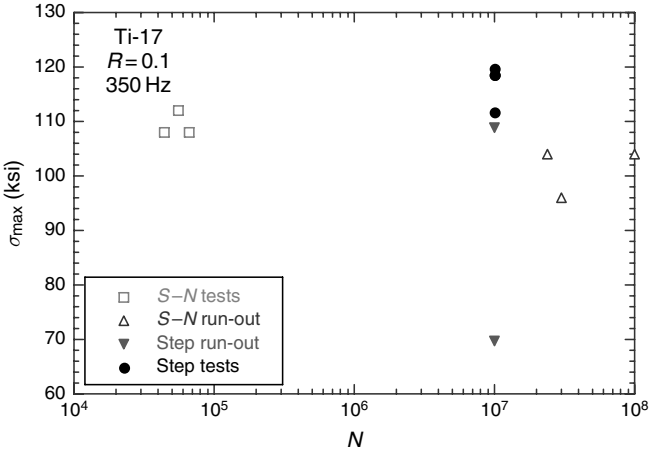


Figure 3.39. Fatigue data for Ti-17 at $R = 0.1$.

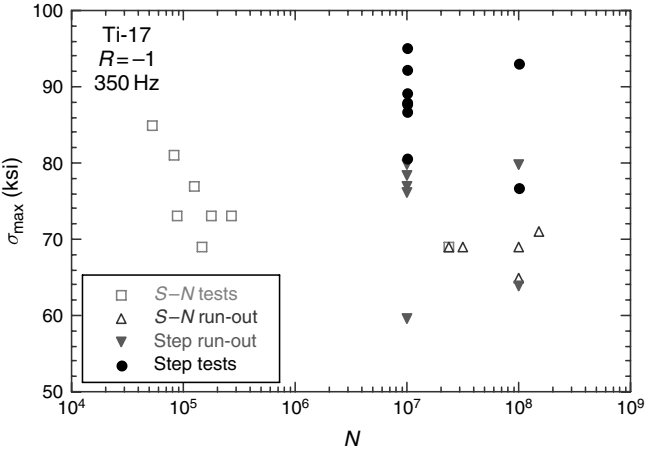


Figure 3.40. Fatigue data for Ti-17 at $R = -1.0$.

has been associated with internal initiations at long lives, and surface initiations at shorter lives in individual specimens,* there were no internal initiations observed in any of the specimens inspected after failure in the longer life (or higher strength) population of the test results.

Another observation that is somewhat puzzling has been made in reviewing HCF limit stress data on titanium. As seen in Figure 2.36 in Chapter 2 as an example, limited data show an unusual amount of scatter for tests conducted at $R = -1$, fully reversed loading, corresponding to zero mean stress. Bellows et al. [26] noted that the scatter in both step tests and conventional tests was highest at $R = -1$. In addition to this being their only test that went into compression, comparison with their other tests showed that these tests had the highest stress (or strain) range and had the lowest value of maximum stress. No readily observable differences were seen between the fracture surfaces of the step tests and conventional tests at the same stress ratio.

The question remains as to whether fatigue lives at stresses above the fatigue limit (infinite life) provide any information about the FLS or the FLS corresponding to a large but finite number of cycles. Inherent in this discussion has to be the question about the exact shape of the *S–N* curve and the extrapolation of this curve to large numbers of cycles or to infinite life. Added difficulties arise from a statistics point of view because the distribution function of lives at stresses producing finite lives and of fatigue limit strengths at long lives or even at the fatigue limit for infinite life have to be known. An evaluation of some aspects of this problem was made by Loren [53], who compared two

* See discussion in Chapter 2.

models for obtaining information on the fatigue limit (infinite life) and the endurance limit defined as the fatigue strength at a given (long) life. The models were evaluated based on numerical simulations of a staircase test procedure. For the fatigue limit model, he assumed the fatigue limit is a random variable having a normal distribution of the logarithm of the stress. If stresses are below the fatigue limit, they have infinite lives. In the second model, the endurance limit (fatigue strength corresponding to a given number of cycles) also is a random variable with a normal distribution of logarithm of stress. If a specimen does not fail at a stress below the endurance limit, it has a life greater than the cycle count at which the staircase testing is terminated. The lives are greater than this cycle count, but not necessarily infinite. A large number of numerical simulations of staircase testing were conducted corresponding to the statistical distribution assumptions for each model. The results were analyzed using maximum likelihood procedures that consider both censored (run-outs) and uncensored (failures) data. Both methods show that it is possible to estimate the distribution of the fatigue limit, but the fatigue limit itself is impossible to observe. The finite lives were found to give additional information on the fatigue limit or the endurance limit in some cases, while in others they simply confirm that the lives are finite. The results depend on the distribution functions as well as on the life where the staircase tests are terminated. The statistical mathematics for conducting these simulations are presented in the paper [53].

3.8. CONSTANT STRESS TESTS

If step or staircase tests are not used to provide information about the fatigue limit, tests at constant stress levels can be used to determine the shape of the *S–N* curve. This is particularly useful for LCF where the cycle counts are lower than in HCF. However, as the *S–N* curve becomes more horizontal near the fatigue limit, the scatter in lives increases. The choice of test method depends on, among other factors, the accuracy desired on both the mean and the variance, the number of available samples, and the test time available. If constant stress level testing is chosen, the number of tests at each level, the specific values of the stress levels, and the stress increment between test levels have to be chosen. While guidelines exist for test planning purposes [54], they are very restrictive and pertain only to *S–N* relationships that are linear on the proper coordinates, that variance in fatigue life is the same at the various stress levels, and that there are no run-outs. For optimum results on real data, the number of tests at each level does not have to be a constant. Beretta et al. [55] conducted a very large number of tests on a 0.43% carbon steel to establish the fatigue properties and scatter for the material. They then conducted a statistical analysis to determine confidence levels of test sequences where the number of tests at each stress level was not constant. The statistical analysis took into account run-outs. As they point out, most existing recommendations are based on assumptions of

the lognormal distribution of lives, the absence of run-outs and, more restrictively, the same variance at each stress level. In their work, they assumed a lognormal distribution of lives at each stress level based on test results, but the distribution was different at each stress level. The largest scatter, as expected, was at the lowest stress level. Three statistical models were considered which have different relationships between the standard deviation and the applied log-stress: exponentially variable according to an exponential model by Nelson [56], linearly variable, and constant. The equations describing these models are shown below. For the mean, μ, the three models use

$$\mu = X_1 + X_2 \left(\log S - \overline{\log S} \right) \tag{3.21}$$

while the three models use the following functions for σ:

$$\sigma = \exp \left[X_3 + X_4 \left(\log S - \overline{\log S} \right) \right] \tag{3.22}$$

$$\sigma = X_3 + X_4 (\log S - \overline{\log S}) \tag{3.23}$$

$$\sigma = \exp (X_3) \tag{3.24}$$

where S is the applied stress, μ is the mean value and σ is the standard deviation of the (log) fatigue life, while $\overline{\log S}$ is the arithmetic average of all the values of $\log S$ in the test series. The constants X_1, X_2, X_3, and X_4 are fitting parameters for each statistical model based on maximum likelihood estimates. While the same function, Equation (3.21), is used for the mean, μ, for each of the models, the values of the parameters X_1 and X_2 are slightly different for each model because of the different distribution functions which they represent.

Using maximum likelihood analysis on the results of fatigue tests they obtained on the 0.43% carbon steel including run-outs, the parameters in the equations were determined for the three models. The models are shown, without the experimental data, in Figure 3.41 (a) through (c) where the mean (50% probability of failure) and 2.5 and 97.5% probability of failure curves are shown for each of the models. The differences in the distributions can be clearly seen, particularly at the lower stress levels.

To evaluate the results of using a small sample size, confidence levels were determined for various sample sizes randomly extracted from the total population of tests run for each model. The first point noted was that the model using a constant standard deviation, σ, Equation (3.24), independent of stress level (Figure 3.41c), provided the worst fit to the data and was not used in subsequent computations. It has been noted that the assumption of constant σ is the most commonly used, and virtually all statistical computer programs for curve fitting make this assumption because the mathematical theory and numerical computations are then simpler [56]. They observed that the Nelson model that uses the exponential variation of σ (Figure 3.41a) provides the best estimates of model parameters

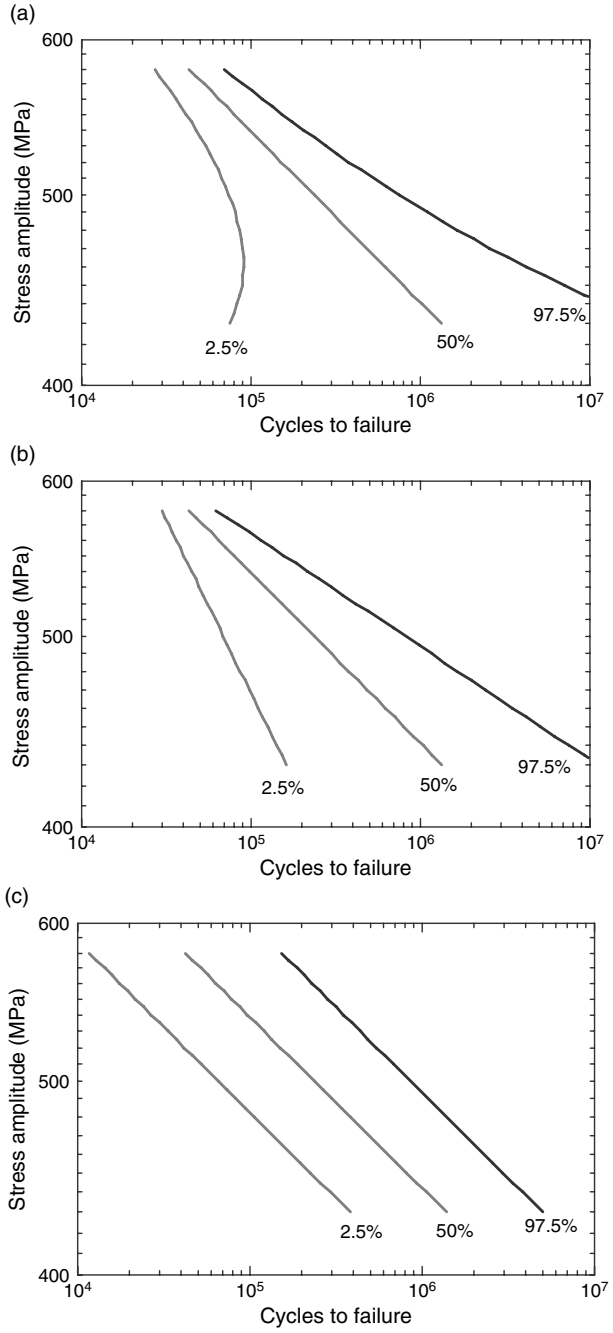


Figure 3.41. Models for fatigue life with standard deviation a function of stress: (a) exponential (Nelson), (b) linear, (c) constant.

and of mean log-lives for a material having variable scatter, provided that the precision at the highest stress level is markedly lower than the others. Their results also showed that results obtained from test programs with different number of specimens per level are better than those of plans with uniform replication. For the particular set of data used, from which experimental results were chosen at random for the statistical analysis, a confidence level of 90% could be obtained over the range $\pm\sigma$ using the following test programs: 10–3–5–6 specimens (a total of 24 specimens) tested at levels 550–520–490–460 MPa for the exponential (Nelson) model, Equation (3.22), and 10–3–6–10 specimens (a total of 29 specimens) tested at the same stress levels for the linear model, Equation (3.23).

3.8.1. Run-outs and maximum likelihood (ML) methods

A unique feature of testing in the HCF regime is the occurrence of run-out tests where the test is terminated after a certain (large) number of cycles. Alternately, a test that fails after N cycles can be used in an analysis describing the behavior for fewer than N cycles, so it can then be treated as a run-out for the fewer cycles being considered. Run-outs, in statistics terms, are considered to be censored data, that is, they fall outside the range of behavior (lives) being considered. In fitting models to data containing run-outs, the run-outs cannot be used in least-square fits because the exact location of the data point is unknown. All that is known is the fatigue life was greater than some quantity. Since least-squares methods cannot use censored data because the data points do not really exist, other methods have been employed. As mentioned in the discussion of the RFL model previously, maximum likelihood (ML) estimation schemes are able to deal with censored data from a statistical point of view. The virtue of the ML method is that it applies to virtually any assumed statistical distribution of lives or fatigue strengths as well as any form of data including run-outs. Details regarding ML theory and its application to fatigue data, particularly in the HCF regime, can be found in the book by Nelson [57], for example. The ML method not only provides valid estimates of the mean and standard deviation of a distribution function, it also provides confidence intervals for coefficients in the distributions or models. The application to various models for variable standard deviation, σ, as a function of stress, for example, was discussed above. ML estimates have good statistical properties for almost any assumed form of the fatigue life distribution and for almost any assumed form for the equation for the distribution parameters as functions of the stress or other variable [56]. In some simple cases where fatigue life is described by a lognormal distribution with constant σ and there are no run-outs, ML estimates of model coefficients are the same as standard least-squares regression estimates. Although ML methods are mathematically complex, they are easy to apply in practice using special computer packages that are now widely available [57]. The procedure involves writing equations for the likelihood of an event (failure in a given lifetime, for example) in terms of the unknown parameters of the distribution

function and/or model. The values of the coefficients that maximize the likelihood are then determined. This procedure generally involves nonlinear equations that cannot be solved algebraically, thus numerical methods are employed. The solution of these types of equations is what statistical computer codes are designed to accomplish using various numerical techniques. It is important that the solutions provide a global maximum of the likelihood function, not a local maximum nor a saddle point. Existence and uniqueness of the solutions also have to be established. There are some models for which the likelihood equations can be solved explicitly [57].

As a simple example of the ML method, we consider a set of ten hypothetical experiments at constant stress where the log lives to failure from each test are tabulated in ascending order in Table 3.10. These data are labeled "actual" and represent a data set where all tests would have been carried out to failure.

If these same tests had been conducted up to 10^7 cycles (log life $= 7$) and terminated at that point if no failure had occurred, then 3 of the tests would be recorded as run-outs (censored). Both sets of data are shown in Figure 3.42 on a probability plot assuming the log lives follow a normal distribution. The actual data are fit with a straight line to determine the constants for the normal distribution that represents this data set.

If the same data are taken with run-outs, the data set including 3 censored points that indicate only that the observed log lives were >7, the ML method can be employed. Using a commercial software package called Minitab, the data were evaluated assuming a normal fit to log life as was the case for the real data [58]. The results of that evaluation are shown in Figure 3.43 which shows both the best fit to a normal distribution of log life (time) as well as the 95% confidence bounds. The fit is almost identical to that of the entire (uncensored) data set shown in Figure 3.42.

For comparison purposes, the results of both fits are presented in Table 3.11. The analyses show that the ML method, using 7 data points and 3 run-outs, produces essentially

Table 3.10. Hypothetical log life data for testing with and without run-outs

Actual	*Censored*
5.8	5.8
6.0	6.0
6.2	6.2
6.3	6.3
6.5	6.5
6.7	6.7
6.9	6.9
7.1	7 run-out
7.3	7 run-out
7.6	7 run-out

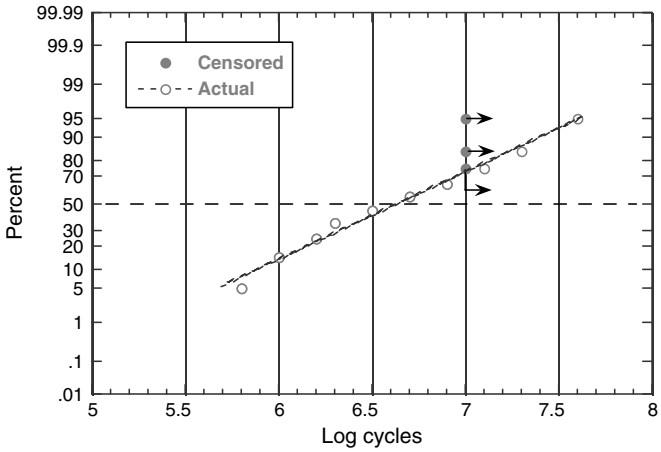


Figure 3.42. Statistical distribution of lives to failure with and without run-outs.

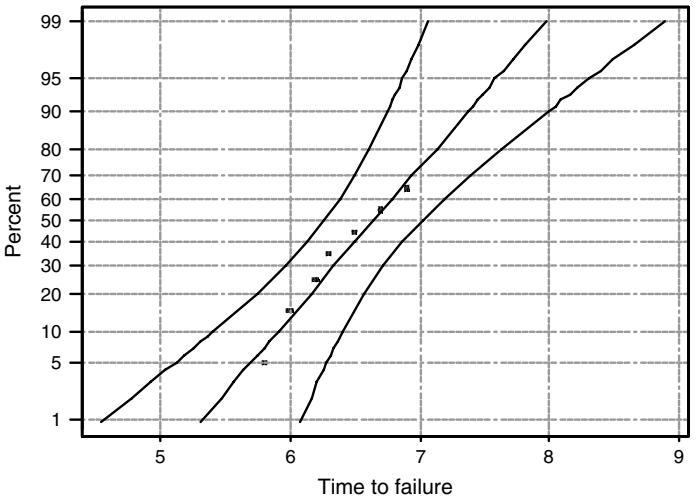


Figure 3.43. Statistical analysis of censored data using ML method.

Table 3.11. Constants for normal distribution of log life from standard and ML methods

Actual		*Censored*	
Mean	Stdev	Mean	Stdev
6.640	0.585	6.644	0.571

the same normal distribution as standard least squares methods for the specific data set of 10 data points chosen for this numerical example.

3.9. RESONANCE TESTING TECHNIQUES

Structural components subjected to high frequency vibrations, such as those used in rotating parts of gas turbine engines, are usually required to be designed using a lifetime failure-free criterion for a very large number of cycles, or an endurance limit. Tools, such as the constant life Haigh or Goodman diagram, described earlier in Chapter 2, are often used, but these diagrams are usually constructed using uniaxial fatigue data only, and the design is based on uniaxial stresses. While it is desirable to have data at many values of mean stress, or equivalent stress ratio, R, there are many cases in design where data at a single value of $R = -1$, fully reversed loading with zero mean stress, are the only data available. Such data, often obtained from vibratory tests on a specimen or component, are then used to construct a Modified Goodman diagram using a straight line extrapolation from the zero mean stress data point to the yield or ultimate strength of the material which is considered as zero alternating stress (see Figure 2.17 in Chapter 2). Alternate approaches such as the Jasper or other equation, as described earlier, can be used to construct a Haigh diagram by using an equation to represent behavior at all values of mean stress or stress ratio, but data for at least one value of R are needed to establish the constants.

Uniaxial fatigue tests on conventional test machines are the type of test normally conducted to obtain the required data for construction of a Haigh diagram. These tests require long time periods to achieve a large number of cycles approaching the endurance limit. Even a servo-hydraulic test machine operating at 60 Hz requires approximately 46 hours to accumulate 10^7 cycles for a point on an S–N curve. Additionally, for each value of mean stress or stress ratio, several data points are needed in order to interpolate the value of stress at the desired life (10^7 in this example) to get a single point on the Haigh diagram. Therefore, significant amounts of time are required to characterize the uniaxial fatigue properties of a material. While newer machines are available which can achieve higher frequencies, and ultrasonic machines that operate at 20 kHz have been developed [2], these tests are typically limited to uniaxial tension. Accelerated test methods, described in previous sections in this chapter, and test procedures such as step or staircase testing, described above, can save some time. However, these provide only uniaxial fatigue data which may be insufficient for assessing high cycle FLSs which often occur in components that are subjected to biaxial loading over a wide range of cyclic frequencies. In turbine blades, for example, fatigue failure often occurs under high order bending or combined bending and twist modes that produce short wave length stress states at very high frequencies. Unfortunately, the current capability to conduct

biaxial fatigue tests, especially under bending or torsion as well as axial stress states, is limited by the high cost of development of such testing methods as well as the lack of existing equipment to conduct the necessary tests at anything other than very low frequencies.

Resonant fatigue testing of some unique geometric configurations has recently been proposed [59] as a method for obtaining data heretofore unavailable because they involve both high frequencies and either uniaxial or biaxial bending stress states. It should be noted that resonant fatigue testing procedures have been in existence for over a century. In reviewing the history of resonant techniques, it can be pointed out that in the time period from 1879 to 1925, no fewer than 35 journal articles appeared describing new test procedures and methods for fatigue testing [60]. The earliest test methods involved coupling a specimen and a driver in order to obtain a resonance or near resonance condition to decrease the power requirements. It was recognized early on that "working in or near the resonance (unstable dynamic equilibrium) demands special controlling devices" [61]. These early machines were only able to achieve frequencies up to approximately 100 Hz and were confined to either pure axial or torsion modes under either resonant or non-resonant conditions [62]. Among the early test machines that operated on the resonance principle were those built by Sontag that produced a constant force at 30 Hz. The Schenck machines, of the 1930s and later [63], operated in a fairly stable manner by using a very large spring coupled to a much smaller specimen and could run continuously under constant load at approximately 30 Hz. Later on, such machines were controlled with automatic feedback from a load cell to correct for any deformation of the specimen during the test such as creep or initiation of a fatigue crack. A very large version of a Schenck machine [64] was used in the Messerschmitt factory during World War II to test large components, but the loading was still uniaxial. Electromagnetic resonant fatigue test machines are currently available having high-test frequencies of 40–300 Hz and boast of the same advantage of the first machines, namely low power consumption.

One of the advantages of a resonant machine where the specimen is part of the mechanical system is that upon incipient failure, the spring constant of the specimen changes and throws the system off resonance which is a warning of impending failure if it is desired to examine the specimen before total destruction of the sample [65]. In addition to mechanically driven machines, magnetic excitation to drive a machine/sample combination into resonance dates back to prior to World War II (see, e.g. [66]).

Tests of structural components and full-scale structures conducted under both resonant and non-resonant conditions [67] date back to the 1860s [68]. Because of the expense of the test articles as well as the test machines, such tests are normally limited to very few components and are not very useful for extracting fatigue properties of the material, even though the stress state at a failure point may be complex. Whatever information is extracted is limited to the specific number of cycles to failure due to the applied loading

condition. Fatigue limit strengths of the structure or the material are rarely obtained for cycle numbers near the endurance limit.

As discussed earlier in this chapter, a step-test procedure has been shown to produce fatigue limit data that are consistent with those obtained from interpolation of *S–N* curves at fixed values of mean stress or stress ratio. With a limited number of samples, since each sample produces a FLS data point, a Haigh diagram can be constructed in a reasonable amount of time. To achieve the goal of determining the FLS under uniaxial or biaxial bending, stress states that are commonly achieved in turbine blades under resonance conditions, a combination of the concepts described above have been utilized and expanded to develop a new testing procedure [59]. This vibration-based fatigue testing concept uses a base-excited plate specimen that is driven into a high frequency resonant mode. Using the step-testing procedure and finite element analysis of the vibrating specimen, the loads and stresses necessary to produce HCF failure corresponding to a fixed number of cycles (10^6 or 10^7) can be determined. The geometry of a plate that is driven into resonance by base excitation on a shaker can be either a square plate for uniaxial bending or a more complicated geometry as shown in Figure 3.44 for biaxial bending. For a square plate of steel with dimensions of 114 mm on a side, the natural frequency under a two-stripe mode is approximately 1200 Hz. The out-of-plane displacement profile and corresponding vonMises stresses are shown in Figure 3.45 for

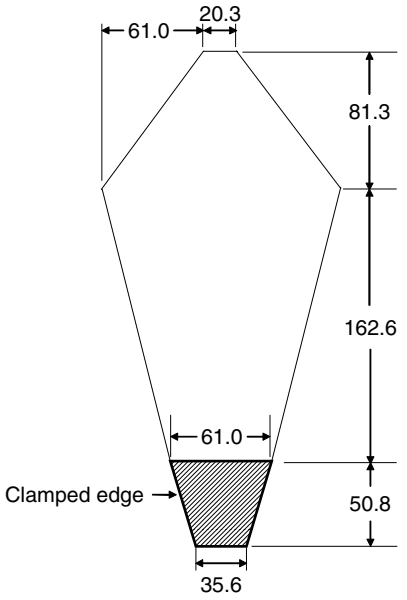


Figure 3.44. Resonant biaxial specimen dimensions (mm).

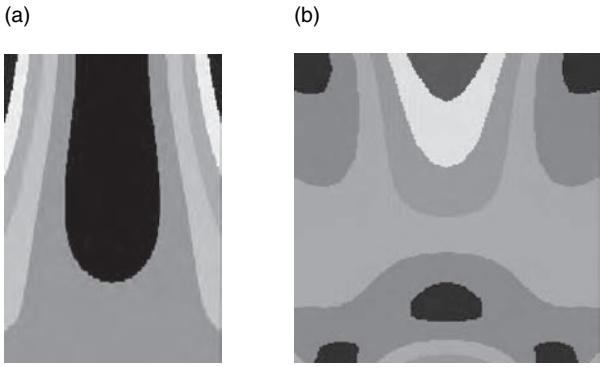


Figure 3.45. Out of plane displacements (a), and vonMises stresses (b), for square steel plate.

the steel plate of 2.4 mm thickness. The maximum stress occurs at the middle of the free end (top of picture) and is higher than any stresses at the fixed end (bottom) which is being excited by the shaker. The stresses at the free end were sufficient to cause cracks to form within 10^6 cycles using a conventional laboratory shaker/amplifier system [59].

For biaxial loading, the specimen shown in Figure 3.44 was base excited into a resonant two-stripe mode frequency of approximately 1600 Hz. The specimen was aluminum with a thickness of 3.1 mm. The out-of-plane displacements and vonMises stresses for the square steel and aluminum biaxial specimens are compared in Figures 3.45 and 3.46.

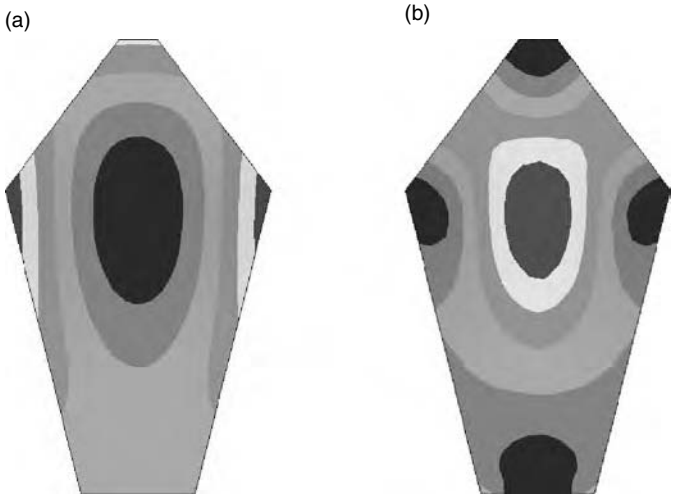


Figure 3.46. Out of plane displacements (a), and vonMises stresses (b), for aluminum biaxial specimen.

Figure 3.46 shows that the maximum stresses for the aluminum biaxial specimen occur along the centerline and away from the free end by approximately one-third of the length. For this particular geometry, the ratio of σ_y (vertical direction) to σ_x (horizontal direction) at the point of maximum stress is approximately 0.59.

These specimen geometries and the resultant two-stripe mode shapes of interest have been used to determine FLSs under uniaxial or biaxial bending with a step-test procedure. The mode shapes that were predicted by finite element method (FEM) and verified experimentally provided a method for calibrating stresses at the critical locations with observed transverse displacement amplitudes recorded with a laser vibrometer.

The fatigue limit strength in typical uniaxial tension tests, performed using conventional testing machines, is determined as the stress at which complete failure occurs under constant load, either by conventional *S–N* or step testing. For long life tests, total life, where the fatigue crack propagates through the specimen and failure occurs, is not distinguished from crack nucleation or crack initiation life. Computations have shown that the fatigue crack propagation life in a tensile bar is only a small fraction of total life when testing at stress levels near the HCF limit defined as 10^7 cycles [69]. In the case of vibration-based fatigue testing under resonance conditions, however, there does not exist a definitive phenomenon such as abrupt failure. Therefore, in the vibration-based tests, from the start of the test until the time of fatigue crack initiation, the response amplitude of the plate as measured by a laser vibrometer has to be monitored and adjusted by changing the amplitude and frequency of the shaker to keep the system in resonance and to maintain the desired stress level. In this technique, the fatigue limit is defined at the instant corresponding to a sudden change in the response of the plate, as opposed to the typical gradual changes in the dynamic response of the plate associated with the stiffness changes associated with fatigue crack development. A resonant frequency shift away from the shaker driving frequency was observable even in the initial stage of fatigue crack development [59].

In the tests conducted by George et al. [59], the vibration testing was continued in one of two ways after the FLS was determined. By varying the experimental technique, they were able to produce both short and long cracks. The technique to produce short cracks, on the order of a few millimeters or less, was to leave the shaker amplitude fixed after the FLS was determined and to propagate the crack by repeatedly re-tuning the shaker driving frequency to the resonant specimen frequency. As the crack propagated, the resonant frequency of the specimen decreased. With this technique, using a constant shaker amplitude, the maximum stress level in the crack tip region ultimately dropped to a level where the crack arrested. This technique produced cracks on the order of 1–2 mm in the case of steel specimens and 0.1 mm in the case of Ti-6Al-4V. To produce long cracks, on the order of tens of mm, the shaker amplitude had to be increased as necessary to continue propagating the crack.

For the biaxial specimen of Figure 3.44, the frequency response exhibited nonlinear hardening which produces specimen response at the natural frequency which is unstable [59]. As the fatigue crack begins to develop and decrease the stiffness of the plate the natural frequency begins to drop and the response immediately decreases drastically. This sudden drop enables small cracks to initiate and then arrest because of the sudden decrease in the forcing function. This phenomenon enabled George et al. [59] to produce an approximately 0.4 mm long series of microcracks in their biaxial specimen.

One of the most important observations from the experiments of George et al. [59] is that the formation of a crack in a specimen reduces the natural frequency of the system. If the frequency of the excitation remains fixed, the level of response at that frequency will be reduced, and a new peak response will be present at a lower frequency. This observation in itself is not new, but its implication on gas turbine engine fatigue could drastically change widely held design and maintenance conventions. From the fatigue perspective, this implies that for a constant level and frequency of excitation, once a crack is initiated, the level of strain in the component is reduced. If this level of strain is reduced below the level needed to propagate the crack, the crack will self-arrest. In order to continue crack growth, the frequency of excitation must be reduced to meet the new peak response frequency, and if it does, the fatigue process continues. For the case of forced response in a gas turbine engine, where the excitation consists of distinct tones, or narrow bands, of aerodynamic drivers, a crack could self arrest once the peak response frequency shifts away from the forcing frequency. For high order modes, where mode shapes tend to have localized areas of high strain, a small crack might form, propagate slightly and then arrest without having an adverse effect on the overall structure. For a broadband excitation, such as inlet distortion or low order excitation of the turbine from combustor effects, the above scenario is less likely and the crack would continue to propagate since an excitation would be strong over a wide range of frequencies. As with classic laboratory fatigue experiments in which a crack is chased by changing frequency to continue crack propagation, as the natural frequency of the component changed, there would be an excitation waiting to continue fatigue through to failure.

3.10. FREQUENCY EFFECTS

Questions have arisen over the years about frequency effects on the HCF behavior and fatigue limit strength of materials and structural components. While laboratory testing has traditionally dealt with frequencies typically below 100 Hz,[*] components in turbine engines can undergo vibratory stresses well into the kHz regime. It is natural to ask, therefore, what effect does frequency have upon the fatigue behavior of materials. Dealing

[*] See Chapter 2, Section 2, for a discussion of gigacycle fatigue and testing at 20 kHz.

solely with material behavior, data on a number of structural materials [70], show that metals exhibit very little difference in strength in terms of strain rate effects up to nominal strain rates in the 1–100 s^{-1} regime. However, these rate effects are confined to the inelastic regime of material behavior, so these numbers should not necessarily apply to fatigue in the HCF regime where behavior is nominally elastic. Further, for the purpose of translating strain rates into equivalent frequencies, consider that nominal maximum strains in the HCF regime are of the order of less than 1% (0.01), so a frequency of 1 kHz would correspond to a strain rate of less than 10 s^{-1}. Finally, gigacycle fatigue testing conducted at frequencies of 20 kHz has shown little or no difference in fatigue strength than results obtained at conventional frequencies. It is significant to note that, for reasons not related to frequency effects, gigacycle fatigue testing is being conducted by many on rotating beam machines that operate at under 60 Hz.

It is with great interest and curiosity that examination of the results of fatigue tests conducted in the 1950s and earlier show what appear to be frequency effects in a number of materials. Lomas et al. [71] summarize many of the findings up to their publication date in 1956 which includes much speculation as to the validity of many of the early results reporting frequency effects. Most of the data were considered unreliable and some of the findings were attributed to heating effects at higher frequencies. They cite the work of Jenkin [72] and Jenkin and Lehmann [73], the latter of who's work they plot in their paper, reproduced here as Figure 3.47. The materials represented here include copper, aluminum, and several steels: 0.86% carbon, 0.11% carbon, rolled, Armco iron,

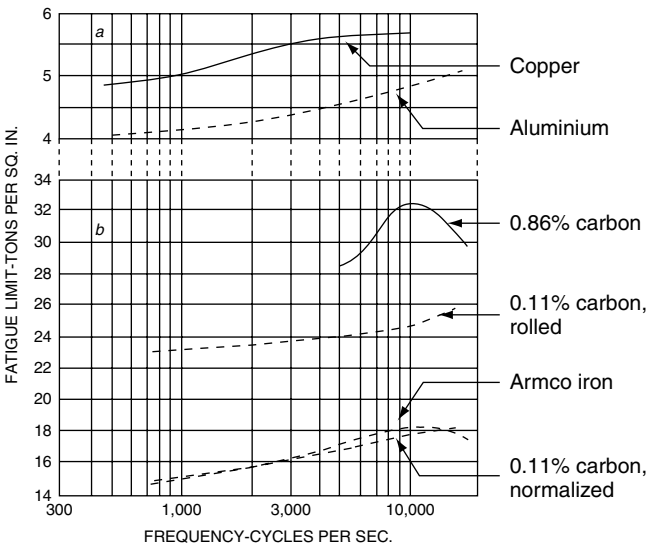


Figure 3.47. Endurance stress data of [73] replotted by Lomas et al. [71].

and 0.11% carbon, normalized. While most of the materials show an increase of fatigue limit strength as a function of frequency, 0.86% carbon steel and, to a lesser extent Armco iron, show a maximum stress at a frequency of approximately 10 kHz.

The early results of Jenkin [72] were obtained using a resonance technique on simply supported beams excited electromagnetically, but the specimen dimensions were much smaller than those used by Lomas et al., thereby producing a range of resonant frequencies that were much higher. Later, Jenkin and Lehmann [73] further extended the frequency range by using even smaller bend specimens excited pneumatically with pressure pulses. The first experiments of Jenkin [72] on copper, Armco iron and mild steel were able to easily cover a frequency range up to 1 kHz. Their results showed that "materials (. . . similar to those tested) gain slightly in their strength to resist fatigue as the speed goes up, but for most practical speeds the gain is insignificant." Jenkin and Lehmann [73] achieved frequencies up to nearly 20 kHz and showed significant frequency effects. They question, however, their own mathematical analysis of the strains based on beam deflection (contributed by Prof. Love) and the purely elastic behavior of the materials which might affect the smaller bar (higher frequency) tests in a systematic manner.

The results of the tests by Lomas et al. [71], shown in Figure 3.48, were obtained from resonance tests on cantilever beams of different dimensions in order to achieve a wide range of natural frequencies. Of note is the characteristic shape of the curves where the fatigue limit strength, corresponding to 10^8 cycles, increases with frequency up to a maximum and then decreases with further increase in frequency for almost all of the ferrous alloys tested. As pointed out by the authors, the grave difference in the results with those of Jenkin is that the peak is obtained at a very different frequency. In Figure 3.48, the peak is seen to occur in the 1–2 kHz regime compared to 10 kHz for Jenkin (Figure 3.47) for a similar class of alloys. While these results are cited sometimes as an example of frequency effects on the fatigue or endurance limit (see Collins [74] for example), it is this author's opinion that aspects of the resonance methods used may be responsible for the apparent effects and discrepancies between investigators. Of greatest concern is that there exists a maximum value of fatigue limit strength with frequency among several different alloys, yet this maximum occurs near the same frequency for each of the alloys. Of unknown significance is that the data point at each frequency is obtained with a different size cantilever beam, but the same geometry beam is used for each of the materials at a given frequency. The observed behavior, however, is in contradiction with observed strain rate effects in many metallic materials [70] and the modeling of such effects where a monotonically increasing effect of strength with strain rate is the norm.* While it is not the intent of this book to critique the referenced observations in detail,

* As pointed out earlier, strain rate effects in metals have been studied almost exclusively in the inelastic regime of material behavior and constitute the field of dynamic plasticity. Strain rate effects under nominally elastic conditions are widely considered to be nonexistent.

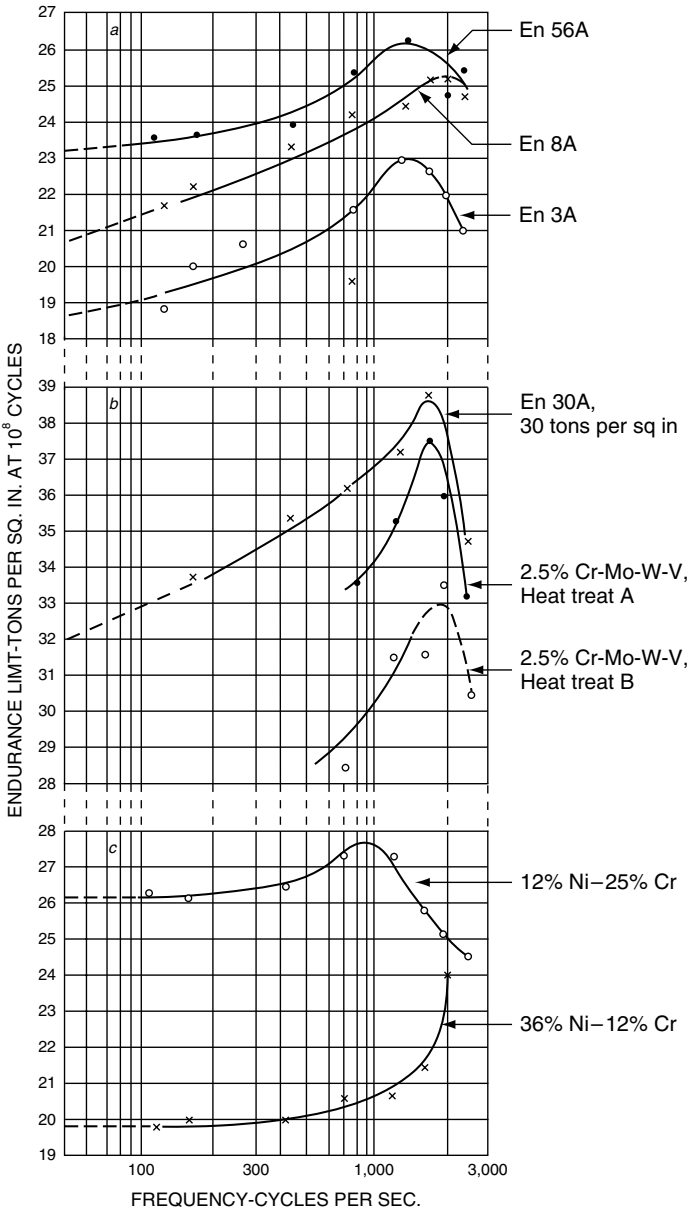


Figure 3.48. Endurance stress as a function of frequency for several materials [71].

it is important to point out some of the potential problems that might be encountered when using resonance tests on simple structural components for obtaining fatigue limit strengths. Of the many concerns, hysteretic heating can lead to changes in behavior even though Morrissey and Nicholas [75] have shown that, in 20 kHz resonance tests on titanium, the effect of temperature rise when running tests without external cooling is negligible. Other issues that have to be considered in conducting resonance tests are the material damping, the structural damping from the experimental apparatus such as supports or grips, and the aerodynamic damping when conducting high frequency tests in air. Of prime concern is that the geometry of the specimen has to be different for each frequency tested in order to achieve different resonant frequencies. This can also raise potential issues regarding the effective stressed area or volume or the stress gradient in bending for different thickness specimens. It should also be noted that these types of tests are not pure resonance tests but, rather, are forced vibrations of lightly damped systems, conducted at or near the resonant frequencies of the test article. The analysis that leads to interpretation of the experimentally observed quantities such as peak displacements is quite complicated, and the ability to maintain the test at a resonant frequency under constant conditions is very difficult. The cited observations of Lomas et al. [71] and the comparisons of his data with similar data from Jenkin and Lehmann [73] serve to point out the need to carefully analyze and interpret experimental findings when using resonance techniques for determination of fatigue limit strengths.

REFERENCES

1. Morgan, J.M. and Milligan, W.W., "A 1 kHz Servohydraulic Testing System", *High Cycle Fatigue of Structural Materials*, W.O. Soboyejo, and T.S. Srivatsan, eds, The Minerals, Metals & Materials Society, 1997, pp. 305–312.
2. Mayer, H., "Fatigue Crack Growth and Threshold Measurements at Very High Frequencies", *International Materials Reviews*, **44**(1), 1999, pp. 1–34.
3. Marines, I., Dominguez, G., Baudry, G., Vittori, J.-F., Rathery, S., Doucet, J.-P., and Bathias, C., "Ultrasonic Fatigue Tests on Bearing Steel AISI-SAE 52100 at Frequency of 20 and 30 kHz", *Int. J. Fatigue*, **25**, 2003, pp. 1037–1046.
4. Gough, H.J., *The Fatigue of Metals*, Ernst Benn Limited, London, 1926.
5. Smith, J.H., "Some Experiments on Fatigue of Metals", *Jour. Iron and Steel Inst., Pt. II*., 1910.
6. Moore, H.F. and Jasper, T.M., "An Investigation of the Fatigue of Metals, Bulleting No. 136", *Eng. Expt. Stat.*, Univ. Illinois, Urbana, 1924.
7. Schütz, W., "A History of Fatigue", *Engineering Fracture Mechanics*, **54**, 1996, pp. 263–300.
8. Ransom, J.T. and Mehl, R.F., "The Statistical Nature of the Endurance Limit", *Metals Trans.*, **185**, 1949, pp. 364–365.
9. Epremian, E. and Mehl, R.F., "Investigation of Statistical Nature of Fatigue Properties", NACA-TN-2719, June 1952.
10. Sinclair, G.M., "An Investigation of the Coaxing Effect in Fatigue of Metals", *ASTM Proceedings*, **52**, 1952, pp. 743–758.

11. Forsyth, P.J.E., *The Physical Basis of Metal Fatigue*, Blackie & Son Ltd, London, 1969.
12. Maennig, W.-W., "Planning and Evaluation of Fatigue Tests", *ASM Handbook*, Volume 19, Fatigue and Fracture, ASM International, Materials Park, 1996, pp. 303–313.
13. Moore, H.F. and Wishart, H.B., "An 'Overnight' Test for Determining Endurance Limit. Proc. ASTM", **33**, Part II, 1933, pp. 334–347.
14. Prot, M., "Un Nouveau Type de Machine D'Essai des Metaux a la Fatigue par Flexion Rotative", *Rev. Metall.*, **34**, 1937, 440; see also: Prot, M., "Fatigue Tests Under Progressive Load. A New Technique for Testing Materials", *Rev. Métall.,* **45**(12), December 1948, pp. 481–489.
15. Ward, E.J., Schwartz, R.T., and Schwartz, D.C., "An Investigation of the Prot Accelerated Fatigue Test", *Proc. ASTM*, **53**, 1953, pp. 885–891.
16. Corten, H.T., Dimoff, T., and Dolan, T.J., "An Appraisal of the Prot Accelerated Fatigue Test", *Proc. ASTM*, **54**, 1954, pp. 875–894.
17. Dolan, T.J., Richart, F.E., Jr., and Work, C.E., "The Influence of Fluctuations in Stress Amplitude on the Fatigue of Metals", *Proceedings ASTM*, **49**, 1953, p. 646.
18. Hempel, M., "Performance of Steel under Repeated Loading", *Fatigue in Aircraft Structures*, A.M. Freudenthal, ed., Academic Press, New York, 1956, pp. 83–103.
19. Epremian, E. and Mehl, R.F., "A Statistical Interpretation of the Effect of Understressing on Fatigue Strength. Fatigue with Emphasis on Statistical Approach", *ASTM STP 137*, American Society for Testing and Materials, 1952, pp. 58–69.
20. Vitovec, F.H. and Lazan, B.J., "Strength, Damping and Elasticity of Materials Under Increasing Reversed Stress with Reference to Accelerated Fatigue Testing", *Proc. ASTM*, **55**, 1955, pp. 844–862.
21. Nicholas, T. and Maxwell, D.C., "Evolution and Effects of Damage in Ti-6Al-4V under High Cycle Fatigue", *Progress in Mechanical Behaviour of Materials, Proceedings of the Eighth International Conference on the Mechanical Behaviour of Materials*, ICM-8, F. Ellyin, and J.W. Provan, eds Vol. III, 1999, pp. 1161–1166.
22. Maxwell, D.C. and Nicholas, T., "A Rapid Method for Generation of a Haigh Diagram for High Cycle Fatigue", *Fatigue and Fracture Mechanics: 29th Volume, ASTM STP 1321*, T.L. Panontin, and S.D. Sheppard, eds, American Society for Testing and Materials, West Conshohocken, PA, 1999, pp. 626–641.
23. Gallagher, J.P. et al., "Improved High Cycle Fatigue Life Prediction", Report # AFRL-ML-WP-TR-2001-4159, University of Dayton Research Institute, Dayton, OH, January, 2001 (on CD ROM).
24. Gallagher, J. et al., "Advanced High Cycle Fatigue (HCF) Life Assurance Methodologies", Report # AFRL-ML-WP-TR-2005-4102, Air Force Research Laboratory, Wright-Patterson AFB, OH, July 2004.
25. Ruschau, J.J., Nicholas, T., and Thompson, S.R., "Influence of Foreign Object Damage (FOD) on Fatigue Life of Simulated Ti-6Al-4V Airfoils", *Int. Jour. Impact Engng*, **25**, 2001, pp. 233–250.
26. Bellows, R.S., Muju, S., and Nicholas, T., "Validation of the Step Test Method for Generating Haigh Diagrams for Ti-6Al-4V", *Int. J. Fatigue*, **21**, 1999, pp. 687–697.
27. Bathias, C., "Relation Between Endurance Limits and Thresholds in the Field of Gigacycle Fatigue", *Fatigue Crack Growth Thresholds, Endurance Limits, and Design, ASTM STP 1372*, American Society for Testing and Materials, West Conshohocken, PA, 2000, pp. 135–154.
28. Bellows, R.S., Bain, K.R., and Sheldon, J.W., "Effect of Step Testing and Notches on the Endurance Limit of Ti-6Al-4V", *Mechanical Behavior of Advanced Materials*, MD-Vol. 84, D.C. Davis et al., eds, ASME, New York, 1998, p. 27.

29. Morrissey, R.J., McDowell, D.L., and Nicholas, T., "Frequency and Stress Ratio Effects in High Cycle Fatigue of Ti-6Al-4V", *Int. J. Fatigue*, **21**, 1999, pp. 679–685.
30. Moshier, M.A., Hillberry, B.M., and Nicholas, T., "The Effect of Low-Cycle Fatigue Cracks and Loading History on the High Cycle Fatigue Threshold", *Fatigue and Fracture Mechanics: 31st Volume, ASTM STP 1389*, G.R. Halford, and J.P. Gallagher, eds, American Society for Testing and Materials, West Conshohocken, PA, 2000, pp. 427–444.
31. Golden, P.J., Bartha, B.B., Grandt, A.F., Jr., and Nicholas, T., "Measurement of the Fatigue Crack Propagation Threshold of Fretting Cracks in Ti-6Al-4V", *Int. J. Fatigue*, **26**, 2004, pp. 281–288.
32. Caton, M.J., "Predicting Fatigue Properties of Cast Aluminum by Characterizing Small-Crack Propagation Behavior", PhD Dissertation, University of Michigan, 2001.
33. Nicholas, T., "Step Loading for Very High Cycle Fatigue", *Fatigue Fract. Engng. Mater. Struct.*, **25**, 2002, pp. 861–869.
34. Lin, S.-K., Lee, Y.-L., and Lu, M.-W., "Evaluation of the Staircase and the Accelerated Test Methods for Fatigue Limit Distributions", *Int. J. Fatigue*, **23**, 2001, pp. 75–83.
35. Dixon, W.J. and Mood, A.M., "A Method for Obtaining and Analyzing Sensitivity Data", *J. Amer. Stat. Assn.*, **43**, 1948, pp. 109–126.
36. Finney, D.J., *Probit Analysis*, 3rd ed., Cambridge University Press, 1971.
37. Fisher, R.A., *Statistical Methods for Research Workers*, 14th Edition, Oliver and Boyd Ltd, Edinburgh, 1969.
38. *A Guide for Fatigue Testing and the Statistical Analysis of Fatigue Data*, ASTM STP 91-A, 2nd ed., American Society for Testing and Materials, 1963, pp. 12–13.
39. Braam, J.J. and van der Zwaag, S., "A Statistical Evaluation of the Staircase and the ArcSin$\sqrt{P}$ Methods for Determining the Fatigue Limit", *Journal of Testing and Evaluation*, JTEVA, **26**, 1998, pp. 125–131.
40. Davoli, P., Bernasconi, A., Filippini, M., Foletti, S., and Papadopoulos, I.V., "Independence of the Torsional Fatigue Limit Upon a Mean Shear Stress", *Int. J. Fatigue*, **25**, 2003, pp. 471–480.
41. Little, R.E. and Jebe, E.H., *Statistical Design of Fatigue Experiments*, Applied Science Publishers, Essex, 1975.
42. Brownlee, K.A., Hodges, J.L. Jr., and Rosenblatt, M., "The Up-and-Down Method with Small Samples", *J. Amer. Stat. Assn.*, **48**, 1953, pp. 262–277.
43. Dixon, W.J., "The Up-and-Down Method for Small Samples", *J. Amer. Stat. Assn.*, **60**, 1965, pp. 967–978.
44. Efron, B. and Tibshirani, R.J., *An Introduction to the Bootstrap*, Chapman and Hall, New York, 1993.
45. Morrissey, R.J. and Nicholas, T., "Staircase Testing of Titanium in the Gigacycle Regime", presented at *3rd International Conference on Very High Cycle Fatigue (VHCF-3)*, Ritsumeikan University, Shiga, Japan, 16–19 September 2004.
46. Pascual, and Meeker, "Estimating Fatigue Curves with the Random Fatigue-Limit Model", *Technometrics*, **41**, No. 4, with comments, November 1999, pp. 277–302.
47. MIL-HDBK-5G, Metallic Materials and Elements for Aerospace Vehicle Structures, **2**, 1 November 1994, pp. 9–100.
48. Berens, A.P. and Annis, C., "Characterizing Fatigue Limits for Haigh Diagrams", *Proceedings of the 5th National Turbine Engine High Cycle Fatigue Conference*, Chandler, AZ, 7–9 March 2000 (see also [24 Appendix B]).
49. Meeker, W.Q. and Escobar, L.A., *Statistical Methods for Reliability Data*, John Wiley & Sons, New York, 1998.

50. Annis, C. and Griffiths, J., "Staircase Testing and the Random Fatigue Limit", *Proceedings of the 6th National Turbine Engine High Cycle Fatigue Conference*, Jacksonville, FL, 6–8 March 2001.
51. Smith, K.N., Watson, P., and Topper, T.H., "A Stress-Strain Function for the Fatigue of Metals", *Journal of Materials*, JMLSA, **5**, No. 4, December 1970, pp. 767–778.
52. Doner, M., Bain, K.R., and Adams, J.H., "Evaluation of Methods for the Treatment of Mean Stress Effects on Low-Cycle Fatigue," *Journal of Engineering for Power*, 1981, pp. 1–9.
53. Loren, S., "Fatigue Limit Estimated using Finite Lives", *Fatigue Fract. Engng. Mater. Struct.*, **26**, 2003, pp. 757–766.
54. ASTM E739-91, Standard Practice for Statistical Analysis of Linear or Linearized Stress-Life (S–N) and Strain-Life (e-N) Fatigue Data, 1998.
55. Beretta, S., Clericic, P., and Matteazzi, S., "The Effect of Sample Size on the Confidence of Endurance Fatigue Tests", *Fatigue Fract. Engng. Mater. Struct.*, **18**, 1995, pp. 129–139.
56. Nelson, W., "Fitting of Fatigue Curves with Nonconstant Standard Deviation to Data with Run-outs", *Journal of Testing and Evaluation*, JTEVA, **12**, 1984, pp. 69–77.
57. Nelson, W., *Accelerated Testing: Statistical Models, Test Plans, and Data Analyses*, John Wiley & Sons, New York, 1990.
58. Berens, A., University of Dayton Research Institute, 2004, private communication.
59. George, T.J., Seidt, J., Shen, M.-H. H., Nicholas, T., and Cross, C.J., "Development of a Novel Vibration-Based Fatigue Testing Methodology", *Int. J. Fatigue*, **26**, 2004, pp. 477–486.
60. Sendeckyj, G.P., *Bibliography on the History of Fatigue*, Air Force Research Laboratory, Materials Directorate 1997 (unpublished).
61. Bernhard, R.K., "Testing Materials in the Resonance Range", *Proc. ASTM*, **41**, 1941, pp. 747–757.
62. Nowack, H., "Fatigue Test Machines", *Fatigue Test Methodology*, AGARD Lecture Series No. 118, North Atlantic Treaty Organization, October 1981, pp. 3-1–3-23.
63. Memmler, K. and Laute, K., "Dauerversuche an der Hochfrequenz-Zuf-Druck-Maschine, Bauert-Schenck [Fatigue tests with the Schenck high frequency tension-compression machine]", *Forschungsarbeiten a. d. Gebiete d. Ingenieur-wesens*, No. 329, 1930, p. 32; Abstract: *Z. Ver. dtsch. Ing*, 8 February, 1930, **74**, pp. 189–190; *Z. Metallk.*, 1930 July, **22**, pp. 249–250.
64. Herzog, A., "Six ton Schenck Fatigue Testing Machine", *Tech. Rep. U.S. Army Air Force*, No. 5623, 15 August, 1947, p. 24.
65. Rawlins, R.E., "Fatigue Tests at Resonant Speed", *Metal Prog.*, 1947, **47**, pp. 265–267.
66. Fehr, R.O. and Schabtach, C., "Resonant Vibration Testing", *Steel*, **109**, 1941, pp. 64–65, 96, 102.
67. *Symposium on Large Fatigue Testing Machines and Their Results*, ASTM STP 216, American Society for Testing and Materials, Philadelphia, 1958.
68. Fairbairn, W., "Experiments to Determine the Effect of Impact Vibratory and Long-Continued Changes of Load on Wrought-Iron Girders", *Phil. Trans. Roy. Soc., London*, **154**, 1864, pp. 311–326.
69. Morrissey, R.J., Golden, P., and Nicholas, T., "The Effect of Stress Transients on the HCF Endurance Limit", *Int. J. Fatigue*, **25**, 2003, pp. 1125–1133.
70. Nicholas, T., "Material Behavior at High Strain Rates", *Impact Dynamics*, Chapter 8, J. Zukas et al., eds, Wiley, New York, 1982, pp. 277–332.
71. Lomas, T.W., Ward, J.O., Rait, J.R., and Colbeck, E.W., "The Influence of Frequency of Vibration on the Endurance Limit of Ferrous Alloys at Speeds up to 150,000 Cycles per Minute Using a Pneumatic Resonance System", *Proceedings of the International Conference on Fatigue of Metals*, Inst. Mech. Engrs, London, 1956, pp. 375–385.

72. Jenkin, C.F., "High Frequency Fatigue Tests", *Proc. Roy. Soc., A*, **109**, 1925, pp. 119–143.
73. Jenkin, C.F. and Lehmann, G.D., "High Frequency Fatigue", *Proc. Roy. Soc., A*, **125**, 1929, pp. 83–119.
74. Collins, J., *Failure of Materials in Mechanical Design*, John Wiley and Sons, New york, 1993, p. 224.
75. Morrissey, R.J. and Nicholas, T., "Fatigue Strength of Ti-6A1-4V at Very Long Lives," *Int. J. Fatigue*, **27**, 2005, pp. 1608–1612.

Part Two
Effects of Damage on HCF Properties

The following four chapters deal with the general subject of the effects of damage on HCF material capability. While HCF alone is a subject that has been well covered in the literature, the effects of damage on the HCF properties of materials have received much less attention. Of concern in design is the effect of any potential damaging mechanism in the form of fatigue cracking, for example, on the fatigue limit strength (FLS) of a material. The terminology HCF implies a potentially very high number of cycles so that HCF capability is discussed here in terms of FLS corresponding to an endurance limit or a threshold for crack propagation when damage can be characterized in terms of an actual fatigue crack. Damage can be in the form of any loading or service event that degrades the properties of a material, whether it be in the form of fatigue cracks or deformation due to creep or corrosion. Chapter 4 starts with a discussion of the influence of LCF cycles on the HCF limit stress of a material. The LCF cycling is loosely categorized here as cycling at higher amplitudes than the HCF limit stress in an undamaged material. HCF cycles that have occasional transients above the FLS also constitute a combined loading spectrum that can be considered as LCF–HCF. The general condition of LCF superimposed with HCF is also considered to be a spectrum load condition where the HCF is subjected to periodic underloads (negative overloads). From both an experimental point of view and a service condition, the LCF loading can occur before any HCF loading or, in the more usual spectrum type loading, can be intermixed with the HCF loads. Causes of damage other than LCF, such as cracks forming at notches or stress concentrations, fretting fatigue that may produce cracks, or FOD, all produce similar conditions where HCF capability may be degraded. All of these subjects are discussed here in Part Two of this book.

This page intentionally left blank

Chapter 4
LCF–HCF Interactions

4.1. SMALL CRACKS AND THE KITAGAWA DIAGRAM

Of primary concern in HCF design is the material capability after it has been subjected to service conditions that may degrade capability over time and cycles. LCF loading, while accounted for in design and not leading to failure during the design life, may degrade the capability of the material regarding its HCF resistance. One other form of potential damage, which is due to transient stresses above the fatigue limit during HCF loading, must also be considered. A practical problem arises when, in designing against HCF, the occurrence of stress transients above the FLS becomes a possibility. Both stress transients above the FLS and prior or combined loading, under conditions where part of the loading is above the HCF limit, constitute conditions that will be referred to as LCF–HCF loading. The LCF portion of the loading is designated as such irrespective of the frequency of loading and is not necessarily restricted to true LCF conditions that normally involve strain-control testing, a low number of cycles to failure, and inelastic deformation in a typical load-displacement loop. It is simply used to designate loading conditions that are different than the HCF conditions being evaluated.

Research into the interactions of LCF with HCF thresholds has spanned the range from tests on smooth bars under LCF loading to the initiation of cracks under LCF, usually in a notched specimen, to determine the threshold for subsequent crack propagation in terms of a threshold stress intensity. In many of these studies, and to bridge the gap between no observable cracks and measurable cracks from prior LCF loading, the concept of a small crack arises. In work reviewed in [1], the threshold for continued fatigue after LCF loading involved analysis of many data points corresponding to crack depths below 100 μm, with many of those below 50 μm, in a titanium alloy. These crack lengths tend towards the region that is commonly referred to as the small or short crack regime. In this regime, it is found that the threshold stress intensity for crack propagation is lower than the long crack threshold, and the behavior is termed “anomalous” by many researchers. An effective way of plotting threshold data for small cracks is to use the Kitagawa diagram [2] shown schematically in Figure 4.1, where stress at threshold is plotted against crack length. The diagram shows a region below the threshold stress intensity and the endurance limit stress, joined by a correction due to El Haddad et al. [3], where cracks

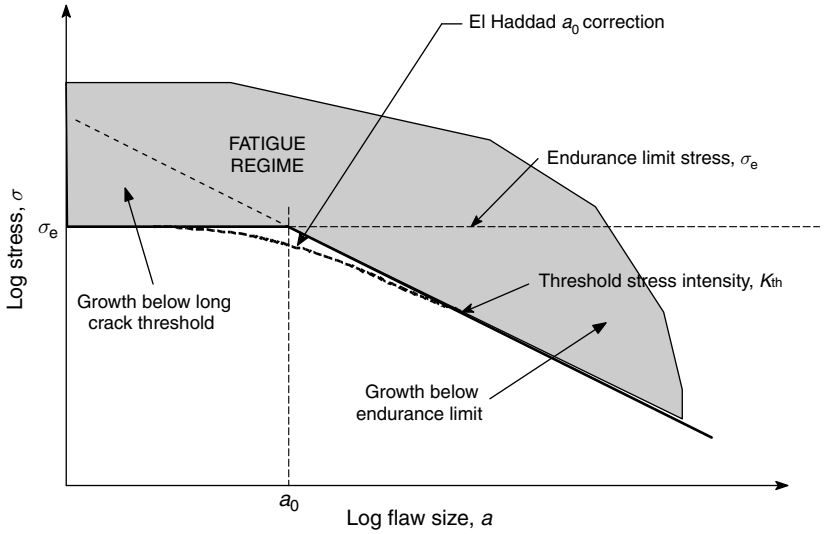


Figure 4.1. Schematic of a Kitagawa diagram.

should not grow.* There are two regions shown in the diagram where cracks can exist either below the endurance limit or the below the extrapolated long crack threshold. In the first case, the crack behavior is dominated by fracture mechanics, not stress. In the second, the small crack correction of El Haddad smoothes out the threshold curve in order to meet the endurance limit at very small crack lengths.

The Kitagawa type diagram [2], shown again schematically in Figure 4.2, is a useful tool to evaluate the potential for a crack to reduce the HCF capability of a material, irrespective of crack size. This plot of stress (σ) against crack length (a) on log–log scales was first suggested for a simple edge-crack geometry where stress intensity is proportional to $\sqrt{a}$. The endurance limit when no crack is present, or the threshold stress intensity when there is a crack, represent the limits above which failure might occur and below which it will not, corresponding to some chosen number of cycles or crack growth rate, respectively. The endurance limit is a horizontal line in Figure 4.2 while the threshold stress intensity is line of slope $= -0.5$ for the simple edge crack. The two

* The terminology for the diagram with log stress plotted against log crack length [2], used subsequently for any crack geometry and stress ratio, is referred to variously in the literature as a Kitagawa–Takahashi diagram, a K–T diagram, a Kitagawa type diagram, or most commonly, a Kitagawa diagram. In this book, the common terminology "Kitagawa diagram" will be used to refer to that type of plot. In a similar manner, the terminology "El Haddad short crack correction" will be used to represent the contribution of El Haddad et al. [3]. The use of this terminology is in no way meant to be disrespectful to, or to ignore the contributions of, the co-authors of Kitagawa or El Haddad in the referenced publications. Rather, the respective terminologies are for convenience only.

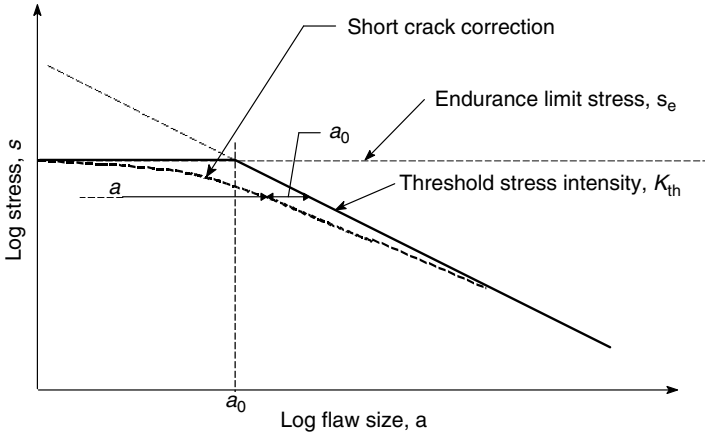


Figure 4.2. Schematic of a Kitagawa diagram for any geometry. Short cracks of length a behave as if they were long cracks with length $a + a_0$.

lines can be connected to form a single curve for all crack lengths using the short crack correction proposed by El Haddad et al. [3]. In the work of Moshier et al. [4], it is shown how the Kitagawa diagram can be used for any crack geometry. In their application, they applied it to a surface flaw in a double-edge-notch tension specimen. Of particular significance in using the Kitagawa diagram for any geometry is that the endurance limit and the value of a_0 for the short crack correction are not material constants but, rather, material parameters for the particular geometry and stress ratio, R, being investigated.

To describe the Kitagawa diagram mathematically for any geometry, the following analysis is presented. The K solution for any crack geometry can be written in the form

$$K = \sigma\sqrt{\pi a}\; Y(a) \tag{4.1}$$

where K is the stress intensity, σ is the stress, a is the crack length, and $Y(a)$ defines the K solution for a particular geometry. If Equation (4.1) is written for the threshold condition of a long crack, and the crack length is represented by a_1, then the long-crack solution for stress as a function of crack length, the threshold line in Figure 4.2, is

$$\sigma = \frac{K_{\text{th,LC}}}{\sqrt{\pi a_1}\; Y(a_1)} \tag{4.2}$$

where $K_{\text{th,LC}}$ represents the long-crack threshold stress intensity, a material constant for a given stress ratio, R. Denoting the intersection of the long crack threshold and the endurance limit stress in Figure 4.2 by a_0, the intersection is defined in the equation

$$\sigma_e = \frac{K_{\text{th,LC}}}{\sqrt{\pi a_0}\; Y(a_0)} \tag{4.3}$$

where σ_e is the endurance limit stress for the particular geometry for which the K solution is given by Equation (4.1). The usual form for this equation solves for a_0,

$$a_0 = \frac{1}{\pi}\left(\frac{K_{th,LC}}{\sigma_e Y(a_0)}\right)^2 \tag{4.4}$$

and is commonly found with the $Y(a)$ term missing or equal to a constant. For the more general case, either of these Equations (4.3) or (4.4), can be solved for a_0 either iteratively or graphically. Equation (4.4) for a_0 will be used extensively in the remainder of the book and will be repeated quite often.

The short crack correction of El Haddad et al. [3], shown graphically in Figure 4.2, uses the concept that a crack of length a behaves as if it had a length $a + a_0$, which has the long crack threshold value. Noting that the crack length a_1 can be written as

$$a_1 = a + a_0 \tag{4.5}$$

the FLS for any true crack length a becomes, from Equations (4.2) and (4.5):

$$\sigma = \frac{K_{th,LC}}{\sqrt{\pi(a+a_0)}\ Y(a+a_0)} \tag{4.6}$$

where, as the crack length goes to zero, the FLS goes to σ_e. The short crack curve in the Kitagawa diagram is easily constructed if the long crack curve exists by taking the value of a for any value of stress from Equation (4.2) and reducing it by a_0. Alternately, if the effective value of K is wanted for a short crack [5], it is easily shown that the effective K is

$$K_{th,SC} = K_{th,LC}\sqrt{\frac{a}{a+a_0}}\ \frac{Y(a)}{Y(a+a_0)} \tag{4.7}$$

where, as in the calculation for a_0, the Y terms can usually be ignored.

The significance of the Kitagawa diagram with the short crack correction is that it shows, if the threshold data follow the curves, that cracks of length a_0 or less, have FLSs which are not significantly lower than the endurance limit for a particular geometry. At a crack length of a_0, the FLS is $1/\sqrt{2}$ or 0.71 of the endurance limit. If cracks are formed at LCF stresses that are higher than the HCF limit, then the cracks that eventually propagate under HCF may act as if an overload occurred which may retard the crack or increase the fatigue limit [6]. Thus, it is not surprising to find that small cracks formed under fretting fatigue [7], or under LCF at notches [8], or in smooth bars, do not have a significant detrimental effect on the FLS. These cases are discussed later in this chapter.

4.1.1. Behavior of notched specimens

A Kitagawa type plot can be used to represent what happens in a notched bar, as has been done by Moshier et al. [4, 9]. A schematic of threshold stress as a function of crack length, assuming no load-history effects in the crack growth behavior, is given in Figure 4.3 for two different cases. The diagram shows two curves, an upper and a lower one, which represent what is commonly termed blunt notch and sharp notch behavior, respectively. Above or below each curve, there is either crack initiation and growth to failure at higher stresses, or no initiation or growth at lower stresses, respectively. The two curves represent the relation between stress and crack length corresponding to the K-solution for a crack emanating from a notch. The solution is corrected for small crack behavior as per the approach suggested by El Haddad et al. [3]. For the blunt notch case, represented by the upper curve through A, a crack that forms will continue to propagate because the stress for crack initiation or threshold crack growth is a decreasing function of crack length. However, in region I below the curve, stresses are below the endurance limit, and cracks should not form in this region unless the history of loading is such to allow formation of a crack. The line through A in the diagram, which is constructed for a specific notch geometry, is valid only for that geometry at a given stress ratio. Cracks formed in region I must, therefore, form from some other loading condition. The point A in the figure, which represents the endurance limit of the notched bar, is often taken to be the smooth bar endurance limit stress, σ_e, divided by k_t. Data such as those of Lanning et al. [8] indicate that this is not necessarily the case for mildly notched titanium bars. While the value of stress at A can be written as σ_e/k_f, where k_f is the fatigue notch factor, this is no more than a mathematical definition of the endurance limit stress for the notched body. The stress at A is not a material constant, but a geometry-dependent, empirically determined quantity. The subject of fatigue thresholds for cracks at notches is discussed in more detail in Chapter 5.

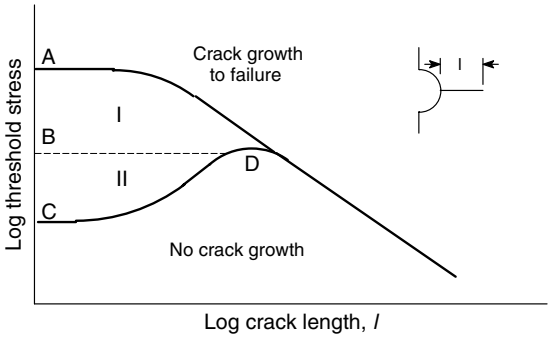


Figure 4.3. Schematic of a Kitagawa type diagram for notched specimens.

A Kitagawa type diagram was used by Moshier et al. [4] for mildly notched specimens which were precracked under LCF. The endurance limit stress for any crack length was found to be well predicted by a load-history dependent model [6], described later in this chapter, combined with the equations that connect the long crack threshold and the notched specimen endurance stress using the small-crack correction from El Haddad et al. [3]. It should be noted that the parameter a_0 used in the El Haddad correction, is not a material constant when used for notches in the manner described here. Rather, it represents the crack length where the long crack K solution for the notch, $K = K_{th}$, intersects the endurance limit given by the stress at point A in the diagram (Figure 4.3).

In region II of Figure 4.3, above the lower curve which represents the K solution for a very sharp notch, typically one with a k_t value in excess of approximately four or five, cracks are known to be able to initiate but not continue to grow. Until the stress exceeds the value at B, and for crack lengths below that indicated by point D, a crack may initiate but arrest. As in the case described above, the stress above which cracks initiate, C, is often taken to be σ_e/k_t, but it is extremely difficult to verify this and, further, this value is of minor engineering significance. What is of greater significance is the empirically determined endurance stress, B, under which a specimen will both initiate a crack and continue to propagate it to failure. Again, this endurance limit is not a material constant but, rather, an empirically determined quantity that depends on the particular sharp notch geometry. While cracks of lengths less than that of point D may initiate and arrest, these crack lengths are generally very small (the so-called small crack or short crack) and not detectable other than in a laboratory setting using sophisticated methods not applicable to real engineering structures. The transition from sharp notch fatigue to cracks, the latter governed by fracture mechanics, is discussed in greater detail later in this chapter.

In the extreme case where a notch starts to behave as a crack, the crack length at point D approaches zero as the notch radius approaches zero, and the geometry becomes that of a crack extending from an existing crack. To illustrate this, a numerical example is used to produce the results shown in Figure 4.4 where an endurance limit of 300 MPa and a threshold K of 5 MPa$\sqrt{\text{m}}$ are assumed. For initial crack (sharp notch) lengths of $c = 5$ or 500 μm, the figure shows the relation between crack extension from the sharp notch and stress required to exceed K_{th} with and without the short crack correction of El Haddad. For the initially very short crack ($c = 5\,\mu$m), the calculated endurance limit (using the short crack correction) corresponds to a value of $k_f = 1.03$ whereas for the 500 μm initial crack, $k_f = 2.58$. As the initial crack length gets longer, k_f increases so that for an initial crack length of 1 mm, $k_f = 3.51$. In this example of a sharp notch represented as a crack, assuming no load-history effects such as those due to overloads, and using Linear elastic fracture mechanics (LEFM), there is no tendency to form a crack that will arrest. Also, as seen in Figure 4.4, as the crack length increases the computations show that all data follow the same long crack threshold.

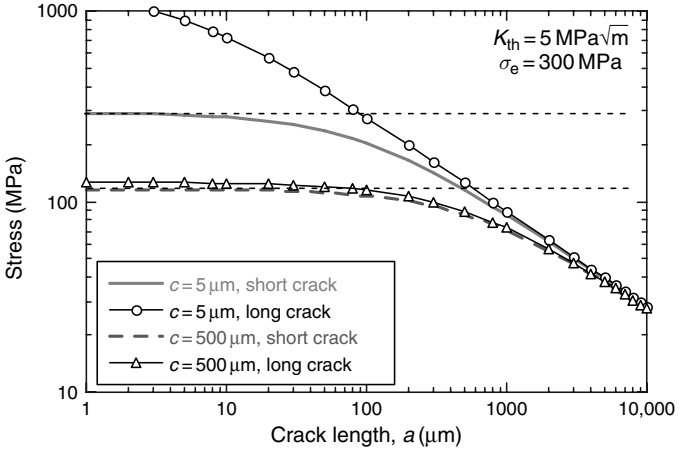


Figure 4.4. Kitagawa type plot for a sharp notch that is treated as a crack.

The Kitagawa type diagram can also be used to examine the effects of defects on the FLS. Materials such as cast aluminum have initial porosity that can be treated as initial defects or cracks of the size of the pores. Assuming that the initial crack size is known, the stress level below which crack propagation should not occur can be predicted from a knowledge of the long crack threshold, the endurance or FLS for the defect free material, and the Kitagawa diagram corrected for short crack effects as shown earlier. If the K solution for the specific specimen geometry is

$$K = \sigma\sqrt{\pi a}\; Y(a) \tag{4.8}$$

then the critical or transition crack length is given [see Equation (4.4) in previous section] as

$$a_0 = \frac{1}{\pi}\left(\frac{K_{th,LC}}{\sigma_e Y(a_0)}\right)^2 \tag{4.9}$$

If the dimensionless quantities

$$\bar{a} = \frac{a}{a_0} \quad \bar{\sigma} = \frac{\sigma}{K_{th}/\sqrt{\pi a_0}\; Y(a_0)} \tag{4.10}$$

are introduced, then the Kitagawa diagram is as shown in Figure 4.5 in log coordinates. If however, the plot is made in linear coordinates, the resultant figure takes the form shown in Figure 4.6. Plots of critical stress versus initial crack size should have this general shape unless the assumptions in the analysis of the material with initial defects are

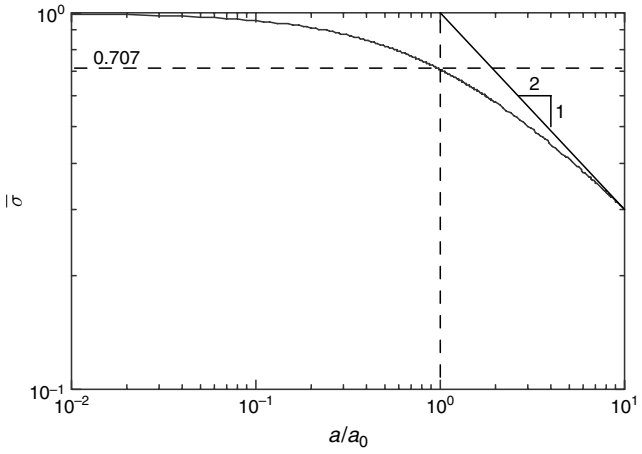


Figure 4.5. Kitagawa plot in dimensionless coordinates.

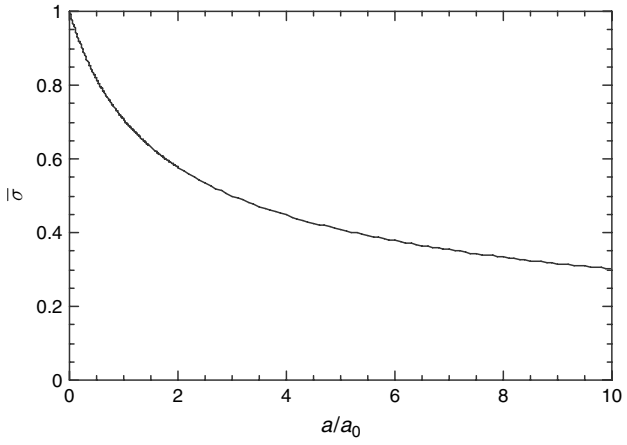


Figure 4.6. Kitagawa diagram in dimensionless coordinates on linear scale.

violated. Caton [10], in his study of 319 aluminum, has attributed the observed behavior being different than that depicted in Figure 4.6 to factors such as small crack effects, crack closure in threshold measurements, and interactions of crack tip plasticity with microstructural features. His data on three different microstructural conditions denoted as low, medium, or high SDAS are shown in Figure 4.7. The initial pore size, measured on the fracture surface of each specimen, is taken as being equivalent to an initial crack length. Thus, the plot should have the features shown in Figure 4.6. In order for all three microstructures to be compared properly as in Figure 4.7, the endurance limit and

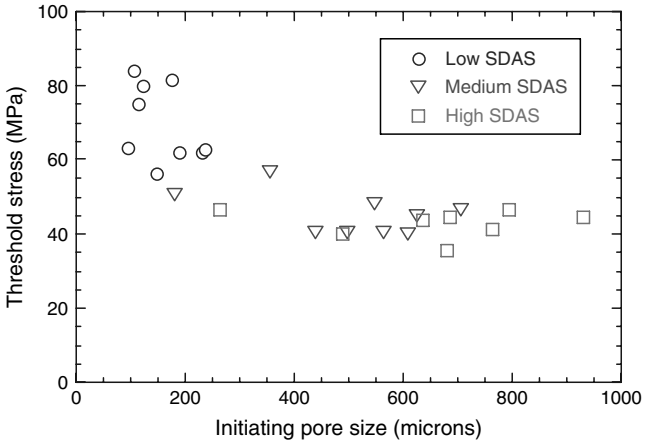


Figure 4.7. Threshold stress levels for step-tested W319-T7 aluminum as a function of initiating pore size.

threshold value of ΔK would have to be the same for all three conditions. This was found not to be true for the values of the threshold stress intensity. The endurance limit for the material without defects was not obtained. Nonetheless, the similarity of the general shape of Figure 4.7 to the dimensionless schematic, Figure 4.6, is surprising. For the two conditions marked medium and high SDAS, however, the data points indicate a threshold stress that is nominally independent of initial crack (pore) size. This led the author to examine other models to relate initial pore size to threshold stress.

4.2. EFFECTS OF LCF LOADING ON HCF LIMIT STRESS

In the USAF HCF program, it was recognized early on that the understanding of LCF–HCF interactions was not only important but, further, that LCF–HCF interactions had not been addressed to any substantial level prior to the program. In response to the lack of research in this area, several series of tests were conducted over the years at the AFRL Materials Directorate (AFRL/ML) where specimens were subjected to LCF loading prior to HCF testing to obtain an FLS [11]. In these types of tests, the LCF stress corresponding to a life in the typical range 10^4–10^5 cycles is determined first from a series of LCF tests and then interpolating on a S–N curve. Some fraction of the LCF life is then applied to the specimen after which it is tested in HCF using the step-loading technique [12] where load-history effects and coaxing have been shown not to be important in Ti-6Al-4V [13]. Two things should be noted in this type of experiment involving preloading under LCF. First, the LCF life is a statistical variable, so testing up to a predetermined fraction of predicted life has an inherent error associated with what fraction of life it really is.

Second, if LCF testing and HCF testing are performed at the same value of stress ratio, R, then the LCF test will be at a higher stress than the HCF test for an uncracked specimen. In the event that a crack is formed during LCF, application of a lower load during HCF testing can amount to having an overload effect, so the fatigue limit may tend to be higher than that obtained without an overload effect. Such a phenomenon was demonstrated by Moshier et al. [4] and is discussed later in this chapter.

Data obtained from different tests on smooth bars subjected to LCF, then HCF, are summarized in Figure 4.8, where the FLS is normalized against the value obtained for the same specimens tested without any prior loading history. Data indicated as "Maxwell" are from the authors' investigations with his colleague David Maxwell while data designated "Park" and "Morrissey" appear in [14] and [15], respectively. The horizontal axis is the number of LCF cycles divided by the expected life at the stress level and R used in the LCF tests. Noting that from a design perspective that the allowable LCF life would be much less than the average, LCF cycle ratios in practice should not be expected to exceed 0.5 of the average, and even less when factors of safety are included. Thus, any reasonable number of LCF cycles that might be encountered are expected to be confined only to the left portion of Figure 4.8. The data show, that within reasonable scatter, the HCF limit does not appear to be degraded by any significant amount in tests covering a range of LCF stress levels and corresponding lives, and stress ratios in both LCF and HCF.

Additional data to evaluate the effect of LCF on the HCF threshold in Ti-6Al-4V were obtained in smooth bar tests in two separate but parallel investigations [14, 15]. In the work by Mall et al. [14], the HCF limit stress corresponding to 10^7 cycles to failure was obtained at 420 Hz at $R = 0.1, 0.5$, and 0.8. These specimens were subjected to initial cycling at the same frequency as in the HCF portion of the tests, but at stress levels

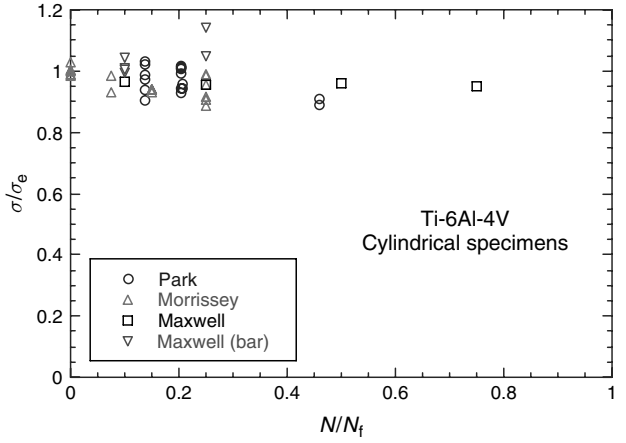


Figure 4.8. Normalized endurance limit stress as function of LCF history.

and values of R that produced shorter lives to failure. These initial cycles, referred to as LCF, were applied at three different conditions: a maximum stress of 700 MPa with $R = 0.1$ (Case A), 790 MPa with $R = 0.5$ (Case B), and 900 MPa with $R = 0.5$ (Case C). These conditions were chosen to cover a range of maximum stresses and cycles to failure. The cycles to failure for cases A, B, and C were approximately 1×10^6, 2.5×10^6, and 0.25×10^6, respectively. The relative amplitudes of these LCF conditions are shown schematically in Figure 4.9. The LCF pre-damage was selected as nominally 20% of life but went from about 15 to 50% of LCF life for Case A at $R = 0.1$. The HCF fatigue limit stresses corresponding to a life of 10^7 cycles are also shown schematically in Figure 4.9. It can be seen that the LCF preloading can result in either an overload or underload (negative overload) condition depending on the combination of LCF loading condition and value of R for the subsequent HCF test.

After applying these pre-damage conditions, the step-loading technique was used to determine the fatigue strength for 10^7 cycles to compare with those without pre-damage. These results are summarized in Figure 4.10. Since a 10% variation is not uncommon in fatigue data, the results clearly suggest that there was practically no effect of pre-damage from LCF on the HCF fatigue strength. Examination of Figure 4.9 shows that for HCF testing at $R = 0.5$, the LCF pre-damage occurred at stress levels which were above the HCF stress levels. If cracks formed during LCF, these cracks could be considered to be overloaded when subsequently tested under HCF, so the stress levels might be expected

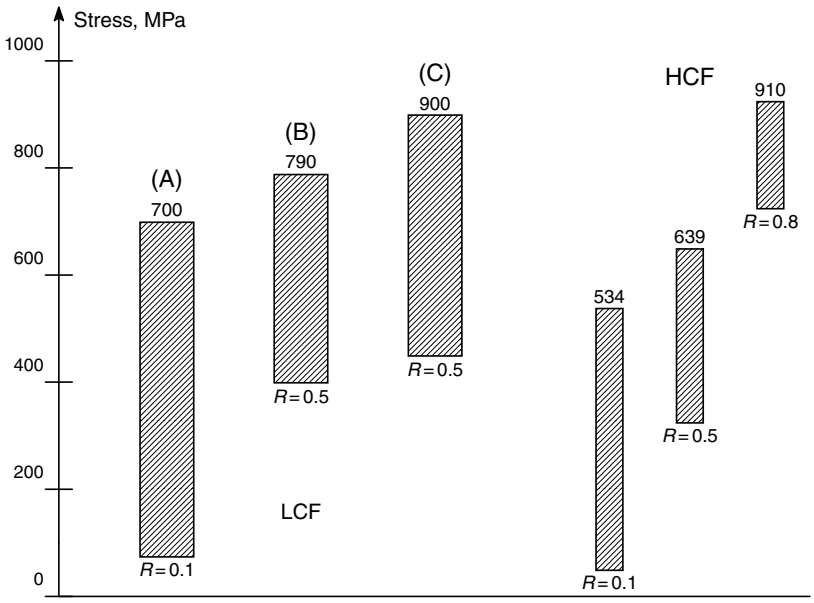


Figure 4.9. Schematic showing amplitudes of LCF and HCF fatigue limit stresses.

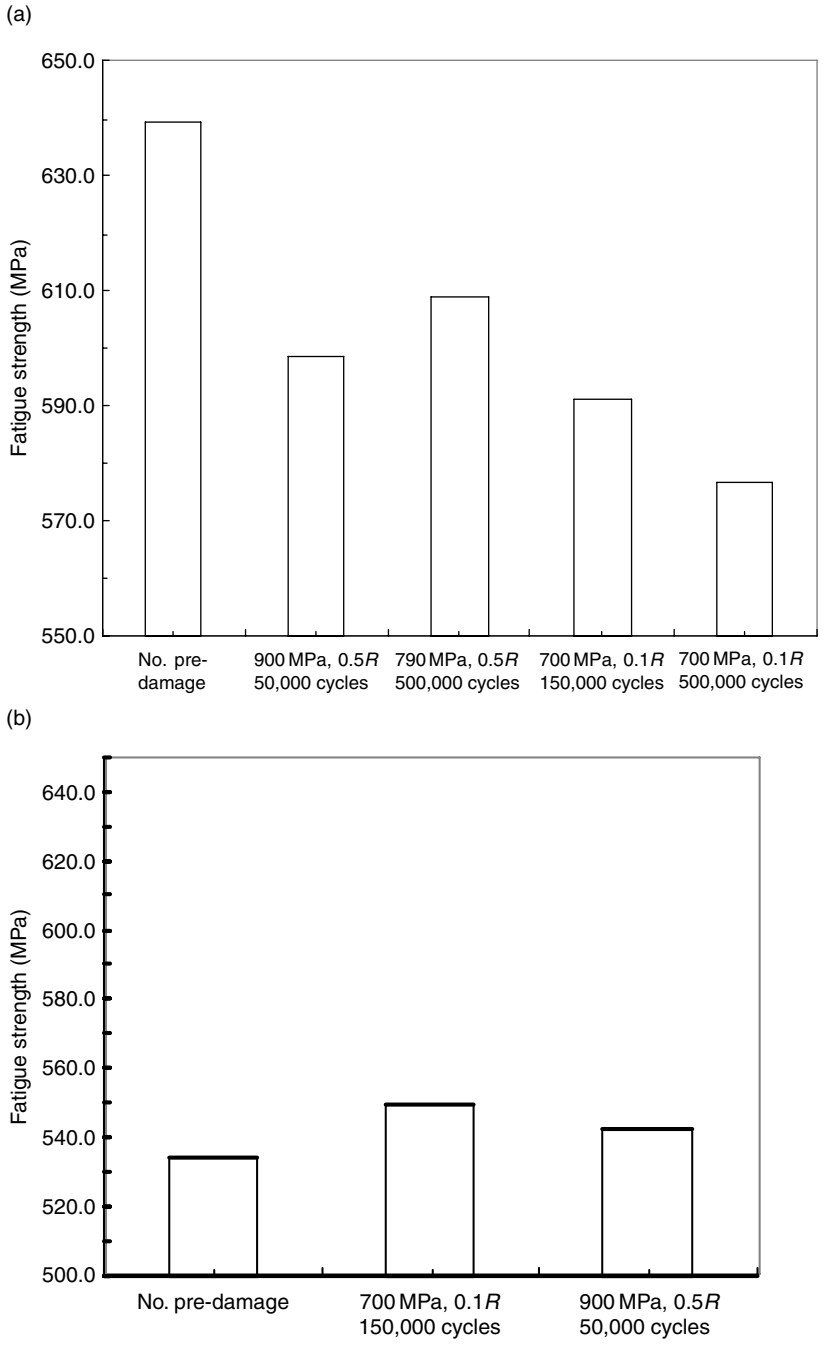


Figure 4.10. HCF limit strength with and without LCF pre-damage: (a) $R_{\mathrm{HCF}} = 0.5$, (b) $R_{\mathrm{HCF}} = 0.1$, (c) $R_{\mathrm{HCF}} = 0.8$.

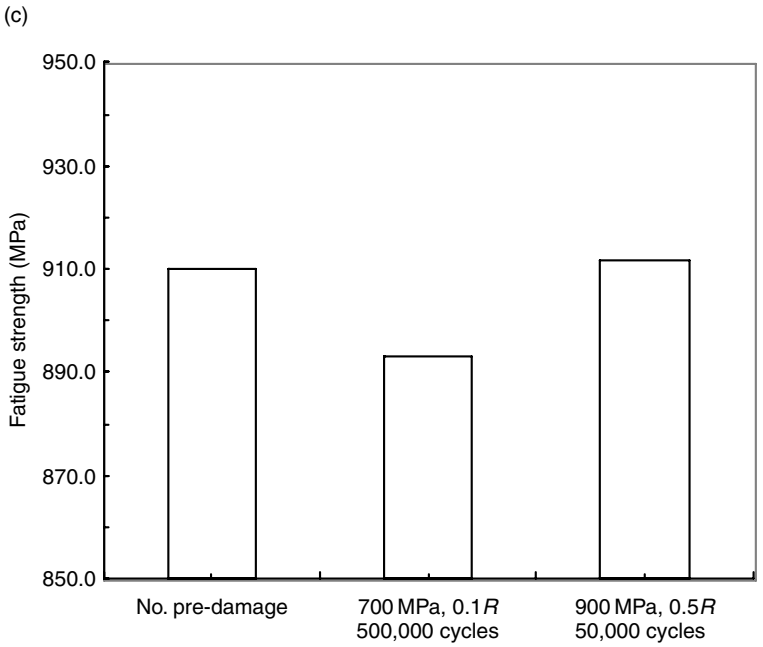


Figure 4.10. (*Continued*).

to be higher than the baseline. The observation that they were lower suggests that there might be an effect of pre-damage due to LCF, but the magnitude is not significant.

In Figures 4.10b, c, results are shown where LCF was applied at a stress of 900 MPa on a titanium alloy that has a yield stress of 930 MPa. In this case, strain ratcheting occurred during the LCF portion of the test, but no ratcheting was observed in the HCF portion of the test under step-loading conditions. Morrissey et al. [16] have reported that time-dependent creep or ratcheting may play an important role at high stress ratios where a portion of each cycle is spent at stresses near or above the static yield stress of the material. They observed measurable strain accumulation dependent on the number of cycles, as opposed to time, at the stress ratio of 0.8 where the applied maximum stress was slightly above 900 MPa. The fracture surfaces for the cases where strain ratcheting was observed in the tests summarized in Figure 4.10 did not show any indication of this phenomenon. This is in contrast to the observations of Morrissey et al. [16] where ductile dimpling was observed on fracture surfaces on specimens tested at $R = 0.8$ with maximum stresses above approximately 900 MPa. In fact, over the range of conditions studied in [14], there appeared to be little or no effect of prior LCF on the subsequent HCF limit stress. If any cracks formed during LCF, they were not observable through fractography and were not of sufficient size to cause any significant reduction of HCF limit stress under subsequent

testing. So, for conditions that covered a range from overloads to underloads from LCF, there was no observable effect on the subsequent HCF limit stress in a titanium alloy.

A similar investigation into load-history effects on the HCF limit stress was conducted by Morrissey et al. [15] where an attempt was made to assess the damage that might occur from HCF transients when these transient stresses exceeded the undamaged HCF limit stress. They addressed a practical problem that arises in designing against HCF because of the possible occurrence of stress transients above the FLS. These stress levels can correspond to lives below the HCF limit, but not necessarily to those which produce LCF. The slope of the *S–N* curve is quite shallow in this region, making the scatter in the cycles to failure quite large and, consequently, making cycle counting difficult from a deterministic life prediction scheme.

As shown in the previous section, the effects of prior loading under LCF seem to have little or no effect on the subsequent HCF limit stress, even when loading under LCF has covered life ranges as high as 50–75% of anticipated life in both smooth and notched specimens. To investigate effects due to transient loading, Morrissey et al. [15] used high frequency blocks of loading to represent the cumulative effect of HCF transients which might cause crack initiation to occur. They determined the effects of these transients for two reasons. First, short duration, high frequency stresses above the fatigue limit (but still within the HCF regime) are typical of what occurs in gas turbine engine applications. Second, in contrast to LCF overloads that would by definition only occur for a very small number of cycles, HCF stress transients could produce large numbers of cycles, even if they only occur for up to 20% of the expected fatigue life at that stress.

The experiments in [15] involved the application of HCF transient stress levels for a certain percentage of life (ranging from 7.5 to 25%) and then using the step-loading technique to determine the subsequent fatigue strength corresponding to 10^7 cycles at $R = 0.5$. Some specimens were either heat tinted or both heat tinted and stress relieved (SR) after the pre-cycling (prior to HCF testing). The results are summarized in Table 4.1 which presents the ratio of the final failure stress under HCF loading conditions, σ_f (after applying stress transient loads) to the 10^7 cycle HCF endurance limit, σ_e. It is clear from the table that preloading at 855 MPa (30% above the endurance limit) for 50,000 cycles (approximately 25% of life) does not reduce the subsequent HCF strength of the

Table 4.1. Summary of fatigue limit stress results for specimens subjected to stress transients

# of tests	σ_{LCF}	N_{LCF}	*% of life*	σ_f/σ_e
3	855	50,000	25	0.99
5	925	25,000	25	0.92
3	925	15,000	15	0.94
1	925	7,500	7.5	0.93
3	925 (SR)	25,000	25	0.81

material. Table 4.1 also shows that cycling at 925 MPa for up to 25% of life has little effect on the HCF strength. However, the HCF strength is reduced by an average of 19% when subjected to prior cycles with a maximum stress of 925 MPa followed by a stress relief process. This implies that there are residual stresses present after the stress transient cycling that act to reduce any loss in HCF strength. The nature of these stresses might be attributed to crack closure, residual compressive stresses ahead of the crack tip, or other phenomena. The net effect is one similar to what is commonly seen in crack growth studies under spectrum loading and is referred to as an overload effect, where prior cracking at a high load level tends to retard crack extension at lower loads.

To analyze the experimental data, a Kitagawa diagram was constructed for a circular bar, the geometry used in the experiments. The resulting diagram is shown in Figure 4.11 where the parameters are given in the figure and no correction is shown for short cracks. The crack growth analysis for the curve is presented below. For comparison, the diagram shows the line for a simple edge-crack geometry for a material having the same endurance limit as well as long-crack threshold stress intensity. This simple example also illustrates the dependence of the shape of the Kitagawa diagram on the specific geometry and value of R being used.

The crack growth analysis in [15] was also made in order to distinguish the initiation stage from the total life observed experimentally. The approach was to subtract the crack propagation time from an initial crack size a_0 from the total life to failure, where a_0 is the transition crack size in the Kitagawa diagram. When repeated over the range of stress levels used for the coupon fatigue tests, the result is a stress-life curve for nucleation life compared to the stress-life curve for total life.

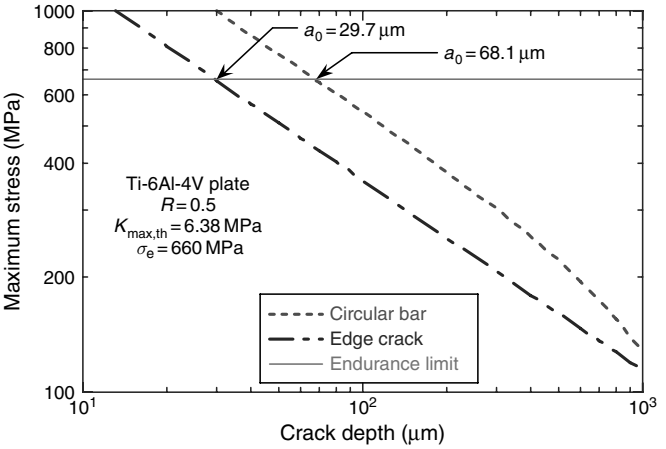


Figure 4.11. Kitgawa diagram for a circular bar.

The Forman and Shivakumar [17] stress intensity factor for a surface crack in a rod can be used for this analysis. This solution assumes that cracks have a circular arc crack front whose aspect ratio starts as 1.0 for small cracks. As the crack propagates, the aspect ratio changes according to experimental observations that are embedded in the K solution. Therefore, only the crack depth, a, is used in the solution. The crack depth is defined as the radial distance from the circumference to the interior of the crack. Equation (4.11) is the general form of the stress intensity factor solution. The geometry correction factor F_0, defined by Equations (4.12) and (4.13), is dependent only on the ratio of crack size to rod diameter, λ [Equation (4.14)].

$$K_{\mathrm{I}} = [\sigma_0 F_0(\lambda)]\sqrt{\pi a} \tag{4.11}$$

$$F_0(\lambda) = g(\lambda)\left[0.752 + 2.02\lambda + 0.37\left(1 - \sin\pi\frac{\lambda}{2}\right)^3\right] \tag{4.12}$$

$$g(\lambda) = 0.92\left(\frac{2}{\pi}\right)\left[\frac{\tan\pi\frac{\lambda}{2}}{\pi\frac{\lambda}{2}}\right]^{1/2}\left(\sec\pi\frac{\lambda}{2}\right) \tag{4.13}$$

$$\lambda = \frac{a}{\mathrm{D}} \tag{4.14}$$

To calculate the propagation life of the fatigue tests from an initial crack size, a crack growth law must be defined. The crack growth rate $\mathrm{d}a/\mathrm{d}N$ versus the stress intensity factor range ΔK was based on experimental data for the same Ti-6Al-4V used in this study [18].

$$\frac{\mathrm{d}a}{\mathrm{d}N} = 4.65 \times 10^{-12}\Delta K^{3.89} \tag{4.15}$$

The propagation analysis procedure is, for each stress level, to start with the defined initial crack size a_0, calculate ΔK, and then calculate the crack growth rate $\mathrm{d}a/\mathrm{d}N$. A small increment of crack growth, Δa, is then applied and the corresponding increment of cycles, ΔN, is calculated. This procedure is repeated until failure when $K_{\max}$ equals the fracture toughness K_{c} that is approximately $60\,\mathrm{MP}a\sqrt{\mathrm{m}}$ for this material.

As discussed above, a Kitagawa type diagram can be useful in evaluating the potential for a crack to reduce the HCF capability of a material. Since stress transients above the HCF endurance limit were being introduced to the material, the possibility that cycling at these stress levels resulted in cracking was evaluated numerically. For this purpose, a Kitagawa type diagram was constructed for the experimental conditions under consideration. The endurance stress, σ_{e}, was taken as the value that had been experimentally determined and the crack growth threshold curve was developed using the K solution above for a crack on the surface of a cylindrical bar. The resulting diagram is shown in Figure 4.12, along with the El Haddad short crack correction. The crack length, a_0, used

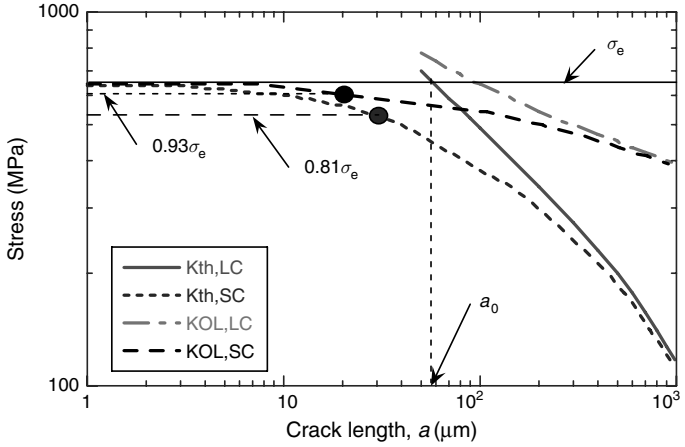


Figure 4.12. Kitagawa diagram with model for overload and short crack corrections. Data points correspond to fatigue limit stresses of LCF–HCF samples with and without stress relief. SRA samples should follow non-model curve, non-SRA should have overload effect. Dots show what fatigue limit stresses imply initial crack lengths might be. No such cracks were found.

for the El Haddad short crack correction was determined from the intersection of the threshold curve with the endurance limit stress as $a_0 = 57\,\mu\text{m}$.

The crack sizes corresponding to the threshold for crack propagation at a given FLS, due to an initial flaw which may have been produced during initial cycling, can be represented on a Kitagawa diagram for the specific geometry used here, a circular bar. For the specimens that were stress relieved to eliminate any prior load-history effects, this diagram shows that, with the small crack correction and the experimentally observed FLS of $0.81\sigma_e$, a crack of length approximately $30\,\mu\text{m}$ in length would produce that threshold stress. On the other hand, specimens that saw no stress relief might exhibit an overload effect due to the initial cycling which occurred at a maximum stress level above the stress obtained during the HCF FLS tests. The magnitude of the overload effect on the threshold for subsequent crack propagation was estimated from a simple overload model developed in [6] that assumes the overload effect is caused by the prior loading history and depends on $K_{\max}$ of the prior loading. The model prediction for the history dependent threshold is

$$K_{\max,\text{th}} = \frac{\Delta K_{\text{th}}^{\text{eff}}}{(1-\beta R_{\text{th}})} + \frac{\beta}{(1-\beta R_{\text{th}})} K_{\max,\text{pc}} \tag{4.16}$$

where $\beta = 0.294$ and $\Delta K_{\text{th}}^{\text{eff}} = 3.23$, are fitting parameters taken from [6]. Subscripts "th" and "pc" refer to the threshold test and the precrack from the prior LCF loading, respectively.

The numerical results using the overload model for a stress of 925 MPa are plotted in Figure 4.12 along with the small-crack correction corresponding to a value of $a_0 = 92\,\mu$m, as determined from the model and the endurance limit stress. This model should correspond to the experimental observations where no stress relief was used, where the fatigue limit for prior loading history at 925 MPa for a range of cycle counts was approximately $0.93\sigma_e$ (see Table 4.1). For this value of stress, the overload model shows that a crack of approximately 20 μm in length would be expected to produce the threshold stresses obtained experimentally. In the case of no stress relief, or with stress relief as indicated above, the initial cycling is expected to produce a crack of length 20–30 μm in order to explain the observed reduction in FLS. In both cases, the size of any crack developed during LCF is near the limit of detection, using either SEM or heat tinting, but more importantly, does not have any serious detrimental effect on the subsequent FLS.

In order to determine the expected flaw size that might occur due to prior cycling, the crack growth life was calculated as noted above. The crack growth life for any value of applied stress is subtracted from the total life to produce a curve corresponding to an initiation life to a crack of length $a_0 = 57\,\mu$m. The results are plotted in Figure 4.13 in terms of percent life spent in nucleation, where it can be seen that the initiation of a crack to the size of a_0 should not be expected after the number of cycles imposed in the experiments as shown in Table 4.1. For example, at the highest stress of 925 MPa, the expected total life is approximately 10^5 cycles. At that stress, the percent of life spent in nucleation to a crack length of a_0 is expected to be about 50%. Thus, initiation corresponds to approximately 50,000 cycles, twice as much as the 25,000 imposed in the experiments. From this it is concluded that fatigue cycling for fractions of life below 50% should not produce a detrimental effect on the subsequent HCF endurance limit.

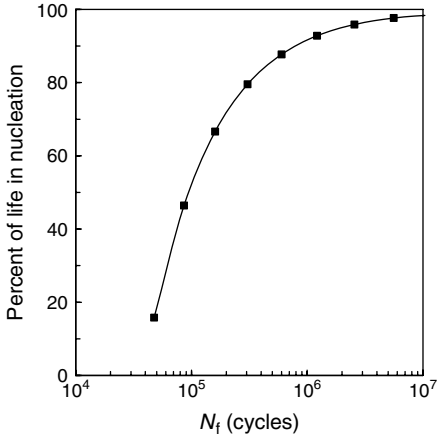


Figure 4.13. The percent life spent during nucleation as a function of the coupon fatigue test failure life.

Since the cyclic life is a statistical variable, a factor of 2 in life should be within expected statistical scatter and the design life should be typically much less than the lives plotted from a limited number of experiments that determine average values.

LCF–HCF interactions have also been studied by applying loading from other than smooth bars subjected to uniform stress. One example is where C-shaped specimens were precracked during fretting fatigue studies and were subsequently evaluated to determine the threshold for fatigue crack propagation [19]. Data for cracks in C-shaped specimens are plotted on a Kitagawa diagram as shown in Figure 4.14 for HCF limit stresses obtained at $R = 0.1$. A similar plot for data at $R = 0.5$ is shown in Figure 4.15. The small crack data for $a < a_0$ seem to be well represented by the El Haddad line and endurance limit stress, while the longer crack data are well represented by the long crack threshold fracture mechanics parameter, $K = K_{th}^{lc}$. A large number of data points for small cracks were obtained because, under fretting fatigue conditions, the contact stress field extends only tens of microns into the contacting bodies. Thus, cracks can initiate at the surface due to very high contact stresses there, but the cracks arrest quickly as they propagate into the fretting pad from which the C-shaped specimens were cut. Fretting fatigue is discussed in more detail in Chapter 6.

Some of the specimens were stress relieved (denoted by Stress relief annealing [SRA] in the figures) to eliminate residual stresses and corresponding load-history effects from the fretting fatigue testing. Each of the figures presents three lines, one is the long crack solution, presented next, one is the short crack corrected solution (dashed line), and one is the FLS for this particular C-shaped geometry obtained experimentally for each value of R. The maximum threshold stress averaged 552 MPa for $R = 0.1$ and 684 MPa for $R = 0.5$.

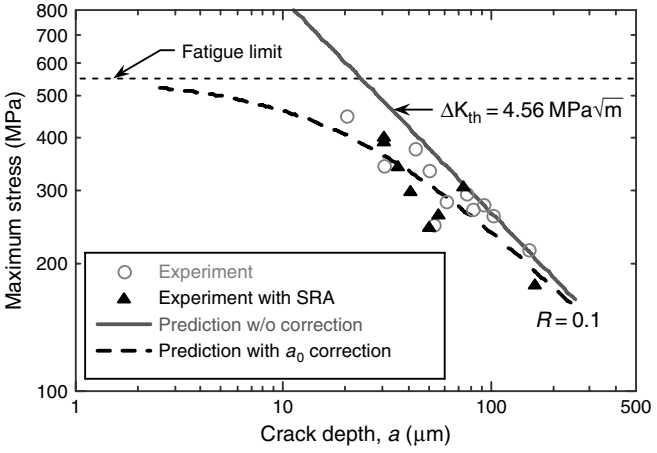


Figure 4.14. Kitagawa type diagram for HCF threshold stresses in C-specimens, $R = 0.1$.

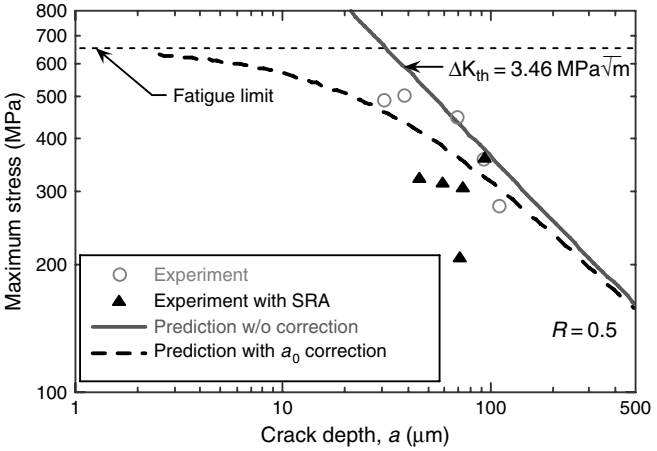


Figure 4.15. Kitagawa type diagram for HCF threshold stresses in C-specimens, $R = 0.5$.

The values of long crack ΔK_{th} used were 4.6 and 2.9 MPa$\sqrt{m}$ for $R = 0.1$ and 0.5 respectively. The $R = 0.1$ data followed the predictions quite well. The $R = 0.5$ data were more scattered but also followed the same trend. A majority of the data fell into the long crack region where LEFM clearly predicted the threshold. Some of the specimens, however, had cracks on the order of a_0 and these data clearly deviated from LEFM and followed the trend of the small crack threshold model. It is also apparent, by observing the trend of the curves in Figures 4.14 and 4.15 that the small crack correction not only represents the trend of the experimental data, but shows that for crack lengths much below a_0 that the FLS is not appreciably below that of an uncracked body. Thus, if assessing the potential damage of a fretting induced crack, the FLS of a body with a "small crack," below a_0, is not much lower than that of an uncracked body even though the calculated value of K may be much reduced from that in a long crack experiment. For small cracks, therefore, stress rather than K should be considered as the governing parameter when assessing potential material degradation from fretting fatigue. Overall, the Kitagawa diagram, using the El Haddad transition modification, provides a reasonable representation of all of the experimental data including those in the small crack regime.

A stress intensity factor (K) analysis of this specimen was required for the fatigue crack growth threshold analysis. The fretting cracks in the C-specimens were modeled as semi-elliptical surface cracks in a plate as drawn in Figure 4.16. The stress gradient of the uncracked specimen was used to calculate K for the cracked specimen by the well-known superposition method. Since this stress gradient was not linear, a generalized weight-function solution was used as presented in Shen and Glinka [20]. Equations (4.17) and (4.18) were used to evaluate K at the depth and surface points of the semi-elliptical crack. In these equations, K_A and K_B are the mode I stress intensity factors at the depth

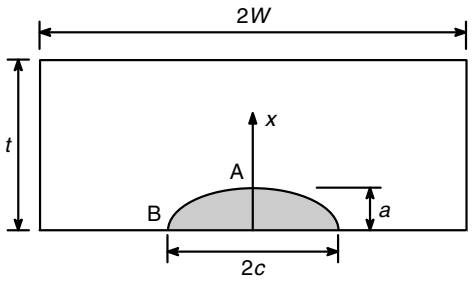


Figure 4.16. Surface crack in plate geometry used for K analysis in C-shaped specimens.

and surface points respectively, $\sigma(x)$ is the stress gradient along the crack depth, and m_A and m_B are the weight functions. The weight functions are defined in Equations (4.19) and (4.20). The six coefficients, M_{iA} and M_{iB}, were derived with the use of known K solutions for tension and bending. The coefficients depend on the crack size, crack shape, and plate geometry.

$$K_A = \int_0^a \sigma(x)\ m_A\left(x, a, \frac{a}{c}\right) dx \tag{4.17}$$

$$K_B = \int_0^a \sigma(x)\ m_B\left(x, a, \frac{a}{c}\right) dx \tag{4.18}$$

$$m_A(x,a) = \frac{2}{\sqrt{2\pi(a-x)}}\left[1 + M_{1A}\left(1-\frac{x}{a}\right)^{1/2} + M_{2A}\left(1-\frac{x}{a}\right) + M_{3A}\left(1-\frac{x}{a}\right)^{3/2}\right] \tag{4.19}$$

$$m_B(x,a) = \frac{2}{\sqrt{\pi(x)}}\left[1 + M_{1B}\left(\frac{x}{a}\right)^{1/2} + M_{2B}\left(\frac{x}{a}\right) + M_{3B}\left(\frac{x}{a}\right)^{3/2}\right] \tag{4.20}$$

In evaluating the results of this investigation, a result of particular interest is the fact that for very small cracks, the stress levels at the threshold are those at or slightly below the endurance limit stress for uncracked specimens. However, the location of failure is found to be at the pre-existing crack as observed from fracture surfaces that were heat tinted before threshold testing in order to provide the dimensions of the pre-existing crack. A legitimate question could be raised about why failure did not occur at a location other than the precrack since the applied stresses were approximately those corresponding to the endurance limit stress. In other words, if very small cracks do not degrade the stress carrying capability of the material, why do they provide the location for subsequent failure? Note that we are dealing with a fatigue limit or threshold condition, not a number of cycles to failure where number of cycles to initiation is an important part of the

process. The proposed answer to this question is based on the concept of a weakest link theory where the location of the fatigue failure initiation point is a random variable in space. However, in precracking of the material in the case of C-shaped specimens, and particularly in the case of notched specimens, the process finds the location of the weakest link and initiates the crack in that location. Threshold testing then samples locations in a larger region, but the weakest link has already been identified. Thus, the crack continues to propagate at the precrack location once the threshold stress is reached.

Further evidence of the relatively small effect of a short crack on the FLS can be found in the work of Lanning et al. [8] where prior LCF loading was followed by step testing to establish the HCF limit stress corresponding to a life of 10^6 cycles. Results for the FLS corresponding to 10^6 cycles as a function of the number of LCF cycles are shown in Figure 4.17 for specimens with small notches having $k_t = 2.7$. The full LCF life was 10,000 cycles at the stress used in the precracking, 609 MPa. Many specimens were heat tinted after LCF loading so the final fracture surfaces could be examined for any cracks formed during the initial LCF loading. One crack was found which was formed in a small notch specimen after 2500 LCF cycles, at 25% of LCF life. The crack had a depth of approximately 25 μm, and a width of about 250 μm. This crack corresponds to the lower of the two data points in Figure 4.17, at 2500 LCF cycles. Since a crack was not observed in the specimen with the data point at a higher HCF fatigue limit, which is only greater by 10 MPa, it appears that a crack of this size may not be significantly detrimental to the HCF limit stress. Note, however, that a crack with lesser depth, perhaps only half of that found, would not be easily detectable using the heat-tinting method.

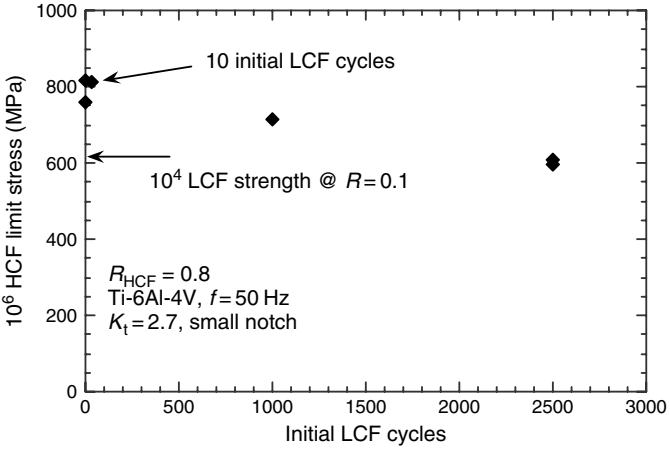


Figure 4.17. HCF limit stress at 10^6 cycles versus number of initial LCF loading cycles for stress relieved small notch specimen, $R_{LCF} = 0.1$ and $R_{HCF} = 0.8$ (from [8]).

Similar data obtained from other tests on notched specimens [8] are presented in Figure 4.18. In these cases, preloading in LCF often involved testing at stress levels that produced plastic deformation near the notch root. The plastic strain field was normally larger than that obtained under pure HCF with no preload, so the comparison of data from LCF–HCF tests with pure HCF tests is much more complicated than in the smooth bar case. In the case of specimens tested at $R = 0.8$, the high peak stresses under HCF combined with the plastic deformation occurring under the prior LCF makes the comparisons even more difficult. It should be noted that in at least two cases of this type of LCF–HCF loading, a crack was found on the fracture surface which indicated that the LCF produced initial cracking which resulted in a reduction of subsequent HCF strength [8]. The effect of precracking is discussed below. Nonetheless, the reduction of fatigue strength due to LCF in notched specimens does not appear to be very significant until at least 25% of LCF life has been expended. As pointed out above, this is based on average life so that with scatter and a factor of safety, it is not reasonable to expect that a material would be subjected to 25% of *average* life in service.

In one of the earliest studies of load-history effects, Kommers [21] pointed out that for small specimens of steel with diameters of about 0.3 in. (7.6 mm) there is no evidence of cracks being formed for large cycle ratios of 0.9 at stresses above the endurance limit. Cycle ratio is defined as the ratio of the number of cycles applied at a given overstress (stress above the endurance limit) to the number of cycles necessary to cause failure at that overstress. It was concluded that a crack is formed only a short time before failure although the author noted that other test results show that this is not true for large specimens.

In addition to studying the effect of prior loading history where the stresses were below the HCF fatigue limit, a brief study was made at AFRL/ML of the effect of prior

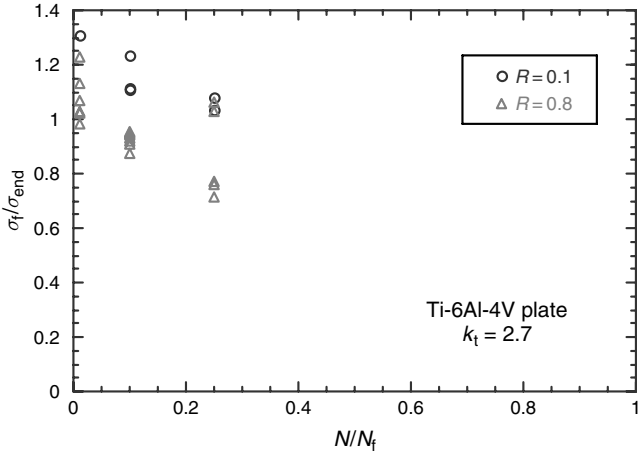


Figure 4.18. Fatigue strength of notched specimens subjected to prior LCF [8].

LCF where stresses are above the HCF fatigue limit [22]. Contrary to the thoughts of Kommers [21], this latter work was conducted under the common belief that cracks initiate under LCF at a smaller fraction of life than under HCF. Consequently, the subsequent HCF life may be shortened after LCF cycling because, if cracks are present, the life to initiation may be drastically reduced. If, however, the LCF and HCF are conducted at different values of R, then the LCF loading may be at peak stresses below the HCF fatigue limit and any cracks may be below the fatigue crack growth threshold. The case of different values of R for LCF and HCF was investigated. The effect of prior LCF at $R = -1$ on the subsequent HCF fatigue limit at $R = 0.5$ was evaluated using the step-loading technique. Specimens were subjected to a predetermined number of LCF cycles and tested subsequently under HCF. The LCF life is approximately 10^5 cycles at $R = -1$ with a maximum stress of 600 MPa at 1 Hz. The results showing the fatigue limit corresponding to 10^7 cycles as a function of prior LCF cycles are presented in Figure 4.19. The data show two things. First, there does not appear to be any significant degradation of HCF fatigue limit due to prior LCF cycling, even up to 75% of life. Second, there does not appear to be a trend in the limited data obtained with the number of steps in the step-loading technique as shown in Figure 4.19.

Another important study of the influence of prior loading cycles at high stress levels on the fatigue limit was conducted by Walls et al. [23]. They noted that many questions have been raised about use of the Haigh diagram for assessing design margins for components subjected to combined LCF and HCF, and they suggested the exploration of the use of fracture mechanics as an alternative. In particular, they emphasized that such an approach needs to be validated under realistic operating conditions on real components. To accomplish this, they subjected two single-crystal blades to two different types of

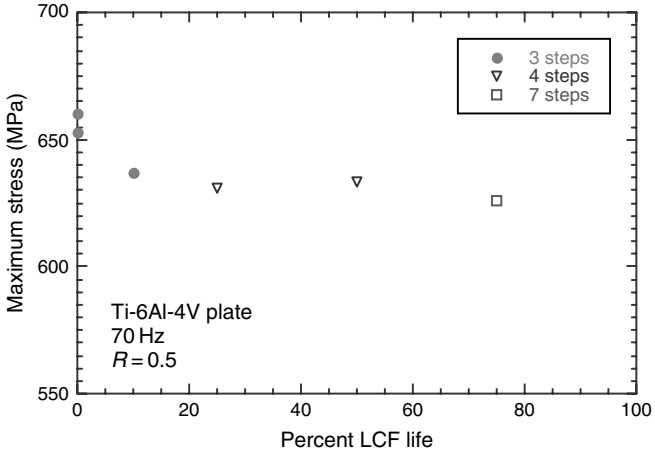


Figure 4.19. Fatigue limit against % LCF life.

vibratory loading modes typically found in engine-operating environments. In the first case, the HCF loading was a high-amplitude, non-resonant vibration (NRV). The high amplitude was well above that observed under normal operating conditions and was chosen so that it would propagate a 0.75 mm initial flaw. In the second case, the blade was subjected to alternately applied NRV and a resonant vibratory mode. In this case, the NRV amplitude was lowered to a level typical of engine operation while the resonant mode was large enough to produce crack propagation from some pre-flaw. In both cases, several large amplitude cycles were interspersed between the applied HCF cycles to represent the LCF driver in a typical mission from major throttle excursions such as takeoff and landing. While details of the complete loading history such as number of HCF cycles and values of R are not available, the following table (Table 4.2) gives some of the basic information of the loading history, where p–p denotes peak to peak amplitude.

The loading conditions were put into a fracture mechanics model that did not consider any load interactions such as overload effects. The material was represented by a crack growth curve and a threshold stress intensity below which no crack propagation takes place. Appropriate K solutions for the blade geometry based on observed crack shapes from fracture surfaces were used. For blade #1, loaded in HCF only by the NRV stresses, the model predicted 4 complete missions from the initial flaw to final fracture. This compared favorably with 3–5 arrest marks on the fracture surface of a blade subjected to that mission. The fracture surface information was enhanced by the nature of the fracture mode in the material used, which changed based on the ΔK range applied to the blade. This made it possible to distinguish between LCF and HCF loading conditions.

For blade #2 subjected to the combined NRV and resonant vibration modes, the fracture surfaces for each individual block of HCF loading were distinguishable due to the different amplitudes of the individual blocks as shown in Table 4.2. The loading block information was put into the fracture mechanics model and resulted in a prediction of 103 complete missions. This compared favorably to the 95 missions evaluated from the fractography. The model was further used to predict the crack size at which the NRV first started to propagate based on threshold data. Crack growth from the NRV mode was predicted to commence at a crack length of 5.5 mm. The fractography, which showed that early propagation was due only to the resonant mode, indicated that NRV-driven crack propagation started at a crack length of 5.1 mm.

Table 4.2. Summary of LCF–HCF loading conditions

Loading mode	*Blade #1*	*Blade #2*
Non-resonant	350 MPa p–p	175 MPa p–p
Resonant	None	295 MPa p–p
LCF	0–875 MPa	0–875 MPa

The results of these two experiments and the corresponding fracture mechanics computations led the authors to conclude that HCF life can be reasonably well predicted under a realistic mission spectrum involving both LCF and HCF. The ability to predict the onset of HCF based on the threshold stress intensity factor was also noted. It should be pointed out that the specific missions investigated for the components selected did not appear to involve any load interactions. Further, the starting flaw sizes were large enough so that small crack effects did not have to be considered.

4.2.1. Studies of naturally initiated LCF cracks

Damage due to LCF cracks can alter the HCF resistance of a material by changing the criterion for crack nucleation and subsequent propagation from one governed by stress (endurance limit) to one governed by fracture mechanics (crack growth threshold). Studies investigating the interaction of naturally initiated LCF cracks and HCF threshold do not appear to have been conducted prior to the USAF HCF program. However, there had been studies that addressed major/minor cycle interaction, lower-bound HCF threshold, and crack growth of both long cracks and artificially induced small cracks including history effects. Akita et al. [24] demonstrated in Ti-6Al-4V with C(T) specimens that repeated loading blocks containing a single overload caused the da/dN crack growth curve to shift down, thereby producing an increase in the threshold level.

Traditional methods for managing HCF have relied heavily on the Haigh (Goodman) diagram approach. The Haigh diagram approach requires smooth bar fatigue data over a range of stresses and stress ratios in order to define a material's fatigue endurance limit. The endurance limit, defined as the stress range below which failure does not occur within a specified lifetime, is then used to specify allowable design stresses. The shortcoming of this approach is that it does not account for any type of defect such as that caused by FOD, fretting fatigue, or cracking due to LCF or combined loading. In the next sections, the effects of loading history on the crack propagation characteristics of a material, particularly the threshold for HCF crack propagation, are discussed.

4.3. CRACK-PROPAGATION THRESHOLDS

As shown above, the fatigue crack-growth threshold, a fracture mechanics concept, can be used to determine a stress level below which a crack of a given size will not grow. Threshold can be used to determine an allowable stress as a function of crack size and is seen as a viable alternative design parameter to the allowable design stress as determined from the Goodman diagram approach. As with the Goodman diagram approach, threshold is a material specific quantity and must be determined under a variety of conditions. The experimental method by which a threshold is determined and the applicability of

that value of threshold to different methods of creating a crack are issues that have not been completely resolved within the technical community. Some examples are presented below. The subject of crack-growth thresholds is presented in greater detail in Chapter 8.

Sheldon et al. used artificially created surface cracks in a so-called K_b specimen geometry to study the effect of specimen geometry and shed rate in Ti-6Al-4V [25]. They found that increased shed rates could be used to arrive at valid thresholds. However, they also noted that the choice of the starting value of K_{max} had an effect on the allowable shed rate that could be used and still measure valid thresholds. As K_{max} was increased, the absolute value of the gradient needed to be decreased in order to distance the crack tip stress field from the plastic wake. Sheldon et al. also found that specimen thickness ranging from 2.54 to 6.35 mm did not influence the measured threshold at $R = 0.1$ and $R = 0.8$. This study showed that both specimen geometry and load history could influence the value of the material threshold. This is just one indication that the threshold may not be an inherent material property.

In another investigation, Lenets and Nicholas [26] used two different methods for determining the fatigue crack-growth threshold in titanium alloy IMI 834. The first test method used a transition from no-growth to growth while the second used a growth to no-growth approach. This is analagous to increasing K or decreasing K in standard threshold testing. A consistent difference between the two thresholds for each test method was found. Increasing ΔK applied to the initially dormant crack produced higher fatigue crack-growth thresholds as compared to the situation when decreasing ΔK values were applied to a growing crack. Lenets and Nicholas concluded that this difference in measured thresholds was attributed to the crack tip shielding associated with residual stresses in front of the crack tip caused by the two different loading histories. These two cited studies, along with results from numerous other investigations, indicate that loading history is an important consideration when determining a threshold for crack propagation and that a single number for a material threshold may not be a valid consideration. The subject is discussed in further detail in Chapter 8.

Loading-history effects are also crucial elements in the study of LCF–HCF interactions in establishing allowable limits for HCF loading. Most of the work in this area has been associated with combined cyclic fatigue (CCF), that is HCF, generally at high R, which is accompanied by periodic underloads to zero or near-zero stress. Several studies have shown that superimposed HCF cycling adversely affects the LCF life of steel [27, 28] and superalloys [29]. Some of the first work in crack growth under combined LCF–HCF was conducted on Inconel 718 at 650 °C [30]. The data showed that crack-growth rate at this temperature was dominated by time-dependent behavior for the LCF cycles and cycle-dependent behavior for HCF. The minor (HCF) cycles had a threshold stress intensity, dependent on stress ratio, below which they had no effect on LCF growth rates, and above which the HCF growth dominated.

Guedou and Rongvaux [31] were among the first to examine the effect of superimposed HCF on the LCF life. In Ti-6Al-4V at 20 °C and Inconel 718 at 550 °C, they examined both initiation life (to a crack depth of 50 μm) and crack propagation life. They found that superimposing HCF cycles ($R = 0.60, 0.80$, and 0.85) on LCF cycles significantly reduced both the initiation and propagation life relative to those measured for LCF-only loading. In agreement with Ouyang et al. [29], the crack propagation life was reduced significantly more than initiation life.

Perhaps the greatest amount of research on combined HCF and LCF loading has been conducted by Powell et al. [32–35] who have examined the crack-growth rate of titanium alloys and other materials under combined HCF and LCF loading. Details of some of these investigations are presented later in this chapter. The earliest investigations [32, 33] were conducted on Ti-6Al-4V and demonstrated the existence of an onset stress intensity, ΔK_{onset}, below which HCF had no effect on LCF growth rate and above which it dominated the growth rate under combined loading. The linear summation of growth rates obtained from LCF and HCF loadings alone was shown to predict the combined behavior for this material. Thus, ΔK_{onset} was essentially equivalent to ΔK_{th} for HCF alone, provided that the ratio of number of HCF to LCF cycles was large enough so that HCF growth rates per block exceeded those due to LCF alone. This condition has led to the requirement for using very high frequency testing apparatus in order to perform these types of tests in a reasonable time. Subsequent work shows Ti-6Al-4V [34] to be less sensitive to load-history effects than nickel-base superalloys. Later work in Ti-6Al-4V [35] showed the effects of multiple LCF underloads and overloads combined with high stress ratio HCF loading on crack growth. The linear summation model showed that the introduction of overloads caused the fatigue-crack-growth curves to shift to lower values of ΔK_{HCF}, when compared with multiple underloads. In the following section, further details are presented on thresholds obtained under LCF–HCF load spectra and studies of history effects in determining such thresholds.

4.3.1. Overloads and load-history effects

While a considerable amount of work has been done to study the effect of transient load cycles on crack-growth rate, only a very small portion of that work has addressed the question of determining a *threshold* for subsequent crack growth. Most of the published literature on underloads and overloads in crack-growth modeling deals with spectrum loading and the retardation or acceleration of growth rates. The work on overloads has concentrated on retardation effects, the slowing down of crack growth for some number of cycles after the overload before the crack resumes its steady-state growth rate. The term "delay cycles," the number of cycles it takes before steady state resumes, is commonly used in describing the retardation phenomenon. A schematic of the growth rate behavior under constant amplitude loading, after an overload, is shown in Figure 4.20. P_{max} refers

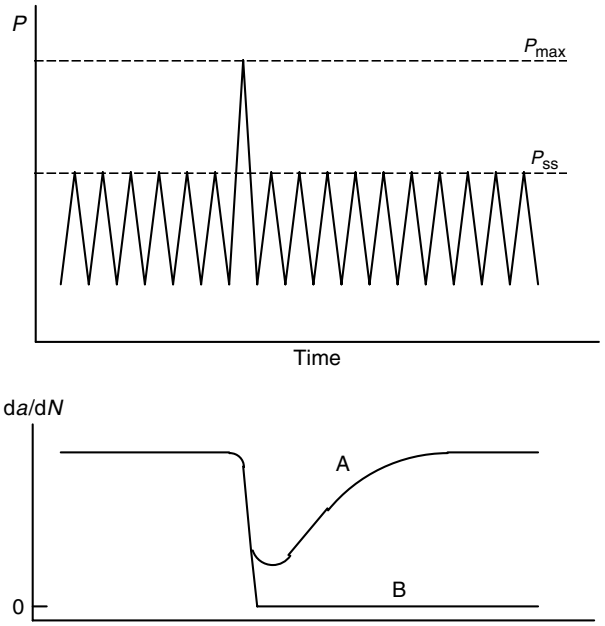


Figure 4.20. Schematic of overload applied to constant amplitude fatigue cycling and the corresponding effect on crack-growth rate; (A) retardation, (B) arrest.

to the peak load of the overload cycle, while P_{ss} refers to the maximum load of the steady-state cycles. Note that minimum loads or stress ratios have to be specified to completely define the loading condition. The usual situation studied is denoted by "A" in the figure, indicating a temporary retardation of growth rate until steady-state growth conditions are resumed.* One subset of this type of study is when the number of delay cycles becomes large enough to consider that subsequent crack growth has been completely arrested, denoted schematically by "B" in Figure 4.20. In this case, the threshold for crack growth following an overload which, in turn, follows the same amplitude steady state crack growth, can be determined. The overload ratio, defined as OLR = P_{max}/P_{ss} from Figure 4.20, is a common terminology used when describing overload effects. No systematic study of the influence of OLR on the threshold for crack propagation after single or multiple overloads seems to have been conducted.

Some of the earliest work on transient loading involved the study of the number of delay cycles after a single peak overload. Probst and Hillberry [36], in conducting a study of crack

* In some cases, an acceleration of crack growth rate occurs immediately after or during the overload cycle. Part of this can be attributed to the overload cycle itself. This is not shown in the figure nor discussed in this book.

retardation under the simple spectrum depicted in Figure 4.20, employed a "zeroing-in" technique to determine the size of the plastic zone required to arrest a crack at any particular fatigue stress intensity level. Their tests involved testing under constant K conditions and their results on overload crack retardation were attributed to some combination of crack blunting, development of residual compressive stresses ahead of the crack tip, and crack closure. Replacing P_{max} by K_0 and P_{ss} by K_{fmax} in Figure 4.20, they observed that the boundary between total arrest and continued crack propagation after the overload was described by a straight line, $K_{fmax} = 0.435K_0$, for a wide variety of test conditions using 2024-T3 Al as the test material. They modeled the phenomenon using the concept of an effective K that is reduced from the applied K by a quantity that can be considered equivalent to a crack closure load. The quantity was related to the overload plastic zone size. This type of modeling has seen considerable use over the years.

In the same time period, Gallagher and coworkers [37, 38] investigated load-interaction models to predict crack growth under different types of overloads resulting from spectrum loading. They modeled the instantaneous crack-growth rate following an overload and showed it was possible to generalize the stress intensity to account for the overload-generated arrest or threshold condition using an overload shut-off ratio. The modeling made use of the concept of plastic zone size and was able to account for the effect in materials with different yield strengths. Since the focus of their work was on the explanation of the retardation phenomenon, the experiments also covered the limiting condition of complete retardation. The overload shut-off ratio was the experimentally determined overload ratio above which crack arrest occurred.

Similar type work was conducted by Alzos et al. [39] where, instead of a single overload, they applied a single transient load that combines an overload with an underload, the latter often referred to also as a negative overload. In Figure 4.20, the minimum load for the single overload cycle would go below the minimum load of the steady-state cycling. They found the growth/arrest boundary corresponding to a subsequent crack-growth rate of $da/dN = 10^{-8}$ mm/cycle which was the limit of resolution in their experiments. Most of the emphasis in their work, like in much of the research in this area, was on delay in crack growth, and very little of the work addressed complete crack arrest.

One of the more significant studies of the effects of prior loading on the subsequent threshold for crack propagation was that of Hopkins et al. [40] who used an increasing-load step test at constant R to determine the overload modified long crack threshold, ΔK^*_{th}. In both a nickel-base alloy and Ti-6Al-4V, they found that for high values of prior overloads that ΔK^*_{th} increased exponentially with the magnitude of the prior applied overload. (Log ΔK^*_{th} was found to be linear with $K_{max,OL}$) It was also found that the ΔK^*_{th}/overload data could be extrapolated to obtain the basic threshold at low stress ratios where valid precracking is impractical for this type of test. Other findings of significance were the effect of frequency on the overload modified threshold and the effect of the number of overload cycles. In both the titanium alloy at room temperature and the nickel-base

superalloy at elevated temperature, their data showed higher thresholds at 1000 Hz than at 30 Hz. Also, when 50 overload cycles were used instead of one, the threshold was 20% higher in the titanium at $R = 0.5$, but unchanged in titanium at $R = 0.9$ and nickel at $R = 0.785$. The authors, after examining all of the data, concluded that crack closure as well as residual compressive stresses that develop at the crack tip due to the overload contribute to in the threshold due to overloads. Closure, however, was not considered to be a factor in tests at high R.

These approach and other methods like them provide models that work well in describing crack retardation regions where crack growth is retarded. However, these approaches require experimentally determined inputs such as the overload shut-off ratio and a baseline K_{th} to successfully correlate such data.

After observing that little work dealing directly with the determination of load-interaction effects on threshold, and even less with small cracks, was available, Moshier and co-workers conducted a series of investigations on load-history effects on the HCF threshold [4, 6, 9]. They studied load-history effects on the crack-growth threshold in notch specimens with LCF precracks on both medium size cracks [9], and later with very small cracks [4]. The experiments were conducted primarily on forged Ti-6Al-4V plate material. Double-notch-tension test specimens having the dimensions shown in Figure 4.21 were used. Stress concentration factors and notch depths of the two notches were chosen so that failure could be confined to the more severe notch having an elastic stress concentration factor, k_t, based on net section stress, of 2.25. The use of equal depth for the two notches produced essentially no bending in the specimen whether fixed or pinned grips were used.

To study the load-history effects on the HCF threshold, the loading schematic of Figure 4.22 was used. The cracks were developed by precracking which, for these investigations, was referred to as LCF. In the earliest investigation [9], precracking was conducted at stress ratios of -1.0 and 0.1. Following the step-loading procedure as shown in Figure 4.22, load was increased until crack growth was detected. ΔK_{th} was defined as the value of ΔK where propagation begins from a no-growth state. The ΔK_{th} determined in the studies by Moshier et al. represents the onset of crack propagation. This quantity is identical to that referred to in the terminology ΔK_{onset} used by Powell et al. (see [32], for example) or ΔK^*_{th} used by Hopkins et al. [40] as an "overload modified threshold" determined from increasing-load step testing on precracked test specimens.

All of the data were obtained at either $R = 0.1$ or $R = 0.5$, whereas the LCF cracks were generated at $R = 0.1$ or $R = -1.0$. The term "overload" or "underload effect" was used in this investigation as described later. The data for the HCF threshold after a LCF crack was initiated are plotted in a Kitagawa type diagram in Figures 4.23 and 4.24 for HCF values of $R = 0.1$ and $R = 0.5$, respectively. In each of the figures, a curve is drawn representing the long crack threshold of $K_{max} = 5.1\,\text{MPa}\sqrt{\text{m}}$ for $R = 0.1$ (Figure 4.23) and $K_{max} = 5.8\,\text{MPa}\sqrt{\text{m}}$ for $R = 0.5$ (Figure 4.24). The curves represent the best bilinear fit of a/c measurements from fracture surfaces for the starting LCF-generated crack.

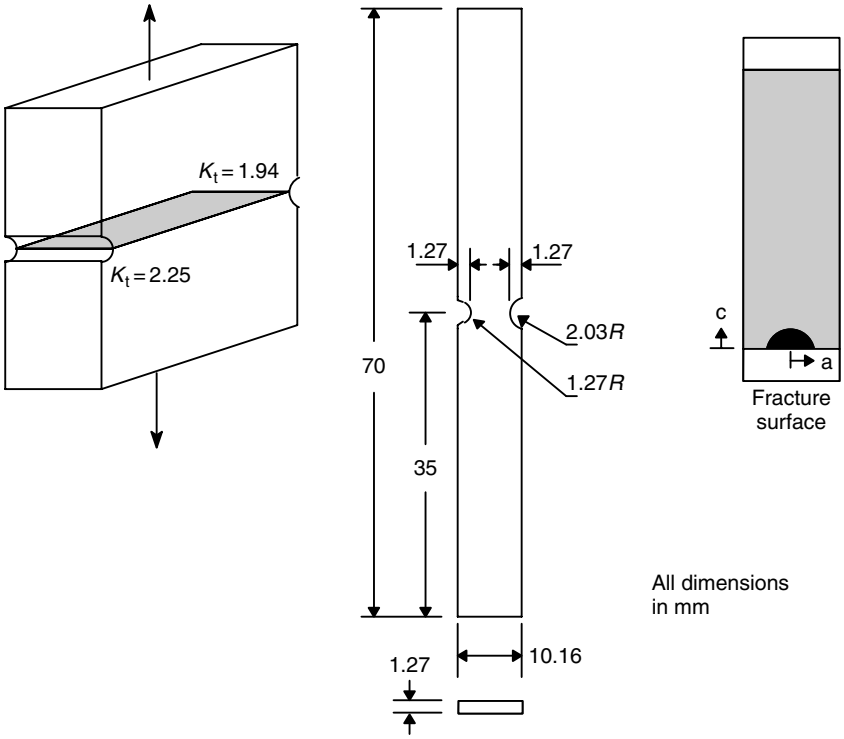


Figure 4.21. Double-notch-tension specimen geometry and crack shape nomenclature.

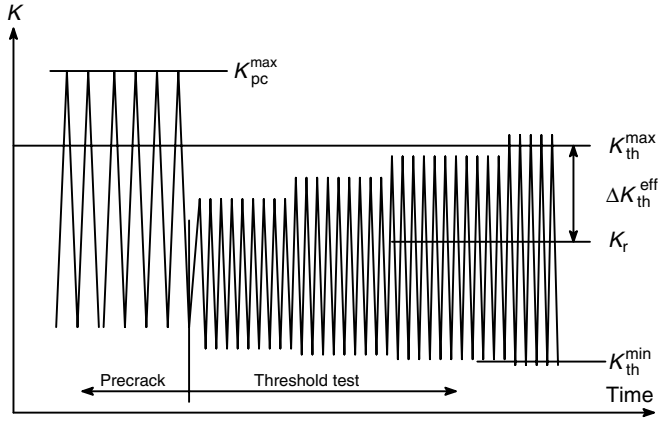


Figure 4.22. Schematic of LCF–HCF loading history and nomenclature.

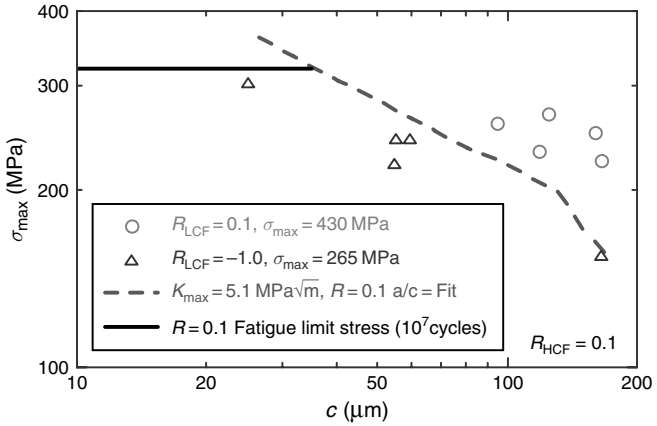


Figure 4.23. HCF thresholds at $R = 0.1$ on a Kitagawa type diagram.

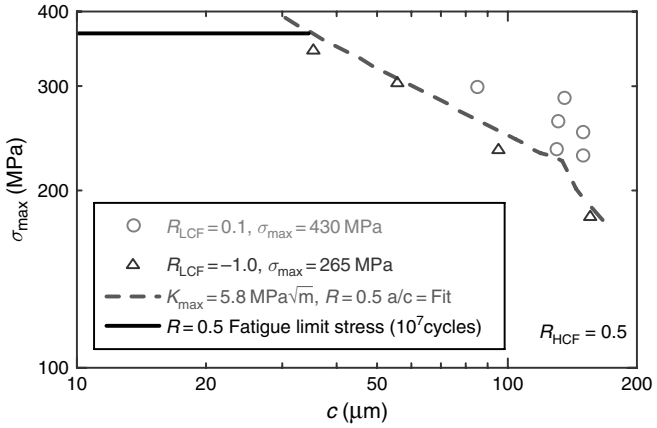


Figure 4.24. HCF thresholds at $R = 0.5$ on a Kitagawa type diagram.

The horizontal line in each figure represents the experimentally determined endurance limit of the uncracked specimen corresponding to 10^7 cycles. It can be seen in both figures that the data obtained using LCF at $R = 0.1$ (circles) show what appears to be equivalent to an overload effect since the threshold values of stress are consistently above the extrapolated long crack threshold. Conversely, data obtained using LCF at $R = -1.0$ (triangles) tend to fall slightly below the projected long crack threshold, the type of effect being representative of what one would expect when a material sees an underload during prior cycling. These results seemed to indicate that an overload type condition (LCF at $R = 0.1$) retards the subsequent HCF propagation while an underload (LCF at $R = -1.0$) might tend to slightly accelerate the subsequent HCF propagation. The apparent overload effect from precracking at a higher stress than that required to propagate the crack

under HCF is the result of multiple "overloads" since constant amplitude loading was used to precrack the specimens. The apparent multiple overload effect is consistent with observations such as those of Frost [41] who noted that cracks formed by precracking at a higher alternating stress are all stronger than expected and that the "propagation stress" (stress to obtain ΔK_{th}) is increased if the initial loading conditions are such as to induce compressive residual stresses at the crack tip. It should also be noted here that the overload ratios (OLR = ratio of precrack stress to FLS) in the works of Moshier et al. were relatively small compared to those used in typical studies of overload effects where values of OLR commonly exceed 1.5 in order to produce noticeable effects [42]. While it is not the intent of this book to discuss the governing mechanisms of retardation due to overloads, the reader is referred to the review article by Sadananda et al. [42] who address that subject.

In the Kitagawa diagram used to present the threshold data above, all combinations of crack length and stress corresponding to a K solution equal to the threshold value can be plotted to establish the threshold crack-growth line. Although small crack corrections were not used here, the concept of data points below the endurance limit represents a threshold for cracks of a particular size. It is clear that such cracks could not be naturally initiated since they represent stress levels below the endurance limit. While such cracks could be preexisting in the material in the form of initial defects, material with such defects in sufficient quantities would have a lower endurance limit (by definition!). It follows, therefore, that data plotted on a Kitagawa diagram representing a crack length and stress below the endurance limit generally represent a condition where the crack was initiated above the endurance limit. The question can be raised as to whether any point on a Kitagawa diagram is unique or, instead, is dependent on the history of loading in getting to that point. The long-crack threshold, for example, represents a data point that may be dependent on loading history. While standards have been set for determining this threshold by following a predetermined loading history, the history dependence and the existence of a unique long-crack threshold still have to be questioned. This subject is discussed further in Chapter 8.

Noting that prior loading history involving multiple overloads and underloads can influence measured FCG thresholds in surface cracks at notches, Moshier et al. [6] conducted a series of long crack experiments to further study the load-history effect on threshold. The study was conducted on both Ti-6Al-4V (Ti-6-4) and Ti-5Al-2Sn-2Zr-4Mo-4Cr (Ti-17). They measured the threshold under constant R, HCF loading, using an increasing ΔK step-loading procedure as shown above (Figure 4.22). LCF precracking was done using a range of ΔK values where the corresponding K_{max} representing LCF loading was greater than those of the subsequently measured HCF thresholds, thereby producing the multiple overload condition. This condition is represented schematically in Figure 4.22.

Data obtained at $R_{HCF} = 0.1$ showed a linear relation between the HCF threshold and the K_{max} and R values of the LCF precrack for long cracks in C(T) specimens. Figures 4.25

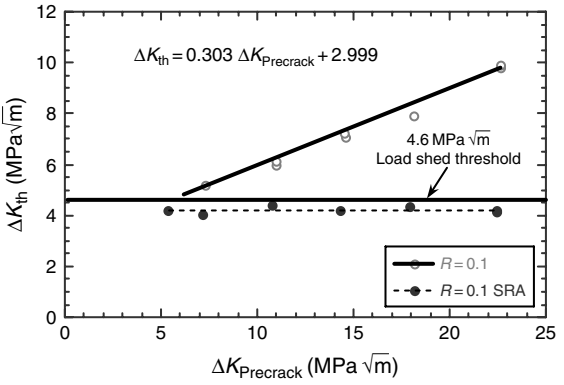


Figure 4.25. Threshold data at $R = 0.1$ for Ti-6Al-4V with and without stress relief annealing (SRA) $R_{LCF} = 0.1$.

and 4.26 show the observed linear relationship between ΔK of the (LCF) precrack and the ΔK threshold for testing at $R_{HCF} = 0.1$ for Ti-6-4 and Ti-17, respectively. A similar plot to Figure 4.25 that includes small-crack specimen data is presented in Figure 4.27 and shows that small-crack data follow the same linear trend. A number of the precracked specimens were SRA to remove any residual stresses developed in the precracking. It can be observed that for SRA, the threshold obtained is independent of precrack history in both materials. The data also agree fairly well with the long-crack threshold obtained under conventional load shed techniques, shown in the figures as "Load Shed Threshold." However, the data from SRA lie slightly below the long crack threshold, more for Ti-6-4 than for Ti-17. The authors speculated that the reason for the slightly lower threshold is that SRA completely eliminates load-history effects and residual stresses whereas the

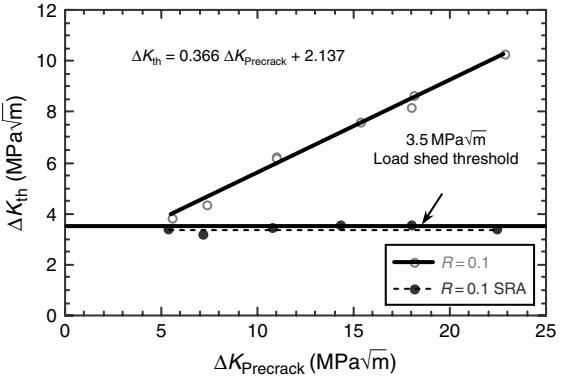


Figure 4.26. Threshold data at $R = 0.1$ for Ti-17 with and without stress relief annealing (SRA) $R_{LCF} = 0.1$.

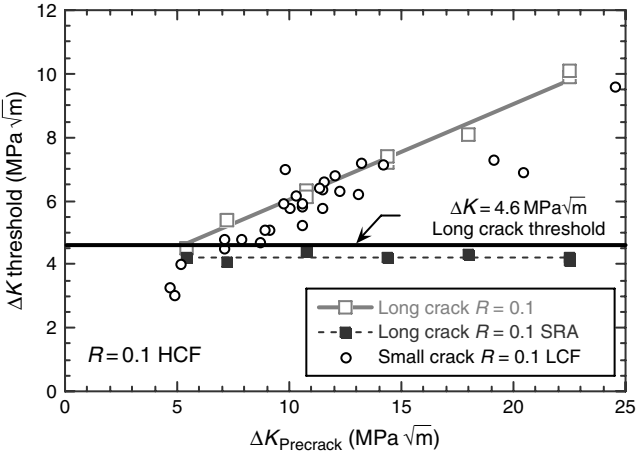


Figure 4.27. Experimental relationship between precrack and threshold stress intensity for $R = 0.1$ threshold tests in long crack C(T) specimens and small surface flaws.

long crack threshold retains whatever residual stresses or closure is present at the end of the conventional load-shed procedure for threshold testing. The resulting threshold could even be considered to be a "true" material threshold, although no such definition of a true threshold seems to exist.

To represent the linear relation between ΔK_{th} of the HCF testing and the $\Delta K_{\text{Precrack}}$, a simple model was developed to fit the data and to use in follow-on analytical modeling of other load-history-dependent threshold test results. The model is purely empirical in nature and was not intended to be a general overload model, many of which already exist in the literature.

4.3.1.1. An overload model

While overload models to estimate FCG retardation abound in the literature, there are few to estimate thresholds. A model for estimating threshold from the LCF precrack level was developed using an approach similar to those used in closure and crack retardation modeling. From the data shown in Figures 4.25 and 4.26 for long cracks in C(T) specimens in both Ti-6-4 and Ti-17, an effective threshold was found to be a material constant. This was used to formulate a relationship between $K_{\max}$ threshold and K_{r}, where K_{r} is defined as the stress intensity factor level above which K is effective and below which it is not. This reduces the stress intensity factor range to an effective range:

$$\Delta K_{\text{th}}^{\text{eff}} = K_{\text{th}}^{\max} - K_{\text{r}} \tag{4.21}$$

where the various terms are defined in the loading schematic, Figure 4.22. K_{r} is analogous to the opening stress intensity factor K_{op} used in closure-based models, and K_{pr}, the crack

propagation intensity factor [42]. After many iterations to consolidate the experimental data, K_r was found to be best represented in the form

$$K_r = \beta\left(K_{pc}^{max} + K_{th}^{min}\right) \tag{4.22}$$

where β is a fitting parameter and subscripts "pc" and "th" refer to the LCF precrack and HCF threshold, respectively. The effective stress intensity factor range, ΔK_{th}^{eff}, is assumed to be a material constant representing the minimum effective ΔK to propagate a crack. The linear relation between ΔK_{th} and ΔK_{pc}, observed experimentally, is then written as

$$\Delta K_{th} = \frac{(1-R_{th})\,\Delta K_{th}^{eff}}{(1-\beta R_{th})} + \frac{\beta\,(1-R_{th})}{(1-\beta R_{th})(1-R_{pc})}\Delta K_{pc} \tag{4.23}$$

The linear fit of threshold data at $R = 0.1$ was used to determine the parameters ΔK_{th}^{eff} and β ($\Delta K_{th}^{eff} = 3.23$ and $\beta = 0.294$ for Ti-6-4 and $\Delta K_{th}^{eff} = 2.29$ and $\beta = 0.353$ for Ti-17). This model was then applied to data obtained at different values of R for the HCF threshold testing. The ability of this equation to represent threshold data obtained at these other values of R after precracking at $R = 0.1$ is illustrated in Figure 4.28 for long cracks in C(T) specimens for Ti-6-4. The empirical fit to the data is made only for the data obtained at $R = 0.1$. The fit at $R = 0.1$ provides the constants which, in turn, produce the model predictions shown for other values of R in the figure. It can be seen that the model provides an excellent representation of the entire data set. An equally good correlation was obtained for T-17 by fitting the data at $R = 0.1$ and predicting the behavior at $R = 0.5$ and $R = 0.7$ (see [6], Figure 4.5).

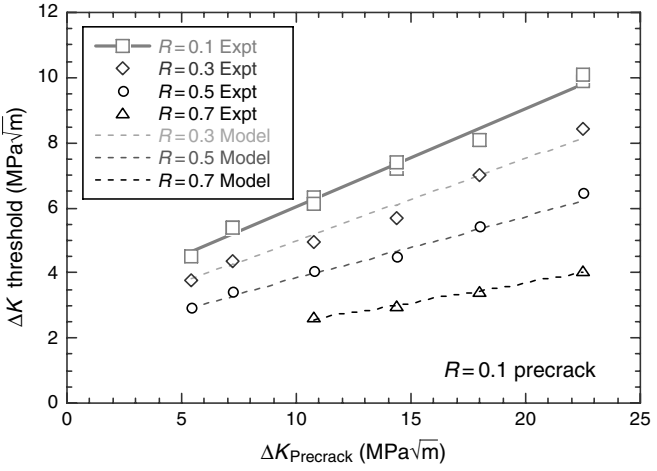


Figure 4.28. Experimental data and model predictions for long crack data.

4.3.1.2. Analysis using an overload model

For the general case of an overload model applied to any geometry, the K solution for the specific geometry is written in the form

$$K = \sigma\sqrt{\pi a}\ \mathrm{f}(a) \tag{4.24}$$

Denoting the precrack condition with subscript pc, the K used to produce an overload condition, which we refer to as the LCF precrack, is

$$K_{\mathrm{pc}} = \sigma_{\mathrm{pc}}\sqrt{\pi a}\ \mathrm{f}(a) \tag{4.25}$$

For the particular overload model used here, the linear relation between K_{th} and K_{pc}, Equation (4.23), requires $K_{\mathrm{th}} = K_{\mathrm{pc}}$ when there is no overload as in the limiting case of steady-state crack growth near threshold. In this case, K is the long crack threshold, $K_{\mathrm{th}}^{\mathrm{lc}}$, a material constant, and Equation (4.23) can be rewritten as

$$K_{\mathrm{th}} = \alpha\ K_{\mathrm{pc}} + K_{\mathrm{th}}^{\mathrm{lc}}(1-\alpha) \tag{4.26}$$

where α is an empirical constant. In these equations, K represents the maximum value of K at a given value of R, but could also represent ΔK throughout.

To extend the modeling to small cracks, the concept of El Haddad et al. [3] is employed to produce the endurance limit stress for arbitrarily small cracks, and the K solution, Equation (4.24) for long cracks. Following the procedure of modifying the material capability (threshold stress intensity) instead of the crack length, the threshold value of K, denoted by $\overline{K}_{\mathrm{th}}$, is reduced for small cracks in the following manner:

$$\overline{K}_{\mathrm{th}} = K_{\mathrm{th}}\left[\frac{a}{a+a_0}\right]^{1/2}\frac{\mathrm{f}(a)}{\mathrm{f}(a+a_0)} \tag{4.27}$$

where a_0, as defined by El Haddad, and modified for the more general K solution of Equation (4.24), is given by Equation (4.4) previously, but repeated here:

$$a_0 = \frac{1}{\pi}\left(\frac{K_{\mathrm{th}}}{\sigma_{\mathrm{e}}\mathrm{f}(a_0)}\right)^2 \tag{4.28}$$

which can be solved for a_0 either graphically or iteratively. The crack length a_0 is usually not considered in the $\mathrm{f}(a)$ term of Equation (4.24) when deriving the effective K in Equation (4.27). For each crack length, the threshold stress is obtained from a combination of Equation (4.27) and the K solution, Equation (4.24), in the following equation:

$$\sigma = \frac{\overline{K}_{\mathrm{th}}}{\sqrt{\pi a}\ \mathrm{f}(a)} \tag{4.29}$$

4.3.2. Examples of LCF–HCF interactions

As an illustrative example, a SEN specimen is cracked at a stress corresponding to the endurance limit, σ_e, and another one at a stress above the endurance limit, $\sigma = 1.25\sigma_e$ in this case. The K solution is approximated in Equation (4.24) by setting $f(a) = 1$. From the K solution, and the small-crack correction, Equation (4.27), the threshold condition for a baseline chosen arbitrarily as $K_{th} = 5\,\text{MPa}\sqrt{\text{m}}$ and $\sigma_e = 300\,\text{MPa}$ is represented in the form of a Kitagawa type diagram in Figure 4.29. The diagram shows the smooth transition from a fracture mechanics dominated long-crack threshold, where the slope on a log-log plot is -0.5, Equation (4.24), to a crack-length independent endurance limit, $\sigma_e = 300\,\text{MPa}$, for arbitrarily short cracks. If, however, the crack is initiated at a stress equal to or above the endurance limit, $\sigma = \sigma_e$ and $\sigma = 1.25\sigma_e$ for the two cases here, then the longer the crack developed under this "LCF" or precrack condition, the higher will be the value of K_{OL} as determined from Equation (4.25). For each case modeled, pairs of values of a and K_{pc} are obtained. Then K_{th} can be calculated from Equation (4.26) and modified for short cracks using Equation (4.27) to get an effective value of K_{th}. The relation between σ and a is obtained from Equation (4.29) to determine points on the Kitagawa diagram as illustrated in Figure 4.29. The divergence of the curves for $\sigma = \sigma_e$ and $\sigma = 1.25\sigma_e$ is due to a combination of the increase in K_{pc} due to increase in LCF crack length, as well as the form of the specific model used here, Equation (4.26), which shows that the threshold increases with increase in K_{pc}. The assumption implied in this illustrative analysis, which could be applied to any actual experimental geometry, is that the endurance limit is a material constant at a given R and does not depend on any prior load history which does not produce cracks. This assumption has been validated under several experimental conditions described at the beginning of this chapter. The net result,

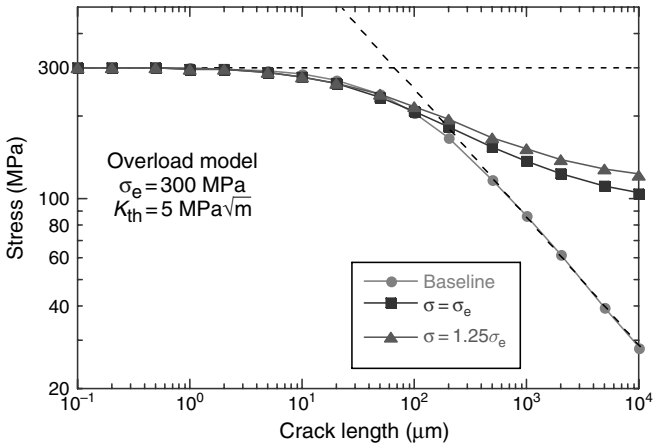


Figure 4.29. Kitagawa diagram for theoretical SEN specimen behavior.

as shown in Figure 4.29, is that the stress required to produce growth of a crack under HCF, which developed under constant load at or above the endurance limit, is below the endurance limit stress but above the baseline stress calculated from fracture mechanics with a small crack correction. The difference is attributed to the load-history effect.

The concept and model described above was applied to an expanded database from experiments on notched specimens in which very small cracks could be detected [4]. The K solution was obtained for the notch geometry with a surface flaw, and the overload effect on the threshold for K was obtained from the model, Equation (4.23). To account for a small crack effect, K was then modified in accordance with Equation (4.27). The specific value of the a/c ratio in the K solution was used for each data point in the calculation of a_0 which is where the endurance limit stress and K_{th} equation cross on a Kitagawa diagram. The data and the model fit are shown in a Kitagawa diagram in Figure 4.30 where the model prediction is based on Equation (4.23) with the appropriate fit to data from long crack experiments.

The data, summarized in Figure 4.30, include tests where both $R = -1$ and $R = 0.1$ were used for the LCF precracking and both SRA and no stress relief were applied prior to HCF testing for both cases. LCF precracking produced cracks with depths covering a range from $c = 16$ to $370\,\mu$m. For modeling predictions, three curves are shown. In one case, the threshold from long cracks ($K_{max} = 5.1\,\text{MPa}\sqrt{\text{m}}$) is used without any overload or small crack correction. This corresponds to Equation (4.24) with K being a constant using the appropriate aspect ratio in the K solution. The second analytical curve corresponds to a prediction without any small crack correction. This simply incorporates the overload effect, Equation (4.23), in the calculation of K_{th}. The third prediction is identical, but the small crack effect is taken into account through the use of Equation (4.27). Several

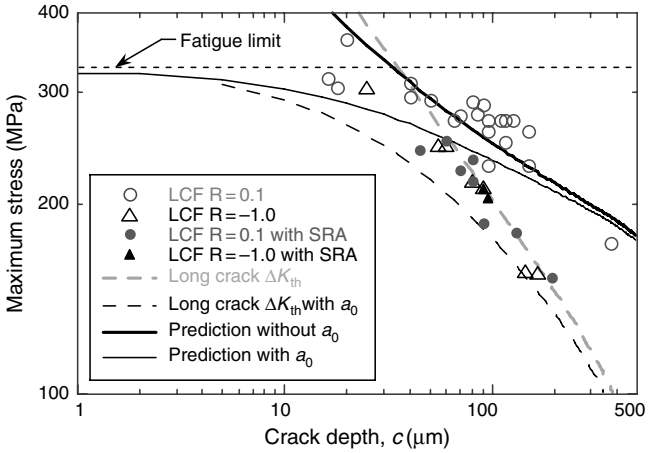


Figure 4.30. Experimental data and model predictions on a Kitagawa diagram.

features of the analytical predictions should be noted. First, the curve for constant K is not a straight line of slope -0.5 as is often noted in a Kitagawa diagram. The reason for this is that the K solution is of a more complex form, Equation (4.24), than for the simple case where $f(a) = 1$ corresponding to the simple $\sqrt{a}$ dependence of K on crack length. The second feature for the cases of a constant load to produce an overload effect is that the model predicts behavior quite different than the constant K solution as illustrated for the simple illustrative example shown in Figure 4.29.

The correlation of the data with the analytical models, as shown in Figure 4.30, shows the ability to extend a long-crack overload model to small surface flaws in a notch geometry. The cracks developed under $R = 0.1$ loading have thresholds at $R = 0.1$ which are predicted, somewhat conservatively, by the linear overload model of Equation (4.23) with the small crack (a_0) correction of El Haddad. It is clear from the data that the threshold is increased when there is an overload history applied during the LCF stage, similar in concept to the retardation effect observed in growing cracks. LCF cracks formed under $R = -1$ loading, on the other hand, produce thresholds which are predicted by the (constant) long-crack threshold value of $K_{max} = 5.1\,\text{MPa}\sqrt{\text{m}}$. The maximum stress or K level in the threshold testing exceeded that of the LCF precracking only for the smallest crack formed in tests at $R = -1$ where precracking was at a maximum stress of 265 MPa. The remainder at $R = -1$ and all at $R = 0.1$ had lower values of K_{max} in threshold tests at $R = 0.1$ than those in precracking. Thus all tests with the exception of one data point could be expected to demonstrate some type of overload effect. However, unlike precracking at $R = 0.1$, precracking at $R = -1$ seemed to have no overload effect on the subsequent threshold. The compression portion of the fully reversed loading cycle appears to negate any beneficial effect of the tension portion of the cycle upon the subsequent threshold. For both prior loading at $R = 0.1$ and $R = -1$, stress relief annealing produced a condition where the subsequent threshold corresponded to the long crack threshold as shown by the solid symbols in Figure 4.30. These data, as well as the data from precracking at $R = -1$ without SRA, show no history-of-loading effect on the subsequent threshold determined at $R = 0.1$. The best representation of these threshold values would be the long crack threshold with a small crack correction for the smallest of cracks in these tests. The small crack correction can be seen in Figure 4.30.

Another important observation from the experimental data of Figure 4.30 is that for cracks having depths, c, less than 30–40 μm (the approximate value of a_0 as determined by the intersection of the long crack threshold curve with the constant endurance limit stress) is the value of the stress to produce crack extension. For these small cracks, while calculated values of K might be considerably below the long crack threshold, the values of *stress* at threshold are only slightly below or at the endurance limit stress within a reasonable scatter band. This indicates that very small cracks are not very detrimental in reducing the fatigue threshold stress, even though the location of the failure corresponds to the location of the initial cracks.

A load-history-free material threshold is equivalent to precracking at threshold. This load-history independent threshold can be calculated from the model by setting ΔK_{pc} equal to the ΔK_{th}. This assumes that the load-history-free threshold would be measured if the LCF cracking could occur at threshold. This substitution gives:

$$\Delta K_{th} = \frac{(1 - R_{th})\,\Delta K_{eff}}{(1 - \beta - \beta R_{th})} \tag{4.30}$$

Experimentally, the history-free threshold is measured using stress-relief-annealed specimens. ΔK thresholds calculated from the model [Equation (4.22)] are $4.3\,\text{MPa}\sqrt{\text{m}}$ for $R = 0.1$ and $2.89\,\text{MPa}\sqrt{m}$ for $R = 0.5$ for Ti-6-4 and $3.37\,\text{MPa}\sqrt{\text{m}}$ for $R = 0.1$ for Ti-17. These compare favorably with the experimentally measured thresholds of 4.23 and $2.8\,\text{MPa}\sqrt{\text{m}}$ for Ti-6-4 at $R = 0.1$ and $R = 0.5$, respectively, and $3.46\,\text{MPa}\sqrt{\text{m}}$ at $R = 0.1$ for Ti-17.

To further investigate the load-history effect on threshold outlined above from the work of Moshier et al. [4, 6], Golden and Nicholas [43] followed the same procedure but precracked at an even lower stress ratio of $R = -3.0$. They examined LCF–HCF interactions at negative values of R under both smooth bar conditions, where LCF generated cracks are difficult to detect and may not even exist, and under notch fatigue, where cracks were deliberately introduced and detected. Their investigation explored the nature of the crack initiation, threshold crack propagation, and any associated load-history effects when a specimen is initially subjected to loading at negative stress ratios. Two types of experiments were conducted. In the first series of tests, smooth bars were loaded at $R = -3.5$ in order to see if this would initiate cracks which might affect the subsequent threshold at a higher value of R. In the second series of tests, LCF cracks were deliberately introduced with loading at $R = -3$ and the subsequent threshold was determined experimentally. The effect of loading history was assessed for both test procedures using Ti-6Al-4V as the test material.

The smooth bar specimens were tested under three conditions: (1) a baseline condition with no preloading; (2) preloaded and then heat tinted prior to threshold step test; and (3) preloaded, heat tinted and stress relieved prior to threshold step test. The 10^7 cycle fatigue strength for each of these three test conditions are reported in Figure 4.31 for $R = 0.1$ and $R = 0.5$ step tests. These tests were conducted on specimens subjected to prior LCF at a value of $R = -3.5$ at a stress level of 240 MPa, which is below the observed failure stress of 265 MPa at that value of R. If it is postulated that cracks nucleate due to some function of total stress or strain range, but will only continue to propagate when subjected to a positive stress range that produces a positive crack driving force, K, then cracks should be found before the HCF testing begins. After subjecting the specimens to 10^7 cycles at $R = -3.5$, the specimens were then tested in HCF until failure at either $R = 0.1$ or $R = 0.5$ using the step-loading procedure. Some of the specimens were stress relieved after the initial loading at $R = -3.5$ in order to remove any history effects on a crack

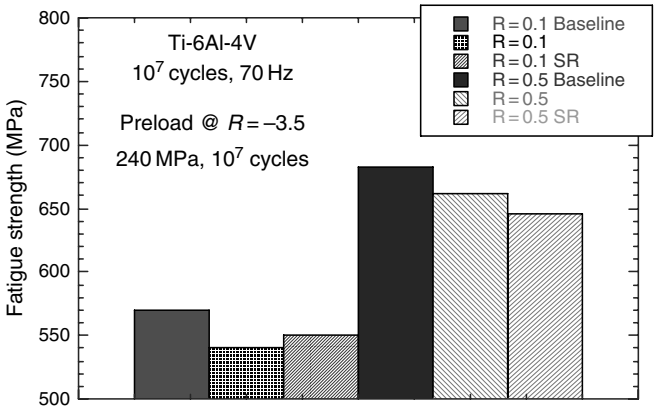


Figure 4.31. Fatigue limit stress for specimens subjected to preloads at $R = -3.5$.

that may have formed. The results are summarized in Figure 4.31 where baseline tests are compared with preload tests with and without stress relief (SR) for both values of R. Note that the peak stress levels applied in the HCF tests are considerably higher than the peak stress used in the preloading (240 MPa). Using an expanded stress scale emphasizes the possibility that a minor reduction in HCF strength may have been obtained due to preloading at $R = -3.5$, but the magnitude of any such reduction is not very significant.

The results show that the pre-loading reduces the 10^7 cycle fatigue strength of the Ti-6Al-4V material by approximately 5%. Given the small difference in fatigue strength and the small number of specimens, this difference is not very significant in a statistical sense. Also, the stress relief did not seem to have a consistent or significant effect on the results. Examination of the fracture surfaces of these specimens showed no obvious heat tint markings. A threshold stress analysis, however, reveals that the calculated a_0 for this material and geometry would be approximately 60 μm. A Kitagawa diagram was drawn for these test conditions (circular bar) as described earlier in the work by Morrissey et al. [15] (see Figure 4.11). The small reduction of strength observed from these tests would indicate cracks approximately 10 μm deep, which is typically too small to detect using the optical microscope. An SEM examination of the fracture surface revealed some possible initial flaws. Examples are shown in Figure 4.32. Here the lines indicate the possible initial crack boundaries. These markings were considered an upper bound to the crack sizes that may have been present after preloading. This was found to be consistent with a Kitagawa diagram analysis. Such features were not observed in baseline specimens which received no stressing at negative R.

In the notched specimens, the precrack test phase was run until cracks were generated and observed with an infrared damage detection system. Therefore, nearly all specimens had a measurable heat tinted crack on the fracture surface and several had multiple cracks.

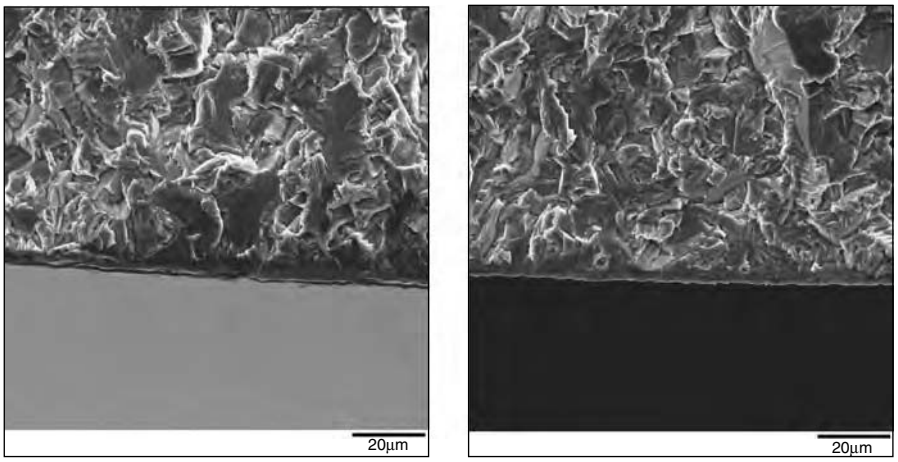


Figure 4.32. Fracture surfaces of specimens subjected to preload at $R = -3.5$.

The threshold stress and crack depths were plotted on a Kitagawa diagram. All of the data for the notch specimens precracked in LCF at $R = -3$ and $R = -1$ followed or fell slightly below the short crack and/or LEFM $R = 0.1$ threshold predictions. The SR did not seem to have a consistent or significant effect on the results.

To compare the results from the smooth bar tests and the precracked notched specimens, a normalized Kitagawa diagram was introduced. Crack length on the x-axis is normalized with respect to a_0 while stress on the y-axis is normalized with respect to the FLS for the specific geometry and value of R. This diagram can be used to compare results from two (or more) entirely separate geometries. Such a plot is shown as Figure 4.33 where the smooth (circular) bar and the notched specimen are represented by their respective long crack (solid) and El Haddad short crack corrected (dashed) curves for $R = 0.1$. Curves for the two geometries for $R = 0.5$ lay nearly on top of the $R = 0.1$ curves in both cases and are not plotted. Nearly identical normalized curves on a Kitagawa diagram at different stress ratios were also observed and documented in Golden [44] for arch-shaped specimens from a fretting fatigue study.

In Figure 4.33, for $R = 0.1$, maximum endurance limit stresses used were 310 MPa, and 570 MPa, for the notched and smooth specimens, respectively. The long crack ΔK_{th} used in the analysis was 4.6 MPa$\sqrt{\text{m}}$. For the notched specimen, $a_0 = 25\,\mu$m for a surface crack with $a/c = 0.6$ and $a_0 = 15\,\mu$m for a through crack while for the smooth specimen $a_0 = 58\,\mu$m. Experimental data points from the notched tests at R = 0.1 are also shown on the curve. Horizontal and vertical dashed lines represent the predicted a/a_0 crack sizes for 95 and 80% of fatigue strength which covers and even exceeds the range of the data shown in Figure 4.31 for specimens preloaded at $R = -3.5$. This leads to predicted

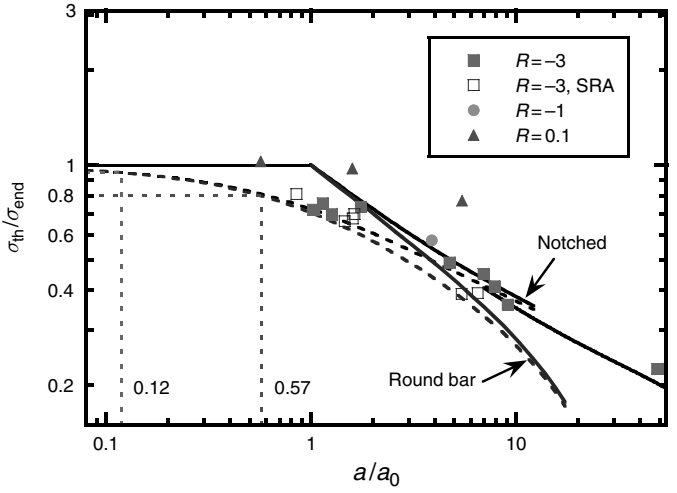


Figure 4.33. Normalized Kitagawa diagram showing curves for circular bar and notched specimens.

crack sizes in the smooth bars of approximately 7–35 μm. As noted above, no indications of such cracks were observed and, further, no load history effects were observed in the notched specimens precracked at $R = -3$ since the data follow the predicted short crack corrected threshold line in the Kitagawa plot.

Another plot that can be used to represent these data is the measured threshold stress intensity factor, K_{max} threshold, versus the applied K_{max} precrack. K_{max} precrack is the stress intensity factor of the final crack size during precracking with the precracking stress applied while K_{max} threshold was calculated using the same crack size but with the threshold stress applied. The plot, shown in Figure 4.34, contains all of the data collected in [43] that have threshold values measured at $R = 0.1$. LCF precracking R values are labeled in the legend. Several curves are added to this plot that represent the predicted or measured threshold behavior for long cracks with and without load-history effects and also for short cracks. The horizontal line is simply the long crack threshold $K_{max} = 5.1\,\text{MPa}\sqrt{\text{m}}$ while the endurance stress, σ_{end}, is the boundary for growth or no growth for material with very short cracks in which failure is controlled by stress rather than LEFM. This boundary was calculated using Equations (4.31) and (4.32) where σ_{pc} is the $R = -3$ precrack maximum stress of 150 MPa and σ_{end} is the $R = 0.1$ endurance stress of 310 MPa. The short crack threshold curve is a transition between the endurance stress and LEFM criteria much like that used in the Kitagawa diagram. Here K_{pc} was calculated by Equation (4.31) and the small-crack threshold stress intensity factor, $K_{th,sc}$, was calculated according to Equation (4.33). Finally, Equation (4.34) is plotted showing the effect of tension overload on the threshold. This line was fit to $R = 0.1$ fatigue crack-growth threshold tests performed by Moshier et al. [6] where the crack-growth

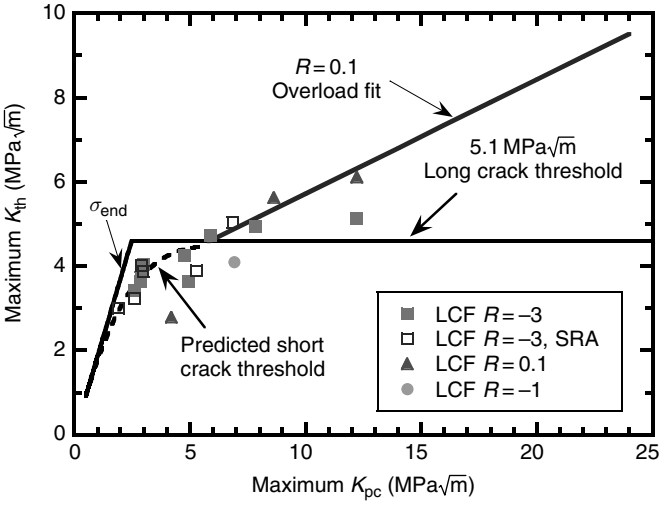


Figure 4.34. Summary of calculated $R = 0.1K_{max}$ threshold of cracks measured in precracked notched specimens. The precracking K_{max} for the endurance stress and short crack threshold predictions are based on the $R = -3$ precracking stress of 150 MPa.

thresholds were measured after different levels of $R = 0.1$ precracking.

$$K_{pc} = \sigma_{pc}\sqrt{\pi a}\ Y(a) \tag{4.31}$$

$$K_{th,end} = \sigma_{end}\sqrt{\pi a}\ Y(a) K_{th,end} = \sigma_{end}\sqrt{\pi a}\ Y(a) \tag{4.32}$$

$$K_{th,sc} = \sigma_{th,lc}\sqrt{\frac{a}{a+a_0}}\ \frac{Y(a)}{Y\,(a+a_0)} \tag{4.33}$$

$$K_{th} = 0.303K_{pc} + 3.33 \tag{4.34}$$

The results plotted in Figure 4.34 are very consistent with the predictive curves. Starting from the lower precracking K_{max}, the $R = -3$ precracked data all seem to have $R = 0.1$ thresholds that match the short crack curve very well. In the K_{max} precrack range of $5-10\,\text{MPa}\sqrt{\text{m}}$, the data precracked at $R = -3$ and $R = -1$ seem to follow the long crack $R = 0.1$ threshold as expected with some scatter. Two points from this study precracked at $R = 0.1$ seemed to follow the load history fit quite well, which was consistent with similar notch data generated by Moshier et al. [4]. What is interesting to note is the data point precracked at $R = -3$ and $K_{max} = 12\,\text{MPa}\sqrt{\text{m}}$ that has an $R = 0.1$ threshold much lower than predicted using the K_{max} overload fit and much lower than the data precracked at $R = 0.1$ with the same precracking K_{max}. Although this result was from only one test, it could only be due to the compression portion of the cycle during the precracking. This result is also consistent with the $R = -1$ precracking data presented by Moshier et al. [4].

The authors conclude that at higher levels of precracking, the compressive "overload" (sometimes referred to as an underload) has the effect of eliminating or canceling the effect of the tensile "overload" load-history effect. At lower levels of precracking K_{max} where a tensile "overload" load-history effect was not expected, the compressive precracking appeared to have very little effect.

The question then arises, could it be possible that the negative stress ratio precracking had an undetected "underload" effect on the crack-growth threshold of many of the tests that didn't appear to show an effect? Single or multiple underload cycles have been shown to accelerate crack growth for a short period of crack extension in constant amplitude crack-growth tests [45]. During threshold step tests it is possible that stress levels are encountered that grow the crack at a ΔK less than the threshold level (either long crack or short crack) due to the "underload" load history. The crack, then, could grow a short distance out of the reduced ΔK_{th} effect and then arrest until the next step increase in stress. This sequence could repeat until a stress is reached that grows the crack to failure. In the analysis, only this final stress would be considered, therefore, the "true" reduced crack-growth threshold stress would not be known and could be lower than has been measured. This scenario, however, is speculative and current experimental procedures and available data cannot prove or disprove this possibility.

Another consideration in the determination of thresholds for HCF crack propagation is crack length. Ritchie points out the importance of the small fatigue crack phenomenon when determining HCF thresholds [46]. Any number of variables including crack size and geometry, mode mixity, applied loading spectra and residual stress may affect the HCF threshold. Ritchie et al. [47] propose a high stress ratio, large-crack-growth test to determine a lower bound HCF threshold. The long-crack lower bound threshold was presented as a way of describing the onset of small crack growth from natural crack initiation and FOD sites. Frequencies of 50 to 1 kHz were used to study large-crack propagation in Ti-6Al-4V using C(T) specimens. The high stress ratio, large crack-growth test is used to simulate the closure-free small-crack behavior and determine a lower bound long crack threshold of 1.9 MPa$\sqrt{\text{m}}$. Comparisons were done with closure corrected lower stress ratio, long crack-growth threshold tests to verify the determined lower bound long-crack threshold. The comparisons, however, indicated that the higher stress ratio threshold was less than the closure corrected lower stress ratio test due to an additional mechanism such as room temperature creep or slip-step oxidation. Although an additional mechanism caused the measured higher stress level threshold to be less, it is in any event still a conservative estimate and thus a lower-bound threshold for Ti-6Al-4V. Additionally, Boyce and Ritchie found that thresholds for Ti-6Al-4V were frequency independent over the range of 50–1000 Hz. Campbell et al. [48] investigated mixed-mode crack-growth thresholds using through cracks in Ti-6Al-4V plate material. They determined that a slight increase in mode I threshold results when the crack kinking

direction increases from 0 to 30 degrees as compared to the pure mode I case. Crack kinking angles greater than 30 degrees produced lower mode I thresholds.

When combined LCF and HCF loading, which is sometimes referred to as combined cycle fatigue (CCF), is present, crack-growth rate behavior has been seen to follow two different patterns as depicted in Figure 4.35. In A, the more common behavior, LCF growth rates follow the rate for LCF alone below the HCF threshold. The transition to an accelerated growth rate occurs when the threshold for pure HCF alone is reached as the crack extends. At that point, if the number of HCF cycles per block is high enough, an accelerated growth rate is observed. The stress intensity at which this occurs is often called ΔK_{onset}. For this type of behavior, a linear summation model seems adequate for describing the behavior. The model can be expressed as

$$\left[\frac{\mathrm{d}a}{\mathrm{d}N}\right]_{\text{Block}} = \left[\frac{\mathrm{d}a}{\mathrm{d}N}\right]_{\text{LCF}} + \mathrm{n}\left[\frac{\mathrm{d}a}{\mathrm{d}N}\right]_{\text{HCF}} \tag{4.35}$$

where the block, or CCF crack-growth rate, is given as the sum of the contribution of one LCF cycle and n HCF cycles, where n is the number of HCF cycles per block. If one considers that crack-growth rate data are normally plotted on logarithmic scales, the model essentially predicts that either LCF or HCF alone determine the observed growth rate, depending on which one is larger. This, in turn, is a function of n, the number of HCF cycles per block, and the value of ΔK with respect to the HCF threshold.

A second type of behavior, depicted as B in Figure 4.35, is similar to that shown as A, but the crack-growth rate at values of ΔK below the HCF threshold is observed to occur at an elevated rate compared to that for LCF alone. The reasons for this behavior do not appear to be very well understood according to published results, but such behavior can be non-conservative from a design viewpoint because the threshold for HCF could be reached in a shorter period of time than that predicted by a simple linear summation

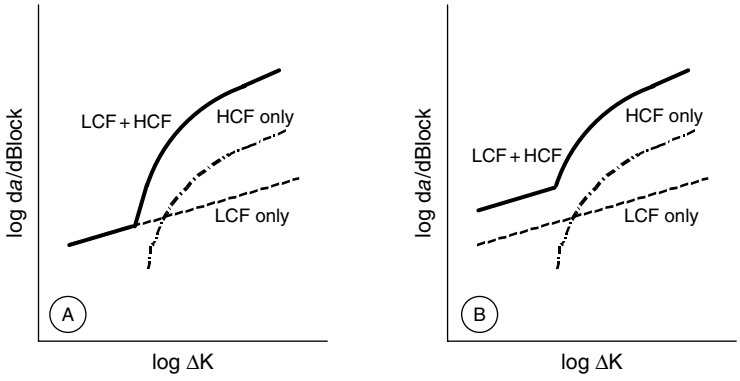


Figure 4.35. Schematic of two types of behavior observed in combined LCF–HCF.

approach to combined LCF–HCF growth rates. Note that the schematic of Figure 4.35 depicts the behavior in a manner that is usually used for presenting such data, namely on log–log plots. What appears to be an elevated growth rate for low values of ΔK for the block loading could easily be more than a factor of two or three, perhaps even higher. No systematic study of the materials for which this accelerated growth rate occurs below the HCF threshold under CCF has been conducted.

4.4. DESIGN CONSIDERATIONS

Damage tolerant design, when applied to LCF alone, is based on inspection size capability for cracks, crack-growth-rate computations, and the determination of proper inspection intervals to locate cracks before they reach a critical size. In an aeroengine, the LCF cycles are related to the number of flights and are fairly well determined by usage. For a component experiencing both LCF and superimposed vibratory (HCF) loading, the HCF contribution to the growth rate must also be considered. In particular, for high frequency vibrations where the number of HCF cycles can be large, reaching the threshold for HCF can be the governing criterion for failure because the crack-growth rate under the combined LCF–HCF loading may accelerate far beyond that for LCF alone. Predicting the onset of the HCF activity thus becomes an important aspect for design and component lifing [49]. Wanhill [50], for example, has pointed out the importance of the use of ΔK_{th} for design. He considers that clearly, the most significant application of fatigue thresholds includes the case of combined LCF–HCF loading where the LCF grows the crack until the threshold for HCF is reached. Whether or not the threshold value obtained from long cracks, ΔK_{th}, can be used to asses the onset of accelerated growth under combined LCF–HCF loading, has yet to be determined for most materials and loading conditions. These conditions involve various combinations of R for the major and minor cycles as well as the number of HCF cycles per LCF "block."

Crack growth under the conjoint action of HCF and LCF was studied by Powell et al. [51]. The objective was to see when the HCF accelerated the steady-state LCF growth rate and how this was related to the threshold for HCF. Two titanium alloys were studied, Ti-6Al-4V and Ti-5331S, the latter also known as IMI829. Using corner-cracked specimens, the crack-growth behavior under pure LCF at $R = 0.1$ with superimposed HCF at $R = 0.9$ ($Q = 0.12$, see below) is illustrated in Figures 4.36 and 4.37 for the two alloys. In these experiments, conducted at room temperature, there were 10,000 HCF cycles for each LCF cycle (denoted as n = 10,000). The plot shows that the threshold for HCF is easy to determine for the Ti-6-4 alloy by locating the intersection of the LCF only and combined LCF–HCF curves. The lack of correlation of LCF only and LCF–HCF curves in Ti-5331S that occurs well below the threshold for HCF alone makes it difficult to determine the point of intersection from Figure 4.37. The Ti-6-4 alloy

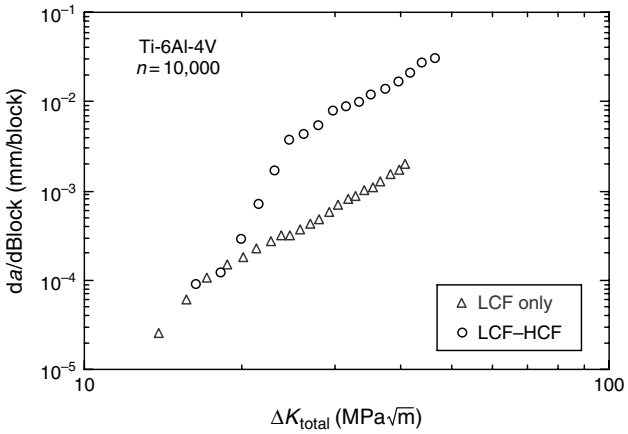


Figure 4.36. Fatigue-crack-growth rates under pure LCF and combined LCF–HCF in Ti-6Al-4V at room temperature.

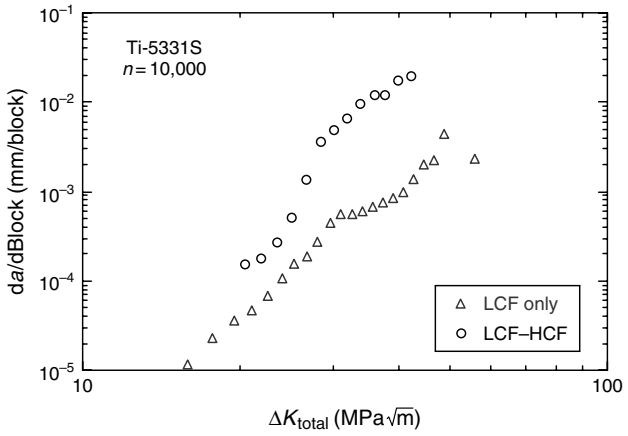


Figure 4.37. Fatigue-crack-growth rates under pure LCF and combined LCF–HCF in Ti-5331S at room temperature.

follows the common behavior denoted as type A in Figure 4.35 while the Ti-5331S follows the unusual behavior depicted as B in Figure 4.35. The authors tried to explain the anomalous behavior below threshold, where the HCF seems to accelerate the LCF growth rate, by a combination of a short-crack effect and the development of crack closure. It was noted that the grain size of the Ti-5331S was approximately 0.6 mm, whereas the Ti-6-4 had a grain size of only 0.025 mm. The accelerated growth rate in Ti-5331S was observed at low values of ΔK when the crack length was of the order of less than 3 grain

diameters. Whatever the explanation, the accelerated LCF growth rate below threshold is an important factor to take into account when determining how many LCF cycles can be sustained before the HCF threshold is reached. In this particular case, the LCF growth rate under combined cycling is a factor of 2–4 above that for LCF alone, thereby decreasing the number of cycles or time it takes to reach the HCF threshold by the same factors. This clearly has to be taken into account when applying a damage tolerant design approach for HCF under combined LCF–HCF loading.

Experiments similar to the ones at room temperature, described above, were also conducted on Ti-5331S at 550 °C. The results are presented in Figure 4.38 where the growth rate per block is compared with the predictions of the linear summation model. The data show that either the HCF threshold is reduced, or that LCF growth is accelerated below the steady-state HCF threshold. The linear summation is carried out for both the average behavior and the worst case, the latter taking into account the scatter obtained in both the LCF and HCF testing. Here is another example where there appears to be an interaction between LCF and HCF in the threshold region for HCF when the two are combined into a simple spectrum. Beyond the threshold, the data appear to follow the average behavior as predicted by the linear summation model.

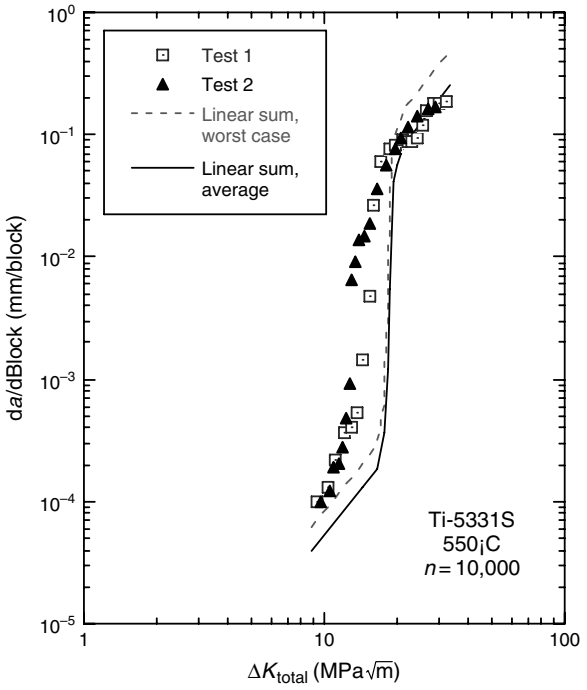


Figure 4.38. Combined LCF–HCF growth rates and model predictions in Ti-5331S at 550 °C.

4.4.1. LCF–HCF nomenclature

Combined LCF–HCF loading has caused some confusion over the years because of nomenclature and the differences that occur when dealing with actual usage versus mathematical formulations involving simple linear summation concepts. Consider the schematic of Figure 4.39 that shows the major cycles (LCF) with a hold or dwell time in between them during which HCF cycles can occur. The problem we deal with is the superposition of the HCF cycles on the LCF behavior. The nomenclature is that of Powell and coworkers at University of Portsmouth, formerly Portsmouth Polytechnic.

LCF loading alone produces a stress intensity level ΔK_{major} and represents the contribution of the major throttle excursions in an engine. During dwell times, at maximum K for the LCF cycle, a vibratory loading occurs whose total amplitude is denoted by ΔK_{minor}. If the total contribution of the individual loading components is considered, then a linear summation law would require that the total growth rate be the sum of $\Delta K_{\text{total}} + \Delta K_{\text{minor}}$, *not* $\Delta K_{\text{major}} + \Delta K_{\text{minor}}$. This is because in the combined case, the effective amplitude of the LCF cycles is ΔK_{total}, not ΔK_{major}, since the LCF cycle now goes from minimum to maximum through an amplitude ΔK_{total}. This concept, while fairly clear, has not been followed consistently in the literature over the years and has led to some confusion when evaluating the applicability of a linear summation concept for crack growth under combined LCF–HCF loading. The confusion arises because the minor cycle amplitude also contributes to the major cycle amplitude as shown in the schematic of Figure 4.39.

Another point to consider in discussing combined LCF–HCF, referred to here as CCF, is the manner in which the data are both recorded and discussed. While the stress or load ratio, R, is a common and well-understood quantity, there are other parameters with which to describe the entire load sequence in CCF, not including spectrum loading where overloads, underloads, and sequencing also have to be considered. For the load ratios we can use R_{minor} and R_{major} to represent the value of R for the HCF and LCF cycles, respectively. The number of HCF cycles per LCF cycle is usually given by n. Unless the value of n is sufficiently high, the contribution of the HCF cycles may not be detected since the HCF is generally applied at a much smaller value of ΔK than are the LCF

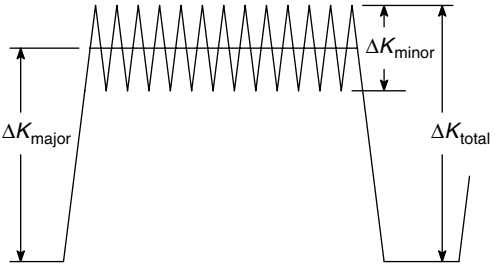


Figure 4.39. Schematic of combined major/minor cycle loading.

cycles. A parameter that is often used to represent the relative magnitude of the combined stress cycles is the amplitude ratio, Q. Q is defined as the ratio of the amplitude of the minor cycles to the magnitude of the major cycles. It can also be written in terms of the ΔK values.

$$Q = \frac{\Delta K_{\text{minor}}}{\Delta K_{\text{major}}} \tag{4.36}$$

Note again that the major cycle amplitude refers to ΔK_{major} as shown in Figure 4.39, not to the value of ΔK_{total} even though the latter is used in linear damage summation. There is no single, yet simple, way of relating the major and minor cycle ratios, other than through the definition of Equation (4.36). The following useful expressions are easily derived and are found frequently in the literature, particularly in the papers coming from University of Portsmouth.

$$R_{\text{minor}} = \frac{2 - Q\left(1 - R_{\text{major}}\right)}{2 + Q\left(1 - R_{\text{major}}\right)} \tag{4.37}$$

$$Q = \frac{2\left(1 - R_{\text{minor}}\right)}{\left(1 - R_{\text{major}}\right)\left(1 + R_{\text{minor}}\right)} \tag{4.38}$$

In the example cited above, Figures 4.36 and 4.37, $Q = 0.12$ for $R_{\text{major}} = 0.1$ and $R_{\text{minor}} = 0.9$. For parallel experiments with the same major cycle, higher amplitude vibratory loading corresponds to $Q = 0.22$ and $R_{\text{minor}} = 0.82$.

The crack-growth rate data from CCF are normally presented with respect to the entire cycle block. Thus, as illustrated in Figures 4.36 and 4.37, the growth rate is shown as da/dBlock where the block consists of a single LCF cycle with n HCF cycles superimposed. For the horizontal axis, ΔK_{total} or K_{max} can be used to describe the block loading. As an alternative, ΔK_{major} can be used. In the latter case, the HCF data cannot be shown superimposed on the block loading. A similar comment can be made for the use of ΔK_{total}. If it is desired to represent the LCF, HCF, and CCF data on the same plot, the use of K_{max} is preferable. However, if a linear superposition concept is attempted graphically, both a vertical shift to account for n HCF cycles per LCF cycle, and a horizontal shift to account for the different maximum values in HCF and LCF has to be used. The reader is cautioned that there is no easy way to show LCF, HCF, and CCF data on the same (log) plot while also demonstrating linear summation graphically.

4.4.2. Example of anomalous behavior

An illustration of the type B behavior of Figure 4.35 observed in combined LCF–HCF testing is taken from [52] where the fracture mechanics of a nickel-based single crystal alloy was studied. The focus was on the interaction of HCF at high stress ratio and at

high frequency combined with LCF at low stress ratio and low frequency in combined cycle loading. The test plan utilized previous threshold data generated at 1100 °F, for $R = 0.1$ and 0.8 in the $<001/010>$ orientation on alloy PWA 1484. After precracking, the specimen was run at a stress ratio of 0.1 at a frequency of 10 CPM (0.167 Hz) until a crack length of a_i was achieved. The target for a_i was selected to be well below the K_{max} threshold value for the $R = 0.8$ test data. A block of 1000 cycles of $R = 0.8$ at 60 Hz was then performed between each $R = 0.1$ LCF cycle. This block loading was continued until the calculated value for threshold at $R = 0.8$ was superseded at crack length a_f. After growing beyond the calculated value of the $R = 0.8$ threshold, the loading was returned to LFC loading only at $R = 0.1$. The test scheme was designed so that all loading blocks could be performed on a single sample so that specimen-to-specimen variation differences would not be included in the results. A schematic of the test approach is shown in Figure 4.40.

For reference purposes, some specimens were tested under constant load to allow stress intensity K to increase with increasing crack length to detect the onset of crack-growth rate behavior of the $R = 0.8$ cycles. The results of the first test under combined LCF–HCF loading are presented in Figure 4.40 which shows that a sharp increase in crack-growth rate occurred at crack length a_i corresponding to the change in waveform from LCF to LCF + HCF indicating that the $R = 0.8$ (HCF) cycles did affect the LCF crack-growth rate. This was in direct contradiction to the anticipated response based on the earlier $R = 0.8$ threshold result that indicated the testing was below the HCF threshold. A return to pure LCF loading resulted in the anticipated return to the original $R = 0.1$ trend. A second specimen was then run to confirm that the data was repeatable and the same result was achieved. The results of the second test sequence are shown in Figure 4.41. The open circles indicate the HCF only test results showing the threshold region for HCF. As in

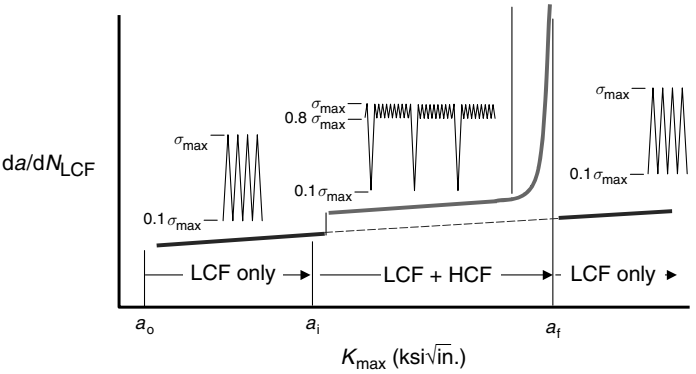


Figure 4.40. HCF–LCF testing approach and prediction.

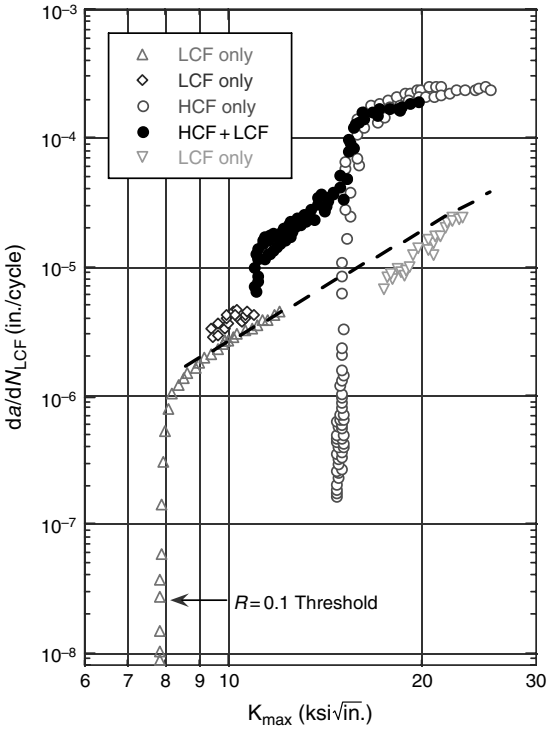


Figure 4.41. LCF–HCF Interaction test results

the first test, the interaction between HCF and LCF produces an accelerated growth rate below the HCF threshold.

To further study this unexpected crack-growth rate acceleration, five loading schemes were devised and performed at a constant ΔK_{LCF} of $10\,\mathrm{ksi}\sqrt{\mathrm{in}}$. The frequency was 10 cycles per minute (CPM) for the LCF portion and 60 Hz for the HCF portion. The loading schemes are shown in Figure 4.42 as Case (a) through Case (f). A single sample was again used to perform all six cases in succession with each case consuming up to 0.020 in (0.5 mm) of specimen ligament before proceeding to the next case.

The results of the test sequence shown in Figure 4.42 are summarized in Figure 4.43. Comparison of the various case loading blocks suggests the higher mean stress or dwell is the significant contributor to the accelerated crack-growth behavior as opposed to the number of HCF cycles. As shown in Figure 4.43, the application of dwell, Case (b), increased the growth rate from the baseline without dwell, Case (a). The dwell produced nearly the same acceleration as adding $1000R = 0.8$ cycles, Case (c). The similarity between Case (c) and Case (d) (1000 versus 500 HCF cycles) suggests that the sensitivity to time-dependent behavior is inclusive of very small differences in hold times and

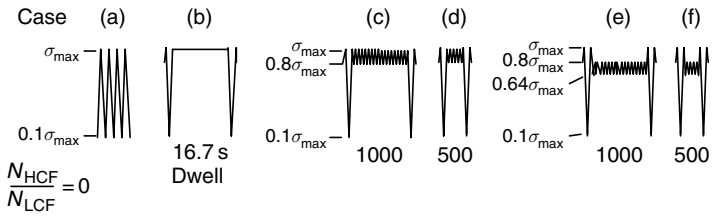


Figure 4.42. Constant K testing to identify crack-growth rate acceleration drivers.

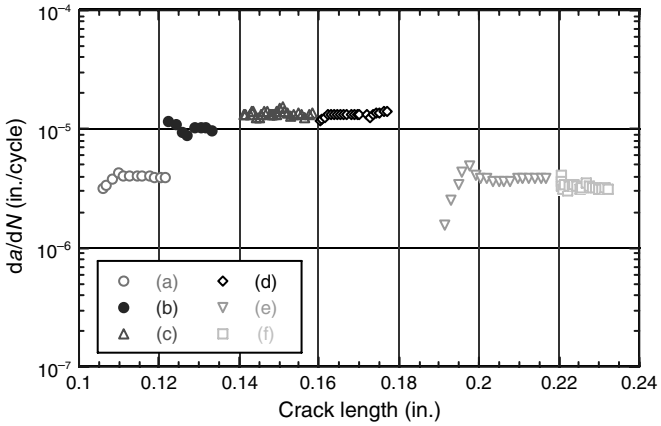


Figure 4.43. Test plan 2 results. Legend refers to loading blocks shown in Figure 4.42.

or cyclic frequency. In fact, threshold testing done previously on that program clearly showed a pronounced frequency effect between 20 Hz, 1 Hz and 10 CPM (0.167 Hz).

An interesting aspect of these findings is that the results indicate that there is a dwell effect present in a temperature regime well below what has typically been called the creep regime. The significance of this finding is that very small decreases in frequency that is 10 CPM alone versus 10 CPM with as little as an 8-second dwell at maximum load, cause up to a 2X–3X acceleration in crack-growth rate. One possible explanation proposed for the LCF–HCF interaction effects was oxidation at the crack tip. Tests in vacuum were recommended.

4.4.3. Another example of anomalous behavior

Another observation of the interaction of LCF and HCF and the subsequent growth rate behavior is that of Russ [45] who conducted studies on Ti-17, a β processed titanium alloy. In that work, LCF cycles with $R = 0.1$ were superimposed on what are referred to

as "baseline" HCF cycles having $R = 0.7$. Both cycles have the same value of maximum load (or stress) for a given crack length. Data were obtained by decreasing the load to obtain a pure HCF threshold and then increasing the load with the LCF–HCF spectrum shown schematically in Figure 4.44. While the study uses the nomenclature of the HCF cycles being the baseline, and the LCF cycles being the equivalent of an underload (also called a negative overload in the literature), the phenomenology is identical to that observed in the works described above (see [32–35] and Figure 4.39, for example). In the work of Russ, the number of HCF cycles per LCF cycle was varied between 10 and 1000. Figures 4.45 and 4.46 show the observed growth rate behavior in the region near the HCF threshold for HCF cycle counts of 200 and 1000 per LCF cycle, respectively. Both figures show the trend expected if no interaction occurs, that is, if linear summation of LCF and HCF growth rates is assumed. The experimental data appear to demonstrate an accelerated growth rate under the combined loading as well as growth rate acceleration below the expected HCF threshold. Although the value of $R = 0.7$ for the HCF cycles is high enough to expect the complete absence of closure, the author finds that a combination of closure during the application of the $R = 0.1$ cycle and residual deformation ahead of the crack may account for the interaction effect. From plane strain finite element modeling, the author shows that closure develops immediately behind the

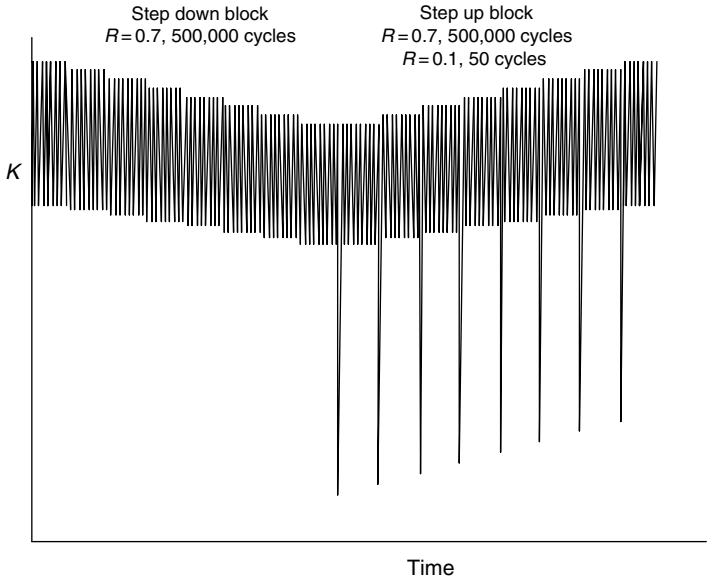


Figure 4.44. Schematic of load history for determining threshold for crack propagation under combined LCF–HCF loading.

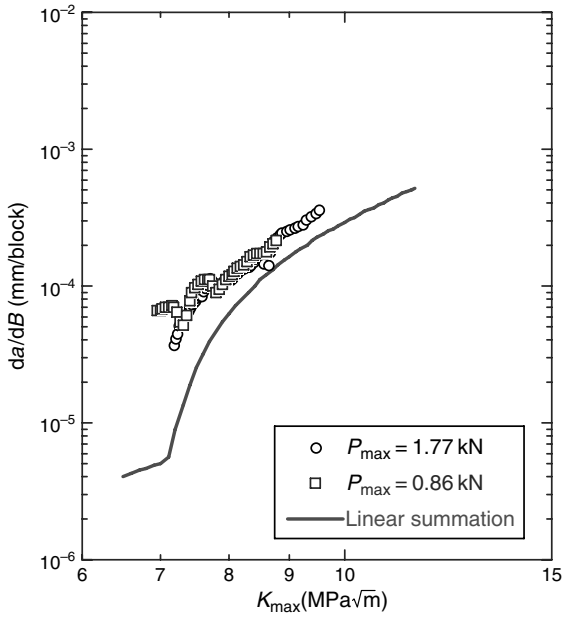


Figure 4.45. Fatigue-crack-growth rate results for 200 HCF cycles per LCF cycle.

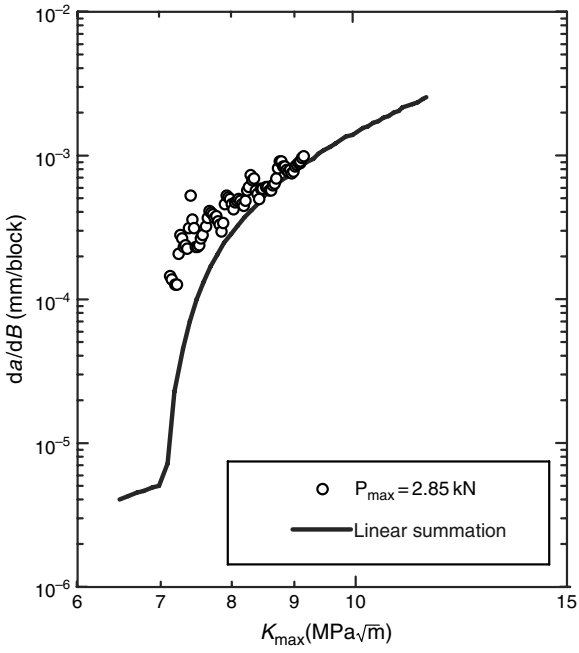


Figure 4.46. Fatigue-crack-growth rate results for 1000 HCF cycles per LCF cycle.

crack and compressive residual stresses develop ahead of the crack tip after the $R = 0.1$ underloads. It should be pointed out that, consistent with FEM results by Sehitoglu et al. [53], compressive residual stresses were observed even in the absence of closure during the $R = 0.7$ cycles. The distances over which the closure and residual stresses develop are only a few microns, inviting speculation as to whether such phenomenology could affect the net growth rate behavior. However, as in the previous examples of Type B behavior as defined in Figure 4.35, the observed behavior is non-conservative when compared to the predictions of a linear summation model.

Another observation by Russ [45] was on the threshold for crack propagation and the differences in the growth rate behavior in the near-threshold regime. For a constant value of $K_{max} = 8\,\text{MPa}\sqrt{\text{m}}$, Figure 4.47 shows the combined-cycle growth rate for different numbers of HCF cycles per block (1 LCF cycle) as well as the results from a simple linear summation of the individual contributions of LCF and HCF. For the maximum number of HCF cycles per block, 1000, the growth rate is dominated by the HCF cycles. For all conditions other than 10 HCF cycles per block, the experimentally measured growth rates are higher than those predicted by the linear summation model. These differences are approximately a factor of two or more. Equally important from a life prediction point of view, the threshold for combined cycle loading is lower than predicted by linear summation. For the spectrum illustrated in Figure 4.44, where the ratio of HCF to LCF cycles is 10,000, the threshold value of K_{max} for pure HCF is $7.27\,\text{MPa}\sqrt{\text{m}}$ whereas, during increasing loading for the combined cycle, the threshold at which crack growth first appears is $6.99\,\text{MPa}\sqrt{\text{m}}$. While these differences in growth rate and threshold do not appear to be very significant, Russ points out that the differences in fatigue lifetimes can be significant when the combined cycling is in the region of the HCF threshold where a significant portion of the total time for crack growth to failure takes place.

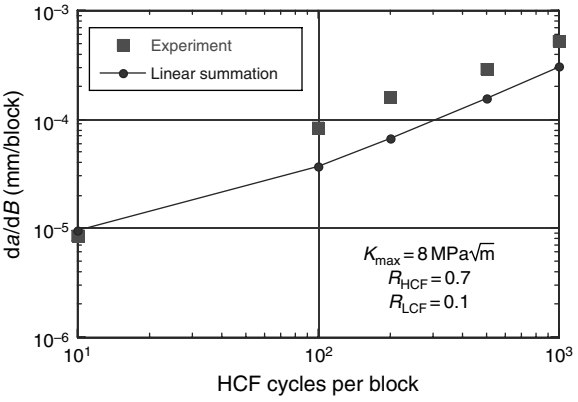


Figure 4.47. Fatigue-crack-growth rates for LCF–HCF spectrum of Russ [45].

4.5. COMBINED CYCLE FATIGUE CASE STUDIES

There are other examples of combined cycle loading where HCF at stress levels below their constant amplitude threshold appear to contribute to the combined cycle growth rate. An example is the study by Zhou and Zwerneman [54] where the cycle block contains small amplitude cycles with periodic overloads. Denoting the major cycles as "overload" (ol) cycles and the other as minor cycles, the ratio $\Delta K_{\text{minor}}/\Delta K_{\text{ol}}$ was chosen as 0.3 and $R_{\text{ol}} = 0.1$. A schematic of the block loading is shown in Figure 4.48. Using ASTM A588 steel as the test material, values of the number of minor cycles per block, n, were chosen as 0, 4, 9, 49, 99, and 999. The results, presented in terms of growth rate per block, are shown in Figure 4.49. The number of cycles per block includes one

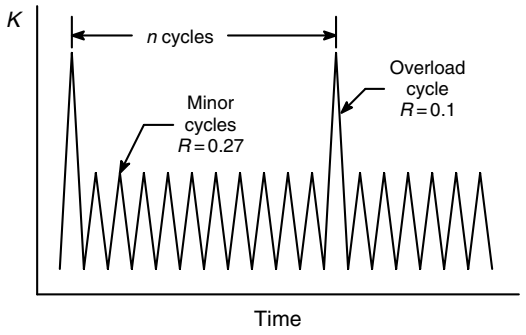


Figure 4.48. Schematic of block loading with periodic overload cycles.

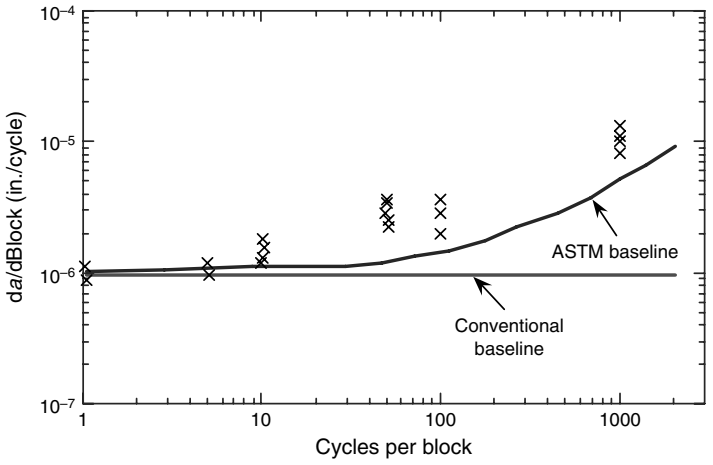


Figure 4.49. Fatigue-crack-growth rate for cycles with periodic overloads.

major cycle and n minor cycles. Since there is only one overload (major) cycle per block, the increase in growth rate per block with increasing values of n can only be attributed to the minor cycles. Yet the minor cycles are applied at K levels that are below their constant amplitude threshold. The "conventional baseline" shown in the figure indicates that there is no contribution due to the minor cycles. The assumed threshold for the minor cycles was taken from an empirical formula for this material. If, instead, the ASTM recommended value for threshold is taken as a growth rate equal to 10^{-10} m/cycle, then this small, but non-zero, contribution to the minor cycle growth results in the curve labeled "ASTM baseline" in the plot. Even under this assumption, the data show that the experimentally observed block growth rate is higher than predicted by a linear summation rule. It is clear that the threshold is reduced by the overload cycles, an effect similar to the acceleration of crack growth due to underload cycles observed by Russ [45], described above. Further evidence of the growth due to the minor cycles was obtained from acoustic emission (EM) monitoring. The intensity of the AE signals was observed to increase with increasing numbers of minor cycles per block. The authors concluded that the increase in AE activity indicated that "the minor cycles below the threshold contribute to fatigue damage." It certainly is possible that the threshold obtained under constant amplitude loading is not applicable to the block-loading situation, an example of load-history effects. Alternatively, the determination of the threshold could be incorrect, also due to load-history effects. This latter condition is discussed in Chapter 8. In both cases, the growth rate of the minor cycles under combined LCF–HCF block loading is affected by the major cycles, whether they are of the overload or underload variety. In both cases, the linear summation approach is non-conservative.

Another example of an LCF–HCF interaction is the overload study of Byrne et al. [55] on a slightly more complicated load spectrum as shown in Figure 4.50. In this case, overloads were superimposed on a baseline LCF–HCF block which combined a major cycle with a number of minor cycles having the same maximum K value. In this block,

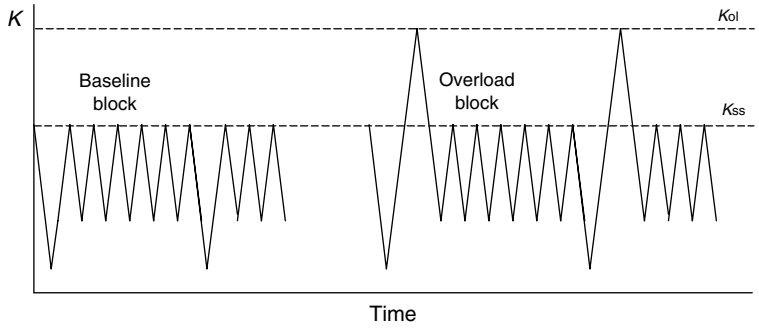


Figure 4.50. Schematic of block loading with superimposed overload cycles.

the LCF cycles can be considered to be an underload on the baseline HCF cycles. On top of this simple spectrum, a single overload is added to the baseline LCF cycle. Defining the overload ratio as OLR $= K_{max}/K_{ss}$, experiments were carried out to see when the onset of HCF activity occurred. The results, based on the use of a number of values of OLR, are presented in Figure 4.51. The curves shown are the best fit to the actual data points which are not shown for clarity. OLR = 1 represents the case where there is no overload in the baseline LCF–HCF cycle. The pure LCF curve is also shown. The results show that as OLR increases, the retardation effect of the single overload diminishes the growth rate until the minor cycles have almost no influence on the baseline LCF cycle at a value of OLR = 2.0. This work, conducted on Ti-6Al-4V, also shows that the apparent onset of HCF activity is delayed by the overload cycle. In this case, there is both an underload in the baseline combined cycle as well as a superimposed overload. While the behavior of the baseline cycle defined by OLR = 1.0 is predictable with linear summation of the LCF and HCF cycles, the additional effect of the overload is both to reduce the minor cycle contribution to the growth rate and to reduce the threshold where minor cycle activity begins.

The natural conclusion arising from these studies is that growth rates and thresholds from constant amplitude loading cannot always be used directly in spectrum loading without consideration of interaction effects. Both retardation and acceleration effects have been noted in various studies, with overloads usually observed to retard crack-growth rates while underloads are found to accelerate the growth rates. While these observations are common, the exceptions prove that a single rule cannot be applied in all cases.

In [52], HCF and LCF tests were used to establish baseline material properties, and simple mission tests were used to assess additional failure modes that may exist if

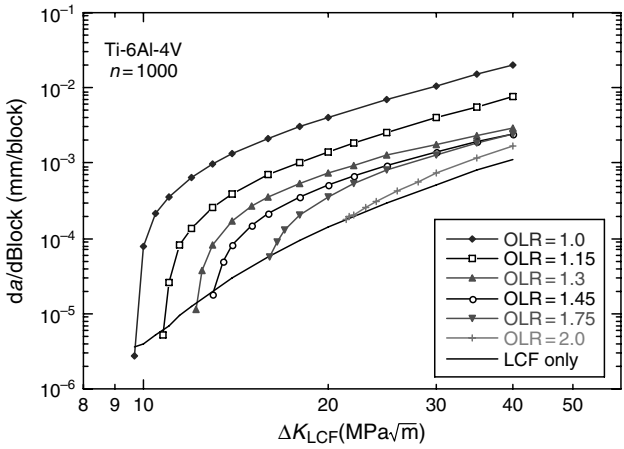


Figure 4.51. Fatigue crack growth for various overload ratios, $R_{HCF} = 0.7$, 1000 minor cycles per block.

LCF–HCF interactions are important. This was explored with mission tests at 75 °F with Ti-6Al-4V and were based on the following criteria: (a) tests that avoid specimen ratcheting failure modes (typically high stress, high R) that are not representative of component failures, (b) LCF stresses that are in the main regime of design interest for turbine engines (average $N_f \sim 10{,}000$ cycles), (c) HCF stresses that are in the regime of design interest ($R > 0.5$ and HCF $> 10^7$ cycles), (d) mission histories that include LCF + periodic HCF cycles until mission failure, and (e) tests that can be run economically in the laboratory. A double-edge V-notch specimen geometry was used to avoid ratcheting for load-control testing and loads were selected to keep the fatigue lives in the regime of design interest. Baseline notch LCF tests at $R = 0.1$ were run to identify stresses for an LCF failure of ~10,000 cycles while baseline notch HCF tests were used to identify the value of R for an average HCF failures of $\sim 10^7$ cycles. All interaction tests were missions or blocks of cycles that were repeated until failure. Missions included an LCF load-up ($R = 0.1$) + 10,000–100,000 repeated HCF cycles ($R = 0.7$–0.9) + an LCF unload reversal ($R = 0.1$) for each mission. The baseline and mission test conditions for the notch geometry are given in Table 4.3. Stresses are reported in units of ksi.

The first group of mission tests was used to assess the HCF capability when minimal LCF damage is present. This was evaluated with 10,000–100,000 HCF cycles/mission with an HCF cycle from 56 to 80 ksi ($R = 0.7$). These conditions were intentionally selected to avoid significant predicted LCF damage. The number of HCF cycles to failure for these mission tests is compared to the number of cycles to failure for HCF alone with probability plots shown in Figure 4.52. Given the similarity of these distributions

Table 4.3. Baseline and LCF–HCF mission tests

LCF S_{min}	*LCF* S_{max}	*HCF* S_{min}	*HCF* S_{max}	*HCF/mission*	*Freq* (Hz)	*Expt HCF cycles*	*Expt missions*	*Pred life with Fs*
9	90	NA	NA	LCF	0.5	NA	9,963	11,365
8	80	NA	NA	LCF	0.5	NA	10,766	16,489
8	80	NA	NA	LCF	0.5	NA	10,821	16,489
NA	NA	56	80	HCF	1k	234,894,301	234,894,301	6,370,632
NA	NA	56	80	HCF	1k	11,694,364	11,694,364	6,370,632
NA	NA	56	80	HCF	1k	2,613,654	2,613,654	6,370,632
8	80	56	80	10,000	0.5/1k	16,400,000	1,640	613
8	80	56	80	10,000	0.5/1k	71,682,975	7,168	613
8	80	56	80	100,000	0.5/1k	14,298,296	142	63
8	80	56	80	100,000	0.5/1k	9,312,872	93	63
8	80	56	80	100,000	0.5/1k	405,933,382	4,059	63
8	80	72	80	10,000	0.5/1k	142,814,527	14,281	16,222
8	80	65	80	10,000	0.5/1k	94,130,587	9,413	16,222

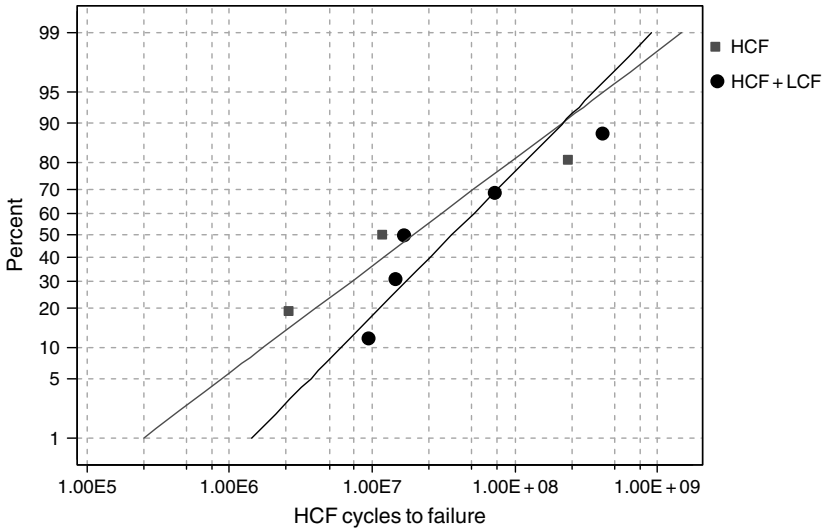


Figure 4.52. Capability of notched HCF tests compared to the HCF capability of LCF–HCF mission tests when HCF damage dominates.

for the small set of data presented, a significant LCF–HCF interaction does not seem to be present for cases when HCF damage dominates.

The second group of tests was run to assess if LCF failure modes are influenced when minimal predicted HCF damage exists. Minimal HCF damage was evaluated with mission tests that included an LCF load-up reversal ($R = 0.1$) + 10 000 repeated HCF cycles ($S_{max} = 80$ ksi; $S_{min} = 72$ for $R = 0.9$ or 65 ksi for $R = 0.82$). The HCF parameters were selected near the minimum allowable stress for a 10^7 HCF limit so that HCF could be ignored as a contributing factor, assuming no LCF–HCF interactions. The number of LCF cycles to failure for the notch mission tests as compared to N_f for the notch specimens with LCF alone is shown in Figure 4.53. The values for predicted N_f used an average smooth specimen S_{equiv} fatigue curve with the modified Manson-McKnight fatigue parameter. The local stresses from the notch were obtained from elastic-plastic analysis and notch life was predicted with the local notch stresses and notch gradients using the effective stressed area, Fs approach described in Appendix E. (see Chapter 5 for a detailed discussion of notch fatigue). The tests are seen to be well predicted within the 2X scatter bands that are representative of a reasonably accurate LCF life method. Neglecting LCF–HCF interactions is shown here to be a reasonable assumption for these mission tests where the predicted HCF damage is minimal. From the viewpoint of design, it appears that one can use an HCF limit based on minimum properties such that HCF can be ignored as a failure mode in the type of mission used here that contains HCF and LCF conditions.

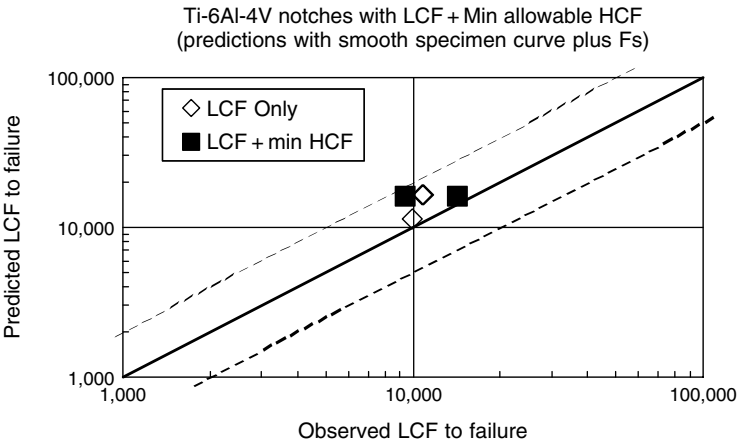


Figure 4.53. Notched LCF tests compared to the LCF of LCF–HCF mission tests with minimal HCF damage.

REFERENCES

1. Nicholas, T., "Step Loading, Coaxing and Small Crack Thresholds in Ti-6Al-4V under High Cycle Fatigue", *Fatigue – David L. Davidson Symposium*, K.S. Chan, P.K. Liaw, R.S. Bellows, T.C. Zogas and W.O. Soboyejo, eds. TMS (The Minerals, Metals & Materials Society), Warrendale, PA, 2002, pp. 91–106.
2. Kitagawa, H. and Takahashi, S., "Applicability of Fracture Mechanics to Very Small Cracks or the Cracks in the Early Stage", *Proc. of Second International Conference on Mechanical Behaviour of Materials*, Boston, MA, 1976, pp. 627–631.
3. El Haddad, M.H., Smith, K.N., and Topper, T.H., "Fatigue Crack Propagation of Short Cracks", *Journal of Engineering Materials and Technology*, **101**, 1979, pp. 42–46.
4. Moshier, M.A., Nicholas, T., and Hillberry, B.M., "High Cycle Fatigue Threshold in the Presence of Naturally Initiated Small Surface Cracks", *Fatigue and Fracture Mechanics: 33rd Volume, ASTM STP 1417*, W.G. Reuter, and R.S. Piascik, eds, American Society for Testing and Materials, West Conshohocken, PA, 2002, pp. 129–146.
5. Chan, K.S., Davidson, D.L., Lee, Y-D., and Hudak, S.J., Jr., "A Fracture Mechanics Approach to High Cycle Fretting Fatigue Based on The Worst Case Fret Concept: Part I – Model Development", *International Journal of Fracture*, **112**, 2001, pp. 299–330.
6. Moshier, M.A., Nicholas, T., and Hillberry, B.M., "Load History Effects on Fatigue Crack Growth Threshold for Ti-6Al-4V and Ti-17 Titanium Alloys", *Int. J. Fatigue*, **23**, Supp. 1, 2001, pp. 253–258.
7. Hutson, A.L., Neslen, C., and Nicholas, T., "Characterization of Fretting Fatigue Crack Initiation Processes in Ti-6Al-4V", *Tribology International*, **36**, 2003, pp. 133–143.
8. Lanning, D., Haritos, G.K., Nicholas, T., and Maxwell, D.C., "Low-Cycle Fatigue/High-Cycle Fatigue Interactions in Notched Ti-6Al-4V", *Fatigue Fract. Engng. Mater. Struct.*, **24**, 2001, pp. 565–578.
9. Moshier, M.A., Hillberry, B.M., and Nicholas, T., "The Effect of Low-Cycle Fatigue Cracks and Loading History on the High Cycle Fatigue Threshold", *Fatigue and Fracture Mechanics:*

31st Volume, ASTM STP 1389, G.R. Halford, and J.P. Gallagher, eds, American Society for Testing and Materials, West Conshohocken, PA, 2000, pp. 427–444.
10. Caton, M.J., "Predicting Fatigue Properties of Cast Aluminum by Characterizing Small-Crack Propagation Behavior", PhD Dissertation, University of Michigan, 2001.
11. Nicholas, T., "Recent Advances in High Cycle Fatigue", *Proceedings of 9th International Conference on the Mechanical Behaviour of Materials*, Geneva, Switzerland, 25–29 May 2003 (on CD-ROM).
12. Maxwell, D.C. and Nicholas, T., "A Rapid Method for Generation of a Haigh Diagram for High Cycle Fatigue", *Fatigue and Fracture Mechanics: 29th Volume, ASTM STP 1321*, T.L. Panontin, and S.D. Sheppard, eds, American Society for Testing and Materials, West Conshohocken, PA, 1999, pp. 626–641.
13. Nicholas, T., "Step Loading for Very High Cycle Fatigue", *Fatigue Fract. Engng. Mater. Struct.*, **25**, 2002, pp. 861–869.
14. Mall, S., Nicholas, T. and Park, T.-W., "Effect of Pre-Damage from Low Cycle Fatigue on High Cycle Fatigue Strength of Ti-6Al-4V", *Int. J. Fatigue*, **25**, 2003, pp. 1109–1116.
15. Morrissey, R.J., Golden, P., and Nicholas, T., "The Effect of Stress Transients on the HCF Endurance Limit in Ti-6Al-4V", *Int. J. Fatigue*, **25**, 2003, pp. 1125–1133.
16. Morrissey, R.J., McDowell, D.L., and Nicholas, T., "Frequency and Stress Ratio Effects in High Cycle Fatigue of Ti-6Al-4V", *Int. J. Fatigue*, **21**, 1999, pp. 679–685.
17. Forman, R.G. and Shivakumar, V., "Growth Behavior of Surface Cracks in the Circumferential Plane of Solid and Hollow Cylinders", *Fracture Mechanics: Sevententh Volume, ASTM STP 905*, J.H. Underwood, R. Chait, C.W. Smith, D.P. Wilhem, W.A. Andrews, and J.C. Newman, eds, ASTM, Philadelphia, 1986, pp. 59–74.
18. Gallagher, J.P. et al., "Improved High Cycle Fatigue Life Prediction", Report # AFRL-ML-WP-TR-2001-4159, University of Dayton Research Institute, Dayton, OH, January 2001 (on CD ROM).
19. Golden, P.J., Bartha, B.B., Grandt, A.F. Jr., and Nicholas, T., "Measurement of the Fatigue Crack Propagation Threshold of Fretting Cracks in Ti-6Al-4V", *Int. J. Fatigue*, **26**, 2004, pp. 281–288.
20. Shen, G. and Glinka, G., "Weight Functions for a Surface Semi-Elliptical Crack in a Finite Thickness Plate", *Theor. Appl. Fract. Mech.*, **15**, 1991, pp. 247–255.
21. Kommers, J.B., Discussion of paper "Fatigue Failure from Stress Cycles of Varying Amplitude" by B.F. Langer, *J. Appl Mech*, 1938, p. A–180.
22. Nicholas, T. and Maxwell, D.C., "Evolution and Effects of Damage in Ti-6Al-4V under High Cycle Fatigue", *Progress in Mechanical Behaviour of Materials*, Proceedings of the Eighth International Conference on the Mechanical Behaviour of Materials, ICM-8, F. Ellyin, and J.W. Provan, eds, Vol. III, 1999, pp. 1161–1166.
23. Walls, D.P., deLaneuville, R.E., and Cunningham, S.E., "Damage Tolerance Based Life Prediction in Gas Turbine Engine Blades under Vibratory High Cycle Fatigue", *Journal of Engineering for Gas Turbines and Power – Transactions ASME*, **119**, 1997, pp. 143–146.
24. Akita, K., Misawa, H., Tobe, S. and Kodama, S., "Fatigue Crack Propagation Behavior of Ti-6Al-4V Alloy under Simplified Loading with a Single Overload", *Fatigue '93*, J.P. Bailon, and J.I. Diskson, eds, 3, EMAS, Warley UK, 1993, pp. 1575–1580.
25. Sheldon, J.W., Bain, K.R., and Donald, K.J., "Investigation of the Effects of Shed-Rate, Initial K_{max}, and Geometric Constraint on ΔK_{th} in Ti-6Al-4V at Room Temperature", *Int. J. Fatigue*, **21**, 1999, pp. 733–741.
26. Lenets, Y.N. and Nicholas, T., "Load History Dependence of Fatigue Crack Thresholds for Ti-Alloy", *Engineering Fracture Mechanics*, **60**, 1998, pp. 187–203.

27. Makhutov, N., Romanov, A., and Gadenin, M., "High-Temperature Low-Cycle Fatigue Resistance Under Superimposed Stresses at Two Frequencies", *Fatigue Engng Mater. Struct.*, **1**, 1979, pp. 281–285.
28. Zaitsev, G.Z. and Faradzhov, R.M., *Metallovedenie i Termicheskaya Obrabotka*, **2**, 1970, pp. 44–46.
29. Ouyang, J., Wang, Z., Song, D., and Yan, M., "Influence of High Frequency Vibrations on the Low Cycle Fatigue Behavior of a Superalloy at Elevated Temperature", *Low Cycle Fatigue, ASTM STP 942*, American Society for Testing and Materials, Philadelphia, PA, 1988, pp. 961–971.
30. Goodman, R.C. and Brown, A.M., "High Frequency Fatigue of Turbine Blade Material", AFWAL-TR-82-4151, Wright-Patterson AFB, OH, October 1982.
31. Guedou, J.Y. and Rongvaux, J.M., "Effect of Superimposed Stresses at High Frequency on Low Cycle Fatigue", *Low Cycle Fatigue, ASTM STP 942*, American Society for Testing and Materials, Philadelphia, PA, 1988, pp. 938–960.
32. Powell, B.E., Duggan, T.V., and Jeal, R., "The Influence of Minor Cycles on Low Cycle Fatigue Crack Propagation", *Int. J. Fatigue*, **4**, 1982, pp. 4–14.
33. Powell, B.E., Henderson, I., and Duggan, T.V., "The Effect of Combined Major and Minor Stress Cycles on Fatigue Crack Growth",. *Second International Congress on Fatigue (Fatigue '84)*, 1984, pp. 893–902.
34. Hawkyard, M., Powell, B.E., Hussey, I., and Grabowski, L., "Fatigue Crack Growth under Conjoint Action of Major and Minor Stress", *Fatigue & Fracture of Engineering Materials & Structures*, **19**, 1996, pp. 217–227.
35. Hall, R.F. and Powell, B.E., "The Effects of LCF Loadings on HCF Crack Growth", US AFOSR Annual Report for Phase II, Report Number F567, University of Portsmouth, England, May 1999.
36. Probst, E.P. and Hillberry, B.M., "Fatigue Crack Delays and Arrest due to Single Peak Tensile Overloads", AIAA Paper No. 73-325, 1973; see also *AIAA Journal*, **12**, 1974, pp. 330–335.
37. Petrak, G.J. and Gallagher, J.P., "Predictions of the Effect of Yield Strength on Fatigue Crack Growth Retardation in HP-9Ni-4Co-30C Steel", *Journal of Engineering Materials and Technology*, **97**, 1975, pp. 206–213.
38. Gallagher, J.P. and Stalnacker, H.D., "Predicting Flight by Flight Crack Growth Rates", *Journal of Aircraft*, **12**, 1975, pp. 699–705.
39. Alzos, W.X., Skat, A.C. Jr., and Hillberry, B.M., "Effect of Single Overload/Underload Cycles on Fatigue Crack Propagation", *Fatigue Crack Growth Under Spectrum Loads, ASTM STP 595*, American Society for Testing and Materials, Philadelphia, 1976, pp. 41–60.
40. Hopkins, S.W., Rau, C.A., Leverant, G.R., and Yuen, A., "Effect of Various Programmed Overloads on the Threshold for High-Frequency Fatigue Crack Growth", *Fatigue Crack Growth Under Spectrum Loads, ASTM STP 595*, American Society for Testing and Materials, Philadelphia, 1976, pp. 125–141.
41. Frost, N.E., "Notch Effects and the Critical Alternating Stress Required to Propagate a Crack in an Aluminum Alloy Subject to Fatigue Loading", *J. Mech. Eng. Sci.*, **2**, 1960, pp. 109–119.
42. Sadananda, K., Vasudevan, A.K., Holtz, R.L., and Lee, E.U., "Analysis of Overload Effects and Related Phenomena", *International Journal of Fatigue*, **21**, 1999, pp. S233–S246.
43. Golden, P.J. and Nicholas, T., "The Effect of Negative Stress Ratio Load History on High Cycle Fatigue Threshold", *Journal of ASTM International*, **2**(5), May 2005.
44. Golden, P.J., "High Cycle Fatigue of Fretting Induced Cracks", PhD Dissertation, Purdue University, 2001.

45. Russ, S.M., "Effect of Underloads on Fatigue Crack Growth of Ti-17", PhD Dissertation, Georgia Institute of Technology, October 2003.
46. Ritchie, R.O., "Small Cracks and High Cycle Fatigue", *Proceedings of the ASME Aerospace Division*, J.C.I. Chang, ed., AMD-Vol. 52, ASME: New York, NY, 1996, pp. 321–333.
47. Ritchie, R.O., Boyce, B.L., Campbell, J.P., Roder, O., Thompson, A.W., and Milligan, W.W., "Thresholds for High-Cycle Fatigue in a Turbine Engine Ti-6Al-4V Alloy", *International Journal of Fatigue*, **21**, 1999, pp. 653–662.
48. Campbell, J.P., Thompson, A.W., and Ritchie, R.O., "Mixed-Mode Crack-Growth Thresholds in Ti-6AL-4V under Turbine-Engine High-Cycle Fatigue Loading Conditions", Proceedings of *4th National Turbine Engine High Cycle Fatigue Conference*, USAF, Monterey, CA, 1999.
49. Powell, B.E. and Duggan, T.V., "Predicting the Onset of High Cycle Fatigue Damage: an Engineering Application for Long Crack Fatigue Threshold Data", *Int. J. Fatigue*, **8**, 1986, pp. 187–194.
50. Wanhill, R.J.H., "Engineering Significance of Fatigue Thresholds and Short Fatigue Cracks for Structural Design", *Fatigue 84,* 2nd *Int. Conf. on Fatigue and Fatigue Thresholds*, Birmingham, UK, **3**, 1984, pp. 1671–1682.
51. Powell, B.E., Henderson, I., and Hall, R.F., "The Growth of Corner Cracks under the Conjoint Action of High and Low Cycle Fatigue", AFWAL-TR-87-4130, Wright-Patterson AFB, February 1988 (ADA190510).
52. Gallagher, J. et al., "Advanced High Cycle Fatigue (HCF) Life Assurance Methodologies", Report # AFRL-ML-WP-TR-2005-4102, Air Force Research Laboratory, Wright-Patterson AFB, OH, July 2004.
53. Sehitoglu, H., Gall, K., and Garcia, A.M., "Recent Advances in Fatigue Crack Growth Modeling", *Int. Jour. Fract*, **80**, 1996, pp. 165–192.
54. Zhou, Z. and Zwerneman, F.J., "Fatigue Damage Due to Sub-Threshold Load Cycles Between Periodic Overloads", *Advances in Fatigue Lifetime Predictive Techniques: Second Volume, ASTM STP 1211*, M.R. Mitchell, and R.W. Landgraf, eds, American Society for Testing and Materials, Philadelphia, 1993, pp. 45–53.
55. Byrne, J., Hall, R.F., and Powell, B.E., "Influence of LCF Overloads on Combined HCF/LCF Crack Growth", *Int. J. Fatigue*, **25**, 2003, pp. 827–834.

Chapter 5
Notch Fatigue

5.1. INTRODUCTION

A notch in a component can be considered to be a defect since it produces a local stress concentration or stress raiser that can ultimately be the location of an HCF failure. Thus, it is important to understand the effect of a notch on the FLS and to be able to predict the strength without having to conduct extensive experiments for each notch geometry. An alternate reason for understanding and modeling notch behavior is that it represents a condition where there are stress gradients in going from maximum stress at the notch root to lower stress at locations beneath the notch. Stress gradients also arise in fretting fatigue, discussed later in Chapter 6. Additionally, FOD, discussed later in Chapter 7, often produces some type of geometric discontinuity. To be able to predict the effect of the discontinuity or damage to stresses induced by vibratory HCF loading requires an understanding of notch effects in fatigue. For these reasons, we present an overview of notch fatigue as related, primarily, to the fatigue limit or threshold for crack propagation.

5.2. STRESS CONCENTRATION FACTOR

In notch fatigue, the primary aim is to be able to predict the fatigue behavior of a material or component with a stress concentration from smooth bar data. The majority of fatigue data available is in either the LCF regime or corresponds to fatigue lives below the endurance limit, if such a limit exists at all. The first aspect of addressing notch fatigue strength is to define the severity of the notch or stress concentration. To do this, the elastic stress concentration factor, k_t, is used.* Here, k_t is defined as the ratio of the peak stress at the root of a notch to the average stress over the net cross section:

$$k_t = \frac{\text{peak stress at notch root}}{\text{average stress over the net cross section}}$$

* The symbol used for the elastic stress concentration factor throughout the literature is either K_t or k_t. The former definition was commonly used before fracture mechanics was developed, when K was introduced as the stress intensity factor. However, K_t is still widely used. In this book, the term k_t will be used wherever possible for consistency. Note, however, that many drawings made early in the preparation of this manuscript or taken from the literature will still show K_t as the stress concentration factor. For this inconsistency and possible confusion, the author expresses his sincere apologies.

Values of k_t can be found in tables or handbooks and have been obtained from closed-form elastic solutions for simple geometries, photoelasticity experiments in the early days, and finite element calculations in the more recent literature. The value of k_t is a measure of the severity of the notch or discontinuity and is used to predict fatigue lives in many engineering applications. There are numerous cases in components with complex geometries where k_t cannot be defined as stated above because there is no well-defined "net-section." An example of such a geometry would be at the root of a notch in a dovetail attachment region where the cross section has a continuing variable geometry. In such a case, the net-section stress is hard to define because a section is difficult to be identified uniquely. Similarly, a notch in a complex 3-d geometry has an undefined value of k_t when the cross-section stresses, wherever the cross section is defined, are highly variable in all directions. Even if k_t is formally defined, it may have no meaning for engineering and design purposes for HCF applications.

In Figure 5.1, three geometries are shown schematically under far-field uniform tensile loading. In (a), a mild notch is depicted, and the stress at the notch tip is slightly higher than the net-section stress over the width, w. Note that if the gross cross section (width $= d$) is used (incorrectly), then a large stress concentration factor will result with resulting misleading approximations for the fatigue strength. All calculations for k_t are based on linear elastic material behavior and are independent of material and depend only on geometry. In (b) and (c), two identical notch radii are shown, but the two do not have the same value of k_t. In (b), the average stress is more influenced by the local notch field than in (c) which is closer to that of an infinite body. The stress concentrations are

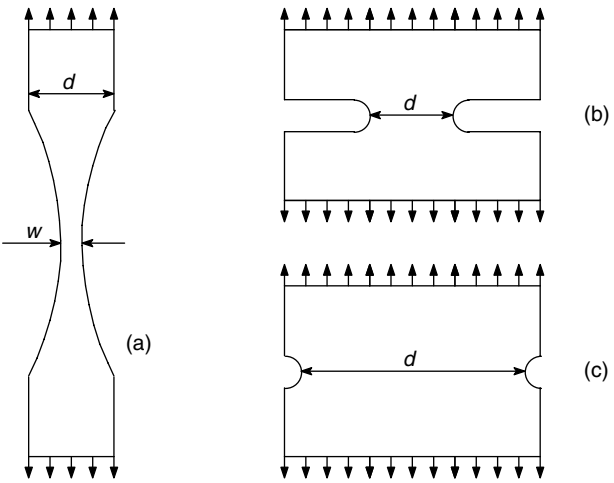


Figure 5.1. Three geometries illustrating the definition of k_t.

different, therefore, and this demonstrates that both the notch geometry and the overall geometry are important in determining k_t.

5.3. WHAT IS K_t?

There are a number of industrial applications where accounting for damage is necessary, even though the amount and severity of such damage is hard to quantify. In cases such as those with FOD, discussed later in Chapter 7, a knockdown factor in the form of an equivalent value of k_t is often used. While the design procedure may quote $k_t = 3$, for example, as the guideline, the intent seems to be to reduce the fatigue limit by a factor of 3 in this example, so the guideline should be $k_f = 3$ instead.* The fatigue notch factor, k_f, is defined and discussed later in Section 5.4.

The ambiguous meaning of quoting a value of k_t to represent damage is illustrated in a simple example here. Not only is k_t not unique in terms of the geometry it represents, but for a given geometry the value of k_t also depends on the loading condition. In this example, a rectangular plate with a U-shaped notch is loaded in tension or bending, as shown in Figure 5.2. With the nomenclature and loading as depicted in the figure, values of k_t are presented for several r/d ratios for tension as well as bending loading in Figure 5.3. For a fixed value of k_t, any of a number of values of r/d can be used to produce that value. Further, for a fixed geometry with specified values of D/d and r/d, the value of k_t is different under axial load than under pure bending. Thus, the specification of a value of k_t to represent a damage state is rather ambiguous and, as mentioned above, is a misuse of the term when a fatigue notch factor, k_f, is probably what was intended.

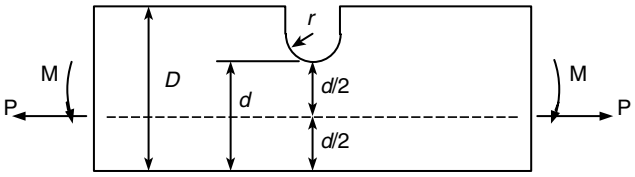


Figure 5.2. Nomenclature for plate with U-shaped notch under tension and bending.

* In recognition of the intent to reduce fatigue strength for FOD damage in ENSIP in preliminary design, $k_t = 3$ was introduced in the original document. The latest versions of ENSIP now use $k_f = 3$ as the guideline.

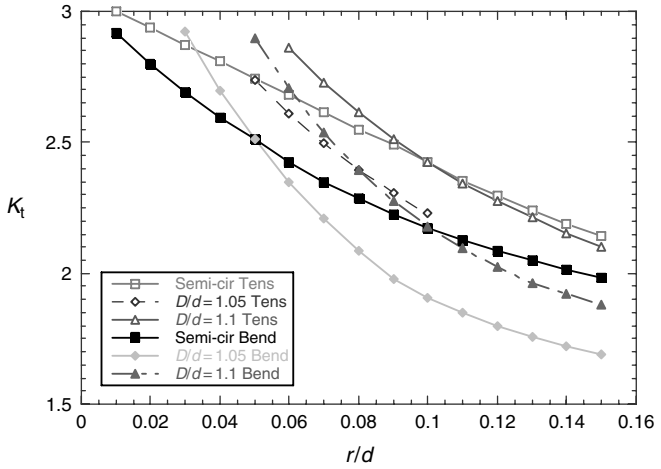


Figure 5.3. Values of k_t for U-shaped notch.

5.4. FATIGUE NOTCH FACTOR

The fatigue behavior of a notched component is not necessarily governed solely by the maximum stress at the notch root. In general, the fatigue life or fatigue strength is greater in a notched component based solely on the stress at the notch root compared to a smooth bar with that same stress distributed uniformly over the entire cross section. Many researchers over the years have attributed this observation to the concept that fatigue behavior depends on the stresses or strains over a critical volume of material. Thus, as the size of a notch becomes very small, the fatigue behavior tends to be governed more by the far-field stresses or average stresses. The notch root radius also plays a significant role in determining the fatigue limit. In the limiting case, as the notch root radius decreases to zero, the notch will behave like a crack as discussed later. On the other hand, as the notch root radius becomes very large, the fatigue behavior is governed more by the peak stress at the notch. In the latter case, in the limit, the stress is given by the far field stress multiplied by k_t. From these observations, and from experimental data developed over many years, equations have been developed for predicting the fatigue behavior in a notched component based on fatigue behavior in smooth bars where the majority of databases can be found. The fatigue notch factor, k_f, is defined as the ratio of the fatigue strength in a smooth bar to the fatigue strength in a notched bar, that is

$$k_f = \frac{\text{unnotched fatigue limit stress}}{\text{notched fatigue limit stress}} \tag{5.1}$$

This equation is defined, in the strictest sense, for fully reversed loading ($R = -1$) as well as for a specific number of cycles and a specific specimen geometry. The fatigue

notch factor generally covers the range $1 < k_f < k_t$, indicating that use of k_t rather than k_f can be overly conservative to describe the notch sensitivity. An alternate quantity used to define the notch behavior of a material is the notch sensitivity, q, defined as

$$q = \frac{k_f - 1}{k_t - 1} \tag{5.2}$$

The notch sensitivity for a material takes the range $0 < q < 1$. When $q = 0$, this represents a material and notch geometry where $k_f = 1$, the case where the material is insensitive to the presence of a notch. When $q = 1$, this corresponds to $k_f = k_t$, where the material is notch sensitive and the behavior is governed exclusively by the local stress at the root of the notch.

From a historical perspective, Schütz [1] points out that A. Thum, one of the most prominent researchers in fatigue in his era, founded the doctrine of "Gestaltfestigkeit," which maintains that for a high fatigue strength the shape of the component, as developed by the designer, is much more important than the material itself. The notch fatigue stress concentration factor k_f was also created by Thum who, according to Schütz, correctly called it a "crutch with which one can limp from the un-notched specimen to the notched component." He knew that it has to be determined anew in every case by exactly those fatigue experiments which it is supposed to make unnecessary.

5.4.1. k_f versus k_t relations

There are many empirical relationships between k_f and k_t, which try to express the combined effects of the gradient of stress at the notch root, the individual contributions of notch root radius and depth of notch, the effect of volume of material being stressed, and the multiaxial stress state which arises at the tip of a very sharp notch. A review of formulas for k_f is presented in [2]. The authors classify all the expressions for k_f into one of the three types according to their assumptions: the average stress (AS) model, the fracture mechanics (FM) model, and the stress field intensity (SFI) model. The latter was a development by the authors and involves determining a weighted average stress over a volume of material ahead of a notch. It is an extension of a model based on average stress over a volume, which, in turn, is a more complicated version of a model that averages stress over a length at the notch tip. This, in turn, is the AS model. The basic differences between the two general types of models, the AS and the FM model, are pointed out in [2]. The AS model assumes that there are no cracks in the material and fatigue occurs when an average stress over some area (or volume) exceeds the stress required for fatigue failure in a uniformly stressed bar. The FM model, on the other hand, assumes that there are cracks in all specimens under fatigue loading. The criterion for the propagation or non-propagation of these cracks forms the basis of the model. Gradient stress field and short crack behavior have to be considered in developing the criterion. For HCF, the threshold for crack propagation is established. The applicability of such a model for finite fatigue life is more difficult and is not a subject that will be dealt with in this book.

Formulas relating k_f and k_t all have one thing in common. For very sharp notches, they all tend to asymptote to a single limiting value of stress, independent of the notch severity. In the limit, this would correspond to a crack which requires a certain level of stress to cause fatigue above a threshold stress intensity factor range. On the other extreme, for very shallow notches, the values of k_f and k_t merge, indicating that the lower stress gradients or stresses away from the notch root tend to have no influence on the fatigue strength as one approaches the case of a smooth bar.

Some commonly used equations for k_f, which are based primarily on experimental data, are listed below. These formulas were based on analysis of stress fields ahead of notches and fall in the category of AS models as defined by Weixing et al. [2]. The equation due to Neuber [3] is of the form

$$k_f = 1 + \frac{k_t - 1}{1 + \sqrt{\frac{a_m}{r}}} \tag{5.3}$$

The equation of Peterson [4] is

$$k_f = 1 + \frac{k_t - 1}{1 + \frac{a_m}{r}} \tag{5.4}$$

The equation of Heywood [5] is

$$k_f = \frac{k_t}{1 + 2\sqrt{\frac{a_m}{r}}} \tag{5.5}$$

where, in all of the above, a_m is a material constant* and r is the notch root radius. For a fixed value of k_t, the fatigue notch factor, k_f, is considered to be a function of notch root radius only. The material constant, a_m, is different for each of the three equations and is most commonly used as an empirical constant to fit experimental data. There have been attempts over the years to relate these constants to tensile properties of materials, but these have met with only limited success. In fact, the relation between fatigue properties and tensile properties is a lofty goal indeed, but such a relationship probably does not exist in the opinion of this writer. The use of k_f in fatigue design is still recommended in some textbooks and handbooks (see, for example [6]).

5.4.2. Equations for k_f

A plot of the value of k_f as a function of notch root radius, r, for each of the three equations, is presented in Figure 5.4 using a dimensionless value, r/a_m, for the root

*The material constants for the equations of Neuber, Peterson, and Heywood are often written as a_N, a_P and a_H, respectively. Here we use the nomenclature a_m to represent any one of them.

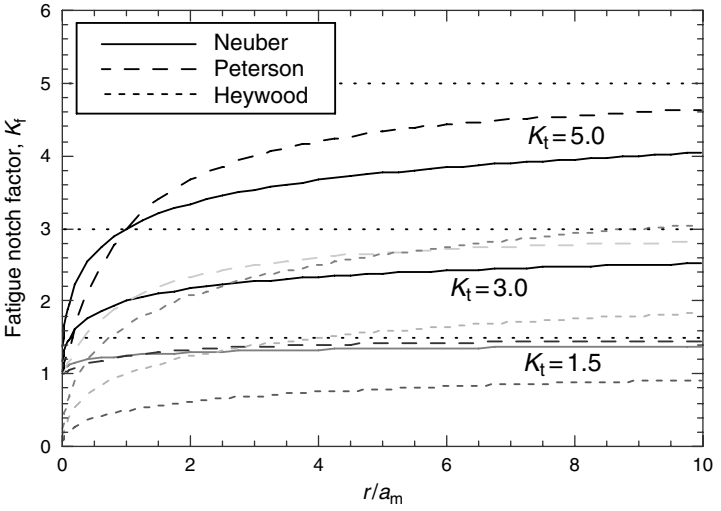


Figure 5.4. Comparison of fatigue notch factor equations.

radius. Here, a_m is a material constant for each of the three equations and would not necessarily be the same for each equation nor for each material. Figure 5.4, plotted for three arbitrarily chosen values of $k_t = 1.5$, 3.0, and 5.0, shows that each equation has a trend of having k_f approaching k_t for large values of r/a_m, but k_f approaches unity for the Neuber and Peterson equations and approaches zero for the Heywood equation as r approaches zero. This indicates that the Heywood equation should not be used for very small values of r because values of k_f under unity are not physically realistic.* For any

* While it would be easy to dismiss the Heywood equation as not being either accurate or physically meaningful as the notch root radius approaches zero, the concepts behind the equation and the limitations of its use are carefully pointed out by Heywood in his paper [5]. In particular, he notes that engineering materials have inherent imperfections that can be treated as very small notches. Thus, Equation (qq05) has validity only above a notch root radius that produces a value of k_f of one. For smaller notches, no further reduction in fatigue strength can occur than is already present in the material due to the inherent imperfections. The equation proposed by Heywood, Equation (qq05), regards the material as "containing a number of stress concentrations due to its heterogeneous nature." For notches of extremely small depth, but for notch radii of "typical proportions," Heywood also proposed the following formula

$$k_f = \frac{k_t}{1 + 2\sqrt{\frac{a_m}{r}\left(\frac{k_t - 1}{k_t}\right)}} \qquad \text{(qq05a)}$$

that has k_f equal to unity when k_t is unity. Heywood, in commenting on the complexity of a fatigue notch factor formula, notes that "more complicated relationships, such as those requiring two or more notch sensitivity constants.…will not be considered, as they are not likely to be used in practice, even though they may have a more satisfactory theoretical basis for their derivation" [5].

particular value of notch root radius, r, the curves in Figure 5.4 can be shifted horizontally left or right by altering the material constant, a_m. While a_m has the dimension of length, it has not been shown to have any real physical significance and should be treated as no more than an empirical curve fit parameter. It is apparent that these equations were meant to show trends for very small and very large values of r/a_m, but were based on data for stress concentrations common in engineering usage.

It is the opinion of the author that such equations, as listed above, which relate to k_f, have limited use in engineering applications unless one is dealing with the same material under nominally identical applications where a fatigue database already exists. Extrapolations beyond where the equations are fit to experimental data are only as good as their validations with more experimental data. In addition to the equations for k_f being material as well as geometry-dependent (both k_t and root radius, r, appear in them), the fatigue notch sensitivity can also depend on stress ratio, R. Most pertinent to the subject of this book, however, is the fatigue life at which the equations are valid. Figure 5.5 is a schematic of S–N curves for a smooth bar as well as that for a notched bar of the same material. No attempt is made to realistically represent the relative slopes, inflection points, or spacing of the two curves. If point A represents the fatigue life of the smooth bar at the indicated stress level, the effect of a notch can be described by either the reduction in fatigue strength by $S1$ for the same fatigue life or the reduction in life by $N1$ for the same applied stress. The former is characterized by the fatigue notch factor, while the latter is often used in design of a component operating under a given stress field. In HCF, the only concern is the reduction in strength or the fatigue notch factor corresponding to a long-life fatigue strength or endurance limit if such exists. For point B

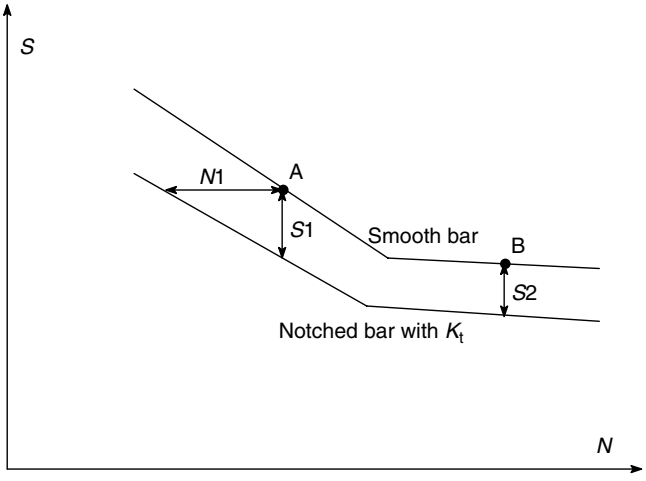


Figure 5.5. Schematic of S–N behavior of smooth and notched specimens.

on the curve, the notch reduces the fatigue strength by $S2$. There is generally no simple relation between the values of $S2$ and $S1$ as either a function of the smooth bar stresses at A and B, or of the fatigue lives corresponding to A and B. Thus, it is speculative to use a fatigue notch factor for point B based on data obtained at lives corresponding to point A in the diagram. It is not surprising to find, therefore, that fatigue notch factors developed mainly for LCF are not applicable to FLSs near the endurance limit for a range of stress concentration factors and stress ratios using a single material constant as demonstrated by Haritos, et al. [7].

An alternate method of representing the trends of equations for k_f as a function of notch root radius, r, as shown in Figure 5.4, is to plot the fatigue strength as a function of elastic stress concentration factor, k_t, as presented in Figure 5.6. If fatigue strength is related simply by the stress at a point, the maximum occurring at the notch root, then the fatigue strength would be simply σ_0/k_t as shown by the heavy solid line labeled $1/K_t$ in the figure. Experimental data show, however, that there is a size effect so that the fatigue strength is higher than that determined strictly by stress at a point, and is given empirically by the fatigue notch factor which was shown in Figure 5.4 for several empirical fits to experimental data. In Figure 5.6, the normalized fatigue strength is shown for several equations, including that of Smith and Miller [8], which represent values for k_f as a function of notch geometry for an elliptical-shaped notch. Smith and Miller represent k_f in terms of notch root radius, r, and notch depth, d, as

$$k_f = 1 + 7.69\sqrt{\frac{d}{r}} \tag{5.6}$$

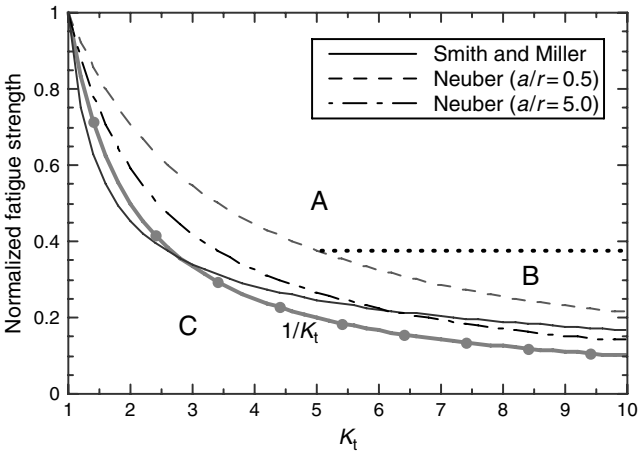


Figure 5.6. Fatigue strength predictions as a function of k_t.

which can be represented as a function of k_t using the equation from Peterson [9], which approximates the stress concentration factor of a circular notch of radius, r, and depth, d, as

$$k_t = 1 + 2\sqrt{\frac{d}{r}} \tag{5.7}$$

5.5. FRACTURE MECHANICS APPROACHES FOR SHARP NOTCHES

The previous equations show that the fatigue strength increases over σ_0/k_t as k_t increases. However, as k_t increases beyond some critical value, the equations for k_f break down and a limiting (minimum) value of fatigue strength is reached. The theory behind this limiting value is that a notch starts to act the same as a crack as the notch becomes sharper and sharper. This, in fact, is the starting point for the theory of fracture mechanics. Smith and Miller [10] have determined this limiting value of stress to be

$$\Delta\sigma = 0.5\frac{\Delta K_{th}}{\sqrt{d}} \tag{5.8}$$

where ΔK_{th} is the threshold stress intensity range, the value of ΔK below which a crack will not grow at a selected arbitrary value of very slow growth rate, commonly taken as 10^{-10} m/cycle. A horizontal dashed line in Figure 5.6 is used to depict this limiting value of stress, whether it be given by Equation (5.8) or any other equation or fit to experimental data. With the establishment of the existence of this limiting stress for high values of k_t, the plot of Figure 5.6 can be broken into three regimes. In regime A, cracks will always initiate and propagate to failure. This defines stress states above the endurance limit for any notch geometry. In region C, cracks will not initiate nor propagate, so this region can be defined as the safe region for HCF. In region B, cracks may initiate because they are subjected to local stresses beyond σ_0/k_f, but they will not propagate because the driving force is insufficient to cause subsequent propagation. The physical reason for this behavior is that there are sufficiently large enough stresses at the notch root, and over a sufficient distance or volume, to cause crack initiation. However, for very large values of k_t, which normally correspond to very small root radii [see Equation (5.7)], the local notch stress field dies out very quickly. The far-field stress field, in addition, is insufficient to cause the initiated crack to continue to propagate because the local stress intensity is below threshold. Part of the reasoning behind this is the fact that the stress intensity for a small crack may be insufficient, or below threshold, if the far-field stress field is low, as would normally be the case for a very high value of k_t.

The equation of Neuber, (5.3), shown in Figure 5.4 for fatigue notch factor can be plotted as FLS, which by definition is equal to $1/k_f$, as a function of the notch root

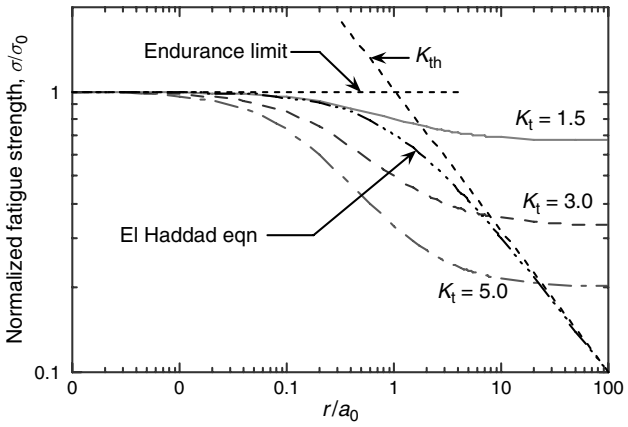


Figure 5.7. Kitagawa diagram for notches with various k_t values.

radius, r, which can be taken as a characteristic length parameter. In this plot, Figure 5.7, logarithmic coordinates are used as was done by Kitagawa and Takahashi [11] to illustrate the dilemma associated with small cracks. For the three particular values of k_t, the FLS is shown as a function of notch root radius normalized with respect to a material constant which will be called a_0. The concepts illustrated in Figure 5.7 involve both fatigue crack initiation and threshold fracture mechanics for the case of smooth bar fatigue. The initiation concept is represented by the endurance limit which is a stress level below which cracks will not initiate and propagate and above which will produce fatigue failure under HCF conditions. The fracture mechanics threshold stress intensity factor is the quantity below which a crack will not propagate and above which it will propagate. For an edge crack in an infinite body, the stress intensity is given as

$$K = 1.12\sigma\sqrt{\pi a_c} \tag{5.9}$$

which, if plotted as stress against crack length, a_c, is a straight line of slope -0.5 on the log–log plot of Figure 5.7, which is equivalent to a Kitagawa diagram. As discussed earlier in Chapter 4, the two limiting cases, that of a smooth bar and that of a bar with crack, have been consolidated in various ways, most notably by El Haddad et al. [12]. They introduce a pseudo-crack length, a_0, which produces a non-zero stress intensity for a smooth bar with no real crack. As the crack length increases, the contribution of the a_0 term becomes small and the long crack fracture mechanics solution is approached. Ignoring the factor of 1.12 in Equation (5.9), the El Haddad relationship has the form

$$\Delta\sigma_{0c} = \frac{\Delta K_{th}}{\sqrt{\pi(a + a_0)}} \tag{5.10}$$

where $\Delta\sigma_{0c}$ is the critical stress range for propagation of a crack of length a. This equation is shown in Figure 5.7 to be asymptotic to the endurance limit and the threshold stress intensity line as discussed previously. Here, a is the actual crack length and a_0 is a material constant which, for the edge crack described by Equation (5.9), and ignoring the factor 1.12, is

$$a_0 = \frac{1}{\pi}\left(\frac{\Delta K_{th}}{\Delta\sigma_0}\right)^2 \tag{5.11}$$

where $\Delta\sigma_0$ is the endurance limit stress for the uncracked body. The quantity a_0 has been interpreted over the years to be anything between a fundamental parameter representing some microstructural aspect of a material to a purely empirical curve fitting parameter. Mathematically, it provides a smooth transition from initiation in an uncracked body to long crack behavior and is claimed to represent much of the small crack threshold data reported in the literature. For almost all materials, however, a_0 is found to be a function of stress ratio, R.

Of significance, in Figure 5.7, is the behavior of notched specimens represented by the equation of Neuber, which provides the FLS as a function of notch root radius, using a_m as a material constant and k_t as a parameter. In the plot, r is normalized with respect to an arbitrary quantity a_0 which is not necessarily the same as a_m, although Taylor [13] indicates that these two quantities, which both have units of length, have been noted to be of the same order of magnitude for many materials. For a notched component, the curves for various k_t values show that as k_t decreases and approaches unity (smooth bar), the FLS approaches the endurance limit. As k_t increases, however, the shape of the curve becomes more like that of El Haddad for small notch root radii. The notch curve for $k_t = 5.0$ can be seen to be almost parallel to the threshold line and, by the proper choice of values of a_m, could be made to be coincident with it. This is another way of showing that very sharp notches tend to produce fatigue limits which can be determined from fracture mechanics by treating the notch as a crack, independent of k_t, as shown in Figure 5.6 and by Equation (5.8). In fact, that equation is simply the fracture mechanics equation for an edge crack, Equation (5.9), where the crack length is replaced by the notch depth, d, for very sharp notches with high values of k_t. Plotted on Figure 5.7, this equation would be parallel to the threshold line. For small values of notch root radius, the region between the fatigue limit curves and the El Haddad fracture mechanics curve corresponds to a region where cracks can initiate but will not propagate because they are below the threshold for crack growth, similar to region B in Figure 5.6. For large values of notch root radius, on the other hand, cracks will both initiate and propagate because the FLS comes directly from the definition of k_f given by Equation (5.1) as shown by the equations in Figure 5.7 and the stresses and root radii are above the crack growth threshold condition.

Evaluation of Figures 5.6 and 5.7 points out some of the difficulties in making generalizations about the transition from crack initiation to crack propagation, particularly as related to the small crack issue in both smooth and notched bars. The transition from a sharp notch to a crack does not depend solely on k_t, as shown in Figure 5.6, nor does it depend solely on notch root radius, r, as shown in Figure 5.7. Instead, it depends on both, even though very sharp notches having large values of k_t are normally associated with geometries that have very small notch root radii. The transition from long to short cracks is also an issue which has to be addressed. Note again, as pointed out previously, that the extrapolation of equations for k_f to either very small notch root radii or very high values of k_t are speculative at best. Figure 5.6 shows the breakdown of those equations for high k_t by a fracture mechanics based parameter. The shape of the curves in Figure 5.7 for very small values of r is nothing more than an extrapolation that eventually approaches the smooth bar behavior.

5.6. CRACKS VERSUS NOTCHES

Taylor [14] has attempted to summarize the scope of the notch problem in fatigue which encompasses a wide range of geometries from a very mild notch to a very sharp notch, the latter acting essentially as a crack. In addition, he incorporates the concept of both very shallow notches and cracks which, in the extreme, have no effect on smooth bar fatigue behavior because of their small size. To do this, a semi-elliptical notch at a surface having depth D and notch root radius r is considered. Using the El Haddad definition of the critical crack length a_0, the behavior of a notch can be broken up into three regimes as shown in Figure 5.8, where the regimes are defined for values of notch size (D/a_0) and notch shape (D/ρ). The three regimes are designated "blunt notches," "crack-like notches," and "short notches," and the boundaries between the regimes are shown schematically in Figure 5.8. The boundary below which a notch is considered to be short is found to be approximately at $D/a_0 = 3$, while crack-like notches occur for notch shapes where D/ρ is greater than approximately 0.25. Taylor goes on to point

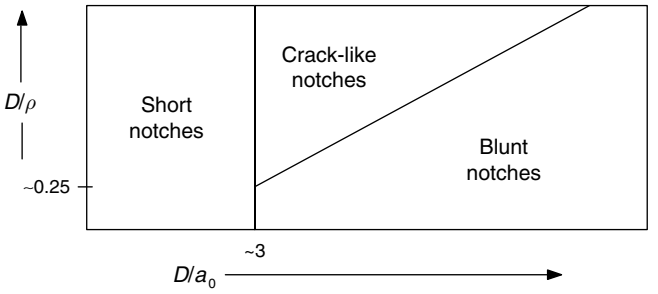


Figure 5.8. Schematic illustration of three regimes of notch behavior [14].

out that close to the fatigue limit (under HCF), blunt notches and sharp notches behave differently in respect to their crack-growth mechanisms.

When notches act like cracks, the mechanism leading to a fatigue limit is the growth of small cracks from the notch tip which may become non-propagating cracks. The criterion for the fatigue limit is the onset of crack propagation from an arrested crack and not crack initiation. Taylor [14] points out that these cracks are always short cracks and they arrest because their threshold values increase faster than the applied stress intensity. This occurs, in general, under a stress field involving steep stress gradients such as at the tip of a very sharp notch. For a plain or blunt-notched specimen, on the other hand, non-propagating cracks are not found, especially for very short crack lengths. Taylor goes on to attribute the fatigue limit in such geometries to the arrest of cracks at a grain boundary, the arrest defining the fatigue limit. This is a material-based limit according to Miller [15] rather than a limit based on the mechanics of the notch.

A numerical example can be used to show the effects of notch geometry on fatigue strength. To illustrate the effect of very small notches on the fatigue strength, the formulas of Peterson for k_t and Neuber for k_f are plotted in Figure 5.9 for two different values of the material parameter a_N and for three different values of notch depth, d (dimensions of the notch and the material parameter a_N are in arbitrary units). The reciprocal fatigue strength,

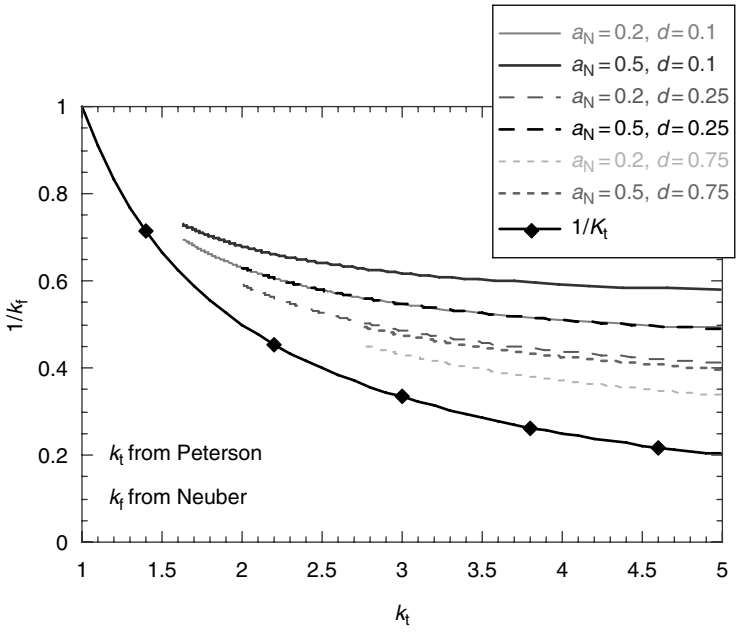


Figure 5.9. Fatigue notch factor as a function of k_t for increasingly small notches. Constants a_N and notch depth d are for Neuber equation for k_f and Peterson equation for k_t.

$1/k_f$ is plotted against k_t and the curve representing $k_f = k_t$ is shown as the bottom (thick line) curve. The higher the curve, as k_f approaches unity, the less is the effect of the notch on the smooth bar fatigue strength. Curves for the various parameters show that the fatigue strength is least effected by the shallowest notch ($d = 0.1$) while the deepest notch ($d = 0.75$) comes closest to taking a fatigue strength debit equal to k_t. In the limit, as the notch depth goes to zero, the fatigue strength is unaffected by the presence of the notch.

Another example illustrating the complex behavior under fatigue loading of a notched specimen can be explained further with the use of Figure 5.10, which plots nominal stress against k_t. The heavy solid line represents the fatigue limit and, as shown, represents a fairly large body of experimental data. The figure is based upon the work of Nisitani and Endo [16]. For low values of k_t the fatigue strength is approximated by σ_0/k_t whereas beyond what is called the branch point [17], the fatigue strength is constant. The difference between the initiation limit curve and the curve due solely to k_t is small as k_t approaches one. This is recognized in many of the formulas for the true fatigue limit strength that

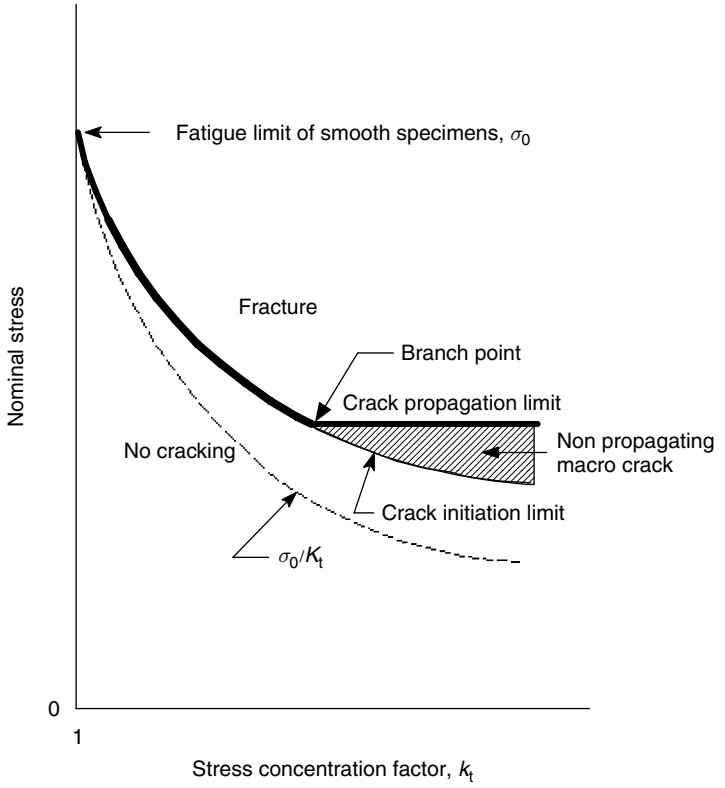


Figure 5.10. Schematic representation of fatigue strength at notch for increasing values of k_t.

show k_f is different than k_t. The crack initiation limit is assumed to be governed by the value of notch tip stress as well as the stress gradient at the notch. It is assumed, therefore, that as k_t increases, the stress necessary to initiate a crack becomes lower. However, because of the steep gradient of stresses at the notch root for high values of k_t, a crack that initiates enters a rapidly decreasing stress field where the tendency to propagate decreases. From a fracture mechanics perspective, the stress intensity decreases to a value below the crack growth threshold and thus the crack arrests. Above the solid line in the figure, fracture will occur after crack initiation and continued propagation. Below the crack initiation limit, no cracks will form. In the intermediate region, shown shaded in the figure, a macrocrack will form but will not propagate. While the authors [16] refer to this region as one where macrocracks form, it is feasible that cracks of any arbitrarily small size may form and a separate crack initiation limit can be established. From a practical point of view, such cracks would have to be observed experimentally in order to establish the microcrack initiation limit and this becomes much more difficult to accomplish.

5.7. MEAN STRESS CONSIDERATIONS

The reduction of fatigue strength of a notched specimen, characterized by the quantity k_f (or alternately, q), is not a unique quantity for a material given by the value obtained at $R = -1$ for very long fatigue life for a given specimen geometry [6]. Instead, the value of k_f is often found to depend on mean stress as depicted in Figure 5.11, as shown in

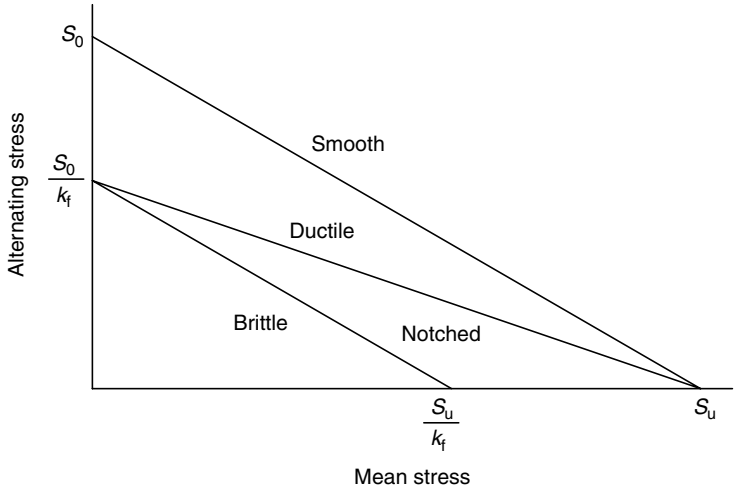


Figure 5.11. Simplified representation of smooth and notched behavior for ductile and brittle materials on a Haigh diagram (after [6]).

[6]. For a brittle material, where local notch plasticity is absent, both the mean stress and alternating stress are reduced on a Haigh diagram since the ultimate stress point is reduced due to a notch. For a ductile material, the ultimate stress is essentially the same in a notched as in an un-notched specimen because of either local or gross-section yielding and the resulting stress redistribution. Thus, the Goodman line in Figure 5.11 goes through the same ultimate strength point as for the un-notched specimen. In reality, notched specimen behavior falls in the region between the two extremes shown in the figure.

If the smooth bar fatigue strength under fully reversed loading is denoted by S_0, as shown in Figure 5.11, then the modified Goodman equation connecting that point with a straight line on a Haigh diagram to the static ultimate stress, S_u, is written as

$$S_a = S_0 \left(1 - \frac{S_m}{S_u}\right) \tag{5.12}$$

The simplest approach to modify this equation for notched specimens is to simply reduce both the mean and alternating stresses by the elastic stress concentration factor, k_t, thus

$$S_a = \frac{S_0}{k_t} \left(1 - \frac{k_t S_m}{S_u}\right) \tag{5.13}$$

This is very conservative, since the reduction in fatigue limit is characterized by k_f, which is less than k_t. A better approach consists of replacing k_t by k_f in Equation (5.13) which produces the line denoted by "brittle" in Figure 5.11. In many cases, a best value of k_f, not necessarily the value for $R = -1$, is used in such an approach. A more realistic approach is to reduce only the alternating stress by a constant factor k_f while maintaining the mean stress. For the line denoted as "ductile" in the same figure, the equation that reduces the alternating stress in this manner is

$$S_a = \frac{S_0}{k_f} \left(1 - \frac{S_m}{S_u}\right) \tag{5.14}$$

Bell and Benham [18] performed an extensive series of notch fatigue tests on stainless steel sheet covering a wide range of both notch geometries and fatigue lives. Concentrating here only on the results for long lives, corresponding to HCF, they observed that the fatigue notch factor was a function of mean stress as suggested above. Using the argument that as the mean stress increases the amount of notch plasticity increases above some critical value, and observing that the static ultimate strength of a notched specimen is somewhat higher than that of an un-notched specimen (referred to as notch strengthening), they proposed an equation which fit their endurance limit data for notched specimens very well, as shown in Figure 5.12. Their equation, used in the figure, is

$$k_f = k_{fav} \left(1 - \frac{S_m}{S_{up}}\right) + \frac{S_m}{S_{un}} \tag{5.15}$$

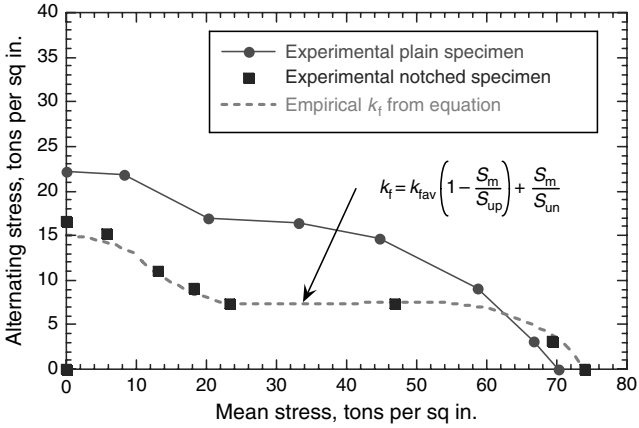


Figure 5.12. Comparison of experimental and empirical curves on Haigh diagram for notched specimens having lives in excess of 10^6 cycles (after Bell and Benham [18]).

where k_{fav} is an average fatigue notch factor at $R = -1$ for a variety of experiments, S_{up} is the tensile strength of an un-notched specimen, and S_{un} is the tensile strength of a notched specimen for the particular notch geometry used in constructing the Haigh diagram. This equation differs from Equation (5.14) in concept because here the fatigue notch factor k_f is reduced as a function of mean stress rather than reducing only the alternating stress by a constant fraction.

To compare the two methods of accounting for the effect of mean stress, numerical examples are provided for a material whose smooth bar behavior can be represented as a straight line (modified Goodman equation) on a Haigh diagram. To illustrate some of the characteristics of Equation (5.15), a Haigh diagram where the un-notched behavior is represented by the straight line modified Goodman equation, Equation (5.12), is shown in Figure 5.13. In this illustrative example, the smooth bar alternating stress is arbitrarily taken as 0.5 of the ultimate strength, S_u (or S_{up} in Equation (5.15)) and all of the quantities are shown in dimensionless coordinates with respect to S_u. Taking $S_{un} = 1.05S_{up}$, values of the notch strength factor $k_f = 1.5$ and 3.0 are chosen. The shape of the curves shows how, as the mean stress is increased, the notch reduction factor decreases. For both cases, where either the alternating stress is decreased according to a constant value of k_f, or the equation of Bell and Benham, Equation (5.15) is used, the reduction in fatigue strength due to a notch is approximately the same. The only noticeable differences are for high values of mean stress. If $S_{un} = S_{up}$ for the straight line case shown here, then the reduction of alternating stress only produces the identical result to Equation (5.15). The two methods for accounting for the notch fatigue strength reduction turn out to be almost identical in this illustrative example.

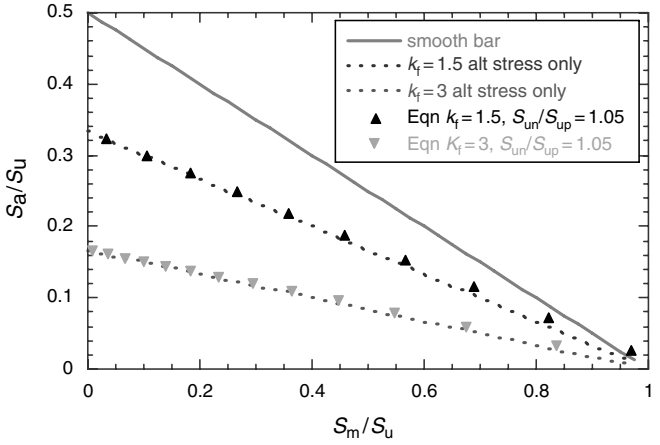


Figure 5.13. Comparison of two equations of Bell and Benham [18] for notched specimen on a Haigh diagram for material represented by modified Goodman equation.

If a nonlinear curve is used to represent the smooth bar fatigue data, then the two equations, modified to take care of the actual shape of the un-notched curve, produce slightly different results as illustrated in Figure 5.14. For an example case where the curve represents data on titanium, shown earlier in Chapter 2, the two methods produce slightly different curves. Nonetheless, both reducing the alternating stress only by a constant factor

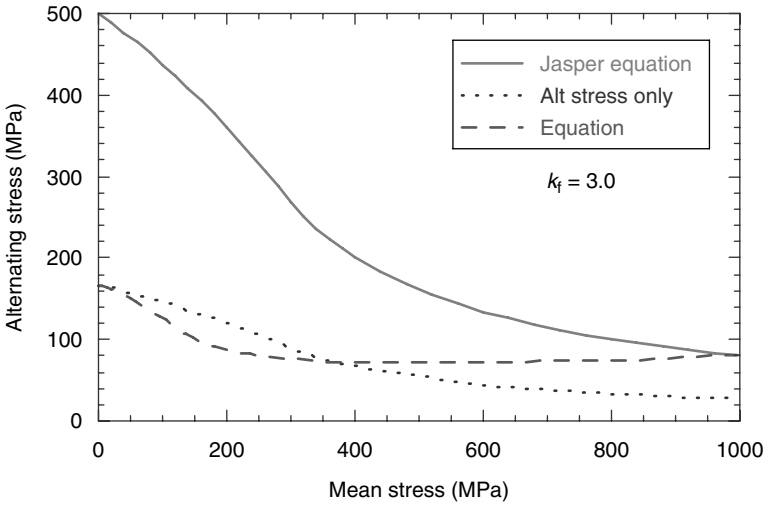


Figure 5.14. Comparison of two equations of Bell and Benham [18] for notched specimen on a Haigh diagram for real material represented by Jasper equation.

k_f and reducing the effective value of k_f as a function of mean stress seem to be effective methods for accounting for the observed dependence of k_f on mean stress in ductile metals.

5.8. PLASTICITY CONSIDERATIONS

One of the earliest and simplest attempts to treat fatigue at notches that undergo plastic deformation at the notch root is due to Gunn [19]. He provided a simplified procedure to use the smooth bar Haigh diagram to create a notched Haigh diagram based solely on the elastic stress concentration factor, k_t, of the notch. The procedure is illustrated in Figure 5.15 for a linear representation of the smooth bar data on a Haigh diagram. The procedure is applied in an identical manner for any shape curve. For purely elastic behavior, the notch stresses are reduced by the same amount for both the alternating and mean stresses. However, when the nominal stress multiplied by k_t equals the yield stress, Y, the notch root will undergo local plastic deformation. Then, it can be assumed that for higher applied peak stresses, the region around the notch root will undergo cyclic plastic deformation for one or more cycles until the entire behavior becomes elastic again. At that point, the mean stress will be reduced from the applied value divided by k_t since the maximum stress at the notch does not exceed the yield stress, but the alternating stress will remain the same. The approximation due to Gunn then uses the smooth bar curve reduced by k_t for stresses below yield at the notch root as indicated by the line AB in Figure 5.15. For regions above where applied stresses cause notch root yielding, the local mean stress remains unchanged since the maximum stress there is limited to the yield stress. The point of local yielding, B, is the intersection of the smooth bar curve reduced by k_t and the line representing maximum stress at the notch root equal to the yield stress, Y. This latter line is shown dotted in the diagram and goes through the point on the

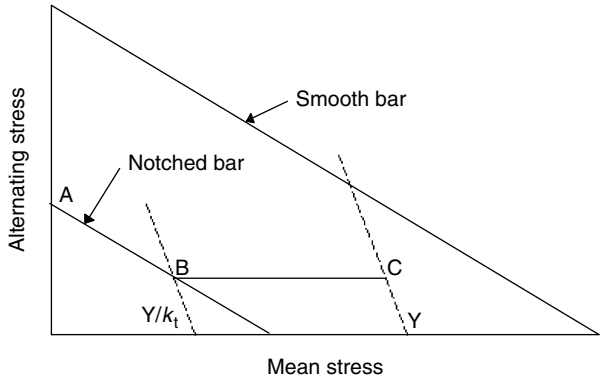


Figure 5.15. Notch Haigh diagram using simplified procedure of Gunn [19].

mean stress axis whose magnitude is Y/k_t. For stresses beyond yield at the notch root, the allowable alternating stress is that at point B since the local mean stress remains constant. This results in a predicted Haigh diagram of ABC as shown in Figure 5.15. Although Gunn [19] developed a more sophisticated model for the Haigh diagram based on the stress–strain behavior of a material, the simplified procedure illustrated by Figure 5.15 was found to be sufficiently accurate for practical purposes [20].

Lanning and co-workers have performed a large number of notch fatigue tests on Ti-6Al-4V to determine the fatigue strength at 10^6 cycles using circumferentially V-notched specimens whose geometry is shown in Figure 5.16. Some of the data, reported in [21], are presented in Figure 5.17 where three combinations of notch dimensions

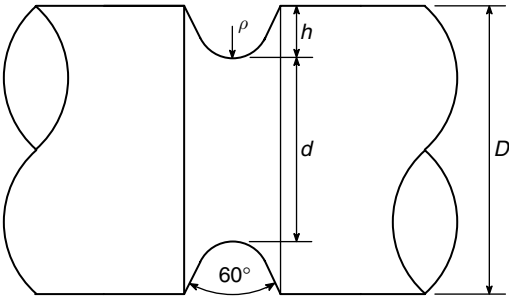


Figure 5.16. Cylindrical fatigue specimen with circumferential V-notch.

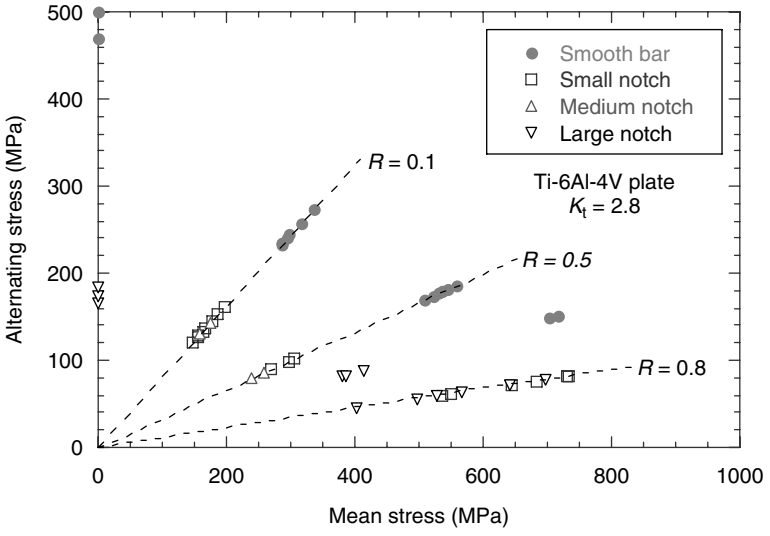


Figure 5.17. Notch fatigue data on Ti-6Al-4V with $k_t = 2.8$.

producing the same value of $k_t = 2.8$ were used. The dimensions of the notches are listed in Table 5.1. For reference purposes, typical values of a_0 for this titanium alloy are around 0.05 mm while the grain size is between 0.015 and 0.020 mm. From the dimensions of the small notch it appears that none of the specimens should be expected to show small notch behavior. Data for these specimens, shown in Figure 5.17, show a reasonably large amount of scatter which the authors attribute to sampling a small volume of material in each test. At the highest value of $R = 0.8$, however, the small notch data seem to lie above the data from the other notch sizes. Calculations show that for values of R above approximately 0.5 that plastic deformation takes place at the notch root. Creep ratcheting, discussed earlier, is also a consideration when the stresses approach the yield stress in this material. This would occur at values of R in the vicinity of $R = 0.8$.

To try to quantify the notch effect for the data in Figure 5.17, we can follow the suggestion of Bell and Benham [18], for example, that the Haigh diagram for a notched specimen may better represent a material if the alternating stress is reduced by k_f but the mean stress is left unchanged. In Figure 5.18, a value of k_f of 2.8 is chosen to represent

Table 5.1. Dimensions for circumferential V-notches with $k_t = 2.8$

Notch type	ρ (mm)	h (mm)	D (mm)	d (mm)
Small	0.127	0.127	5.72	5.47
Medium	0.203	0.254	5.72	5.21
Large	0.330	0.729	5.72	4.26

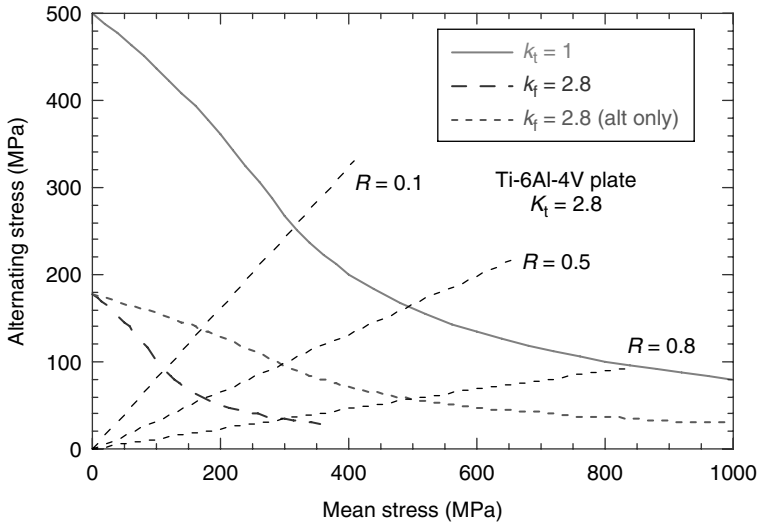


Figure 5.18. Representation of fatigue notch data with k_f reductions.

the data of Figure 5.17. The Jasper equation, used earlier in this book (see Chapter 2), is used to represent the smooth bar data. For comparison purposes, the smooth bar curve is reduced by k_f for the maximum stress in one case. This amounts to reducing both the mean and alternating stresses by the same amount. The value of $k_f = 2.8$ is taken from Figure 5.17 based on the zero mean stress ($R = -1$) data points. In this particular case, $k_f = k_t$ for the $R = -1$ condition. This same value of k_f is used to reduce only the alternating stress and the resulting curve is also shown in Figure 5.18. Comparing Figure 5.18 with the data in Figure 5.17 shows that the reduction of only the alternating stress, as suggested in [18], produces a more reasonable representation of the notch data for this particular material, Ti-6Al-4V plate.

While it is always convenient to have a simple formula to predict notched behavior from smooth bar behavior, even if it is just for mildly notched specimens, the scatter in fatigue limits and the tendency for real materials not to follow the laws we create for them makes predicting notch behavior a cumbersome task. As an example, taking the same titanium alloy as discussed above in [21] and the data presented in Figure 5.17, we look at data obtained at a fatigue limit of 10^7 cycles from a recent Air Force program [22]. These data were obtained on smooth and notched specimens that were both stress relieved after machining and chem milled. While this process is aimed at producing a pristine material, the experimental data may be different than those obtained after stress relieving only as was done for the data in [21] (corresponding to a fatigue limit at 10^6 cycles). It should also be noted that the fatigue properties of titanium alloys are very sensitive to surface finish [23]. In the work in [22], a nominal value of $k_t = 2.5$ was obtained for double-edge V-notch rectangular specimens with a nominal root radius of 0.033 in. (0.84 mm). The experimental data are presented in Figure 5.19 where each data point is the average of several tests. The Jasper equation is used to fit the smooth bar data and produces a good representation of the data points obtained at $R = -1$, 0.1, 0.5, and 0.8. Three methods of representing the notch data are shown. In the first, only the alternating stress is reduced by the value of k_f for $R = -1$, which is approximately $k_f = 2.0$. This produces the poorest fit to these notch data. The second method uses a value of k_f that is linearly dependent on mean stress between a mean stress of zero and the ultimate stress, following the suggestion of Bell and Benham discussed above. This method produces a slightly better fit to the data and has the right general shape, but the curve falls above the experimental data points for non-zero mean stresses. The third and final method is just to apply the same value of k_f to all of the smooth bar data. This method produces a very good fit to all the data except at $R = 0.8$ where both plasticity and time-dependent ratcheting or creep are known to occur. In this particular example, the ability to fit the notch data with a model produces results somewhat different than in the earlier example where the surface finish and notch geometry were different, but the material was identical.

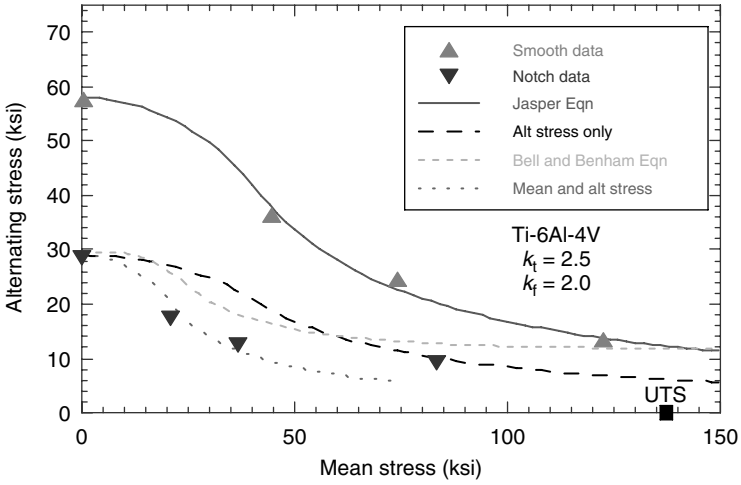


Figure 5.19. Smooth and notch fatigue data from [22] and methods for representing the notch curve.

It is often tempting to take a small amount of data that includes inherent scatter and postulate a new or modified theory that will fit the data better than existing models. So, not heeding my own advice, I offer the following as a method for fitting notch data based on the results shown in Figure 5.19. Following the concepts presented above that were put forth by Bell and Benham [18], the modification for the value of k_f is further modified slightly for the following reasons. If the notch behavior is purely elastic, then the value of k_f should not change for a given notch geometry. This region, on a Haigh diagram, will cover values of mean stress from zero until the value at which the maximum stress, S_{max}, equals the yield stress, S_y, or in terms of mean and alternating stress

$$S_m = S_m^* \quad \text{when} \quad S_m + S_a = S_y \tag{5.16}$$

where S_m^* is defined as a transition mean stress. For values of S_m below S_m^*, the fatigue notch factor is constant and equal to the value of k_f at $R = -1$, or zero mean stress, which we denote by k_{f0}. For mean stress values above S_m^*, we can allow the value of k_f to decrease linearly up to the ultimate strength, S_u. This can be expressed by the equation, which I will modestly call the "Nicholas equation," as

$$k_f = k_{f0}\left(1 - \frac{S_m - S_m^*}{S_u - S_m^*}\right) + \frac{S_m - S_m^*}{S_u - S_m^*} \tag{5.17}$$

In the above, the transition mean stress is calculated from Equation (5.16) based on the assumption that for a mild notch k_f is approximately equal to k_t. In reality, k_t relates the peak stress to the average stress so that k_t will govern when first yielding occurs

based on average stress values. Then, first yielding would occur as per Equation (5.16) which is based on smooth bar values. The concept behind proposed Equation (5.17) is that when the ultimate strength of the material with a notch is approached, the notch and the smooth bar ultimate strengths are nearly the same because both involve net-section yielding. Therefore, at the ultimate strength point, $k_f = 1$ for the notched specimen. The linear variation is the simplest way to transition from the mean stress where yielding first occurs to the ultimate strength. In the example shown in Figure 5.19, the value of k_f is overestimated for data at high R when using a constant value of k_f. If the "Nicholas equation" (5.17) is used, as shown in Figure 5.20, the resulting curve, based on a Jasper equation for representing the smooth bar data, produces an amazingly good fit to the limited experimental data points. For this material, the yield strength was 135 ksi and the transition mean stress $S_m^* = 122$ ksi. While the fit to a limited data set in itself does not completely prove or validate any such theory, the method has an advantage over using a single value of k_f. With a single value, the highest mean stress that can be predicted for notch data is S_u/k_{f0}. Since smooth bar data are not available beyond a mean stress equal to S_u, the range in which predictions can be made is limited as shown in Figure 5.19 (also in Figure 5.20), where the constant k_f equation terminates at a mean stress of under 75 ksi. The effect of using a constant value is to shrink the smooth bar curve radially inward along lines of constant R on a Haigh diagram. It makes no sense to try to extend the smooth bar equation to mean stresses beyond the ultimate strength. With the new formulation, the notch curve is extended to the ultimate strength of the material without having to extrapolate smooth bar data.

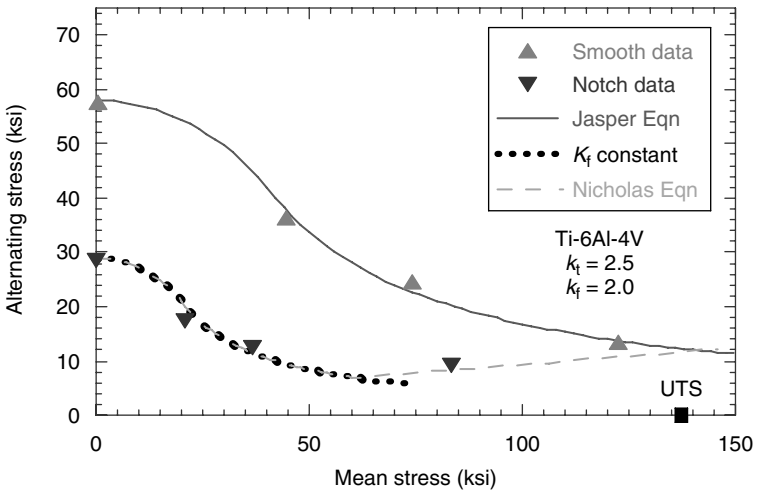


Figure 5.20. Illustration of the proposed Nicholas equation ability to fit notch data.

For the case of a straight-line modified Goodman equation used to represent smooth bar data, this new approach would be equivalent to following the line called "brittle" in Figure 5.11 from zero mean stress up to the transition mean stress, and then continuing with a straight line to S_u.

5.8.1. Negative mean stresses

Notched fatigue behavior for negative values of mean stress has received essentially no attention in the open literature. With the recent increased usage of compressive residual stresses for component fatigue life improvement, an increase in emphasis in this subject can be expected. The use of surface treatments that produce compressive residual stresses is discussed in Chapter 8. Here we discuss both uniform stress fields and those produced by notches. In Figure 5.21, three possible methods of extrapolating the modified Goodman equation* into the negative mean stress region are shown. Each one is a straight line, and the three lines are denoted by A, B, and C. There is no physical basis for any of the three lines, but lacking data in the negative mean stress region, these three lines cover a wide range of possible behavior in this region. For each of the lines, the notch fatigue behavior is assumed to be governed by either of the two equations. First, the fatigue notch factor is assumed to be linearly proportional to the mean stress so that

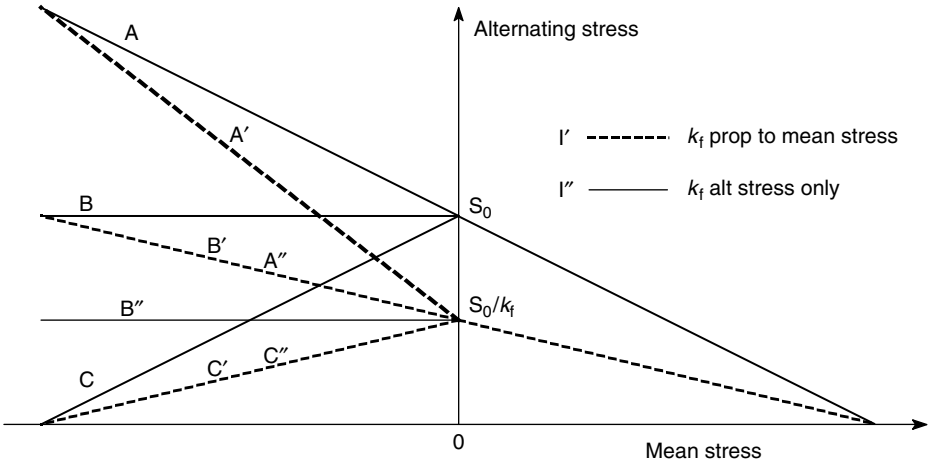


Figure 5.21. Representation of notch fatigue behavior for negative mean stress using three straight-line representations of a Haigh diagram.

* The modified Goodman equation is a straight line from the value of the alternating stress at zero mean stress to the ultimate stress at zero alternating stress.

the value of k_f goes from its reference value at $R = -1$ (zero mean stress) to unity at the ultimate strength point in both tension and compression. This is equivalent to using Equation (5.15) above with the added condition that $S_{un} = S_{up}$. The alternating stress at zero mean stress is this s_0/k_f. These curves are denoted by A′, B′, and C′ in the figure, corresponding to the un-notched curves A, B, and C, respectively. The second method of representing the notch fatigue behavior is to reduce only the alternating stress by the same factor, k_f, obtained (and defined) for $R = -1$. The curves for this condition are denoted by A″, B″, and C″. In the positive mean stress region, the two methods produce the same curve when the straight line is used to represent the un-notched behavior, as pointed out earlier. In the negative mean stress region, a range of predicted behavior can be seen. The wide variety of possible behavior, both for smooth and notched specimens, provides a compelling argument for the generation of data in the negative mean stress region before any meaningful modeling can be expected to be accomplished. At the time of this writing, no such data have been found. This discussion is limited to relatively blunt notches because the possibility of very sharp notches with small root radii closing under compressive loading is a distinct possibility.

5.9. FATIGUE LIMIT STRENGTH OF NOTCHED COMPONENTS

An engineering approach to notches of arbitrary size and geometry which may or may not have initial cracks has been developed by Hudak et al. [24]. It was developed to explain the behavior of specimens subjected to FOD which can cause both craters and cracks. It is based on a fracture-mechanics analysis using a concept similar to that of El Haddad, et al. [12] described earlier, that attempts to predict the type of behavior shown schematically earlier in this Chapter in Figure 5.6 where there are regions of growth to failure, no initiation or growth, and an intermediate region of initiation but no growth. The concepts are illustrated in Figure 5.22(a) where the regions of initiation and growth to failure (A), initiation and arrest (B), and no initiation (C) are shown schematically. The authors define a "worst case notch" as a value of k_t, defined as K_w, above which further increase in k_t no longer results in a decrease in threshold stress. In Figure 5.22(b), the same regimes are shown as a function of crack size for a fixed value of notch depth and different values of root radius. The upper and lower curves represent a large (ρ_3) and small (ρ_1) root radius, respectively, while the horizontal line represents the limiting radius, ρ_w, corresponding to K_w, above which crack arrest cannot occur (discussed earlier in this chapter). What distinguishes this work from previous analyses is that the crack-size effect is addressed by defining a crack-size dependent threshold in the form

$$\Delta K_{th}(a) = \Delta K_{th}(R)\sqrt{\frac{a}{a + a_0}} \tag{5.18}$$

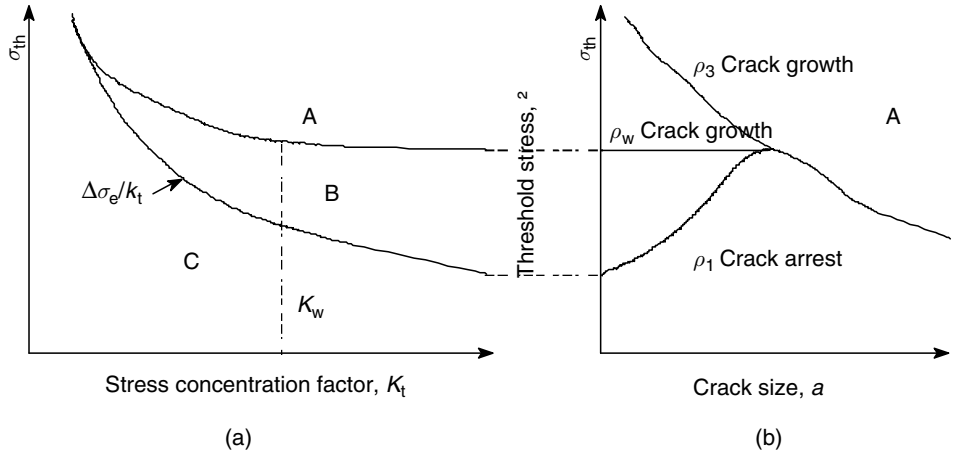


Figure 5.22. Schematic of regions of notch behavior.

where a_0 is the parameter defined by El Haddad in Equation (5.11) and ΔK_{th} is a function of stress ratio, R. The curves shown in Figure 5.22(b) are generated for a specific geometry and far-field loading by taking into account the actual stress field ahead of the notch and calculating K as a function of crack length. The analysis allows for the prediction of crack arrest or growth from a fracture-mechanics-based analysis and precludes the need to use an empirical relationship for k_f as a function of k_t. It further has demonstrated that the crack arrest which occurs at sharp notches depends both on the notch root radius and depth, as well as on the crack and specimen geometry. The authors contend that simple correlations between k_f and k_t are bound to break down for very deep, sharp notches of the type that can be produced by FOD (see Chapter 7). This same type of analysis can be used in contact fatigue problems (Chapter 6) where a complicated stress field, involving steep stress gradients, is produced by the contact loading and not by sharp notches. A further advantage over empirical approaches is that residual stresses, such as those occurring during FOD, or those produced by surface treatments such as shot peening, can be taken into account when calculating the stress intensity field ahead of the notch.

The worst-case-notch concept has been extended to take into account local notch plasticity. In addition, an approach that takes into account the surface area in the vicinity of a notch, similar in concept to the critical volume or critical distance approaches to notches, has been developed and is discussed later in this chapter. These two developments, that were accomplished under a recently completed HCF program within the Air Force, are described in detail in Appendix E.

5.9.1. Non-damaging notches

One of the earliest attempts to quantify the size of a non-damaging notch, a notch that does not reduce the fatigue limit strength of a material, is due to Lukas et al. [25]. Using linear elastic fracture mechanics, they compared the stress intensity of an edge crack of length l in a plate with that of a crack of the same length, l, emanating from an elliptical notch having a notch root radius ρ. For the former, the stress intensity is given as

$$K_{\text{plain}} = 1.12\sigma\sqrt{\pi l} \tag{5.19}$$

whereas for the crack from a notch, they used an approximation of results from FEM analysis of Newman [26] in the form

$$K_{\text{notch}} = \frac{1.12k_{\text{t}}\sigma\sqrt{\pi l}}{\sqrt{1+4.5(l/\rho)}} \tag{5.20}$$

where k_{t} is the elastic stress concentration factor for the notch with root radius ρ, and σ is the uniform far-field tensile stress. For both equations, a crack length $l = l_0$ is introduced for which length the stress intensity is the threshold stress intensity for a long crack, and the stress is the endurance limit stress for the smooth (σ_{e}) and notched (σ_{en}) specimens, respectively. Applying their assumption that the depth of microcracks on the surface of smooth specimens and the depth of microcracks at the notch root is the same at the fatigue limit, Equations (5.19) and (5.20) are combined to produce the following formula for the endurance limit at the notch,

$$\sigma_{\text{en}} = \frac{\sigma_{\text{e}}}{k_{\text{t}}}\sqrt{1+4.5\,(l_0/\rho)} \tag{5.21}$$

From a large number of experiments on specimens having various radii, the best value of l_0 was determined by trial and error fitting to Equation (5.21) for the FLS to be $100\,\mu$m for 15313 steel and $90\,\mu$m for copper.

The condition for a notch to be non-damaging with respect to the fatigue limit for the same applied stress level and the same crack size (l_0) is shown to be

$$\left(k_{\text{t}}^2 - 1\right)\rho \le 4.5 l_0 \tag{5.22}$$

If Equation (5.19) is used to relate l_0 to the long crack threshold and the smooth bar endurance limit, then l_0 becomes the same as a_0 in a Kitagawa diagram and the criterion for a non-damaging notch takes the form

$$\left(k_{\text{t}}^2 - 1\right)\rho \le 1.14\,(K_{\text{th}}/\sigma_{\text{e}})^2 \tag{5.23}$$

This approach, which attempts to correlate the behavior of a notch with that of a smooth bar, both of which have a crack, is essentially the same as using a Kitagawa diagram for

the notch geometry (with a crack) and finding the crack length (a_0) where the endurance limit and long crack threshold curve intersect. In this particular case, there is no El Haddad small crack correction.

5.10. SIZE EFFECTS AND STRESS GRADIENTS

Continuing attempts have been made over the years to predict the fatigue limit of notched components from data on smooth bars. The physical reasoning used has been that a critical volume of material must be subjected to a critical stress level, the smooth bar fatigue limit, in order for fatigue failure to occur. This postulate means that stress at a point, for example at a notch root, is not the sole governing criterion for fatigue to occur. The observations made that sharp notches have higher fatigue strengths than mild notches is partial evidence for such a theory. Since the calculation of average stresses over a volume is computationally intensive and impractical for many sharp notch geometries, the problem is often simplified to one or two dimensions. This still would involve determination of the average stress over some critical length. The simple solution for such a problem, adopted by many, has been to use the stress at a critical distance from the surface to represent the average stress over a larger distance. Critical volume approaches have been reviewed by Sheppard [27] and Taylor and O'Donnell [28]. The empirical relations between k_f and k_t, in many cases, are derived from determination of stresses over a critical length and some simplifying assumptions about the distribution of stresses in order to come up with a critical distance (see, for example, Peterson [4] who assumes a linear variation of stress from the notch root).

5.10.1. Critical distance approaches

The critical distance approach has the advantage over many other empirical approaches because it deals with both stress gradients and size effects. Taylor [13] shows, in fact, that sharp notches and fatigue cracks have some commonality, as observed experimentally, that the two behave similarly when the notch has a k_t or sharpness beyond which the FLS becomes coincidental with that of a crack of the same size. Taylor shows that the stress determined at a critical distance $a_0/2$, is the same for a sharp notch and a crack, where a_0 is the length parameter of El Haddad determined from Equation (5.11). Numerical results showing the stress distributions ahead of a circular notch of radius r, and of a crack of length a, are shown in Figure 5.23, for three different values of a/a_0; 0.1, 1.0, and 10. The thick lines show the stress distribution for the notch, while the thin lines represent that of the crack. The figure shows the overall distribution in (a), and a more detailed distribution near the notch or crack tip, in (b). The vertical dashed line is the location $a_0/2$ which represents the location where the local stress determines the fatigue

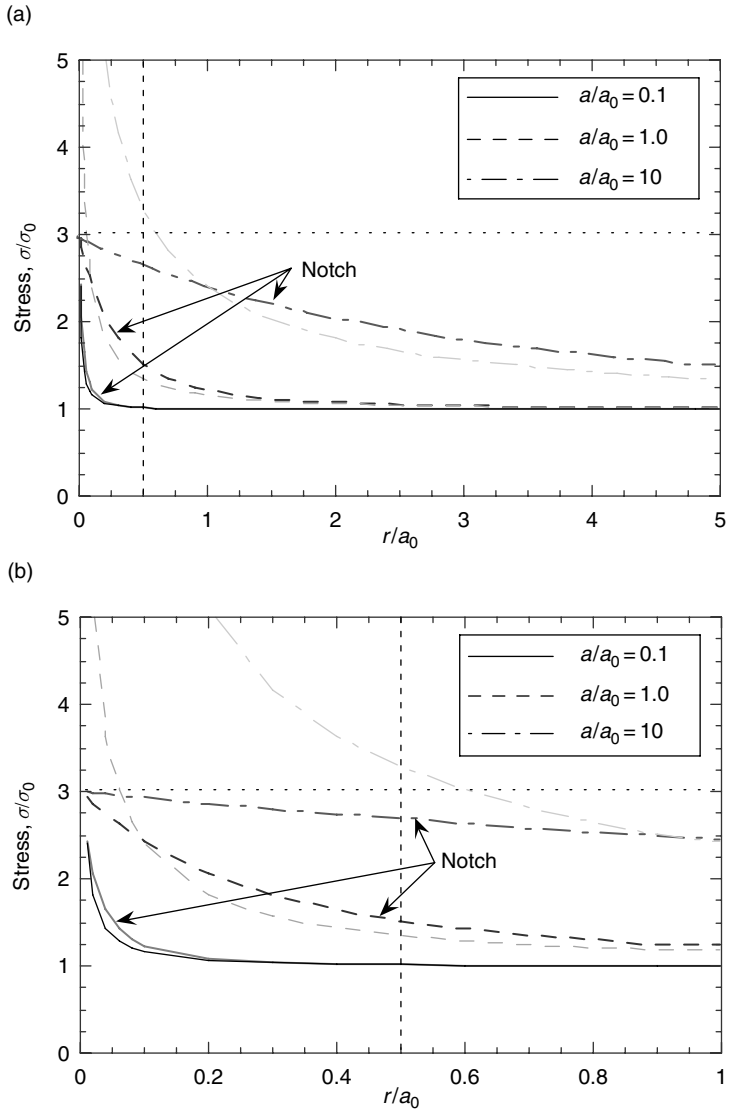


Figure 5.23. Numerical results showing the stress distributions ahead of a circular notch of radius, r, and of a crack of length, a. Dashed line is at $r = 0.5a_0$. Plots (a) and (b) have different scales for r/a_0.

strength based on smooth bar data at the same stress. As Taylor points out, for a very sharp notch having a small radius, or a crack of the same length, the stresses at this point are identical. For a large notch, the normalized stress approaches that corresponding to the stress concentration factor which is three for the circular notch. Taylor also shows

that the average stress over a length equal to $2a_0$ provides the same numerical results as the stresses at a point and, further, that the method produces the same prediction for small crack behavior as that of El Haddad et al. [12] as given in Equation (5.11).

The critical distance concept for notch fatigue may involve quantities other than uniaxial stress. Lanning et al. [21] review some approaches that involve use of a combination of hydrostatic and shear stress and crack propagation thresholds. From a large body of notch fatigue limit data generated on Ti-6Al-4V, they explored other quantities in a critical distance approach to see if the data could be consolidated. In addition to evaluating a quantity at a critical distance, they also used both an average value of a quantity and a weighted average over some distance. Quantities evaluated included stress range, mean stress, and elastic strain energy density. From FEM computations to obtain these quantities for cylindrical notched specimens of varying notch depths and radii including variations of applied stress ratio, R, some of which produced local notch plasticity, they found best-fit parameters for each modeling concept. The use of a single critical distance where the local stress range was evaluated produced the best overall correlation with the experimental data. The authors conclude that the approach is moderately successful but point out the difficulties that occur when local plasticity produces variations in R with distance from the notch and when very small notch sizes are included in the database.

A further attempt to find a quantity that can be used to consolidate notch data with smooth bar fatigue data using averaging over some critical distance was made by Naik et al. [29]. Two approaches were used involving the Findley parameter, one was evaluating the parameter at a critical distance, a_c, and the other used the average value of the same parameter over the same critical distance, a_c. They used the Findley parameter, FIN, for uniaxial stress in the form

$$\mathrm{FIN} = \tau_a + k\sigma_{max} \tag{5.24}$$

where k is a fitting parameter and τ_a and σ_{max} are the maximum shear stress amplitude and maximum normal stress on a critical plane that is defined as the plane where FIN is maximum. The parameter was shown to fit a large body of smooth bar fatigue data on Ti-6Al-4V at several values of stress ratio, R, as illustrated in Figure 5.24 from [29]. For those data, the best fit to the data is when the parameter has the form for an S–N type curve,

$$\mathrm{FIN} = 65{,}739N^{-0.6779} + 433.5N^{-0.0415} \tag{5.25}$$

To apply the parameter to notch data, the average value of the parameter over a distance a_c is called G_r, and is given by

$$G_r(N) = \frac{1}{a_c}\int_0^{a_c} \mathrm{FIN}(x, N)\,\mathrm{d}x = G_F \mathrm{FIN}_{smooth}(N) \tag{5.26}$$

where G_F is defined as a notch gradient parameter. In this formulation, the critical distance is not a material constant. Rather, the quantity G_F is found to be a constant

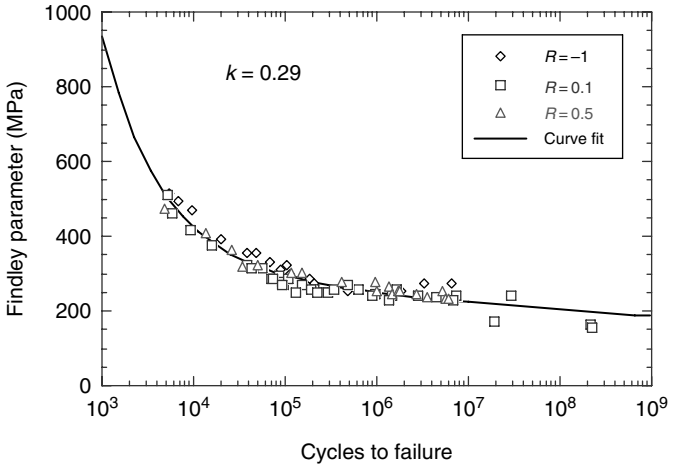


Figure 5.24. Findley parameter for cycles to failure in Ti-6Al-4V from smooth bar data [29].

from calculations involving a wide range of notch geometries. With G_F as a constant, a quantity s is computed for any value of stress ratio, R, from

$$s = \sqrt{1 + \left(\frac{1-R}{2k}\right)^2} \tag{5.27}$$

where k is the constant in the Findley parameter, Equation (5.24). A quantity A_0 is defined as

$$A_0 = \left(1 + \frac{2a_c}{\rho}\right) \tag{5.28}$$

where ρ is the notch root radius and a_c is the critical distance (not a constant). The authors derive the relation

$$(G_F - 2)\, A_0{}^2 + [G_F(s-1) + 2s]\, A_0 - 2(s-1) A_0{}^{3/2} - G_F s = 0 \tag{5.29}$$

from which A_0 can be calculated since G_F is a material constant and s is obtained from Equation (5.27) for any value of R. Once A_0 is found, the critical distance can be obtained from Equation (5.28) and used in Equation (5.26) to obtain the value of FIN from which number of cycles is determined using the equation that fits the smooth bar data – Equation (5.25) in this example. The ability to consolidate notch data using this approach is illustrated in Figure 5.25 where the constant $G_F = 1.16$. This constant was slightly different than the value of 1.21 obtained from a more limited set of notch fatigue data, but the correlation was quite similar. For the results shown in Figure 5.25, the critical

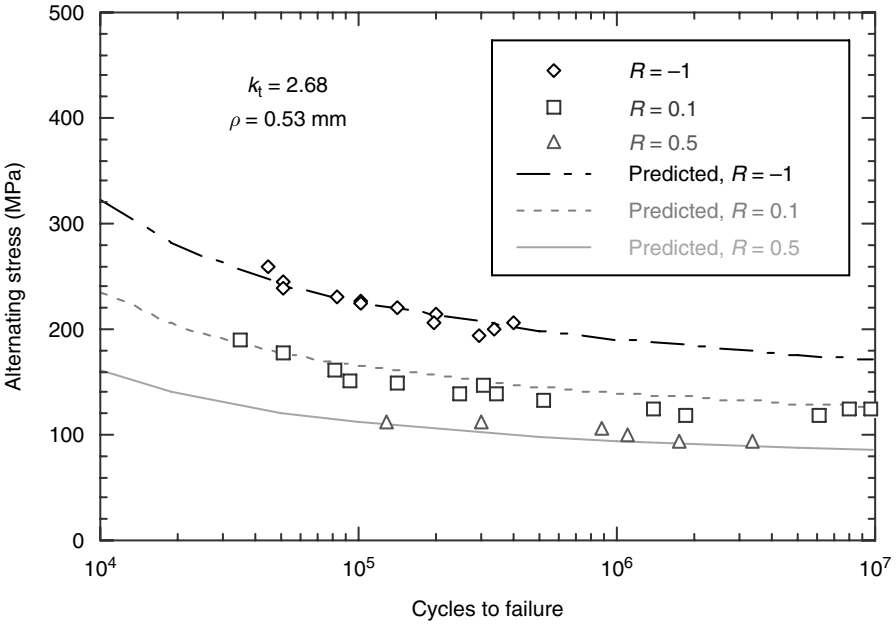


Figure 5.25. Comparison of predictions and experimental data for notch fatigue data in Ti-6Al-4V [29].

distance, a_c, was 0.074, 0.086, and 0.094 mm for $R = -1$, 0.1, and 0.5, respectively. What makes this approach work so well is the fact that G_F turns out to be a constant for a large body of data. This is analogous to finding a critical distance which is a constant for a material. In this case, the critical distance is computed from Equation (5.28) and is dependent on both stress ratio, R, and notch root radius, ρ.

It is also shown in [29] that the fatigue notch factor can be obtained from the following equation.

$$k_f = k_t \left(\frac{A_0 + s}{{A_0}^{3/2}(1+s)} \right) \tag{5.30}$$

5.11. ANALYSIS METHODS

In the work of Nisitani and Endo [16], the stress field ahead of an elliptical hole in an infinite plate subjected to remote tension, as shown in Figure 5.26, is reported as

$$\sigma_y(x) = \sigma_\infty \frac{m^4\xi^3 + m^2(m^2 - m - 3)\xi + m + 1}{(m-1)(m^2-1)} \tag{5.31}$$

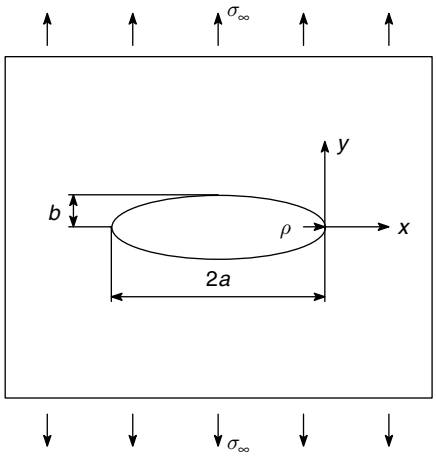


Figure 5.26. Schematic of elliptical hole in tension.

$$\xi = \sigma_\infty \frac{a+x}{\sqrt{a\rho + 2ax + x^2}} \sqrt{\frac{\rho}{a}}, \qquad m = \sqrt{\frac{a}{\rho}} \tag{5.32}$$

$$k_t = 1 + 2m \tag{5.33}$$

The authors note that the branch point in Figure 5.10, where a notch starts to behave like a crack, has a constant root radius, ρ, independent of notch depth for a given material. This constancy is attributed to the fact that the relative stress distribution near a notch root is determined by the notch root radius ρ alone. From experimental results and the analysis of a crack at the root of an elliptical hole, they demonstrate that the crack initiation limit curve and the crack propagation limit, and their intersection at the branch point (see Figure 5.10), can be determined by using only σ_{max} at the notch root and the notch root radius, ρ. The determination of these quantities, however, is based on fitting of experimental data to the theoretical curves. The unified treatment proposed in [16] can be summarized in a schematic of their approach shown in Figure 5.27. The limiting values of the nominal stress times k_t for crack initiation and propagation are shown as a function of $1/\rho$ for the elliptical notch. Points A and B correspond to the fatigue limit of a smooth bar and the branch point, respectively. The curves B–C and B–D bound the region where fatigue limit stresses for a sharp notch will fall whereas milder notch results will be on curve A–B. The experimentally observed dependence of the fatigue limit of an elliptical notch solely on notch root radius, ρ, and k_t, allows the construction of the curves in Figure 5.27 from results of only a limited number of fundamental experiments.

An alternate method for bridging the gap between fatigue limit of a notch (initiation limit) and the threshold stress intensity for a very sharp notch or crack has been developed

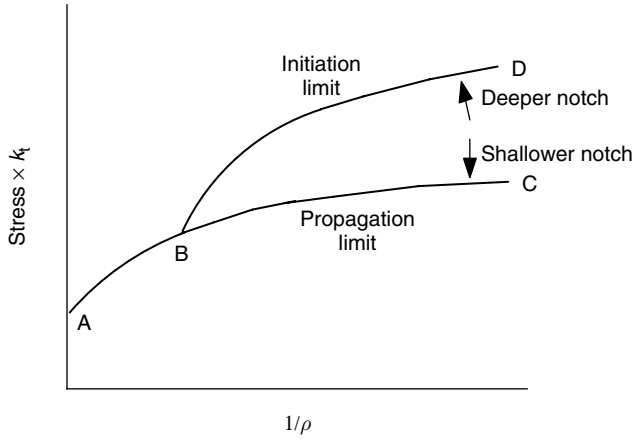


Figure 5.27. Schematic figure of crack initiation limit and crack propagation limit [16].

by Atzori and Lazzarin [30]. They extended the Kitagawa diagram for cracks to include blunt cracks (i.e. U-shaped notches) as illustrated schematically on Figure 5.28. Note the similarity to Figure 5.7 and the accompanying discussion earlier. For a very blunt notch, where a becomes large, the fatigue limit stress is simply $\Delta\sigma_0/k_t$, where $\Delta\sigma_0$ is the smooth bar fatigue limit and k_t is the elastic stress concentration factor. As the length factor a, which would be the depth of a U-shaped notch, decreases, this approximation becomes more conservative (line CD) so that below some critical value at $a = a^*$, the notch becomes a crack and the Kitagawa diagram becomes applicable as shown. It is easily shown from the definitions of the intersections of the ΔK_{th} line with σ_0 and

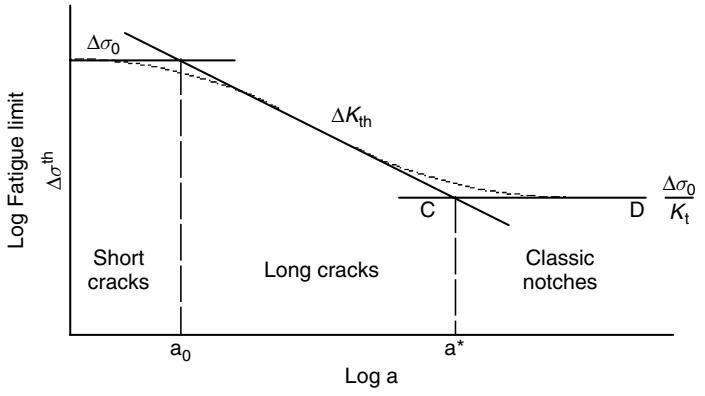


Figure 5.28. Fatigue behavior of a material weakened by notches or cracks [30].

σ_0/k_t being $a = a_0$ and $a = a^*$, respectively, that the following expression provides the value of a^*

$$k_t^2 = \frac{a^*}{a_0} \tag{5.34}$$

where a_0 is the standard definition used in a Kitagawa diagram for an edge crack characterized by

$$\Delta K_{th} = \Delta\sigma_{th}\sqrt{\pi a} \qquad a_0 = \frac{1}{\pi}\left[\frac{\Delta K_{th}}{\Delta\sigma_0}\right]^2 \tag{5.35}$$

If the theoretical elastic stress concentration factor for a notch is used, that is

$$k_t = 1 + 2\sqrt{\frac{a}{\rho}} \tag{5.36}$$

then for a very deep notch, where $a \gg \rho$, the notch root radius corresponding to $a = a^*$ is defined as ρ^* and is found to be $\rho^* = 4a_0$. Then, the threshold stress intensity for such a notch becomes

$$\Delta K_{th} = \frac{\Delta\sigma_0\sqrt{\pi\rho^*}}{2} \tag{5.37}$$

which the authors relate to the generalized stress intensity factor suggested by Tanaka [31] and Glinka [32] for rounded notches.

These results are interpreted as bridging the gap between the concepts of sensitivity to defects and notch sensitivity. The former refers to crack-like defects whereas the latter represents geometric stress raisers imposed into a material. From a phenomenological point of view, these can be substantially different. The modeling concepts tend to bridge this gap and provide a way of looking at the two as essentially the same problem.

The work in [30] has been extended to a more general geometry than the elliptical notch in an infinite plate by Atzori et al. [33] through the introduction of a shape factor as is done in fracture mechanics. Using a more general form of the stress intensity factor

$$\Delta K = \alpha\Delta\sigma\sqrt{\pi a} \tag{5.38}$$

the ΔK_{th} curve of Figure 5.28 is shifted down and to the left. The transition points $a = a_0$ and $a = a^*$ are replaced by $a = a_D$ and $a = a_N$, respectively, where the new points are defined as

$$a_D = \frac{a_0}{\alpha^2} \qquad a_N = \frac{a^*}{\alpha^2} = \frac{k_t^2 a_0}{\alpha^2} \tag{5.39}$$

where a_D is the intrinsic defect size. If the small crack correction of El Haddad is introduced, then the fatigue limit behavior of a component in the presence of a defect size close to a_D is given by

$$\frac{\Delta\sigma_{th}}{\Delta\sigma_0} = \frac{1}{\sqrt{\alpha^2 \frac{a}{a_0} + 1}} \tag{5.40}$$

If k_t is kept constant, the depth of a completely sensitive notch is now a_N.

This extension of previous work in [30] is presented as a "universal" diagram able to summarize experimental data related to different materials, geometry, and loading conditions. The diagram is applied both to the interpretation of the scale effect and to the surface finishing effect.

Ciavarella and Meneghetti [34] reviewed some of the empirical formulas developed for the fatigue strength of notched components that were based on concepts involving the relation of the fatigue strength with the stress at a certain distance or averaged over a certain distance ahead of a notch. This distance, often thought to be a microstructure-based quantity, has generally been used more as a fitting parameter for experimental notch fatigue data. Extrapolation to extremely sharp notches, where fracture mechanics controls, is often found to be inaccurate. The use of averaging of the stress ahead of a notch including very sharp notches (cracks) or using stress at some distance ahead of the notch is no better than the accuracy of the stress field solution for the particular notch. In comparing the formula for crack-like behavior as cracks get small due to El Haddad, often shown on a Kitagawa diagram, a modified version of the notch formula of Neuber is proposed in [34]. This involves simply using the definition of k_t for the elliptical notch in an infinite plate, resulting in a "Neuber modified" equation

$$k_f = 1 + \frac{k_t - 1}{1 + \frac{k_t - 1}{\sqrt{a/a_0}}} \tag{5.41}$$

which compares favorably with the El Haddad formula

$$\Delta K_{th} = \Delta\sigma_{th}\sqrt{\pi(a + a_0)} \tag{5.42}$$

The modified Neuber formula is shown to be slightly more conservative in the small crack regime. Further, it has the correct asymptotic behavior for blunt notches as $\rho \to \infty$, namely that $k_f \to k_t$.

Tanaka [31] first noticed that for a sharp notch, averaging the stress over a characteristic distance l_0 then, in order to match the fatigue limit for arbitrarily small cracks, l_0 must be equal to $2a_0$, where a_0 is the El Haddad transition point on the Kitagawa diagram (see also Taylor [13]). From this, it is shown that the following expression holds true:

$$k_f = \sqrt{1 + \frac{a}{a_0}} \tag{5.43}$$

This is referred to as the El Haddad formula. Ciavarella and Meneghetti then proposed two possible formulations for describing the notch fatigue limits covering the entire range from sharp notches, which act like cracks, to blunt notches. In the dual models proposed, the two curves covering different parts of the diagram shown earlier in Figure 5.28 are made continuous at a transition point. The first model proposes Equation (5.43) for $a < a_c$ and the following equation from Lukas and Klesnil [35] for $a > a_c$

$$k_f = \frac{k_t}{\sqrt{1 + \dfrac{(k_t - 1)^2}{a/a_0}}} \tag{5.44}$$

where the transition point is found as:

$$a_c = a_0(k_t - 1) \tag{5.45}$$

The second proposed formulation uses Equation (5.43) for $a < a^*$ and simply $k_f = k_t$ as illustrated in Figure 5.28 where a^* is defined in Equation (5.34). Both formulations were found to provide a reasonably good representation of FLSs from a large body of notch fatigue data. What the results illustrate is that there is no one single formulation that is able to represent the wide range of notch data available in the literature. By representing portions of the data, a better fit can be achieved. Notice that in both cases, the authors use the El Haddad representation of sharp notch, crack-like data, which appears to provide a good fit in the sharp notch region. The difference between the two formulations for this region is in the transition point to a blunt notch model. In the first method, the transition is at a_c, while in the second, it is at a^*. These quantities can be compared through the following formula, using Equations (5.34) and (5.45):

$$a^* = k_t^2 a_0 > a_c = a_0(k_t - 1) \tag{5.46}$$

which illustrates that the two criteria coincide when the notch depth is lower than a_c. For $a > a_c$, the second criterion using $k_f = k_t$ is more conservative but it lacks the smooth transition of the other.

5.12. EFFECTS OF DEFECTS ON FATIGUE STRENGTH

While much analysis has been conducted on what may be described as ideal cracks, many applications requiring use of a fatigue threshold in HCF design deal with real defects in the form of voids or inclusions, for example. For these irregular shapes, an engineering stress intensity has been developed that is based on the "area" of the crack. The area is defined as the projection of the actual area of the crack or defect onto a plane

normal to the applied stress. The maximum value of the stress intensity can be written, approximately, as

$$K_{\text{Imax}} = C\sigma_0\sqrt{\pi\sqrt{\text{area}}} \tag{5.47}$$

where σ_0 is the maximum applied tensile stress and "area" is defined as the projected area. The constant C has been estimated to be 0.5 for surface defects and 0.65 for internal defects [36]. These approximations are a good engineering tool but are subject to limitations on crack size, crack geometry, and material microstructure. The evolution and limitations of these equations and their application to engineering problems is discussed thoroughly in the book by Murakami [36]. These equations have seen extensive use in the work on gigacycle fatigue, discussed in Chapter 2, where failure at ultra-long fatigue lives and establishment of fatigue limit stresses or endurance limits deal with crack initiation from internal defects.

If a fracture mechanics approach using a threshold value is not adapted for small inclusions in a material, then the FLS approach can be used. Problems such as foreign object damage (see Chapter 7) can be addressed with a threshold for an equivalent crack. Many other problems in HCF center around the issue of the effect of odd-shaped inclusions on the FLS of a material. The effects of small defects in materials, particularly steels, is discussed in detail by Murakami [36]. In that book, he provides formulas for the fatigue limit strength, σ_{w}, of a steel with a non-metallic inclusion as

$$\sigma_{\text{w}} = \frac{C(H_{\text{V}} + 120)}{(\sqrt{\text{area}})^{1/6}} \tag{5.48}$$

where H_{V} is the Vickers hardness in units of kgf/mm^2, $\sqrt{(\text{area})}$ is in μm, and C is a constant depending on the location of the inclusion. For an inclusion in contact with the surface, $C = 1.41$, while for an internal inclusion, $C = 1.56$ [36]. Murakami also provides an empirical formula for the upper bound to the FLS of a steel having no inclusions as

$$\sigma_{\text{wu}} = 1.6H_{\text{V}} \tag{5.49}$$

For the two cases of internal and surface connected inclusions, the maximum size of an inclusion that will have no effect on the fatigue strength of a steel is easily calculated from Equations (5.48) and (5.49). The results, in terms of the parameter $\sqrt{\text{area}}$, are presented in Figure 5.29 which shows that for all but the softest of steels, as measured by the Vickers hardness, inclusions have to be smaller than several microns in order not to affect the FLS. On the other hand, as the Vickers hardness decreases below approximately $H_{\text{V}} = 200$, the material is very intolerant to inclusions of much larger sizes.

It can be noted that the form of the Murakami Equation (5.48) involves an inclusion dimension to the 1/6 power in the denominator. Contrast this with the equations for a

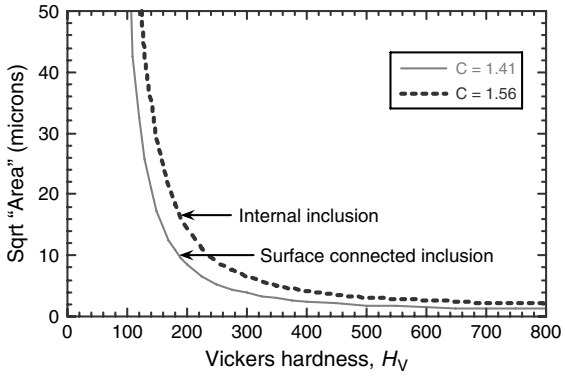


Figure 5.29. Critical dimensions for inclusions in steels (formulas from [36]).

long crack that have the crack length raised to the $-1/2$ power, denoting a square root singularity. If the Kitagawa diagram is used to compare FLSs to a corresponding crack length, the resultant diagram in dimensionless form is shown in Figure 5.30 where the El Haddad short crack correction has been introduced. As shown in the diagram, long cracks corresponding to $a/a_0 \gg 1$ have a slope $= -1/2$ while short cracks approach zero slope corresponding to the normalized endurance limit stress $= 1$. At $a/a_0 = 1$, the slope on this log–log plot is -0.25. The Murakami equation provides for a slope of $-1/6$ which is indicated in the figure. This slope is tangent to the Kitagawa diagram curve for a range of crack lengths slightly below the region where $a = a_0$, the El Haddad short crack parameter. The actual tangent point where the slope $= -0.167$ $(-1/6)$ is at $a/a_0 = 0.46$. The values shown in Figure 5.29 correspond to where this curve would intersect the endurance limit for given values of Vickers hardness number. These computations and

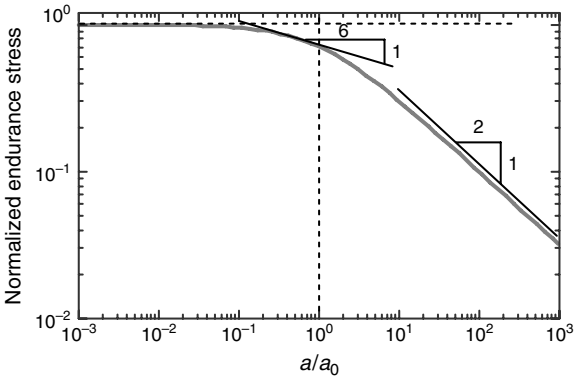


Figure 5.30. Normalized Kitagawa diagram showing slope of Murakami equations.

plots indicate that the simplified formula of Murakami, Equation (5.48), for different values of H_V, seems to follow the same trend as the El Haddad equation for the endurance limit stress for small cracks.

5.13. NOTCH FATIGUE AT ELEVATED TEMPERATURE

In Section 2.6, the construction of a Haigh diagram at elevated temperature was illustrated for a single crystal material that showed evidence of creep behavior at certain maximum or mean stress levels. In this chapter, Section 5.8, the effects of plastic deformation of notches on the shape of a Haigh diagram for notched components were discussed. Here, that discussion is expanded to include the effects of creep, typical of elevated temperature behavior, on the construction of a Haigh diagram for a notched component. There are two main considerations in this problem: the stress gradient present at a notch or stress concentration and the redistribution of stress due to inelastic deformation (creep), particularly at a region of high stress and stress gradients such as a notch. There are many analytical and empirical methods for tackling such a problem and the specific material, geometry, and loading conditions will dictate which approach is better. For illustrative purposes, we refer to the work of Harkegard [37] who provides details for a rather simple approach.

The starting point for development of a Haigh diagram for notched components in the creep regime is to consider the smooth bar behavior at temperatures below the creep regime. Such behavior can be easily represented as a straight line in a Haigh diagram that goes from the fully reversed ($R = -1$) alternating stress to the true fracture stress, σ_f. This slight variation of the Goodman equation is accurate only if there is no yielding at the notch root. This differs from some of the previous formulations for notch behavior because it considers only the local stresses at the notch root as opposed to average stresses and the use of the elastic stress concentration factor, k_t. Because of stress gradients, this is a conservative approach based on k_t, not k_f. The use of true fracture stress changes the Goodman equation for smooth bar behavior [Equation (5.3) in Chapter 2],

$$\sigma_a = \sigma_{-1}\left(1 - \frac{\sigma_m}{\sigma_u}\right) \tag{5.50}$$

that ends at the ultimate stress, σ_u, to the modified form

$$\sigma_a = \sigma_{-1}\left(1 - \frac{\sigma_m}{\sigma_f}\right) \tag{5.51}$$

where the true fracture stress, σ_f, is defined as

$$\sigma_f = \frac{\sigma_u}{(1 - Z)} \tag{5.52}$$

and Z is the reduction in area in a tension test. It is recognized in the construction of the Haigh diagram for use in notched components that at the root of a notch, localized plastic flow can take place upon the first load application. Thus, the maximum stress that takes place is limited to the yield strength of the material if there is little strain hardening or small plastic strains. To account for this, the "fictitious" mean stress is used in plotting the Haigh diagram as depicted in Figure 5.31. The fictitious or nominal stress is computed assuming purely elastic behavior. However, the notch root stress is limited by the yield strength, thus the curve is limited by the line denoted by $s_{\max} = s_y$ as shown in the figure (see also Figure 5.15 and the discussion accompanying it). For elastic behavior at the notch root, the smooth bar and notched behavior are assumed to be governed by the local stress, with gradients not considered. As the local stresses increase with increasing mean stress, the behavior at the notch root becomes inelastic, but the stresses are assumed to not exceed the yield strength. For nominal (fictitious) stresses above the yield stress, the maximum local stress is assumed to be the yield stress. Thus, in Figure 5.31, for fictitious mean stresses above that where yielding first takes place, the allowable alternating stress is the same as that at the yield condition, as shown by the horizontal line in the figure.

If the behavior of the material is only known at room temperature, it can be extended to higher temperatures below the creep regime through the use of the fatigue ratio, V_w,

$$V_w = \frac{\sigma_0(T)}{\sigma_u(T)} \tag{5.53}$$

by assuming V_w to remain constant as temperature increases. In this definition, σ_0 is the alternating stress at zero mean stress and σ_u is the ultimate stress. For the case where creep occurs in the material at high temperatures, a fatigue limit no longer exists [20]. Now, the behavior is time-dependent and number of cycles is eventually replaced by time as illustrated in Chapter 2 when discussing the Haigh diagram for a single crystal material at elevated temperature (see Section 2.6). In the present approach, the fatigue ratio, Equation (5.53), is used in the following form:

$$V_r = \frac{\sigma_A(t, T)}{\sigma_u(t, T)} \tag{5.54}$$

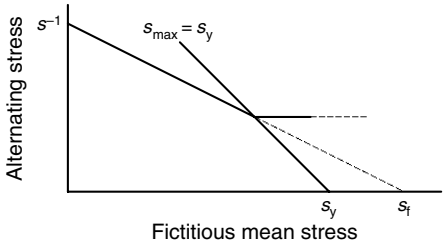


Figure 5.31. Haigh diagram of a notch component below the creep regime (after [37]).

where σ_A is the fatigue strength at an arbitrary mean stress and depends not only on temperature but on time in order to account for the time-dependent behavior. This formula is based on the assumption that the fatigue ratio is a function of the creep rupture strength only. The formulation goes on to use a "universal" empirical relation between the fatigue ratio, V_r, and the normalized creep rupture strength, r,

$$r = \frac{\sigma_u(t, T)}{\sigma_u(20\,^\circ\mathrm{C})} \tag{5.55}$$

The empirical relationship is of the form

$$V_r = A_r r^{-\alpha} R \tag{5.56}$$

By applying this relation to data at two values of stress ratio, $R = -1$ (fully reversed loading at zero mean stress) and $R = 0$ (pulsating tension), the coefficients A_r and α_R can be obtained. From these, the fatigue strength of a smooth bar at $R = -1$ and $R = 0$ can be determined at any temperature in the creep regime. At that temperature, the Haigh diagram is plotted as shown in Figure 5.32 where the two quantities representing the fatigue strengths at two values of R are connected by a straight line. Using the recommendation of Forrest [20], the diagram is cut by a vertical line through the creep rupture strength, indicating a weak interaction between fatigue and creep damage.

To apply this diagram to a notched component, consideration has to be given to the fact that stresses at the notch root ($= k_t S_m$), where the geometry can be defined by an elastic stress concentration factor, k_t, will relax with time toward the nominal (fictitious) mean stress level, S_m. The fatigue loading is then considered to be allowable by comparing the nominal mean stress level, S_m, and the alternating stress at the notch with the FLS based on smooth bar tests as illustrated in Figure 5.33. The lower curve is that shown in Figure 5.32 when the value of k_t is not known. According to Forrest [20], it is reasonable to assume that the mean stress component will not be affected by a notch and that the alternating stress component will be reduced by the fatigue notch factor, k_f. If k_t is known, k_t can be substituted for k_f for a conservative estimate. This produces the upper curve in Figure 5.33 for a known k_t.

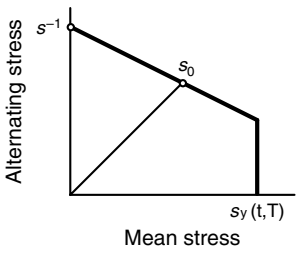


Figure 5.32. Haigh diagram of a smooth component in the creep regime (after [37]).

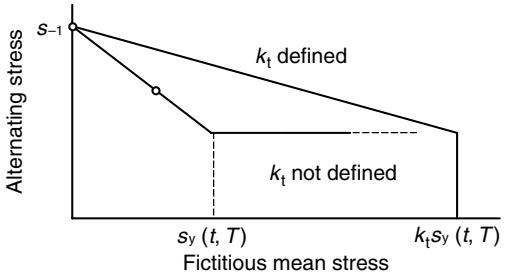


Figure 5.33. Haigh diagram of a notched component in the creep regime (after [37]).

As pointed out by Forrest [20], the fatigue strength at elevated temperature can be represented on a Haigh diagram by a series of contours that represent failure at a given time. Each point on a contour represents a combination of mean and alternating strength corresponding to that particular time. For low mean stress, the alternating stress is dominated by the fatigue behavior (number of cycles), whereas for large mean stresses, the behavior is primarily creep. The behavior thus goes from the alternating fatigue strength ($R = -1$) to the creep rupture strength. A plot such as Figure 5.34 is for a single temperature so that a complete description of a material would have to include a sufficient number of Haigh diagrams, or analytical expressions, to represent the material behavior at different temperatures. One method for representing the Haigh diagram for creep–fatigue behavior is to represent the mean and alternating stresses in normalized form as shown in Figure 5.35 [20]. The alternating stress is normalized with respect to the alternating fatigue strength corresponding to an appropriate (large) number of cycles as is done in a conventional Haigh diagram. The mean stress is normalized with respect to the creep rupture strength based on an acceptable (large) time to rupture for a given application. Experimental data show that, for many materials, both the Goodman straight line and the Gerber parabola are overly conservative under combined creep and fatigue loading. A circular arc is suggested as being more representative of real material behavior [20].

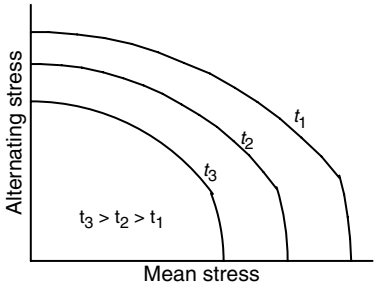


Figure 5.34. Creep rupture curves at elevated temperature.

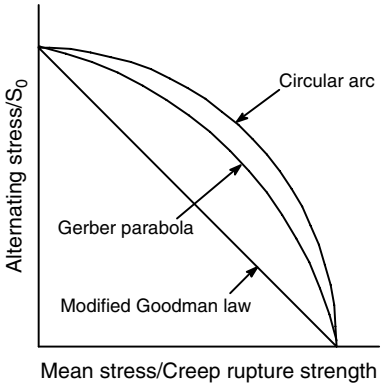


Figure 5.35. Normalized creep curves (after [20]).

Finally, an alternative empirical relation that involves a straight line Goodman equation on a Haigh diagram, but using the tensile strength as discussed earlier, can be used to represent the combined creep and fatigue behavior on a Haigh diagram at elevated temperatures. For each temperature, a different line represents the data as illustrated in Figure 5.36 which appears in [35]. The restriction in this method of representing data is that the static stress does not exceed the creep rupture strength at any temperature. Forrest claims that the straight line curves, truncated by the creep rupture stress, represent data as well as the circular arc method at high temperatures and is "a better guide to fluctuating fatigue strengths at moderate temperatures. That this criterion fits the experimental data reasonably closely is an indication that in general there is little interaction between the creep and fatigue processes" (see [20], p. 248).

The discussion above illustrates some of the complexities in designing for fatigue under non-zero mean stress in the creep regime where the static (creep rupture) strength depends on time (or frequency of loading) whereas the alternating stress capability under zero

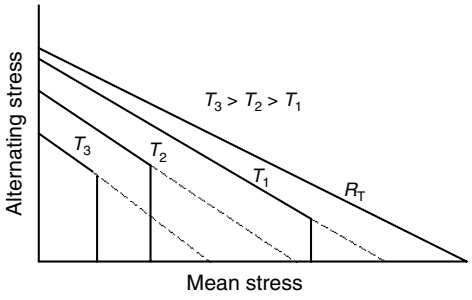


Figure 5.36. Creep–fatigue Haigh diagram (after [20]).

mean stress depends on number of cycles. For a fatigue limit, both a maximum number of cycles as well as a maximum exposure time have to be established for a particular design, whether or not the application is for a smooth component or one containing a notch or other stress raiser.

REFERENCES

1. Schütz, W., "A History of Fatigue", *Engineering Fracture Mechanics*, **54**, 1996, pp. 263–300.
2. Weixing, Y., Kaiquan, X., and Gu, Y., "On the Fatigue Notch Factor, K_f", *Int. J. Fatigue*, **4**, 1995, pp. 245–251.
3. Neuber, H., *Theory of Notch Stresses: Principle for Exact Stress Calculations*, Edwards, Ann Arbor, Mich., 1946.
4. Peterson, R. E., "Notch Sensitivity", *Metal Fatigue*, G. Sines and J.L. Waisman, eds, McGraw-Hill, New York, 1959, pp. 293–306.
5. Heywood, "Stress Concentration Factors, Relating Theoretical and Practical Factors in Fatigue Loading", *Engineering*, **179**, 1955, pp. 146–148.
6. Dowling, N.E., in *Mechanical Behavior of Materials*, 2nd Edition, Prentice Hall, Upper Saddle River, New Jersey, 1999.
7. Haritos, G.K., Nicholas, T., and Lanning, D.B., "Notch Size Effects in HCF Behavior of Ti-6Al-4V", *Int. J. Fatigue*, **21**, 1999, pp. 643–652.
8. Smith, R.A., and Miller, K.J., "Fatigue Cracks at Notches", *Int. J. Mech. Sci.*, **19**, 1977, pp. 11–22.
9. Peterson, R.E., "Stress Concentration Factors", John Wiley & Sons, Inc., New York, 1974, p. 22.
10. Smith, R.A., and Miller, K.J., "Prediction of Fatigue Regimes in Notched Components", *Int. J. Mech. Sci.*, **20**, 1978, pp. 201–206.
11. Kitagawa, H. and Takahashi, S., "Applicability of Fracture Mechanics to very Small Cracks or the Cracks in the Early Stage", *Proc. of Second International Conference on Mechanical Behaviour of Materials*, Boston, MA, 1976, pp. 627–631.
12. El Haddad, M.H., Dowling, N.F., Topper, T.H., and Smith, K.N., "J Integral Applications for Short Fatigue Cracks at Notches", *Int. J. Fract.*, **16**, 1980, pp. 15–24.
13. Taylor, D., "Geometrical Effects in Fatigue: A Unifying Theoretical Model", *Int. J. Fatigue*, **21**, 1999, pp. 413–420.
14. Taylor, D., "A Mechanistic Approach to Critical-Distance Methods in Notch Fatigue", *Fatigue Fract. Engng Mater. Struct.*, **24**, 2001, pp. 215–224.
15. Miller, K.J., "The Two Thresholds of Fatigue Behaviour", *Fatigue Fract. Engng Mater. Struct.*, **16**, 1993, pp. 931–939.
16. Nisitani, H. and Endo, M., "Unified Treatment of Deep and Shallow Notches in Rotating Bending Fatigue", *Basic Questions in Fatigue: Volume I, ASTM STP 924*, J.T. Fong and R.J. Fields, eds, American Society for Testing and Materials, Philadelphia, 1988, pp. 136–153.
17. Isibasi, T., *Prevention of Fatigue and Fracture of Metals*, Yokendo, Tokyo, 1954.
18. Bell, W.J. and Benham, P.P., "The Effect of Mean Stress on Fatigue Strength of Plain and Notched Stainless Steel Sheet in the Range from 10 to 10^7 Cycles", *Symposium on Fatigue Tests of Aircraft Structures: Low-Cycle, Full-Scale, and Helicopters, ASTM STP 338*, American Society for Testing and Materials, Philadelphia, 1962, pp. 25–46.

19. Gunn, K., "Effect of Yielding on the Fatigue Properties of Test Pieces Containing Stress Concentrations", Aeronautical Quarterly, **6**, 1955, pp. 277–294.
20. Forrest, P.G., *Fatigue of Metals*, Pergamon Press, Oxford, 1962 (U.S.A. Edition distributed by Addison-Wesley Publishing Co., Reading, MA).
21. Lanning, D.B., Nicholas, T., and Haritos, G.K., "On the Use of Critical Distance Theories for the Prediction of the High Cycle Fatigue Limit in Notched Ti-6Al-4V", *Int. J. Fatigue*, **27**, 2005, pp. 45–57.
22. Gallagher, J.P. et al., "Improved High Cycle Fatigue Life Prediction", *Report # AFRL-ML-WP-TR-2001-4159*, University of Dayton Research Institute, Dayton, OH, January, 2001 (on CD ROM).
23. Wagner, L., "Effect of Mechanical Surface Treatments on Fatigue Performance of Titanium Alloys", *Fatigue Behavior of Titanium Alloys*, R.R. Boyer, D. Eylon, and G. Lutjering, eds, The Minerals, Metals & Materials Society, 1999, pp. 253–265.
24. Hudak, S.J., Jr., Chan, K.S., Chell, G.G., Lee, Y.-D., and McClung, R.C., "A Damage Tolerance Approach for Predicting the Threshold Stresses for High Cycle Fatigue in the Presence of Supplemental Damage", *Fatigue – David L. Davidson Symposium*, K.S. Chan, P.K. Liaw, R.S. Bellows, T.C. Zogas and W.O. Soboyejo, eds, TMS (The Minerals, Metals & Materials Society), Warrendale, PA, 2002, pp. 107–120.
25. Lukas, P., Kunz, L., Weiss, B., and Stickler, R., "Non-Damaging Notches in Fatigue", *Fatigue Fract. Engng Mater. Struct.*, **9**, 1986, pp. 195–204.
26. Newman, J.C., "An Improved Method of Collocation for the Stress Analysis of Cracked Plates with Various Shaped Boundaries", *NASA Technical Note D-6376*, 1971.
27. Sheppard, S.D., "Field Effects in Fatigue Crack Initiation: Long Life Fatigue Strength", *Jour. Of Mech. Design, Trans ASME*, **113**, 1991, pp. 188–194.
28. Taylor, D. and O'Donnell, M., "Notch Geometry Effects in Fatigue: A Conservative Design Approach", *Engineering Failure Analysis*, **1**, 1994, pp. 275–287.
29. Naik, R.A., Lanning, D.B., Nicholas, T., and Kallmeyer, A.R., "A Critical Plane Gradient Approach for the Prediction of Notched HCF Life", *Int. J. Fatigue*, **27**, 2005, pp. 481–492.
30. Atzori, B. and Lazzarin, P., "Notch Sensitivity and Defect Sensitivity under Fatigue Loading: Two Sides of the Same Medal", *Int. J. Fract.*, **107**, 2000, pp. L3–L8.
31. Tanaka, K., "Engineering Formulae for Fatigue Strength Reduction due to Crack-Like Notches", *Int. J. Fract.*, **22**, 1983, pp. R39–R46.
32. Glinka, G., "Energy Density Approach to Calculation of Inelastic Stress-Strain Near Notches and Cracks", *Engng Fract. Mech.*, **22**, 1985, pp. 485–508.
33. Atzori, B., Lazzarin, P., and Meneghetti, G., "Fracture Mechanics and Notch Sensitivity", *Fatigue Fract. Engng Mater. Struct.*, **26**, 2003, pp. 257–267.
34. Ciavarella, M., and Meneghetti, G., "On Fatigue Limit in the Presence of Notches: Classical vs. Recent Unified Formulations", *Int. J. Fatigue*, **26**, 2004, pp. 289–298.
35. Lukas, P. and Klesnil, M., "Fatigue Limit of Notched Bodies", *Mater. Sci. Eng.*, **34**, 1978, pp. 61–69.
36. Murakami, Y., *Metal Fatigue: Effects of Small Defects and Nonmetallic Inclusions*, Elsevier Science, Ltd, Kidlington, Oxford, 2002.
37. Harkegard, G., "High-Cycle Fatigue Design of Steam-Turbine Blades at Elevated Temperature", *Swedish Symposium on Classical Fatigue*, N.-G. Ohlson and H. Norberg, eds, Uddeholm Research Foundation, Sunne, Sweden, 1985.

Chapter 6
Fretting Fatigue

6.1. INTRODUCTION

Fretting fatigue is a type of damage occurring in regions of contact where small relative tangential motion occurs between the two bodies in contact that are under compressive load. Fretting fatigue typically involves a contact region where both complete and partial slip occur as discussed below. It is usually associated with loading conditions where one of the components is subjected to bulk loading, which can cause cracks formed locally near edges of contact to propagate. Such conditions can lead to premature crack initiation and failure. Fretting-fatigue damage in blade/disk interfaces has been indicated as the cause of many unanticipated disk and blade failures in gas turbine engines. As the magnitude of relative motion in the contact region increases, the nature of the damage changes to what is commonly referred to as "galling" or "wear." The emphasis in this chapter will be on fretting fatigue that involves very small relative motion.

Under laboratory conditions, the synergistic effects of the many parameters involved in fretting fatigue make determination and modeling of mechanical behavior extremely difficult. In particular, the stress state in the contact region involves very high peak stresses, extremely steep stress gradients, multiaxial stress states, and differing mean stresses. Further, there is controversy over whether the problem is primarily one of crack initiation or one involving a crack propagation threshold, and whether or not stress states rather than surface conditions play a major role in the observed behavior. All of these issues will be addressed in this chapter.

Fretting fatigue is generally associated with HCF, whereas wear and galling are more concerned with LCF. This is a broad generalization, but for the purposes of discussing HCF it is adequate to make such a distinction. In particular, fretting fatigue under HCF conditions is normally associated with contact conditions where a part of the contact region is in total contact (stick) while the edges of contact undergo small relative displacements in the tangential direction (slip). Such relative displacements are typically of a magnitude of tens of microns or less. The slip region may be very small, only at the very edge of contact, or may cover a considerable percent of the contact area. Additionally, due to the back and forth sliding that takes place and the general nonlinearity of contact problems, the boundary between stick and slip may move back and forth on every cycle and never reach a single constant location. A schematic of fretting-fatigue contact between a pad (top) and a specimen (bottom) is shown in Figure 6.1. There, the specimen represents half of a real specimen thickness (by symmetry) and is loaded by a bulk load T. The applied

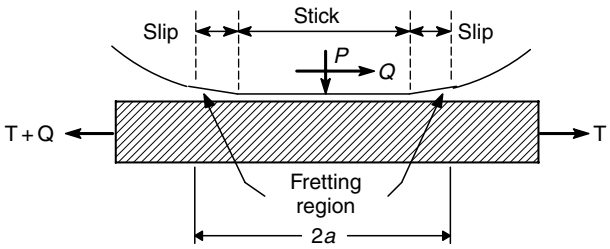


Figure 6.1. Schematic of fretting region showing applied forces.

normal and tangential loads are denoted by P and Q, respectively. Under typical stick–slip conditions, part of the contact region undergoes no relative displacements between pad and specimen (stick) while the edges undergo slip. The maximum slip occurs at the deformed edge of contact, at the positions that are at a distance $2a$ apart in the figure. Beyond those locations, there is no contact. Under large shear forces, specifically when the ratio Q/P reaches the value of the average coefficient of friction (COF), the entire region may undergo slip.

From both experimental observations and theoretical analysis it has been found that contact conditions in fretting change with increasing displacement amplitude [1]. Three regions are normally defined under constant normal force and oscillating tangential force. These regions are referred to as "stick," "mixed stick–slip," and "total slip." Each corresponds to a range of displacement amplitudes as depicted schematically in Figure 6.2 taken from [1]. The damage in these three regions can be characterized as low damage fretting, fretting fatigue, and fretting wear, respectively. As noted in the schematic, the lowest fatigue lives are associated with the fretting-fatigue region, the subject of this section. It is noteworthy that the lowest lives are not associated with the lowest or largest slip amplitudes, but with intermediate values. These values can cover a range of from about 5 to 50 μm, but will depend in general not only on the materials but also on the contact stresses. In addition to these three regions, a limiting region of large amplitudes in which wear mechanisms and wear rates become identical to those in unidirectional sliding is defined as the reciprocating sliding regime [1]. This occurs at the right side of the schematic of Figure 6.2 where both amplitude and fatigue life would be represented on a logarithmic scale and amplitudes in this region could approach 1 mm. It can be noted that the same experimental conditions are not necessarily used when obtaining data on effects of slip amplitude and even the local conditions are somewhat different. Very small values of slip are normally obtained under stick–slip conditions where computations or indirect measurements are used to deduce the slip values. These slip values are not constant but will vary from zero at the stick–slip boundary to a maximum at the edge of contact. Further, the boundary may move during a complete load cycle. Large values of slip, on the other hand, occur under full slip conditions and may only be obtained for

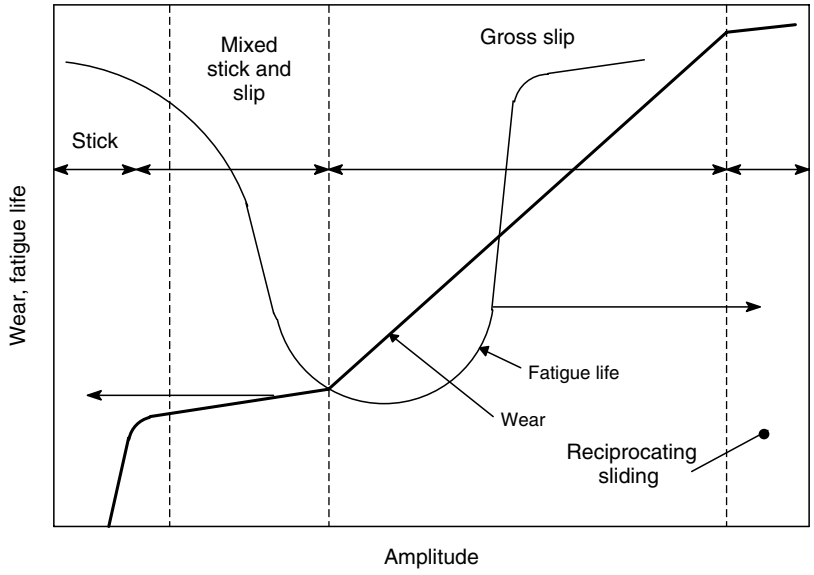


Figure 6.2. Schematic of fretting regimes showing relative wear and fatigue lives as a function of relative displacement amplitude (after [1]).

specific experimental configurations and loading conditions including various aspects of how load or displacements are controlled.

6.2. OBSERVATIONS OF FRETTING FATIGUE

The author's first real exposure to fretting fatigue was in the early part of a major HCF program where baseline long life fatigue tests were being conducted in the laboratory. Under load control, using tapered cylindrical dog bone type specimens, a number of failures occurred in the grip region as depicted in a two-dimensional schematic of the test in Figure 6.3. The failures, as shown, were soon identified as fretting fatigue, and occurred at average stress levels in the grip area that were considerably lower than the nominal fatigue strength of the titanium alloy being tested. Only by reducing the nominal stress by thinning the gage section of the specimen were these failures eventually eliminated. This experience was certainly not unique since fretting in the grips is a common occurrence in testing laboratories. This experience, however, and the related observations eventually led to the design of a fretting-fatigue apparatus used by Hutson and co-workers (see [2] for example) described later in Section 13 (Figure 6.47). This apparatus made use of the propensity for fretting-fatigue failures in a contact region under cyclic loading when gross sliding is not present.

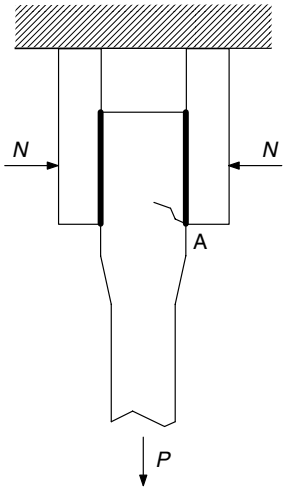


Figure 6.3. Schematic of uniaxial fatigue test showing fretting fatigue at grip.

One of the more common applications where fretting fatigue is a design issue and where numerous failures have occurred is the dovetail joint in an engine where the blade is inserted into a slot as shown schematically in Figure 6.4. Here, the contact interface is normally composed of two flat surfaces in contact with blending radii in both the blade and the disk. The general problem is three-dimensional in nature with loading taking place in the directions shown in the two-dimensional schematic of Figure 6.4 as well as out of the plane of the figure. The loading can be a combination of LCF due to start up and shut down of the engine, producing primarily an axial load in the blade as shown, and HCF due to vibratory motion of the blade, producing lateral cyclic loading as well as axial or bending (not depicted here) contributions. The contact region, where the flat surfaces mate, sees both normal and tangential loads as well as bulk loads in both the blade and the disk. At a contact interface, the normal and shear stresses at any point

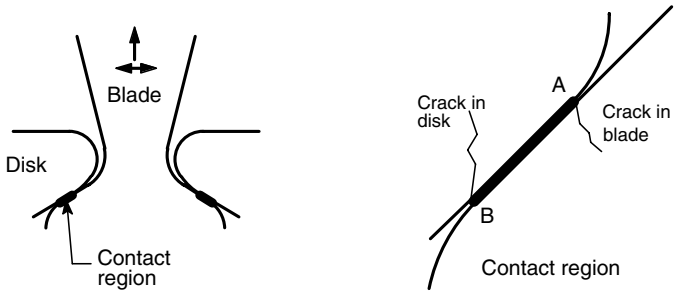


Figure 6.4. Schematic of blade/disk contact region.

are equal and opposite, but the bulk stresses can be different in the two bodies at the interface. For this region, fretting-fatigue failures can occur in either the blade or the disk as depicted schematically in the blowup of the contact region in Figure 6.4. For the blade, the highest bulk load parallel to the interface occurs at the upper edge of contact, shown as point A in the figure. In the disk, however, the highest bulk load occurs at the lower edge of contact, point B in the figure. The two potential failures occur at two different locations so that generally either one or the other occurs first in reality. But in design or analysis, both locations have to be examined as potential sites for fretting-fatigue failure.

In addition to the location of crack initiation and the stresses needed to cause initiation, the subsequent propagation of the crack also has to be considered. In the dovetail region in an engine, cracks initiated in the blade nearly always propagate due to the severity of the bulk load from centrifugal forces. However, cracks initiated in the disk frequently arrest when they are still very short [3].

Another application where fretting-fatigue failures are known to occur is at fastener joints where a rivet or bolt is used to join two members that are subjected to oscillatory loading. Riveted joints in airframe construction are one of the most common places where fretting fatigue can occur. A schematic of a riveted lap joint is shown in Figure 6.5 where a symmetrically loaded joint is depicted. While the joint is designed to function with essentially no relative motion anywhere, small relative displacements can occur in the region between the rivet and the plate as indicated by the solid lines in the figure. This very small relative motion, produced by fatigue loading of the joint, is due primarily to the elastic strains in the adjacent materials at the contact interface. The high stresses that develop in this contact region can lead to fretting-fatigue crack nucleation and subsequent propagation due to the bulk loads in the plate as depicted in the figure.

Another common example of a structural configuration where fretting fatigue can occur is where a hub is press-fitted onto a shaft. A characteristic of this and other applications where fretting fatigue occurs is the small amplitude of the relative motion between

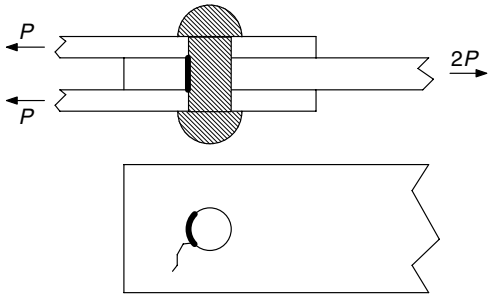


Figure 6.5. Schematic of rivet joint showing fretting fatigue region.

the contacting surfaces. It was shown by Tomlinson et al. [4] as early as 1939 that if relative motion (slip) occurs, even at a level as small as 10^{-6} in. (0.025 μm), fretting will result.

One rather ironic example of a fretting-fatigue failure is that experienced while conducting fretting-fatigue experiments in the laboratory. Figure 6.6 is a schematic of the upper part of a dovetail fixture used to conduct fretting-fatigue experiments [5]. The fixture is free to rotate because it is held by a pin which, in turn, is held in a clevis which supports it as shown in the figure. Similar to the case of the riveted joint described above, small relative motion can occur between the pin and the fixture in the region shown as a thick line in the figure. After numerous tests to typical cycle counts of 10^6 or 10^7 per test, the very large number of cycles (approaching one billion) eventually produced failure of the grip as depicted in Figure 6.6. This ironic example is one where fretting-fatigue failure of the grip assembly halted the conduct of real fretting-fatigue experiments.

Another scenario where fretting-fatigue failure can occur is at a bolted joint as depicted schematically in Figure 6.7. While such a failure mode is rare, it is not nonexistent. In a set of rotating components bolted together, excessive vibration of one of the components can lead to cyclic loads that produce a combination of normal, shear and transverse loads in the contact region shown as the thick line in the figure. These loads, combined with the initial static axial load in the bolts due to tightening, can lead to fretting-fatigue crack initiation in the bolt and potential failure of the bolt as depicted by a crack initiating in Figure 6.7. In this example, and in all of the prior examples, the conditions that produce fretting-fatigue cracks are assumed to be ones where partial slip occurs in the contact region. This is in contrast to the condition of total slip that is produced by higher loads and larger slip amplitudes. Although the latter is normally associated with LCF, and shows up as wear or galling, the one-to-one correlation between fretting fatigue and partial slip, and wear and galling to total slip, is only a generalization and not an all inclusive rule. Thus, while HCF is normally associated with fretting fatigue, there are questions regarding the

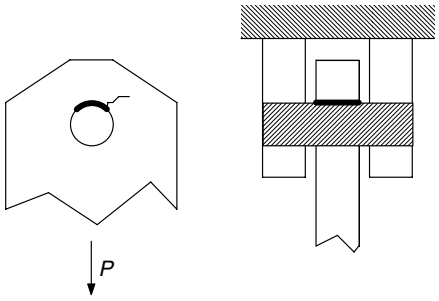


Figure 6.6. Schematic of fretting fatigue failure in pin-held fixture.

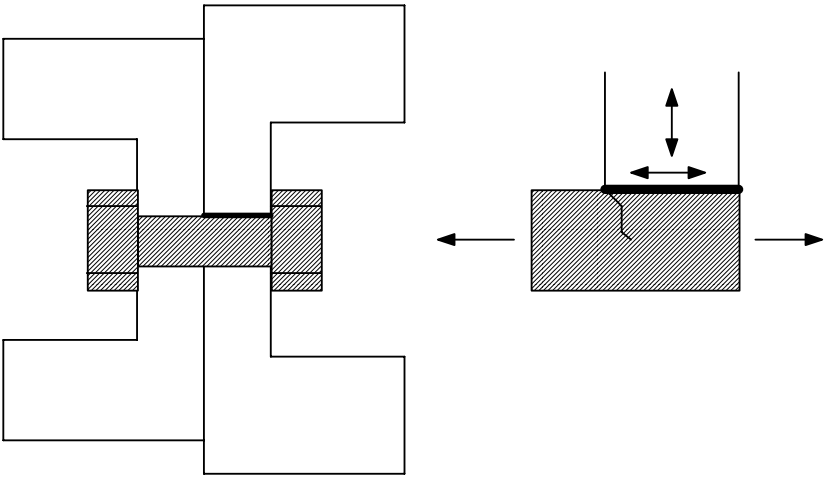


Figure 6.7. Schematic of fretting fatigue in bolted joint.

possible role of LCF in fretting fatigue and whether fretting fatigue is attributable to HCF exclusively.

6.3. REPRESENTING TOTAL CONTACT LOADS, *Q* AND *P*

A common method for describing the general fretting conditions in an experiment or a component, particularly to distinguish between partial slip and total slip conditions, is to plot the total shear force, Q, as a function of the total normal force, P, in the contact region. Such a plot, particularly if it includes the first several load cycles as well as occasional cycles to trace any changes of the forces with cycles, will provide information on the evolution of the stick or slip nature of the region of contact.

For most of the laboratory experiments used to study fretting fatigue, the loads P and Q are applied directly or are a direct consequence of applied bulk loads. In many of these experimental configurations, the clamping load, P, is maintained essentially constant. In such cases, the plot of Q versus P provides very little information unless the cycle goes through a stick and slip condition during the cycle. In such a case, the hysteresis loop of that plot provides evidence of this phenomenon.* Real applications and simulated experiments involve geometries, where the Q versus P conditions are more complicated. Two specific cases are shown schematically in Figure 6.8, (a) a dovetail slot and (b) a simulated dovetail apparatus for laboratory testing. While the two geometries possess

* The hysteresis would also be evident in plots of Q against bulk load or Q against relative displacement.

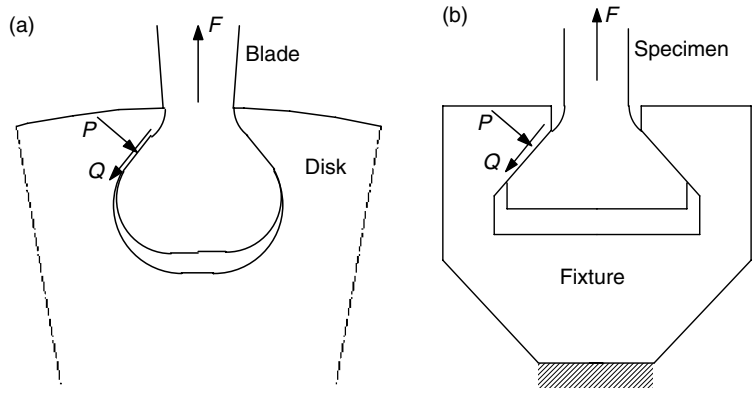


Figure 6.8. Schematic of (a) dovetail slot in engine and (b) dovetail laboratory simulation experiment.

many of the same features, the dovetail load F develops from centrifugal forces which also act on the disk while the laboratory apparatus only experiences the applied load F. As will be shown later, the reactive loads P and Q are different in the two cases shown. In the case of a dovetail slot in an engine, or in a simulated dovetail experiment, the Q versus P relation throughout the cyclic loading history provides much useful information and, in general, is difficult to obtain. The calculation of conditions for such a plot involves analysis of a configuration where the structure and loading are statically indeterminate, meaning that the elastic compliance of the system must be considered in the computations. The resultant Q and P values are then load-path dependent, especially when the loading conditions produce conditions of both total slip and partial slip (stick–slip) at the contact interface.

Figure 6.9 shows a Q against P plot for any two bodies in contact. Two lines bound the region where all combined values of Q and P can take place. The one boundary is when the bodies slide with respect to each other in one direction while the other is when they slide in the other direction. All other points in the enclosed region represent partial slip conditions. The boundaries are given by

$$Q = \mu P \text{ and } Q = -\mu P \tag{6.1}$$

where μ is the average COF. All sliding must take place along these lines. The lines are denoted as the "slide out line" and the "slide in line" as described by Gean [6] in characterizing the conditions in a dovetail slot in an engine where the blade can tend to slide out of the disk or back into it.

In Figure 6.9, conditions are also shown for a common laboratory experiment conducted under constant clamping load. The clamping load is normally applied first, so line O–A represents the initial loading. Then, a typical experiment will involve partial slip conditions

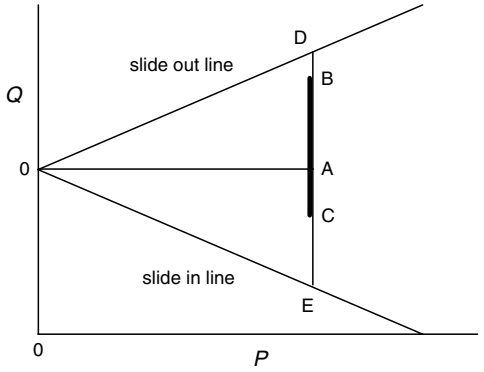


Figure 6.9. Plot of Q against P for any two bodies in contact. Possible paths for simple laboratory experiment with constant P are also shown.

as the specimen is subjected to cyclic shear loading between points B and C, for example. In some experiments, the initial shear load may produce slip, such as at point B. If the COF increases, then the slide out line will take on a higher slope and the remainder of the test will be conducted in partial slip. If the conditions are such that slip takes place at one point in the cycle for each cycle, such as in cycling through D–C, then a ratcheting condition will occur. If slip takes place at both maximum and minimum shear load, then the cycle would be represented by D–E. In either of the last two cases, the hysteretic nature of the cycle does not show as a hysteresis loop in a Q–P plot such as Figure 6.9. Rather, it has to be recognized that once a point in the cycle is reached that touches either of the slide lines in the figure that sliding will take place. The amount of sliding is not reflected in such a plot. A third dimension would have to be added to the diagram to account for the magnitude of the slip.

A Q–P plot for an engine mission that shows the paths that Q and P can follow in a dovetail slot due to changes in engine rpm is shown in Figure 6.10. Starting at rest with zero-applied load, the first increase in engine rpm produces sliding to point A. A decrease in rpm from that point produces a further increase in crush load, P, even though the centrifugal load from the blade is decreasing [6]. The reason for this is the compliance of the disk changes with rpm (or centrifugal load) so that the net effect is to increase the load P with decrease in rpm. If the engine goes through small throttle excursions after the maximum rpm at point A, then the Q–P path will involve points somewhere along the line A–B with the direction of movement due to increase or decrease in rpm as shown in the figure. If the decrease in rpm is large, the path can go from maximum rpm at A to point B, where sliding-in starts to take place, to point C where minimum rpm is reached. An increase in rpm from that point will take the path from C to D and then along the line D–A. Complete shut down will follow the path from A to B to the origin. Thus, for small throttle excursions, the behavior will be somewhere along the line A–B while for

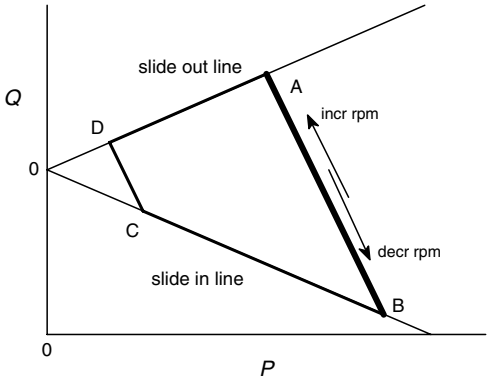


Figure 6.10. Q–P plot for an engine dovetail slot.

large excursions, where low rpms are reached, the path can follow A–B–C–D–A. Note again that unless points A or B are reached during some throttle excursion, the dovetail slot remains in partial slip.

The behavior in a dovetail slot, Figure 6.10, is different than that in a simulated dovetail fixture in a laboratory, described later in this section. In a laboratory experiment, centrifugal loading is absent so that the compliance of the fixture does not change due to the loading. The external loading is that applied by a specimen representing a blade. The *Q–P* path followed during a laboratory experiment on a simulated dovetail fixture is depicted in Figure 6.11 [7]. Here, the specimen slides along the fixture as load is increased until point A is reached. A decrease in load will then follow a path from A in the direction of B. Continual cycling with no sliding will then take place somewhere along the A–B line, never reaching A or B during the test. Increasing and decreasing

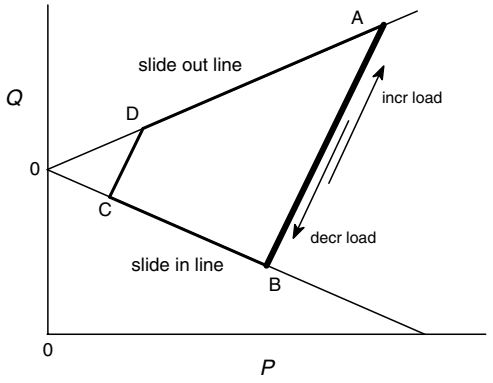


Figure 6.11. Q-P plot for laboratory dovetail fixture.

load will produce motion as indicated in the figure. If the load decrease is very large, however, sliding will take place at point B and continue along B–C until minimum load is reached at point C. When the load is increased, the lines C–D (partial slip) and D–A (total slip) will be followed until maximum load is reached at point A. In the dovetail experiment, a complete hystersis loop A–B–C–D–A can be followed for low values of load ratio, R, while for large R a path somewhere along the A–B line will be followed.

In making comparisons, the three plots, Figures 6.9, 6.10, and 6.11, show the conditions involving only partial slip. The line followed on a Q–P plot for the constant load experiment, the engine dovetail slot, and the laboratory dovetail specimen has a slope that is zero, negative, or positive, respectively. In developing models for fretting fatigue based on stress and stress histories, the load and load histories play an important role and the differences between laboratory simulations and actual usage, as demonstrated above, should be taken into account.

6.4. LOAD AND STRESS DISTRIBUTIONS

To derive criteria for fretting-fatigue failure, based solely on a mechanics analysis, requires determination of the stress–strain behavior in the contact area. A complete analysis of the fretting-fatigue process should include deriving criteria for both the initiation of cracks in the contact region, and criteria for the propagation or non-propagation of fretting fatigue–induced cracks. A major issue with such an approach, whether for fretting fatigue or fatigue in general, is the size of a crack associated with the concept of initiation. Criteria for crack propagation, particularly with the onset or threshold, are fundamentally dependent on the crack size chosen in any definition of initiation. It is not clear whether such a crack length is independent of load level, number of cycles, or other parameter such as stress ratio, R, in developing a model for fretting fatigue. Further, while HCF should normally be associated with a threshold condition, the behavior at stresses corresponding to a finite life are also of engineering importance and, more importantly, are easier to obtain in experiments than those corresponding to a fatigue limit corresponding to a very large number of cycles.

Experiments from which fatigue models are developed for fretting fatigue can be classified under two categories: those associated with a finite number of cycles to failure, and those associated with the determination of a FLS. The latter can be obtained corresponding to some cycle count, typically 10^7 or higher, and usually involve either step testing or staircase testing (see Chapter 3). For the first category of test types, typically LCF tests or tests at constant stress (or strain) corresponding to a finite life, data can be obtained on the stress conditions in the contact region corresponding to the conditions to develop a given initiation crack size. The total life of the test, obtained experimentally, consists of both the initiation and the propagation phase. For modeling purposes, it is important

to subtract out the propagation life. This can be done using an accurate representation of the $da/dN - \Delta K$ behavior of the material at the appropriate value of R, the K solution for the crack geometry which emanates from the fretting region, and a suitable choice for an initial crack length corresponding to initiation. The criteria developed for initiation will depend on this choice of crack length. What cannot be determined from a test of this type is the threshold for crack extension under the type of stress fields typical of those in the fretting region. What typically happens is that a crack will initiate and then continue to propagate because the initiated crack will have a stress intensity range above the threshold value. Thus, the crack propagation calculation will cover a range of ΔK values from above threshold to either a critical value or one corresponding to a reasonably large crack where further propagation life will be very small.

The second type of test, corresponding to the determination of conditions producing a threshold for fretting-fatigue failure at a large number of cycles, usually involves some type of step testing. In this situation, the stresses associated with the equivalent of a fatigue limit provide information on the threshold for fatigue crack propagation. It is usually easy to produce a stress field which will initiate a crack because of the high intensity of local stresses in the contact region, but the K field has to be of sufficient magnitude to produce continued crack propagation. Tests of this type, corresponding to a fatigue limit test, can provide information on the threshold for crack propagation under fretting fatigue. One of the great misuses of this type of test is to assume that the stresses corresponding to failure are those that lead to crack initiation. It is possible that cracks formed at much lower stresses during the step testing and the final stresses are the ones that produce stress intensity values above the threshold. Examples of this condition are presented later in this section. Again, as in the previous scenario, the crack size corresponding to initiation has to be chosen. The reverse situation can also take place where the crack does not initiate until the maximum load is reached during a step test, and then the crack will continue to propagate because it is already above the threshold value of K. This appears to be the less likely of the two scenarios because of the very high stresses in the region of contact. Because of this, it is anticipated that there may be many case of fretting fatigue where tiny cracks are initiated, but then arrest. This can be a dilemma for those owners of systems who do not like to have cracked parts in service, where the cracks are below the inspectable level, and the analysis and testing indicates that the cracks will not propagate unless the stresses are higher than those that initiated the cracks.

6.5. EFFECTS OF LOCAL AND BULK STRESSES ON STRESS INTENSITY

While it is generally thought that crack initiation is governed primarily by the local contact stresses, and propagation is more related to the far-field or bulk stresses, the local stresses can have a significant effect on the K field over much larger distances than where

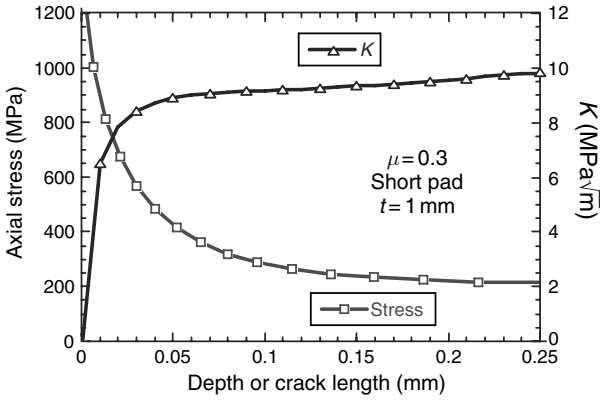


Figure 6.12. Stress distribution and resulting K solution for short pad specimen case.

the local stresses are high. An example of this is the stress and K fields for two fretting pad geometries in an experimental configuration where the bulk stresses are high on the trailing edge of contact and go to zero on the leading edge [8]. The numerical results for stress intensity, K, for a crack normal to the contact surface are shown in Figures 6.12 and 6.13 for two different pad lengths referred to as the "short" and "long pad cases," respectively. The results are based on analysis at the deformed edge of contact. Also shown is the stress distribution, σ_x, at the same location into the depth of the specimen. The values of K were found to be relatively insensitive to the exact location in the x direction when going away from the edge of contact 10 μm in either direction [8]. For these particular cases, where the values of σ_x become constant at large distances from the surface, the values of K are seen to be larger for the short-pad configuration than for the

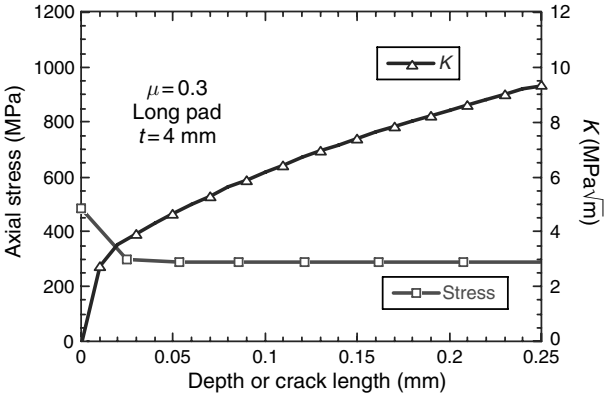


Figure 6.13. Stress distribution and resulting K solution for long pad specimen, $\mu = 0.3$ case.

long pad, consistent with the magnitudes of the local stress fields as shown in the figures. At much larger crack lengths, the K fields appear to be converging. However, for short crack lengths, the higher local stresses which occur over the first 0.1 mm in the short pad case, and over a much shorter distance in the long pad case, produce much higher values of K for distances beyond those at which the stresses are high. The higher local stresses in the short pad case clearly produce higher values of K over a distance beyond 0.25 mm.

This problem can be looked at in a more general manner. For a very simplified approach, one can treat the local contact stresses as a point load at the mouth of a crack, and treat the far-field or bulk stresses as a uniform stress field far from the crack as illustrated in Figure 6.14.

The K solutions are written individually for the bulk load and the concentrated load [9]:

$$K_{\mathrm{I}}^{\sigma} = \sigma\sqrt{\pi a}F_1(a/b) \tag{6.2}$$

$$F_1(a/b) = 1.12 - 0.231(a/b) + 10.55(a/b)^2 - 21.72(a/b)^3 + 30.39(a/b)^4 \tag{6.3}$$

$$K_I^P = \frac{2P}{\sqrt{\pi a}}F_2(a/b) \tag{6.4}$$

$$F_2(a/b) = \frac{3.52}{(1-a/b)^{3/2}} - \frac{4.35}{(1-a/b)^{1/2}} + 2.13(1-a/b) \tag{6.5}$$

where a is the crack length, b is the total width of the plate, P is the concentrated load representing the local contact stresses parallel to the edge of the plate, and σ is the far-field uniform stress. Only Mode I stresses on a crack normal to the contact surface

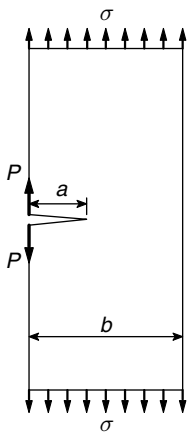


Figure 6.14. Schematic of equivalent stresses in contact problem.

are considered here.* Simple numerical examples are solved for the far-field stress, σ, assuming values of 10, 100, or 1000 and the concentrated load is assumed to be $P = 1$. A value of $\sigma = 10$ represents a situation where the contact stresses are very large and the bulk stress is very small. The case where $\sigma = 1000$ represents the other extreme where the bulk stress dominates and/or the local contact stresses are very small. The calculated values of K are normalized with respect to the bulk stress, so graphs are presented for a normalized stress intensity K/σ. Figure 6.15 compares the total K, the sum of K's due to σ and P, for the three cases. The solution is shown up to a value of $a/b = 0.2$. It can be seen that the case for $\sigma = 10$ has very high values of K for small crack lengths, governed mainly by the local fretting-induced contact stresses. In this case, it would appear to be a situation where initiation could be easily followed by crack arrest since the driving force, K, decreases by such a large magnitude. Conversely, for $\sigma = 1000$, the far-field stress dominates and any crack that initiates can be expected to continue to propagate because of the continually increasing value of K with increase in crack length. The intermediate case of σ = 100 shows a small decrease in K at very small crack lengths followed by a continual increase. Here, there may be a slight chance for crack arrest when the combination of contact stresses and far-field stresses is just right. In Figure 6.15, this would occur at a crack length corresponding approximately to $a/b = 0.01$.

The individual contributions of σ and P, the far-field, and local contact stresses, respectively, can be seen in Figures 6.16, 6.17, and 6.18, corresponding to $\sigma = 10, 100,$

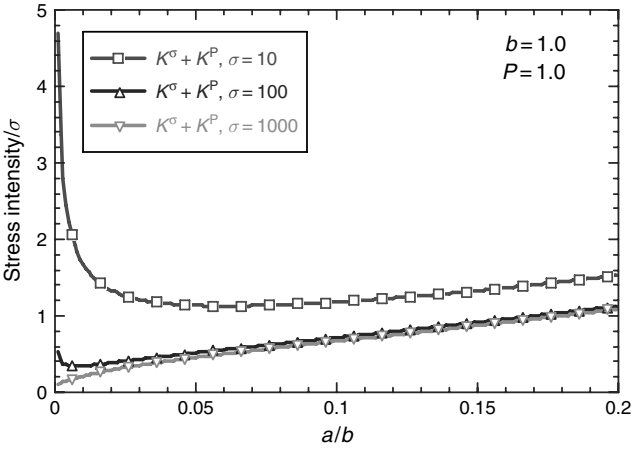


Figure 6.15. Total K solution for three different values of applied far field stress.

* In this simple numerical example, the thickness of the plate is taken as 1. For this reason, the equations do not appear to be dimensionally correct (the thickness does not appear in them explicitly).

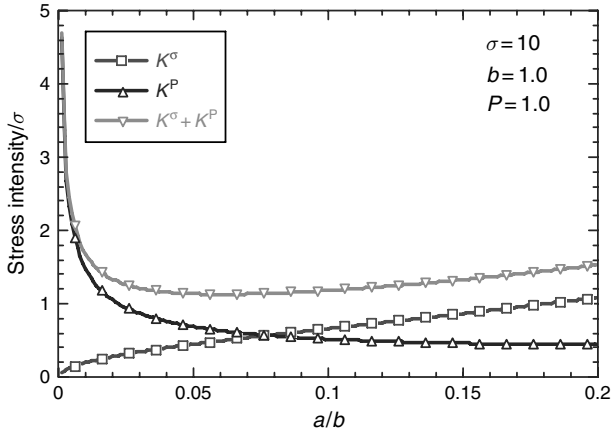


Figure 6.16. Stress intensity from contact stresses and far field stress = 10.

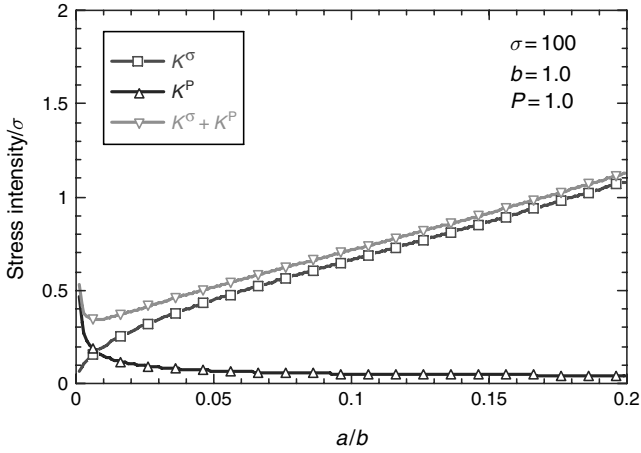


Figure 6.17. Stress intensity from contact stresses and far field stress = 100.

and 1000, respectively. In Figure 6.16, it is clearly seen that for $\sigma = 10$, the local contact stresses are dominant up to a crack length of approximately $a/b = 0.05$ and, as mentioned above, there is a significant decrease in K up to that crack length. Figure 6.18, on the other hand, shows that the far-field stress, σ, is dominant for all crack lengths and K is a continually increasing function. Finally, the intermediate case shown in Figure 6.17 illustrates a similar contribution from σ and P at a crack length of approximately $a/b = 0.01$. From these observations, it is demonstrated that the relative magnitude of the local contact stresses compared to the far-field stresses is a major factor in determining the

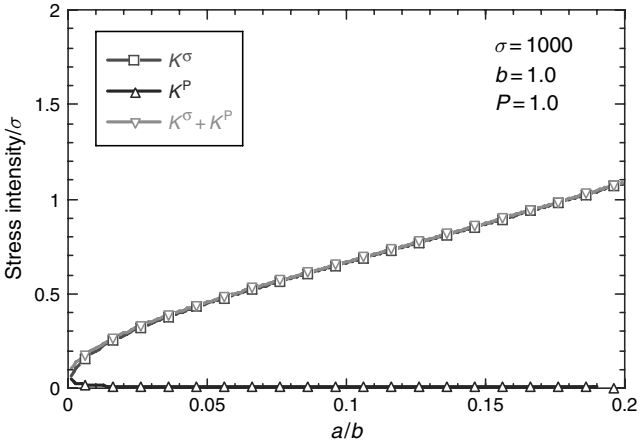


Figure 6.18. Stress intensity from contact stresses and far field stress = 1000.

tendency or lack thereof for a crack to initiate and then to either continue propagating or arrest. A consequence of this is the interpretation of experimental data and observations where the far-field stresses should be considered in deciding if a crack arrest phenomenon is likely or possible to occur.

6.6. MECHANISMS OF FRETTING FATIGUE

The history of fretting goes back almost an entire century. The first report of fretting appears to be that of Eden et al. [10] in 1911 while the first systematic experimental investigation of the process is attributed to Tomlinson [11] in 1927. Fretting has traditionally been linked closely with corrosion, oxidation, or other environmental effects. In the early days of fretting-fatigue research as we now define it, the topic was commonly called "fretting corrosion" (see Forrest [12], for example). The definition of the phenomenon does not seem to have changed. According to Forrest [12] in 1962,

> If two solid surfaces in contact are subjected to a repeated relative movement of small amplitude, some damage to the surfaces may occur and this is known as fretting corrosion. Its presence is usually recognized by the corrosion products formed, which consist of finely divided oxide particles. . . . The appearance of oxide particles is usually accompanied by localized pitting of the surfaces in the fretted region and this can result in serious reductions in fatigue strengths. The mechanism of fretting corrosion is not yet fully understood and this is reflected by the number of alternative terms used to describe the same process, for example friction oxidation, wear oxidation, chafing, and false brinelling. The process is a form of mechanical wear which can occur without corrosion, but which can be greatly aggravated if corrosion occurs simultaneously . . .

In recent times, fretting fatigue has been addressed by some researchers almost entirely from a mechanics viewpoint, irrespective of the corrosion process. There is no question, however, that environmental effects play an important role in the process, even if the only consideration in a mechanics approach is the evolution of the COF. Poon and Hoeppner [13], for example, found that the number of cycles to failure in fretting-fatigue experiments on 7075-T6 aluminum in vacuum was between 10 and 20 times longer than that tested in laboratory air. They concluded that the chemical factor plays the dominant role in reducing specimen life when fretting occurs simultaneously with fatigue. It is hoped and certainly believed by the author that the purely mechanics approach that uses realistic values of the COF, as successful as it has been, will not fall into the following category noted by Schütz [14] in his review of the history of fatigue: "In every time period there are one or more unrealistic ideas and solutions which at the time are followed enthusiastically by some distinguished scientists and engineers; with the benefit of hindsight, however, their delusions appear incredible!"

The effects of corrosion cannot be dismissed in a mechanics-based approach to fretting fatigue, even if it is just to adjust the COF to represent what occurs during the fretting process. In one of the earliest works on fretting corrosion, Tomlinson et al. [4] concluded that for surfaces in closely fitting contact subjected to vibration, that corrosion is mechanical rather than chemical in character. Vibration or alternating surface stress alone was not expected to cause corrosion. It was the relative surface slip, alternating in direction, that was the necessary condition. They surmised that slip effectively causes corrosion, even if it is reduced to the order of molecular dimensions, and is always present including on lubricated surfaces. In one experiment where a total slip amplitude of 2.3×10^{-6} in. (0.058 μm) was used, surfaces subjected to 300 000 reversals resulted in a slight but narrow ring of corrosion debris [4]. In an earlier experimental investigation, Tomlinson [11] concluded that the fretting action was a particular manifestation of molecular cohesion between the surfaces. These early observations led to conclusions that the fretting-fatigue process involved corrosion in association with slip and the attrition of the mating surfaces is caused in some way by the severance of cohesion bonds. For these and other reasons, the terminology "fretting corrosion" was widely used to describe an event that occurs on and near the surface as distinguished from fatigue that is associated with cyclic straining of the material as a whole.

It is not surprising, therefore, to find that adhesion has been considered in developments in the mechanics of contact fatigue. Giannakopoulos et al. [15] have shown, for example, that in the contact between a cylinder and a flat surface the pressure is bounded and zero at the edge of contact without adhesion, but that the presence of strong adhesion would cause the pressure to become singular at the new edge of contact. Even for weakly adhered surfaces, stresses near the adhered stick zone boundary are square root singular. These local stress fields are entirely different than those calculated without consideration of adhesion.

The environment in which fretting takes place still has to be considered in fretting-fatigue life prediction. Taylor [16], in a review of environmental effects on fretting fatigue, points out that the environment "can have a profound effect on the nature and degree of the resultant surface damage and fatigue crack generation." He points out the need to consider the possible interactions between fretting and corrosion in the crack initiation stage. In particular, he notes that the resultant corrosion products can lead to a reduction in the COF and development of protective surface films. The major conclusions of the overview by Taylor [16] are:

> The mechanism of fretting fatigue includes chemical and mechanical factors, the observed damage commonly resulting from both. The factor which dominates is dependent on the particular circumstances prevailing. Most researchers favour the chemical factor as playing the major role in reducing fretting fatigue life with the mechanical damage serving to disrupt surface films and expose underlying chemically reactive sites. Cathodic protection which removes deleterious electrochemical effects on both the generation and propagation of fatigue cracks greatly improves fretting fatigue performance, usually returning values to or above those found in air.
>
> The fretting fatigue behaviour can be significantly affected by the nature of the corrosion products forming within the fretted region. Thick layers of such product may reduce the coefficient of friction between contacting surfaces and also provide some protection to the surfaces, thereby delaying the generation of fatigue cracks.

Another aspect of the corrosion effect in fretting fatigue that has not received a large amount of attention, at least in a quantitative sense, is the role that corrosion debris has on the crack propagation behavior in the contact region. In particular, debris that forms and lodges in the crack can play an important role in developing crack closure that, in turn, can reduce the effective stress intensity by keeping the crack tip open at low applied loads. Conner et al. [17] characterized the mechanisms of damage in fretting fatigue using three different test systems and four different pad geometries. They observed that the wear mechanism, which is reported to increase with slip displacement as described in the work of Vingsbo and Söderberg [1], also results in an increase in the production of wear particles that can enter cracks and retard crack propagation. They observed cracks of the order of 5 μm in length that were filled with debris. The growth of such cracks would be influenced by the presence of debris in the crack wake, and the presence of this debris was observed to be independent of contact geometry or loading conditions. This is just another factor that should be considered in the development of a robust analysis of the fretting-fatigue phenomenon.

6.7. MECHANICS OF FRETTING FATIGUE

The application of mechanics to predict fretting-fatigue lives has used crack initiation (or nucleation), crack propagation, or a combination of both as the basis for life prediction

or the determination of fatigue limit conditions for HCF applications. An investigation by Faanes and Fernando [18] used a fracture mechanics approach because the authors determined that the "fracture process is dominated by crack growth." Using a BS L65Al 4% Cu alloy, the authors used a simple short crack correction, like the one described for treating short cracks at notches in Chapter 5, by correcting the fatigue threshold. Using a bridge pad fixture where a wide range of slip amplitudes could be achieved, they found good correlation of experimental fretting-fatigue lives with crack propagation analysis as shown in Figure 6.19. Their experiments covered a range in lives from below 10^5 cycles to beyond 10^6 cycles as shown in the figure. They found that the behavior of short cracks, accounted for in their analysis, was especially important for long lives approaching the HCF regime. They also noted that the behavior of short cracks seemed to have less influence on the lifetime in fretting fatigue compared to plain fatigue. Of particular note is their use of an initial crack length for the fracture mechanics (crack growth) calculations assumed to be equal to the surface roughness which was reported to be of the order of 5μm for polished specimens. The assumption of crack growth being dominant in fretting fatigue is also supported by the observations of Waterhouse [19] who observed that in normal fatigue, crack initiation may account for 90% of fatigue life. However, in fretting fatigue, he observes that initiation could occur in only 5% or less of the fatigue life.

Other investigations, such as that of Hills et al. [20], support the contention that fretting fatigue is an initiation-controlled process. In that study, a standard fretting-fatigue fixture (described later as a "partial load transfer fixture") was used to conduct experiments on HE15-TFAl-4wt.%Cu alloy up to run-out at 10^7 cycles. The authors concluded that initiation is the dominant part of life in these long-life tests because fracture mechanics was

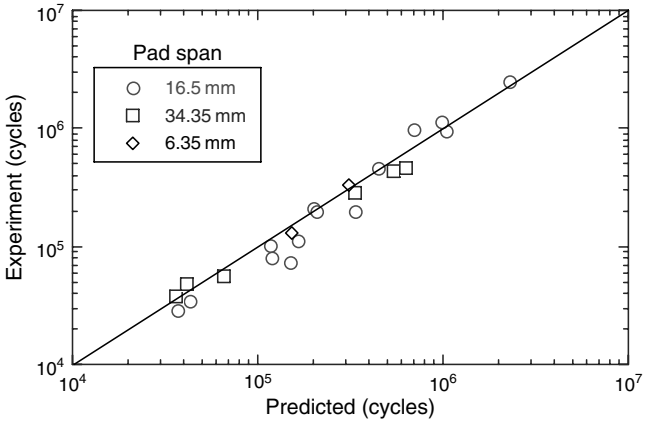


Figure 6.19. Comparison of fretting fatigue lives with experiments for fracture mechanics calculations corrected for short crack threshold [18].

found to predict that "the time taken for the crack to grow from threshold to catastrophe is only a small fraction of the measured life." Similar conclusions have been drawn by Szolwinski and Farris [21] from calculations for experiments on a 4% Cu aluminum alloy. For a life in excess of 10^6 cycles, nucleation was found to consume over 95% of the total life of the specimen. In their fracture mechanics calculations, an initial crack length of 1 mm deep was assumed as the transition size from nucleation to crack propagation.

Contrast these findings with those of Golden and Grandt [22] who found, in experiments on a Ti-6Al-4V titanium alloy, that at long lives in excess of 10^6 cycles, crack propagation life is an order of magnitude longer than initiation life. In their fracture mechanics calculations, the initial crack length was assumed to be 25 μm although the crack propagation life was found to be relatively insensitive to the starting crack size for the apparatus they were using. Mutoh and Xu [23] reached similar conclusions based on their experiments using bridge-type fixtures. They note that a fretting-fatigue crack generally initiates in the very early stage (few percent of the whole life) for most metallic materials. However, they point out that some materials like titanium alloys show very long fretting-fatigue crack initiation life.

While no definitive conclusion can be drawn from the above examples, it is important to note that crack propagation life can be sensitive to the material and its COF, the assumed initial flaw size that separates the initiation from the crack propagation phases, and the geometry of the test fixture or component. The sensitivity of the analytical fracture mechanics computations to the type of test fixture and geometry, particularly at long lives or threshold conditions for HCF, is discussed later.

6.8. STRESS ANALYSIS OF CONTACT REGIONS

One of the features that makes the analysis and life prediction of a fretting-fatigue problem so difficult is the unusual nature of the stress field in a region of contact. While a square punch on an elastic body is known to have a singular* stress field at the edge of contact (see [24] for example), even a flat pad with a blending radius produces a locally intense stress field with steep gradients. Solution of such problems with finite element methods demands sophisticated approaches involving very fine mesh sizes as well as methods for handling sliding contact between two bodies. The case of a rounded punch on an infinite body with a flat surface was one of the first problems to be solved analytically. While the stress field due to a normal force is smoothly distributed, a shear force produces a singular (shear) stress field at the edge of contact if displacements are assumed to

* A singular stress field is one where the stresses become mathematically infinite as the distance from the origin of the singularity goes to zero according to elasticity theory. Stress ahead of a crack in fracture mechanics is an example of a common singularity.

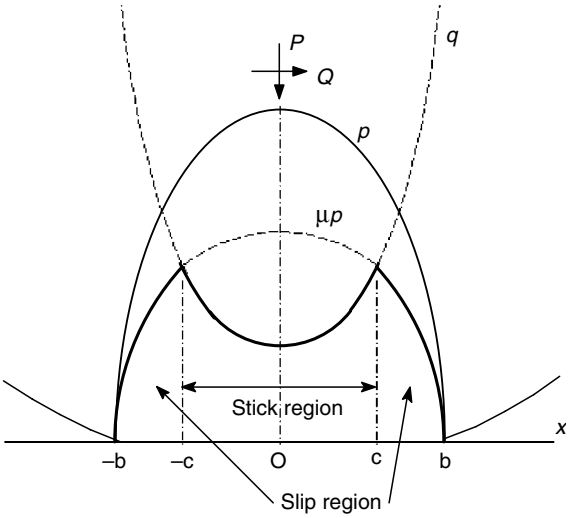


Figure 6.20. Stress distribution for cylinder on flat contact.

be continuous across the interface [25]. Figure 6.20 illustrates the stress field of the cylindrical or spherical indentor on a flat, infinite surface. The so-called Mindlin problem[†] assumes identical elastic materials, an infinite body, and no oscillatory bulk stresses. The cylindrical contact pad is used widely because of the availability of a closed-form analytical solution. Figure 6.20 illustrates some of the features that are characteristic of fretting-fatigue contact problems. In this case, the normal stresses, p, due to the applied normal force, P, are smoothly distributed going from zero at the edge of contact, $\pm c$, to a maximum at the center. The shear stresses, q, due to an applied shear load, Q, are singular if the contact is perfect. In the Mindlin solution, the displacements are assumed continuous between the contacting bodies, that is no slip occurs. In reality, the shear stresses are limited by assumed Coulomb friction and, therefore, cannot exceed μp at any location [25], where μ is the COF. This results in a stick–slip contact, shown in the figure, where the bodies do not slide in the "stick" region between $x = \pm c$, and sliding occurs in the "slip" zone between $x = \pm c$ and $x = \pm b$, where $q = \mu p$.

[†] The Mindlin solution is widely reported to have been developed independently by Cattaneo in Italy. The paper by Cattaneo is referenced in Mindlin's article as having been pointed out to him by Dr. Stewart Way, since two identical equations had been developed by Cattaneo. The author is only familiar with the Mindlin solution because he studied elasticity under Prof. Mindlin at Columbia University and, further, speaks or reads no Italian. For completeness, the other reference is: Cattaneo, C., "Sul Contatto di Due Corpi Elastici: Distribuzione Locale Delgi Sforzi," *Rendiconti dell' Accademia dei Lincei*, **27**, Saeries 6, 1938, pp. 342–348, 434–436, 474–478 (in Italian).

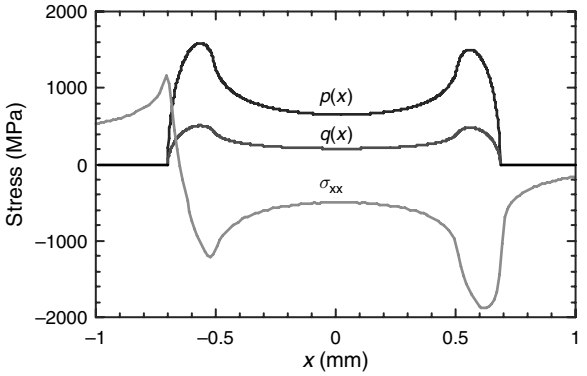


Figure 6.21. Stress field distribution in contact region of a dovetail fretting experiment [26].

Other contact geometries produce complex but not necessarily singular stress fields in the contact region. An example of a typical stress distribution under a contact pad is shown in Figure 6.21, taken from [26], where the contact pad has a 1 mm wide flat and a 3 mm blending radius. The figure shows that the local normal and shear stresses near the edge of contact have high local peaks. The deformed edge of contact is beyond the flat portion of the pad due to the local elastic deformation due to the applied pressure. Here, $p(x)$, the pressure at the interface, is shown positive in compression. The stress of greatest interest is the axial stress in the specimen parallel to the surface denoted as σ_{xx}. At the edge of the specimen where the applied bulk load is the highest (commonly referred to as the "trailing edge of contact"), the axial stress is maximum and has a very steep stress gradient in the x direction. It will be seen later that a steep gradient also exists in a direction normal to the surface into the depth of the specimen. The steep gradients combined with the biaxial stress states make life prediction from a fatigue initiation viewpoint a difficult problem. In the example cited, where the material was Ti-6Al-4V, the peak stresses determined from an elastic analysis exceed the yield stress of the material (930 MPa). The complexity of the stress analysis increases significantly if elastic-plastic analysis has to be conducted.

6.8.1. Multiple crack considerations

The analysis of fretting fatigue is difficult because the damage process may involve multiple cracks [27, 28]. The aspect ratio for a single crack changes drastically when individual cracks link up and produce long shallow cracks with highly irregular shapes. The existence of multiple cracks that eventually link up is an equally difficult problem for developing initiation criteria as well as for applying fracture mechanics to track crack growth. An example of multiple cracks developed under fretting fatigue is shown in Figure 6.22 where the fracture surfaces show the linking up of multiply initiated cracks.

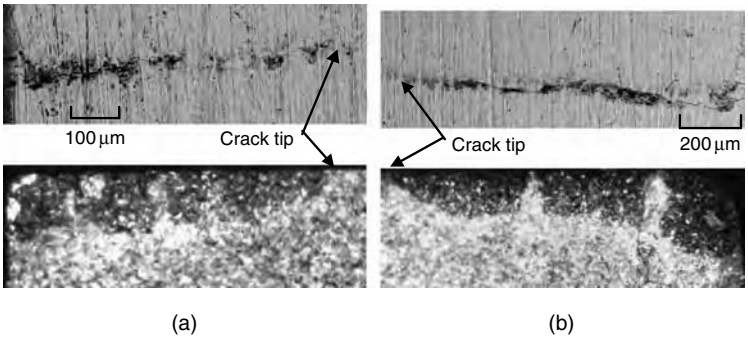


Figure 6.22. SEM images of fretting fatigue cracks (contact region is on the top half of the images) and corresponding fracture surface (below). The dark region on the fracture surface indicates the depth of the crack at the time the contact was removed. (a) 700 μm cracks. Specimen edge is shown to the left of the images. (b) 1.2 mm crack. Specimen edge is shown to the right of the images. The three separate dark region on the fracture surface indicate the size of the cracks at the time the contact was removed [29].

The reality of the formation of multiple cracks serves to point out the extreme difficulty that can be encountered when trying to develop models for the fretting-fatigue process.

6.8.2. Analytical solutions

A common contact geometry that is used widely in fretting-fatigue experiments and one which models actual contact geometries such as those in a dovetail slots in turbine engines is the flat pad with blending radii, shown in Figure 6.23. Closed-form solutions now exist for this contact geometry subject to the assumptions of a semi-infinite body as the substrate, elastic behavior for both materials, no bulk loads in the substrate, and similar properties for the two materials. For the simplest case of two identical materials for the punch and substrate, the equations below are due to Ciavarella et al. [30] who also handle the case of dissimilar materials. In the nomenclature for Figure 6.23, the semi width, a,

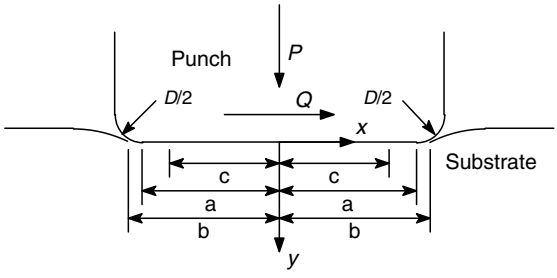


Figure 6.23. Schematic of flat indentor with blending radius.

represents the flat portion of the punch that is in contact with the substrate. The deformed edge of contact is at $x = \pm b$, while the boundary between the slip region and the stick region is denoted by $x = \pm c$. For the case of the cylindrical punch, a subset of the more general case shown here, the flat dimension goes to zero and $a = 0$ in the solutions below. For the cylindrical case, the exact solution given in [30] gives the contact pressure as $a \to 0$ for the cylinder on flat as

$$p(x) = \frac{2P}{\pi b}\sqrt{1-(x/b)^2}; \quad |x| \le b \tag{6.6}$$

while for the other extreme of a flat punch with a sharp corner, where $D \to 0$ and $b \to a$, the flat-on-flat contact pressure is given by

$$p(x) = \frac{P}{\pi\sqrt{1-(x/b)^2}}; \quad |x| \le b \tag{6.7}$$

The relation between the contact half width, b, and the normal load, P, is [30]

$$\frac{PD}{a^2E^*} = \frac{\pi - 2\phi}{2\sin^2\phi} - \cot\phi \tag{6.8}$$

where the composite contact stiffness, E^*, for identical materials, is

$$E^* = \frac{E}{2(1-\nu^2)} \tag{6.9}$$

and the parameter ϕ is defined by

$$\sin\phi = a/b \tag{6.10}$$

From the same paper [30], the size of the stick zone due to a tangential load, Q, is

$$\frac{Q}{\mu P} = 1 - \left(\frac{c}{b}\right)^2 \frac{\pi - 2\theta - \sin(2\theta)}{\pi - 2\phi - \sin(2\phi)}; \quad c > a \tag{6.11}$$

or

$$\frac{Q}{\mu P} = 1 \quad c \le a \tag{6.12}$$

where

$$\sin\theta = a/c, \quad \sin\phi = a/b \tag{6.13}$$

and mu is the COF. In the limit, as $a \to 0$, the classic case of the cylinder on flat is recovered

$$\frac{Q}{\mu P} = 1 - \left(\frac{c}{b}\right)^2 \tag{6.14}$$

The complete stress distributions for normal stress, p(x), and shear stress, $q(x)$, along the contact boundary can be found in [30].

Of greatest interest in the determination of the FLS for fretting fatigue is the maximum value of the axial stress, σ_{xx}, at the interface as shown in Figure 6.21, for example, at the edge of contact. Such stress can be used in a fatigue initiation criterion. In Giannakopoulos et al. [31] the value of this stress is taken as the sum of the contributions due to the contact shear load, the normal pressure, and the bulk applied stress. The endurance limit stress can then be formulated as

$$\sigma_{\text{end}}(R) = \max\ \sigma_1^{\text{tot}} = \sigma_{xx}^{Q} + \sigma_{xx}^{P} + \max\ \sigma_{\text{b}} \tag{6.15}$$

where $\sigma_{\text{end}}(R)$ is the endurance limit stress for a smooth bar at the appropriate stress ratio, R. If $q(x)$ is the shear stress due to a tangential load Q, the maximum tension is given in [32] as

$$\sigma_{xx}^{Q} = \frac{2}{\pi}\int_{-b}^{b} \frac{q(x)}{b-x}\mathrm{d}x \tag{6.16}$$

For the maximum stress due to the pressure, σ_{xx}^{P}, numerical results from [31] are plotted in Figure 6.24 which shows that the value of this stress depends on the ratio of the thickness of the substrate to the width of the contact region (t is the half thickness and b is the half width). For the infinite thick substrate, the tension stress vanishes.

Analytical or semi-analytical solutions have been developed for obtaining fretting-fatigue stress fields for more general contact geometries than a cylinder or flat with rounded corners on a half space. Murthy et al. [33] present details of a computationally efficient mechanics-based approach using discrete Fourier transformations to obtain contact stresses. The approach is based on the solution to singular integral equations that

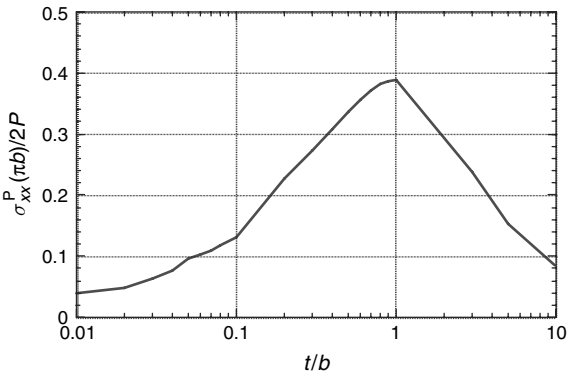


Figure 6.24. Normalized maximum tensile stress for different strip thickness [31].

characterize the contact of two surfaces and takes into account the details of the shape of the contact surfaces. Of particular significance is the ability to account for distortion or irregularities in the contact interface from experiments themselves or from imperfect machining. This particular formulation was eventually incorporated into a computer code at Purdue University that was referred to subsequently in the literature as CAPRI. Later, modifications were made to the code that accounted for the finite thickness of typical specimens as well as accounting for superimposed bulk stresses in the specimen. A description of the mathematics and procedures for determining the surface and internal stresses using semi-analytical procedures and the codes for conducting these analyses is presented in Appendix F.

An alternate method for determining the stress fields in a contact region where fretting fatigue takes place is the use of finite element methods. Finite element modeling, in addition to requiring the necessary mesh refinements to capture the steep stress gradients in the contact region, has to represent the boundary conditions appropriately. A comparison of a quasi-analytical approach and FEM results is presented in [34]. There, two different models are used as shown schematically in Figure 6.25. The first, (a), shows the scheme used to represent contact interaction when a normal and shear load are applied to an indentor. In this configuration, no account is taken of the bulk stress but it is used to validate analytical or quasi-analytical solutions to the contact problem which normally do not consider bulk loads. The second model, (b), represents a typical experimental configuration where bulk loads are applied, thereby inducing a tangential load on the indentor through the resistance of the fretting fixture. The displacement boundary conditions are represented with rollers as shown schematically in Figure 6.25. The spongy layers represent forces applied with hydraulic fixtures and are represented with elements

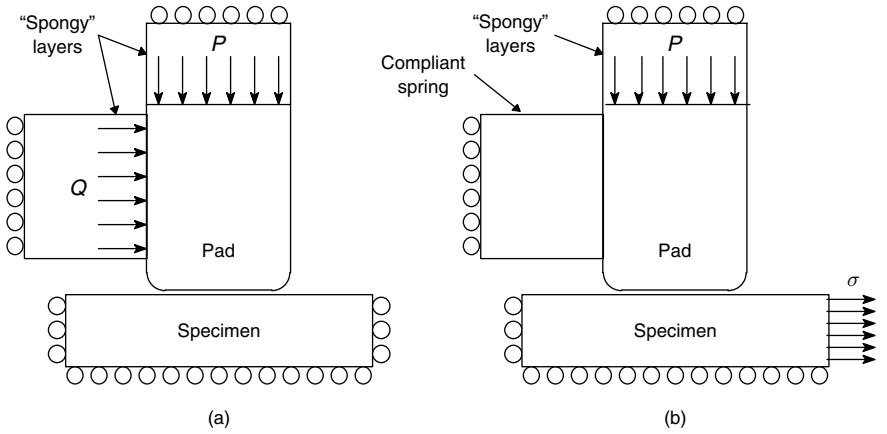


Figure 6.25. Schematic of finite element configurations for fretting contact, (a) for loading validation, (b) for experimental configuration (after [34]).

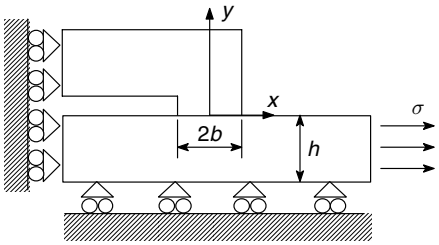


Figure 6.26. Schematic of finite element modeling of bridge pad with specimen loaded in tension [23].

with a relatively insignificant modulus. The compliant spring is used to represent the resistance of the experimental fixture and creates the shear load Q which is in-phase with the applied bulk stress, σ.

For a bridge-type fretting-fatigue fixture, shown schematically in Figure 6.34, modeling using the FEM also has to adequately represent the proper boundary conditions. An example of a model for a bridge-type pad is shown in Figure 6.26, after [23], where structural steel JIS SM430A was used for both pad and specimen. The model shown represents the condition where the bulk load, σ, was 180 MPa in tension and the clamping pressure was 60 MPa with a value of coefficient of friction $\mu = 0.8$. With values of $h = 4$ mm and $b = 1$ mm, a relative displacement of $\Delta = 1.56\,\mu$m was achieved as shown in the exaggerated deformed profile shown in Figure 6.27. The bulk loading was conducted at $R = -1$, and under compression the relative displacement was $\Delta = -0.55\,\mu$m. The corresponding stress distributions obtained by finite element analysis are shown in Figures 6.28 and 6.29 for tension and compression, respectively. It can be seen that, in general, there are three regions on the contact interface: sticking, slipping, and gapping (separation of the two bodies). As the authors point out, it is obvious that there is no stress singularity at the boundary points between the gap and slip or stick and slip regions. In general, the existence of singular stress fields near the edge of contact

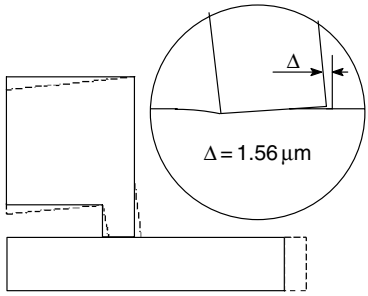


Figure 6.27. Deformation under tension with bridge type fretting pad [23].

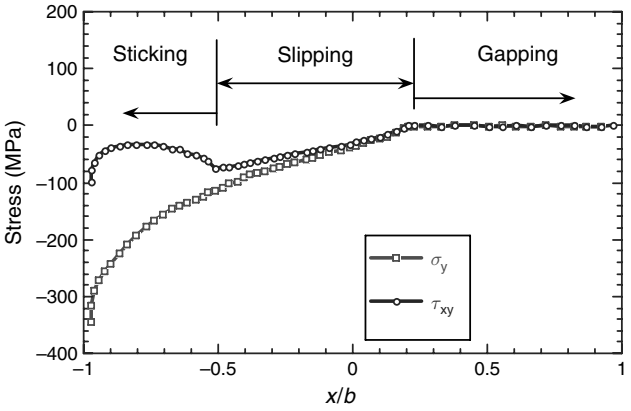


Figure 6.28. Stress distribution on interface under tension [23].

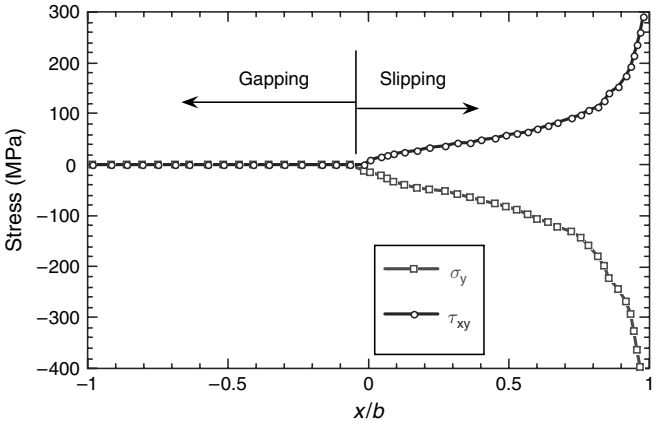


Figure 6.29. Stress distribution on interface under compression [23].

depends on the geometry, material combinations, and the type of deformation. In the case cited, the singularity appears at the external contact edge under compression loading and at the internal contact edge under tension. Moreover, the singular stress field will dominate crack initiation under fretting fatigue but may not be dominant once the crack tip moves out of the local region. For the bridge-type pad illustrated here, crack initiation and subsequent propagation may take place either at the edge of contact or in the center region of the contact, the latter being the case when there is either no edge singularity or when the singularity disappears due to the wear of the pad and the specimen [23]. The difference in initiation sites is generally a function of the variables mentioned above as well as loading conditions such as stress ratio, R.

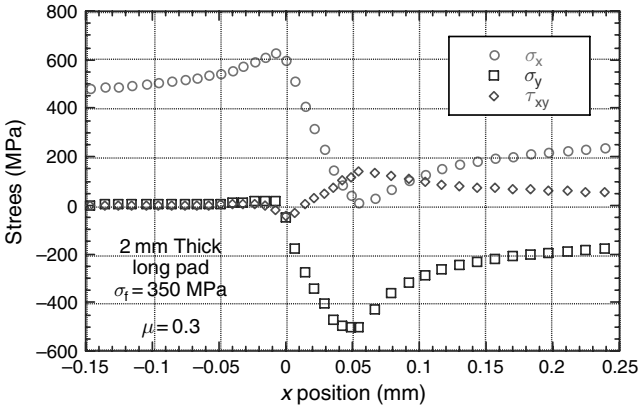


Figure 6.30. Stress distribution along surface at trailing edge of contact [8].

The non-singular, yet steep stress gradients encountered in the contact region between a flat pad with blending radii and a flat specimen are of concern in developing stress-based models for fretting-fatigue initiation or total life. Reasonably accurate stress profiles have been obtained using finite element computations with mesh refinement down to sizes of approximately 6.5 μm near the edges of contact where maximum stresses are reached [8]. An example of the nature of the stress distribution near the edge of deformed contact is shown in Figures 6.30 and 6.31 [8]. In both plots, $x = 0$ corresponds to the edge of deformed contact (EDC) as determined from the finite element computations. The maximum tensile stress occurs just outside the EDC, but at a distance not exceeding about 10 μm. Obviously, σ_y and τ_{xy} go to zero outside the contact region. Compared to σ_x and σ_y, the values of τ_{xy} are relatively small and spread out more while the compressive stresses, of the same order as σ_x, peak at about 50 μm inside the EDC. From Figure 6.30, the axial stress, σ_x, is seen to decay from a maximum to near zero in a distance of approximately 50 μm.

The stress gradients into the thickness are plotted in Figure 6.31. Shown is σ_x at several distances into the thickness direction. The coordinate $y = 1$ corresponds to the surface of the specimen in contact with the pad and the corresponding stress profile is identical to that shown for σ_x in Figure 6.30. The stress profiles show that the σ_x stresses decay rapidly, with stresses at 50 μm below the surface being almost the same as those much deeper. Thus, stress gradients into the thickness are of the same order of magnitude as those along the surface. Similar observations were made for other cases involving different pad geometries and pad thicknesses [8].

Given the capability to determine the stress field in a contact region where fretting fatigue takes place, it is tempting to try to develop a parameter that can adequately characterize the degradation of fatigue strength due to fretting fatigue. Unfortunately,

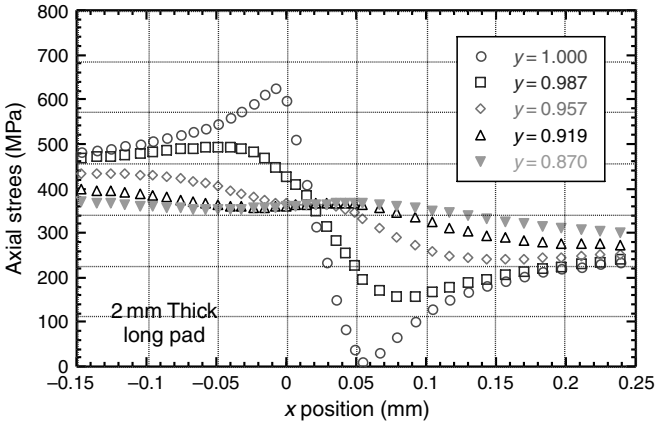


Figure 6.31. Stress distribution at various depths at trailing edge of contact [8].

there are many parameters and variables that seem to affect the behavior [28], and many of them can have a synergistic effect with others on the observed behavior. Many parametric studies, too numerous to mention or cite, have been conducted over many years.

In addition to the effect of environment on the fretting-fatigue behavior of materials, parameters such as slip amplitude, magnitude and distribution of contact stresses, and friction are widely accepted as major influences on the observed behavior. The earliest and simplest approaches for quantifying the degradation of fretting-fatigue lives or fatigue strengths is with the use of S–N curves obtained under fretting-fatigue conditions and comparing them with those obtained on smooth specimens. The resulting fretting-fatigue strength reduction factor, k_{ff}, is analogous to the fatigue notch factor (see Chapter 8) and is probably equally useful (useless) because the data themselves are necessary to validate any formulas developed to quantify such a parameter. Further, the S–N curves are normally neither parallel nor proportional in stress amplitude over a range of values in N. For the purposes of HCF design, the value of k_{ff} is needed at very high values of N where fretting-fatigue data are normally not obtained because of the time required to perform such experiments.

Generally speaking, fretting exerts its maximum effect in HCF since its main effect is the initiation of a propagating crack at stresses well below the normal fatigue limit [19]. A typical example of such a reduction is shown in Figure 6.32, taken from [19], for an annealed austenitic stainless steel tested at $R = 0$. In the HCF regime, corresponding to 10^7 cycles, the knockdown factor is approximately two whereas at 10^5 cycles, plain and fretting fatigue have nearly identical strengths under the specific test conditions. Similar results are shown in Figure 6.33, taken from [23], for a structural steel JIS SM430A tested in a bridge-type fixture at $R = -1$. There, the knockdown factor at 10^7 cycles is about one-third and the fretting and plain fatigue behavior is the same at about 10^4cycles. While

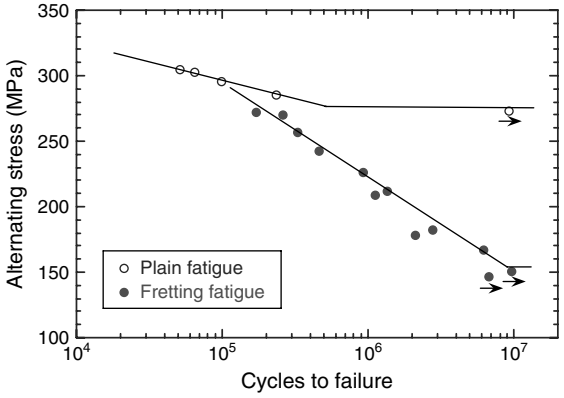


Figure 6.32. *S–N* curves for austenitic stainless steel ($R = 0$) in plain and fretting fatigue (after [19]).

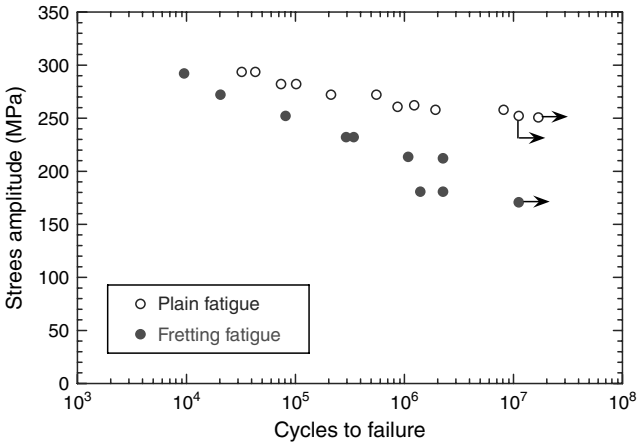


Figure 6.33. *S–N* data for structural steel JIS SM430A ($R = -1$) in plain and fretting fatigue (after [23]).

these two examples provide evidence that fretting fatigue is primarily a HCF problem, the results of these types of tests are dependent on many variables and a general conclusion about fretting fatigue being strictly an HCF problem should not be drawn.

6.9. ROLE OF SLIP AMPLITUDE

Of the many parameters that influence fretting fatigue, slip amplitude has been considered to be a primary driver in reducing fatigue strength in fretting fatigue [35]. In order to assess the influence of slip amplitude, the appropriate experiments must be performed.

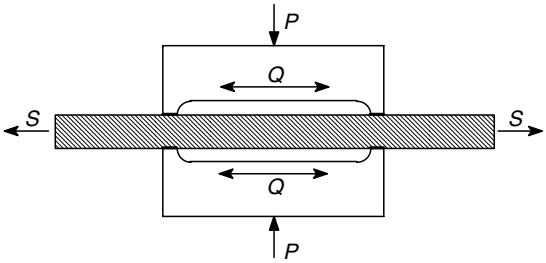


Figure 6.34. Schematic of bridge type pad for fretting fatigue experiments.

A bridge-type pad shown schematically in Figure 6.34 has been used extensively because it is particularly convenient for studying the effects of slip amplitude [35]. For very small slip amplitudes, however, where stick–slip conditions may occur under the pad, the variability of slip from one pad to another under nominally identical conditions makes it difficult to determine the actual conditions under each pad, either experimentally or computationally.

Slip amplitude has been incorporated into a fretting-fatigue parameter developed by Ruiz et al. to quantify the extent of fretting-fatigue damage [36]. They postulated that both slip amplitude, δ, and interface shear stress, τ, in combination, cause the damage that leads to reduction of fatigue strength. The amount of work done in overcoming friction per unit surface area in the slip zone can be characterized by the product, $\tau\delta$. If taken at the point where the product is a maximum, they postulated that the fretting damage is a maximum and is given by the product. Arguing also that the crack development is influenced by the stress, σ_t, tangential to the surface, they ended up with a fretting-fatigue damage parameter (FFDP) that combines aspects of initiation as well as propagation* in the form

$$\text{FFDP} = \sigma_t \tau\delta \tag{6.17}$$

A crack is predicted to initiate at the point where the parameter FFDP reaches a critical value. While it is difficult to establish the values of the variables in the parameter in a real component, it may provide guidelines in design for mitigating the effects of fretting fatigue by attempting to minimize the value of FFDP by tweaking the values of the individual terms.

Doing this, however, has no physical basis and although trends may be established for some combinations of material and geometry, the general applicability of this parameter has not been established.

* This type of formulation has little, if any, mechanics-based justification.

While much attention has been paid to the role of slip in fretting fatigue, stress analysis of the contact region in conjunction with a fracture mechanics analysis can shed light on criteria such as the growth or arrest of a crack that initiates in the contact region. Observation of a distinct transition from short to long life in fretting-fatigue experiments on aluminum using cylindrical pads led to a fracture mechanics-based analysis to explain the effect [3]. Results from a series of experiments using different cylindrical radii and different contact widths were plotted as shown in Figure 6.35 where fatigue life is seen to decrease suddenly when the contact width is increased. In this figure, a_0 is the critical contact size in one series of experiments where fatigue lives transition from in excess of 10^7 cycles (run-outs are shown schematically with arrows in the figure) to shorter lives ($<10^6$ cycles). Individual data points are not shown, but the transition from run-out to short lives occurs over a small range in contact length. In the various experiments, the peak stress in the Hertzian (cyclindrical) contact was maintained as a constant. The local stress field, including the gradient, changed as contact width was changed. By comparing the crack driving force due to the combination of contact stresses and applied stresses, K, to the threshold for crack propagation, K_0, corrected for short crack effects, Araújo and Nowell [3] were able to demonstrate the existence of a transition from crack arrest to crack growth depending on the particular stress field. Their numerical values based on contact widths agreed quite closely with those observed experimentally.

A plot very similar to Figure 6.35 was obtained by Magaziner et al. [37] in a similar set of fretting-fatigue experiments using cylindrical pads and a titanium alloy. However, their explanation was quite different. Whereas the experiments reported in [4] involved stick–slip conditions, those in [37] were found to have gross slip under certain combinations of loading. The data reported in [37] are plotted in Figure 6.36 and show that small contact

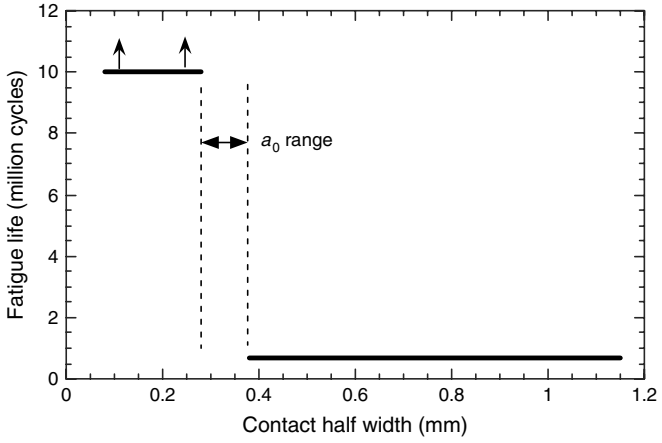


Figure 6.35. Schematic of observed fretting fatigue life behavior for Hertzian contact [7].

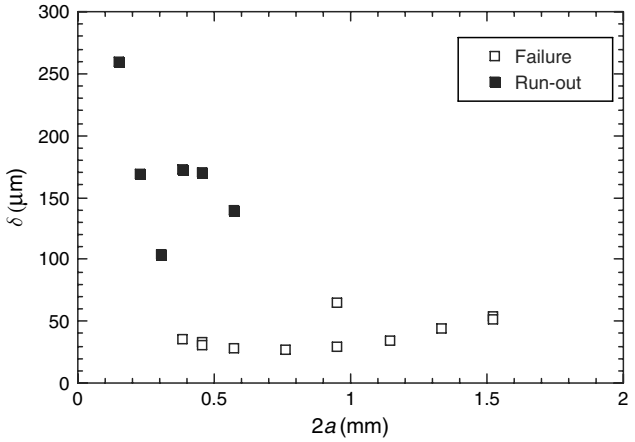


Figure 6.36. Comparison of slip distance with contact width in fretting fatigue. Data from [37]

widths are associated not only with run-out conditions but with large slip distances that involve total slip rather than stick–slip. In the data reported, run-out was taken as having lives greater than 10^6 cycles whereas the shorter lives, denoted as "failure" in Figure 6.36, involved failure in less than 10^5 cycles.

While the cycle count range and slip amplitudes in the two cited studies differed somewhat, both studies related the observed phenomenon of a jump in life with size of contact as a size effect. The individual analyses show that size is not the effect, it is either the stress field in the first study or the change from gross slip to slip–stick in the latter. The differences in test type (the latter controlling slip amplitude directly), material, and COF may have a greater effect on the observed behavior than just a "size effect." As for a stress analysis, as the authors of the latter study point out, there are concerns when trying to conduct a stress analysis when gross slip occurs. Both the possible wearing away of cracks as well as the exact location of the maximum stress (which may vary from cycle to cycle) make it difficult to apply a fracture-mechanics type of analysis to establish the conditions where crack arrest may occur.

6.10. STRESS-AT-A-POINT APPROACHES

Many approaches to life prediction under fretting-fatigue conditions have dealt with stress at a point, the value of a parameter at a point, or the stress or parameter at some distance from the surface, or an average value over some surface area or volume. In HCF, the notion that most of the life of a material is consumed in the nucleation or initiation stage has led to the widespread use of the maximum value of a parameter at

or near the edge of contact where stresses are normally at a maximum. Because of the steep stress gradients that are present in a contact region, parameters that are used for notch fatigue (see Chapter 5) should also have merit in fretting-fatigue life prediction. Parameters used for notches such as a modified SWT, Walker equivalent stress, modified shear stress range, or Findley parameter have been tried in an attempt to consolidate data from different fretting-fatigue experiments or from a range of conditions in a single experiment. These parameters are either unidirectional, representing a maximum stress in a direction normally parallel to the contact surface, or take into account the stresses in different orientations with respect to the contact plane and require consideration of values on all planes in order to find the maximum value.

Naboulsi and Mall [38] investigated three critical-plane-based parameters for crack initiation by computing their values over a process volume and compared the results with those obtained by averaging stress or strain over some region and then computing the parameter based on the average value. They used a modified SWT parameter on a plane where the value is maximum. The parameter, proposed in [21], had the form

$$\mathrm{SWT} = \sigma_{\max}\varepsilon_{\mathrm{a}} \tag{6.18}$$

where $\sigma_{\max}$ is the maximum normal stress and ε_{a} is the normal strain range. A second parameter, the Shear Stress Range (SSR), proposed in [39] has the form

$$\mathrm{SSR} = \Delta\tau_{\mathrm{crit}} = \tau_{\max}(1 - R_{\tau})^{m} \tag{6.19}$$

where $\tau_{\max}$ is the maximum shear stress on the critical plane where $\Delta\tau$ is maximum, R_{τ} is the shear stress ratio on the critical plane, and m a fitting parameter obtained from smooth bar fatigue data. The third parameter used is that of Findley [40] in the form

$$\mathrm{FP} = \Delta\tau + k\sigma_{n}^{\max} \tag{6.20}$$

where $\Delta\tau$ is the shear stress amplitude on a critical plane, $\sigma_{n}^{\max}$ is the maximum stress normal to the maximum shear plane, and k is a fitting parameter.

Numerical results were obtained based on averaging the parameter over a critical process zone and averaging the stresses over the same volume and computing the parameter based on the averaged stress. These did not differ significantly when obtained from fretting-fatigue experiments on Ti-6Al-4V using cylindrical pads. It was found, however, that the SWT parameter (based on normal stresses) had a steeper gradient than either the SSR or the FP parameters (based on shear stresses). For the SSR or the FP parameters, the values decreased less than 10% from their peak values at the surface when averaged over a process volume that extends 50 μm from the peak. This corresponds to approximately 4 grain sizes for this material. The use of a process volume, in this case, is somewhat dependent on the specific parameter being used if attempts are made to consolidate data with smooth bar fatigue data.

To add further fidelity to a fretting-fatigue parameter, Namjoshi et al. [41] introduced a modified shear-stress-range (MSSR) parameter that contains the better aspects of the SSR parameter, equation (6.19), and the Findley parameter, equation (6.20). The MSSR parameter considers both the shear stress range on a critical plane and the normal stress on that same plane. The critical plane is defined as the one where the MSSR parameter has its maximum value. The MSSR parameter has the form

$$\text{MSSR} = A\ \Delta\tau_{\text{crit}}^{B} + C\ \sigma_{\text{max}}^{D} \tag{6.21}$$

where $\Delta\tau_{\text{crit}}$ is as defined in Equation (6.19) and represents the maximum shear stress range on any plane, and σ_{max} is the maximum stress in the direction normal to the critical plane. It is of interest to note that the coefficients B and D have been chosen as 0.5 resulting in a parameter that is less sensitive to stress amplitude than one where stress is not raised to a power.* In [41], this MSSR parameter was found to be able to represent data better than the earlier SSR parameter by including effects of normal stresses on a critical plane. While it will be shown later that crack propagation can also be an important part of fretting-fatigue life prediction, even in the HCF regime, critical plane-based initiation parameters such as MSSR have been shown to be able to predict both the location of crack initiation as well as the angle of inclination of the crack formed at the surface [41, 42].

Neu et al. [42] point out that although fretting-fatigue life involves both crack initiation as well as crack propagation, the formation of a crack (initiation) is often desirable to avoid in design of complex structures. In a series of experiments on PH 13-8 Mo stainless steel, they observed that maximum shear strain amplitude predicted the location and orientation of the nucleated crack, but was unable to separate differences in life due to mean stress. Several other parameters investigated showed deficiencies in predicting all aspects of crack nucleation. For their material and test conditions, the Fatemi-Socie parameter (see below), Equation (6.22), was found to be the only parameter that predicted both the location and the orientation of a nucleated crack and captured the correct trend in life with change in mean stress. While many theories exist for fretting-fatigue crack nucleation, and some are able to consolidate data from selected experiments on specific materials, most of them fall short of quantitatively predicting the cycles to crack nucleation, however that condition is defined [21]. “Since the fretting damage process involves a myriad of interacting mechanical and chemical phenomena – wear, corrosion and fatigue – the notion of an all-inclusive model for fretting fatigue crack nucleation borders on the absurd.” [21]. For this and other reasons, attention has been directed toward the role that crack propagation plays in determining total life under fretting-fatigue conditions.

---

* See the discussion in Chapter 8 under Section 8.1, “Factors of Safety” for the implications of using a stress-based parameter that is in units of stress raised to a power.

Of particular concern in developing a fatigue initiation model is the combined effect of a local biaxial stress field with the steep stress gradients typically found in the contact region where cracks are likely to form. Noting that multiaxial criteria normally do not account for stress gradient effects, Araújo and Nowell [43] investigated the applicability of two critical plane models to rapidly decaying contact stress fields. Using a modified version of the SWT parameter, Equation (6.18) above, as well as a fatigue parameter suggested by Fatemi and Socie [44], they found that direct application of the models using the peak stresses at the edge of contact produced highly conservative predictions of initiation life compared to experimental data. The FS parameter used has the form

$$\mathrm{FS} = \frac{\Delta\gamma}{2}\left(1 + \alpha\frac{\sigma_{\max}}{\sigma_{\mathrm{y}}}\right) \tag{6.22}$$

where $\Delta\gamma$ is the difference between maximum and minimum values of the shear strain in a cycle, $\sigma_{\max}$ is the maximum stress normal to the critical plane, σ_{y} is the yield strength, and α is a constant that approaches unity at long lives.

The experimental data for total life were corrected for initiation life by subtracting out a computed crack propagation life. The predictions were worse for small contacts than for large contacts because of the steeper stress gradients at smaller contacts which also correspond to the HCF (long life) regime. To get better correlation with experimental results, the gradient effect was addressed by either averaging the stress over some volume or averaging the parameters over a volume, similar to the procedure used in [38] described above. The differences between the two methods were small. The most critical aspect of this approach was the size of the averaging volume which was determined not to be a material constant for consolidating data under several different test conditions on two different alloys, Al-4% Cu and Ti-6Al-4V. However, the best values for a critical volume were of the order of the grain size of the material to give the best estimates of fatigue initiation life as observed experimentally.

For life prediction, [33] used an equivalent stress parameter, $\sigma_{\mathrm{equiv.}}$, to consolidate stresses at various values of R as

$$\sigma_{\mathrm{equiv}} = 0.5(\Delta\sigma_{\mathrm{psu}})^{w}(\sigma_{\max})^{(1-w)} \tag{6.23}$$

where $\Delta\sigma_{\mathrm{psu}}$ is the alternating pseudo-stress range defined as

$$\Delta\sigma_{\mathrm{psu}} = \frac{1}{\sqrt{2}}\left[\begin{array}{c}(\Delta\sigma_{\mathrm{xx}} - \Delta\sigma_{\mathrm{yy}})^2 + (\Delta\sigma_{\mathrm{yy}} - \Delta\sigma_{\mathrm{zz}})^2 \\ (\Delta\sigma_{\mathrm{zz}} - \Delta\sigma_{\mathrm{xx}})^2 + 6(\Delta\sigma_{\mathrm{xy}}^2 + \Delta\sigma_{\mathrm{yz}}^2 + \Delta\sigma_{\mathrm{zx}}^2)\end{array}\right]^{(1/2)} \tag{6.24}$$

and $\Delta\sigma_{\mathrm{ij}}$ defines the pseudo-stress range for each stress component based on maximum and minimum points in the fatigue cycle.

The Walkerized equivalent stress, Equation (6.23), was used with the definition of pseudo-stress, Equation (6.24) in a multiaxial model to predict the cycles to crack initiation in their fretting-fatigue experiments. This approach had been previously used for

predicting notch fatigue behavior and was found to work only if the values of σ_{psu} were averaged over some volume to account for the stress gradients typical of notched specimens. However, even averaging over a few elements of a FEM model over the surface was not sufficiently accurate to consolidate results with smooth bar fatigue data. This led to the use of a weakest link model which was referred to as the stressed surface area, or Fs approach, described in Appendix E. The inability of this approach to consolidate fretting-fatigue data with smooth bar fatigue data was attributed to both the inability to account for local plasticity in the fretting region near the edge of contact and the neglect of crack propagation life when comparing results from an initiation model to total life experimental values.

One additional consideration in trying to predict crack initiation under a contact stress field with steep stress gradients is surface finish. Whereas the surface finish is smooth and can be controlled somewhat in notch fatigue, the surface where maximum stresses occur in fretting fatigue is in the slip regime where material damage and surface irregularities can be produced. In order to compare crack initiation in fretting fatigue to crack initiation under a similar gradient stress field at a notch, Nowell and Dini [45] proposed using notch fatigue tests. Using a notch such as depicted in Figure 6.37, they demonstrated that a notch geometry could be found that has a stress gradient very similar to that obtained in several fretting-fatigue contact stress geometries. While their analysis was for complete sliding, any conditions could be modeled. Also, while $p(y)$ in Figure 6.37 implies a stress that varies in the y-direction, the analysis for comparing stress gradients in fretting with those from a notch was conducted for a uniform stress field and considered the stresses at $x = 0$ starting at the root of the notch. These stresses, in turn, were compared with fretting stresses starting at the contact surface. For a best fit notch angle of $2\Psi = 60°$, best fit notch root radii of 0.03 to 0.12 mm were found, indicating that such dimensions could

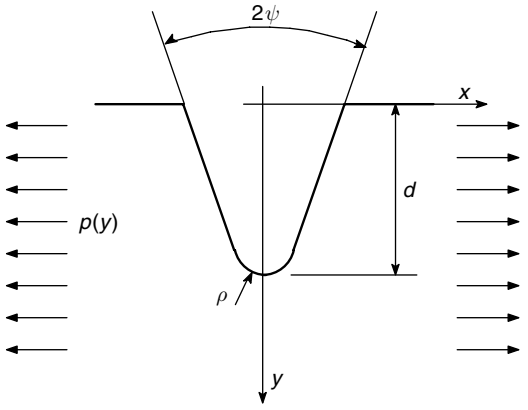


Figure 6.37. Geometry of notch to simulate fretting fatigue [45].

be achieved without any special machining necessary. Notch and fretting experiments with equivalent stress gradients are therefore possible and these would provide a possible means of separating out surface damage and stress gradient effects.

6.11. FRACTURE MECHANICS APPROACHES

One of the early applications of fracture mechanics to fretting fatigue was that of Nix and Lindley [46] who computed the critical size of a defect that could eventually propagate under fretting-fatigue conditions. For 2014A aluminum specimens with 3.5NiCrMoV steel fretting contact pads, they obtained the results shown in Figure 6.38 for two contact pressures. No attempt was made to account for possible small crack effects (probably not important in their case). For a non-fretting condition, the curves shown represent the constant threshold stress intensity (denoted by ΔK_0) and the applied stress intensity for a smooth specimen as a function of crack depth, a. For the fretting case, the applied stress intensity is derived from the combination of the local contact stress field as well as the applied bulk stress in the specimen. Because of the complexity of the local contact stress field, the stress ratio changes with increasing crack depth as reflected in the figure. This, in turn, causes a variation in the threshold stress intensity because ΔK_0 is a function of R. The intersection of the applied K and the threshold K defines the crack depth above which a crack or defect could propagate whereas for smaller crack depths, the driving force (applied value of $K = K_a$) is below the crack growth threshold. An alternate way in which data of this type can be interpreted would be to suggest that a fretting-fatigue crack of that critical size would have to be initiated or nucleated without growing as a crack. This would normally be the case for very small cracks, probably on the order of the microstructural features of the material.

Attempts to use the stress states in the contact region of fretting fatigue in models for the initiation and subsequent propagation of cracks have generally been less than successful. In particular, similar stress states have not been found using different specimen geometries that produce the same fretting-fatigue life of 10^7 cycles [8]. Further, these stress states have been found to depend highly on the assumed COF, μ [48]. Finally, the stress states generally are multiaxial and involve steep stress gradients, making it difficult to predict the values that might lead to crack initiation based on smooth bar fatigue data. This is essentially the same problem as that in notches, discussed in Chapter 5. An alternate approach has been to look at the problem from a fracture mechanics viewpoint, with an attempt to see if crack driving forces exceed the threshold for crack propagation [47, 49]. The primary questions to be answered in this approach are what constitutes an initiated crack length and along what direction should the crack be expected to propagate. To help answer some of these questions, a detailed analysis of the fracture-mechanics parameters in the contact region was conducted by Nicholas et al. [47]. There, several

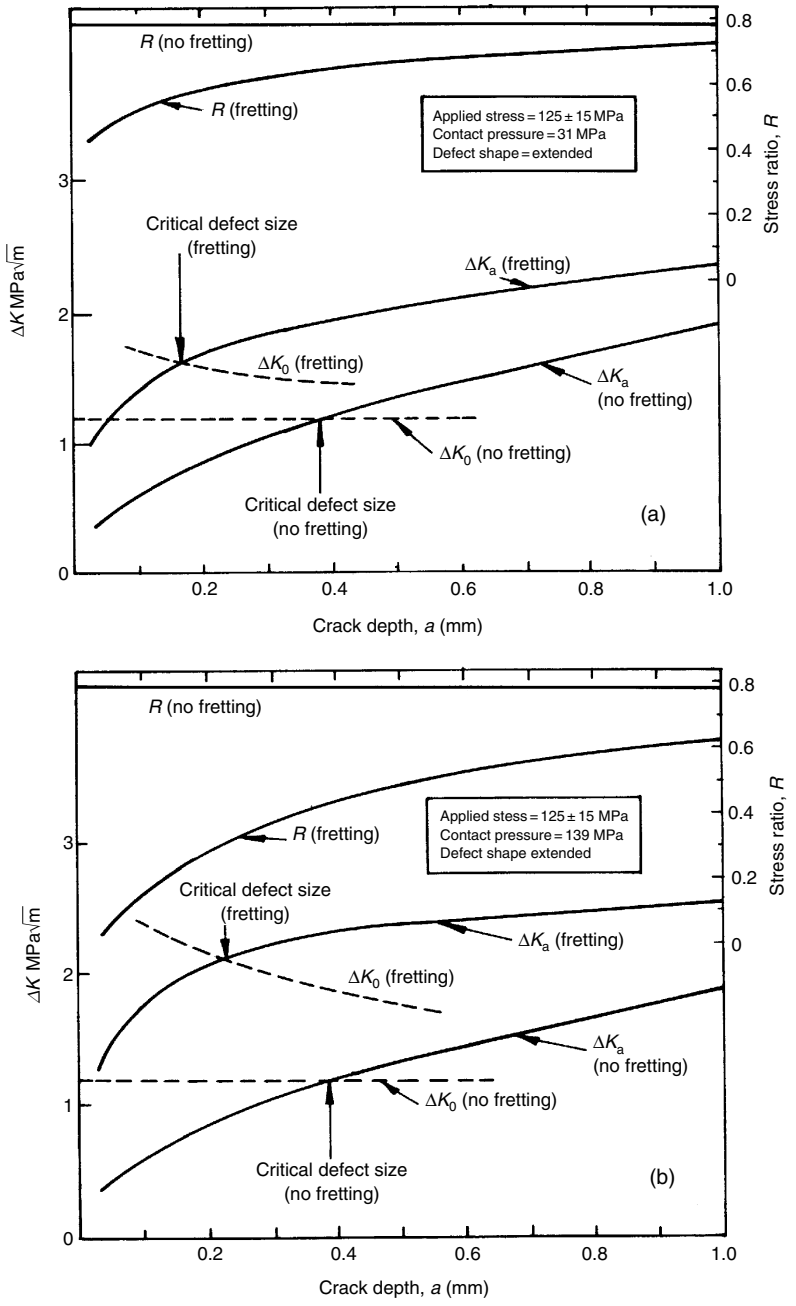


Figure 6.38. Applied and threshold stress intensity factors with and without fretting. (a) Contact pressure = 31 MPa, (b) contact pressure = 139 MPa [46].

different fretting-fatigue conditions were analyzed that produced long lives using a step-loading procedure. This type of experiment was analogous to determining the FLS under uniaxial fatigue using a step-loading procedure corresponding to a chosen HCF life. From analysis of these experiments, both multiaxial stress fields and mixed-mode stress intensity factors for specific cases were obtained. The results were analyzed in order to find some commonality which could lead to development of parameters having broad application to fretting fatigue. Variations in COF, μ, were also evaluated.

Stresses in the region of contact were computed using the 2-dimensional FEM assuming linear-elastic material behavior and plane-stress conditions. The FEM analysis of stresses in the contact region was made for an uncracked body. The development of a crack would influence the local contact stresses which, in this case, are treated as "far-field" for the purpose of the stress analysis and in the subsequent K analysis. The stress analysis for the contact region was made using the common assumption that the development of a crack and accounting for its compliance does not alter the computed stress fields. It is noteworthy that such a procedure was accomplished and showed, somewhat surprisingly, that the K analysis of the crack emanating from a contact region does not change appreciably if the crack is accounted for in the FEM analysis [50].

The approach taken to establish the threshold for propagation of a crack in the fretting region was similar to that of Chan et al. [49] where they employed a worst case notch (WCN) concept and applied it to a fretting-fatigue problem. For the biaxial plane-stress state, the Mode I and Mode II stress intensity factors were calculated along a crack having an arbitrary orientation with respect to the plane of the contact as depicted in Figure 6.39. From the computed stresses, the weight function method was used to calculate the Mode I and Mode II stress intensities along the crack.

To be able to represent conditions at different values of R ($R = K_{\mathrm{I,min}}/K_{\mathrm{I,max}}$) with a single parameter, an equivalent Mode I stress intensity was used in the form

$$\Delta K_{\mathrm{I,eq}} = \Delta K_{\mathrm{I}}(1-R)^{m-1} \tag{6.25}$$

The value of m was assumed to be identical for the threshold and low growth rates, and was found to be $m = 0.56$. For $R < 0$, the equivalent ΔK was taken as the maximum value of K and when $K_{\mathrm{I,max}}$ was negative, ΔK was taken to be zero.

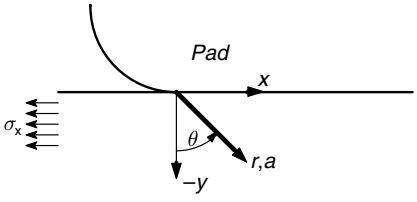


Figure 6.39. Nomenclature for orientation in K analysis.

For mixed-mode behavior, the effective stress intensity factor was defined as

$$\Delta K_{\text{eff}} = \sqrt{\Delta K_{\text{I,eq}}^2 + \Delta K_{\text{II,eq}}^2} \tag{6.26}$$

where $\Delta K_{\text{I,eq}}$ is determined from the stress field and corrected for different values of R using equeation (6.25) while $\Delta K_{\text{II,eq}}$ is taken simply as ΔK_{II} with no correction for R.

The effective threshold was modified to account for small crack effects by introducing the El Haddad parameter, a_0, as shown in previous sections. This produces an ever-decreasing threshold as the crack length, a, gets smaller as seen on a Kitagawa diagram.

$$K_{\text{eff}} = K_{\text{LC}} \sqrt{\frac{a}{a + a_0}} \tag{6.27}$$

where K_{LC} is the long crack threshold and a_0 is defined as

$$a_0 = \frac{1}{\pi} \left(\frac{K_{\text{th}}}{\sigma_{\text{e}}} \right)^2 \tag{6.28}$$

In Equation (6.28), K_{th} is the effective long crack threshold, corrected for R while σ_{e} is the endurance limit stress, also corrected for R.

The values of K along a straight line inclined at an arbitrary angle θ to the line normal to the contact surface (see Figure 6.39) were obtained through the equations:

$$K_{\text{I}}(a, \theta) = \int_0^a h_{11}(r, \theta, a) \sigma_{\theta\theta}(r, \theta) \mathrm{d}r + \int_0^a h_{12}(r, \theta, a) \tau_{\text{r}\theta}(r, \theta) \mathrm{d}r \tag{6.29}$$

$$K_{\text{II}}(a, \theta) = \int_0^a h_{21}(r, \theta, a) \sigma_{\text{qq}}(r, \theta) \mathrm{d}r + \int_0^a h_{22}(r, \theta, a) \tau_{\text{r}\theta}(r, \theta) \mathrm{d}r \tag{6.30}$$

where $\sigma_{\theta\theta}(r, \theta)$ and $\tau_{\text{r}\theta}(r, \theta)$ represent the normal and shear stress on the crack surface, respectively, and h_{11}, h_{12}, h_{21}, and h_{22} are the mixed-mode weight functions developed by Beghini et al. [51] for an edge crack in an infinite medium.

One of several cases analyzed was a 4 mm thick specimen with a bulk stress of 200 MPa. From the FE analysis the stresses at the maximum and minimum applied load were found to stabilize within the first complete cycle. For this case, the stresses were computed along lines at angles of 0°, 10°, 30°, and 50°. The normal and shear stresses along the crack at an angle of 0° are shown in Figure 6.40. For this and all angles evaluated, the computations showed that the shear stress amplitude is small. Further, the stress ratio for the stresses normal to the crack surface, $\sigma_{\theta\theta}$, is nominally about 0.5 for the crack oriented at $\theta = 0°$. Normal stresses were also seen to decay rapidly with crack length, a, and became compressive for larger angles, $\theta = 30°$ and $\theta = 50°$.

From these stresses, values of K_{I} and K_{II} were determined using the weight-function method, and the short-crack-corrected threshold for the value of R at each point was

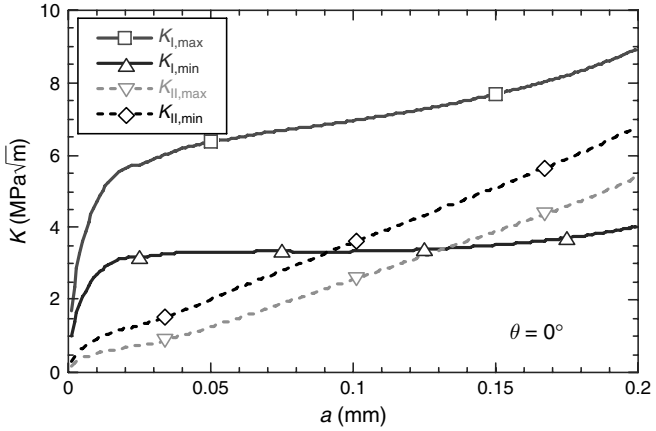


Figure 6.40. K distribution as function of crack depth for Modes I and II [47].

computed for comparison. The mixed-mode driving force and threshold for each of the four angles were determined for crack lengths up to 200 μm. The results showed that the threshold is exceeded at crack lengths that are fairly large compared to the value of a_0 which tends to be about 30 μm for these computations. From the computations, crack growth would occur only at crack lengths above 185 μm for the crack at 0° as shown in Figure 6.41. Experimental observations of crack orientations were made and indicate that crack nucleation angles are typically around 45° as shown in Figure 6.42. These cracks turn towards a direction normal to the contact surface within crack lengths of the order of tens of microns where they become primarily Mode I cracks. Based on these observations,

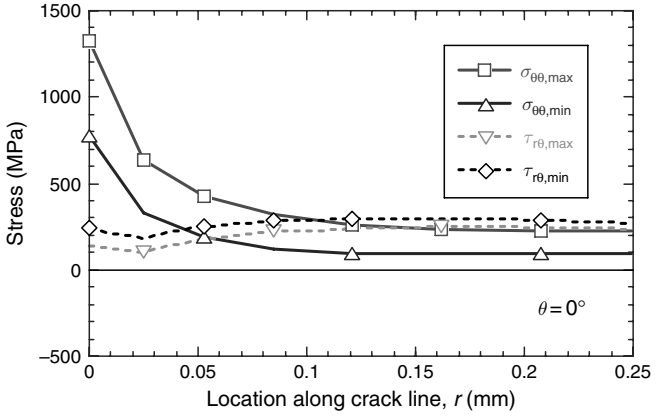


Figure 6.41. Shear and normal stress distribution as function of depth [47].

the analysis only of what happens along a line $\theta = 0°$, which is perpendicular to the contact surface, is deemed important.

From Figure 6.41 at 0°, the maximum and minimum values of the Mode I stress intensity show that the stress ratio, R, used in the equations for K ($R = K_{\mathrm{I,min}}/K_{\mathrm{I,max}}$), is very close to the applied stress ratio for the bulk load which was 0.5. Figure 6.41 also shows that at 0°, the Mode II component is smaller than that for Mode I but, more importantly, that ΔK_{II} is quite small.

Comparisons were made to evaluate the effects of specimen thickness, clamping load, and COF on the tendency of a crack to grow or not grow under the experimentally observed loading conditions corresponding to a fatigue life of 10^7 cycles. In one case the crack growth was close to occurring for all crack lengths even though the growth condition does not occur until the crack is over 100 μm long while in another case, the driving force was well below the threshold until the crack reached a length of almost 200 μm. There appeared to be more of a tendency for crack growth to occur at either a higher clamping stress or a higher shear stress. Overall, it was found that the fracture mechanics methodology holds more promise for predicting failure or FLSs than analysis of the stress field. The reason for this is that a threshold stress intensity is available for long cracks either under Mode I only or under mixed-mode conditions and can be easily corrected for short crack effects. On the other hand, knowledge of the stress field involving steep gradients requires a gradient stress failure model which is not readily attainable from smooth bar failure data. Further, the stress fields were very sensitive to the value of the COF, μ, whereas the K solutions were less sensitive other than for extremely short crack lengths. The role of μ in fretting-fatigue analysis is discussed in the next subsection.

The length of an inclined crack before it turns 90° to the fretting surface varies widely with material, pad geometry, and fretting fixture and loading conditions. Whereas Figure 6.42 shows a crack that is normal to the surface within 10 μm for Ti-6Al-4V, the same alloy at 260 °C is reported to develop cracks that do not turn perpendicular to the loading direction before achieving a length from 200 to 500 μm [52]. An example of such a crack is shown in Figure 6.43 which was obtained using different loading conditions and a somewhat different fretting-fatigue fixture than that for which the crack in Figure 6.42 was obtained.

In yet another fretting-fatigue fixture, that of the bridge type, cracks are reported to initiate at an angle of 60° to the surface and then to gradually turn normal to the bulk loading direction. For a case where the pad and specimen material were SM430 steel, the crack did not become perpendicular to the surface until a depth of over 700 μm which the authors attribute to where the fretting effect is eliminated [23].

Mutoh and Xu [23] propose that an accurate assessment of crack propagation life must take into account the mixed-mode loading conditions and the combination of Mode I and Mode II loading on a crack, even when the crack is normal to the surface in a fretting-

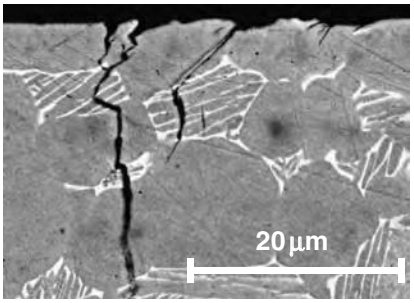


Figure 6.42. Cross-section of a fretting fatigue cracked specimen prior to fracture [47].

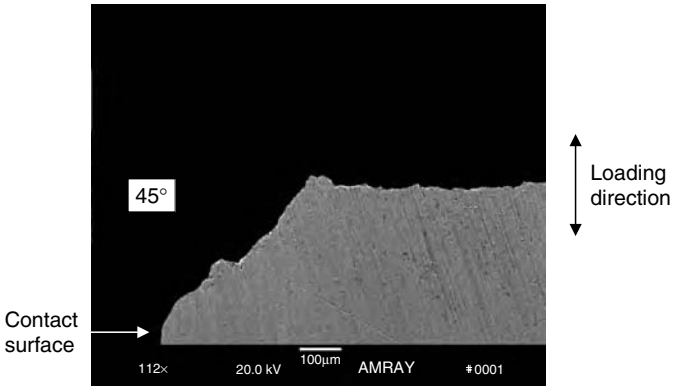


Figure 6.43. Cross-section of failed fretting fatigue sample showing crack orientation [52].

fatigue experiment. Their criterion for initiation of a crack is related to the direction of maximum shear stress range, but propagation is governed by the direction of the maximum tangential stress range around the crack tip. They propose a numerical integration scheme where the crack length is incremented and the orientation continually updated. In the numerical example presented, however, they find that "the fretting fatigue crack growth curve under mixed mode agrees well with the fatigue crack growth curve under mode I, except for the initial first few data points."

6.12. A COMBINED STRESS AND K APPROACH

An example of an investigation where many of the features needed for an accurate life prediction scheme are incorporated is that of Golden and Grandt [22]. There, they combined an initiation model with fracture-mechanics-based crack growth modeling to try to predict experimental data from several fretting-fatigue experiments. The crack growth

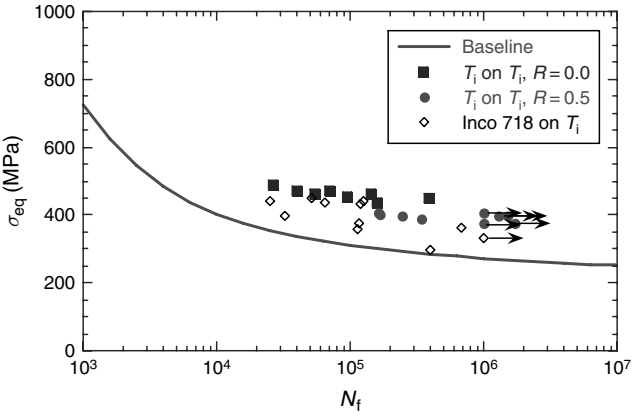


Figure 6.44. Smooth bar and fretting test data adjusted for stressed surface area using equivalent stress [22].

portion accounted for the three-dimensional nature of the cracks and their subsequent growth, accounting for aspect ratios. The initiation modeling accounted for multiaxial and mean stress effects while making use of an equivalent stressed surface area as done in [33] (see also Appendix E). From their initiation modeling alone, Figure 6.44 shows how the use of an equivalent stress parameter that is adjusted to account for the gradient of stress using the Fs approach can consolidate data from a number of fretting-fatigue tests but does not match smooth bar fatigue data. The reason for this is the assumption that the initiation model represents total life. The authors then introduce the crack growth life prediction to subtract from the total life observed experimentally. The computations, based on a assumed crack depth of 25 μm, are shown to produce crack propagation lives that are relatively insensitive to the assumed initial crack size. Table 6.1, taken from [22], illustrates the insensitivity of crack propagation lives to initial crack size, a_i, for four different fretting-fatigue experiments. Note for Experiment # 4, which comes closest to the HCF region, that an initial crack size as small as 6.4 μm produces a crack propagation

Table 6.1. Crack propagation lives* from four experiments for different values of a_i (from [22])

Exp't	*Initial crack size, a_i,* (μm)				
	6.4	12.7	25.4	50.8	101.6
1	51	46	41	36	31
2	188	166	146	125	97
3	199	178	158	135	104
4	677	641	595	511	329

* Lives are given in thousands of cycles.

life that is not significantly different than that for an initial crack size of 50 μm. In this study, the initial crack size for all of the computations was chosen to be equal to the El Haddad transition crack length, a_0, which was approximately 25 μm.

The predicted lives for several sets of experiments using either the initiation model alone or the combined initiation and propagation modeling are compared with experimental lives in Figure 6.45. The figure shows how the combined predictions match reasonably closely with the experimental results up to lives in excess of 10^6 cycles. These results can be seen better in Figure 6.46 where the predictions for total life are compared with

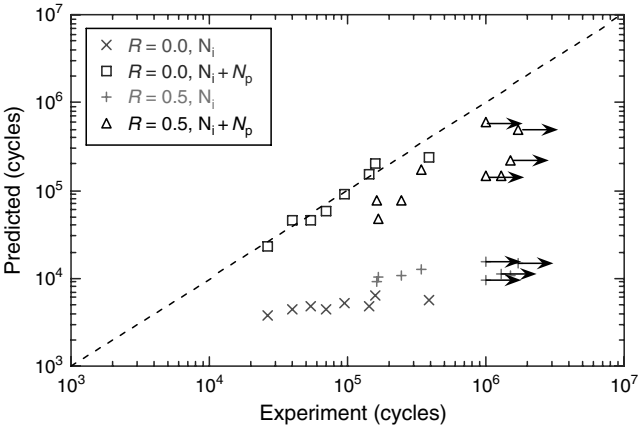


Figure 6.45. Comparison of predicted versus experimental fretting fatigue lives for initiation and total life calculations [22].

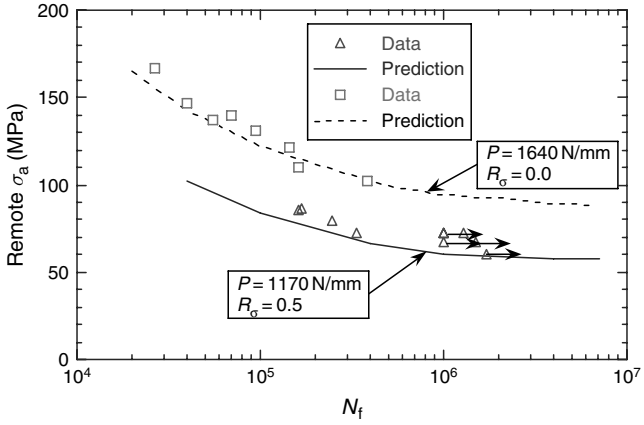


Figure 6.46. Experimental fretting fatigue lives and model predictions for two data sets plotted against remote applied stress [22].

experimental results for two sets of data obtained at different applied stress ratios. To display the data better, the plot uses applied (remote) stress.

6.13. COMPARISON OF FRETTING-FATIGUE FIXTURES

In [53], three experimental fixtures were compared to assess their characteristics regarding the propensity for crack propagation after initiation. The first system, denoted "A," has been used to test relatively thin (2–4 mm) flat specimens against flat pads with blending radii at the edges and is shown in Figure 6.47 [2]. Unlike classical fixtures, the entire load applied to the specimen is transferred to the fixture through the fretting pads since the portion of the specimen beyond the contact area is stress free. As a result, gross slip throughout each test is eliminated (for valid tests), thereby simplifying calculation of the shear stress on the contact. Thin specimens are used in order to keep the shear force, Q, low compared to the clamping force, P, while still maintaining high enough values of bulk stress to represent the conditions that occur in actual components.

The second system, denoted "B," uses a flat specimen with cylindrical or short flat pads with blending radii on both sides, as is shown in Figure 6.48. This fixture is typical of many reported in the literature and produces partial transfer of the load through the fretting pads to a nominally rigid-fixture device that controls the applied clamping load and pad alignment. The fixture compliance controls load transfer from the specimen to the pads. Gross slip occurs early in each test until surface interactions change local friction behavior, after which partial slip conditions prevail. A modified fixture where the slip distance is controlled by a independent loading device, thus controlling the shear force indirectly, has been developed [54].

The third system is a simplified laboratory dovetail fixture (Figure 6.49), denoted "C," in which the shear and clamping loads are the reactive forces to the applied loading and, therefore, are both cyclic and in-phase with the applied load. Cylindrical or short flat

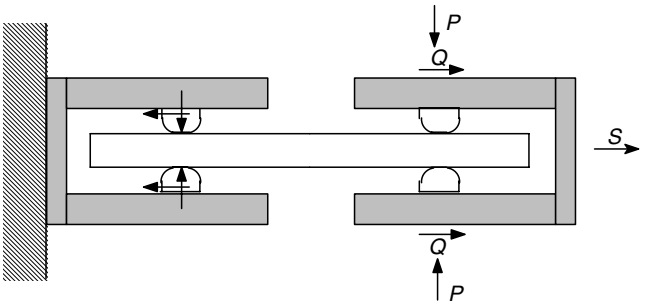


Figure 6.47. Schematic of full load transfer fixture "A".

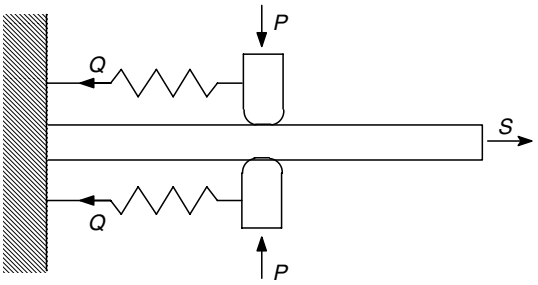


Figure 6.48. Schematic of partial load transfer fixture "B".

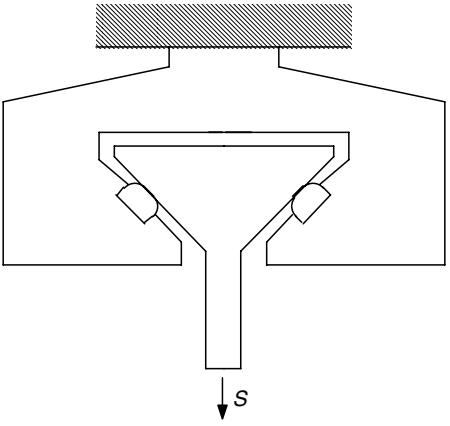


Figure 6.49. Schematic of laboratory dovetail fixture "C".

pads with blending radii may be used. As in fixture B, gross slip can occur early in the test until partial slip conditions prevail.

The distributions of σ_{xx} below the edge of contact at maximum load for experiments conducted on the three fixtures are shown in Figure 6.50 on a semi-log plot. Here, y is the coordinate into the specimen depth. For fixtures A and B, y is normal to the surface. For fixture C, y is inclined 15° away from the contact area, since this was the crack growth path. For the dovetail experiments (C1 and C2), the subsurface stresses decay the most rapidly and become compressive at a local minimum that occurs at $\sim 100\,\mu$m. The local minimums for fixtures A and B are not as well defined. They are tensile and occur closer to the surface, between ~ 50 and $100\,\mu$m (A1, A2, B1). For the cylindrical pad (B2), the stress field does not decay as rapidly as in the other cases, and the local minimum is not present.

The effective stress intensity factor range, K_{eff}, for each experiment as well as the short crack ($K_{\text{th,sc}}$) and long crack ($K_{\text{th,lc}}$) thresholds for a given crack depth, a, are

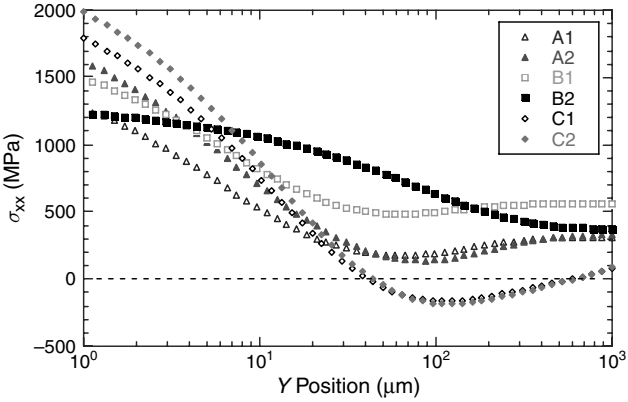


Figure 6.50. Axial stress as a function of depth from surface for three fretting fixtures.

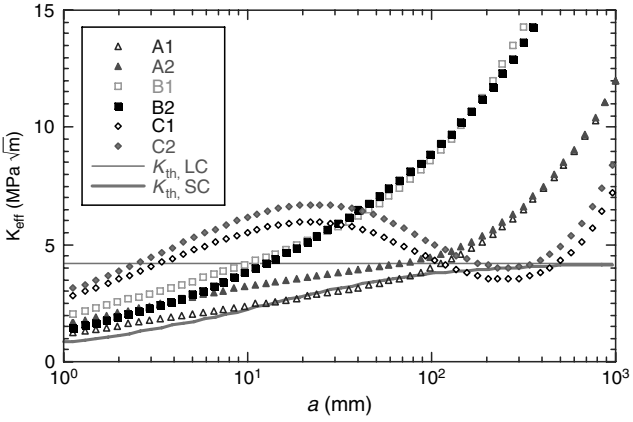


Figure 6.51. Effective stress intensity factors for three fretting fatigue fixtures.

shown in Figure 6.51. K_{eff} for all three fixtures under nearly all tested conditions falls above $K_{\text{th,sc}}$ for cracks below $\sim$100 μm, suggesting that all cracks will propagate to some length, however, not always to failure. K_{eff} for fixture A is shown to cross the short crack threshold near 10–20 μm crack depths under some loading conditions. The dovetail fixture experiments, however, have a local minimum for K_{eff} at approximately 100 μm where long-crack fracture mechanics dominates, indicating a potential for these cracks to arrest. Fixtures A and B have K_{eff} continuously increasing and without a local minimum. The most rapidly increasing K_{eff} is shown for fixture B. K_{eff} is similar in magnitude for fixtures A and B for very small flaw sizes, but the rate of increase of K_{eff} for fixture A does not occur until after $\sim$100 μm. Crack growth lives, therefore, would be expected to

be much longer for experiments using the A fixture than those for the B fixture. If the total lives are similar, then initiation would have taken place earlier in the A experiments than for those in B. The results for the dovetail fixture, on the other hand, show a distinct possibility that initiation could have taken place at stress levels below which were recorded for total failure. Some critical stress level had to be achieved, according to the K analysis, in order to prevent crack arrest because of the observed dip in the applied K. The difference in the initiation and threshold behavior of fixtures A and B compared to the dovetail fixture C can be primarily attributed to the differences in thickness.

For experimental data generated corresponding to similar total lives in the range of 10^6 to 10^7 cycles, the stress intensity factor fields are somewhat different. Only the dovetail fixture appears to closely approach a condition where the effective threshold, corrected for small crack behavior, overcomes the applied stress intensity factor, thereby leading to crack arrest. In the other two fixtures, propagation appears to always be taking place for any crack length. The stress intensity factor fields are rather insensitive to the local contact stresses, which vary with μ.

Based on the experimental conditions covered, the dovetail fixture is the only one where cracks always can initiate and arrest until the load for exceeding the crack growth threshold is exceeded. Thus, the load causing failure should relate to the threshold stress intensity factor and not to any initiation criterion. On the other hand, fixture B produces conditions where the load that produces failure should be related to a criterion for initiation since any crack that initiates will continue to propagate. In fixture A, the load for failure may be related to either an initiation criterion or a fracture mechanics threshold, depending on the specific conditions. In general, for any fixture, it would seem to be important to compute the fracture mechanics driving force, K_{eff}, and compare it with the threshold stress intensity factor corrected for small crack behavior if the data are to be interpreted correctly.

The data comparisons among the three fixtures demonstrate that a simple fracture mechanics model, involving exceeding a material threshold condition, is insufficient to explain all of the experimental results. Rather, both crack initiation and crack propagation appear to be necessary considerations for this total life range of 10^6–10^7 cycles.

6.14. ROLE OF COEFFICIENT OF FRICTION

Fretting-fatigue experiments normally result in the degradation of the mechanical properties of material in a region of contact where cyclic tangential loads occur in the presence of normal or clamping loads. Such a process involves cyclic material damage accrual where many mechanical factors affect the degradation process. Included in these are the contact pressure, the slip amplitude at the interface, the COF and the magnitude of the tangential shear stress, and bulk stress at the contact interface. In fretting fatigue, as opposed to wear or galling, the contact region is one where the two bodies experience

relative motion only near the edges of contact ("slip") while the central region remains in full contact, normally referred to as "stick." Of the many variables associated with the phenomenon [28], one parameter, the relative COF between the contacting bodies, has been shown numerically to have a significant influence on the magnitude of the stresses and relative slip displacements in the contact region [8].

In many modeling efforts it is assumed that fretting-fatigue life prediction criteria are predicated on contact stress state. For example, in a critical plane stress criterion, (see, for example, [21, 31, 55]), the crack is assumed to initiate along the plane with the maximum value of some stress-based parameter. Other criteria, for example Nicholas et al. [47] and Naboulsi and Mall [38], also require the determination of the contact stress field. Hence, considering various pad configurations and load conditions with nominally identical experimental fretting-fatigue life, in these cases, it is sufficient to compare their maximum stress. Also, the history dependence of fretting fatigue during cycling causes the stress state to undergo changes, for example Naboulsi and Mall [55]. Such a consideration is beyond the scope of what has been investigated.

Experiments have shown that the magnitude of the average COF changes with number of cycles in fretting of titanium against titanium [56]. While no direct measurements have been made of COF in the slip region where relative motions are of the order of only tens of microns, several computational efforts have deduced values by matching results from models to experimentally observed phenomena. In fretting-fatigue experiments on a stainless steel material, elastic–plastic finite element modeling using a higher COF, $\mu = 1.5$ was found to better model the experimentally observed extent of local plasticity than using $\mu = 0.5$ or 1.0 [57]. In another study, Goh et al. [58] found that in crystal plasticity calculations for Ti-6Al-4V fretting-fatigue experiment simulations, a value of $\mu = 1.5$ provided the best simulation of the experimentally observed dimensions of the slip regions of the contact. It is to be noted that these values of COF are considerably higher than average values generally measured in contact experiments and subsequently used in modeling of contact geometries. For example, Farris et al. [59] have reported a saturated value of $\mu = 0.5$ after a large number of fretting-fatigue cycles in the same titanium alloy. In other fretting-fatigue experiments, a saturated value of an average COF = 0.5–0.7 was obtained using flat pads with a blend radius against 1 mm thick specimens of identical Ti-6Al-4V [60]. The saturated value was reached after approximately 1000 cycles and an initial value of about $\mu = 0.25$. In another study, McVeigh et al. [56] analytically modeled the interfacial conditions in nominally flat contacts and obtained good correlation of computations with experimentally observed amounts of interfacial damage in Ti-6Al-4V specimens using an average value of 0.4 for the COF. In the same material, $\mu = 0.33$ has been used in one investigation as an average value for computations of contact stress fields [61] while $\mu = 0.3$ has been used in another [8].

In Nicholas et al. [62], the K solution for a Mode I crack at the edge of the region of contact where stresses are maximum was obtained. Although the local stress fields were

different for two cases of fretting geometries and loads corresponding to the same life of 10^7 cycles, there was also no correlation of the K fields from the two cases compared. From this observation, the possibility that initiation took place at stress levels lower than the final one obtained in the step test procedure in two cases, and that the final stresses were based on a threshold for crack propagation, was eliminated. Subsequently, Naboulsi and Nicholas [48] investigated the possibility that the COF is not a constant in the region of slip but, rather, that f may depend on the relative slip amplitude. While the results of their numerical simulations indicated that a variable COF might reproduce the experimental conditions in [8] better than a constant COF, the findings pointed clearly toward the need to have a higher COF, perhaps greater than $\mu = 1.0$, in order for the stress fields from several different experimental conditions to approach each other. These stress fields which resulted in similar fretting-fatigue lives of 10^7 cycles were postulated to be similar since they produced similar fretting-fatigue lives. Only a high COF could produce such trends for the experimental conditions modeled. In their simulation of experiments with short and long fretting pads, both the static and the dynamic COF were assumed to have a range of values, but the static coefficient, μ_s, was assumed to be larger than the dynamic coefficient, μ_d. Based on the cases analyzed, the static coefficient of friction, $\mu_s = 2.0$, and the dynamic coefficient of friction, $\mu_d = 1.0$, produced the best match of stress state for the long and short pad configurations.

In Hutson et al. [63], experimental observations in fretting-fatigue experiments similar to those in [8] and [47] indicated that for a low average clamping stress (200 MPa), the propagation life should be short since no cracks were found at a life of 10^6 cycles which was 10% of the expected life under the imposed stress conditions. Calculations using $\mu = 0.3$ indicated that initial cracks with depths of 80 μm or less would have infinite or very long propagation lives. Changing the coefficient of friction to $\mu = 1.0$, however, produced the short propagation lives that were expected. This indirect evidence that the local coefficient of friction is higher than the average values measured experimentally is consistent with that of the computations of Naboulsi and Nicholas [48] described above.

One of the problems in modeling fretting fatigue with a single value of the coefficient of friction, μ, is that μ is not constant throughout the experiment and may take many cycles to reach a stabilized value. If an average value of μ is obtained too early in the test, it may not adequately represent the phenomena and stress field calculations that represent what happens later in the test when initiation takes place. Friction experiments where the shear load is increased until the onset of total slip is reached are commonly used to obtain average values of the coefficient, $\mu_{ave} = Q/P$. Figure 6.52 shows a best fit to actual data for determining μ, the actual data are not shown. In this particular case involving titanium, over 10^4 cycles are required before equilibrium is achieved.

Similar findings on the evolution of the coefficient of friction in fretting-fatigue experiments are reported by Hills et al. [20]. In work on an aluminum −4% Cu alloy, they

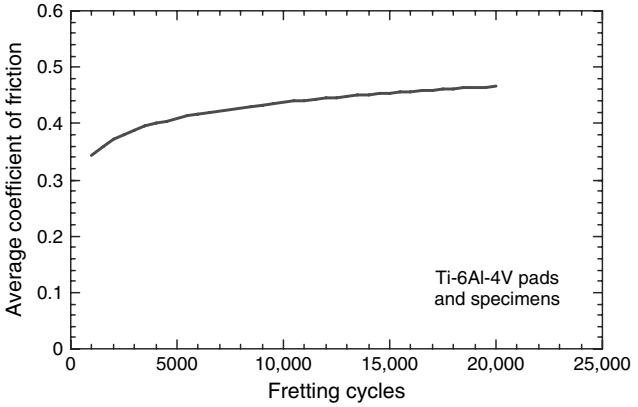


Figure 6.52. Evolution of coefficient with number of fretting cycles (from [33]).

report the value of μ to go, in one case, from an initial value of 0.2 to 0.55 in only 20 cycles. In another case, at lower contact pressure, μ is observed to go from 0.2 to 0.75 in 150 cycles. Based on these examples, the number of cycles to reach a stable value of μ depends on both the materials and the contact conditions, both geometry and loads.

If the two bodies in contact are subjected to fretting under partial slip conditions, the surfaces may undergo modification resulting in an increase in the COF, f [64]. Values of the average COF have been reported to increase over the first numbers of cycles as illustrated above. However, the relation between the average coefficient and the local coefficient is not known. The local coefficient may have a large effect of the local stresses in the contact region. Following this line of reasoning, Dini and Nowell [65] conducted an analysis of the contact region between a flat pad with a blending radius and a half plane to establish the relationship between the average (mean) COF, μ_m, and the COF that exists within the slip zone after n cycles of loading, μ_n. Their assumption is that the local relative displacements in the slip zone will result in a surface modification and will produce an increase in the local value of μ. The average value of μ is determined experimentally by increasing the shear load, Q (Figure 6.53) until the onset of slip. Using the nomenclature of Figure 6.53, calculations were carried out for geometries that ranged from Hertzian contact where the flat contact length a is zero to an almost sharp punch where $a/b = 0.99$. For various combinations of normal to shear load ratios, the calculated values of μ_m and μ_n (denoted f_m and f_n) are shown in Figure 6.54. Two important conclusions can be drawn from these results. The first is that the local value of μ is higher than the average value. The second is that the local value is very sensitive to the measured average value for the sharp punch case, and less sensitive for the Hertzian (rounded punch) case. However, the numerical results show that fairly large values of the local coefficient, μ_n, up to 1.0 are predicted for some cases where the average coefficient, μ_m, is in the range closer to 0.3–0.5 for nominal values of Q/P in the same range 0.3–0.5.

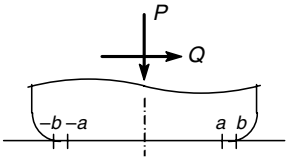


Figure 6.53. Contact geometry for flat pad with radius. b is the semi-width of the overall contact and a is the semi-width of the central flat part.

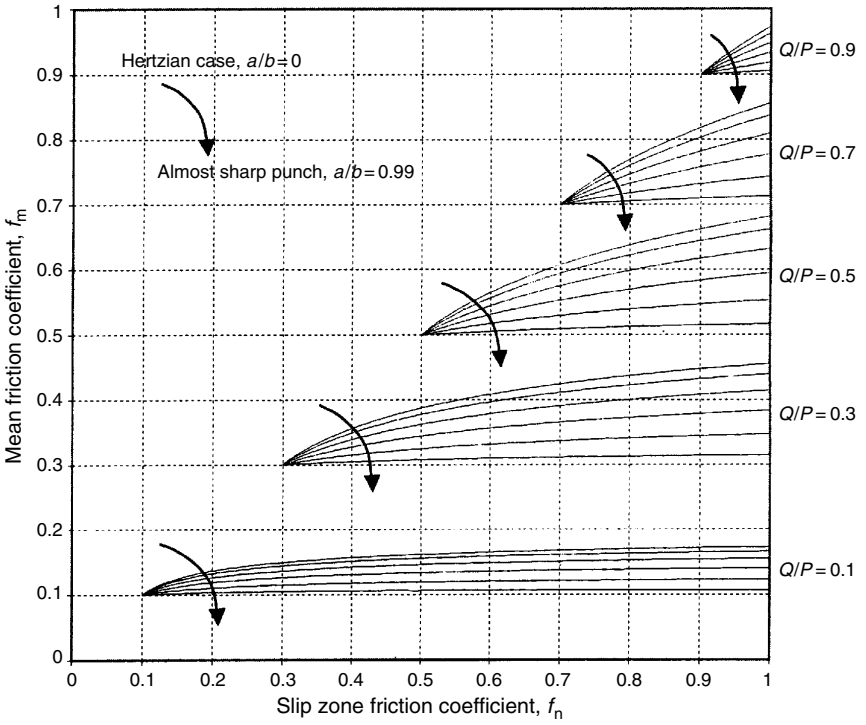


Figure 6.54. Numerical results for different contact geometrics, $a/b = 0, 0.2, 0.45, 0.7, 0.9, 0.99$ [65].

These numerical findings are consistent with those of the previously cited references where larger local values of COF are deduced from combined experimental and numerical findings. These higher values are known to affect the local contact stresses which, in turn, can have a significant impact on crack initiation criteria and a lesser impact on crack growth behavior away from the local contact stress field. Thus, the value of COF becomes an important aspect in the analysis of fretting-fatigue conditions and, unfortunately, is not an experimentally measurable quantity.

6.14.1. *Average versus local coefficient of friction*

The average COF, μ, is commonly obtained experimentally by increasing the shear load in a contact region until the bodies in contact just start to slide with respect to each other. Of greater importance, however, for modeling purposes, is the local value of m in the slip region in stick–slip contacts. The average value and local slip zone value have been shown to be different. The slip zone coefficient of friction, μ_s, is obtained from the average value as follows [27]

$$\mu_s = \mu + \frac{2}{\pi}\int_{\mu_0}^{\mu_s} (B\sqrt{1-B} + \sin^{-1}\sqrt{1-B})\mathrm{d}\mu_s \tag{6.31}$$

where $B = Q/\mu_s P$, μ_0 is the initial value of COF, and μ is the average value. Equation (6.31) ignores the effect of the bulk load on the contact tractions and assumes that the friction coefficient in the stick zone does not change.

Araújo and Nowell [43] later reported a change in the equation due to a slight error that they describe as affecting the final form of the equation but the values are little changed. The revised equation has the form

$$\mu_s = \mu + \frac{4Q}{\pi P}\left[\frac{\pi}{2} - \cot\theta_s - \theta_s\right] - \frac{2}{\pi}\left[\mu_s\varphi_s - \frac{Q}{P}\tan\varphi_s\right] \tag{6.32}$$

where

$$\theta_s = \sin^{-1}\sqrt{\frac{Q}{\mu_s P}} \qquad \varphi_s = \cos^{-1}\sqrt{\frac{Q}{\mu_s P}} \tag{6.33}$$

6.15. SUMMARY COMMENTS

Three main factors have to be addressed in a robust life prediction scheme for fretting fatigue:

1. The initiation life has to be treated separately from the propagation life. While no definition can be given for the flaw size that separates initiation from propagation, many instances arise where the crack propagation results are insensitive to the actual value used. The use of the value of a_0 from the El Haddad short crack formulation appears to be a reasonable approach, but a_0 takes on different values depending on stress ratio, R, in many cases. It is also somewhat dependent on the geometry of the body into which the crack propagates, but generally only for long cracks.
2. Point stresses in the presence of steep stress gradients cannot be used as part of a realistic criterion for crack initiation. Instead, they must be modified as in notch

fatigue in order to be able to consolidate them with smooth bar fatigue data. In fretting fatigue we are normally dealing with stress fields that are the equivalent of those encountered at the tip of a very sharp notch. Multiaxial stress states can be an important consideration when establishing initiation criteria.

3. The stresses necessary to initiate a crack in fretting fatigue in the contact region may be altered by the presence of damage from the fretting process itself, by changes in COF, μ, by changes in the surface roughness, or through local plasticity and/or material removal at the surface. These considerations should be taken into account in model development.

In all of the above, the application to HCF as opposed to LCF can be addressed in some cases by treating the problem as one where the threshold for crack propagation is the governing criterion, whether or not a real crack has initiated. In such cases, it would have to be shown whether or not an initiated fretting-fatigue crack would continue to propagate based on the combination of a local stress field from the contact conditions and a far-field stress field from the loaded component into which the crack is propagating.

There have been many successes using fracture-mechanics-based criteria for HCF thresholds (and LCF lives) in fretting fatigue based on the use of a friction coefficient that is appropriate for the particular experimental configuration. For HCF thresholds, it is assumed, further, that the threshold crack growth value in a gradient stress field is the same as that obtained under uniform stress (see Chapter 8 for a discussion of factors that affect crack growth threshold values).

For an extensive coverage of fretting fatigue including background, experiments and experimental results, and analytical methods including life prediction, the reader is referred to the review article by Farris et al. [66].

REFERENCES

1. Vingsbo, O. and Söderberg, D., "On Fretting Maps", *Wear*, **126**, 1988, pp. 131–147.
2. Hutson, A.L., Nicholas, T., and Goodman, R., "Fretting Fatigue of Ti-6Al-4V Under Flat-on-Flat Contact", *Int. J. Fatigue*, **21**, 1999, pp. 663–669.
3. Araújo, J.A. and Nowell, D., "Analysis of Pad Size Effects in Fretting Fatigue Using Short Crack Arrest Methodologies", *Int. J. Fatigue*, **21**, 1999, pp. 947–956.
4. Tomlinson, G.A., Thorpe, P.L., and Gough, H.J., "An Investigation of the Fretting Corrosion of Closely Fitting Surfaces", *Proc. Inst. Mech. Engrs, London*, **141**, 1939, pp. 223–237.
5. Conner, B.P. and Nicholas, T., "Using a Dovetail Fixture to Study Fretting Fatigue and Fretting Palliatives", ASME *Jour. Eng. Mat. Tech.*, **128**, 2006, pp.133–141.
6. Gean, M.C., "Finite Element Analysis of the Mechanics of Blade Disk Contacts", M.S. Thesis, School of Aeronautics and Astronautics, Purdue University, West Lafayette, IN, May 2004.
7. Golden, P.J. and Nicholas, T., "The Effect of Angle on Dovetail Fretting Experiments in Ti-6Al-4V", *Fatigue Fract. Engng Mater. Struct.*, **28**, 2005, pp.1169–1175.

8. Hutson, A.L., Nicholas, T., Olson, S.E., and Ashbaugh, N. E. "Effect of Sample Thickness on Local Contact Behavior in a Flat-on-Flat Fretting Fatigue Apparatus", *Int. J. Fatigue*, **23**, 2001, pp. S445–S453.
9. Tada, H., Paris, P.C., and Irwin, G.R., Stress Analysis of Cracks Handbook, Del Research Corp., Hellertown, PA, 1973.
10. Eden, E.M., Rose, W.N., and Cunningham, F.L., "The Endurance of Metals – Experiments on Rotating Beams at University College", *Proc. Inst. Mech. Engrs., London*, **4**, 1911, pp. 839–974.
11. Tomlinson, G.A., "The Rusting of Steel Surfaces in Contact", *Proc. Roy. Society (London)*, **A115**, 1927, pp. 472–483.
12. Forrest, P.G., *Fatigue of Metals*, Pergamon Press, Oxford, 1962 (U.S.A. Edition distributed by Addison-Wesley Publishing Co., Reading, MA).
13. Poon, C. and Hoeppner, D.W., "The Effect of Environment on the Mechanism of Fretting Fatigue", *Wear*, **52**, 1979, pp. 175–191.
14. Schütz, W., "A History of Fatigue", *Engng Fract. Mech.*, **54**, 1996, pp. 263–300.
15. Giannakopoulos, A.E., Venkatesh, T.A., Lindley, T.C., and Suresh, S., "The Role of Adhesion in Contact Fatigue", *Acta Materialia*, **47**, 1999, pp. 4653–4664.
16. Taylor, D.E., "Environmental Fretting Fatigue", *Fretting Fatigue*, ESIS 18, R.B. Waterhouse and T.C. Lindley, eds, Mechanical Engineering Publications, London, 1994, pp. 375–389.
17. Conner, B.P., Hutson, A.L., and Chambon, L., "Observations of Fretting Fatigue Micro-Damage of Ti-6Al-4V", *Wear*, **255**, 2003, pp. 259–268.
18. Faanes, S. and Fernando, U.S., "Life Prediction in Fretting Fatigue using Fracture Mechanics", *Fretting Fatigue*, ESIS 18, R.B. Waterhouse and T.C. Lindley, eds, Mechanical Engineering Publications, London, 1994, pp. 149–159.
19. Waterhouse, R.B., "Fretting Fatigue", *Int. Mater. Rev*., **37**, 1992, pp. 77–97.
20. Hills, D.A., Nowell, D., and O'Connor, J.J., "On the Mechanics of Fretting Fatigue", *Wear*, **125**, 1988, pp. 129–146.
21. Szolwinski, M. and Farris, T., "Mechanics of Fretting Fatigue Crack Formation", *Wear*, **198**, 1996, pp. 93–107.
22. Golden, P.J. and Grandt, A.F. Jr., "Fracture Mechanics Based Fretting Fatigue Life Predictions in Ti-6Al-4V", *Eng. Fract. Mech*., **71**, 2004, pp. 2229–2243.
23. Mutoh, Y. and Xu, J.-Q., "Fracture Mechanics Approach to Fretting Fatigue and Problems to be Solved", *Tribology International*, **36**, 2003, pp. 99–107.
24. Hills, D.A., Nowell, D., and Sackfield, A., *Mechanics of Elastic Contacts*, Butterworth-Heinemann, Oxford, 1993.
25. Mindlin, R.D., "Compliance of Elastic Bodies in Contact", ASME *J. Appl. Mech*., **16**, 1949, pp. 259–268.
26. Golden, P.J. and Calcaterra, J.R., "A Fracture Mechanics Life Prediction Methodology Applied to Dovetail Fretting", to be published in *Tribology Int.* **Lyon presentation**.
27. Hills, D.A. and Nowell, D., *Mechanics of Fretting Fatigue*, Kluwer Academic Publishers, Dordrecht, The Netherlands, 1994.
28. Dobromirski, J.M., "Variables of Fretting Processes: Are There 50 of Them?", *Fretting Fatigue, ESIS 18*, R.B. Waterhouse and T.C. Lindley, eds, Mechanical Engineering Publications, London, 1994, pp. 60–66.
29. Hutson, A.L., Neslen, C., and Nicholas, T., "Characterization of Fretting Fatigue Crack Initiation Processes in Ti-6Al-4V", *Tribology International*, **36**, 2003, pp 133–143.
30. Ciavarella, M., Hills, D.A., and Monno, G., "The Influence of Rounded Edges on Indentation by a Flat Punch", Proc. Inst. Mech. Engrs., *J. Mech. Eng. Sci*., **212C**, 1998, pp. 319–328.

31. Giannakopoulos, A.E., Lindley, T.C., Suresh, S., and Chenut, C., "Similarities of Stress Concentrations in Contact at Round Punches and Fatigue at Notches: Implications to Fretting Fatigue Crack Initiation", *Fatigue Fract. Eng. Mater. Struct*, **23**, 2000, pp. 562–571.
32. Johnson, K.L., *Contact Mechanics*, Cambridge University Press, Cambridge, 1985.
33. Murthy, H., Farris, T.N., and Slavik, D.C., "Fretting Fatigue of Ti-6A1-4V Subjected to Blade/Disk Contact Loading", *Developments in Fracture Mechanics for the New Century*, 50th Anniversary of Japan Society of Materials Science, Osaka, Japan, May 2001, pp. 41–48.
34. McVeigh, P.A., Harish, G., Farris, T.N., and Szolwinski, M.P., "Modeling Contact Conditions in Nominally Flat Contacts for Application to Fretting Fatigue of Turbine Engine Components", *Int. J. Fatigue*, **21**, 1999, pp. S157–S165.
35. Lindley, T.C., "Fretting Fatigue in Engineering Alloys", *Int. J. Fatigue*, **19**, Supp. No. 1, 1997, pp. S-39–S49.
36. Ruiz, C., Boddington, P.H.B., and Chen, K.C., "An Investigation of Fatigue and Fretting in a Dovetail Joint", *Expt. Mechanics*, **24**, 1984, pp. 208–217.
37. Magaziner, R., Jin, O., and Mall, S., "Slip Regime Explanation of Observed Size Effects in Fretting", *Wear*, **257**, 2004, pp. 190–197.
38. Naboulsi, S. and Mall, S., "Fretting Fatigue Crack Initiation Behavior Using Process Volume Approach and Finite Element Analysis", *Tribology International*, **36**, 2003, pp. 121–131.
39. Lykins, C.D., Mall, S., and Jain, V.K., "A Shear Stress-Based Parameter for Fretting Fatigue Crack Initiation", *Fatigue Fract. Eng. Mater. Struct*., **24**, 2001, pp. 461–473.
40. Findley, W.N., "Fatigue of Metals Under Combinations of Stresses", Trans. ASME, **79**, 1957, pp. 1337–1348.
41. Namjoshi, S., Mall, S., Jain, V., and Jin, O., "Fretting Fatigue Crack Initiation Mechanism in Ti-6Al-4V", *Fatigue Fract. Eng. Mater. Struct*., **25**, 2002, pp. 955–964.
42. Neu, R., Pape, J., and Swalla, D.R., "Methodologies for Linking Nucleation and Propagation Approaches for Predicting Life Under Fretting Fatigue", *Fretting Fatigue; Current Technology and Practices, ASTM STP 1367*, D.W. Hoeppner, V. Chandrasekaran, and C.B. Elliot, eds, American Society for Testing and Materials, West Conshohocken, PA, 2000, pp. 369–388.
43. Araújo, J.A. and Nowell, D., "The Effect of Rapidly Varying Contact Stress Fields on Fretting Fatigue", *Int. J. Fatigue*, **24**, 2002, pp. 763–775.
44. Fatemi, A. and Socie, D.F., "A Critical Plane Approach to Multiaxial Fatigue Damage Including Out of Phase Loading", *Fatigue Fract. Eng. Mater. Struct*, **11**, 1988, pp. 149–165.
45. Nowell, D. and Dini, D., "Stress Gradient Effects in Fretting Fatigue", *Tribology International*, **36**, 2003, pp. 71–78.
46. Nix, K.J. and Lindley, T.C., "The Application of Fracture Mechanics to Fretting Fatigue", *Fatigue Fract. Eng. Mater. Struct*., **8**, 1985, pp. 143–160.
47. Nicholas, T., Hutson, A., John, R., and Olson, S., "A Fracture Mechanics Methodology Assessment for Fretting Fatigue", *Int. J. Fatigue*, **25**, 2003, pp. 1069–1077.
48. Naboulsi, S. and Nicholas, T., "Limitations of the Coulomb Friction Assumption in Fretting Fatigue Analysis", *Int. J. Solids Struct*., **40**, 2003, pp. 6497–6512.
49. Chan, K.S., Davidson, D.L., Lee, Y-D., and Hudak, S.J., Jr., "A Fracture Mechanics Approach to High Cycle Fretting Fatigue Based on The Worst Case Fret Concept: Part I – Model Development", *Int. J. Fract*., **112**, 2001, pp. 299–330.
50. McVeigh, P.A. and Farris, T.N., "Analysis of Surface Stresses and Stress Intensity Factors Present During Fretting Fatigue", *Proceedings of the* 40th *AIAA/ASME/ASCE/ASC Structures, Structural Dynamics, and Materials Conf., vol. 2*, St Louis, MO, April 1999, pp. 1188–1196 (CD-ROM). See also: McVeigh, P.A., "Analysis of Fretting Fatigue in Aircraft Structures:

Stresses, Stress Intensity Factors, and Life Predictions", Ph.D. Thesis, School of Aeronautics and Astronautics, Purdue University, West Lafayette, IN, 1999.
51. Beghini, M., Bertini, L., and Fontanari, V., "Weight Function for an Inclined Edge Crack in a Semi-plane", *Int. J. Fract.*, **99**, 1999, pp. 281–292.
52. Jin, O., Mall, S., and Sahan, O., "Fretting Fatigue Behavior of Ti-6Al-4V at Elevated Temperature", *Int. J. Fatigue*, **27**, 2005, pp. 395–401.
53. Golden, P.J., Hutson, A.L., Bartha, B., and Nicholas, T., "A Comparison of Fretting Fatigue Test Fixtures", presented at ICEM 12 – 12th International Conference on Experimental Mechanics, Bari, Italy, 29 August–2 September 2004. Conference proceedings only.
54. Jin, O. and Mall, S., "Effects of Independent Pad Displacement on Fretting Fatigue Behavior of Ti-6Al-4V", *Wear*, **253**, 2002, pp. 585–596.
55. Naboulsi, S. and Mall, S., "Investigation of High Cycle and Low Cycle Fatigue Interaction on Fretting Behavior", *Int. J. of Mechanical Sciences*, **44**, 2002, pp. 1625–1645.
56. McVeigh, P.A., Harish, G., Farris, T.N., and Szolwinski, M.P., "Modeling Contact Conditions in Nominally Flat Contacts for Application to Fretting Fatigue of Turbine Engine Components", *Int. J. Fatigue*, **21**, 1999, pp. S157–S165.
57. Swalla, D.R. and Neu, R.W., "Influence of Coefficient of Friction on Fretting Fatigue Crack Nucleation Prediction", *Tribology International*, **34**, 2001, pp. 493–503.
58. Goh, C.-H., Wallace, J.M., Neu, R.W., and McDowell, D.L., "Polycrystal Plasticity Simulations of Fretting Fatigue", *Int. J. Fatigue*, **23**, 2001, pp. S423–S435.
59. Farris, T.N., Murthy, H., and Matlik, J.F., "Fretting Fatigue", *Comprehensive Structural Integrity Fracture of Materials from Nano to Macro; Volume 4: Cyclic Loading and Fatigue*, R.O. Ritchie and Y. Murakami, eds, Elsevier, 2003, pp 281–326.
60. Hutson, A.L., Niinomi, M., Nicholas, T., and Eylon, D., "Effect of Various Surface Conditions on Fretting Fatigue Behaviour of Ti-6Al-4V", *Int. J. Fatigue,* **24**, 2002, pp. 1223–1234.
61. Namjoshi, S.A., Jain, V.K., and Mall, S., "Effects of Shot-Peening on Fretting Fatigue Behavior of Ti-6Al-4V", *ASME Journal of Engineering Materials and Technology*, **124**, 2002, pp. 222–228.
62. Nicholas, T., Hutson, A.L., Olson, S., and Ashbaugh, N., "In Search of a Parameter for Fretting Fatigue", *Advances in Fracture Research, Proceedings of ICF-10*, K. Ravi-Chandar, B.L. Karihaloo, T. Kishi, R.O. Ritchie, A.T. Yokobori Jr., and T. Yokobori, eds, Paper # 0809, CD ROM, Elsevier, 2001.
63. Hutson, A.L., John, R., and Nicholas, T., "Fretting Fatigue Crack Analysis in Ti-6Al-4V", *Int. J. Fatigue*, **27**, No. 10–12 (Special Issue on Fatigue Damage of Structural Materials), 2005, pp. 1582–1589.
64. Hills, D.A., Nowell, D., and Sackfield, A., "Surface Fatigue Consideration in Fretting", *Interface Dynamics, Proceedings of the 14th Leeds-Lyon Symposium on Tribology*, D. Dowson, C.M. Taylor, M. Godet, and D. Berthe, eds, Elsevier, Amsterdam, 1988, pp. 35–50.
65. Dini, D. and Nowell, D, "Prediction of the Slip Zone Friction Coefficient in Flat and Rounded Contact", *Wear*, **254**, 2003, pp. 364–369.
66. Farris, T.N., Murthy, H., and Matlik, J.F., "Fretting Fatigue", *Comprehensive Structural Integrity Fracture of Materials from Nano to Macro; Volume 4: Cyclic Loading and Fatigue*, R.O. Ritchie and Y. Murakami, eds, Elsevier, 2003, pp. 281–326.

Chapter 7
Foreign Object Damage

7.1. INTRODUCTION

Foreign object damage, commonly referred to as FOD, involves the damage caused by objects ingested into turbine engines. These events typically take place upon takeoff and landing. Ingested objects, which involve a range of soft and hard materials of all sizes and shapes, cause damage when they strike rotating blades, static vanes, or other parts of the engine where they cause a reduction in strength of the component. The damage is typically in the form of a notch covering a wide range of notch depths, radii, and possible cracking at the root of the notch. The problem is most severe when the extent of the damage causes instantaneous failure of a component. Such events are difficult to prevent although methods such as the use of screens have been unsuccessfully attempted at times in the past. Debris on runways can be ingested into engines and is taken care of by routine inspection of runways and taxiways and removal of such debris. Nonetheless, objects are commonly ingested and can cause damage in the form of nicks, dents, tears, and so forth. Damage, if not severe, can cause a reduction of the static strength of a component which is handled in design by the use of some type of knockdown factor to account for FOD in regions where such events are expected or known to take place from prior experience. A greater concern arises when the component that is damaged is also undergoing some type of forced or resonant vibration that can lead to HCF in the damaged area. The problem of FOD is somewhat related to fatigue of notches, discussed in Chapter 5, but is much more complicated because it involves additional aspects that are discussed later. The severity of a notch, from a geometric point of view, is characterized by a stress concentration factor, k_t, which, under FOD, can vary significantly in service. Different types of damages are illustrated later in this chapter as well as in Appendix G involving a wide variation in geometry and corresponding values of k_t. Robust engineering methods are needed to predict the influence of these geometric variables on HCF threshold stresses.

It is the HCF failure and the HCF strength of damaged materials that is the main subject of this chapter dealing with the HCF properties of materials and components that are subjected to FOD. Both real and simulated FOD are discussed, the latter based on the assumption that damage from an impacting object can be simulated by other impact events. Low velocity and quasi-static impact events can produce damage that appears to be geometrically similar to that obtained under ballistic impact. How representative these events are in reproducing actual FOD is an important consideration in the study of FOD. A further concern is the nature of the ingested object that causes the damage in

engines and is rarely identified in total after the event. Only the damaged component is left behind to study the nature of FOD.

In turbine engines, FOD is caused most by the ingestion of birds, sand, dust, ice, and other debris. This general problem is addressed by the US Department of Defense through a specification guide that is applicable to all of the Services – Army, Navy, Air Force, Marines, and Coast Guard. The specification guide, however, does not deal with methods for designing against FOD or conducting analysis of damaged hardware. Rather, it provides guidance for the testing of engines to qualify them for tolerance to ingested objects of specified materials and sizes. Often, in the introduction of a new engine, the objects that the engine may see in service are left up to the discretion of the organization or service that builds the engine for specific applications and missions. This highly empirical approach to FOD, detailed in a *Joint Service Specification Guide* (JSSG), is summarized in Appendix H. Although the guide, in general, deals with the types of debris noted above, it does not specifically deal with large sand particles or small stones which have been found to be both common and very damaging to airfoils in gas turbine engines. This type of debris will hereafter be referred to as *hard particles*. FOD can also be caused by soft body impact such as due to birds. A common misconception is that ice acts as a hard body impactor. Depending on temperature, ice can often appear to display the characteristics of hard body impact, but the majority of time ice should be thought of as a soft body impactor.

In addition to objects ingested into an engine that cause what we term FOD, there are instances where the debris causing damage comes from an internal failure. For example, tips of blades have been known to break off, usually due to some type of resonant fatigue condition. Such an object can then proceed further down the engine and cause impact damage on another component. Objects that are produced from internal failures and subsequently impact some other engine component are considered to cause domestic object damage (DOD). Although this section deals with the general subject of FOD, there is no attempt to distinguish between FOD and DOD because both involve a dynamic impact event. Thus, the terminology FOD will be used to describe all impact events irrespective of the origin of the impacting object.

In this section, some observations and approaches to FOD from small hard objects are presented. While no "standard" object for engine qualification exists, work is continuing to define objects that might be impacted into blades that will cause the same level and geometry of damage as is experienced in operational engines. For example, in one case, a steel cube whose dimensions are approximately 3 mm on a side has been impacted sideways against a blade and has been shown to cause damage that closely represents what is seen in field hardware (see Appendix G). The damage, however, is specific to one engine on one aircraft that performs certain missions and is probably not applicable to all blades in all engines. In what follows, damage from a variety of sources, and methods for predicting such damage and the resultant debit in HCF capability of a material, is discussed.

The author is fortunate to have a contribution to this book in the form of Appendix G, which supplements this section on FOD with detailed discussions of experimental simulations of impact events, a discussion of the field events from which the impact conditions were deduced, and details of analytical and numerical simulation methods. In this section, we will concentrate on the nature of the FOD event and the resultant damage and relevant parameters related to the damage and resulting debits to fatigue limit strength.

7.2. FIELD EXPERIENCE AND OBSERVATIONS

Foreign object damage is of great concern for both military and commercial engines. Field experience has shown that FOD results in nicks and dents and reduces life expectancy of those components exposed to vibratory loading. Most of the FOD experienced in the field comes from sand ingestion with depths of about 0.076 mm (0.003") or less (see Appendix G). Figure 7.1 illustrates engine blades with several types of FOD indicated by the circles. Due to these types of events, supplementary FOD inspections and guidelines

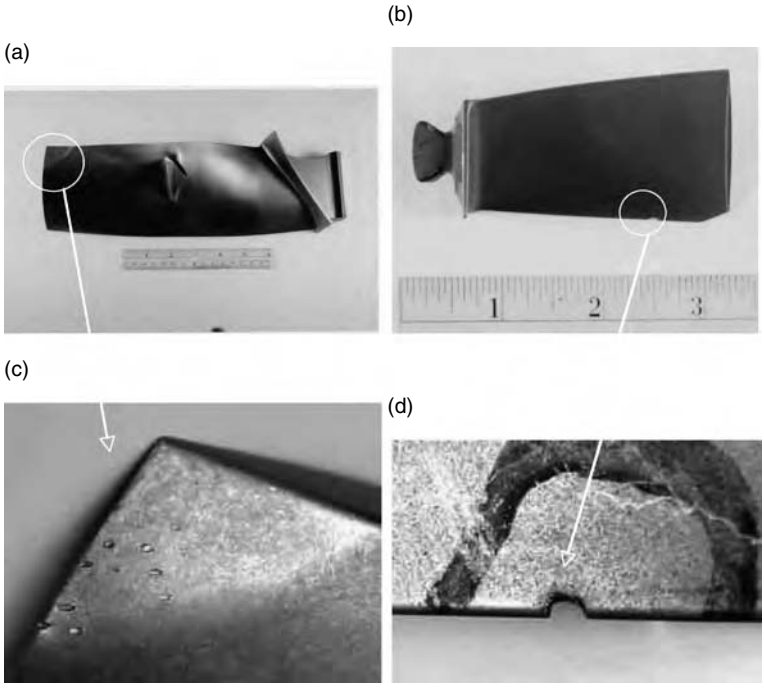


Figure 7.1. In-service FOD: (a) 1st stage fan rotor blade; (b) compressor rotor blade; (c) close-up of (a); (d) close-up of (b).

have been implemented into engine maintenance. The guidelines provide instructions on serviceability and repair limits for damaged engine blades, which are based on the depth of the damage. For numerous engines, field FOD inspection is conducted before and after each flight by the maintenance crew chief, in order to prevent catastrophic in-flight failure [1].

Written requirements in the form of technical orders (TO) for both flight-line and engine shop maintenance provide direction on the execution of the FOD inspection as well as serviceability limits for each rotor blade and stator vane in the engine. Limits for FOD found during a flight-line inspection are generally specified. The serviceability limits determine whether the damage needs to be serviced or not. If the damage depth is below the limit noted in the TO, it is recorded in the maintenance log. If the damage depth exceeds the serviceability limit, it is then blended out by filing the blade. In addition, if the damage depth exceeds the repairable limit, the engine is pulled out of the aircraft and sent into the engine shop for replacement. If the FOD depth found on the 1st stage fan rotor blade exceeds the serviceability limit, the 2nd and 3rd stage rotor blades must also be inspected using a borescope.

As an example, the current serviceability limit for the first stage fan rotor blade on one Air Force fighter engine is 0.76 mm (0.030"). If the damage depth exceeds the maximum repairable limit of 3.8 mm (0.120"), the engine is pulled out of the aircraft for blade replacement. In addition, the entire compressor section must be borescoped to determine if there has been further engine FOD. Once blade replacement is accomplished, the engine is thoroughly re-inspected before returning the engine to operation [1].

7.3. REPAIR BY BLENDING

There is no solid technical ground on which blend and repair limits have been established. Rather, it is an experience-based approach that works well if the only stresses that a blade sees are those due to centrifugal loading. The LCF stresses due to engine speed variations and the corresponding cycle counts are all taken into account with adequate safety factors. Two aspects of FOD and the resulting HCF capability are not well taken care of in a blending operation. Little consideration is given to the possibility of a resonant vibration occurring on the blended blade geometry, especially if the blended area becomes the hot spot for the vibratory stresses. More important, possible damage may exist beyond the depth of the nick that is blended out. In addition to the remaining damage, the area beyond the blend may retain residual tensile stress from the FOD event. Characterization of residual stress fields and microstructural damage from FOD events is certainly not a mature technical area at this point in time. There have been instances where blending of FOD indents has exposed a deeper region that contains residual tensile stresses. These residual stresses, combined with centrifugal and vibratory stresses in the region, have led to HCF failures in the “repaired” region.

While the maximum serviceable limits for FOD in some jet engines in operation today range from 0.36 to 0.76 mm (0.014"–0.030"), the damage depths found in service vary significantly (see Appendix G). Of major concern is if FOD as small as sometimes found in service provides a significant fatigue strength debit in simulated engine blade specimens. Whether the damage should be blended out or the component be removed from service and replaced is very difficult to ascertain in many cases. Another item of concern is the determination of whether damage depth is a good indicator of the actual remaining fatigue life of an FOD impacted blade.

7.4. BACKGROUND

There has not been a substantial amount of work done relating FOD to fatigue strength. Peters et al. [2] researched the effects of FOD on HCF thresholds by shooting steel spheres onto the flat surface of modified K_b (edge cracked) specimens. They found that the overall effect of FOD markedly reduced the fatigue life, compared to that obtained on undamaged smooth-bar specimens, by providing preferred sites for the premature initiation of fatigue cracks. Mall et al. [3] tested both diamond cross section and uniform rectangular cross section samples to study the effects of FOD. The samples were either ballistically impacted or damaged by quasi-static indentation or shearing. They found that the different damage methods created distinctly different damage mechanisms. It was suggested that a total damage depth parameter could be utilized to allow the use of inexpensive and easily controlled methods of simulating FOD, such as the quasi-static chisel indentations, to replace more difficult and expensive means, such as ballistic impacting.

Due to the continuing concern of FOD, studies characterizing the damage sites have been conducted in order to understand the effects of FOD on the HCF strength of engine blades. There are several ways of simulating FOD in a laboratory environment which do provide an impact site and fatigue strength debit; however, each method produces different types of damage which could lead to different crack initiation mechanisms. Characteristic material, geometries representing the leading edge of engine blades, and "realistic" impact conditions have been explored. In this section we attempt to quantify the various measurable damage parameters and to determine if they play a role in controlling the fatigue strength in simulated blades.

7.5. FOD DATA MINING AND INVESTIGATION

While FOD is not solely an HCF problem, many incidents involve FOD damage and, at some later time, vibratory loading that can lead to HCF failure. It is important therefore, from a damage tolerance perspective, to find damage from FOD before the component is exposed to sufficient HCF loading cycles to lead to failure. For this reason, military turbine

engines are inspected routinely to preclude the existence of FOD damage as well as understand the nature of FOD before they are returned to service. The steps in a typical FOD investigation have been documented by Franklin and Kleinakis in a NATO report [4]. The procedure includes, in general, the following steps which are extracted from that report:

- *Visual examination of the inlet and the compressor for missing parts or indications (marks) of foreign material with the use of light source*. The first step is to collect every available component from the engine. It is best if the entire engine is available, but investigators can work with less. The most important components are those two stages upstream and two stages downstream of the failed stage. If the FOD is repaired prior to investigation, this will eliminate nearly all of the evidence and make the investigation very difficult if not impossible. Therefore, the first step of collecting all of the available components and debris from the engine is very important.
- *Visual examination of the area and the stages upstream and downstream of the FOD damaged blades*. This inspection may be performed using flexible boroscopes in accordance with the manufacturers' recommendations. Once the debris is collected, the investigators will start looking at the two damaged stages that are farthest forward in the engine. Looking at these two stages will provide useful information that helps separate primary and secondary damage. The first step is to look at the witness marks. Basically the direction of the damage origination can be determined from the witness marks and that will be used to determine where to focus investigation efforts. If the majority of FOD sites are on the pressure side of the airfoils, there is a good chance that the damage came from the first damaged stage or from in front of that. If the damage is on the suction side, this usually means the damage came from behind which would indicate some sort of stall in the airflow. If none of the engine components actually failed, the witness marks have to tell the entire story.
- *Disassembly of the engine and examination of the blade*. Once the primary damage component is located, the witness marks will be subjected to microscopic inspection using both optical and scanning electron microscopes. The shape of the damage can be determined from these inspections and potential components (such as bolts, nuts, washers) that match the damage geometry can be isolated. After the detection of the most likely damage origination, the broken surfaces must be examined. Hopefully, at least one of the fracture surfaces will have 'beachmarks', crack growth striations or the general appearance of brittle fracture – as these are all indications of fatigue. If all of the components have signs of tensile rupture, the cause of failure is difficult to determine. Once the components with fatigue damage are identified, a more complete microscopic examination can be performed. Using a combination of experimentation and numerical analysis, both 'beachmarks' and striations can be counted to determine approximately when the damage was initiated. Basically, the prediction is based on the identification of the stresses, in conjunction with experiments in the lab using specimens to simulate the loadings if the necessary data are not available from the bibliography or the engineering data provided from the manufacturer. If there is the appearance of brittle fracture (a relatively flat and featureless fracture surface) without crack growth striations, this can indicate high R-value fatigue as a damage mechanism. This could be indicative of HCF

or LCF, but the appropriate type of fatigue must fall within the realm of what is predicted numerically.

- *In addition, a spectrographic inspection of the fracture surface can be used to determine if any material has been deposited on the blades from the impactor.* This is crucial to determining which of the geometrically compatible components is most suspect. For example, if the spectrographic inspection of the blade indicates trace amounts of cadmium, and one of the bolts is cadmium coated, then the process of determining what caused the FOD will focus on those bolt locations. When the suspected impactors are narrowed down to the smallest possible list, the locations of the suspects are inspected. If a failed component is found, the fracture surface is inspected to determine if it failed before the larger incident. If it did, this will probably be called the cause of the incident.

Nearly all of the investigation procedures are useless if heating is involved in the incident. Heating can and will distort fracture surfaces, melt material, and just make a general mess of things.

This is the general FOD incident investigation process. For determining what caused a damaged component to fail, optical and scanning electron microscopes are used almost exclusively (Figure 7.2). If these workhorse tools do not indicate what went wrong with the part, then the investigators will use any possible tool to determine the cause of damage, but the majority of these tools are mostly only proven in a laboratory setting.

7.6. DEFINITION OF FOD

Similar to the use of the terminology HCF, there is no formal definition of FOD other than "foreign object damage." The foreign object is typically either a soft object like a bird or ice, or a hard object like a stone, wrench or other similar object ingested into an engine. While these could formally be classified as FOD events, the mid-air collision of

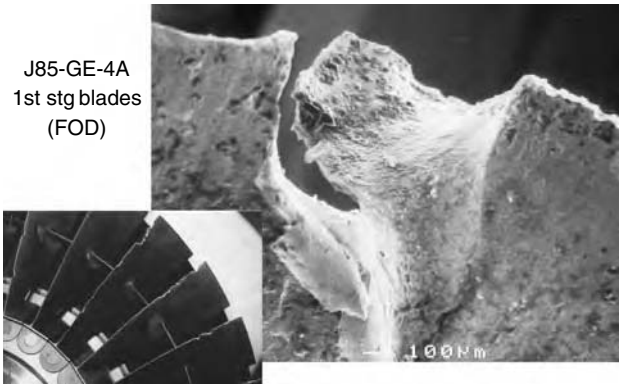


Figure 7.2. SEM photo of a damaged blade (FOD).



Figure 7.3. F/A-18 aircraft after suffering severe FOD from mid-air collision.

two F/A-18 aircraft is not treated in any analysis and is not considered as potential FOD in the design process. Figure 7.3 shows that the radome, radar and all of the avionics equipment, everything, are gone. This "FOD incident" created several problems for the pilot: aerodynamics, eventual loss of hydraulics due to loss of fluid, navigation, and probably the most amazing, as the pieces fell away, some debris had to be ingested by the engines (real FOD) and he still was able to bring it home.

The story behind this is that two F/A-18 Hornets made a head on pass, just a bit too close. One got home with part of the left wing and left vertical fin and rudder missing, while the other jet, shown in Figure 7.3, is missing everything forward of the cockpit pressure bulkhead – and is a flying convertible because the canopy is shattered too. This illustrates the extreme nature of FOD and the possible consequences. In this chapter, we will deal primarily with small hard objects that are commonly ingested into engines.

7.7. TYPES OF DAMAGE

When an engine blade experiences FOD, the damage can be in many different forms. Some of these, like curling, denting, and distortion, have little effect on the fatigue properties of the component. In a recent report [5], in Annex C, the definitions of the

various forms of engine blade damage from FOD have been summarized along with photos showing examples. Figures 7.4–7.15 are taken directly from that report, defining the different types of damage.

Burred: Rough edge or sharp projection on edge or surface of parent material. Most commonly associated with surge damage.



Figure 7.4. Example of a burred blade.

Chipped: Breaking away of surface of parent material usually caused by heavy impact (not flaking). Most commonly associated with snubber abutment face damage.



Figure 7.5. Example of a chipped blade.

Cracked: Partial separation of material which may progress to a complete break, either visible or detected by NDT.



Figure 7.6. Example of a cracked blade.

Curled: Condition where edges of outer portion of blade have been rolled over. Often associated with rubbing on casing or vanes, or sometimes soft body.



Figure 7.7. Example of curled blades.

Dented: Indentation with rounded bottom, usually on leading/trailing edge, sometimes on surface. Parent material is displaced, seldom separated.

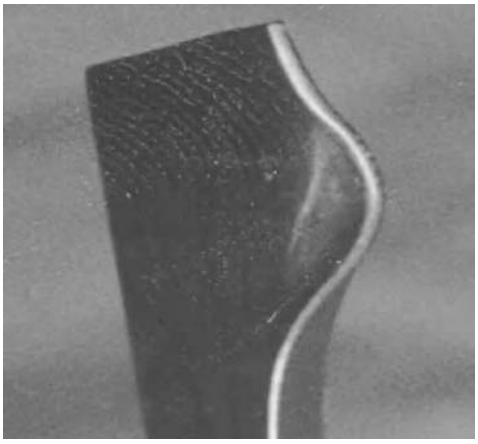


Figure 7.8. Example of a dented blade.

Deposits: Build-up of material (on blades and vanes).



Figure 7.9. Example of blades with deposits.

Disintegrated: Separated or decomposed into fragments. Excessive degree of fracturing (breaking) as with disintegrated bearings. Complete loss of original form.

Distorted: Extensive deformation (whole or major part of aerofoil) of original contour of part.



Figure 7.10. Example of a distorted blade.

Erosion: Gradual removal of metal due to continuous action of impact from very small particles.

Gouged: Scooping out of material, usually associated with surface of aerofoil.



Figure 7.11. Example of a gouged blade.

Nicked: Relatively short, sharp indentation, usually associated with leading/trailing edges. Parent material is displaced, sometimes removed.

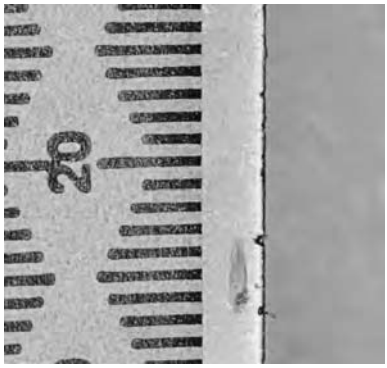


Figure 7.12. Example of a nicked blade.

Peeled: Breaking away of surface finishes such as coating, platings, etc; peeling would be flaking of very large pieces; blistered condition usually precedes or accompanies flaking.

Piece Out: Complete material removed from leading/trailing edge.

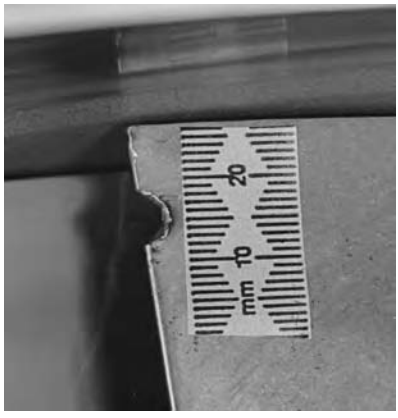


Figure 7.13. Example of a blade with a piece out.

Pitted: Small irregular shaped cavities in surface of parent material.

Scored: Relatively long, deep scratch or scratches made by sharp edges of foreign particles. Usually associated with aerofoil surfaces.

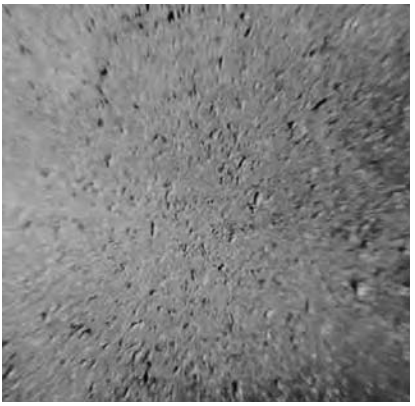


Figure 7.14. Example of a pitted blade.

Scratched: Light, narrow, shallow mark or marks caused by movement of sharp object or particle across surface. Material is displaced, not removed.
Torn: Separation by pulling/ripping apart.

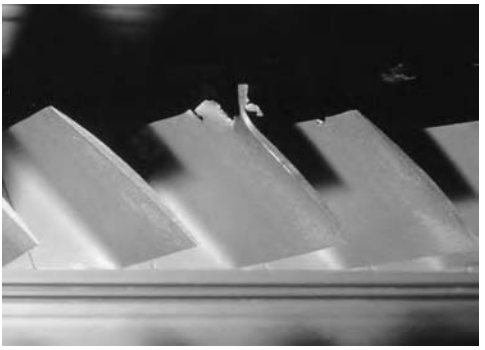


Figure 7.15. Example of a torn blade.

As noted above, not all of these damage modes are related to HCF. The specific types of damage treated in this book are, using the definitions above, burred, chipped, cracked, nicked, pierce out, scored, scratched, and torn. These, in turn, can be analyzed using some of the tools dealing with notches, particularly including the extension to cracks and short crack/shallow notch behavior discussed in Chapter 5. In some cases, these tools are inadequate because of the many complex mechanisms associated with FOD.

7.8. SCOPE OF THE FOD PROBLEM

As noted in Appendix G, FOD can even be of a size that can barely be detected by the unaided eye. A majority of FOD involves damage sizes that are less than 2 mm (0.080") in depth. There have been instances in service usage where concerns over HCF failures originating at extremely small FOD sites have led to frequent inspections of leading edges of fan blades using both a finger nail inspection or running dental floss up and down to find small FOD nicks or dents. More important, it is not yet known whether HCF failures which emanate from very small FOD are due to the degradation of material properties or are, instead, due to excessive vibratory stress amplitudes which just happen to choose the FOD location as the origin site based primarily on statistics of there being a very slight reduction in material capability at that site.

Fan and compressor blades at the front end of jet engines are the components that receive the majority of damage, particularly at the leading edge of the airfoil. Due to the high frequency vibratory stresses that can be present in the fan and compressor sections associated with normal engine operation, it is not uncommon for fatigue cracking to initiate from FOD sites and grow catastrophically within minutes to hours of engine running time. The HCF caused by steady state or transient vibrations of the component is one of the leading causes of in-service failures of blades that have been subjected to FOD. It is important, therefore, to know the fatigue strength of materials and airfoil geometries that have been damaged by foreign objects of various types, sizes, velocities, and incident impact angles.

Evaluation of FOD resistance of materials and structural components has been conducted in a highly empirical manner over the years. Engine companies generally subject individual components such as fan and compressor blades to simple vibratory loading to determine fatigue resistance. FOD is then introduced at anticipated critical locations and the damaged component is tested to determine the debit in fatigue resistance due to FOD. For laboratory specimens, there is little reported work on the introduction of FOD and subsequent evaluation of the fatigue resistance, particularly under HCF conditions. Some of the relevant research is described later in this section. For either real components or laboratory test samples, the method used for inflicting real or simulated FOD is extremely important. “Real” FOD can be produced by shooting typical objects ingested into an engine at velocities and incident angles expected under operational conditions. Other simulations of FOD can be achieved by machining a notch in the material of a size to match real FOD observed from field experience, by using quasi-static indentation of a chisel with a appropriate radius to the proper depth, by pendulum or drop weight impacts at various angles to the leading edge including a side impact chisel, or any other method such as a solenoid gun to produce the required geometry of notch. It has not yet been established that any of the simulation methods produce conditions identical to those of real FOD from ballistic impacts in terms of residual stress fields or material damage

ahead of the notch. In fact, it is shown below that ballistic impacts and quasi-static chisel indents that produce nearly similar size craters in a leading edge do not produce the same HCF resistance under axial fatigue loading.

Current design practice establishes allowable vibratory stresses on a pristine material through the use of a constant-life Haigh diagram that presents material data as alternating stress as a function of mean stress for either run-out conditions (infinite life) or a fixed number of cycles, typically 10^7 or higher (see Chapter 2). For FOD, the allowable vibratory stress is reduced by some percentage to account for the possibility of FOD in non-critical areas. For critical areas such as the leading and trailing edges of a blade, a notch severity corresponding to the worst case expected damage is assumed in the form of an equivalent stress concentration factor, k_t, with perhaps a maximum notch depth associated with it. Such assumptions are usually based on field experience with similar geometries and usage in engines. The notch sensitivity can be further refined by converting from a stress concentration factor to a fatigue notch factor, k_f (see previous section on notches), using empirical relations that have been developed for a number of materials and notch geometries, or by using actual notch fatigue test data on the material under consideration [6].

While the literature on notch fatigue is extensive (see Chapter 5), including both LCF and HCF, its extension to the solution of FOD problems is not direct or even applicable in many cases. There are several aspects of FOD that make it more complicated than a problem dealing solely with a notch induced by an impacting object. First, the impacting object causes material or microstructural damage ahead of the ensuing notch that, in turn, may reduce the fatigue properties of that material. Second, the impact event usually involves plastic deformation that leads to a state of residual stress in the notch vicinity. These residual stresses must be taken into account in any analytical modeling of the fatigue behavior of a sample subjected to FOD. Third, cracks or tears may be produced during the impact event which changes the problem from one of notch fatigue to that of determination of the threshold stress intensity for subsequent crack propagation due to HCF loading. Finally, the geometry of the damage produced by FOD on a typical geometry of a fan or compressor blade from impacts at various angles to the leading edge can be quite complicated and not easily described solely by conventional methods that utilize parameters such as depth and radius of notch. It is not surprising, therefore, to find little in the way of systematic investigations on the effects of FOD on the fatigue properties of materials. Furthermore, most investigations focus on the reduction of fatigue life due to FOD and subsequent loading at a given mean and vibratory stress level. Nicholas et al. [7] conducted a series of impact experiments on titanium leading edges and compared results with those on machined notches. The projectiles and velocities used in that investigation produced much higher levels of damage than are of interest in the present discussion. Further, the emphasis for comparison was on fatigue life, generally in the LCF regime. For HCF design, what is needed is a description of the reduction

of the FLS defined as the maximum stress that will not lead to fatigue failure for a predetermined (large) number of cycles. In other words, HCF design for FOD must be able to establish the allowable combination of steady-state and vibratory stress levels for a component.

7.8.1. Laboratory simulation methods

Simulation methods for inducing damage representative of real FOD are intended to be easier to conduct than real ballistic impact. Different methods being used are discussed in Appendix G. Here we discuss the three methods that have been most widely used in recent investigations of FOD and its effect on the fatigue strength of materials and simple components. These methods were used in the recent US Air Force HCF program [8].

7.8.1.1. Solenoid gun

This is the current baseline used by General Electric Aircraft Engines Co. where they have developed extensive experience in producing simulated FOD. It was selected over the ballistic method which is very erratic and difficult to control. The solenoid gun provides a very controlled input energy to the specimen and produces the typical nick depths (0.005"–0.025") experienced in service. The main problem with the solenoid gun is that the impact energy is controlled, not the notch depth. As a result, the notch depth will vary depending on the dimensions of the leading edge region. The mass of the solenoid is relatively heavy; therefore, impact velocities are relatively low for low energy impacts. The velocity for low energy impact on a sharp-tip specimen (described later) is less than 10 ft/s. Therefore, the description of this method as a "dynamic" simulation is questionable. The advantage of the solenoid gun is its ease of use and repeatability of impact velocity. The terminology "gun" in "solenoid gun" is somewhat misleading if one thinks of a gun as a method of launching projectiles at high velocities.

7.8.1.2. Pendulum

The pendulum systems also impact with a controlled energy level and at relatively low velocity. A 5 foot pendulum arm gives a 9 ft/s impact which is roughly the same impact velocity as that of the solenoid gun at the lowest power setting. The pendulum system also needs some type of catch system to prevent multiple impacts. One advantage of the pendulum system is that the energy at impact is simple to calculate. Unfortunately, where that energy goes to during the impact event is largely unknown even though it has been studied extensively. The pendulum system does not seem to offer anything over the solenoid gun, both being fairly low velocity methods of inducing damage with a mass much larger than that used in a ballistic impact experiment. On the other hand, the pendulum is a test device that is commonly found in many mechanical testing laboratories.

7.8.1.3. Quasi-static

A quasi-static method involves loading a specimen into a servo-hydraulic or screw-driven test frame and pushing on the specimen with an indentor. The cross-head is lowered until the indentor just touches the specimen, and then the FOD nick is controlled by cross-head displacement or maximum load. Since cross-head displacement is not the same as nick depth due to compliance in the load train and variability in establishing the exact point where contact starts, this makes overall control of the depth somewhat difficult. In addition, it is necessary to calibrate the relationship between cross-head displacement and nick depth for each specimen configuration and notch depth (similar to what has to be done for the solenoid gun or pendulum method). The advantage of the quasi-static method is that if cross-head displacement is controlled, this may provide a more controlled nick depth than controlling with impact energy like with the solenoid gun or pendulum methods. In addition, the quasi-static method can provide continuous load versus displacement information which may be useful in terms of determining net energy input into the target and its fixture. On the positive side is that for any reasonable size test machine and fixture, the energy available to deform the specimen is essentially unlimited.

7.8.2. Simulations using a leading edge geometry

Foreign object damage is a common occurrence in blades and vanes of turbine engines and is most common on the leading edges of those components. FOD can be in the form of a crater or tear in the impacted component and can reduce the fatigue capability of the material at the location of the impact. The degradation of the fatigue strength can be attributed to three primary factors: a stress concentration due to a notch-like geometry, the generation of residual stresses during the formation of the crater, and microstructural damage which can range from microcracking through the formation of shear bands to the transformation of the microstructure [2, 9]. At certain levels of severity of the impact conditions, the formation of cracks during the impact event can occur, necessitating consideration of the threshold for crack propagation of initially very small cracks from a notch-like geometry [10]. In addition, changes in the geometry of the airfoil leading edge and residual stresses due to plastic deformation may produce local stress ratios at the notch tip which are, in general, different than the far-field applied stress ratio and may even drive the initiation location from surface to sub-surface [3]. Of the factors affecting the fatigue strength, the stress concentration is easiest to handle by using theoretical or empirical notch fatigue factors applied to measured deformation profiles.

In many engineering and design applications, the geometry of the notch is simulated in the laboratory using quasi-static methods as opposed to resorting to ballistic impact. There are certainly questions related to this procedure if the damage produced differs

from that which occurs in the real event even though the notch geometry produced is identical [3].

In studying FOD on leading edges, the geometry and orientation of the blade or vane has to be considered. For a rotating blade, the angle of incidence (see Figure 7.16c) between an ingested particle and the blade can be estimated by considering the relative vector velocities of the angular velocity of the blade, dependent on radial location and rotational speed, and the forward velocity of the engine. In addition, the twist of the blade provides the angle between the rotational direction and the angle of the leading edge of

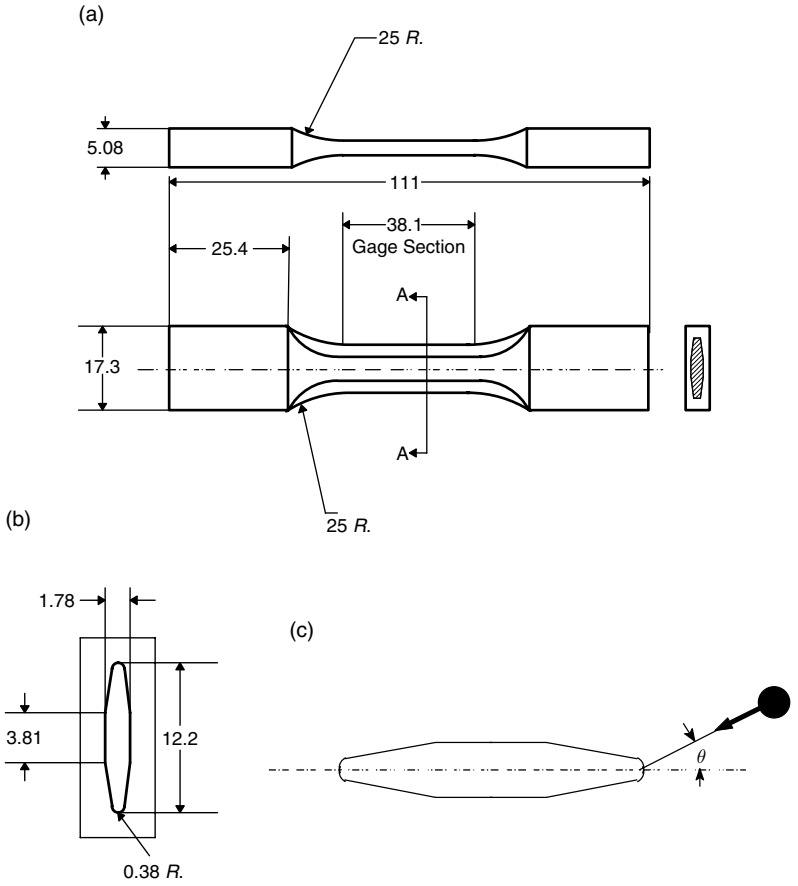


Figure 7.16. Leading edge (LE) specimen. All dimensions in mm (a) Overall dimensions (b) Section A-A (c) Schematic showing orientation of impacting sphere.

the blade with respect to that direction. Typical angles of incidence range between 0 and 60° and impact velocities can be in the several hundred m/s regime.

Laboratory simulations conducted by Ruschau et al. [11] used a representative velocity of 300 m/s and incident angles covering 0–60° on two different leading edge geometries on the axially loaded leading edge specimen shown in Figure 7.16. Further, the fatigue strength was evaluated using step loading at stress ratios of both $R = 0.1$ and $R = 0.5$. To study the influence of impact angle, results were obtained on Ti-6Al-4V bar stock samples for a range of FOD impact angles for a cyclic life of 10^6 cycles. The data are presented in Figure 7.17 and are normalized with the smooth bar fatigue strength at the same life for each value of R. Results show little debit in fatigue life for the 0° impact angles, while a large loss in fatigue strength is noted for the other impact angles examined. The greatest loss in fatigue strength occurred with the 30° samples for both values of R examined. The lowest fatigue strengths for the 30° samples are similar to reference data of Haritos et al. [6] for the same titanium alloy tested with a machined notch of $k_t = 2.7$.

Some of the difference in fatigue strength between 0° and higher angle impacts may be attributed to the residual stress state produced during the impact event. The states of residual stress and plastic deformation that result from the dynamic impact have been evaluated analytically for a hard spherical ball striking a simulated leading edge. Details are presented later in Section 7.14 and in Appendix G. Those results show that for an ideal normal (0°) impact at the center of the leading edge sample, a compressive residual stress field is created in a region surrounding the FOD notch, with a residual tensile stress field existing some distance interior of the impact site. Such a residual stress state would thus reduce the elastic stress concentration created by the FOD notch, and, if the tensile

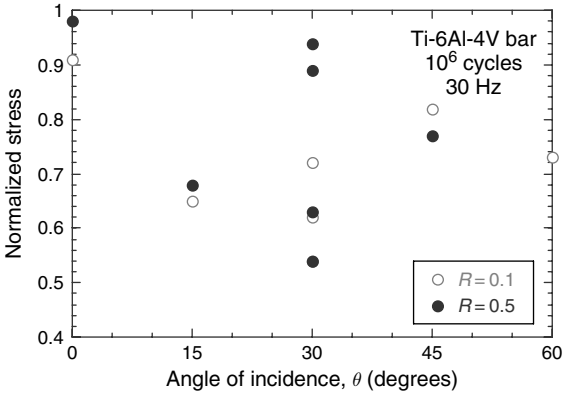


Figure 7.17. Normalized fatigue strength for various foreign object impact angles.

region is sufficient in magnitude, would lead to fatigue initiation in the interior region of the sample, as observed in [12].

For the case of non-normal impact angles, analysis (see Appendix G) shows that while a large compression stress region is created from the impact, a small tensile stress field is created near the surface at the entrance side of the damage site. This tensile stress region at the surface would offset any beneficial influence from the compressive stress field, hence the fatigue strength of a non-normal FOD impact would be reduced to some extent [11]. However, since it is difficult to hit the *exact* center of the leading edge sample, particularly with angled impacts, such a tensile stress region would be expected to vary significantly in size and magnitude with slight differences in impact location, thus leading to a large variability in fatigue behavior [11]. The large degree of scatter in fatigue results makes it difficult to demonstrate any trend of decreasing fatigue strength with increasing impact angle. However, as seen in Figure 7.17, impacts other than 0° can be deduced to produce more damage in terms of tensile residual stresses that can greatly reduce the fatigue strength. This explanation of the variability in fatigue strengths is from the standpoint of the residual stress field alone. Such a scenario assumes an ideal, "clean" damage crater with no cracking, tears, nicks, of other type of damage acting in conjunction with the FOD notch. This is not generally the case, and is discussed further in later sections.

Further tests were performed to examine the influence of leading edge thickness on fatigue strength, but were limited to 0° and 30° impact angles only [11]. The fatigue strength was determined for a cyclic life of 10^7 cycles at a test frequency of 350 Hz. The results of samples with leading edge radii of 0.38 and 0.127 mm, using Ti-6Al-4V forged plate, showed similar fatigue behavior in the 0° and 30° impacts.

This differed from the forged bar data which demonstrated a larger debit in fatigue performance resulting from the simulated FOD at a 30° impact angle over the 0° impact. Even with a large amount of scatter in the data, the 0° data showed a larger debit in fatigue strength than expected. While the 0° impact should produce a compressive residual stress field behind the impact crater, thereby providing higher fatigue strength over a 30° impact, the impact sites for several specimens were slightly off-center and produced damage that appeared similar to that observed in samples impacted at 30°. Thus, off-centered 0° impacts can cause some residual tensile stresses in the FOD notch vicinity similar to the 30° impacts, thus explaining the lower than expected results for 0°.

Of particular importance in the results of the study of the influence of the leading edge thickness was the observation that while the samples with the 0.127 mm edge radius were much thinner and thus more prone to deeper FOD impacts, fatigue strength losses were, in general, similar to the thicker leading edge sample results. There was no apparent influence of sample edge radius (or thickness) on the degree of fatigue strength losses for the type of FOD investigated. In that study [11], only 1 mm glass spheres at a single velocity of 305 m/s were used. Different impact parameters (e.g., FOD material, size,

shape, velocity, etc.) may have an influence on the trends reported. In general, off-angle impacts were found to be more detrimental than head-on (0°) impacts. Fatigue strength losses, some as high as 50%, showed little or no correlation with leading edge thickness or depth of notch.

Mall et al. [3] simulated FOD with a quasi-static indentor against a flat plate whose width was 1.27 mm as shown in Figure 7.18. The use of this simple geometry allowed them to conduct elastic-plastic FEM analysis to study the deformation profiles and to compute residual stresses. Chisel indentors of hardened steel were loaded against the edge of a flat plate under displacement control to achieve various depths of damage. The indentors had a tip diameter of either 1, 2, or 5 mm. The fatigue strength of the damaged specimen that was indented twice, once on each opposing edge (for symmetry), was obtained in tension–tension fatigue at 350 Hz at values of $R = 0.1$ and 0.5. The results are shown in Figure 7.19 as a function of the permanent depth of the indent. These are not small indents compared to the ones used in the previous studies cited. In this case, extensive plastic deformation was observed which was verified with the finite element calculations that showed permanent strains in excess of 15% in some cases. For damage depths in excess of 2000 μm, the authors observed damage in the form of shear cracks along with plastic deformation. For depths less than 2000 μm, on the other hand, there

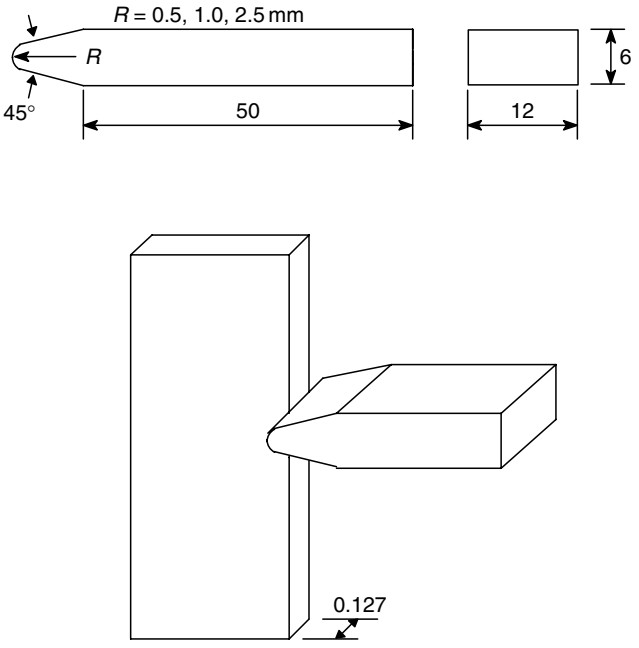


Figure 7.18. Specimen and impactor geometry used in [3]. Dimensions are in mm.

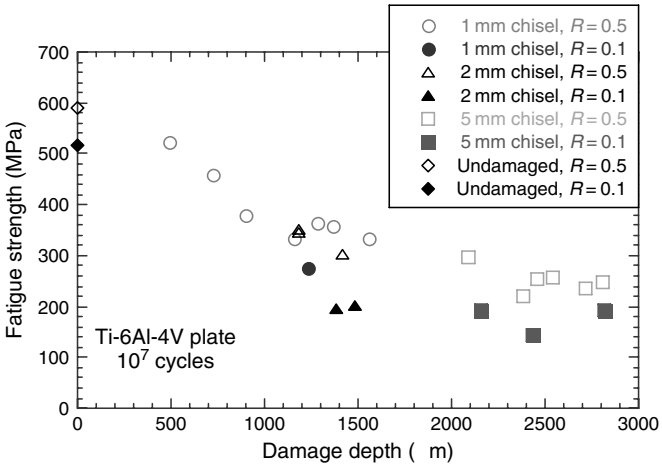


Figure 7.19. Fatigue strength versus damage depth [3].

was no evidence of damage other than the plastic deformation in the vicinity of the indent. The shear cracking in the case of deeper indents is reflected in the fatigue strengths which were approximately 200 MPa, as shown in Figure 7.19, which is approximately one-third that of the undamaged material. The fatigue strength appears to level off as depths beyond 2000 μm are reached. For this particular scenario, a value of $k_f = 3$ appears to represent the worst-case data reasonably well.

7.8.3. Role of residual stresses

These results of leading-edge impact studies, including analytical modeling, point out the important role of residual stresses in altering the fatigue strength of material subjected to FOD. To study the influence of residual stresses, stress relief annealing has been used in titanium specimens [13, 14]. By annealing, residual stresses are effectively eliminated while preserving the microstructural and mechanical characteristics of the material. Whether or not this applies to material that has been subjected to very large local strains, such as at the tip of a notch produced by an impact event, has not been ascertained.

Damage induced by FOD in a leading edge geometry was studied in a series of experiments involving variations of impact energy, size of impactors, and various methods of inducing damage, ranging from quasi-static to ballistic impact [12]. The specimen geometry was that shown above in Figure 7.16. Samples were ballistically impacted with steel spheres of nominal diameters of 0.5, 1.33, and 2.0 mm at velocities ranging from approximately 60 to 500 m/s. The impact conditions were chosen to obtain similar kinetic energy impacts from different size projectiles. The samples were shot on each leading edge, two shots per sample, in the center of the gage section at an impact angle

of 30° relative to the centerline of the test sample cross section. The nomenclature for the definition of impact angle is furnished in Figure 7.16(c). Because of the use of two impacts on each sample, each data point generated represents the behavior of the worst of two nominally identical impact conditions.

For comparison with the ballistic impact specimens, quasi-static indents were imparted using a testing machine under displacement control to produce notches that were geometrically similar to those obtained under ballistic impact. This was accomplished using a steel indentor geometry with the same radius as the ballistically impacting spheres and accounting for the elastic rebound in the quasi-static indentation. The radius of the ballistically impacted crater was nominally the same as the radius of the impacting sphere [9, 14].

A third method of imparting damage was through the use of a pendulum fitted with chisel indentors whose radii were identical to the three impacting spheres. A single mass at two different incident velocities was chosen to produce similar values of depth of penetration to those of the sphere impacts. The incoming and rebound velocities of the pendulum were recorded for subsequent energy calculations.

All of the impacted and indented specimens were fatigue tested using the step-loading procedure with load steps of 10%. The initial load block was taken well below the anticipated fatigue strength of the damaged specimen.

7.8.4. Energy considerations

The depth of crater was examined as a function of the energy for each of the three impact methods and the results are presented in Figure 7.20. For the quasi-static indents, the energy is obtained from the load-displacement records by taking the area bounded by the loading–unloading curve for each specimen. This represents the net energy absorbed in the specimen and is not influenced by any (elastic) compliance of the specimen under the end supports used during the indentation process. A straight line in the figure is an approximation to the quasi-static indent data obtained using a chisel indentor whose radius was 0.67 mm (half the diameter of the 1.33 mm sphere). The two clusters of quasi-static data points represent attempts to produce two different values of the permanent displacement with the same indentor. The same indentor geometry was used for the pendulum impacts. The energy absorbed is calculated from the net kinetic energy used to produce the deformations, the vector sum of the input, and rebound kinetic energy as measured in the experiments. The two clusters of pendulum data points represent two different input velocities used to produce two nominally different depths. The data follow the quasi-static data quite closely.

The remaining data in Figure 7.20 represent those from the ballistic impact experiments. These data represent impacts with all three sphere diameters and, in addition, several different velocities chosen to duplicate the kinetic energy of a different size sphere.

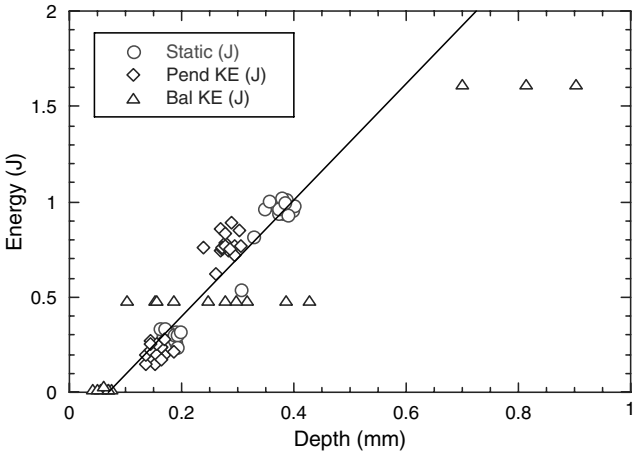


Figure 7.20. Relation between depth of crater and energy.

The energy plotted in the figure represents the input kinetic energy only. There was no information obtained experimentally about the residual velocity of the spheres. If it is assumed that the spheres did not rebound, then the energy plotted can be considered to be an upper bound of what went into deforming or fracturing the target. At any given energy level, the figure shows that there is a lot of scatter in the permanent depth.

Careful examination of the individual points revealed that at the highest energy level, obtained with the 2.0 mm diameter spheres at 305 m/s impact velocity, most of the leading edge specimens were chipped or fractured and showed what has been termed loss of material (LOM) [9, 13]. Such a condition is shown in the SEM photo, Figure 7.21(a). The points having such a fracture appearance lie to the right and below the trend line of the quasi-static data. Some of the data points to the left had only permanent deformation as seen in the SEM photo in Figure 7.21(b). This shows that the energy required to produce a fracture is less than that needed to produce a crater of equivalent size through

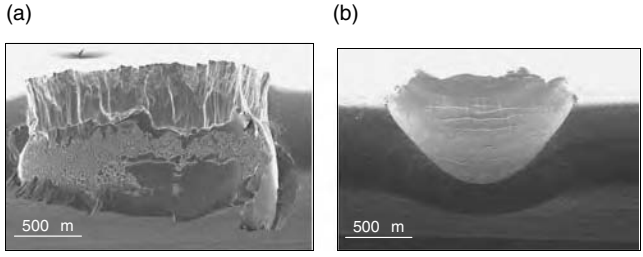


Figure 7.21. SEM photos of indents showing: (a) loss of material and (b) indentation.

plastic deformation. A similar observation was made for the data points to the right at an energy level of approximately 0.5 J which represent the 1.33 mm diameter sphere impacts at 305 m/s. Here, again, chipping and local fracture led to the formation of the crater rather than extensive plastic deformation. Thus, the depth of penetration of all of the impacts can be correlated well with impact energy, as would be expected, except for cases where fracture occurred locally. In that case, the depth of penetration is generally higher and represents the worst case scenario regarding fatigue strength debit as noted also in previous research [9, 13]. Of significance is the observation that the two types of permanent distortion, LOM and crater formation, occur under nominally identical impact conditions. In these cases, the differences were in the location of the actual impact with respect to the targeted point exactly in the middle of the airfoil leading edge.

As an overall observation, for the range of conditions covered in [12], quasi-static and pendulum indenting used to produce craters of the same depth as the ballistic impacts resulted in plastic deformation in all cases. While the depth of penetration was correlated with the input energy, this quantity cannot be predicted *a priori* because the unloading load-displacement curve or rebound velocity is not known for the quasi-static or pendulum indenting, respectively. These types of FOD simulations that produce plastic deformation can over-predict the fatigue strength for the same depth of penetration compared to the ballistic case where LOM occurs.

7.9. FATIGUE LIMIT STRENGTH

For different impact conditions that produce craters, the reduction of fatigue strength can be characterized by a fatigue notch factor, k_f, defined as the ratio of the smooth bar fatigue strength to that of the notched bar based on net cross-sectional area, as indicated in earlier in the discussion of notches, Section 5.4,

$$k_f = \frac{\text{unnotched fatigue limit stress}}{\text{notched fatigue limit stress}} \tag{7.1}$$

In [12], predicted values of k_f were calculated based on the elastic stress concentration factor, k_t, through an empirical formula that fits experimental data. The notch was assumed to have a radius equal to the impacting sphere or the static indentor, an assumption that was verified in prior investigations on the same material [9, 13, 14]. Finite element analyses of ideal 30° notches were used to determine k_t for several different combinations of radius and depth. These values were found to be close to those calculated for a circular notch of depth, d, and radius, r, from Peterson [15],

$$k_t = 1 + 2\sqrt{\frac{d}{r}} \tag{7.2}$$

The fatigue notch factor used was that given by Peterson [16] in the form,

$$k_f = 1 + \frac{k_t - 1}{1 + \frac{a_p}{r}} \tag{7.3}$$

where $a_p = 300\,\mu m$ is a material constant obtained from fitting notch fatigue data on the same material [17].

The results for the FLS, normalized with respect to the smooth bar fatigue strength at $R = 0.1$, 10^7 cycles (568 MPa), are presented in Figure 7.22 as a function of the measured notch depth. Most of the data in this investigation were obtained for impacts with a ball diameter of 1.33 mm and quasi-static indents with the same diameter chisel. Shown also is a reference line corresponding to the fatigue notch factor as calculated for a notch radius of 0.67 mm from Equation (7.3). In the nomenclature used, hollow symbols refer to stress-relieved (SR) specimens, whereas solid symbols are for specimens tested as-received (AR) after impacting or indenting. Data obtained at three different ballistic velocities (having significantly different kinetic energies) are noted, as well as results for the quasi-static and pendulum indents of similar impact depths.

A prediction, based solely on notch geometry using k_f, is also shown in the figure. (Since the fatigue strength is normalized, the prediction appears as a line calculated as

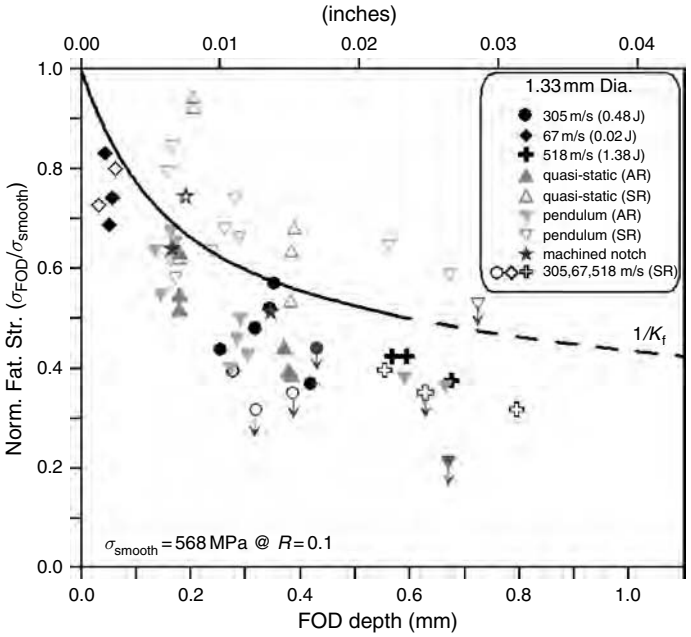


Figure 7.22. Normalized fatigue strength as a function of FOD depth for 1.33 mm diameter indents.

$1/k_f$.) It should be noted that this line does not take into consideration any microstructural damage imparted by the impacts or any residual stresses produced during the impacts. The data of the as-impacted (AR) specimens follow essentially the same trend, which is slightly lower than the prediction regardless of the impacting technique. By comparison, the fatigue strength of specimens with machined notches* of depths of approximately 0.2 and 0.4 mm were essentially that as predicted by the k_f formula. This confirms the validity of the k_f formulation for these notch geometries.

The hollow triangles, in Figure 7.22, show the effect of removing residual stress effects from the quasi-static and pendulum indents, which indicates that the fatigue strength increases due to stress relief. This would imply that the indenting procedures imparted tensile residual stresses. The apparent strengthening effect over that predicted by k_f analysis can be partially explained by observing the geometry of the non-ballistic notch after indentation as compared to a machined notch, as shown in Figure 7.23. The indent produced by quasi-static methods produces substantial bulging, plastic deformation, and distortion of the notch, as shown in Figure 7.23(b). The net effect seems to be a shielding effect on the notch and invalidates the k_t approximation because of the distorted geometry. By comparison, the fatigue strength of specimens with machined notches of depths of approximately 0.2 and 0.4 mm was essentially that as predicted by the k_f formula.

Another possible contribution to the apparent strengthening effect on the SR samples is the strain hardening that takes place during the deformation process when the crater is formed. Both the quasi-static and pendulum impacts show an apparent strengthening effect when stress relieved, but the net effect produces fatigue strengths above that predicted solely by the geometry. In addition to the difference in deformation pattern discussed above, it is thought that some strengthening in fatigue from strain hardening in compression during the impact event may have occurred.

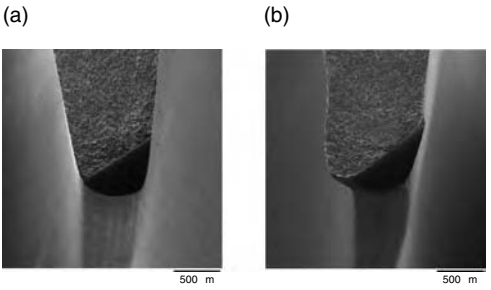


Figure 7.23. Comparison of (a) machined notch with (b) quasi-static indentation.

* The machined notches were not stress relieved because low stress grinding (LSG) was used in machining the notches. It was assumed that LSG produced little or no residual stress and that final polishing reduced any possible residual machining stresses even further.

Stress relief of the specimens that were ballistically impacted, on the other hand, produced little or no change in fatigue strength as shown by the hollow circles and crosses in Figure 7.22. Here it would appear that the ballistic impacting produces minimal residual stresses and perhaps beneficial compressive stresses dominate. (A downward arrow in a data point indicates that it failed during the first loading block of the step test procedure.) This observation of apparent compressive residual stresses is consistent with observations from numerical simulations of spherical ball impacts on this leading edge geometry, which show tendencies for compressive stresses to develop near the exit side of the crater for an ideal impact [8].

Data for the impacts with the 2.0 mm diameter spheres/indentor is shown in Figure 7.24. For these spheres causing the deepest notches, the formula corresponding to k_f tends to over-predict the FLSs, particularly when the notch depth approaches 1 mm. Here, for the ballistic impacts, the stress relief procedure has little or no effect on the fatigue strength, indicating the absence of significant residual stresses in the vicinity of the damage site. The quasi-static indented specimens, on the other hand, exhibit the same type of behavior as seen in the 1.33 mm diameter specimens described above. Again, this may be attributed to some combination of the deformation pattern observed (Figure 7.23) and possible strain-hardening effects.

Data from the impacts using the 0.5 mm diameter spheres, Figure 7.25, show that these smaller diameter spheres produce FLSs which are higher in the stress relieved case than

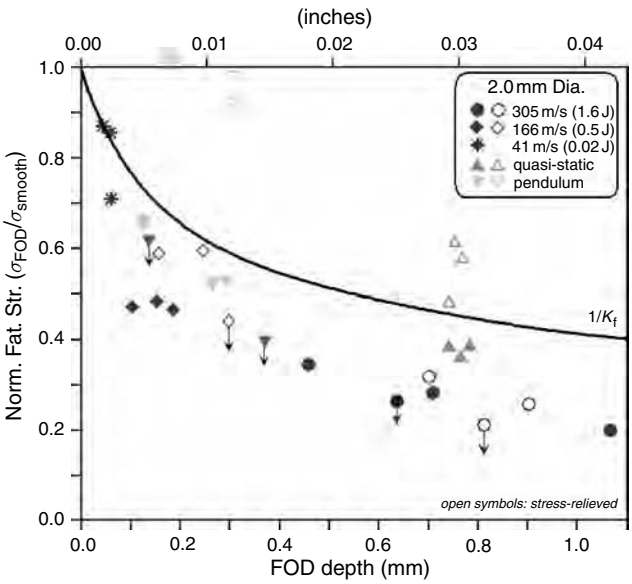


Figure 7.24. Normalized fatigue strength as a function of FOD depth for 2.0 mm diameter indents.

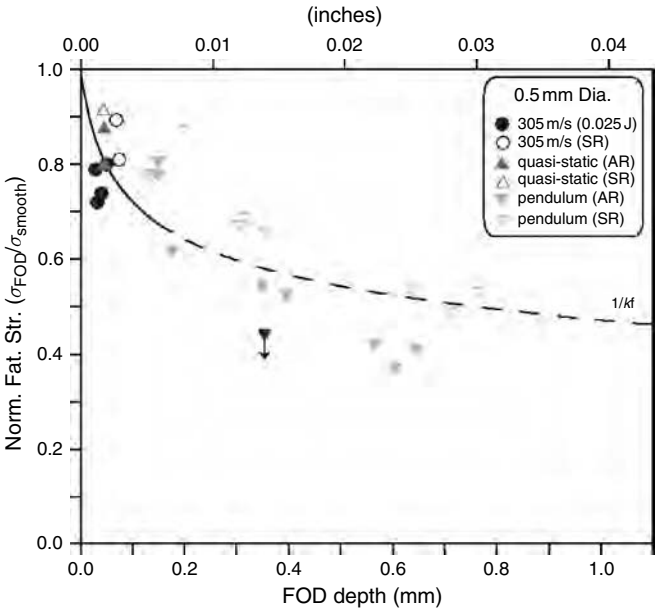


Figure 7.25. Normalized fatigue strength as a function of FOD depth for 0.5 mm diameter indents.

for those without SR. This would tend to indicate that some residual tensile stresses were present in the impacted specimens, the opposite of which was observed for the 1.33 mm diameter sphere impacts (Figure 7.22). Note that for the 0.5 mm case, the depths of craters are less than 0.1 mm whereas for the 1.33 mm case, the depths are typically five times as large.

One reason for the lower strength of ballistic damage after stress relief is attributable to the physical appearance of the damage sites. For the impacts with the larger ballistic damage sites, most of the leading edge specimens were chipped or fractured and exhibited what has been termed LOM, discussed earlier (see Figure 7.21a). Some of the specimen impacts had only permanent deformation (dents) (see Figure 7.21b).

A general observation that can be made is that residual stresses that are produced by ballistic impact depend on the size and velocity of the impacting sphere. These stresses may be different in magnitude and type (tension versus compression) depending on their appearance when going from ballistic impacts to quasi-static indentation. One significant observation is that the FLS of a ballistically impacted leading edge specimen can be reduced by as much as 70–80% in the specimens that have the largest amount of damage. While these were the most severe impact conditions in the reported experiments, they still involved rather small impacting objects compared to the stones, tools, and even some

sand particles that have caused FOD in gas turbine engines in both military and civilian aircraft.

We can conclude that the fatigue limit strength of a ballistically impacted leading edge specimen is influenced not only by the geometry of the notch produced by the impact, but by the residual stress field and mechanisms producing the notch. For notches with lesser amounts of damage, the impact site was predominately plastic deformation that resulted in a notch fatigue strength that was reasonably predicted by conventional notch analysis using k_f. Some strengthening effect, observed after stress relief annealing, was attributed to possible strain hardening. Residual stresses, which tend to alter these strengths somewhat, are very sensitive to the nature of the impact and can be either tensile or compressive and very hard to predict. For larger ballistic damage levels, the notch crater exhibited damage such as chipping, local failure, and LOM. In these cases, the fatigue strength was degraded compared to that predicted by k_f analysis and the energy absorbed was lower than for a similar geometry notch caused by plastic deformation. The fatigue strength was degraded most when LOM occurred. The types of FOD simulations that provide low impact velocities (pendulum) or are quasi-static, where only plastic deformation occurs, can slightly over-predict the fatigue strength for the same depth of penetration when compared to the ballistic case where LOM occurs. While some of the quasi-static and pendulum impacts produced fatigue strengths that were similar to those from ballistic impacts of the same depths, the mechanisms producing the altered strengths were not always the same in the ballistic case compared to the simulated indents at much lower velocities. Of greatest concern, however, is the scatter in fatigue strengths that is attributed to the sensitivity of deformation and damage to the exact location of impact in a leading-edge geometry.

7.9.1. Simulations using a flat plate

While it is both common and desirable to study FOD and the resulting fatigue strength in actual components, the extreme difficulty and variability in results led to the use of simple leading edge geometries under axial fatigue loading to better understand the problem. While the use of axial loading as opposed to axial and bending loads in a real component simplified the problem, and complexities such as twist and camber in real blades were avoided, variability in results due to extreme sensitivity to the impact conditions has made a thorough understanding of the FOD event rather difficult as noted above. Noting this large amount of scatter in evaluating FOD in leading edge geometries, simpler geometries were evaluated by Nicholas et al. [18]. They followed the procedure of Peters et al. [2] who investigated the ballistic impact damage on the same Ti-6Al-4V alloy in a flat plate geometry under normal impact and tensile fatigue loading. However, they extended the study to a wider range of test conditions involving both axial and torsional loading on rectangular specimens as well as introducing extensive use of stress relief (SR) annealing

to separate out the role of residual stresses as was done in the LE studies described above. The conditions chosen covered those found to impart deformation only at low velocities as well as microcracking under higher velocity ballistic impact [2]. In addition, low velocity pendulum impacts and quasi-static indenting were used. Because of the simple impact geometry of a flat plate impacted normally, as opposed to impacting a leading edge at a non-zero angle of incidence, the scatter in material behavior was reduced somewhat.

The procedures that were followed are close to those described in the previous section for leading edge impact studies where ballistic impact, pendulum impact, and quasi-static indentation were used to produce damage of similar depths. For the ballistic impacts, steel spheres, 3.18 mm in diameter, were impacted normally at velocities of either 200 or 300 m/s onto 3.18 mm thick flat plates. Half of the specimens were stress relief (SR) annealed in order to eliminate any residual stresses produced during the impact event. For either the quasi-static ball indentation or the low velocity pendulum, the ball used for producing the indent was of the same diameter and material as that used in the ballistic impacts. The depth of indent for the quasi-static and pendulum indents was chosen to be the same as the average value for the ballistic impacts, 0.22 and 0.41 mm for the 200 and 300 m/s impacts, respectively.

All of the plate specimens were fatigue tested in tension or torsion using the step-loading technique to determine the FLS, σ_{FLS}, corresponding to a life of 10^6 cycles. The torsion tests were added to axial testing previously performed on airfoil samples in order to produce different failure locations where residual stresses might be different.

For the simple plate geometry with an indent, the stress distribution and a modified elastic stress concentration factor were determined for the two notch depths using FEM. In the analysis it was assumed that the notch had a spherical surface with a radius of one-half of the impacting sphere whose diameter was 3.18 mm. A schematic of the cross section at the indent or notch is shown in Figure 7.26.

Results for the axial stresses on the notched specimen due to an average axial stress of 100 MPa or a torque that produces 100 MPa at the surface were calculated and are presented in Figure 7.27 for the deep notch as a function of the *y*-axis location, denoted

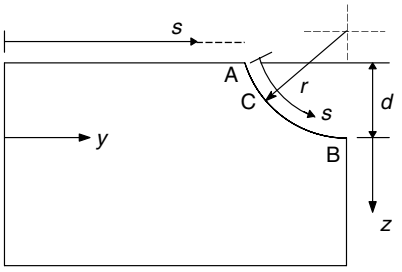


Figure 7.26. Geometry of half cross section through middle of notch.

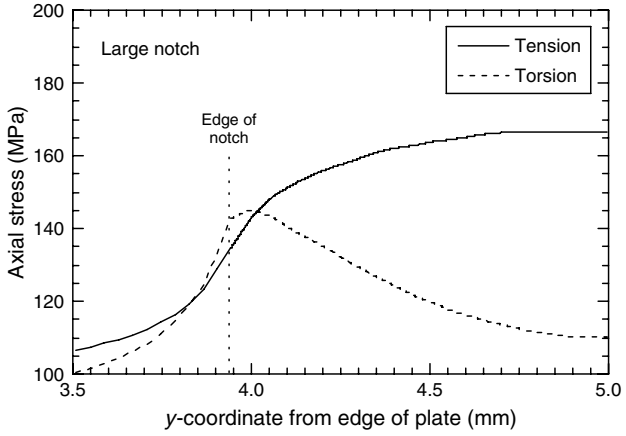


Figure 7.27. Axial stress distribution along surface of plate with large notch.

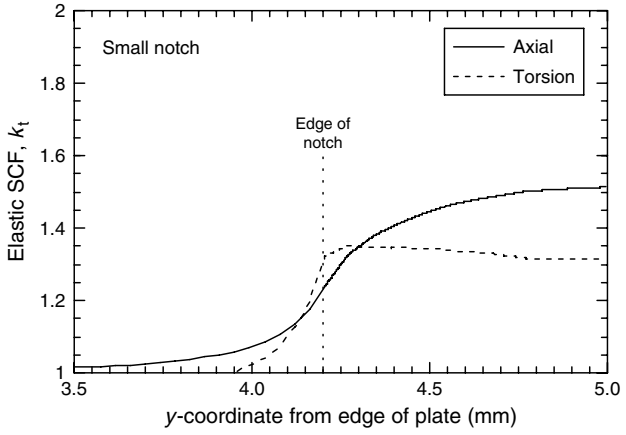


Figure 7.28. Elastic stress concentration factor along surface of small notch.

in Figure 7.26. The stresses for the shallow notch are shown in Figure 7.28. The center of the notch corresponds to $y = 5$ mm (10 mm wide plate) and the coordinates for the point A in Figure 7.26, where the notch intersects the surface of the plate, are $y = 4.201$ and $y = 3.939$ mm for the shallow and deep notches, respectively. This location is shown as the edge of notch using a dotted line in the figures.

Values of k_t can be obtained based on the true definition of a stress concentration factor: the actual stress at a location divided by the stress at that same location if the notch were not present. For axial loading, this is no problem since the smooth bar stresses are uniform across the cross section. However, for bending or torsion where the stresses

in a smooth bar vary linearly through the cross section, the value of the smooth bar stress decreases from the surface towards the notch bottom. A better measure of the notch effect is to use an effective stress concentration factor, denoted by k'_t, defined as the local stress in the notched specimen divided by the maximum stress at the surface in the smooth bar. The value of k'_t is then simply the value of the stress, shown in Figure 7.27 for the deep notch or in Figure 7.28 for the shallow notch, divided by the reference far field stress, 100 MPa in this case. Values for the effective stress concentration factor are summarized in Table 7.1. For most cases, the locations for the maximum value of the local stress concentration are either at A along the surface at the edge of the notch or at B at the root of the notch as shown in Figure 7.26. However, for the deep notch under torsion, the maximum value of k'_t occurs at point C at the interior of the notch as seen in Figure 7.27. It is slightly higher than the value at point A on the surface for the torsion case.

The FLS, σ_{FLS}, corresponding to a life of 10^6 cycles was determined from step tests in both tension and torsion. For reference purposes, the value of σ_{FLS} for smooth bar tension tests on this material at 10^6 cycles is 600 MPa at $R = 0.1$. The results for the average value of k_f from two tests at each of the conditions shown are summarized in Table 7.2 for tension tests conducted at $R = 0.1$. The symbol "AR" is used to denote as-received material (material as tested without stress relief after the indents were put in) while "SR" denotes samples that were stress relieved after indentation. Three types of indentation are represented in this database: ballistic, pendulum, and quasi-static, all to the same depth. The results of the tensile fatigue tests show that SR improved the fatigue strength in all cases, although the improvement was not very large. This implies that some tensile residual stresses were present after all three indentation procedures, since

Table 7.1. Computed values of k'_t for notches

	Small notch		*Large notch*	
	Bottom	*Surface*	*Bottom*	*Surface*
Axial	1.51	1.24	1.67	1.35
Torsion	1.13	1.26, 1.32*	1.10	1.38, 1.46**

* @ $y = 4.25$ mm, ** @ $y = 4.00$ mm

Table 7.2. Experimental values of k_f for notches under tension, $R = 0.1$.

Notch type	*Ballistic*	*Pendulum*	*Quasi-static*
AR shallow	1.31	1.20	1.19
AR deep	1.69	1.31	1.26
SR shallow	1.26	1.10	1.07
SR deep	1.53	1.11	1.09

nothing changes during the SR process other than the removal of residual stresses. This finding is consistent with that discussed in the previous section for impact on leading edge geometries. Of greater significance is the observation that ballistic impacts to the same depth as pendulum or quasi-static indentations are more severe in terms of the resulting fatigue limit strength reduction. This is especially true for the deeper indents corresponding to ballistic impacts at 300 m/s. In the work of Peters et al. [2], the impacts at 300 m/s produced small amounts of cracking at the crater whereas the impacts at 200 m/s produced no observable cracks. This shows that low velocity (pendulum) or quasi-static indentation does not produce the same amount of damage as ballistic impact for this material under the specific impact conditions (depth of indent) described, particularly at higher velocities.

Results for the tests in torsion are summarized in Table 7.3. Here, only ballistic impacts were evaluated at $R = 0$ for both AR and SR samples, and $R = -1$ for AR only. The SR samples show a reduction in k_f which is equivalent to an increase in σ_{FLS}. This is attributed to the implied existence of tensile residual stresses in the failure region. The value of k_t in Table 7.1 for a deep notch in tension indicates that fracture would be expected at the bottom of the notch. This is confirmed by the observed location of initiation near the notch bottom as shown in Figure 7.29(a). On the other hand, torsion tests of a specimen

Table 7.3. Experimental values of k_f for ballistic notches under torsion

Notch type	$R = 0$	$R = -1$
AR shallow	1.31	1.62
AR deep	2.00	2.00
SR shallow	1.01	–
SR deep	1.47	–

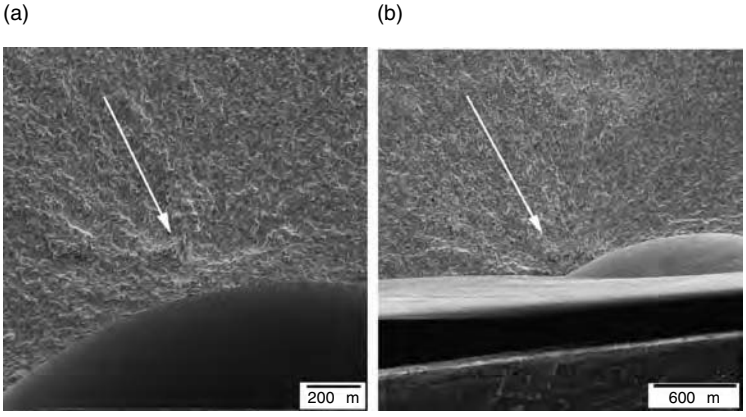


Figure 7.29. Fractographs showing initiation sites in (a) tension, (b) torsion.

with a shallow notch would be expected to produce a failure near the surface because of the higher value of k_t as listed in Table 7.1. The fractograph, Figure 7.29(b), confirms such a finding. In both cases illustrated, the specimen was subjected to SR, so only microstructural damage or hardening could account for fracture initiating at any other location. In one extreme case initiation occurred near the surface of a deep notch from high velocity (312 m/s) ballistic impact. While initiation would be expected to occur at the bottom according to k_t analysis for tension fatigue loading, damage in this case was sufficient in the form of local tearing to reduce the fatigue strength below that of most of the other specimens. This resulted in fracture initiating near the location of extensive damage at the surface.

The difference in σ_{FLS} between AR and SR in the tension and torsion cases for ballistic impact seems to indicate that the tensile residual stresses are somewhat higher near the surface than at the bottom although scatter in test results makes this observation somewhat tenuous. In both the tension and torsion cases, for ballistic impact at 300 m/s which produces the deeper crater, the debit in fatigue strength is greater than that expected due solely to the stress concentration factor, indicating some type of microstructural damage near the failure location whether it be at the bottom, for tension tests, or near the surface, for torsion tests. Finally, for the shallow indents produced by ballistic impact at 200 m/s, there is no apparent reduction in fatigue strength under torsion testing after SR, even though the value of k_t is 1.32 at the failure location. This implies that some type of strengthening mechanism is present that retards fatigue failure, most likely delaying fatigue initiation. In a study of deep rolling and other surface treatments in this same alloy, Nalla et al. [19] identified a strengthening mechanism in the form of an induced work hardening near-surface layer that improves the fatigue resistance of the material.

Figure 7.30 shows high resolution SEM images of a region at the deformed surface where a different microstructure can be seen over the first several microns from the free surface. This region of intense plastic deformation seems to have a retarding effect on fatigue crack initiation as deduced from the experimental data, particularly from the SR specimens.

All of the data obtained in tension at $R = 0.1$ and torsion at $R = 0$ are summarized in Figure 7.31 where hollow symbols represent the SR specimens and solid symbols are for specimens that were not stress relieved and are designated AR. The data are plotted as a function of k_t for the various notches, where it should be noted that k_t is different for the same geometry notch when tested in tension or torsion as discussed earlier. This figure illustrates the trend of SR specimens to have higher strengths than AR specimens, even higher than would be expected from a k_t analysis. For reference purposes, the line representing $1/k_t$ is shown. Ideally, a line showing theoretical values of $1/k_f$, which would be somewhat higher, should be shown. However, for the notch geometry and loading conditions used here, there is no model for values of k_f.

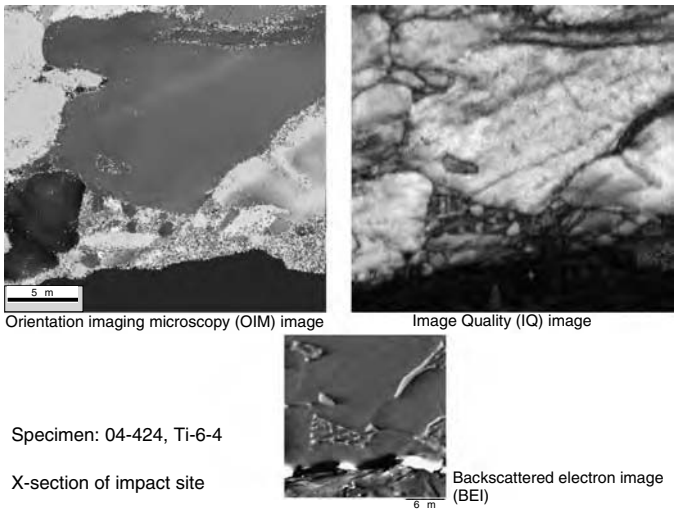


Figure 7.30. SEM images of region near impacted surface.

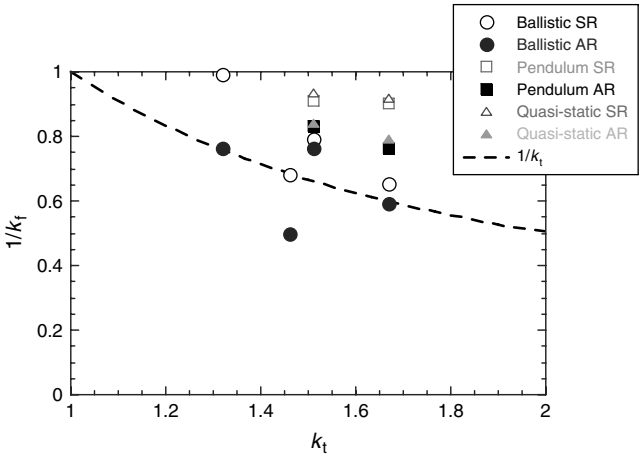


Figure 7.31. Fatigue limit strength for all tension ($R = 0.1$) and torsion ($R = 0$) tests.

Figure 7.31 shows that the ballistically impacted specimens show degradation in strength beyond that predicted simply by k_t. The results are in agreement with those shown in the previous section for 2.0 mm ball indents on leading edges where damage under ballistic impact was greater than from quasi-static or pendulum indents.

The observations discussed above indicate that FOD, even under carefully controlled laboratory conditions, involves a number of mechanisms that contribute to the fatigue

strength of a material. Normal impacts on flat plates under ballistic and slower velocity conditions that produce craters of a given depth produce damage involving a number of mechanisms. The fatigue strength, that is a reflection of the damage severity, is also a function of loading conditions under axial or torsion stress states. Residual stresses are deduced to be tensile in most cases while some type of strengthening mechanism from the indenting exists that is not removed by stress relief annealing. The result of plastic deformation near the surface seems to have a beneficial retardation effect on crack initiation. For the deeper of the impacts discussed here, the impact damage from ballistic or lower velocity conditions reduces the fatigue strength beyond that predicted from the geometry of the resultant crater as characterized by the equivalent elastic stress concentration factor. However, quasi-static and low velocity pendulum indents produce different damage mechanisms than equivalent depth craters from ballistic impacts even though the fatigue strengths may be similar. These results, combined with observations of damage in leading edge specimens in the previous section, indicate that simulating FOD using quasi-static or low velocity methods may not produce identical results to true FOD in terms of either fatigue strength or damage mechanisms.

7.9.2. Other laboratory FOD simulations

This section illustrates several methods for analyzing FOD data obtained from several specimen geometries using different techniques based primarily on concepts developed for notches as described earlier in Chapter 5. In the HCF program of the US Air Force [8], the fatigue properties of specimens subjected to well-controlled laboratory FOD simulations were deduced based on the geometry of the notch produced. An extensive experimental investigation was conducted where the fatigue limit strength of a material subjected to real or simulated FOD was characterized. All tests were run on Ti-17 material at room temperature using two different test specimen geometries to simulate the leading edge of an airfoil. The axial specimen geometry, similar to the one shown earlier in Figure 7.16 (see also Appendix G), was machined with a 12-mil root radius that simulates a blunt tip airfoil leading edge geometry.

The bending specimen geometry is shown in Figure 7.32. This specimen is tested under 4-point bending to simulate the stress gradients in an airfoil. The use of this specimen is described in more detail in Appendix G. The edge of this specimen was machined with 7-mil and 14-mil root radii to simulate a sharp and blunt tip airfoil geometry, respectively.

The FOD to the leading edge was simulated on the axial and bending specimens with a steel chisel indentor fired from a solenoid gun described earlier in this chapter (see also Appendix G). The FOD indentor had a nominal root radius of 5 mil with a 60° included angle. Several depths of penetration were obtained at a 30° impact angle using different energy levels on the solenoid gun. At a depth of ~10 mil, the onset of shear cracks in the material being extruded was observed. The FOD at ~20 mil produced more extensive

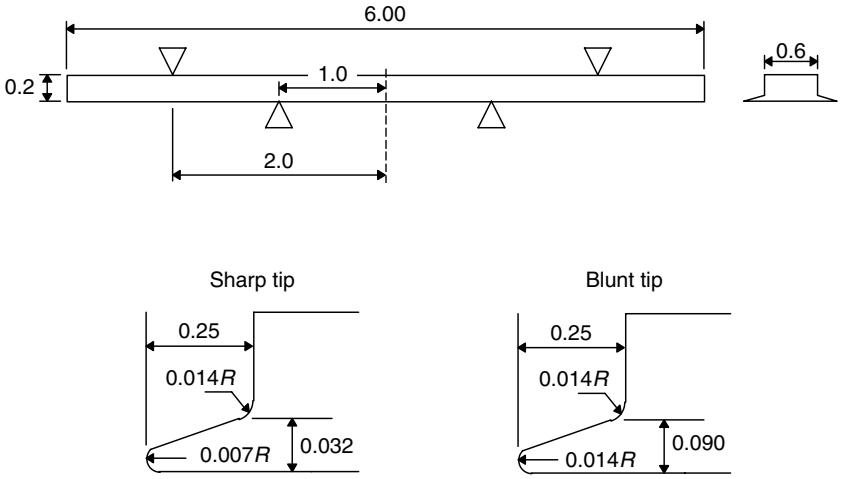


Figure 7.32. Bend bar simulating sharp and blunt airfoil leading edge. All dimensions in inches.

damage as expected. Numerous shear cracks were observed on the flanks of the FOD in the extruded material, but no tears or cracks were observed at the root of the FOD notches.

The FOD depth was determined with a line normal to the FOD as a notch depth profile. The FOD impact angle was determined from a line normal to the FOD impact with respect to a line tangent to the specimen leading edge face. An example of deep FOD in a sharp tip bend specimen is given in Figure 7.33. Lines to obtain the FOD impact angle and depth are shown schematically in the figure.

Fatigue tests on the axial specimens were predominately run at $R = -1$ under step testing to 10^7 cycles. Three different FOD impact angles were evaluated for the axial tests in the "as-FODed" and "FODed + stress relief (SR)" conditions. Tests with FOD + SR were used for comparison to assess the role of residual stresses in the analysis. The SR condition was obtained on the Ti-17 material in a vacuum furnace for 8 hours at 1130°F after the FOD impact.

The Ti-17 bending tests were run under step loading to 10^6 cycles. Bending tests were run at one nominal impact angle for both the sharp and the blunt tip leading edge geometries. Tests were run for the geometries in the as-FODed and FODed + SR conditions. The results are presented as k_f as a function of geometry, impact angle, stress relief, and FOD depth. To account for different values of R, k_f is defined as S_{equiv} for the smooth specimen data normalized by S_{equiv} at the specimen failure stress calculated for the notched specimen.

Several methods were used to predict allowable HCF limits for specimens with FOD. Crack initiation methods were used, where baseline HCF capability for Ti-17 was obtained

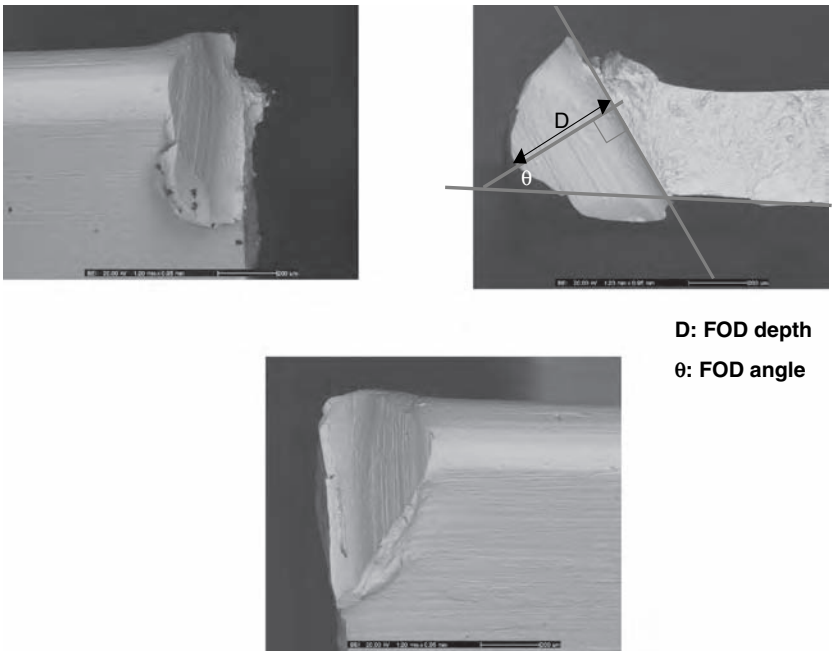


Figure 7.33. Fractography for deep FOD in the sharp tip geometry.

from the best-fit curve to the smooth specimen data using equivalent stress to consolidate data obtained at different values of R. The first prediction ignored the FOD notch stress concentration and damage, and was based solely on the calculated maximum stress at the notch location. This approach is easy to implement, but is inaccurate for FOD tests as shown in Figure 7.34. The term $S_{\text{un-notched}}$ refers to the local stress at the location of the FOD, uncorrected for the notch effect or any stress gradient due to the notch. In this and subsequent plots, S_{curve} refers to the baseline smooth bar data. This result is generally non-conservative as expected. This method of data analysis simply shows the debit in fatigue strength at the notch location. By definition, k_{f} is the reciprocal of the y-axis value that appears to range from slightly over one to as high as five.

The next approach utilized the calculated local peak stresses with the smooth specimen fatigue curve. For this approach, stress components are obtained from the measured notch geometry with maximum and minimum load cases at the interpolated loads with 3D elastic-plastic stress analysis. This approach is generally conservative (Figure 7.35) as expected. There does not seem to be any trend with stress relieved specimens compared to those without SR, indicating that residual stresses are neither compressive nor tensile consistently. Rather, they appear to be scattered and probably depend on the specific conditions at each impact site and the specific failure initiation location.

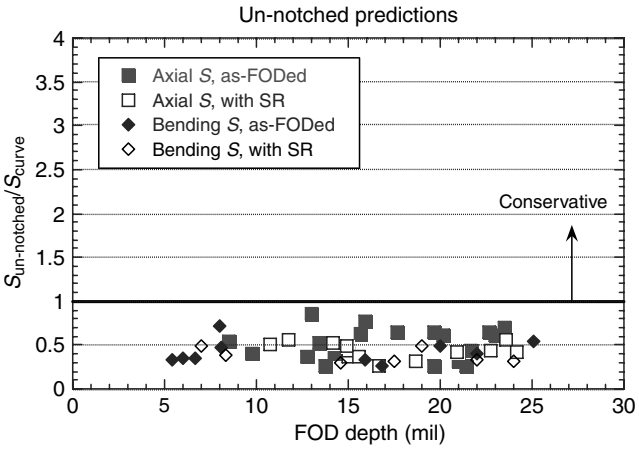


Figure 7.34. Prediction of the HCF capability of specimens with FOD using the unnotched stresses.

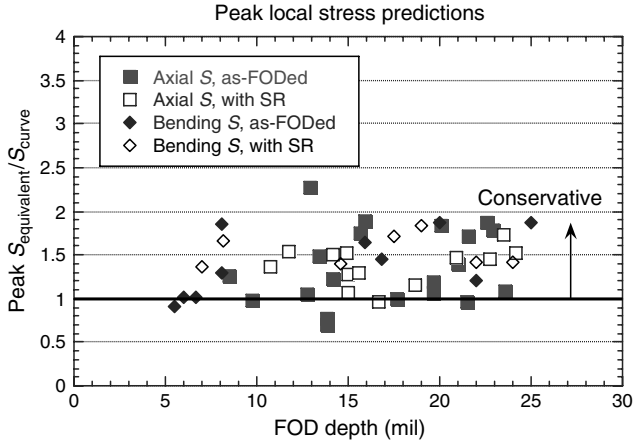


Figure 7.35. Prediction of the HCF capability of specimens with FOD from the peak concentrated stress.

Machined notch data for the same material are shown in terms of equivalent peak local stress as a function of fatigue life in Figure 7.36. In the plot, the RFL model (see Chapter 2) was used to represent the smooth bar data. Data for specimens with very small notches are shown along with those that were obtained for machined U- and V-notches. The local stress approach with smooth specimen fatigue curves under-predicts the HCF capability of specimens for small notches. On the other hand, the V-notch data are over-predicted based on the local stress at the notch tip. The notch data and the smooth bar

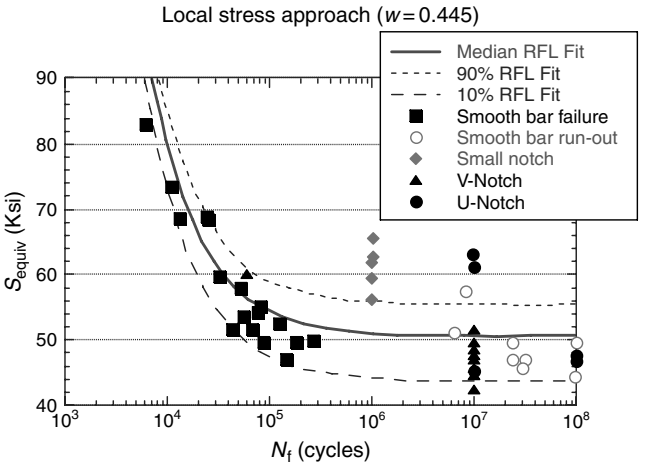


Figure 7.36. Smooth and notched bar fatigue results with the peak local stress approach.

data would match on this plot if $k_f = k_t$. As seen, the small notch data exhibit a size effect that would produce higher strengths as the notch size became smaller. The V-notch data indicate that the notch may be sharper at the tip than measured.

Local stress approaches were modified with notch fatigue stress concentration (q–k_f) and feature stress (Fs) approaches. Both methods try to account for stress gradients at the notch root by recognizing that fatigue in that location is not governed solely by the peak stress. The first notch method evaluated is a q–k_f approach, alternately referred to simply as the q approach. This approach is used to predict FOD capability from the combination of k_t and an equation for k_f. Note that this approach is essentially an empirical approach using the fatigue notch factor, k_f, applied to notch geometries. It is summarized by the following three equations:

$$\sigma_{\text{equiv, } q\text{adj}} = k_f(\sigma_{\text{equiv, unnotched}}) \tag{7.4}$$

$$q = \frac{k_f - 1}{k_t - 1} \tag{7.5}$$

$$q = \frac{1}{\left(1 + \frac{a}{\rho}\right)} \tag{7.6}$$

where $\sigma_{\text{equiv, unnotched}}$ is calculated at the critical location without the notch present, $k_t =$ notch concentrated stress/unnotched stress, ρ is the notch root radius, and "a" is a material constant. Equation (7.6) is the empirical equation for k_f, shown earlier as Equation (7.3). k_t can be difficult to define for 3D component geometries, but the approach is well suited

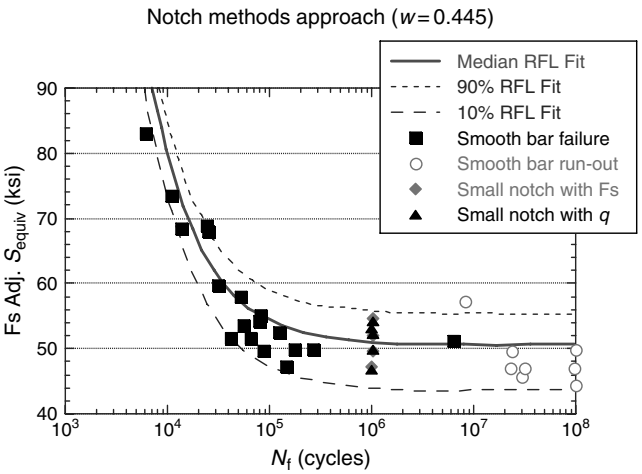


Figure 7.37. Small notch correlation with Fs and q–k_f approaches as compared to smooth specimen fatigue curves.

to small FOD or machined notches where the local stress can be referenced to the stresses in the unnotched geometry. For this approach, the material constant $a = 1.8$ mil was found to best correlate small machined notch test data as shown in Figure 7.37.

The Fs approach or equivalent stressed surface area takes into account the stress distribution about the peak stress at a notch root. This approach is described in Appendix E. Both the q and the Fs approaches do a credible job of consolidating small notch data with smooth bar data as shown in Figure 7.37. Since the two approaches produced almost equivalent results, the q approach was used to consolidate the FOD test results because it is much simpler to apply than the Fs approach described in Appendix E.

The results of the axial and bend specimen FOD tests for the various impact angles (in the axial tests) and the different tip radii (for the bend tests), modified using the q approach, are presented in Figures 7.38 through 7.42. In all cases, the notch geometry was measured as described above. The predictions for a constant notch root radius of 4.4 mil are represented with solid black lines for the different geometries and impact angles. Significant scatter exists in the FOD test results, but calculated k_f with the q approach generally provides a reasonable prediction of the mean HCF behavior of specimens with FOD for different impact angles and FOD depths. For reference purposes, the k_t values are also shown in the plots.

Results are summarized for tests in the "as-FODed" and "as-FODed + stress relief (SR)" conditions in Figures 7.43 and 7.44. The predictions are best with a reduction in test scatter when the stress relief cycle is employed after FOD to reduce residual stresses (Figure 7.44).

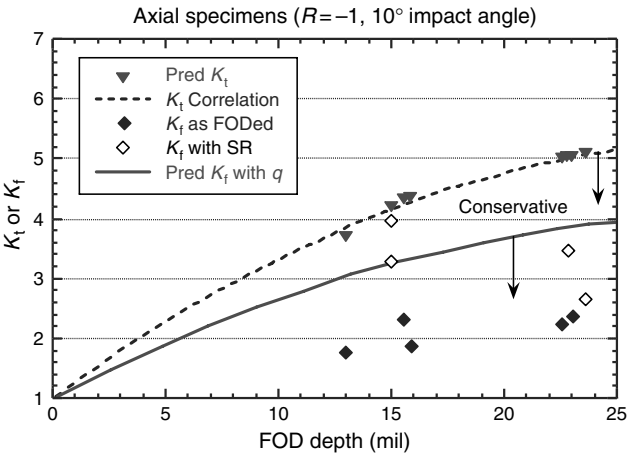


Figure 7.38. Predicted and experimental k_f for FOD tests in the axial specimen geometry with a 10° impact angle.

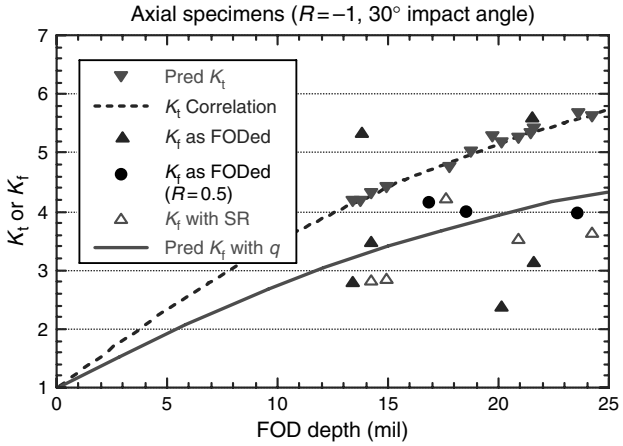


Figure 7.39. Predicted and experimental k_f for FOD tests in the axial specimen geometry with a 30° impact angle.

Results with both the q and Fs approaches for the axial and bend specimens are similar as summarized in Figures 7.45 and 7.46. For the axial specimens, the SR samples appear to have less scatter and consolidate better with smooth bar data than those without SR. While the authors of this report [8] propose implementation of these approaches for design applications, it should be noted that the indentor geometry and notch conditions covered only a limited range of FOD variables. As noted in the previous notch section, extending

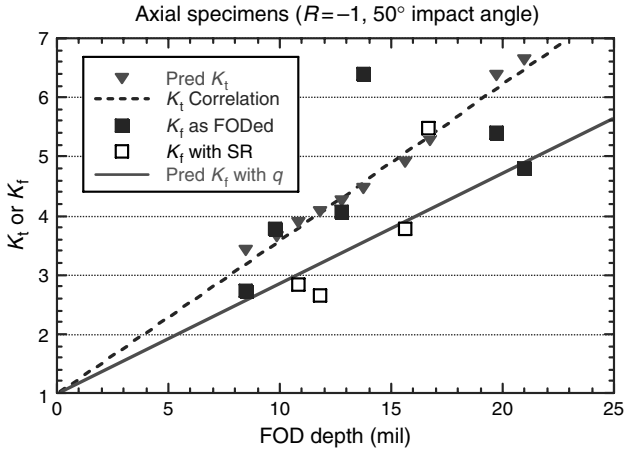


Figure 7.40. Predicted and experimental k_f for FOD tests in the axial specimen geometry with a 50° impact angle.

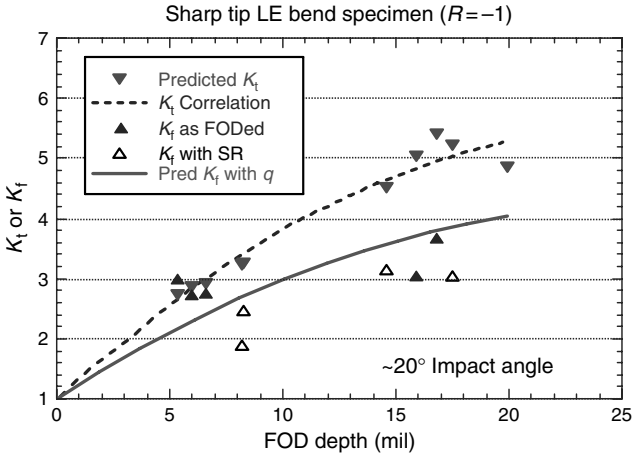


Figure 7.41. Predicted and experimental k_f for FOD tests for a bending specimen with the sharp tip geometry.

approaches such as the one based on q or k_f to a wider range of notch geometries can lead to errors. For FOD, as will be shown later, changes in the residual stress states, and material damage, as severity of the impact increases, make it even more difficult to extend the approaches described herein.

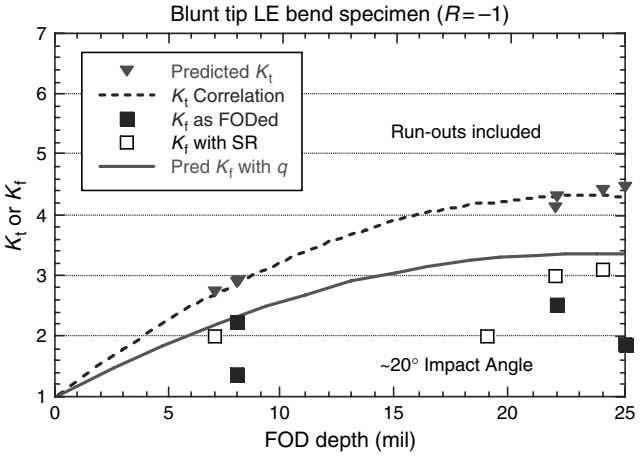


Figure 7.42. Predicted and experimental k_f for FOD tests for a bending specimen with the blunt tip geometry

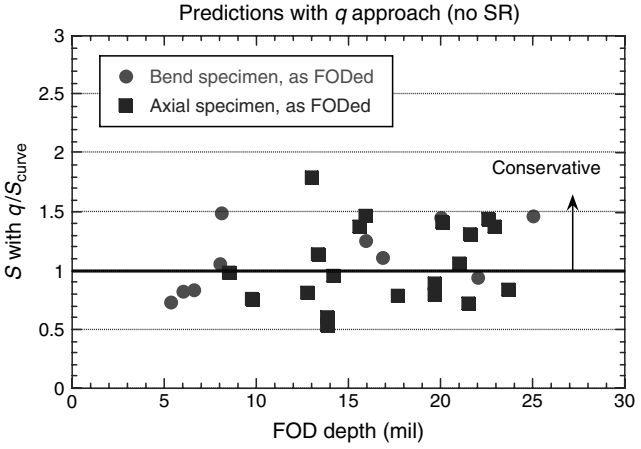


Figure 7.43. Predicted HCF capability vs the baseline fatigue behavior for as-FODed tests.

7.10. ANALYTICAL MODELING OF FOD

Appendix G describes, in detail, both experimental and analytical simulation methods for the prediction and modeling of FOD. It describes some of the procedures that can be used to measure and predict the effects of FOD and gives current state-of-the-art examples of techniques and methodologies that are in use and/or are being developed. In this section, some analytical procedures and findings are described which relate to hard body FOD. More extensive studies and observations are contained within the Appendix.

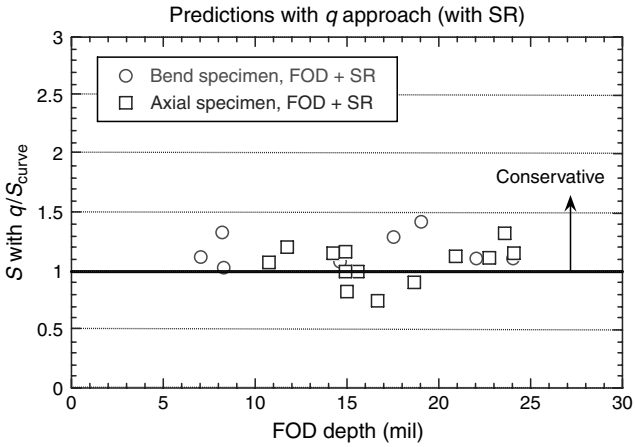


Figure 7.44. Predicted HCF capability vs the baseline fatigue behavior for as-FODed tests with a stress relief cycle to minimize residual stresses.

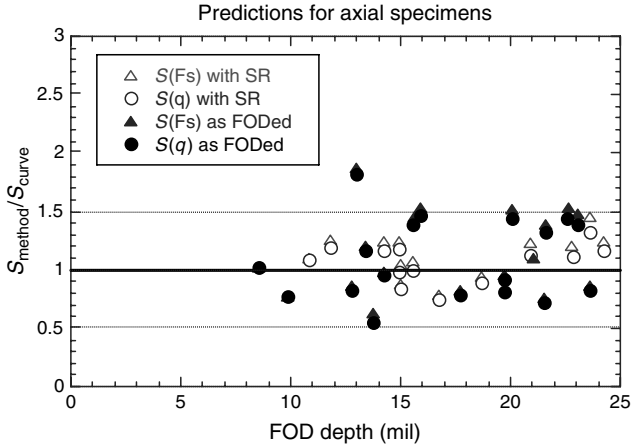


Figure 7.45. Similar predicted HCF capability with q and Fs approaches for axial specimens with FOD.

While experimental observations of FOD show wide variability with little or no change in impact conditions, analytical modeling should be expected to provide more consistency. This is true only if the actual conditions occurring during FOD are modeled accurately. This is not always the case, either analytically or experimentally. In particular, the role of centrifugal loading can be important in an impact event. In [8], analytical modeling studies of leading edge FOD impact events were conducted to determine the effects of various parameters on leading edge damage, residual stress distribution, and predicted

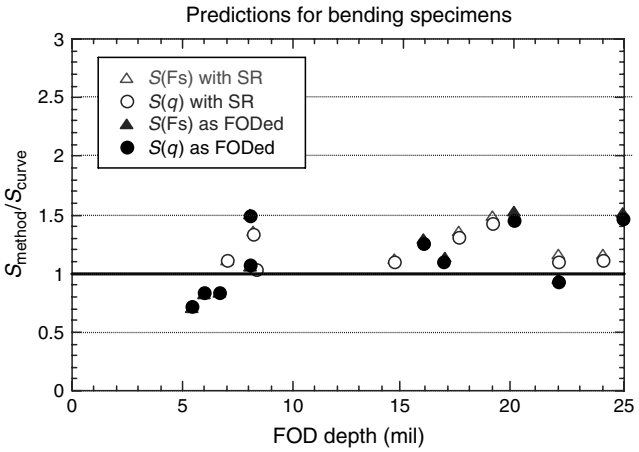


Figure 7.46. Similar predicted HCF capability with q and Fs approaches for bending specimens with FOD.

HCF capability. The parameters investigated were impact velocity, impact angle, blade centrifugal loads, projectile geometry, and imperfect impact. MSC/DYTRAN was used for analysis of the high-speed impact events. Existing DYTRAN finite element models of the specimen shown in Figure 7.16, referred to earlier, were utilized for the analysis. The specimen finite element model geometry and a close-up of a steel ball projectile can be found in Appendix G.

The dynamic analysis modeling included strain-rate-dependent material properties and material failure. The material failure model was based on the Von Mises yield function. Material strain-rate dependency was included. The chosen material failure model allowed for failure of the element by definition of an effective plastic strain at failure. The high-strain-rate effective plastic strain at failure utilized in this analysis was 35%. The single effective-plastic-strain variable utilized does not distinguish between different material failure modes such as tension, compression, shear, and mixed modes. A more accurate failure model would provide a better residual stress state and deformation of the FOD site location. An HCF–LCF cycles-to-failure model based upon a Walker methodology was developed and used to investigate parameter influences on predicted fatigue life to failure. The Walker strain is defined as

$$\varepsilon_{\text{Walker}} = \frac{\sigma_{\max}}{E}\left(\frac{\Delta\varepsilon_{\text{eq}}E}{\sigma_{\max}}\right)^{m} \tag{7.7}$$

where $\sigma_{\max}$ is the maximum stress, m is the Walker strain exponent, and $\Delta\varepsilon_{\text{eq}}$ is the equivalent strain range. The ability of this formulation to consolidate fatigue data at different values of R is illustrated in Figure 7.47 which shows data from smooth bar as well as notched specimens and lines indicating the degree of scatter.

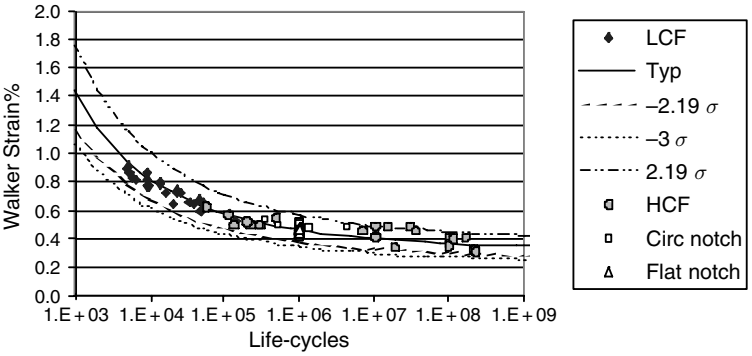


Figure 7.47. Ti-6Al-4V RT consolidated HCF and LCF results.

One of the analytical studies performed was an investigation of blade preload effects (due to centrifugal load) on the residual stress distribution around the FOD site. Residual stress distributions and predicted cycles to failure were investigated and compared. Specimens were impacted at different angles and impact velocities while experiencing 0 ksi, 20 ksi, and 40 ksi static stress fields simulating the blade centrifugal load. A 1.33 mm diameter steel ball with a 1000 ft/s velocity was used. The study indicated that as blade preload increased, higher compressive and tensile residual stresses would be produced at the FOD site. Although the influence of preload on predicted fatigue life was not clearly observed, it might be attributed to a relatively coarse mesh density, and the use of a simple material failure model. It was observed, however, that including residual stress reduced the predicted fatigue life to failure by more than a few orders of magnitude as indicated in Figure 7.48, which also shows that increasing the impact angle reduces

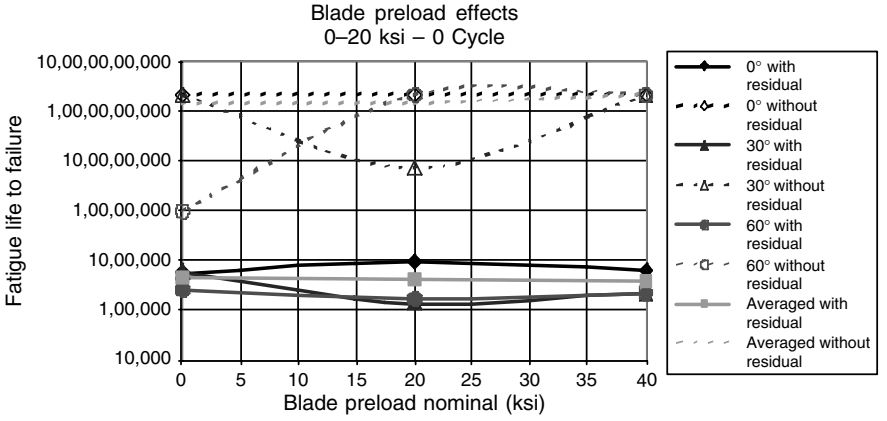


Figure 7.48. Predicted fatigue life of preloaded blade cycled to 20 -ksi nominal stress.

the predicted fatigue life. More variance exists in the "without residual stress" predicted fatigue life results. Model mesh density might affect the variance. After impact, the finite element model is faceted at the local FOD. Local facets produce sharp angles that are stress risers. Including the residual stress reduces the predicted fatigue life and smoothes out the curves.

Figure 7.49 illustrates that as the cyclic stress increases to 0–40–0 ksi, residual stress due to impact has less effect on the predicted life. Comparing Figures 7.48 and 7.49 suggests that residual stress is more critical in the HCF regime than the LCF regime. Figure 7.49 shows that as impact angle increases, fatigue life decreases.

One interpretation of this analysis is that performing experiments on FOD in blades under laboratory environments, absent of centrifugal loading, may produce results that are not representative of real engine conditions and could be misleading. Similarly, reproducing the correct impact angle, particularly for low angles, can influence the fatigue life of the specimen.

7.10.1. Perturbation study

As shown in Appendix G, FOD test results can exhibit a great deal of scatter in both the fatigue life of specimens and the nature of the damage when impacted under nominally identical conditions. It has proven to be very difficult to reproduce exactly the same FOD from one test specimen to the next. To study this analytically, an impact site perturbation

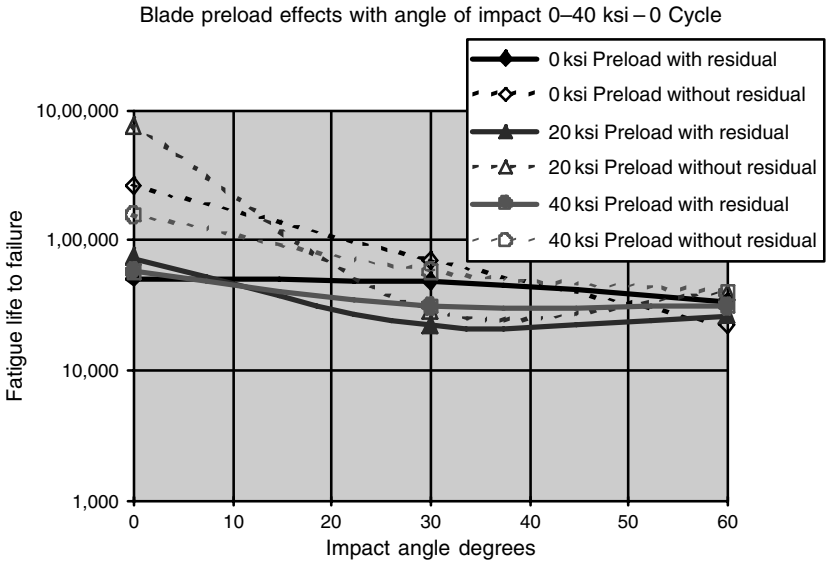


Figure 7.49. Predicted fatigue life of preloaded blade cycled to 40 ksi nominal stress.

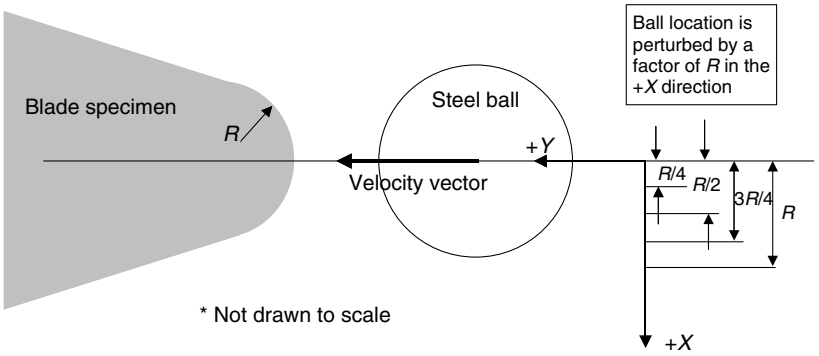


Figure 7.50. Perturbation study definition for the 0° impact angle study.

study was performed [8]. Similar to the study in the previous section, the effect on fatigue life for the 0° impact angle of the blunt edge radius (0.381 mm/0.015") blade specimen was addressed. Here, a 1.33 mm ball with a velocity of 1000 ft/s was investigated by offsetting the vector of the incoming ball by amounts ranging from 0.25 to 1.0 times the radius of the leading edge as shown in Figure 7.50.

It was found that increased impact site offset in the $+X$ direction (down) produced increased tensile residual stress on the top side of the blade. The effect of the offset in fatigue life is summarized in Figure 7.51 which illustrates that with increased impact site offset there is a reduction in fatigue life. For the $X = 0$ location, the case of 0–20 ksi produces a fatigue life is calculated to be 3,370,000 cycles, while increasing the offset to

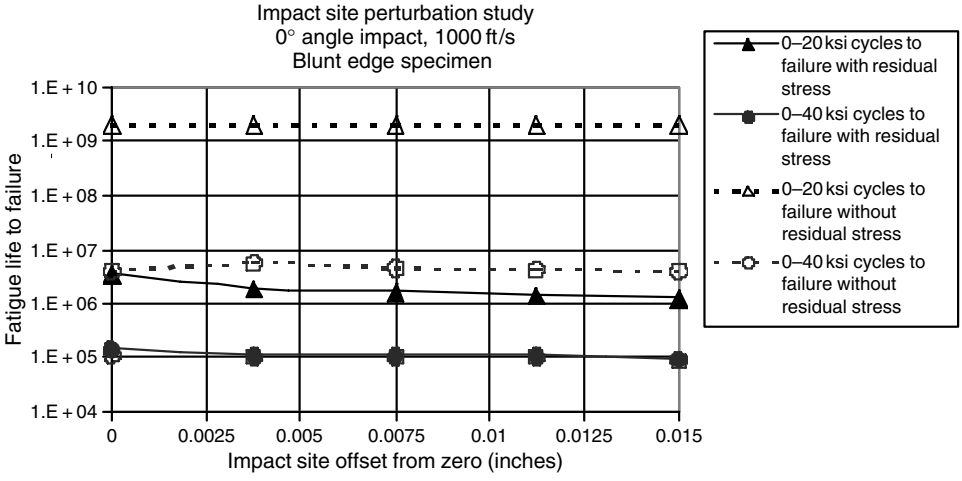


Figure 7.51. 0° Impact site offset study on fatigue life.

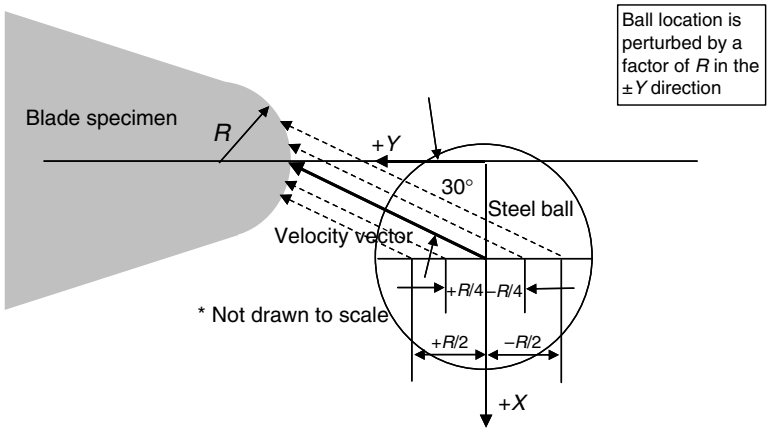


Figure 7.52. Perturbation study definition for the 30° impact angle study.

$X = R$, fatigue life decreases by a factor of 2.9 to 1,180,000 cycles. The 0° perturbation study suggests that a good deal of fatigue life variation could be observed due to imperfect impacts.

Another study looked at the effect of impact offset when the incoming angle of the projectile was 30° as shown in Figure 7.52. Five impact cases were investigated with the blunt edge specimen. It was observed that as Y goes from $-R/2$ to $+R/2$ the depth of the FOD site increases. The $-R/2$ and $-R/4$ impacts removed elements through the thickness of the blade tip. For $Y = 0$ and greater, some elements remained on the exit side of the impact, and there were more elements removed at the entrance side. The compressive stress distribution was found to be driven from a more interior distribution for $Y = -R/2$ toward a surface distribution for $Y = +R/2$. Figure 7.53 compares the fatigue life results for this perturbation study. For the 0–20 ksi cyclic case with residual stresses, the calculated maximum number of cycles to failure was 9,80,000 cycles at the $Y = -R/4$ location. The minimum of 2,00,000 cycles occurred at the $Y = 0$ location. There is a factor of 4.9 between the maximum and the minimum calculated fatigue life.

These results demonstrate that there can be a significant difference in predicted fatigue life given an imperfect impact. The 0° impact angle perturbation study of the blunt edge specimen shows a 2.9 factor between the maximum and the minimum calculated fatigue life values. For the 0° impact, fatigue life decreased as offset increased. For the 30° impact of the blunt edge specimen, a 4.9 factor between the maximum and the minimum fatigue life was observed. The two impact site perturbation studies performed here suggest there is a variation in fatigue life due to imperfect impacts. Further analysis would need to be done to more accurately address the actual magnitude of the variation.

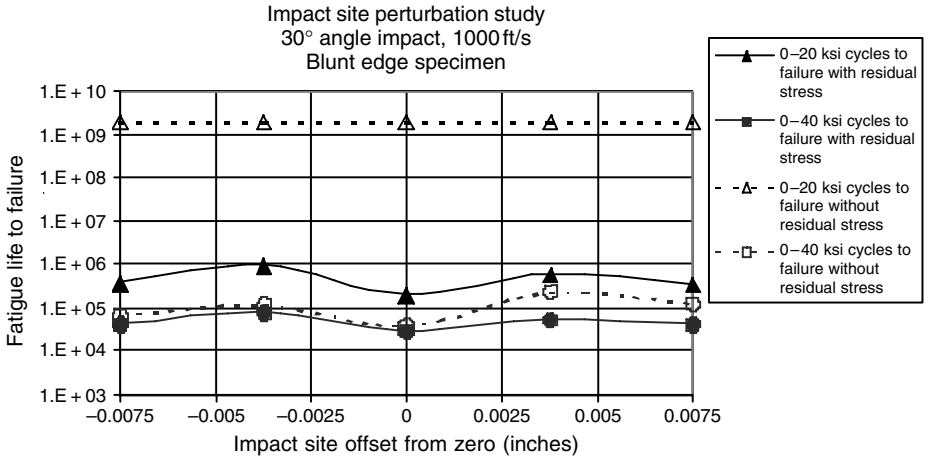


Figure 7.53. 30° Impact site offset study on fatigue life.

7.11. SUMMARY COMMENTS

The nature of the FOD problem that involves objects impacting static or rotating components, as well as some of the research findings summarized in this chapter, clearly distinguish FOD as the most difficult subject to deal with from an HCF (materials) design and analysis perspective. While extensive FOD occurs on a regular basis, fortunately only a small percent of damaged components actually fail from HCF. Thus, the combination of damage and vibratory stress is what must be assessed to establish the potential for a combined FOD/HCF failure to occur. Adding to the complexity of the problem, as pointed out in this chapter, is the very wide variety of damage modes that may occur. This variability is due not only to the type of impacting object that causes the damage, covering a range in sizes, shapes, and materials, but also to the geometry of the component being impacted. For the latter, the susceptibility of the component to vibratory stress is an important aspect for design against FOD/HCF failure. Another consideration is the consequence of a component failure, for example, whether a blade is contained within the engine housing and how much potential damage such a blade or piece of blade might cause downstream in the engine. Most of all, however, is the question of what objects cause FOD. The word "foreign" in FOD is very appropriate because it is rare when the foreign object can be identified. Only the damage remains after the event and, in extreme cases, no evidence remains at all when catastrophic failure occurs. One organization is currently using steel cubes to simulate FOD, one is 3.2 mm on a side and one is 4.8 mm on a side. While these cubes, when specifically oriented, produce damage that is very similar to what is observed in the field or provide a worst case scenario, it is obvious that steel cubes are not the real objects being ingested into engines in the

field. Although standard size birds have been identified for bird ingestion simulations and engine qualification, no hard objects have been identified to produce FOD similar to what is encountered in the field beyond the steel cubes mentioned above. Will there ever be a "standard" sand particle or stone with which to evaluate the FOD tolerance of an engine or an engine component? It is this author's opinion that some sort of standardization should be developed for the purpose of at least comparing the FOD tolerance of different designs or FOD tolerance enhancements.

One aspect of FOD that has not been addressed in this book is the subject of FOD repair. Current methods involve either replacing the component when damage is severe or blending out the damaged region by grinding or filing. Blend limits and specifications depend not only on the extent of the damage but also upon the location of the damage such as radial position along the leading edge of a blade. As noted in this chapter, residual stresses can be produced during the FOD event. The extent and magnitude of such stresses have not been quantified to any great extent, so blending may or may not eliminate all residual stresses or, worse, may expose detrimental (tensile) residual stress fields. Concurrently, microstructural damage may occur beyond the crater in the form of shear bands, internal cracking, or other. Such damage may not be detectable or visible on a component. Current repair specifications are highly empirical and do not consider the extremely complex nature of the damage imparted to a material during an FOD event as noted in this chapter. Simulations of FOD events may not produce the actual damage encountered in service because the impacting object is not known or the method of imparting damage (quasi-static for example) may not produce the same damage as a ballistic impact.

Finally, the very complex nature of the FOD event lends its treatment to statistical methods where the probabilities of the event itself as well as the vibratory loading and the material capability should all be considered. This subject is discussed in Chapter 8.

REFERENCES

1. Martinez, C.M., "Effects of Ballistic Impact Damage on Fatigue Crack Initiation in Ti-6Al-4V Simulated Engine Blades", M.S. Thesis, School of Engineering, University of Dayton, Dayton, OH, April, 2000.
2. Peters, J.O., Roder, O., Boyce, B.L., Thomson, A.W., and Ritchie, R.O., "Role of Foreign Object Damage on Thresholds for High-Cycle Fatigue in Ti-6Al-4V", *Metallurgical and Materials Transactions*, **31A**, 2000, pp. 1571–1583.
3. Mall, S., Hamrick, J.L., II, and Nicholas, T., "High Cycle Fatigue Behavior of Ti-6Al-4V with Simulated Foreign Object Damage", *Mech. of Mat*., **33**, 2001, pp. 679–692.
4. Franklin, J. and Kleinakis, E., "FOD Data Mining and Investigation", Chapter 2 in Ref. [4].
5. "Best Practices for the Mitigation and Control of Foreign Object Damage–Induced High Cycle Fatigue in Gas Turbine Engine Compression System Airfoils", Work performed by RTO AVT Task Group-094, NATO RTO Technical Report TR-AVT-094, December 2004.

6. Haritos, G., Nicholas, T., and Lanning, D., "Notch Size Effects in HCF Behavior of Ti-6Al-4V", *Int. J. Fatigue*, **21**, 1999, pp. 643–652.
7. Nicholas, T., Barber, J.P., and Bertke, R.S., "Impact Damage on Titanium Leading Edges from Small Hard Objects", *Experimental Mechanics*, **20**, 1980, pp. 357–364.
8. Gallagher, J. et al., "Advanced High Cycle Fatigue (HCF) Life Assurance Methodologies", Report # AFRL-ML-WP-TR-2005-4102, Air Force Research Laboratory, Wright-Patterson AFB, OH, July 2004.
9. Birkbeck, J.C., "Effects of FOD on the Fatigue Crack Initiation of Ballistically Impacted Ti-6Al-4V Simulated Engine Blades", Ph.D. Thesis, School of Engineering, University of Dayton, Dayton, OH, August 2002.
10. Peters, J.O. and Ritchie, R.O., "Influence of Foreign-Object Damage on Crack Initiation and Early Crack Growth During High-Cycle Fatigue of Ti-6Al-4V", *Eng. Fract. Mech.*, **67A**, 2000, pp. 193–207.
11. Ruschau, J.J., Nicholas, T., and Thompson, S.R., "Influence of Foreign Object Damage (FOD) on Fatigue Life of Simulated Ti-6Al-4V Airfoils", *Int. Jour. Impact Engng*, **25**, 2001, pp. 233–250.
12. Ruschau, J.J., Thompson, S.R., and Nicholas, T., "High Cycle Fatigue Limit Stresses for Airfoils Subjected to Foreign Object Damage", *Int. J. Fatigue*, **25**, 2003, pp. 955–962.
13. Martinez, C.M., Birkbeck, J., Eylon, D., Nicholas, T., Thompson, S.R., Ruschau, J.J., and Porter, W.J., "Effects of Ballistic Impact Damage on Fatigue Crack Initiation in Ti-6Al-4V Simulated Engine Blades", *Mat. Sci. Eng*., **A325**, 2002, pp. 465–477.
14. Thompson, S.R., Ruschau, J.J., and Nicholas, T., "Influence of Residual Stresses on High Cycle Fatigue Strength of Ti-6Al-4V Leading Edges Subjected to Foreign Object Damage", *Int. J. Fatigue*, **23**, 2001, pp. S405–S412.
15. Peterson, R.E., "Stress Concentration Factors", John Wiley & Sons, Inc., New York, 1974, p. 22.
16. Peterson, R.E., "Notch-Sensitivity", *Metal Fatigue*, G. Sines, and J.L. Waisman, eds, McGraw-Hill, New York, 1959, pp. 293–306.
17. Lanning, D.B., Nicholas, T., and Haritos, G.K., "On the Use of Critical Distance Theories for the Prediction of the High Cycle Fatigue Limit in Notched Ti-6Al-4V", *Int. J. Fatigue*, **27**, 2005, pp. 45–57.
18. Nicholas, T., Thompson, S.R., Porter, W.J., and Buchanan, D.J., "Comparison of Fatigue Limit Strength of Ti-6Al-4V in Tension and Torsion after Real and Simulated Foreign Object Damage", *Int. J. Fatigue*, **27**(10–12) (Special Issue on Fatigue Damage of Structural Materials), 2005, pp. 1637–1643 presented at *International Conference on Fatigue Damage of Structural Materials V*, Hyannis, MA, 19–24 September 2004 (to be published in *Int. J. Fatigue*).
19. Nalla, R.K., Altenberger, I., Noster, U., Liu, G.Y., Scholtes, B., and Ritchie, R.O., "On the Influence of Mechanical Surface Treatments – Deep Rolling and Laser Shock Peening – on the Fatigue Behavior of Ti-6Al-4V at Ambient and Elevated Temperatures", *Mat. Sci. Eng.*, **A355**, 2003, pp. 216–230.

Part Three
Applications

In the previous chapters, some of the technical aspects of HCF have been addressed, many as a result of research efforts in the particular areas. Emphasis was placed mainly on the scientific basis and fundamental principles of observed phenomena related to HCF. In the following Chapter 8, an attempt is made to address some of the more practical aspects related to HCF design. Many of the issues are directly related to topics covered in the prior chapters, whereas some of the considerations are not previously addressed. Although the aspect of HCF design could be an entire book in itself, it is hoped that the following chapter provides guidance and stimulates consideration of the issues that a designer faces when dealing with HCF. Some research findings that are relevant to HCF design are discussed in detail here, particularly those dealing with fatigue-crack-growth-thresholds and some dealing with the beneficial effects of compressive residual stresses.

This page intentionally left blank

Chapter 8
HCF Design Considerations

8.1. FACTORS OF SAFETY

Factors of safety are applied in structural design to account for both variability and uncertainty. In HCF, the variability in the fatigue strength of a material is accounted for by considering the statistical variation and employing a -2σ or -3σ (for a normal distribution) or some other factor to account for the lowest value of a material variable within some statistical limits. These allowable values can then be plotted on a Haigh diagram or incorporated into some other design tool. The ignorance associated with not knowing the value of the applied load, such as from stresses due to some vibratory condition, can also be accounted for by further reducing the allowable stresses due to expected values of the applied loads. For example, if the vibratory stresses are not known very well and the maximum vibratory stress is projected to be up to 50% higher than the calculated design value, then the material capability can be taken to be 1/1.5 or 0.67 of the original design allowable. For vibratory loading, one must be careful to distinguish whether the reduction is taken on the maximum stress or only on the vibratory portion of the cycle. On a Haigh diagram, the vibratory portion is clearly distinguished since it is the vertical axis, the alternating stress. One of the main reasons why the Haigh diagram has become a design tool for vibrating components or structures, particularly rotating machinery, is because the mean stresses are normally reasonably well known or easily determined, while the vibratory stresses are much less known and subject to larger uncertainties. For the particular example of a 50% error in vibratory stress, a Haigh diagram based on the straight line-modified Goodman equation is shown in Figure 8.1 for a titanium alloy, Ti-6Al-4V. The straight line representing the allowable alternating stress goes from a value of 500 MPa at $R = -1$ (fully reversed loading, zero mean stress) to the ultimate strength of the material, 980 MPa. The line is drawn for positive mean stress only in this discussion. Behavior at negative mean stress values and the associated uncertainty was discussed earlier in Chapter 2. In addition to the alternating stress, the maximum allowable stress is also shown as a function of mean stress on this Haigh diagram. These two lines, shown thick, represent the material capability. While the values shown are nominal, not statistically minimum values, these will be considered material allowables for the sake of illustration here. Two cases can be considered in reducing the material allowables to account for uncertainties in the applied loads. First, the alternating and maximum stress values are reduced to account for an uncertainty of 50% only in the alternating stress. The curves in Figure 8.1 representing this case for alternating and maximum stress are designated as “FS on alt” denoting that the factor of

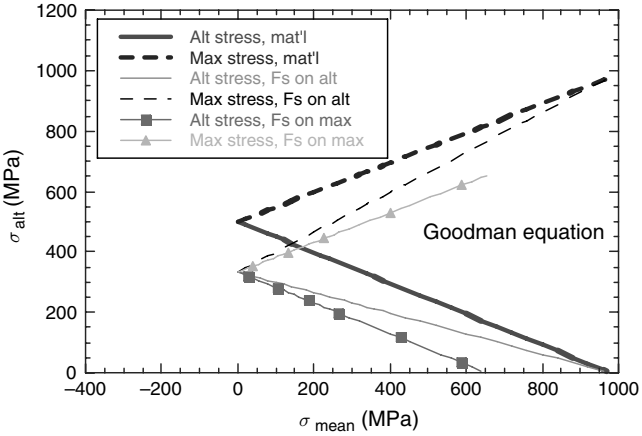


Figure 8.1. Haigh diagram showing factor of safety (FS) on alternating or maximum stress for Goodman equation.

safety (uncertainty) is applied only to the alternating stress. Second, similar reductions are shown to account for uncertainty in the maximum value of the loading and are denoted by "FS on max." In this case, the uncertainty is on both the mean stress and the alternating stress. From Figure 8.1 it is seen that the reduction due to uncertainty in alternating stress only results in a proportional reduction of the alternating stress capability that goes to zero at the maximum value of mean stress on the plot. At the same time, the reduction in maximum stress is numerically the same as for the alternating stress. For this case, the effects at high mean stress which also correspond to high values of R is less than at lower mean stresses or lower values of R. If, on the other hand, the total stress is reduced due to uncertainty, then the reduction of either the alternating stress or the maximum stress is a constant value at all values of the mean stress as shown on the plot. Note that a fixed value of R is represented by a radial line from the origin on a Haigh diagram. The reduction is a proportion of the total along a radial line, but shows as a constant value when plotted here against mean stress.

If something other than a straight line is used on a Haigh diagram, the results of reducing the material capability to account for uncertainty in the applied loading show up in a slightly different fashion. For illustrative purposes, the Haigh diagram described by the compression modified Jasper equation described in [1] (see Chapter 2) is used to represent the material capability including behavior under negative mean stress as shown in Figure 8.2. The heavy solid line is the conventional alternating stress while the heavy dashed line is the corresponding maximum stress. As in the previous case, material capability is decreased to account for uncertainty in either the alternating stress or the maximum stress. While the alternating stress reduction is a fraction of the material

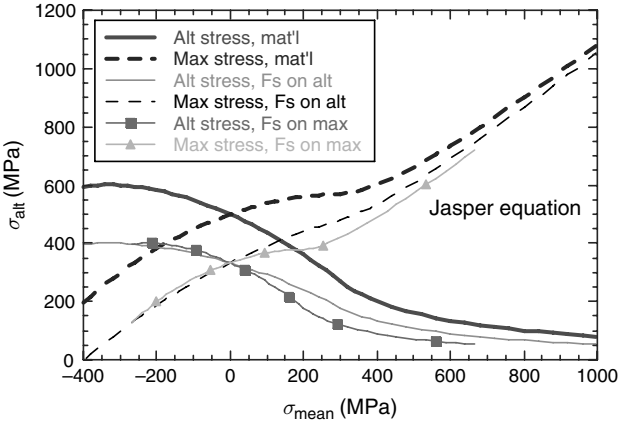


Figure 8.2. Haigh diagram showing factor of safety (FS) on alternating or maximum stress for Jasper equation.

capability at all values of mean stress due to uncertainty in the applied alternating stress ("Alt stress, FS on alt"), the reduction in alternating stress capability is not proportional to mean stress when the maximum stress capability is reduced due to uncertainty in loading ("Alt stress, FS on max"). The reason for this is the non-linear nature of the curve representing material capability on the Haigh diagram. Similarly, the maximum stress capability reduction reflects the non-linear nature of the material capability curve. It can also be seen in this Haigh diagram, as well as in Figure 8.1 above for the Goodman equation, that when the maximum stress is reduced due to uncertainty in applied loading, the corresponding reductions in material capability cover a new (reduced) range of mean stress on the plot.

8.1.1. Modeling errors

In establishing factors of safety, representing design allowables or just presenting data, the parameters used to represent the data can have an influence on the perceived error between experimental data and model representation. Most fatigue and FLS data are normally presented as stress. However, where other variables are involved, for example stress ratio, parameters are introduced which help to consolidate the data in terms of a single parameter such as effective stress, Smith–Watson–Topper (SWT) parameter, pseudostress, or some other quantity. In more complicated cases, such as for multiaxial loading or complicated stress states such as in the contact region for fretting fatigue (Chapter 6), the parameters used to represent data from a wide range of conditions can take on more complicated forms. Data obtained in terms of stress can then be converted into a parameter that does not necessarily have the units of stress. The units of the model parameter can then have an effect on the perceived or apparent error between the

experimental data and the model. This, in turn, can have an effect on the true factor of safety or allowable stress. As a simple example, consider an S–N curve of a material which covers a range in cycle count from 10^4 to 10^9. While real numbers are used here, they have no intended meaning other than for illustrative purposes. To represent the S–N curve, we use the following:

$$P = 3500\,N^{-0.5} + 37\,N^{0.0007} \tag{8.1}$$

where P represents a parameter such as stress. If stress is the actual parameter, then the S–N curve is as shown in Figure 8.3 by the solid line. The constants in the equation and the curve are taken to represent a material that has an endurance limit for a very large number of cycles as shown in the diagram. If it is assumed that experimental data are obtained that have values of stress that are 25% different than the average curve, then a number of points at different values of N can be computed and are plotted for values of N covering the range of the curve plotted in Figure 8.3. These points represent either $1.25\,P$ or $0.75\,P$ and show what a 25% spread in experimental data points would look like in a plot when the behavior is represented by Equation (8.1). If a reduction of 25% from the average were to be used as a design allowable, the lower set of points in Figure 8.3 would constitute the design allowable curve.

If we now assume that the model does not use a parameter in terms of stress, but depends instead on the square root of stress, then the exact same data plotted as square root of stress are those shown in Figure 8.4. A quick glance at this plot and comparison with Figure 8.3 seems to indicate that the parameter does a better job of representing or correlating the data than the linear representation using stress. In a similar fashion, if the allowable stress were taken as 0.75 of the average model behavior based on a parameter

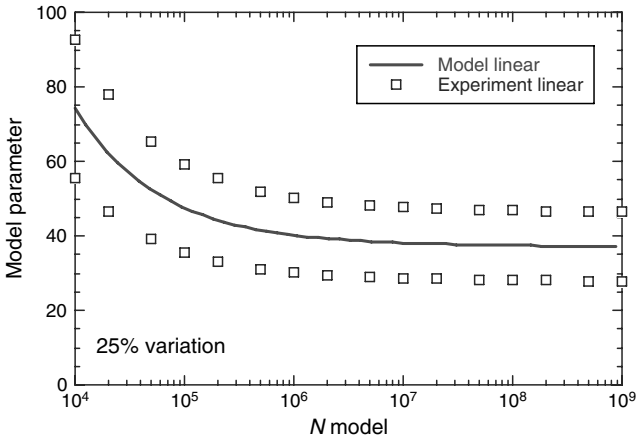


Figure 8.3. Representation of model using actual stress with 25% error.

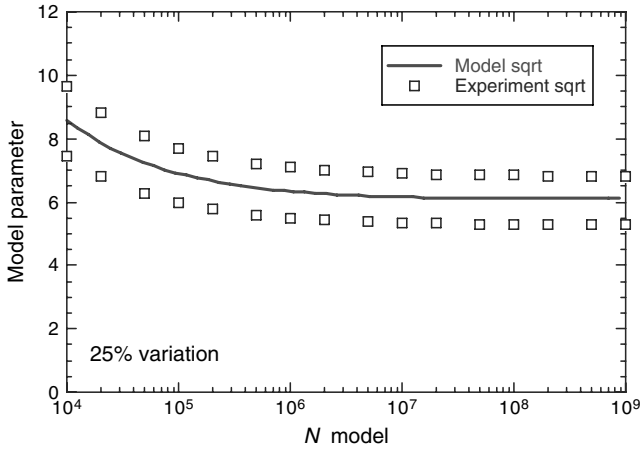


Figure 8.4. Representation of model using square root of stress with 25% error.

that uses square root of stress, the allowable curve (not shown) would be lower (on the basis of percentage of the parameter) in Figure 8.4 than the data representing 0.75 times the actual stress. Following this same logic, the use of a parameter that involves the square of the stress would appear to produce much larger scatter as shown in Figure 8.5. Here, a design curve for 0.75 of the model behavior would be higher than the data with a true error of 25% in stress. This example illustrates that care has to be taken when dealing

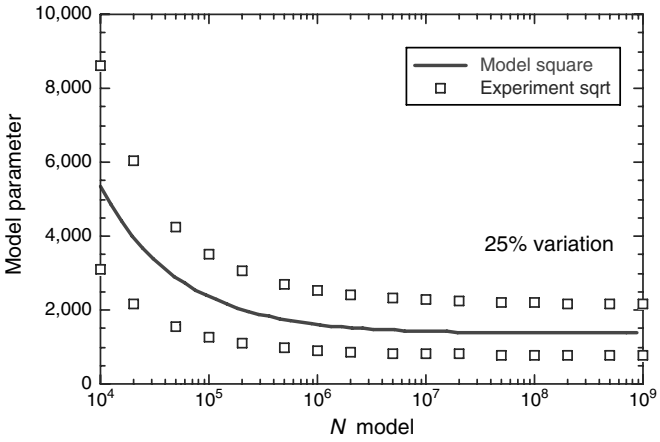


Figure 8.5. Representation of model using square of stress with 25% error.

with parameter representations of real data in determining allowable stresses when the parameter is not in the units of stress.*

If data are represented by a model that consolidates data from, for example, different values of R, then the scatter in the data and the fidelity of the model both have to be taken into account when establishing a design allowable. This subject is discussed later in Section 8.4.1 dealing with "Representing fatigue limit data."

8.1.2. Material variability

Another concern in using the Haigh (Goodman) diagram is the statistical variability of fatigue data, particularly in the long-life regime where S–N curves tend to be nearly horizontal. A Haigh diagram could represent average data or a statistical minimum such as a -2σ or -3σ confidence limit (for a normal distribution). For the latter cases, a large amount of data are required, along with some physical or statistical evidence that the scatter follows any assumed distribution trend. While most of the data in many cases, particularly for endurance limits, are obtained at $R = -1$, representing fully reversed loading with no mean stress, the application of the Haigh diagram to HCF often involves conditions at high values of R such as 0.7–0.9. These conditions represent high mean stresses with small, superimposed vibratory stresses. There are often very few data available in this region, and the extrapolation of data from low values of R and the assumption that statistical distributions of data are the same at high R as they are at low R are questionable.

It is not surprising, therefore, to note that (straight line plot) Modified Goodman Diagrams (MGD) were replaced in MIL-HDBK-5 with equivalent stress diagrams. MIL-HDBK-5 (a military design handbook) used the term "Modified Goodman Diagram" to be consistent with the older nomenclature that referred to any linear relation (on a Haigh diagram) as an MGD. The main reasons they were replaced were that the old diagrams showed no actual data, and were constructed from S–N curves that were extrapolated, often from limited data. Many times these original S–N curves covered only a small portion of the range of stress ratios and/or mean stresses represented on an MGD; thus extensive extrapolation was sometimes involved. Further, once the MGDs were constructed and placed in the Handbook it became impossible for anyone to assess the adequacy of the original data, the reasonableness of the extrapolated curve fits, or the extent of scatter/variability in the data. One classic case was Ti-6Al-4V mill annealed sheet, where it was found that the entire MGD was constructed based on 12 highly scattered data points, covering only a small range of maximum stresses and stress ratios.

* A similar situation arises in LCF where the number of cycles to failure is determined for a given applied stress. Use of a parameter based on the square root of stress, for example (Figure 8.4), makes the S–N curve flatter and hence, the uncertainty in life for a given stress, larger. On the other hand, the model gives the appearance of providing a better fit to actual data!

A statistically significant diagram would be expected to have a minimum of 4–5 points for each of approximately 10 stress ratios. The current equivalent stress fatigue data presentations have their limitations too, but at least these limitations are evident and can be evaluated by any concerned user of MIL-HDBK-5.

Material quality is another parameter that has to be considered when using the Haigh diagram in the design process. If the data are obtained in the laboratory on smooth specimens, then the heat treatment, processing, microstructure, surface finish, and specimen size must all be considered when applying the data to actual components. Perhaps the single most critical issue in the use of a Haigh diagram, however, is the degree of initial or service-induced damage which the material in a component may contain when such damage is not present in the material used for the database. If, for example, microcracks or other damage develops in service, then the Haigh diagram has no meaning for this material because it represents "good" or undamaged material. A design methodology which considers the development of damage from any source other than the constant amplitude HCF loading must be used to account for the different state of the material. For example, if cracks develop due to LCF, then the tolerance of the material might be evaluated using fracture mechanics and the concept of threshold stress intensity factor. The Haigh diagram, which does not represent fatigue life in the presence of other damage mechanisms, has no validity under this situation. The effects of damage on HCF strength were reviewed in Chapters 4–7 for several common types of damage.

One method for developing a Haigh diagram which represents material in a real component is to develop the data on actual hardware. In this case, a combination of LCF and HCF loading, or general spectrum loading, could be used to obtain a single point on the diagram. Extrapolating this point to any other region on a Haigh plot based on straight line or other assumptions has little or no physical basis and meaning, and most probably will be misleading. It is also important to note that plotting a mix of fatigue life data from combinations of LCF and HCF loading on a single diagram is dangerous because the physical processes are different and extrapolations and interpolations are difficult. LCF usually involves high amplitude, low frequency loading which leads to crack initiation early in life; a considerable fraction of life is spent under crack propagation. It is this aspect that has allowed for the successful application of damage tolerance using fracture mechanics in design. HCF, on the other hand, generally involves low amplitude, high frequency loading, with a considerable portion of life spent in crack initiation. Interaction of the two types of loading, therefore, can involve the processes of crack initiation and growth under LCF, and subsequent propagation under HCF. The Haigh diagram which represents total life, most of which constitutes initiation under HCF, represents material behavior in the absence of initial cracks and, therefore, has no meaning under combined LCF–HCF loading. While the subject of LCF–HCF interactions was discussed extensively in Chapter 4, the same concepts have to be applied for any other type of damage that may affect the HCF behavior such as creep or corrosion or other damage mode.

8.2. FRACTURE MECHANICS CONSIDERATIONS

The implications of the shape of the Haigh diagram, as described by the modified Jasper formulation, for example, can be examined in terms of the fracture mechanics parameter related to the threshold for crack growth, namely ΔK_{th}. The FLS, which can be defined as the maximum stress under which a crack will not initiate and grow, should be related to the threshold for crack propagation using the following logic. At a stress just above the fatigue limit, a crack will both initiate and grow to failure in a smooth bar. If it is assumed that crack initiation can be defined as initiation or nucleation to a defined size, then the driving force in terms of ΔK must be equal to or exceed ΔK_{th} in order for failure to occur. As an illustrative example, the locus of stresses in terms of the alternating and maximum stresses corresponding to the modified Jasper equation used to fit the data on Ti-6Al-4V plate material are plotted against mean stress in Figure 8.6. The fit to experimental data is extended into the negative mean stress region in this plot. A line corresponding to $R = 0$ is also shown for reference purposes in this Nicholas–Haigh diagram.* At values of the stress ratio above $R = 0$, all stresses are positive throughout the load cycle. One can consider two extreme cases for ΔK_{th} for a fixed crack size, independent of R, for crack initiation. First is the case where crack propagation, and hence the threshold for crack extension, is governed by the total stress range. In this case, ΔK_{th} is proportional to the alternating stress and would be represented by a horizontal line marked "ΔK_{th} = constant" in Figure 8.6. A second scenario, one commonly used in fatigue crack

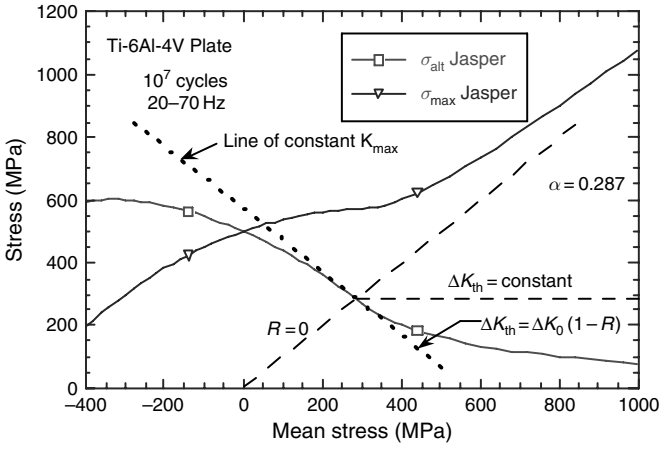


Figure 8.6. Locus of maximum and alternating stresses corresponding to modified Jasper equation fit to experimental data.

* The Nicholas–Haigh diagram that plots both alternating and maximum stress was discussed in Chapter 2.

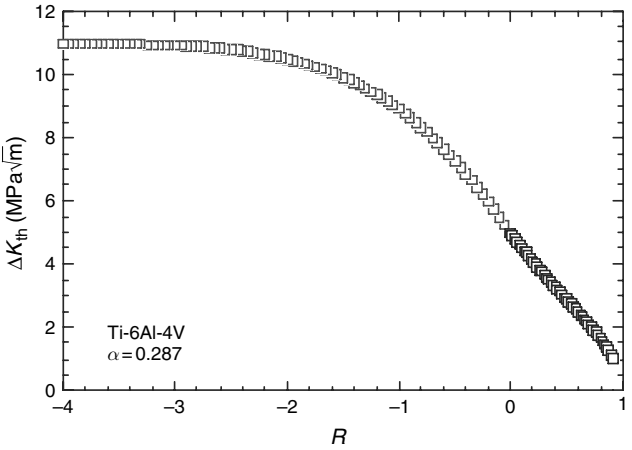


Figure 8.7. Computed ΔK_{th} corresponding to a fixed size to crack initiation and modified Jasper equation fit to experimental data. It is assumed that $\Delta K_{th} = 5\,\text{MPa}\sqrt{\text{m}}$ at $R = 0$.

growth modeling, is that only the positive stresses contribute to crack extension. Under this second hypothesis, the maximum stress is proportional to the threshold, ΔK_{th}, for a fixed crack length. For positive values of R, this is equivalent to a $K_{max} =$ constant criterion for threshold compared to a $\Delta K =$ constant criterion which is represented by the horizontal line in Figure 8.6. The dotted line, shown in Figure 8.6, is the line of constant K_{max} and is arbitrarily drawn through the same point at $R = 0$ as the line of constant ΔK_{th}. It can be seen that neither line corresponds to the lines representing the modified Jasper equation which is a best fit to the experimental data. These comparisons do not consider that ΔK_{th} may depend on crack length in the small crack regime (see [2], for example), or that ΔK_{th} is a function of stress ratio, R, as demonstrated in [2] and [3], for example. These considerations notwithstanding, the simplified analysis presented here indicates that crack initiation to a specific crack length requires either a different crack length for each mean stress, or that the value of ΔK_{th} is different for each value of mean stress. Pursuing the latter postulate, the value of ΔK_{th} can be calculated for each value of mean stress using the modified Jasper equation fit to the experimental data. Based on data for the test material that indicates the value of ΔK_{th} is approximately $5\,\text{MPa}\sqrt{\text{m}}$ at $R = 0$, the values of ΔK_{th} for other values of R are plotted in Figure 8.7. While the shape of the curve is similar to that seen often in the literature for positive values of R, it is of interest to note that the computed threshold is approximately constant as the values of R become more negative. For high values of R, however, there is no indication of the value of ΔK_{th} becoming constant above some critical value of R as observed experimentally in some titanium alloys [3]. Noteworthy, however, is the almost linear variation of ΔK_{th} with R for values of $R > -1$ which represents fully reversed loading. Note again that these numbers are based on a best fit to the experimental data on FLS using the modified

form of the Jasper equation which accounts for the lesser contribution of compressive stresses to the fatigue process near the endurance limit as explained in Chapter 2. For high R values, in this case, the data are extrapolated based on the Jasper equation fit which has very little physical meaning as R approaches unity.

The predicted values of threshold ΔK based on a constant crack length for initiation, and the value of fatigue limit strength, can be computed for other shapes of the Haigh diagram. While the previous calculations were conducted for the modified Jasper equation that fits some experimental data, we examine here Haigh diagrams represented by the more common forms of equations, namely the Goodman (straight line) and Gerber (parabola) formulas discussed in Chapter 2. These two equations, shown again here, are

$$\frac{\sigma_{\text{alt}}}{\sigma_{\text{y}}} = \frac{\sigma_0}{\sigma_{\text{y}}}\left(1 - \frac{\sigma_{\text{mean}}}{\sigma_{\text{y}}}\right) \tag{8.2}$$

$$\frac{\sigma_{\text{alt}}}{\sigma_{\text{y}}} = \frac{\sigma_0}{\sigma_{\text{y}}}\left[1 - \left(\frac{\sigma_{\text{mean}}}{\sigma_{\text{y}}}\right)^2\right] \tag{8.3}$$

where the mean stress axis is intercepted at the yield strength while the alternating stress axis takes on the value denoted here as σ_0. The value of σ_0 is normally taken from experimental data, so we can examine several cases where the values of σ_0 are taken as a fraction of the yield stress. In particular, we arbitrarily choose σ_0/σ_y to have values of either 0.33 or 0.5 for illustrative purposes. The curves that are represented by these values for both the Goodman and the Gerber equations are shown on a Haigh diagram in Figure 8.8. Using the same logic as before, namely that these (alternating) stress levels provide values of ΔK_{th} for a fixed crack length, the computed values of ΔK normalized to σ_{y} are plotted in Figures 8.9 and 8.10 for the Goodman and Gerber

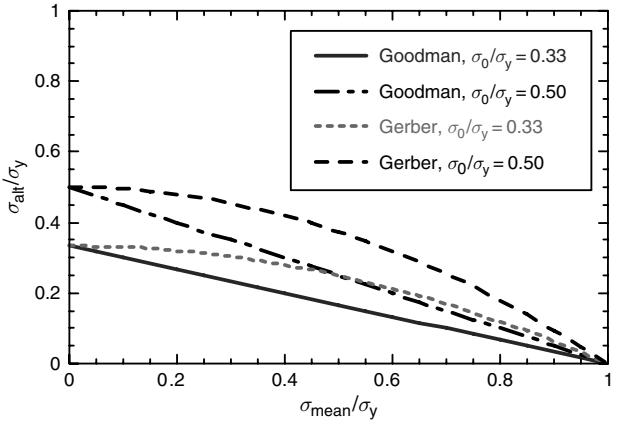


Figure 8.8. Haigh diagram for modified Goodman and Gerber equations

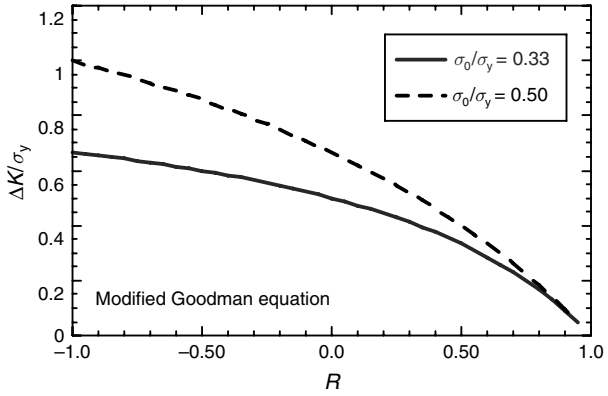


Figure 8.9. Threshold ΔK corresponding to modified Goodman equation.

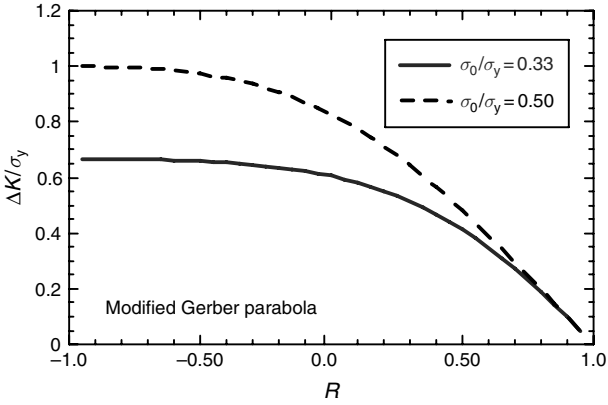


Figure 8.10. Threshold ΔK corresponding to modified Gerber equation.

equations, respectively. These plots only cover the range of R from -1 to $+1$ because the two equations are only valid for positive values of mean stress. Based on the shape of these curves, it is questionable whether either of these representations of data on a Haigh diagram predicts a ΔK_{th} curve that is more representative of actual data than the Jasper equation did (Figure 8.7), or whether the assumptions of a threshold corresponding to a fixed crack length and having a constant value are valid.

An alternate manner in which to compare the implications of the shape of the Haigh diagram on the relation between ΔK_{th} and R is to start with the $\Delta K_{th} - R$ relation and see what shape the corresponding Haigh diagram takes. To do this, the threshold is assumed to be linear in R, starting at $R = 0$ and decreases to a value at $R = 1$ that is greater than zero. The ratio of ΔK_{th} at $R = 0$ to ΔK_{th} at $R = 1$ is taken as a parameter α. For illustrative

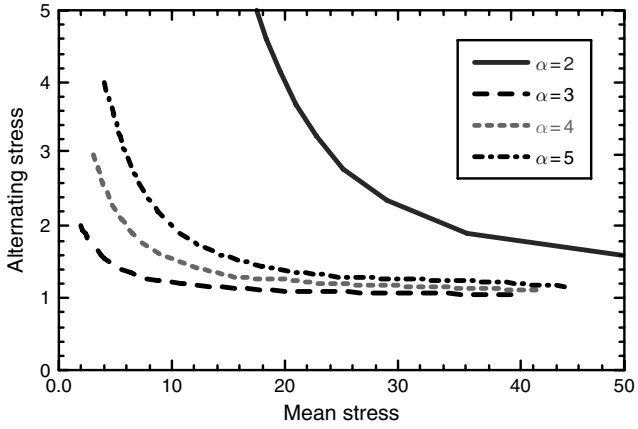


Figure 8.11. Haigh diagram for linear ΔK_{th} relation.

purposes, the quantity $\sqrt{(\pi a)}$ is taken $= 1$ and σ_{alt} is proportional to ΔK_{th} for a fixed value of the crack length, a. The results of this numerical exercise are shown in Figure 8.11 for several values of α but where the numerical values of the alternating and mean stresses have no meaning. Only the general shapes of the curves are of importance. It can be seen that all of the curves are concave upward over the range in stress ratio covered by the assumptions, namely $0 < R < 1$. Of interest is the comparison between these results and those of the previous section where a Gerber parabola in a Haigh diagram (Figure 8.10) produced a ΔK_{th} curve that was nearly linear with R for higher values of R. The Jasper equation formulation, however, produces more of a linear fit for ΔK as a function of R for a wider range of R. These numerical examples simply point out that the shapes of the curves in the Haigh diagram are quite sensitive to the shape of the ΔK_{th} vs R curve and vice versa.

8.2.1. Effects of defects

A number of years ago, concern was raised in the design community within the turbine engine manufacturing companies when fracture mechanics concepts were applied in order to assess the vulnerability of fan or turbine blades to FOD. As one designer related to me, if fracture mechanics worked for FOD, they would have experienced failures in almost every blade that was flying. Calculations such as the ones presented in the previous section showed that there was a major issue in trying to connect threshold fracture mechanics data with endurance limit data from a Haigh diagram. To try to shed light on this problem, a major contractual effort was conducted by Pratt and Whitney (P&W) for the Air Force Materials Laboratory [4]. While the focus of the work was on defects in the form of FOD, the findings are equally relevant to actual defects in materials.

When trying to connect threshold data with endurance limit data for different values of stress ratio, R, one of the findings widely reported is that the threshold ΔK depends, to some extent, on the test technique being used. Arguments persist as to what is a real material ΔK_{th} as well as how closure might be taken into account in evaluating the experimental data. Note that such concerns are not as prevalent when obtaining endurance limit data if the fatigue limit corresponding to a given number of cycles is arbitrarily defined as the endurance limit. This is little different than the definition used for ΔK_{th} that corresponds to a specific (slow) growth rate, 10^{-10} m/cycle for many cases. Thus, it is not surprising that P&W found that ΔK_{th} measurements varied with both test specimen and test procedure. The problem was somewhat circumvented by using closure corrections or using a technique that minimizes closure and load-history effects.

P&W generated data for a Haigh diagram by conducting smooth bar fatigue tests at constant stress levels to obtain lives up to nearly 10^7 cycles and then extrapolating the data to 10^7 cycles. These tests were conducted at stress ratios of $R = -1$, 0.1, 0.5, and 0.7 at both room temperature, 27 °C, and at an elevated temperature of 260 °C for titanium alloy Ti-8Al-1Mo-1V, hereafter referred to as Ti 8-1-1. A regression analysis to all of the data at different values of R was used to establish the behavior of the material as

$$N_f = A\left(\sigma_{mean} + \frac{\Delta\sigma}{2}\right)^B (\Delta\sigma)^D \tag{8.4}$$

where N_f is the number of cycles to failure and A, B, and D are empirical constants used to fit the data. This information, in turn, provided data for the mean and −97.5% data points which were plotted on a Haigh diagram at 27 °C and 260 °C as shown in Figure 8.12.

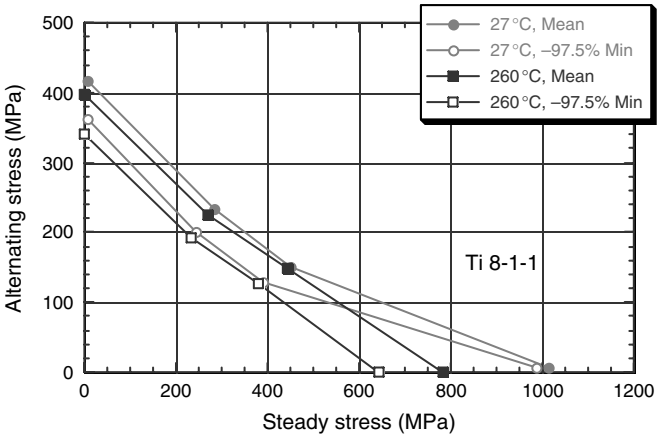


Figure 8.12. Haigh diagram for Ti 8-1-1 at 27 °C and 260 °C.

The minimum curves, representing the −97.5% lower bound from the statistical analysis of the data, are often used for HCF design [4]. The values of mean stress on the Haigh diagram at zero alternating stress were taken as the material's monotonic ultimate and yield strengths, for the mean and minimum curves, respectively (another version of the "modified Goodman diagram"). The data show that the fatigue strength at 260 °C is only slightly lower than that at 27 °C. The major difference is in the yield and ultimate strengths which are used as anchor points for the Haigh diagram and may not be related directly to fatigue strength at all.

To evaluate the use of fracture mechanics for construction of a Haigh diagram from threshold data, values of ΔK_{th} were obtained from three different methods as detailed in [5]. The methods involved both increasing and decreasing ΔK tests and a closure corrected version of the decreasing ΔK tests. These tests are designated as $\Delta K_{th,inc}$, $\Delta K_{th,dec}$, and $\Delta K_{th,eff}$ respectively. The threshold values at 260 °C at $R = 0.1$, 0.5, and 0.7 for the various methods are shown in Figure 8.13.

To construct a fracture mechanics-based Haigh diagram from threshold data, an initial or reference crack size has to be defined. In the study by Pratt and Whitney, the initial material quality (IMQ) defect distribution was used as the initial crack size. The IMQ, in turn, was determined using a probabilistic approach from measurements of the size of alpha particles from which fatigue failures were observed to originate. A lognormal distribution with measured sizes ranging from approximately 7 to 17 microns with a mean slightly above 10 microns was used to represent the initial defect size. The statistics of the smooth bar fatigue strength as well as the statistics of the initial flaw sizes were used to construct the Haigh diagrams of Figures 8.14 and 8.15 where the mean and

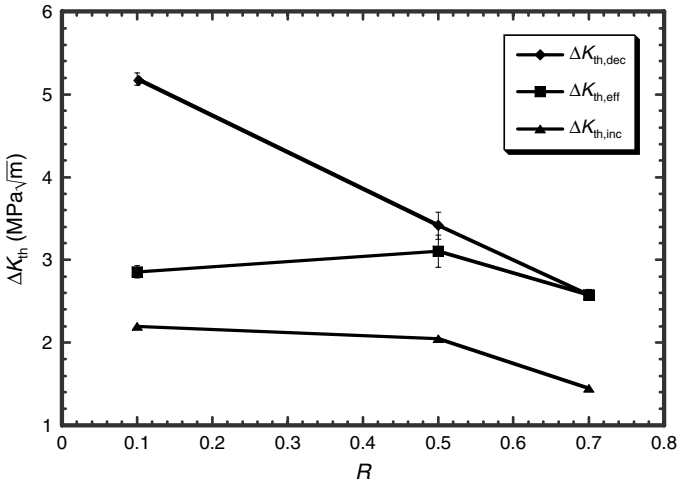


Figure 8.13. Threshold stress intensity as a function of stress ratio at 260 °C.

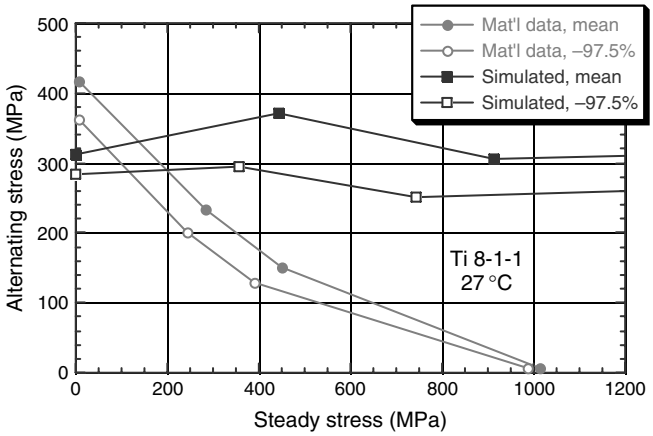


Figure 8.14. Haigh diagram for Ti 8-1-1 at 27 °C.

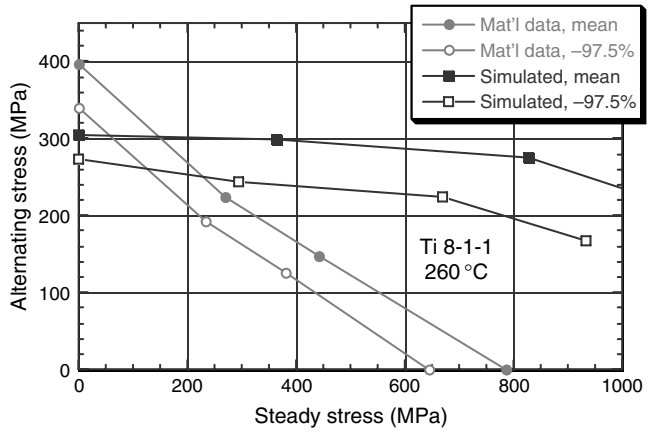


Figure 8.15. Haigh diagram for Ti 8-1-1 at 260 °C.

minimum (−97.5%) curves are labeled "predicted" to indicate the fracture-mechanics-based predictions using deterministic values of ΔK_{th} obtained from the increasing ΔK_{th} tests (see Figure 8.13). It is immediately apparent that the fracture mechanics approach to establishing a Haigh diagram does not work well because the values of ΔK_{th} obtained from the increasing ΔK_{th} tests are nearly independent of R. Further, the predicted results are conservative at zero mean stress but substantially anticonservative at higher mean stresses corresponding to higher values of R. Increasing the value of the initial crack size, with no physical basis for doing so, would lower the curve but not change its shape significantly. Although using the decreasing ΔK_{th} test data would provide a curve whose

shape would be closer to the smooth bar Haigh diagram, the stress levels would be much higher. At the same time, the validity of such ΔK_{th} data can be questioned because of the presence of significant amounts of closure in the tests at lower values of R and the inability to reproduce such data with other test techniques.

Since the primary purpose of the P&W program was to evaluate the use of fracture mechanics to determine the susceptibility of engine blades to service-induced damage in the form of FOD, the procedure described above was repeated for specimens with initial notches [4]. The effects of defects was only studied at 260 °C. Simulated FOD was put into specimens with notch depths of either 0.20 or 0.38 mm. These specimens were then fatigue tested to obtain data from which a Haigh diagram was constructed. For comparison, a fracture mechanics approach was used based on initial defects of the size of the notches, a distribution of fatigue strengths as characterized by Equation (8.4), and deterministic values of ΔK_{th} as obtained from the decreasing ΔK_{th} tests as shown in Figure 8.13. The choice of these threshold values apparently stems from the general shape of the curve which shows the threshold to decrease with increasing values of R since the Haigh diagrams show the same trend.

The distribution of initial flaw sizes was determined from a database of FOD sizes measured in the field. The data were separated into repairable FOD and non-repairable FOD. The 0.20 mm deep notch was considered representative of repairable FOD whereas the 0.38 mm deep notch was representative of non-repairable FOD. For each type of FOD, a distribution function of FOD depths was constructed from 162 measurements of repairable and 104 measurements of non-repairable damage. This resulted in a Weibull distribution as best representing the repairable FOD and a lognormal distribution representing the non-repairable FOD. The notch depths measured in the field covered a range from 0.075 to 0.40 mm (mean of 0.16 mm) for the repairable damage and from 0.075 to 2.5 mm (mean of 0.60) for the non-repairable damage. The notch depths chosen for testing, 0.20 and 0.38 mm, were somewhat representative of these two distributions. For the mathematical procedure to determine the allowable stresses in a Haigh diagram, the notch depths used in the testing were chosen as the mean values of the initial flaw size while the distribution function of initial sizes was taken from the FOD data. Following the statistical procedure outlined above, mean values of the stresses for the Haigh diagram were obtained. These results, as well as the baseline notch behavior, are plotted in Figure 8.16. It can be seen that for the FOD simulations with the accompanying assumptions, particularly the choice of threshold values, the fracture mechanics procedure appears to work fairly well for data obtained in the range from $R = 0.1$ to $R = 0.5$.

In a review article, Cowles [6] summarizes the findings of the P&W study by noting that the fracture mechanics approach to constructing a Haigh diagram for defect-free material does not work very well whereas the same approach, using a different set of ΔK_{th} values, seems to work much better for large initial defects from FOD. The challenge, he notes, is in the smaller size range for initial damage or defects where small crack behavior

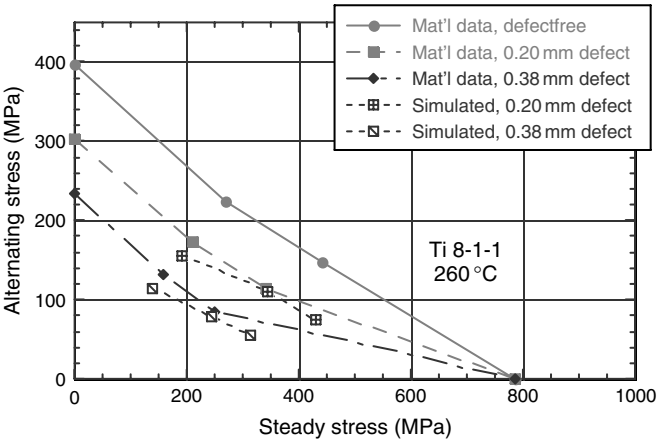


Figure 8.16. Haigh diagram for defect containing specimens at 260 °C.

and crack closure become important considerations. Further, he notes, the results are very sensitive to the threshold stress intensity factor and that crack initiation might also have to be considered.

Following this thought, Larsen et al. [5] also conducted a reassessment of the work performed by P&W. They performed fracture mechanics calculations based on the decreasing ΔK_{th} data of Figure 8.13. For the computations, they treated the notch not as an equivalent crack as had been done previously [4], but as a notch with an initial semi-circular surface flaw of depth a_i at the root of the notch. Further, they chose the value of a_i for the notch specimens, and the initial flaw size for the baseline smooth bars, to best match the experimental data as shown in Figure 8.17. For the notch data, this crack size was 13 microns which is close to the mean size of initial defects found from fractographic observations of failed specimens. However, for the smooth bar data, an initial crack size of 110 microns had to be assumed to match the experimental data. Use of 13 microns for the initial crack size would produce stresses far above those on the smooth-bar Haigh diagram. They also concluded that the anomalously high value of initial crack size of 110 microns could be associated with lack of consideration of the combination of initiation and propagation making up the total life in smooth bar tests as well as the possible fast growth of small cracks. For the notches that were produced by the shearing action from the impact of a sharp tool, the assumption that initiation life is small or negligible seems reasonable. The same, however, cannot be said about the smooth specimens. Even if calculations are performed for smooth bars with no initiation life, there does not seem to be a way of consolidating fracture mechanics-based FLS levels with those obtained for total life tests on smooth bars when the total life is in the endurance limit range of 10^7 or higher cycles.

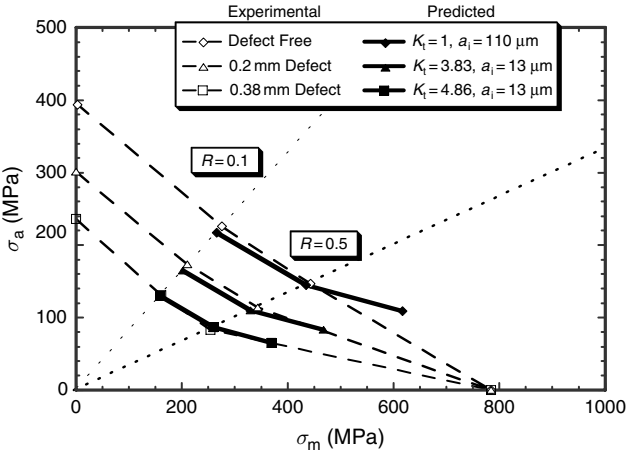


Figure 8.17. Haigh diagram for smooth and notched specimen data compared with fracture mechanics-based computations of allowable stresses based on initial flaw size a_i.

8.2.2. Application to LCF–HCF

Looking at the same general problem of relating a Haigh diagram to a threshold plot, Nicholas and Zuiker [7] evaluated behavior under combined LCF–HCF loading. Using another set of data and addressing the problem from yet another perspective, an analysis was conducted to create a Haigh diagram corresponding to an initial crack size based on actual threshold data. Details of the analysis for general LCF–HCF loading conditions are presented in Appendix I. The specific problem addressed the initiation of a crack from LCF loading and the propensity for that crack to grow when subjected to HCF loading. No load history or interaction effects were assumed in this study. The analysis considered the initiation phase using the threshold stress intensity, ΔK_{th} and was handled with a Haigh diagram that was treated as representing a damaged material having an equivalent crack depth of 0.05 mm. This crack depth was chosen to correspond to that used on experimental data in the literature where this depth was taken to be the definition of initiation [8]. The Haigh diagram for initiation to a crack of depth of 0.05 mm in Ti-6Al-4V, obtained from data of Guedou and Rongvaux [8] and others, was represented as a straight line that went from $\sigma_{alt} = 240\,\text{MPa}$ at $\sigma_{mean} = 0$ to $\sigma_{alt} = 0$ at $\sigma_{mean} = 1200\,\text{MPa}$, the ultimate strength of the material. For essentially the same alloy and heat treatment, threshold data were also taken from Hawkyard et al. [9] which show that ΔK_{th} decreases linearly from $5\,\text{MPa}\sqrt{\text{m}}$ at $R = 0$ to $2.25\,\text{MPa}\sqrt{\text{m}}$ at $R = 0.7$, and remains constant at that value for $R > 0.7$. As a second assumption, the straight-line decrease of ΔK_{th} was continued beyond $R = 0.7$ by Nicholas and Zuiker for comparison purposes.

To compare initiation criteria from a Haigh diagram to those based on threshold fracture mechanics for this material, the alternating stress was plotted against mean stress for the

two threshold stress intensity relations described above: one for ΔK_{th} constant for $R \geq 0.7$, and one for ΔK_{th} linearly decreasing for all R. The calculations were carried out for three initial crack lengths, 0.05, 0.1, and 0.15 mm using, for simplicity, the approximate relation for an edge crack, $\Delta K = \Delta\sigma\sqrt{\pi a}$, where $a = a_{initial}$ is the starting crack size. For each crack size, the threshold for crack propagation is plotted along with the Haigh diagram for initiation in Figures 8.18 and 8.19 for the two relations. Dashed lines in the figures represent constant values of R as indicated. The differences between the two sets of relationships for the threshold for crack propagation above $R = 0.7$ were found to be relatively minor for these conditions. It is observed that the value for ΔK_{th} for high R

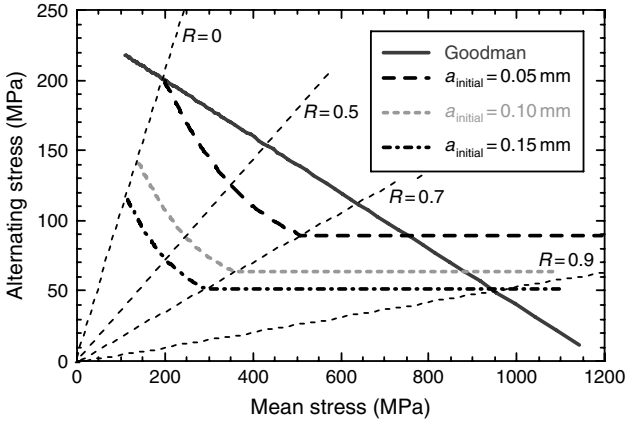


Figure 8.18. Damage tolerant Haigh diagram: ΔK_{th} constant for $R > 0.7$.

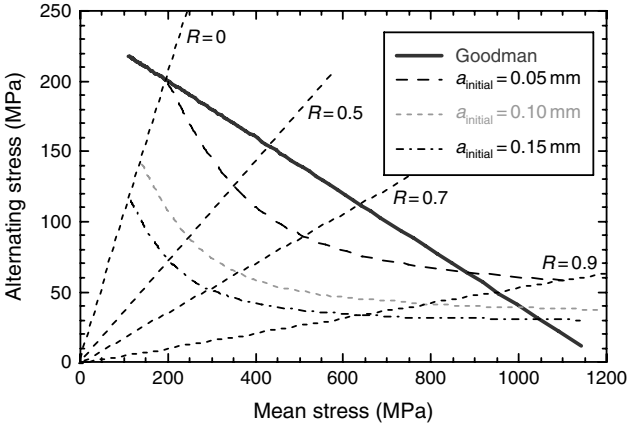


Figure 8.19. Damage tolerant Haigh diagram: ΔK_{th} linearly decreasing.

seems to have little effect on the damage tolerant Haigh diagram plot which shows the stress states at which an initial crack will start to propagate.

It is of interest to compare the shape of the modified Goodman line (linear) with that predicted based on the assumption of an initial crack using fracture mechanics as shown in Figure 8.18. Note that these curves are essentially the same as those shown in Figure 8.11, where the assumption of a linear representation of threshold data as a function of R was used. The damage tolerant curves are seen to have a much steeper slope at low mean stresses. Taking, for example, the curve for a 0.05 mm crack (which is equivalent to the initiation criterion used to determine the modified Goodman line [8]), it can be seen that the damage tolerant curve is below the Goodman line at intermediate mean stress levels ($0 < R < 0.75$). On the other hand, the curve is above the Goodman line at very high mean stresses and also at low mean stresses ($R < 0$) if the curve is extended. When the damage tolerant curve is below the Goodman line, this implies that if a crack were present in the material, it would grow at stresses that would otherwise not cause crack initiation in 10^7 cycles. On the other hand, when the damage tolerant curve is above the Goodman line, this indicates that a crack could initiate but would not propagate. These two separate regions constitute two types of material behavior: damage intolerant when the damage tolerant curve is below, and damage tolerant when the damage tolerant curve is above the Goodman initiation line. While these specific curves are based on a number of assumptions and limited experimental observations, there appear to be trends that indicate the Haigh diagram, as constructed from smooth bar fatigue limit data, does not accurately characterize the damage tolerance of a material as a function of mean stress.

8.3. DAMAGE TOLERANCE FOR HCF

The natural tendency in the implementation of a "damage tolerant" approach to fatigue would be to relate remaining life based on predictions of crack propagation rate to inspectable flaw size. In Chapter 1, the concepts involved in damage tolerance were discussed. As pointed out there, this has been shown to work well in LCF, and such an approach was adapted by the US Air Force in 1984 as part of the ENSIP Specification for critical engine structural components [10]. For HCF, direct application of such an approach cannot work for "pure" HCF because required inspection sizes are well below the state-of-the-art in non-destructive inspection (NDI) techniques and the number of cycles in HCF is extremely large because of the high frequencies involved. Thus, crack propagation times to failure could be extremely short, and the resultant inspection intervals would be too short to be practical.

The basic problem is illustrated schematically in Figure 8.20 which shows that LCF involves early crack initiation and a long propagation life as a fraction of total life as

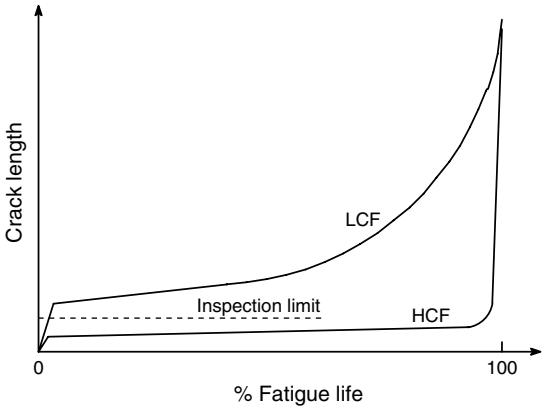


Figure 8.20. Schematic showing conceptual differences between HCF and LCF.

discussed in Chapter 1. There is no attempt in this schematic to represent the complex processes in the early stages of crack nucleation and initiation, nor to distinguish between fatigue of smooth bars versus notched samples. In general, LCF cracks are typically of an inspectable size early enough in total life so that there is a considerable fraction of life remaining during which an inspection can be made. HCF, on the other hand, requires a relatively large fraction of life for initiation to an inspectable size, or the creation of damage which can be detected, to occur. This results in a very small fraction of life remaining for propagation.

It is therefore impractical to apply the damage tolerant approach as used for LCF to pure HCF. While considerable research is being conducted at the present time to identify and detect HCF damage in the early stages of total fatigue life, conventional damage tolerance seems impractical at present for HCF. However, the problems that arise in the field are generally not related to material capability under pure HCF. Rather, the problems fall into two main categories. First, and foremost, is the existence of vibratory stresses from unexpected drivers and structural responses which exceed the material capability as determined from laboratory specimen and sub-component tests. Design allowables are normally obtained on material which is representative of that used in service including all aspects of processing and surface treatment and are often represented as points on a Haigh or "Modified Goodman diagram." (This point is qualified in the following paragraph.)

The second category involves the introduction of damage into the material during production or during service usage. The three most common forms of damage, either alone or in combination, are LCF cracking, FOD, and contact or fretting fatigue. These damage mechanisms and their effect on material HCF capability were discussed in Chapter 4. As pointed out there, methods appear to be available to quantify the fatigue limit of a material subjected to HCF, and to establish a threshold for a crack of an inspectable size.

However, the main issue in design for HCF is to quantify the severity of damage induced by LCF, FOD, or contact fatigue. This requires establishing what material allowables should be used to account for such damage. Other modes of service-induced damage, such as creep, thermo-mechanical fatigue, corrosion, erosion, and initial damage from manufacturing and machining, must also be taken into account in establishing material capability and inspection intervals.

To account for various forms of damage, or to design for pure HCF, the concept of a threshold below which HCF will not occur is necessary because of the potentially large number of HCF cycles which can occur over short service intervals. This is due to the high frequency of many vibrational modes, often extending into the kHz regime. In fact, current design for HCF through the use of a Haigh diagram seeks to identify maximum allowable vibratory stresses so that HCF will not occur in a component during its lifetime. The current ENSIP specification requires this HCF limit to correspond to 10^9 cycles in non-ferrous metals, a number which is hard to achieve in service and even harder to reproduce in a laboratory setting. Consider that a material subjected to a frequency of 1 kHz requires nearly 300 hours to accumulate 10^9 cycles. Superimposed on these considerations is the probability of the occurrence of high-amplitude vibratory stresses combined with the simultaneous probability of the material capability being at the design minimum or design allowable level.

8.3.1. Material allowables

The diagram most used for design purposes in HCF is a constant life diagram (see Chapter 2) as illustrated in Figure 8.21, where available data are plotted as alternating

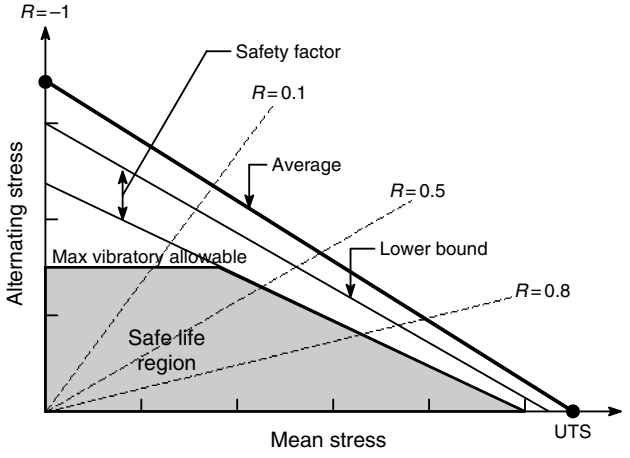


Figure 8.21. Constant life diagram.

stress as a function of mean stress for a constant design life, usually 10^7 or higher. As explained in Chapter 2, in the absence of data at a number of values of mean stress, it is often constructed by connecting a straight line from the data point corresponding to fully reversed loading, $R = -1$, with the ultimate tensile strength (UTS) or yield strength of the material. Data at $R = -1$ can be obtained readily from a number of techniques using shaker tables to vibrate specimens or components about a zero mean stress, while data at other values of mean stress are often more difficult to obtain, particularly at high frequencies. Alternatives to the straight line approximation in Figure 8.21 involve various curves through the yield stress or UTS point on the x-axis, or through actual data if available, to represent the average behavior. Scatter in the data can be handled by statistical analysis which establishes a lower bound for the data as discussed in Chapter 3. On top of this, a factor of safety for vibratory stress can be included to account for the somewhat indeterminate nature of vibration amplitudes, particularly those of a transient type. Finally, design practices or specifications may limit the allowable vibratory stress to be below some established maximum value, independent of the magnitude of the mean stress. The safe life region, considering all of these factors, is shown as the shaded area in Figure 8.21. What the shaded region provides, therefore, is an allowable threshold vibratory stress as a function of mean stress, the latter being fairly well defined because it is closely related to the rotational speed of the engine. If the vibratory stress is maintained within the allowable region on the Haigh diagram, there should be no failure due to HCF and, further, no periodic inspection required for HCF. Provided that the maximum number of vibratory cycles experienced in service does not exceed the number for which the Haigh diagram is established, 10^9 for example, then such a design procedure is one of "infinite" life requiring no periodic inspection. The implication of this procedure is that cycle counting is not necessary because it is inherently assumed that an unlimited number of cycles will not produce failure if stresses are maintained below the HCF design limit. Further, it is assumed that there is no damage accumulation due to HCF if this design or endurance limit is not exceeded.

As pointed out in Chapter 2, there are some pitfalls in the use of a Haigh diagram in design, particularly when basing it only on data at $R = -1$. For example, Figures 8.22 and 8.23 show such diagrams for the same material, Ti-6Al-4V, processed into two different product forms, hot rolled bar, and forged plate, respectively. In addition to the alternating stress, the peak or maximum stress is also shown. The data in Figure 8.23 are obtained from two independent sources (denoted as ML and ASE) on the same material, yet an unusual feature of the data is the relatively large amount of scatter which occurs under $R = -1$ (fully reversed, zero mean stress) loading. This phenomenon has been observed in several other alloys and is under further investigation. Note also that a straight line (see Figure 8.22) does not provide a good representation of the alternating stress data. Note, further, that for high values of mean stress, the maximum stress is quite high, approaching the static ultimate stress of 1030 and 980 MPa for the bar and plate material, respectively.

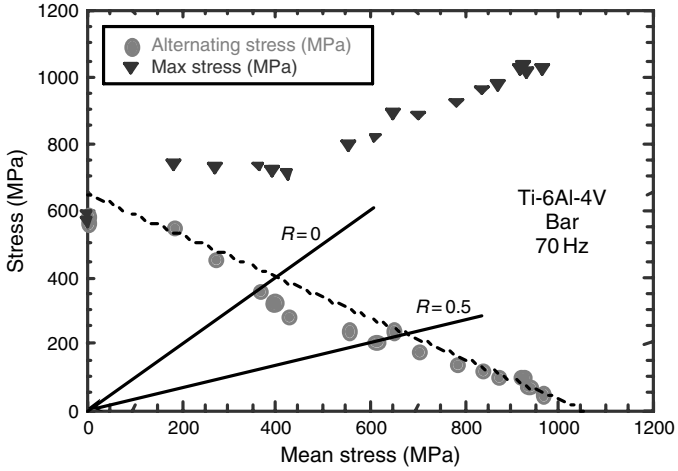


Figure 8.22. Haigh diagram for Ti-6Al-4V bar.

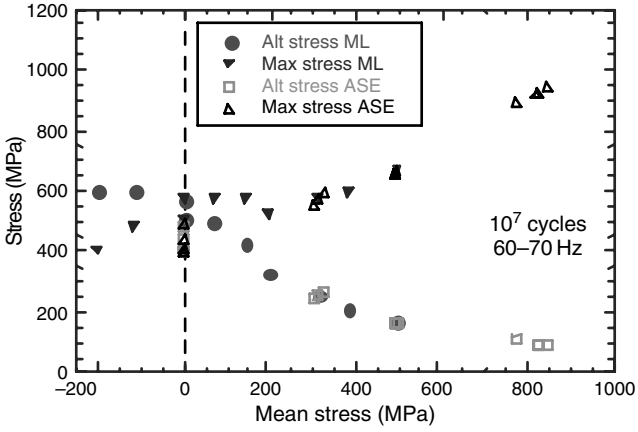


Figure 8.23. Haigh diagram for Ti-6Al-4V plate.

Research on fatigue life at high mean stresses in a titanium alloy [11] has shown that at high mean stress, the fracture mode changes from one of fatigue to one of creep. A plot of maximum and minimum stress, Figure 8.24, shows the range of vibratory stresses (min to max) at each mean stress tested. The stress above which creep occurs is shown along with the line denoted as "Cyclic creep limit" which delineates the region of fatigue, at low mean stresses, from the region of creep, at high mean stresses. Thus, in the creep regime, consideration has to be given to the amount of time during which such vibrations occur, not only to the number of cycles. Allowable vibratory stresses, while very low

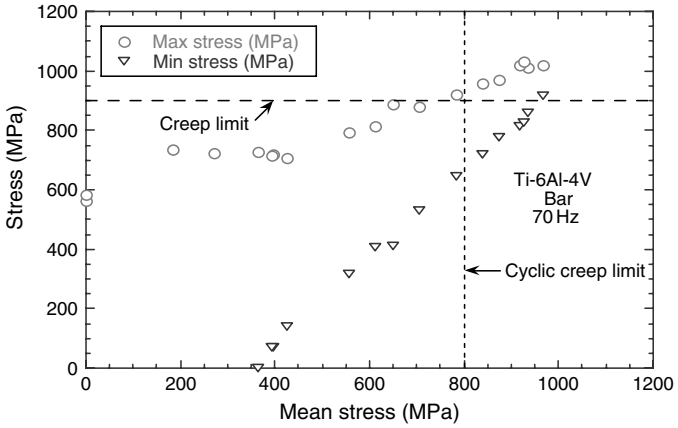


Figure 8.24. Haigh diagram showing region of transition in mechanism for high mean stress.

in this region, should also be supplemented with consideration of maximum stresses. It is for these reasons in some cases that designers shy away from the high mean stress regime, often for reasons that cannot be quantified.

8.4. THRESHOLD CONCEPT FOR HCF

As explained earlier, because of the large number of HCF cycles that may occur in service due to high frequency vibrations in a component, a threshold concept is necessary to insure structural integrity. Whether this threshold involves crack growth rates below some operational threshold, or the use of a fatigue limit corresponding to a large but fixed number of cycles, the concepts involve "infinite life," at least within the number of cycles that may be assumed to occur during the lifetime of a component. These could be either from steady-state vibrations or from transient phenomena and would correspond to a different number of total expected cycles in general. The engineering approximation to an "infinite life" concept is illustrated schematically in Figure 8.25 for crack growth and fatigue. In crack growth, a preexisting crack or one that develops during the service life of a component should not grow at a rate beyond some threshold rate so that crack extension can be neglected during the expected life of the material. Similarly, for a material without a crack, the stress level has to be maintained below a fatigue limit such that fatigue failure does not occur within an expected number of cycles. If the number of expected cycles can be established, and the crack growth rate and S–N curves can be estimated, then a threshold growth rate and a fatigue limit can be determined which are consistent with each other and account for "infinite" life for the expected number of

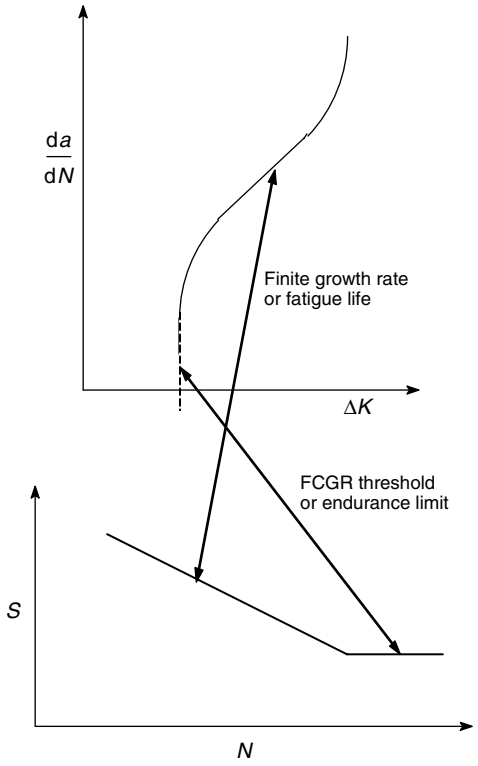


Figure 8.25. Schematic illustrating threshold concept in fatigue and crack growth.

cycles. In establishing such limits for fatigue, the shape of the *S–N* curve has to be taken into consideration. As an example, Figure 8.26 shows *S–N* data for Ti-6Al-4V at several values of stress ratio, *R*. It is to be noted that the slopes of the curves are different, and the transition point where the curves become nearly flat differs depending on the value of *R*. Therefore, stress ratio becomes an important parameter in establishing the fatigue limit, just as is shown in the Haigh diagram where mean stress is used as the variable to establish allowable alternating stress.

The concept of consolidating data from smooth bar fatigue limits and from threshold crack growth rates in cracked bodies was addressed in Section 4.1 through the use of a Kitagawa diagram. There it was pointed out that such a diagram is a valid method of representing data only for a specific value of *R* and only for one specimen geometry for a single plot. In this chapter we explore further the methods for obtaining data that can be used in a threshold design approach, particularly with respect to obtaining useful crack growth thresholds for use in engineering design.

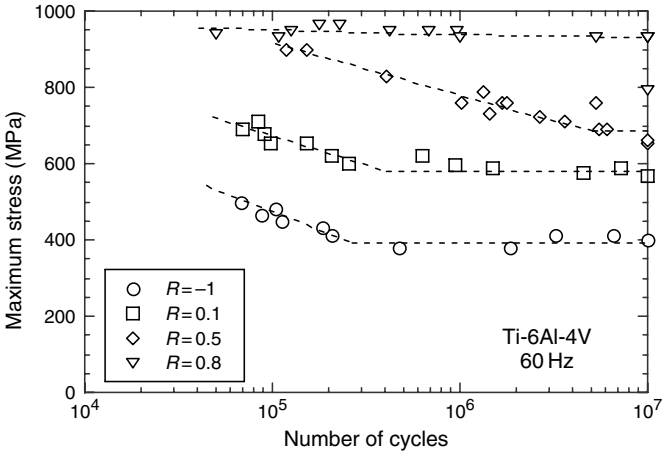


Figure 8.26. *S–N* data at different values of *R*.

8.4.1. Representing fatigue limit data

In determining a threshold for HCF for different values of R, parameters are often introduced which attempt to consolidate data obtained at different values of R at different numbers of cycles of fatigue life. Such an approach was discussed in Chapter 3 using the RFL model with an effective stress parameter. Parameters such as the SWT, Walker, or Jasper equation, discussed in Chapter 2, are commonly applied to data such as those presented in Figure 8.26. That figure shows, however, that any attempt to consolidate data with a single function of R, for all values of cyclic lives, will never be able to bring all of those data into a single curve because of the varying shape of each curve at a different value of R. Certainly, the data can be brought closer together, but never with a very good fit. In evaluating models for threshold stresses, using a function of stress to consolidate data from different values of R, the accuracy of the consolidating parameter as well as the ability of the model to represent the consolidated data both have to be taken into account. In many, perhaps most cases, the amount of data available is insufficient to be able to distinguish between capability to consolidate data with a single function and the ability of the model to represent the entire database including the endurance limit.

The concept of representing a body of data with a single function can be illustrated using the data of Figure 8.26. Assuming that the linear or bilinear fits to the individual data sets at different values of R represent a good approximation to the actual data, the fits can be consolidated using the SWT equation. The SWT model is a simplified version of the Walker equation, Equation (8.5), where $m = 0.5$. Applying this model to the straight lines in Figure 8.26 results in the plot of Figure 8.27. There it can be seen that the lines are consolidated into a single band with the exception of the line representing the data at $R = 0.8$. To better represent the data, the Walker model, Equation (8.5), was used

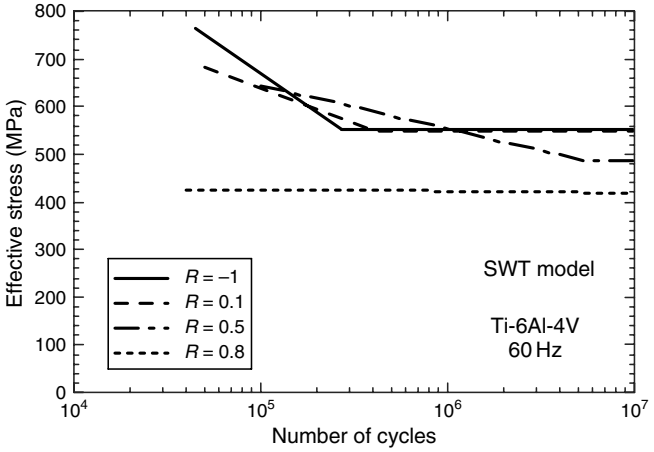


Figure 8.27. Representation of straight line fits using SWT parameter for various values of R.

by finding the best value of the exponent m using a least squares fit to a straight line representation of all of the lines in Figure 8.26. The resulting model has a value of $m = 0.34$ and is shown in Figure 8.28. Here, all of the lines are brought together in a single band, but the degree of scatter is somewhat large. To illustrate the scatter on the original data of Figure 8.26, Figure 8.29 is drawn along with the best fit straight line shown as a solid line in the figure. While the single straight line seems to represent all of the data reasonably well, the degree of scatter is quite broad. What these plots illustrate is that when data from different values of R are represented by a single function, the

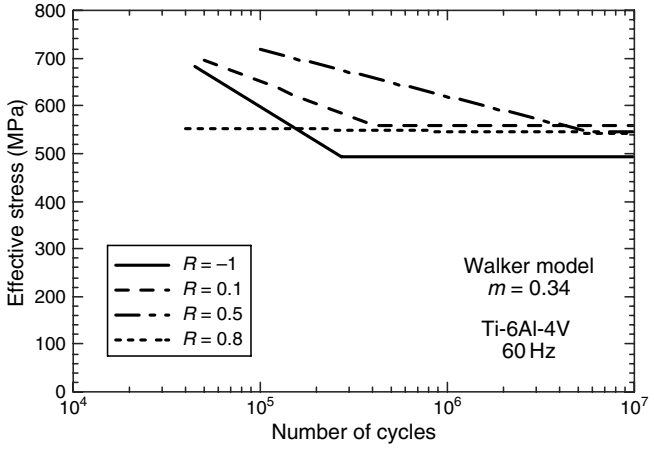


Figure 8.28. Consolidation of straight line fits to data using Walker model.

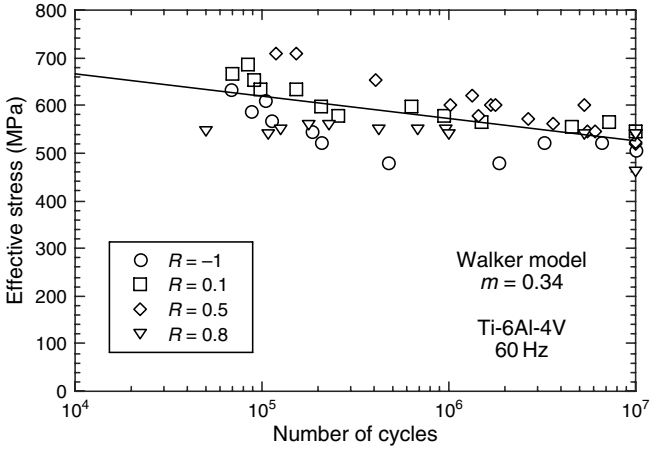


Figure 8.29. Consolidation of all data using Walker model.

resulting scatter is a combination of the true scatter as illustrated in Figure 8.26 as well as the inability of the function to consolidate results obtained at different values of R. For the particular data sets shown here, the data at $R = 0.8$ are considered to be different than the other data because at this high value of R, time-dependent behavior has been observed. The data at $R = -1$, on the other hand, may be represented by a different value of the exponent m in Equation (8.5) because it has been found that a different exponent can consolidate data at negative R better than the one used for positive R. In general, this provides another degree of flexibility in representing data at various values of R with a single function. This becomes an exercise in curve fitting that has little or no physical significance.

$$\sigma_{\text{eff}} = \sigma_{\max}(1 - R)^m \tag{8.5}$$

The example above illustrates the issue of distinguishing between true material scatter and the capability of a model to represent data obtained under a variety of conditions or in terms of various parameters. An extreme case of this dilemma is when fatigue data are obtained under multiaxial conditions at lives both at the endurance limit and lower. Even if load-history effects are ignored and are unimportant, the number of parameters used in testing can result in only a few tests under a single condition and a large body of data at different conditions. The evaluation of a model to fit such a data set requires the ability to distinguish between inherent material scatter and the capability of the model to represent the various conditions. As illustrated above, the scatter is due to a combination of both and it is often very difficult to distinguish between modeling capability and material scatter. While duplicate tests under a single condition are generally very useful to

evaluate material scatter, tests covering a wide variety of conditions do not always allow for sufficient replicate tests for practical reasons such as total test number limitations.

8.4.2. Threshold considerations

In dealing with a cracked component using fracture mechanics rather than a fatigue limit using stress, the concept of a threshold for crack growth has to deal with ever-decreasing growth rates and the possible existence of a true threshold. The concept of a crack growth threshold, ΔK_{th}, and its very existence, has been addressed in the literature for decades and will not be discussed in any detail in this book. For a brief review of the discovery of the threshold concept, see Paris and Tada [12]. There, they discuss the variables that affect the threshold at various values of mean stress or stress ratio. In much of the published literature, the variation in the threshold with different values of R is attributed to crack closure as well as small crack behavior. It is interesting to point out that in smooth bar fatigue, when establishing fatigue limits or endurance limits, closure has little or no meaning except in the crack growth region which is very small for long-life fatigue.

The subject of load-history and interaction effects in fatigue crack growth, with particular attention to threshold behavior and small crack effects, have been reviewed by Skorupa [13, 14]. In [13], many of the observed phenomena are reviewed, with the author noting that trends are not always consistent from one investigator to another and from one material to another. In [14], mechanistic arguments are used to explain what controls load-interaction effects and to explain the generally observed trends. Again, the author points out that there is no consistent explanation and understanding of many of the complex phenomena observed when non-constant fatigue cycling is applied to materials. At the end of his review article on the history of fatigue, Schütz [15] gives his outlook on remaining problems. He offers the opinion that prediction of fatigue life under variable amplitudes remains unsolved, as much as ever, "despite innumerable claims to the contrary in the literature." It can be stated here that this problem also remains largely unsolved when considering the FLS or endurance limit under variable amplitude loading.

The interaction of LCF and HCF in terms of the observable growth rates and the results of the interaction was discussed in Chapter 4. There, emphasis was placed on the "threshold" conditions above which infinite life can be expected, particularly in terms of applied stress. In the following section, we extend the discussion in terms of the interactions when trying to determine a fatigue crack growth threshold that can be used in the design process. In this case, we are dealing with damage that can be quantified in terms of a measurable crack size. Many of the features of LCF–HCF interactions discussed in Chapter 4 are relevant to this section. Conversely, many of the aspects of the interactions of LCF with HCF in determining a suitable threshold for design could easily have been put in Chapter 4. In this discussion, we deal primarily with the history effects in determining a threshold stress intensity that is applicable to the design process

for the determination of the condition that leads to the onset of crack propagation once a LCF crack has formed. The emphasis here is on the determination of the value of the threshold stress intensity. Concepts such as an inherent material threshold, a lower bound for such a threshold, the variability of such a threshold with conditions such as the value or history of stress ratio, R, and the existence of fundamental laws that govern such a threshold are discussed. Finally, the section concludes with an engineering definition of a threshold that can be used in the design process.

8.4.3. Experimental threshold measurements

Reliable knowledge of the load conditions corresponding to the onset of fatigue crack growth (FCG) becomes a critical issue as damage tolerance concepts are increasingly applied to a variety of engineering applications. Such knowledge can be obtained from failure analysis of real structures and/or from laboratory tests performed on samples of a material. The latter way is usually preferable since it is more economical and effective, which points out the importance of the role which experimental techniques play in FCG studies. Further efforts to improve the accuracy of design and life estimation technologies dependent upon FCG analysis must consider and minimize, whenever possible, any substantial differences between testing and real service conditions.

The existing procedure for FCG testing outlined in ASTM E 647-93a [16] provides for the special care which must be taken to approach threshold conditions in a continuous and gradual manner. As a result, the FCG threshold values are measured for the smallest cyclic plastic zone possible under respective loading parameters. In real components, especially those operating under high stress ratios, R, FCG usually commences in the presence of larger cyclic plastic zones created in the vicinity of preexisting crack-like defects by previous load excursions.

8.4.3.1. "Jump-in" method

To account for the possible influence of cyclic plastic zone size on the fatigue threshold at high R, other methods for defining a threshold that can be used in design have been proposed. Döker et al. [17], Castro et al. [18], Lenets and Nicholas [19], and subsequently Mall et al. [20] used a so-called "jump-in" or "step-down" threshold test method with an abrupt load change while keeping a constant value of R [17, 20] or K_{max} [18]. With this procedure (Figures 8.30 and 8.31), the fatigue crack is grown under certain load conditions ($K_{max\,0}, \Delta K_0$) long enough to develop corresponding monotonic and cyclic plastic zones. Subsequently, ΔK is instantaneously decreased to a value ΔK_1 (slightly above the expected threshold for FCG) and then held constant until clear evidence of crack propagation is obtained. The above load sequence is repeated with successively smaller ΔK values: $\Delta K_1 > \Delta K_2 > \Delta K_3$ until no crack growth can be detected after an abrupt load change within a specified number of cycles. The FCG threshold, ΔK_{th}, is

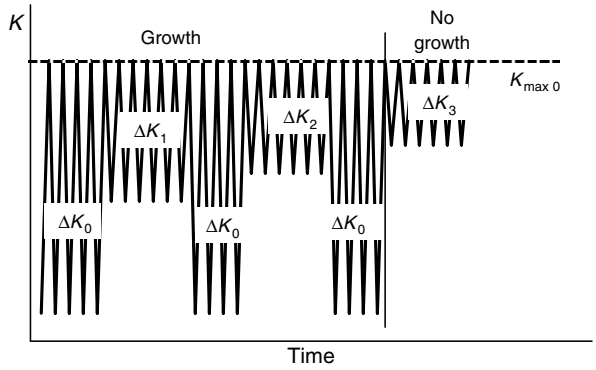


Figure 8.30. Load pattern for "jump-in" threshold method for constant K_{max}.

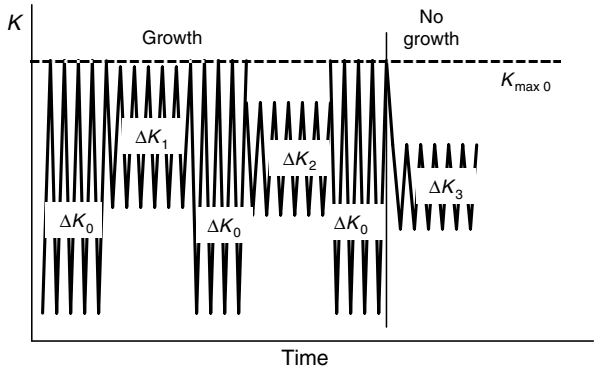


Figure 8.31. Load pattern for "jump-in" threshold method for constant R.

considered to be bracketed by the stress intensity range corresponding to the last loading block that produces crack propagation and that corresponding to the dormant crack (e.g. $\Delta K_2 > \Delta K_{th} \geq \Delta K_3$ in Figures 8.30 and 8.31). Note that the crack length at which FCG threshold conditions are approached depends on the threshold value and therefore cannot be specified prior to the test. For a nickel-based superalloy Inconel 617 and a titanium alloy Ti-6246, lower ΔK_{th} values have been obtained after the "jump-in" tests as compared to the gradual load shedding toward threshold conditions [18, 20]. Such findings indicate that a difference in the cyclic plastic zone size between a laboratory specimen subjected to FCG testing via existing procedures and a real component in service may result in non-conservative design solutions.

Lenets and Nicholas [19] used two methods, shown schematically in Figure 8.32, where thresholds were obtained from increasing and decreasing ΔK experiments after growing

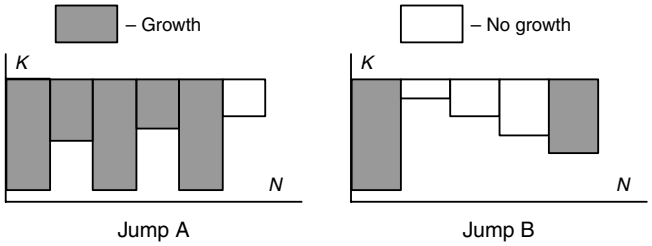


Figure 8.32. Schematic of jump loading history.

the crack under large amplitude loading. Figure 8.33 presents the results which show that the decreasing ΔK threshold (Jump A) is smaller than the increasing ΔK threshold (Jump B), although the authors feel that the lower threshold is not realistic because service conditions usually produce loadings below threshold until a severe event occurs in which HCF becomes critical, as in Jump B.

With both the "jump-in" [17, 18, 20] as well as the ASTM E647 load-shed [16] methods, the fatigue threshold value is obtained at the transition between the two conditions "growth – no growth." Figures 8.30 and 8.31 depict the load (stress intensity, K) pattern used for conducting such tests under constant K_{max} and constant R conditions, respectively. Engineering applications, however, are typically characterized by initially non-propagating (sometimes even non-existent) cracks. Therefore, fatigue threshold values obtained at the transition from no growth to growth seem to be of greater practical interest. Fortunately, it appears that the "jump-in" method can easily be modified so that it better represents service conditions in terms of non-propagation of the initial defects. To achieve this, a smaller ΔK value (insufficient for the FCG to occur after the instantaneous load change) should be applied first. For example, in Figures 8.30 and 8.31, ΔK_3 should be applied instead of ΔK_1. Then, provided that the crack does not grow, successively

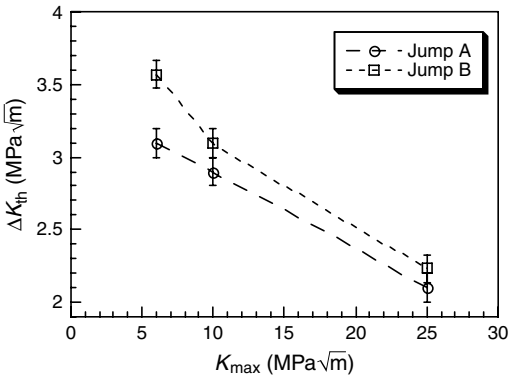


Figure 8.33. Threshold data for jump tests.

higher ΔK values should be applied until crack propagation begins. Note that such modification does not affect the main advantage of the method, that is the possibility to obtain FCG threshold values in the presence of cyclic plastic zones of any size. Further, unlike the approach discussed above, such a modified "jump-in" method is not limited to a threshold determination only. After the conditions for the onset of FCG are reached, the stress intensity or load can be kept constant to monitor subsequent (post-threshold) crack propagation behavior. Another advantage of this proposed technique is that, similar to real behavior in service, no crack growth occurs before threshold is reached. Thus, it should be possible to reproduce threshold conditions at certain pre-determined crack lengths. This becomes especially important when the influence of local microstructure or stress–strain state is to be taken into account (e.g. short crack, welding residual stress, or notch effect). It is obvious that with such a modified "jump-in" method, threshold conditions for FCG are preceded by rather extensive loading which produces ΔK values smaller than or equal to ΔK_{th} and during which the crack remains dormant. The opinion exists [21] that such cycling at small amplitude has no influence on the subsequent FCG behavior of metallic alloys as long as the boundaries for $K_{\text{max,th}}$ and $K_{\text{min,th}}$ are not surpassed and the crack does not grow. However, no attempt has been made so far to evaluate experimentally the load-history effects on the FCG threshold values furnished by the "jump-in" threshold test method.

For damage in the form of cracks from FOD, fretting or LCF, for example, the use of a fracture mechanics threshold to determine the allowable vibratory stress seems to be a promising approach for HCF, and follows the concept now being used successfully for LCF. Provided that an inspection can be made, and crack lengths measured, knowledge of the threshold for crack propagation can be used to assess the susceptibility of the material to HCF crack propagation from the damaged area. If the stresses are maintained below this limit, and the limit corresponds to a sufficiently low growth rate, perhaps 10^{-10} m/cycle or lower, then safe HCF life is assured. The potential growth of such cracks under LCF, and the time interval where such growth produces a crack where HCF might occur, must also be considered. This would establish the required inspection interval. One key issue in this proposed scenario is the determination of a suitable threshold for the types of cracks which may occur in service, some of which could be quite small. Various types of loading conditions can be used to determine a threshold, most of which are for long cracks. The effects of loading history on the threshold for HCF under spectrum type loading has already been discussed in Chapter 4. The determination of a threshold condition applicable to design is still a subject of some controversy.

8.4.4. Mechanisms in threshold testing

The study by Lenets and Nicholas [19] mentioned above, for example, revealed a consistent difference between the FCG thresholds obtained via two loading patterns, both

utilizing an abrupt change in the ΔK value at constant K_{max} (see Figure 8.32). Increasing ΔK applied to the initially dormant crack resulted in higher FCG thresholds as compared to the situation when gradually decreasing ΔK values were applied to the growing crack. The discrepancy was larger for lower K_{max} and much less significant at the highest value of K_{max}. It is important to understand the possible reasons for the observed differences in threshold due to different loading or testing histories. Since the loading pattern itself cannot change an intrinsic material's resistance against crack propagation, one should assume that the difference in the FCG threshold behavior revealed in that study originates from the loading history and was attributed by the authors to an extrinsic (crack tip shielding) mechanism.

A close similarity can be pointed out between threshold behavior in the referenced study by Lenets and Nicholas and observations from previous studies of the influence of fatigue underloads on FCG close to threshold in a pressure vessel steel [22]. In the latter case, an underload (i.e. cyclic loading at stress intensities below the fatigue threshold) was shown to retard subsequent crack propagation at $\Delta K > \Delta K_{th}$. A proposed mechanism for the influence of such subthreshold cycling was associated with a fatigue crack closure phenomenon arising from the crack flank fretting-oxidation. Thus, it can be argued that the initial loading block during the Jump B tests, while being insufficient to propagate the crack could, nonetheless, result in excessive fretting-corrosion deposits on the fracture surfaces. Such deposits would wedge the crack tip open, thereby decreasing the effective driving force for its propagation. As a result, the crack would not propagate even at the next load level, $\Delta K_i = 3.2\,\mathrm{MPa}\sqrt{\mathrm{m}}$, that was sufficient to maintain crack propagation during the Jump A test (see Figure 8.32) where conditions for extensive crack flank oxidation (i.e. subthreshold cycling) were absent. However, at least two reasons exist which do not allow one to accept the above explanation. First, unlike a low-alloyed pressure vessel steel used in [22], the Ti-alloy of the referenced study is not prone to fretting-oxidation. Second, the fracture surface contact behind the crack tip was observed in [22] for a low stress ratio $R = 0.05$ whereas in the referenced study, the values of R were much higher, varying from 0.4 (the lowest R at $K_{max} = 6\,\mathrm{MPa}\sqrt{\mathrm{m}}$) to 0.98 (the highest R at $K_{max} = 25\,\mathrm{MPa}\sqrt{\mathrm{m}}$). For this range of R values, the fracture surface contact as well as all related crack shielding processes, if any, should be less significant. Lenets and Nicholas concluded that the FCG threshold behavior that they observed can only be explained if some other crack tip shielding or load-history induced mechanisms, not associated with fracture surface contact, are involved.

An observation, somewhat helpful in this respect, was reported by Mall et al. [20] where crack-tip opening was recorded with extremely high accuracy using an interferometric displacement gage (IDG). During a varying ΔK test at $R = 0.5$ and $K_{max\,0} = 20\,\mathrm{MPa}\sqrt{\mathrm{m}}$, they observed a higher closure level than that obtained from either crack opening displacement (COD) or back face strain (BFS) methods. Further, immediately after a sudden load change, the IDG measurements indicated some crack tip shielding even though

conventional crack closure measurements via COD or BFS methods gave negative results. In another study, using a completely different indirect method for the crack opening load measurement, Döker and Bachmann [21] showed that a certain amount of crack tip shielding may exist even if the COD or BFS measurements give no indication of the fracture surface contact. They found that after a sudden load change, the crack driving force does not immediately follow an externally applied load, but retains, at least for a certain number of load cycles or certain crack length increment, a memory about the shielding level characteristic of the previous load regime. In other words, the FCG process depends on a load history even in the absence of the fracture surface contact. This line of reasoning brings one to the conclusion that, immediately after a load change, the Jump A test should provide a higher driving force for FCG than does the Jump B method, even under conditions where the same ΔK is applied in both cases.

A delayed transition in the crack tip shielding after a sudden load change (jump) can also explain an influence of the load history applied to an initially dormant crack (see Figure 8.32). In this case, under the Jump B test conditions, the driving force acting at the crack tip after a sudden load change increases toward its stable (nominal) value characteristic of the constant amplitude loading. Therefore, the onset of crack propagation at a certain ΔK value depends additionally on the number of previously applied cycles. For example, at $K_{max} = 6\,\text{MPa}\sqrt{\text{m}}$, no crack growth occurred at $\Delta K_i = 3.4\,\text{MPa}\sqrt{\text{m}}$ when this loading block was preceded by 8 million cycles. However, when applied after about 20 million cycles, the same $\Delta K_i = 3.4\,\text{MPa}\sqrt{\text{m}}$ immediately resulted in crack propagation.

8.4.5. Load-history effects

Other studies, too numerous to mention, have demonstrated the effect of loading history on the experimentally observed threshold, a number that is critical for design under combined LCF–HCF cycling. For example, Ritchie et al. [23] addressed the problem of determining the threshold for initially small cracks whose behavior has been shown to produce growth rates in excess of those observed for long cracks at the same values of ΔK and R. Further, they note that small cracks have been shown to have thresholds which are below the long crack threshold using LEFM analysis. Possible reasons for this anomalous behavior are discussed in [19], for example. To accomplish this, Ritchie et al. evaluated two procedures for obtaining a lower bound threshold by conducting tests where crack closure is absent, a condition believed to be present and responsible for the behavior in small cracks. The standard load-shedding procedure recommended by ASTM E-647 was applied to tests at various load ratios, R. The load shedding follows the sequence described by the following equation:

$$\Delta K = \Delta K_{\text{initial}} \exp[C(a - a_{\text{initial}})] \tag{8.6}$$

where subscript "initial" refers to the crack length and ΔK values after precracking where the load-shed sequence is started. The K-gradient, C, is recommended by ASTM E-647

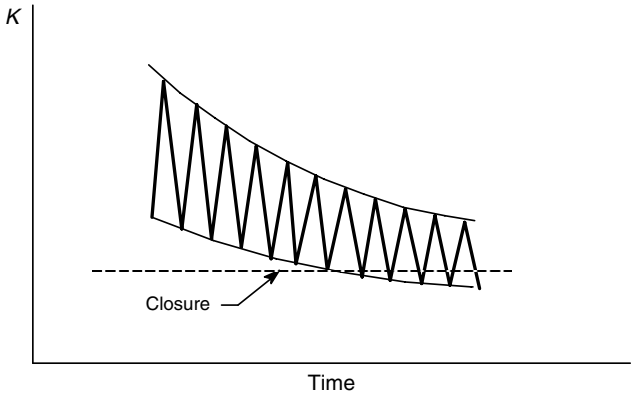


Figure 8.34. Schematic of conventional load-shedding history.

to be $-0.08\,\mathrm{mm}^{-1}$. As depicted in Figure 8.34, if tests are conducted at low values of R, crack closure may influence the behavior and, thus, the measured threshold. To avoid closure considerations, only data at high values of R are of interest.

The second procedure employed by Ritchie et al. consisted of testing under a constant value of $K_{\max}$, and increasing $K_{\min}$, until the crack is arrested. This test procedure, shown schematically in Figure 8.35, maintains conditions where the loading stays above any possible closure level if a high enough value of the starting (constant) $K_{\max}$ is chosen. The test is conducted under varying (increasing) R conditions, unlike the standard load-shed test, thereby making it hard to obtain the threshold at a specific targeted value of R.

From these two test sequences, both designed to obtain a threshold value in the absence of closure, results were obtained at 1 kHz frequency. Under standard, high R load shedding,

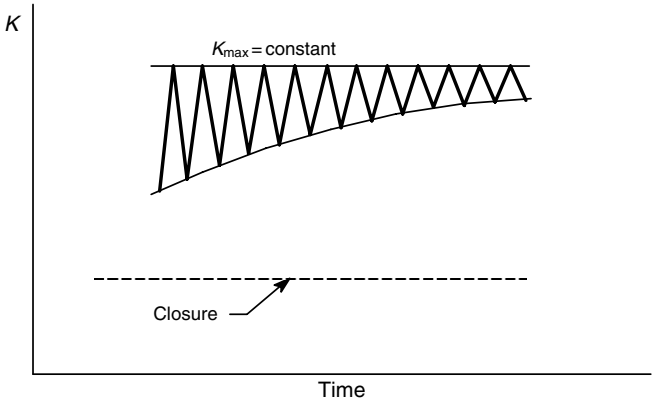


Figure 8.35. Schematic of constant $K_{\max}$, decreasing ΔK test history.

a value of $\Delta K_{th} = 2.4\,\mathrm{MPa}\sqrt{\mathrm{m}}$ at $R = 0.8$ was found. For the constant K_{max}, increasing K_{min} test, a value of $\Delta K_{th} = 2.2\,\mathrm{MPa}\sqrt{\mathrm{m}}$ at a final load ratio of 0.92 was obtained. They conclude that this latter value corresponds to a lower bound threshold for small crack propagation, even though the test is conducted on a long crack specimen. By comparison, for the identical material, Ti-6Al-4V, small crack growth behavior from naturally initiated and FOD-induced small cracks was not observed below a ΔK of $2.9\,\mathrm{MPa}\sqrt{\mathrm{m}}$.

8.4.5.1. Compression precracking

The concern for history effects in determining a threshold that can be used for engineering purposes in design has led to considerations of alternate techniques. Forth et al. [24] present data using the conventional load-shedding technique recommended by ASTM at constant R and constant K_{max} on 7075-T7351 aluminum. In addition, they tested using a compression precracking scheme to avoid development of plasticity-induced closure during the precracking. From the results for this particular material, and from other reported observations, they conclude that the threshold and near threshold growth rates obtained during the K-shedding portion of a test are not necessarily the same as those obtained under constant load, increasing K tests. In their work, constant load levels were maintained after reaching threshold. Although these tests are generally conducted at the load level (and K level) where the decreasing K tests were terminated at the defined threshold of 10^{-10} m/cycle, there are many cases where the load has to be increased in order to start the crack growing again. In the work of Forth et al. [24], however, the crack grew immediately. In their case, they conclude that remote crack closure may still be present in decreasing K tests dependent on the load history, thus producing an artificially high threshold. Further, oxide buildup is also observed when plane stress conditions occur at the specimen surface. By comparison, the authors introduced a compression–compression precracking scheme and a K-increasing test procedure at constant R to determine a threshold that they consider to be independent of load history. In the case of the aluminum alloy that they tested using middle through-crack M(T), specimens, they observed that the crack growth curve generated using the constant R load-reduction method can be non-conservative by more than an order of magnitude in growth rates near threshold. In summarizing this work [25], the authors conclude that tests with history effects do not accurately describe the material threshold. They observed the constant R load-reduction test generated artificially high threshold values when compared to steady-state data.

8.4.5.2. Load-shed rates

The ASTM standard for threshold testing defines the threshold as the asymptotic value of ΔK at which $\mathrm{d}a/\mathrm{d}N$ approaches zero. The operational definition recommends that the growth rate be 10^{-10} m/cycle and that the rate of decrease of K be limited. To

explore the possibility of obtaining a realistic threshold for design, Bain and Miller [26] used a surface flaw specimen (Kb bar). This specimen geometry represents the (high) stress levels as well as the surface flaw geometry constraint expected in many highly stressed turbine engine components. This work was a continuation of earlier work by Sheldon et al. [27] where the effects of high load shed rates were explored. The very gradual shed rate recommended by ASTM, $C = -0.08\,\mathrm{mm}^{-1}$ [see Equation (8.6)], cannot be used with the surface flaw geometry in the Kb bar because the specimens are not physically large enough to allow the stress intensity factor to be shed at this rate before the crack would break through the specimen at the back face. Larger specimen sizes would require extremely high loads to achieve the required K levels. With these constraints on specimens and testing, much higher shed rates than those recommended by ASTM were explored. Experiments were conducted using shed rates from $C = -0.295\,\mathrm{mm}^{-1}$ to $C = -1.181\,\mathrm{mm}^{-1}$ on Ti-6Al-4V titanium alloy. The threshold measured from these tests was similar to that obtained using a compact tension specimen with a conventional shed rate of $C = -0.08\,\mathrm{mm}^{-1}$ [27]. Statistical analysis of the data showed that the results using high shed rates had similar scatter and threshold values as compared to those obtained using either compact tension or single-edge-notched specimens and, most significant, resulted in a much faster determination of threshold. The results for the value of threshold from this study are summarized in Table 8.1.

Threshold data such as the type described above can be used in design for both the threshold conditions when a crack exists or to compute the crack growth rate in the near threshold regime. To do this, a crack growth model that relates $\mathrm{d}a/\mathrm{d}N$ to ΔK is needed. Since data on threshold and low growth rates normally exist for different values of R, and design conditions also exist at various values of R, a method of consolidating data at various values of R is also required. The threshold data discussed above, which were obtained at values of R from -1.0 to 0.8 [28], were incorporated into a sigmoidal crack growth model using an effective K defined using a dual Walker exponent relation [29]:

$$K_{\mathrm{eff}} = \Delta K\ (1 - \mathrm{R})^{\mathrm{m}-1}$$

$$m = m^{+} \text{ for positive values of } R$$

$$m = m^{-} \text{ for negative values of } R$$

Table 8.1. Summary of threshold values on Ti-6Al-4V at room temperature, $R = 0.1$, from study by Bain and Miller [26]. (K in MPa$\sqrt{m}$)

Specimen type	*Shed rate, C* (mm^{-1})	*Number of tests*	*Low value*	*High value*	*Average value*	-3σ *minimum*
SEN	-1.181	13	3.83	5.98	4.58	3.18
C(T)	-0.236 to -1.181	11	4.14	5.34	4.70	3.67
Kb-bar	-0.295 to -1.181	5	3.87	4.60	4.23	3.46

For the Ti-6Al-4V titanium alloy, a values of K_{eff} at threshold of 3.829 ksi $\sqrt{\text{in.}}$ was used with values of $m^+ = 0.72$ and $m^- = 0.275$. This approach seems to provide an engineering method for representing threshold data over a wide range of values for R. The curve representing this dual Walker model, shown in Figure 8.36 (without data), was found to represent data on the same material from a variety of sources using several different specimen geometries. The shape of this curve is discussed later.

An extensive review of fatigue thresholds as well as their relationship to fatigue limits, including an extensive bibliography, can be found in the paper by Lawson et al. [30].

8.4.6. Crack closure

Crack closure is mentioned often in the discussion of crack growth at rates anywhere from threshold and near threshold to rapid propagation. The concept of crack closure is attributed to Elber [31, 32] and relates to the phenomenon of a crack closing above the minimum cyclic applied load due to some obstacle in the crack wake. Closure in the early days of the concept was attributed mainly to plastic deformation at the crack tip leaving a wake of deformed material behind as the crack advances. This is one reason why small cracks are commonly assumed to be open since they have not propagated a sufficient distance for closure to develop in the wake of the crack. In subsequent years, closure has been observed and attributed to many different phenomena including debris such as oxides forming behind the crack tip [33], roughness from the irregular deformation and fracture patterns (crack tortuosity) forming on the mating surfaces [34], and a number of other phenomena [35, 36]. If closure is present, the effective crack driving force is considered to be ΔK_{eff} as shown schematically in Figure 8.37 rather than the total applied

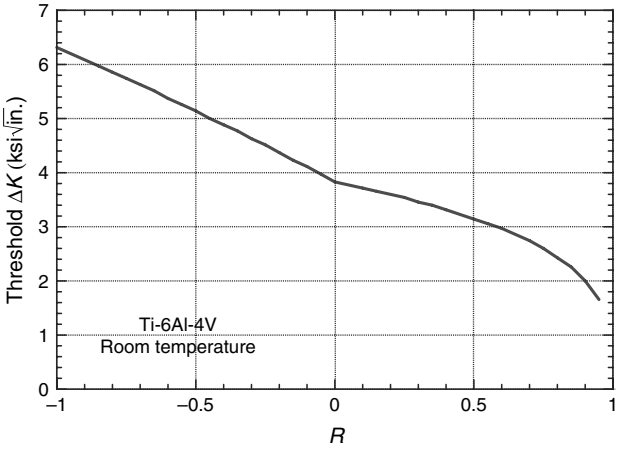


Figure 8.36. Representation of crack growth threshold with Dual Walker model.

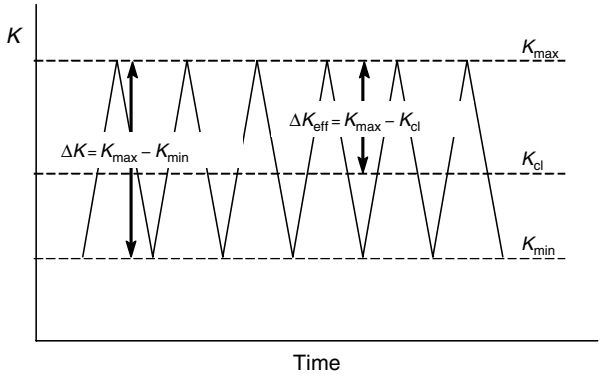


Figure 8.37. Schematic showing definitions of ΔK and ΔK_{eff}.

driving force, ΔK, obtained from LEFM. The rationale behind this formulation is that the crack tip sees no driving force when it is closed.

8.4.6.1. K_{max}–ΔK concept

Crack-growth-threshold data reported earlier in this chapter and many other sets of data reported elsewhere (see [37, 38], for example) follow a trend described and modeled by Schmidt and Paris [39] which is shown schematically in Figure 8.38. The model is based, in part, on the crack closure concept using the notion that two threshold quantities, $K^*_{max,th}$ and ΔK^*_{th}, both defined in the figure, are constant and independent of R. Threshold conditions for various values of R are illustrated schematically in Figure 8.39. If the concept of crack closure is introduced, a constant value of K_{cl} can be assumed (as shown) in order to produce a condition where $\Delta K_{eff} = \text{constant}$ (see Figure 8.37) is

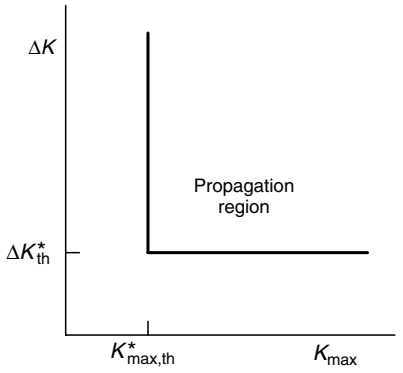


Figure 8.38. Schematic of threshold boundary of Schmidt and Paris [39].

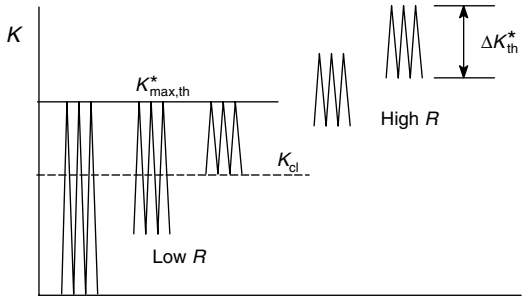


Figure 8.39. Schematic of threshold conditions at various values of R for K_{max}–ΔK threshold concept.

the threshold condition. It is significant to point out that closure does not have to be introduced, measured, or assumed when applying the K_{max}–ΔK threshold concept. As seen in Figure 8.38, it predicts that the measured values of thresholds, ΔK_{th} and $K_{max,th}$, will be load-ratio independent, respectively, above and below a transition R. In the work of Ritchie [36], this value was estimated to be approximately $R = 0.5$.

Thus, while the arguments explaining the observed behavior of the values of threshold (and near-threshold growth rate behavior) have commonly been linked to the concept of crack closure, the data can also be interpreted in terms of intrinsic behavior governed by two distinct parameters, a threshold for the range of stress intensity, ΔK^*_{th}, and a threshold for the maximum stress intensity, $K^*_{max,th}$, both shown in Figure 8.38 [40]. The K_{max}–ΔK threshold concept simply requires that two thresholds have to be exceeded before crack growth can occur.

Instead of the "ideal" or simple behavior of the threshold stress intensity depicted by the right angle in the K_{max}–ΔK plot of Figure 8.38, the behavior in some cases cannot be described by a constant value of ΔK above some critical value of R. Rather, the threshold is found to decrease in many cases with increasing R [41] as depicted by curve B in Figure 8.40(a) rather than being constant as depicted by the curve A in the same figure. The threshold data of [41], as well as those from other sources [28] were well represented by the dual Walker curve shown above in Figure 8.36. Note that the data include values obtained at negative R. Noting the simple relations among K_{max}, K_{min}, ΔK, and R,

$$\Delta K = K_{max} - K_{min} = K_{max}(1 - R), \quad R = \frac{K_{min}}{K_{max}} \tag{8.7}$$

and noting that the loading condition can be completely described by two independent quantities, we find that an alternate manner of representing threshold data is the often-used plot of the threshold stress intensity as a function of R as in Figure 8.40(b) for the two cases of the data representation shown in Figure 8.40(a). Note that the linear plot for case B in Figure 8.40(a) using K_{max} as the x-axis is nonlinear in the plot against R in Figure 8.40(b). To further add confusion to the representation of threshold data, often

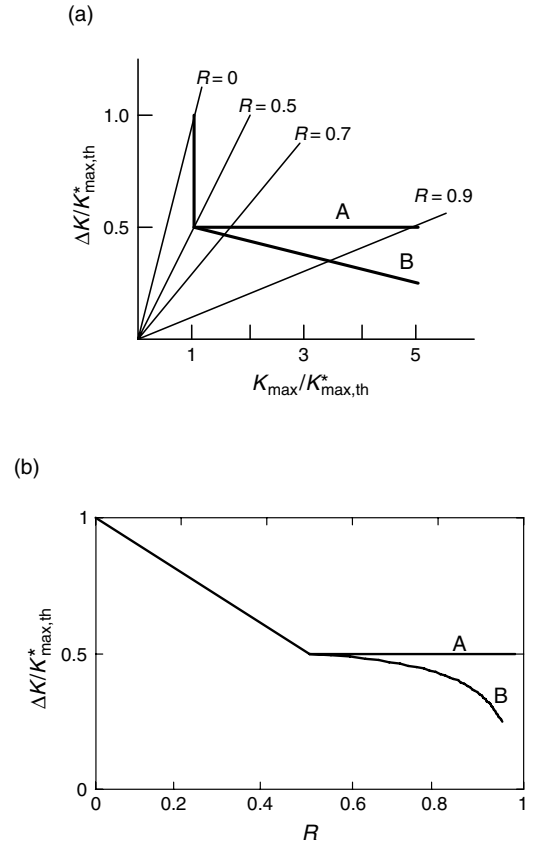


Figure 8.40. Schematic of two-parameter threshold in plots of (a) ΔK versus K_{max} and (b) ΔK versus R.

in an attempt to explain governing mechanisms, the threshold can be represented as a plot of K_{max} as a function of R as shown in Figure 8.41 for the same cases A and B from Figure 8.40. The data represented by case B in the above are often interpreted as representing an additional mechanism in addition to being governed by fixed values of K_{max} and ΔK as governing parameters. Boyce and Ritchie [41], for example, raised the possibility of high R thresholds being associated with sustained load cracking because of the high values of K_{max} associated with high R threshold values as shown in Figure 8.41. In their case, from experiments on Ti-6Al-4V, they concluded that in the observed behavior, similar to that represented by case B above, the intrinsic threshold behavior is itself K_{max}-dependent and such sensitivity to K should be considered in developing threshold models. In a similar manner, a constant value of ΔK_{th} for small values of R may only be an approximation and the actual shape of the curve should be taken into account.

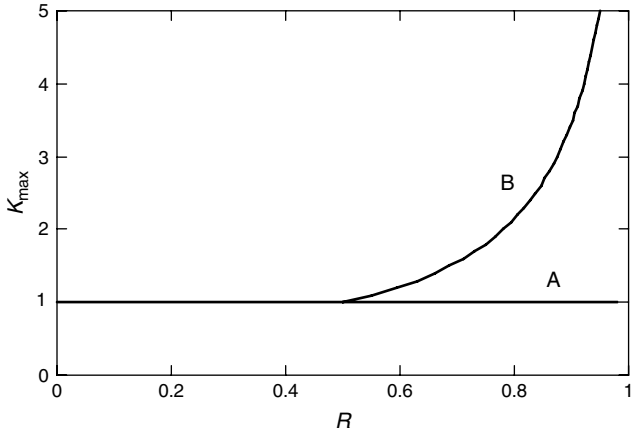


Figure 8.41. Schematic of two-parameter threshold in plot of K_{max} versus R.

So, when plotting threshold data or examining the consequences of such data for design purposes, the possible governing mechanisms or consequences of extrapolating to other conditions should be considered. It is important to recognize the various ways in which the data can be represented and some of the interpretations of the meaning of the shape of the various plots. A review of some of the key considerations that have evolved over many years in the use of the two parameter approach to fatigue thresholds involving the use of K_{max} and ΔK is given in [42].

8.4.6.2. Crack propagation stress intensity factor

Lang [43] introduced an alternate to a crack-closure-based model for threshold using a crack propagation stress intensity factor, K_{PR}, which is defined in the equation

$$\Delta K_{eff} = K_{max} - (K_{PR} + \Delta K_T) \tag{8.8}$$

where the term $(K_{PR} + \Delta K_T)$ has the same mathematical significance as the K_{cl} term in closure-based threshold models. In the interpretation of the Lang formulation, ΔK_T is an inherent material threshold and K_{PR} is an experimentally derived quantity that is determined from the onset of crack propagation in an increasing K test started below the material threshold until the onset of crack growth is detected. The mathematical description and the experimental determination of K_{PR} are not related to closure in any manner and no measurement of closure is either defined or attempted. While ΔK_T is defined as an inherent threshold or a material constant, K_{PR} is a variable with R, for example, under constant amplitude cycling. The variation of K_{PR} with R is determined experimentally and produces a threshold plot of ΔK versus K_{max} which is not necessarily

linear nor does it represent a constant value of ΔK above some critical value of R. After certain load sequences involving overloads or underloads are applied, "master curves" can be obtained for a given material, but only after extensive testing. Essentially, K_{PR} must be determined as a function of the prior loading history which includes K_{max}, unloading ratio, and number of overloads.

A notable difference of the K_{PR} approach relative to crack closure modeling is that the K_{PR} approach predicts that even under very high R ($R > 0.8$) steady-state conditions, K_{PR} is found to be greater than K_{min}. Further, the observed behavior is not attributable to crack closure. Lang [43] hypothesizes that K_{PR} is controlled primarily by the residual stress state ahead of the crack tip, and that it represents the point in the loading cycle where these stresses become tensile. As in crack-closure modeling where closure is difficult to measure and those measurements are subject to interpretation, the crack tip stress field is even more difficult if not impossible to measure. In both methods, however, finite element modeling can be used to justify the approach and to correlate with experimental observations.

8.4.7. An engineering approach to thresholds

We introduce here an engineering approach to the determination of a threshold stress intensity that can be used in design when a spectrum that involves a combination of LCF and HCF is present in the operating environment. In many cases, a component is subjected to such a spectrum during qualification testing. The test sequence is often used to determine the condition under which the HCF starts to affect the LCF growth rate using step-testing procedures. The condition where the HCF starts to have a significant affect is deemed to be the threshold for HCF crack propagation, namely the threshold stress intensity for HCF. For complex spectra as well as complex geometries where the K analysis is not fully validated, an engineering approach can be used. This approach is nothing more than the threshold approach described in Chapter 4 for simple LCF–HCF load spectra. Here, it is applied to any complex spectrum that contains an HCF component that may lead to failure when the crack length due to crack propagation from the spectrum exceeds the critical threshold value for the HCF component. Overload and retardation effects are automatically considered even though they are not specifically identified. This approach involves the use of a Kitagawa type diagram for the specific geometry and the specific load spectrum. Applied load (stress) levels at which the HCF part of the loading spectrum starts to have an appreciable effect on the crack growth rate can be plotted as a function of the crack length at which this occurs on a Kitagawa diagram as shown schematically in Figure 8.42. The K solution for a crack in the specified component geometry can then be fit to the experimental data on the Kitagawa diagram. The best-fit curve can then be used to infer the crack growth threshold stress intensity, without having to resort to a laboratory sample test procedure to obtain that same quantity.

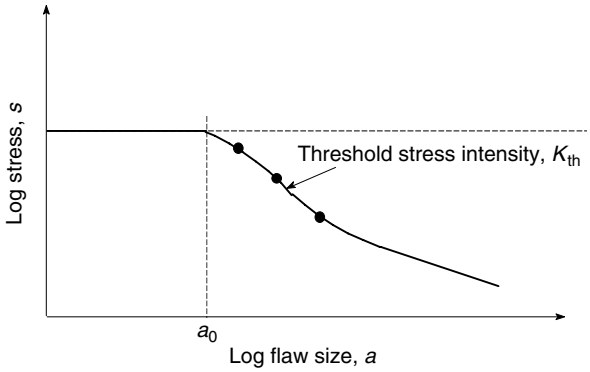


Figure 8.42. Schematic of Kitagawa diagram for component with complex geometry and complex K solution.

Even if the K solution is not of the highest fidelity, but that same solution is used in design, the threshold for the onset of crack growth due to the HCF portion of the loading can be accurately determined. For the endurance limit stress, the same spectrum applied to the same component geometry is used to establish the FLS of the uncracked body, typically using step testing or staircase testing as described in Chapter 3. Without consideration of small crack effects, this approach will provide an accurate assessment of the threshold conditions without having to resort to laboratory testing and considerations of history effects in the method used for threshold determination as described in the section above.

8.4.8. Observations from field failures

One of the methods for the evaluation of the conditions leading to HCF failures under combined LCF–HCF loading, as described in Chapter 4, is examining the fracture surfaces of failed parts. In examples cited, LCF often precedes the onset of HCF, the latter consuming only a small fraction of life. The determination of LCF life is typically much easier than determining the HCF threshold, which may be loading-history dependent, since LCF loading in rotating components is related to rotational speeds and the resultant centrifugal load-induced stresses which are well characterized in many instances. HCF loading, on the other hand, is usually related to some type of vibratory condition that is not always well defined, particularly in cases where the vibration is somewhat random. If a crack initiates in LCF, and then accelerates in HCF, the crack length at which this transition takes place can sometimes be determined from examination of the striations on a fracture surface of a failed part. Several instances of this situation have occurred in field incidents on US Air Force engines. The fracture surfaces revealed the crack length at which the transition took place. Knowing, or speculating, on the HCF stress ratio present when the vibratory stresses started contributing to the crack extension, and assuming the

threshold stress intensity at that value of R was the one corresponding to long crack laboratory data with no load-history effects, the vibratory stress magnitude could be deduced from either a Kitagawa diagram (including a short crack correction, if necessary) or a fracture mechanics analysis. In some cases, the HCF markings on the fracture surface were not easily discernable because the HCF growth rates were extremely small and the resulting striations were observable only under very high magnification under SEM. Nonetheless, LCF–HCF interactions can produce markings on a fracture surface which allow an indirect determination of the HCF stresses that were present. In the presence of a complicated mission cycle, such an approach may be the only way to determine the role of HCF and HCF threshold on the failure conditions when LCF–HCF conditions prevail.

Several limitations exist on the use of fracture surface markings to establish thresholds for HCF under combined LCF–HCF loading conditions. First is the fact that striations can be distinguished on a fracture surface only for certain combinations of material and growth rate regime. Materials such as aluminum show striation markings much better than other materials such as titanium. Second, under loading spectra where some of the cycles go into compression ($R < 0$), the fracture surfaces come into contact and the features may be obliterated because of the smearing due to compressive loading on the surfaces. What appears at first to be a very useful tool for analyzing threshold behavior from fractography then turns out, unfortunately, to be non-applicable in certain cases.

8.5. PROBABILISTIC APPROACH TO HCF/FOD DESIGN

The technical issues of the FOD problem in terms of experimental and analytical determination of the severity of damage were discussed in Chapter 7 and the accompanying Appendix G. Here we consider some of the aspects of getting information of that type into the design process. We can note that probability-based methods are becoming increasingly important in the design process. The present ENSIP document contains requirements dealing with the probability of failure due to HCF in terms of the acceptable number of failures per 10^7 engine flying hours whereas the original version did not deal at all with probability of failures. Of the many aspects of HCF design, the problem of FOD is certainly one that lends itself to a probabilistic design approach. FOD not only involves the probability of incurring damage of a certain severity at a certain location in a component, but it also involves the probability of a vibratory stress of a given amplitude occurring at the location of the FOD site as well as the variation in the endurance limit of undamaged material. An attempt to incorporate the various aspects involved in the probability of failure from FOD is presented conceptually in Figure 8.43. "Material failure strength" in HCF is shown for an undamaged material. The mean or median fatigue strength, represented by the dashed line, is usually the quantity used in design. Additionally, a -3σ

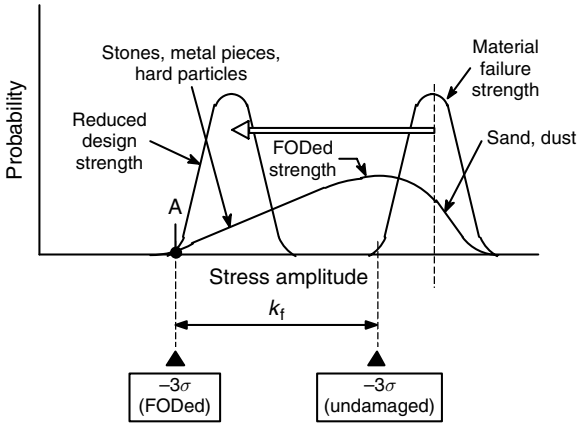


Figure 8.43. FOD/HCF probability diagram.

value for a normal distribution or some other measure of spread in the distribution curve is needed for a robust probabilistic design as indicated in the figure. The diagram also shows a hypothetical distribution of fatigue strength of a material subjected to FOD ("FODed strength"). Again, both the mean and the spread of the distribution of material strength and FODed strength are important for design purposes. (This representation is purely conceptual so the amplitude and shape of each of the distribution functions are not intended to represent any real distribution nor to be related to each other in any manner.) The schematic shows that there can be a region where the FODed strength is below the minimum or allowable fatigue strength of the undamaged material. Such a low strength of FODed material may be produced by FOD from stones, metal pieces, or hard particles as indicated in the figure. These damaging objects will generally produce more severe damage, in terms of reduction of fatigue strength, than smaller objects such as sand and dust. These latter objects may reduce the fatigue strength only slightly. The type and number of potential particle impacts will, therefore, provide the input for determining or estimating the overall shape and limits of the FOD strength distribution curve. As in the case of the undamaged material strength, the spread of the distribution curve as well as the mean are of importance in a probabilistic design.

Similar to the method for accounting for notches in fatigue, the material allowable would have to be reduced by a factor k_f so that the minimum fatigue strength of the FODed material, point A in the figure, is at or above the reduced design strength of the material in order to minimize the possibility of failure. This constitutes moving the undamaged fatigue strength distribution curve over by a factor of k_f as shown in Figure 8.43, even though the entire curve will be used in defining the probability of failure. If there is overlap of the distribution functions for undamaged material strength and FODed strength in the region near point A, the probability of failure has to be established as corresponding

to some chosen level that is acceptable for a given application.* Single engine versus multiple engine aircraft is another consideration if system failure is being predicted rather than component failure. Values of k_f in the range from 3 to 5 are often necessary to account for the potential debit in fatigue strength due to FOD. At the higher values of k_f, a severe penalty will be paid in material capability to account for FOD in design.

The distribution curve for the FODed material is sensitive to the type of FOD that may be encountered in service and is based on usage and field experience. As noted above, FOD from sand and dust is not as severe as FOD from stones, metal pieces, and hard particles. For design purposes, the expected rate of FOD incidents from each type has to be established. On many airfields, both military as well as commercial, FOD walks are conducted regularly by the maintenance personnel to search for and remove any debris that may be ingested into an engine. Such walks would likely reduce the probability of ingestion of larger objects and would tend to skew the FODed strength curve of Figure 8.43 to the right as well as truncate the tail of the curve on the left. This would have the effect of reducing the value of the required k_f in design. An additional complexity in this design concept is the exact location of the expected FOD and the stress magnitude as well as stress ratio at that location. In general, curves such as those depicted in Figure 8.43 would have to be established for each location or region along the leading edge of a blade, for example. A more realistic approach, however, might use only one probabilistic model that accounts for randomness in location and its correlation with FOD size.

An illustration of the severity of FOD encountered on a representative blade is shown in dimensionless form in Figure 8.44.† Here, individual FOD incidents are depicted on a plot of FOD size against location from the blade tip. Both quantities are presented in non-dimensional form. The data for this specific blade show a trend of large damage sizes occurring near the blade tip. However, it can be seen that smaller damage occurs all along the blade. Additionally, the material capability either has to be taken into account at each location based on probability of vibratory stresses of a given amplitude occurring at that location, or the vibratory forcing function has to be described in terms of its probability of occurrence. The latter is the more common method of accounting for vibratory stress amplitude in a probabilistic design as depicted schematically in Figure 8.45. There, at any given location, the probability of a vibratory stress of a specified magnitude has to be

* Note that a normal distribution curve has non-zero probability over the entire range $0 - \infty$. Thus, there could generally be overlap at any value of stress in the figure. In the figure used here, an attempt is made to convey a concept. The location of the overlap region is a concept, NOT a mathematical entity, even though such curves are often found in the literature. The statistics of the individual curves and the determination of the joint probability causing failure must be established in determining an appropriate value of k_f. Further information and explanations on this matter can be found at http://www.StatisticalEngineering.com/FORMSORM2.htm.

† The data for Figure 8.44 and the ideas dealing with the use of probabilistic methods for FOD design are courtesy of Patrick Conor of the New Zealand Defence Technology Agency to whom the author is deeply grateful.

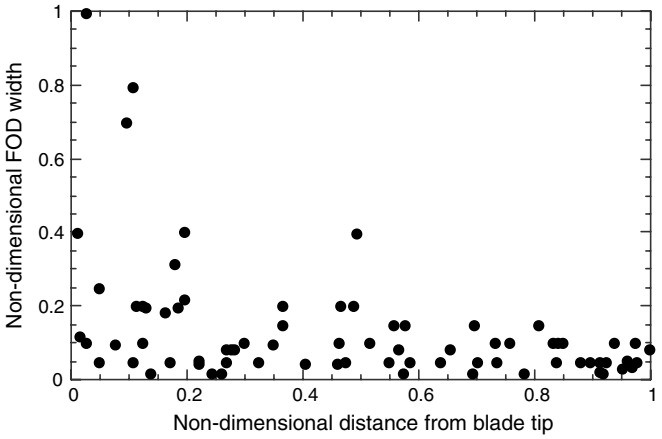


Figure 8.44. Representative distribution and severity of FOD damage on a blade.

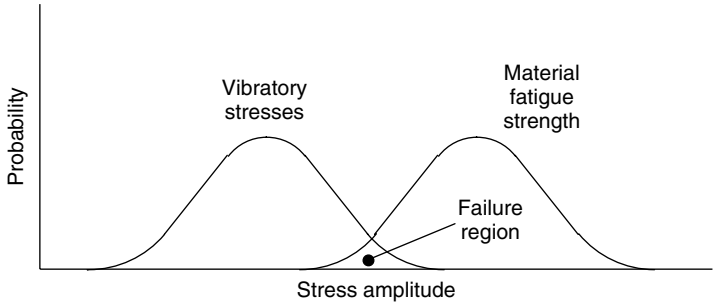


Figure 8.45. Schematic of probabilistic approach to HCF design.

established. Concurrently, the material capability in terms of fatigue limit strength also has to be established. If there is overlap of the two curves, a region of potential failure exists as shown in the figure (see discussion in earlier footnote). The probability of failure in this region can be established by statistical means if the two distribution functions are known. As noted earlier, the area of overlap denoted as "failure region" in Figure 8.45 is *not* proportional to the probability of failure. As a simple illustrative example, assume that the distributions of vibratory stress and material fatigue strength are identical and are normal with the same standard deviation. If the distance between the mean (μ) of each curve is given as z standard deviations (σ), that is

$$\mu_{\text{strength}} = \mu_{\text{vib stress}} + z\sigma \tag{8.9}$$

then the probabilities of failure are easily obtained assuming the individual quantities (vibratory stress and fatigue strength). The values are provided in Table 8.2. Note that

Table 8.2. Failure probabilities for identical normal distribution curves for undamaged strength and damaged strength separated by $z\sigma$

z	0	1	2	3	4	5
Prob	0.50000	0.23975	0.07865	0.01695	0.0023389	0.0002035

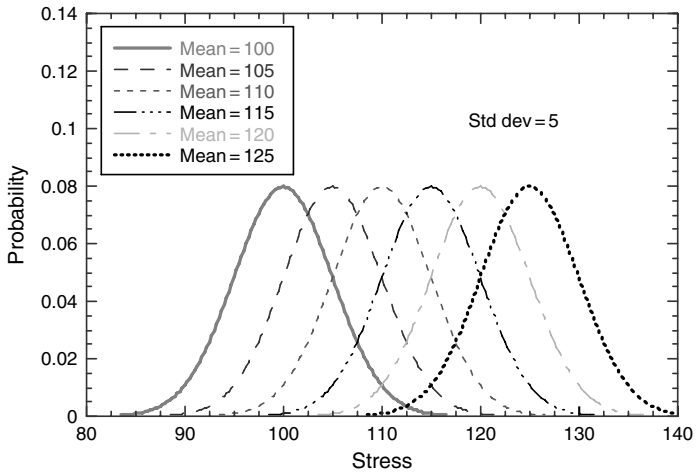


Figure 8.46. Normal distribution functions for various values of mean stress that have the same value of variance ($\sigma = 5$).

$z = 0$ indicates that the two distributions fall on top of each other. To illustrate the distributions graphically a value of $\mu = 100$ is taken for the vibratory stress function and σ is assumed to be $= 5$. The distributions for various values of μ corresponding to $z = 1$ to $z = 5$ are shown in Figure 8.46. When $z = 0$, the so-called overlap is 100% but the probability of failure is 0.5 since the values of vibratory stress and fatigue strength are chosen randomly from the same distribution and the criterion for failure is if the vibratory stress exceeds the fatigue strength.

The numbers in Table 8.2 indicate that, for these normal distributions, the mean values for the two curves would have to be separated by over four standard deviations in order for the probability of failure to be below one in a thousand or 0.001. Figure 8.46 shows that the "overlap" between the two curves for $z = 4$ ($\mu = 100$ and $\mu = 120$, respectively) is clearly visible even for a probability of approximately 0.002. When $z = 5$, the probability of failure is only 0.0002 yet the figure shows a region of overlap indicated as a "Failure region" in Figure 8.45. This numerical example clearly shows that overlap and probability of failure are not related numerically, contrary to the common misconception that they are. This example is only for an assumed normal distribution function representing the fatigue strength as

well as the material capability. Unfortunately, as discussed in Chapter 3, determination of the actual distribution function is difficult unless a very large database is available. The knowledge of the real distribution function (normal versus lognormal, for example) to represent either vibratory loading or material fatigue strength is often quite limited.

8.6. RESIDUAL STRESSES IN HCF DESIGN

Residual stresses can play an important role in affecting fatigue crack initiation or crack propagation under both LCF and HCF loading conditions. Residual stresses can either be introduced deliberately during fabrication or can result from usage of a component. Most of the early work on residual stresses dealt with those stresses that occur during the production process or those that occur in service such as stresses that develop due to plastic deformation in a notch region. Later, residual compressive stresses were deliberately introduced in many applications to improve the resistance of a material to crack initiation and/or crack propagation. In many engine components, for example, shot peening is now used routinely on surfaces where fatigue may occur. While the process has been shown to improve fatigue properties in many cases, no credit is taken in design or analysis. Rather, the surface treatment is considered as an added margin of safety. In recent years, new processes like laser shock processing (LSP), low plasticity burnishing (LPB), ultrasonic peening, or cavitation peening have provided a method for introducing compressive residual stresses to greater depths than those from conventional shot peening. For leading edges on airfoils, the FOD resistance can be improved significantly with the deeper compressive residual stress techniques. While the vibratory loading on an airfoil, specifically the stress *range*, is not affected by the introduction of residual stresses, the effective mean stress or the maximum stress is lowered by the introduction of compressive residual stresses. The stress ratio due to vibratory loading at a certain location, and the shape of the Haigh diagram for the material, will determine the potential beneficial effects of the compressive residual stresses [1]. A Haigh diagram for Ti-6Al-4V including the negative mean stress region is shown in Figure 8.47. It can be seen that moving to the left (decrease in mean stress) will increase the allowable alternating stress when in the high mean stress region, but the benefit decreases when the mean stress is zero (fully reversed loading) or it is negative. This would affect the initiation of a crack. The propagation of a crack is governed by the stress intensity field, which is made up of the applied K less the K due to residual stresses as discussed below. Because the residual K (negative) is often an increasing function of crack length, and may increase faster than the K due to applied loading, a crack may arrest at a constant load. Experimentally, this is often found to be the case as illustrated in Figure 8.48 where each successive P is larger than the previous one. Here, cracks propagate and arrest as the load is increased successively until finally the specimen fails. Because of the beneficial effects of surface treatments such as LSP

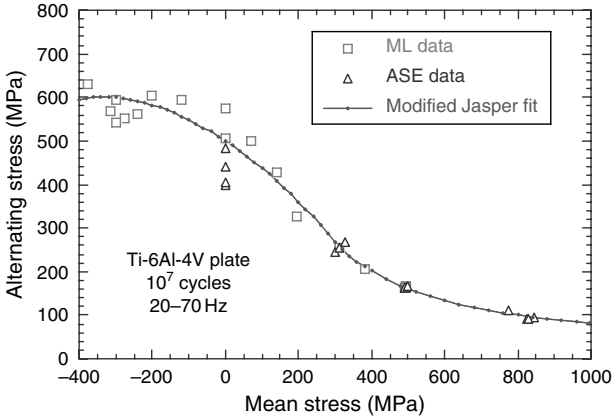


Figure 8.47. Haigh diagram for Ti-6Al-4V including negative mean stress [1].

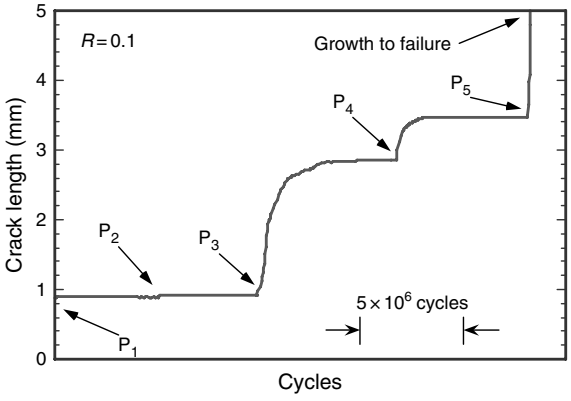


Figure 8.48. Crack length history for specimen with residual stresses from LSP.

and LPB, the latest versions of ENSIP are allowing credit to be taken provided that the process and related analysis can be adequately validated.

The dilemma raised earlier in Chapter 6 for fretting cracks being present but not catastrophic also arises for residual stress benefits as illustrated in Figure 8.48. Here, for a typical laboratory test on a specimen that has LSP near the edge, it is seen that cracks at load levels between P_2 and P_4 will arrest and not cause failure. However, the question arises regarding how to handle this behavior in analysis and in field maintenance when a crack can be shown to exist and not be potentially damaging. The answer on how to handle this situation has not yet been resolved in the engine community, but the trend in thinking seems to be not to allow cracked parts to remain in service.

In evaluating the effects that occur due to the introduction of residual stresses from surface treatments such as conventional shot peening, burnishing, laser shock processing, cavitation peening, or others, several features have to be considered. In addition to the effects due solely to the residual stresses that develop, both local and far field in a specimen or component, microstructural or material damage resulting from the process itself as well as effects from inelastic deformation such as strain hardening must be considered. Further, any net geometric effects from the process such as distortion must be considered when the loading may be altered due to such deformation. In particular, a member loaded in compression may be more susceptible to buckling in a slightly distorted configuration than when it was initially straight.

The process of using residual stresses to improve the fatigue capability should consider the resulting capability to slow or retard crack growth. Much of the work on the effects of overloads on crack growth retardation, described earlier, has focused on the identification of the governing mechanisms and phenomena associated with the event. One aspect of the explanations has focused on the effects of compressive residual stresses ahead of the crack tip. These are both difficult, if not impossible, to measure (especially in 3-d geometries) and hard to compute because they can be so localized that continuum modeling tends to break down. Nonetheless, it is an example of the potentially beneficial effects of compressive residual stresses in fatigue crack growth. Heywood [44] was one of the first to show that the fatigue life of full-sized airplane components could be increased by the application of preloads (overloads). Heywood's results were substantiated by Gerber and Fuchs [45]. The latter pointed out that two assumptions are usually made to predict the beneficial effects of residual stresses (what have also been referred to as self-stresses) on fatigue resistance: "(1) self-stresses are assumed to have the same influence on fatigue strength or fatigue life as a mean stress and (2) the self-stresses that are assumed to be significant to fatigue are those at or near the surface." The second point has been validated over many years by the observation that fatigue, under most circumstances not involving internal defects, originates at free surfaces. To the above observations should be added the comment that the local value of stress, from the applied load plus the residual stress, does not solely determine the fatigue strength. The gradient of the stress field, much like that at the tip of a notch, also has an influence on the fatigue properties. The methods for development of compressive residual stresses and the nature of such stresses are discussed below. These can be applied to either smooth or cracked bodies. Concepts that are useful for delaying crack growth and increasing fatigue life, such as overload retardation, can be extended to the condition of complete crack arrest for HCF applications where a threshold condition may be required.

The simplest and most straightforward method of improving fatigue resistance through the development of compressive residual stresses is illustrated schematically in Figure 8.49 where the stress field ahead of a notch is depicted. Denoting tensile stresses as positive (upward), the schematic shows the development of residual stresses by plastic deformation

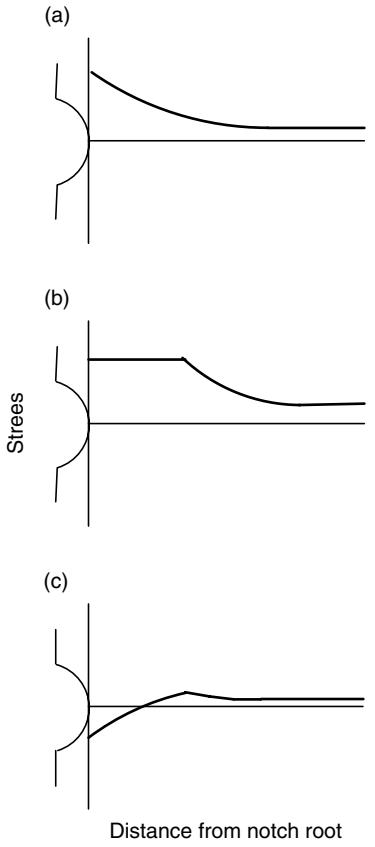


Figure 8.49. Schematic of stresses ahead of a notch: (a) elastic loading, (b) loading beyond yield, (c) residual stress after unloading.

at the notch root for an assumed elastic–perfectly plastic material. In (a), the elastic stress field for an applied load that does not cause plastic deformation at the notch root is depicted. The maximum stress occurs at the root of the notch and then decays with distance from the notch root. In (b), the load is increased to a level that causes local plastic deformation (yielding) in the vicinity of the notch. When this load is removed, the material unloads elastically, leaving a residual stress field as shown in (c). In the most general problem, the actual stress distribution near the notch, whether 2-d or 3-d, has to be computed. Further, the actual elastic–plastic behavior including strain hardening has to be properly represented. If the specimen or component is further subjected to compressive loading such as from a far-field fully reversed load cycle, then the notch region may be subjected additionally to compressive yielding. This loading may wash out the beneficial effects of the compressive residual stresses. The calculation of such an

effect must take into account the reversed yielding characteristics of the material using the appropriate strain-hardening law to represent what might be isotropic or directional hardening or something in between, depending on the specific material involved.

Some of the basic concepts regarding the beneficial effects of residual compressive stresses in fatigue are summarized in the following quote from a paper that dates back to 1956. In his paper, Gadd [46] states:

> . . . a finish or treatment which produces a compressive stress in the surface layer will cause a diminution in the level of the applied tensile stress thus improving fatigue resistance. It must be remembered however that the imposition of a compressive stress on the surface layer will produce an equal and opposite effect in the underlying layers in order to maintain equilibrium. A point will be reached therefore when both the core stress and applied tensile stress are both of a like sign, with the consequence that a subsurface tensile peak is formed. Since failure occurs at the point where the tensile stress is greatest, sub-surface fractures will take place in those instances. If the relationship between the depth of surface layer compressively stressed and the cross-section of the bar is correct, that is, the ratio is low, the stress peak will still be less than the value of the nominal stress applied. In other words, the fatigue resistance of the material will be improved. If, on the other hand, the ratio is high, the sub-surface stress peak may well exceed the nominal value applied, and failure will consequently be accelerated.
>
> The effect of compressive stress in the surface layers of test bars free from notch effects is most marked under bending and torsion and only to a minor degree under true axial fatigue conditions. When notches are involved, however, even test bars subjected to axial loading derive considerable benefit from surface compressive stresses. Under notched conditions, compressive stresses in the surface produce even greater benefits than under plain conditions, the treatment diminishing the tensile stress concentration at the root of the notch, and in some instances even eliminating it. This is of great importance in engineering design where changes in section cannot be avoided and the surface finish is not always all that can be desired.

While issue cannot be taken with these statements that are as true today as they were then, the scenario under which these were arrived at involved surface treatments such as shot peening where the depth of the residual stress field is small compared to the total thickness of a part. Further, shot peening generally is, and can be, applied over most if not all of the surface of a component. Such a condition is depicted in Figure 8.50(a) where the magnitude of the tensile stresses is held below that of the surface compressive stresses, shown shaded in the figure. What was probably not considered many years ago was the development of techniques such as laser shock processing (LSP), low plasticity burnishing (LPB), cavitation peening, or others where the depth of the compressive residual stress field can be considerable with respect to the total thickness of the specimen. Compared to shot peening, where the depth of residual compression is of the order of 0.1 mm, LSP and LPB can reach depths of the order of 1 mm or more. When applied to components such as a leading or trailing edge of an airfoil whose total thickness may be under 1 mm,

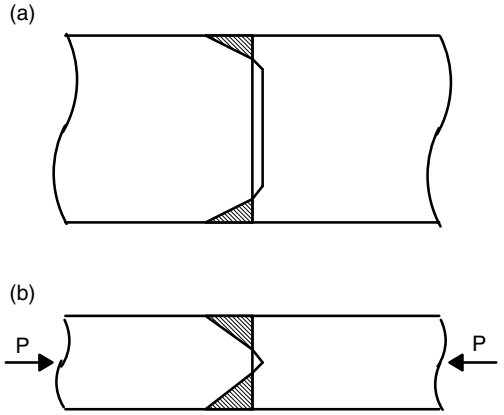


Figure 8.50. Schematic of residual stress profiles developed during surface treatment. Compressive stresses are shown shaded.

the residual compression can develop throughout the entire thickness. The difference in application between these "deep" compressive stress fields and shallow shot peening is illustrated in Figure 8.50(b) where the depth of the residual compressive stress field is significant with respect to the total thickness of the part. To achieve such a stress field, the region at which this cross section is taken from has to be constrained in the far field. For example, LSP or LPB applied along an airfoil leading edge is constrained by the overall stiffness of the airfoil. For this reason, it can only be applied over a limited region of the specimen in order to be able to develop far-field constraint. Such constraint is shown schematically as a compression load P in Figure 8.50(b). In (b) of that figure, the stresses through the cross section are not in equilibrium because of the existence of the far-field constraint. The section shown is only a part of an overall geometry that allows for a far-field constraint to develop. Without that constraint, for example in the case where surface treatment is applied over most of the surface, equilibrium of the cross section has to be achieved. It is surprising how often this concept of equilibrium gets forgotten in actual applications! On the contrary, for thick sections where the depth of compression is relatively small, the cross section can be in equilibrium without any far-field constraint.

Noting the prior comments about residual stresses having the effect of shifting the mean stress, the initiation of a crack may not be retarded significantly due to compressive stresses. The continued propagation of such a crack, however, may be influenced a great deal. The depth of initiation, one of the great unknowns in fatigue, and the subsequent crack growth, must both be considered in any analytical modeling of the potential beneficial effects of surface treatments that impart compressive residual stresses. For LCF, where cracks initiate early in life and spend a large portion of life in propagation, and HCF, where initiation consumes a major portion of life, the beneficial effects of a

surface treatment may be different. Specifically, in HCF, cracks may take a long time to initiate but, with the aid of compressive residual stresses, they may arrest. This may provide a measurable improvement in the endurance limit or the fatigue limit strength at a large cycle count.

8.6.1. Application to notches

As noted above, the effect of residual compressive stress is to move the mean stress in the negative direction. For a smooth bar, this simply shifts the Haigh diagram, a plot of alternating stress against mean stress, to the left. In most cases, for a smooth bar, the compressive residual stress near the surface produces a tensile residual stress field in the interior, the magnitude of which is dependent on the compressive stress profile and the cross-sectional dimensions. In most cases, under tensile loading, fatigue failures will occur in the interior rather than at the surface. Under bending, however, failure can occur at the surface or interior to the surface depending on the geometry of the specimen (applied stress gradient) and the residual stress distribution profile.

If there is a notch in a specimen or component, a residual compressive stress field will also reduce the local stresses in the vicinity of the notch. The residual stress field, produced by a surface enhancement procedure such as conventional shot peening (CSP), low plasticity burnishing (LPB), laser shock processing (LSP) or other, will depend on whether the surface treatment is applied before or after the notch is introduced. The notch depth as well as the depth of the residual compressive stresses must also be considered. For illustrative purposes, the assumption will be made in the following that the residual stress field extends beyond the notch depth so that the local notch stress field due to applied loading is reduced uniformly by the residual stresses that are assumed to be uniform over this depth. The net effect will be to shrink, rather than just shift, the Haigh diagram as illustrated in the following examples. The first case examined will be a modified Goodman equation that connects the fully reversed alternating stress with the UTS on the mean stress axis. For the examples presented here, the fully reversed alternating stress (corresponding to $R = -1$), σ_{-1}, is taken to be 500 MPa while the ultimate strength is assumed to be 1000 MPa. This is somewhat representative of Ti-6Al-4V plate material where $\sigma_{\text{ult}} = 980$ MPa.

Figure 8.51 is a Haigh diagram where the modified Goodman equation (straight line between σ_{-1} and σ_{UTS}) is arbitrarily extended into the compressive mean stress region. For stress concentration values of $k_{\text{t}} = 1.5$, 2, and 3, the FLSs are reduced as shown in the figure and are still straight lines. If the reduction is due to the effect of a notch on the fatigue limit, then k_{f} would replace k_{t} in the diagram. Also shown in the diagram are the ultimate and yield stress lines which limit the smooth bar response in both tension and compression.

Another equation that can be used to represent the fatigue limit is the Smith Watson Topper (SWT) equation that, if extended into the negative mean stress regime, has the

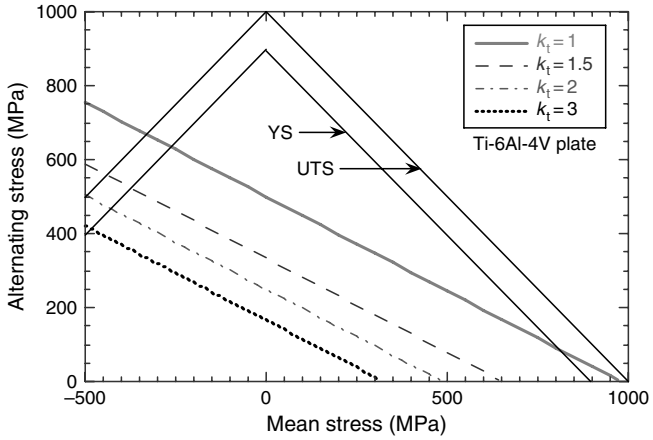


Figure 8.51. Haigh diagram showing allowable regions for several values of k_t using modified Goodman equation extended into negative mean stress region.

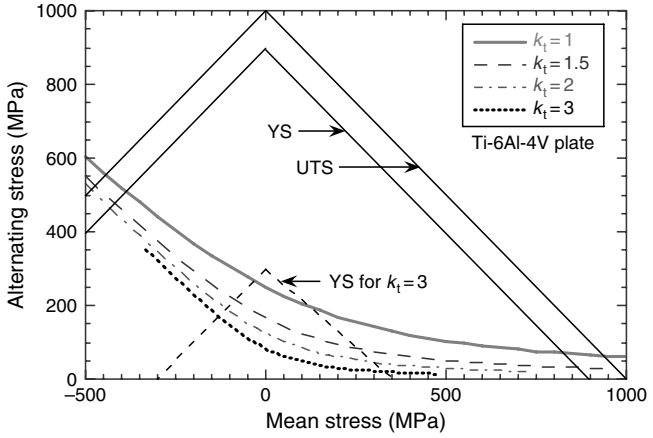


Figure 8.52. Haigh diagram showing allowable regions for several values of k_t using Smith–Watson–Topper (SWT) equation.

shape shown in Figure 8.52 for purely elastic behavior which is generally representative of HCF. Prevey et al. [47] have used this formulation to define what they term "safe" regions. If the reduction for an equivalent k_t is considered, then the curves are as shown in the figure. Since the local stress at the notch root is k_t times the applied stress, the applied stress to produce yielding is also reduced by the value of k_t, producing a reduced yield zone as shown in the figure for the case of $k_t = 3$.

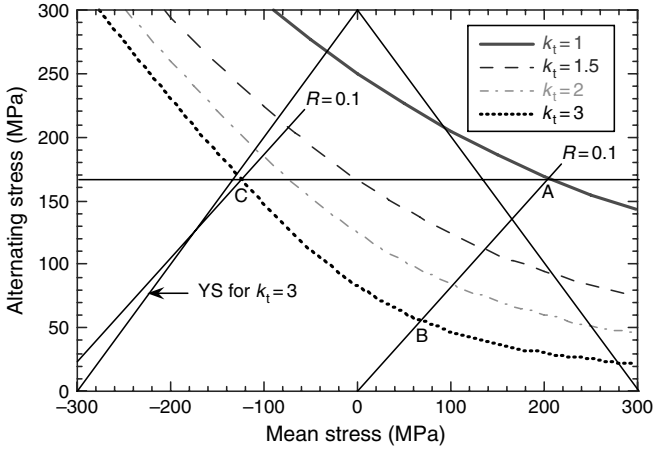


Figure 8.53. Blowup of SWT equation plot showing safe region and example of benefit of compressive residual stress.

Following the approach of Prevey et al. [47], a blowup of Figure 8.52 is shown in Figure 8.53 where the behavior for applied loading is indicated along the line denoted by $R = 0.1$. Assuming the allowable load in an unnotched specimen is at point A, a notch with an equivalent k_t (actually an equivalent k_f) reduces the allowable stresses to those indicated by point B in Figure 8.53. If the introduction of compressive residual stresses seeks to retain the allowable alternating stress to be that of the undamaged specimen without a notch, then the stress state would have to be along the $k_t = 3$ line, namely at point C in the figure. To accomplish this, a residual compression of magnitude CA in the figure would have to be introduced. The net effect of the residual compression is to shift the Haigh diagram to the left by the amount of the residual compressive stress. Lines of constant R remain parallel to their original orientation, but are all shifted to the left. In the cited example, the point C is just inside the reduced compressive yield line, indicating that yield at the notch root would not yet have taken place in the specimen subjected to residual compressive stresses of the amount CA.

It is of interest to note that the SWT equation reaches a limiting value in the compressive region as the value of k_t is increased [47]. Figure 8.54 shows the Haigh diagram for values of $k_t = 3$, 5, and 10, the latter representing the extreme value of a very sharp notch or a crack. While the line of constant life appears to asymptote to a fixed value, the compressive yield stress line, shown for the value of $k_t = 3$, would continually shrink toward the origin in the Haigh diagram.

Other equations such as that due to Jasper can be used to represent the constant life curve in a Haigh diagram as shown in Figure 8.55. Here, the equation was modified to fit data in the compressive mean stress regime, and applying values of k_t to that equation

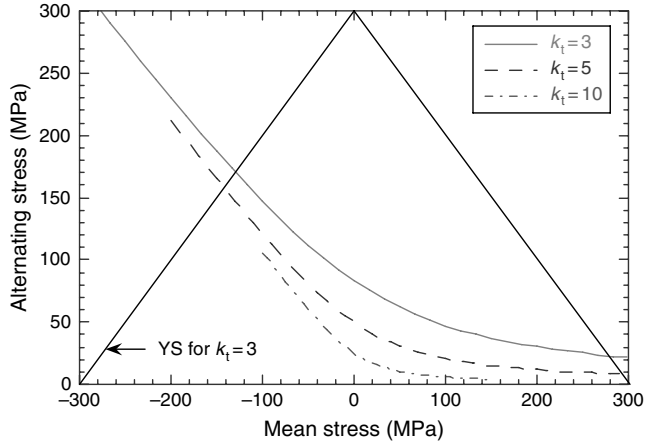


Figure 8.54. SWT equation plot for high values of k_t.

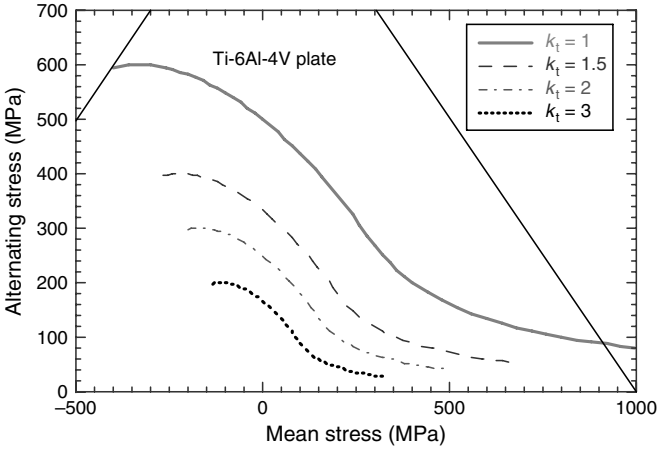


Figure 8.55. Haigh diagram showing allowable regions for several values of k_t using compression modified Jasper equation.

produces the plot shown. If the curve for $k_t = 3$ is extrapolated beyond the range where it was fit to the data corresponding to $k_t = 1$ (smooth bar), the curve starts to bend down as shown for the curve of $k_t = 3$. There are no experimental data nor is there a theoretical basis for the downward trend in the curve. To extrapolate the curve for notches, a modified version of the modified Jasper equation is shown where the curve is extrapolated at a constant value of alternating stress into the negative mean stress regime. The extrapolation is for illustrative purposes only, and no data are available to

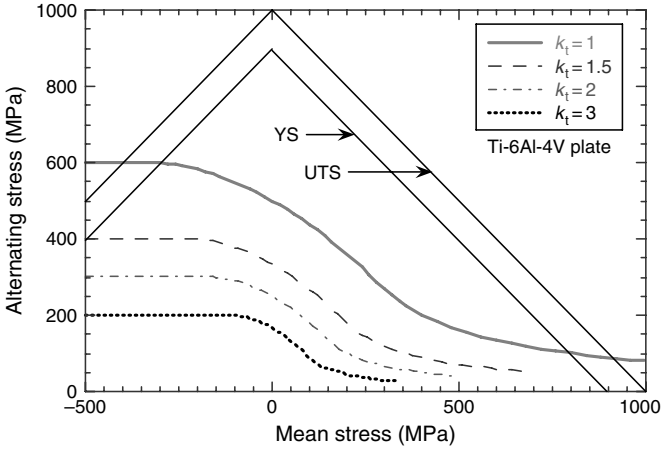


Figure 8.56. Haigh diagram showing allowable regions for several values of k_t using further modified version of compression modified Jasper equation.

indicate that this might be the actual trend of data. Nonetheless, the extrapolated curves are shown in Figure 8.56 and provide the reader with an idea of how the allowable stress states at a notch shrink with increasing k_t or k_f. As in the example above for the SWT equation, the addition of compressive residual stresses would provide a region where the allowable alternating stresses for positive values of R could be expanded because of the higher allowables in the compressive mean stress region. The possible shrinking of the allowable alternating stress in the compressive mean stress region would also have to be taken into account.

The examples provided above show that the allowable region for HCF design at a stress concentration, which is below the specific constant life curve chosen and below the yield surface, depends heavily on the curve chosen. This, in turn, depends on the shape of the curve, particularly in the negative mean stress region where data are generally not available. Further, if the curves for given values of k_t or k_f are shifted to the left due to the presence of compressive residual stresses, the resultant curves should be based on experimental values of the endurance limit. In most cases, these values would be based on tests using the appropriate geometry with a k_t value tested in the negative mean stress region. Shrinking of smooth bar data by the appropriate value of k_t will often not cover a sufficient range into the negative mean stress region if compressive residual stresses are added to the applied stress state. However, in the cases cited above, the extended range of stresses available in the negative mean stress region, compared to those in the positive mean stress region (values of $R > -1$), clearly shows the potential benefits available from the introduction of compressive residual stresses for either smooth bars or those containing a defect in the form of an equivalent k_t or k_f.

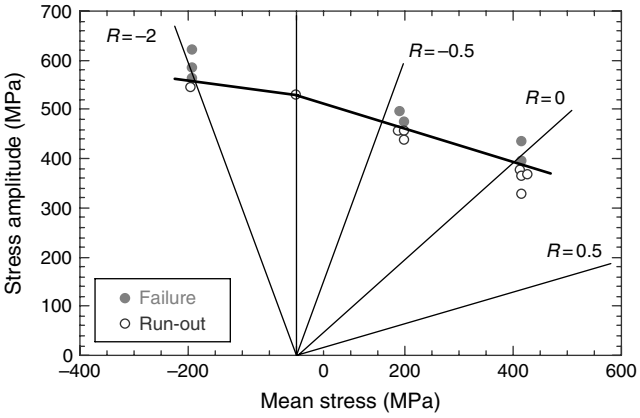


Figure 8.57. Fatigue limit stresses for maraging steel with drilled hole [48].

An example of the limited data available on notched fatigue limit behavior into the negative mean stress regime is shown in Figure 8.57 [48]. Here, small drilled holes of depth and diameter of 100 μm were used to produce stress concentrations in a maraging steel. Although the data cover only a limited range of mean stresses, the lowest corresponding to $R = -2$, there does not appear to be any significant trend of an increase in alternating stress with decrease in mean stress in the negative mean stress region. These and other similar data, combined with the general lack of data of this type, make it difficult to accurately predict, analytically, the potential beneficial effects of surface enhancement procedures that produce compressive residual stresses.

For design, consideration must also be given to the possible variation of k_f with k_t for different values of stress ratio, R, since many materials do not follow a single formula like the Neuber equation [49]*

$$k_f = 1 + \frac{k_t - 1}{1 + \sqrt{\frac{a_m}{r}}} \tag{8.10}$$

where the dependence is based solely on notch geometry and not on R.

8.6.2. Shot peening

The subject of the effect of residual stresses on fatigue, including the effects on threshold which are important for application to HCF, has been studied for many years. A general

* In this equation for a notch, a_m is an empirical material constant and r is the notch root radius (see Section 5.4.2). The value of k_t can be determined from formulas developed for common notch geometries or from FEM analyses for more complex geometries.

overview of the effects of residual stresses on fatigue, particularly in the use of conventional shot peening, can be found in the book by Almen and Black [50], for example. On the history of the process, they write:

> The discovery of the improvement in fatigue properties from shot peening stemmed from efforts in 1928 to 1929 by the Buick Motor Division of General Motors Corporation to remove spots of scale from valve springs by blasting them with grit. It was found that the fatigue properties of the springs were markedly improved by grit blasting. This provided the impetus for an extensive program which led to the development of modern shot-peening methods and applications.
>
> In the early days it was thought that the improvement in fatigue properties secured by shot peening was due to work hardening of the surface material, but it was soon learned that the major part of the benefits lay in the compressive stress induced at the surface of the shot-peened part.

In the preface to their book, Almen and Black [50] point out the simplifying assumptions that must be considered in the application of surface treatments such as shot peening to the fatigue life or fatigue limit of a material. Specifically, they note that it is generally assumed that "practically all machine-part fractures occurring in normal service are fatigue fractures," and "metal surfaces are weaker in fatigue than sound subsurface material." The latter, in particular, is used and justified as a basis for developing methods for imparting surface residual compressive stresses in a material through methods such a shot peening.

There has been much research conducted over many years on the effects of shot peening on the fatigue properties of materials. Only a limited number of those studies are cited here to illustrate some of the significant findings. In a study to optimize the parameters to improve the HCF strength of a titanium alloy, Hanyuda and Nakamura [51] evaluated the fatigue strength of titanium alloys as a function of the two dominating parameters, surface roughness and residual stress. Wagner et al. [52], in studying the effect of shot peening on the fatigue strength of Ti-6Al-4V, had found that an increase in the surface roughness promotes fatigue crack initiation. In [51], however, they found that surface residual stress has a dominating influence on fatigue strength in comparison with other factors such as surface roughness, depth of work hardening layer, and depth of the compressively stressed layer. The conclusions on the latter two factors were made solely in the context of the constraints of the shot-peening process. A more important finding in their work, one that reinforces a recurring theme in much of the research on the beneficial effects of compressive residual stresses, is that the resistance to crack propagation at the surface is more effective on fatigue strength as compared with the resistance to crack initiation or propagation below the surface at an early stage.

Hasegawa et al. [53] found that in 0.5% carbon steel, the increase in fatigue strength at room temperature due to shot peening was due to both work hardening as well as compressive residual stress at the surface. The benefit, however, was minimal in the LCF regime and increased as the HCF regime is approached as seen in Figure 8.58.

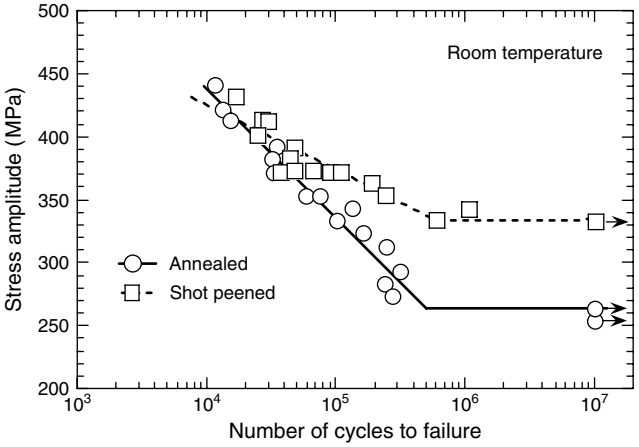


Figure 8.58. *S–N* curves for annealed and shot-peened specimens of 0.5% carbon steel from rotating bending tests at room temperature (from [53]).

When the same tests were conducted at elevated temperatures, however, the magnitude of the residual stresses was reduced which resulted in a decrease in the fatigue strength benefits. The shot-peened specimens still had higher fatigue strengths than the annealed specimens. This was attributed to the existence of work hardening which remained after cyclic loading at elevated temperature.

Dorr and Wagner [54] studied the effects of shot peeening on the fatigue strength of Timetal (Ti-1100) in both fully lamellar and duplex microstructural conditions. Their work was aimed at evaluating optimum shot-peening conditions for fatigue life improvement in both smooth and notched components under fully reversed ($R = -1$) conditions, using electro-polished (EP) specimens as the baseline. They noted that among the factors affecting the fatigue strength were local residual tensile stresses at a nucleation site (subsurface), the mean stress sensitivity of the material due to the microstructural condition, and the sensitivity of the material/microstructural condition to environment for subsurface initiations. These factors, in combination, could increase or decrease the fatigue strength after application of shot peening. Results for two of the microstructural conditions tested under axial loading at $R = -1$ are illustrated in Figure 8.59 for (a) duplex and (b) lamellar microstructures. In these cases, particularly in (a), the benefits of the shot peening appear to be concentrated in the LCF regime with perhaps even a debit in the HCF regime. Based on the known increase in fatigue strength in vacuum versus that in air in titanium alloys, the lack of benefit or deterioration of fatigue strength in the HCF regime was attributed to the "marked tensile residual stresses at the crack nucleation site" in the shot-peened specimens. They summarize their findings by noting that the fatigue crack nucleated below the residual compressive stress field in the shot-peened specimens. This crack

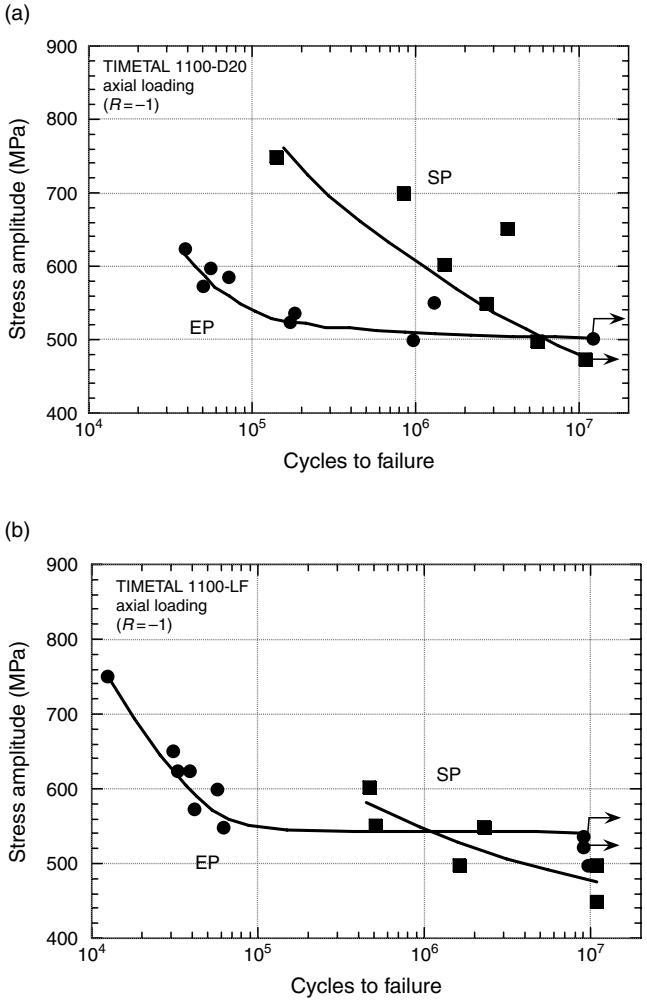


Figure 8.59. *S–N* curves for Ti 1100 in (a) duplex and (b) lamellar microstructural condition under axial loading (from [54]). SP = shot peened, EP = electro polished.

does not have to interact with the residual compressive stress field because it can first propagate rather easily deeper into the specimen interior. So, in addition to mechanical effects, environmental effects should be considered since subsurface cracks nucleate and propagate under vacuum conditions until they reach the surface.

Further light in the study of subsurface initiation in shot-peened specimens was shed by Shao et al. [55] in a study on 300 M steel under rotating bending conditions. Their work extended a concept proposed earlier in [56] where the terminology for another

kind of fatigue strength called "internal fatigue strength" was introduced. The concept was based on observations of internal initiations below the shot-peened layer where tensile residual stresses were present and there was no work-hardening effect due to the shot peening. Through calculations of the tensile residual stress field where the failure occurred, they found that in a 40 Cr steel tested under three-point bending at $R = 0.05$, the internal fatigue strength corresponding to 5×10^6 cycle life was approximately 35% higher than the "surface fatigue strength" obtained on unpeened specimens under identical test conditions. There was no attempt to relate this increase to environmental effects. In the later work of Shao et al. [55], the concept of an internal fatigue limit was extended and verified with tests under rotating bending ($R = -1$) on 300 M steel. Using calculated values of the tensile residual stress field at the failure location, the authors found that the ratio of the internal fatigue limit to the surface fatigue limit was about 1.39. The results were obtained for a fatigue life of 10^7 cycles using the up-and-down (staircase) test method (see Chapter 3).

The beneficial effects of shot peening can be attributed, in some cases, to the retardation of crack initiation at the surface due to the compressive stress field that is developed there. In other cases, the retardation of crack growth is credited with fatigue improvements. In this latter case, the beneficial effect can be attributed to the residual stress field which, in turn, affects the closure behavior of the cracks. Song and Wen [57] studied fatigue crack growth in AISI 304 SS in C(T) specimens. The surfaces of the specimens were shot peened in various locations and closure measurements were made as the crack was grown. This produces a complicated 3-dimensional stress state where closure can be related to surface distortion. Under these complex conditions, they concluded that the location of the shot-peened region has an influence on the re-initiation life and growth-rate behavior. When a crack is embedded within a peened region, crack closure develops. This appears to be another way of saying that residual compressive stresses affect the crack growth rate or threshold through a change in the effective stress intensity as will be discussed later in an example related to laser shock processing.

Drechsler et al. [58] conducted a study to compare fatigue improvements from shot peening to those of roller-burnishing where, in the latter, the depth of the affected region is greater. Using various titanium alloys under rotating bending fatigue, they attempted to sort out the effects of surface roughness and work-hardening characteristics of a material on fatigue property enhancement when surface treated. For the two processes used, the shot peening produced much higher surface roughness than roller-burnishing. With several different alloys, they covered a range of cyclic hardening/softening characteristics in the test materials. This would be less significant in the HCF regime than in LCF since cycling in the HCF regime is mainly elastic. The results from the surface-treated specimens showed slope changes in the S–N curves compared to baseline electro-polished specimens. Very marked improvements in fatigue performance were observed in Ti-2.5 Cu while the improvement in the S–N curve of Ti-10-2-3 was significantly less pronounced.

Intermediate improvements in fatigue performance were observed on Ti-6-7/AC. Marked changes in the slope of the *S–N* curves were observed in Ti-6-7/WQ owing to pronounced lifetime improvements in the HCF regime while finite life was only slightly improved. These results serve to illustrate the complex nature of the effect of surface treatments on fatigue behavior, particularly in the HCF regime, and the dependence of such behavior on the characteristics of the specific material such as strain hardening/softening.

The ability of a surface treatment, and the resulting residual stresses that are produced, to slow or stop a fatigue crack is probably the most important aspect in fatigue life improvement, particularly in the HCF regime where complete crack arrest defines the condition for determining an endurance limit. Guagliano and Vergani [59] address the problem of predicting the conditions for non-propagation of cracks in shot-peened specimens. They adopt the premise that fatigue alleviation due to shot peening is mainly due to the ability of the residual stresses to stop crack propagation and not in preventing fatigue crack initiation. Their approach is based on fracture mechanics and the existence of a threshold for crack propagation, ΔK_{th}. With the aid of an FEM model which considers both the applied loading and the compressive residual stress field, and taking into account crack closure and contact between crack faces, they are able to explain the presence of non-propagating cracks with typical depths from 0.15 to 0.3 mm in a low alloy steel. They note that the depth at which the cracks have stopped is entirely dependent on the residual compressive stress field induced by shot peening. Such a finding can be used as motivation for the use of other surface treatments that provide greater depths of residual compressive stresses.

The control of the initiation and early phase of crack propagation of surface cracks is considered to be paramount for prolonging the fatigue life and improving the HCF strength of engineering components subjected to cyclic loading. The extensive use of shot peening to achieve these purposes through the development of near-surface plastic deformation is based on the widely accepted concepts that work hardening and high magnitude compressive residual stresses are responsible for these benefits. Work hardening is expected to increase the resistance to flow in the material while compressive residual stresses can reduce the mean stress for crack initiation or produce closure to retard subsequent crack propagation. For many years, the benefits of the residual stresses were used as motivation for shot peening, and methods for optimizing the depth and magnitude of these stresses were sought after. While many of the approaches have been highly empirical and dependent upon large databases, work such as that by Rodopoulos et al. [60] has endeavored to develop scientifically based optimization procedures for shot peening of aluminium alloys. Their approach treats residual stress profiles, work hardening profiles, and surface roughness as the major parameters which control the final fatigue life improvements. The methodology also predicts crack-closure stress profiles to address the early statges of crack propagation [61]. The surface roughness due to shot peening is treated in terms of elastic stress concentration based on surface roughness

measurements. The authors also acknowledge that shot peening has been reported to produce distortion of the near surface microstructure, but such an effect was not considered in their process optimization modeling. The results of the optimization process produced shot-peening conditions that showed a significant improvement in the fatigue life of a 2024-T351 aluminium alloy, but the benefits were mainly in the LCF regime. The life improvement was attributed to a prolonged period of crack arrest. The benefits in the HCF regime, where crack growth is a go, no-go situation, were much less obvious. As pointed out previously, "beneficial effects" have to be examined in terms of the life range in the *S–N* curve where such observations are made.

One of the more significant observations in [60] is the relaxation of the residual stresses during fatigue cycling. An example of such reduction for two values of applied stress under the same shot-peening conditions is shown in Figure 8.60 from that reference. It is noted in this and other examples given in [60] that the relaxation of the residual stresses seems to depend on the applied stress while the basic shape of the residual stress profile remains unaffected. The authors caution, therefore, that credit for residual stresses as a far-field parameter in terms of $\Delta\sigma_{\text{eff}}$ should be avoided since it will overestimate the true effect of the residual stresses because of the relaxation of the stress field.

8.6.3. Deep residual stresses

The realization that a compressive residual stress layer at the surface can improve the fatigue properties of a material, particularly by retarding crack growth, has encouraged the development of processes where the depth of the layer has been increased over that obtained with conventional shot peening. The concept of a deeper layer is related to the length of crack that may be retarded by having residual stresses that go deeper into the material. In airframe applications where holes are expanded in order to produce a compressive residual stress field around the hole, the length of crack that has to be considered in a damage tolerant analysis can be increased over that used in analysis on an untreated hole. Thus, as compressive residual stresses are imparted deeper into a material, the resistance to crack propagation is improved for longer crack lengths. An investigation into the fatigue behavior of Ti-6Al-4V subjected to deep rolling and laser shock processing (LSP) was conducted by Nalla et al. [62] at both ambient and elevated temperatures. Deep rolling, as used in that investigation, involved high pressures on a spherical rolling element that produces surface plastic deformation from which deep compressive residual stresses and a work-hardened surface layer are induced. LSP, another method of inducing deep compressive residual stresses, is discussed in more detail below. For both procedures, the residual stress field was more than 0.5 mm deep. For the specific process parameters and test specimen geometry used, deep rolling produced more intense compressive residual stresses as well as a higher degree of work hardening. Both processes produced enhanced HCF resistance at ambient temperature that was attributed

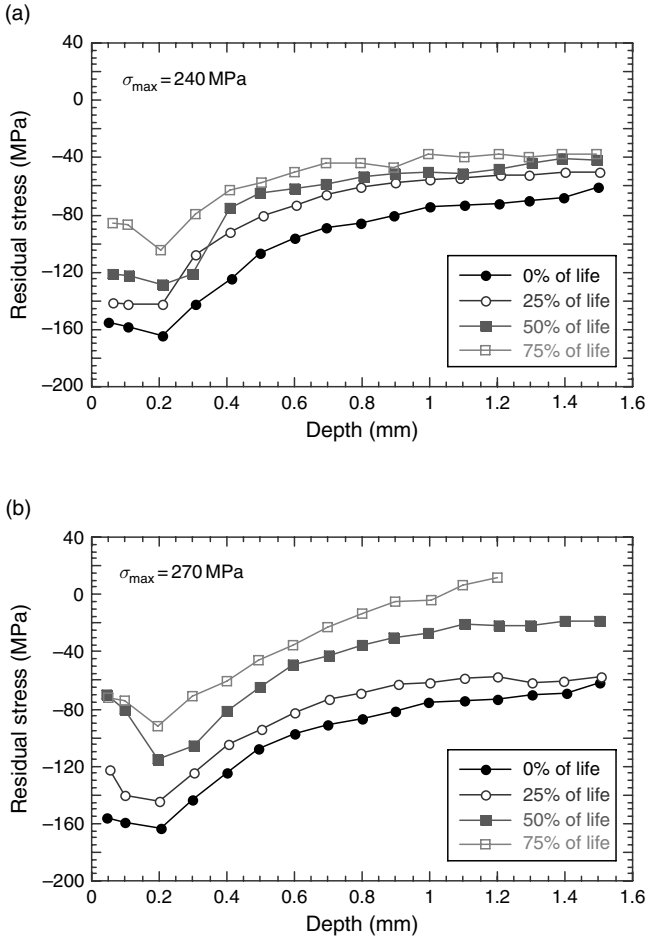


Figure 8.60. Residual stress relaxation pattern in an aluminium alloy at a maximum stress of (a) 240 MPa, (b) 270 MPa (from [60]).

to both the deep residual stress field and the formation of a work-hardened near-surface layer. At elevated temperature, the near-surface compressive residual stresses were almost completely relaxed, but the fatigue properties were still enhanced, although not as much as at ambient temperature. The authors believe that the benefit at elevated temperature (450 °C) is associated primarily with the induced work-hardening near-surface layer that is particularly stable, even at high temperature. In this particular example, as well as in carbon steel discussed earlier [53], the beneficial effects of surface treatments are not associated solely with the residual stress fields that are produced in shallow as well as deep layers near the surface.

It is of interest to note that processes such as laser shock processing (LSP), where deep compressive residual stresses are induced into the surface region of a material, were originally thought to derive their benefits from changes in the material. Early theories assumed that the increases in fatigue performance were due to work hardening effects, but gradually it became apparent that LSP-induced compressive residual stresses were also a contributing, if not dominating, factor [63].

In the discussions above, no mention has been made of the effects of defects on the fatigue properties in surface-treated specimens or components. It has been noted that fatigue failures in compressively loaded components such as ball or roller bearings can be traced to the presence of defects such as slag inclusions in steels. Almen and Black [50] comment on this type of failure in the following:

> From previous experience, it is known that fatigue cracks could be caused only by tensile stresses, but the tensile stress in bearing contacts, as calculated by the Hertzian equation, was too low to cause fatigue cracks. …it became clear that microresidual tensile stresses of great magnitude were developed in the steel adjacent to the slag inclusions, voids, and similar defects. …
>
> Residual tensile stress develops in such local, compressively deformed metal because the adjacent sound metal does not suffer such plastic deformations and therefore recovers elastically when the elastic load is removed. The drastically deformed metal does not so recover but is forceably restored to nearly its original dimensions by the greater volume of elastically recovered metal. The result is high-magnitude residual tensile stress adjacent to the inclusion. The stress in this small volume of steel ranges from high-magnitude residual tensile stress when no external load is acting to compressive stress when external load is applied. These repeated tensile stresses eventually result in fatigue cracks that grow at acute angles to the surface and form the well-known but variously named pits, flakes, spalls, or cavities that destroy ball bearings, roller bearings, cams, railroad rails, and probably gear teeth.

8.6.3.1. Application to an airfoil geometry

In recent years, surface treatments that impart residual stresses much deeper into the surface than conventional shot peening have been studied in specific geometries and applications. The approaches in both understanding and modeling have followed much of the work on shot peening, described above in Section 8.6.2. For example, the beneficial effects of LSP in a simulated airfoil geometry were demonstrated in a study on Ti-6Al-4V [64, 65]. The results of those investigations are presented here in detail because they provide a representative example of many features that are involved in the use of deep compressive residual stress fields, irrespective of the process used to induce them into a component. In the investigations of Ruschau et al., LSP, developed in the 1970s as a fatigue-enhancement surface treatment for metallic materials (see [66] for example), was used as the method for introducing deep compressive residual stresses into a simulated

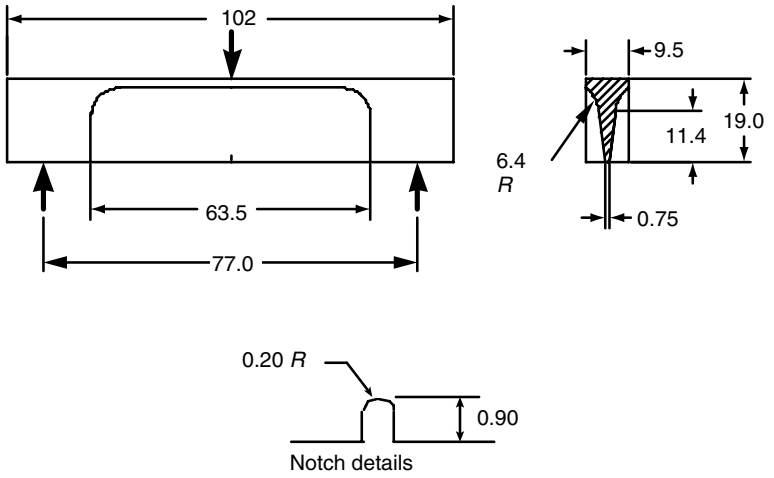


Figure 8.61. Geometry of 3-point bend airfoil specimen (dimensions in mm).

airfoil leading edge geometry. A unique 3-point bend test specimen, shown in Figure 8.61, was designed and employed to study the effect of LSP on the FCGR properties of Ti-6Al-4V. The specimen had a typical airfoil leading edge thickness of 0.75 mm and an overall cross section that included sufficient area to counterbalance the residual compressive stresses that developed due to the LSP treatment along part of the leading edge. The back edge of the sample (opposite the leading edge) was considerably thicker to provide constraint as well as to prevent buckling during the 3-point bend loading. Finally, the cross section of the sample was sufficiently tapered so that fatigue crack growth information could be obtained both from regions containing through-thickness residual compressive stresses, as well as in sections where the compressive stresses were not completely through the thickness. This is of particular concern in airfoil applications because, as the thickness increases away from the edge, a tensile residual stress or reduced compressive stress region may be present near the centerline, possibly compromising any benefits created by LSP.

The actual shock processing, conducted by LSP Technologies, Inc., consisted of approximately 13 hits or strikes that produced a laser spot pattern as shown in Figure 8.62. The resulting *surface* residual stress field is shown in Figure 8.63 as a function of distance from the leading edge in the direction of crack growth (y). These measurements were made using conventional X-Ray diffraction (XRD) techniques and, in the case of titanium, interrogate a surface layer of approximately 10 μm thickness. The average compressive stress in the x direction (σ_x), perpendicular to the crack plane, is approximately 850 MPa at the specimen surface and is reasonably constant throughout the LSP processed region over an area beginning $\approx$ 1–2 mm back from the leading edge. Near the leading

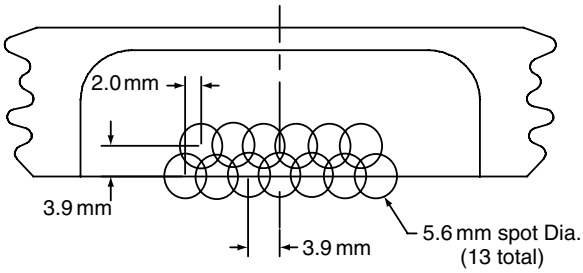


Figure 8.62. Laser spot pattern.

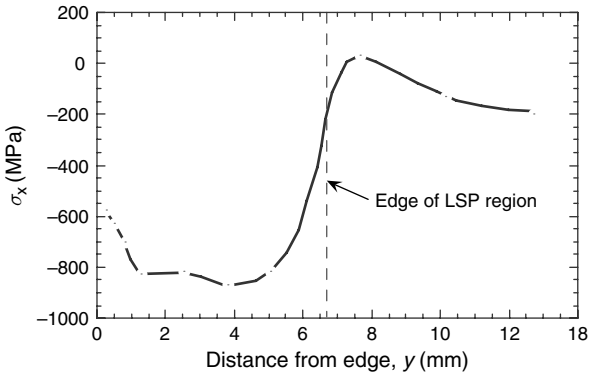


Figure 8.63. Surface residual stresses for an LSP sample along the direction of crack growth (at $x = 0$).

edge, the residual surface stresses are significantly lower as a result of lack of constraint at the free edge of the sample. Likewise at the back edge of the LSP region ($y \approx 7$ mm), the compressive *surface* stresses drop rapidly to zero, and become tensile just outside of the LSP processed region. The compressive surface stresses measured well outside the LSP region (i.e. 8–14 mm from edge) are believed to be attributable to low stress grinding operations used in specimen fabrication. Residual stresses measured at the surface in the direction perpendicular to the direction of loading (σ_y) were minimal due to the narrow LSP processed region as well as the lower constraint at the leading edge where the free surface requires $\sigma_y \cong 0$.

Residual stress into the depth was examined at two locations in the LSP processed area, and the resulting stress profiles are shown in Figure 8.64 for two locations, 0.5 and 5 mm from the leading edge. A compressive stress field is evident throughout the sample thickness at both locations, dropping from a peak compression of 600–800 MPa at the surface to a minimum compressive stress of 200 MPa at the interior. Notice that at both locations the peak compression at the surface decays to the lesser value over a depth of

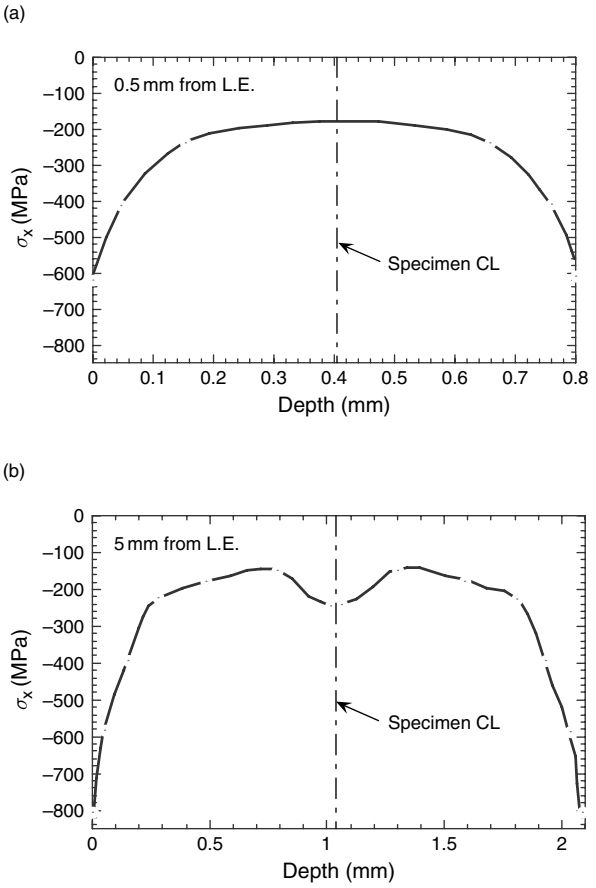


Figure 8.64. Through-thickness residual stress profile for an LSP sample as a function of depth; (a) stress profile 0.5 mm from leading edge; (b) stress profile 5 mm from leading edge.

approximately 0.2 mm. At the 5 mm location where the sample thickness is approximately 2 mm, the magnitude of the compressive stress field increases slightly at the center of the sample.

To compare crack growth characteristics of a treated sample with those of an untreated sample, fatigue testing of the simulated airfoil samples was carried out under 3-point bend, constant amplitude (CA) loading (see Figure 8.61). To examine mean stress effects, two stress ratios (R) were examined: $R = 0.1$ and 0.8. Crack initiation and growth was monitored on all samples using an electric potential difference (EPD) technique where crack length changes of typically 2–3 μm were readily detected.

An equation was developed using the results from a 3-dimensional elastic finite element analysis of the geometry and loading conditions shown in Figure 8.61 and is valid for all $a/W \leq 0.6$. Using the strength of materials equation for bending stress,

$$\sigma = Mc/I \tag{8.11}$$

where $M =$ bending moment (one-half of the applied load $\times$ one-half the support span), $c =$ distance from the centroid of the cross section to the leading edge, and $I =$ moment of inertia of the specimen cross section. The K solution for this specimen is found to be:

$$K = \sigma\sqrt{\pi a} f(a/W) \tag{8.12}$$

$$f(a/W) = \frac{1.1215 - 5.0402(a/W) + 14.4979(a/W)^2 - 22.0211(a/W)^3 + 12.9270(a/W)^4}{[1-(a/W)]^{3/2}} \tag{8.13}$$

where a is the crack length measured from leading edge, and W is the total height of the specimen (19 mm).

The crack growth response of a non-processed airfoil sample, as well as from a standard C(T) sample, were obtained at both $R = 0.1$ and $R = 0.8$. The results from the two sample types agreed reasonably well and are denoted as "baseline" hereafter.

The FCGR results for the LSP samples at $R = 0.1$ are presented in Figure 8.65 (solid symbols), along with the curve representing the baseline data and closure-corrected data (open symbols), discussed later. Data obtained from the LSP samples clearly demonstrate a significant advantage in FCGR resistance over baseline material when plotted as a function of applied ΔK. Growth rates for the LSP samples in the range of ΔK of 30–40 MPa$\sqrt{\text{m}}$ are nearly three orders of magnitude slower than for the unprocessed material; however, as the applied maximum stress intensity factor approaches the fracture toughness of the material the two data sets appear to converge.

For the purpose of comparing results from baseline and LSP samples, compliance measurements were made to evaluate crack closure levels and thus compute the effective crack driving force. For the baseline samples, the compliance traces appear linear over a wide range of crack lengths, indicating no apparent evidence of crack closure. The compliance traces for LSP samples, on the other hand, displayed clear evidence of crack closure. For the tests at $R = 0.1$, the opening load value, P_{open}, corresponding to the fully opened crack tip was approximately 80% of the maximum applied load throughout the LSP region. Outside the LSP region (corresponding to crack lengths in excess of 7 mm) the closure levels began to drop off drastically. The magnitude of the residual compressive stress field is directly responsible for the degree of crack closure observed.

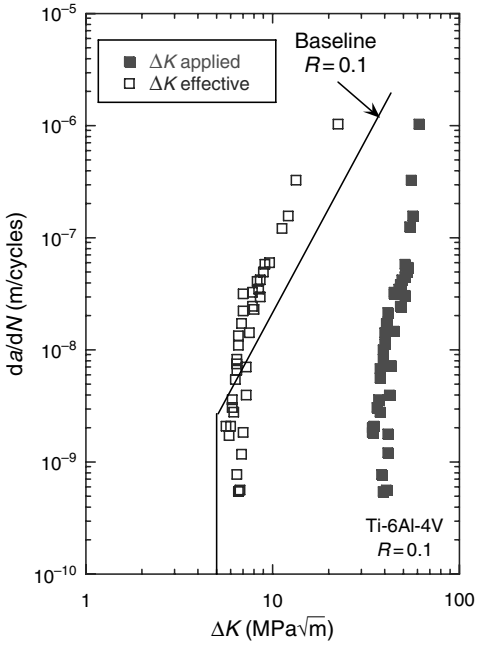


Figure 8.65. The FCGR data for LSP samples at $R = 0.1$ as a function of ΔK and ΔK_{eff}.

Using this opening load and conventional closure concepts to define an effective stress intensity range, ΔK_{eff}, the $\mathrm{d}a/\mathrm{d}N$ data for different stress ratios can be consolidated into a single curve. This value of ΔK_{eff} is defined simply as:

$$\Delta K_{\text{eff}} = K_{\text{max,applied}} - K_{\text{open}} \tag{8.14}$$

In the absence of closure, K_{open} equals the minimum applied K, and hence the applied ΔK is equal to ΔK_{eff}.

The LSP crack growth data in Figure 8.65 were corrected for crack closure by using the experimentally measured values of P_{open}. The data then shift to the left and fall reasonably along the baseline curve at $R = 0.1$ which displayed little or no closure. The enhanced FCGR resistance for LSP processed material can be attributed to a superimposed residual stress field shielding the crack tip, producing crack closure.

The results of LSP samples tested at $R = 0.8$ are presented in Figure 8.66 along with the baseline curve for the same stress ratio. Advantages in the FCGR resistance of LSP at this higher value of R clearly diminish and, in fact, disappear completely since the data fall along the trend line for the baseline material. Compliance traces obtained at $R = 0.8$ were linear throughout the entire loading range, suggesting that no closure is present. The advantages of LSP do not appear at the higher stress ratio since, for any stress ratio, once

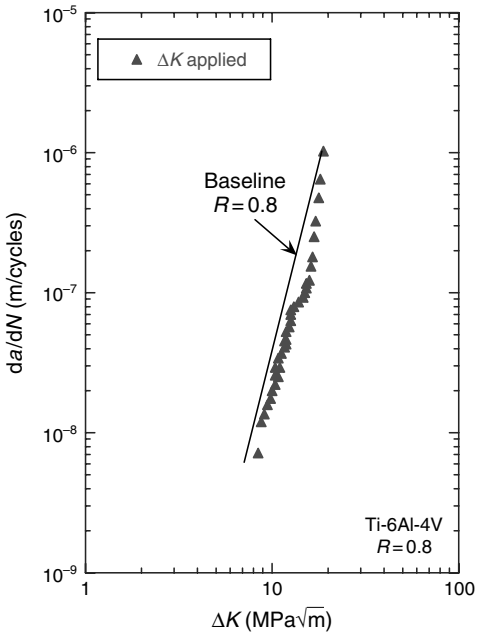


Figure 8.66. The FCGR data for LSP samples at $R = 0.8$.

the minimum stress in the loading cycle equals or exceeds the stress due to the residual stress field created in the LSP process, crack growth rates are unaffected.

It must be noted that in correcting crack growth rate data for closure, it is inherently assumed that stress ratio has no measurable effect on the growth rate, that is ΔK is the sole correlating parameter. Thus, for the case of an applied ΔK at $R = 0.1$ in an LSP sample, closure at 80% of maximum load would correspond to an effective $R = 0.8$. The data obtained in the reported investigation, represented by the baseline curves in Figures 8.65 and 8.66, show that tests at either $R = 0.1$ or $R = 0.8$ produce no significant degree of closure and produce comparable growth rates, thereby validating the use of a closure correction for the LSP data.

The beneficial effects of surface treatments can be quantified with the aid of fracture mechanics. If residual stresses are present, they produce a residual stress intensity factor, K_{res}, at the crack tip that can be calculated using methods such as weight functions (see below). In the absence of other closure-related mechanisms, the effective values of K at maximum and minimum loads are given by:

$$\begin{aligned} K_{\text{max,eff}} &= K_{\text{max,applied}} + K_{\text{res}} \\ K_{\text{min,eff}} &= K_{\text{min,applied}} + K_{\text{res}} \end{aligned} \tag{8.15}$$

and an effective stress ratio can then be defined as:

$$R_{\text{eff}} = \frac{K_{\text{min,eff}}}{K_{\text{max,eff}}} \tag{8.16}$$

Note that in this case, ΔK does not change due to residual stresses, but R_{eff} decreases if K_{res} is a negative number. Since the residual stresses are compressive, the computed K_{res} is negative. While it should be recognized that K_{res} being negative has no formal meaning, a negative K_{res} is used to represent the contribution of the compressive loading across the crack surfaces. This, in turn, is added to the K of the applied loading. If closure is observed at a given crack length, then the measured value of P_{open} corresponds to the point where K_{min} overcomes K_{res}.

In the reported investigation, at the higher stress ratio test condition,

$$R_{\text{applied}} = \frac{K_{\text{min}}}{K_{\text{max}}} \tag{8.17}$$

and

$$K_{\text{min}} = 0.8K_{\text{max}} \tag{8.18}$$

Since closure was absent in the load-displacement traces at $R = 0.8$, with or without LSP, then,

$$K_{\text{min}} + K_{\text{res}} \geq 0 \tag{8.19}$$

and, therefore, combining Equations (8.18) and (8.19) yields:

$$K_{\text{res}} \geq -0.8K_{\text{max}} \tag{8.20}$$

Equation (8.20) implies that the magnitude of K_{res} is less than or equal to 80% K_{max} during the $R = 0.8$ test. For the case of $R = 0.1$ testing where K_{max} is the same as the $R = 0.8$ test, it follows from Equations (8.15) and (8.16) that:

$$R_{\text{eff}} = \frac{0.1K_{\text{max}} + K_{\text{res}}}{K_{\text{max}} + K_{\text{res}}} \tag{8.21}$$

and

$$R_{\text{eff}} = \frac{0.1K_{\text{max}} - 0.8K_{\text{max}}}{K_{\text{max}} - 0.8K_{\text{max}}} \tag{8.22}$$

or

$$R_{\text{eff}} \approx -3.5 \tag{8.23}$$

Note that R_{eff} equal to -3.5 is a limiting value or *upper bound* (in magnitude) because it is based on the assumption of $K_{\text{res}} = -0.8K_{\text{max}}$ [Equation (8.20)]. The above calculations imply an apparent closure level of $\approx 80\%$ during crack growth with $R_{\text{eff}} \approx -3.5$ at the crack tip.

It is important to point out that closure contributions at a certain value of K, and residual stresses producing a value of K at the crack tip, are different and independent concepts. The effect of closure, quantified by Equation (8.14), reduces the range of ΔK whereas residual stresses reduce the mean stress. The behavior of a cracked specimen that has a residual stress can be further understood with the aid of Figure 8.67 where compliance curves are shown for a material that exhibits no crack closure in (a) and for a material having a closure or opening value, K_{op}, as shown in (b). In both cases, curves denoted by "A" represent the cracked body with no residual compressive stresses. Curves "B" and "C" depict the behavior for two different degrees of residual stress producing a calculated K_{res} of magnitudes $K_{\text{res},1}$ and $K_{\text{res},2}$. From Equation (8.15), the compliance curves are shifted in the negative K direction by different magnitudes. For the material with no closure in (a), the point where the resultant value of K is zero represents the point in the compliance curve where the slope will change. The portions of the compliance curves that are dashed, for "negative K," have no meaning in terms of K and will have slopes in the dashed regions corresponding to a closed crack. In terms of applied load, the apparent closure load will be some fraction of the total applied load. If the material exhibits crack closure as depicted in (b), the superposition of residual K will produce compliance curves as shown. In case B, the inherent closure of the specimen is at a higher K than the closure produced by the residual stresses. In case C, however, the residual

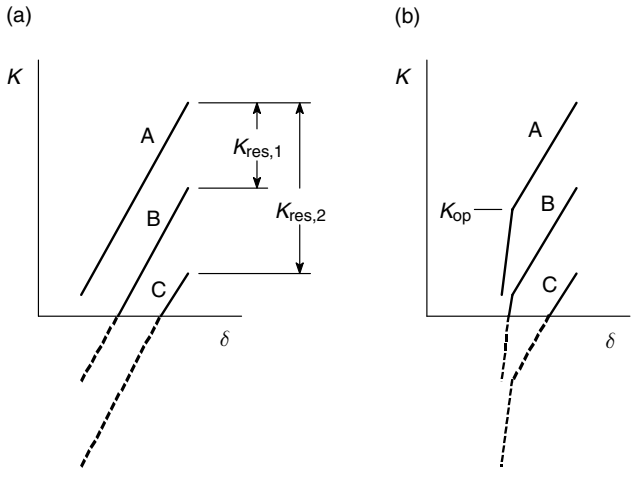


Figure 8.67. Schematic diagram of compliance curves for (a) closure free specimen, (b) specimen with crack closure.

stress produces an apparent closure at $K_{\text{eff}} = 0$ such that the material closure is at a lower load level and would not be detected. In this case, as in the previous one, negative values of K have no physical meaning and the compliance below $K = 0$ is simply that of an uncracked body. It should be recognized that the superposition of K_{res} and K_{applied} only has physical meaning if the crack is open at all points along the crack face. If the crack is closed, the linear superposition of Equation (8.15) is no longer valid and the mathematical quantities obtained for negative values of K are incorrect. The computations of negative values of R for crack growth analysis are also of dubious value or have little physical meaning. Note also, in the compliance curves shown schematically in Figure 8.67, the top and bottom of each curve corresponds to the maximum and minimum applied load, respectively. Thus, the point where the effective value of K becomes negative has to be considered with respect to where it occurs on the applied load cycle.

8.6.3.2. Crack arrest

In the discussion above of crack growth behavior, the load levels applied to obtain continuous crack growth were of a sufficient magnitude to avoid crack arrest as depicted earlier in Figure 8.48. In many of the experiments performed by Ruschau et al. [64, 65], the crack growth behavior of an LSP sample indicated that cracking initiated under similar loading levels as those of the baseline samples, grew a short distance, then arrested as shown in Figure 8.68. This crack arrest behavior for LSP samples required that the maximum cyclic stress had to be increased (5–10%) in order to re-initiate cracking. Again, this re-initiated crack often arrested after minimal growth, forcing the continual process of increasing the peak cyclic stress to re-propagate the crack until steady state crack growth eventually took place and the crack propagated to failure.

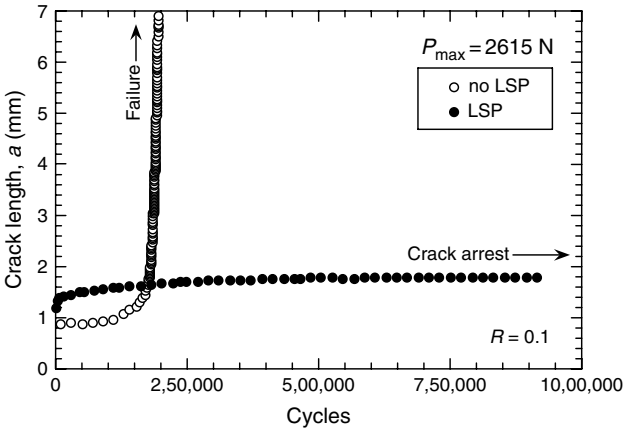


Figure 8.68. Crack length vs cycles data for baseline and LSP samples.

The crack arrest behavior can be attributed to large compressive residual stresses in the LSP region which display a steep gradient near the leading edge, increasing in intensity a short distance from the leading edge as illustrated in Figure 8.63. For a propagating crack, as discussed above, this non-uniform stress field results in a residual compressive stress field at the crack tip and hence an effective compressive stress intensity, K_{res}, that increases in absolute value with increasing crack length, thus producing crack arrest. For crack growth to continue, the applied maximum stress intensity, K_{max}, at the crack tip must exceed K_{res} as well as the inherent threshold stress intensity range, ΔK_{th}, of the material. The sequential growth and arrest behavior can be explained with the aid of Figures 8.69 and 8.70 which were constructed using the stress intensity solution for the airfoil geometry, Equations (8.12) and (8.13), and an expression for K_{res}. The latter could be derived, in principal, from the residual stress profiles shown in Figures 8.63 and 8.64 and a lot of interpolation, taking into account the three-dimensional nature of the problem due to the increase in specimen thickness with increasing crack length (see Figure 8.61). Instead, Figures 8.69 and 8.70 are constructed using some numerical simulations that include a crude approximation of the residual stress profile deduced by Lykins and John [67] for the same airfoil geometry and the same material used by Ruschau et al. These figures are discussed later.

In [67], as in [64], crack arrest occurred when the crack was in the LSP processed region, requiring an increase in load to continue the crack growth. The sequence of crack growth and arrest that was obtained with incremental increases in the applied load is shown in Figure 8.71, where the dashed line represents the experimental observations. From numerous measurements of the applied load and crack length where arrest occurred, Lykins and John [67] were able to calculate the value of the applied K at that point. Then, having data for the threshold stress intensity for the corresponding values of R, the

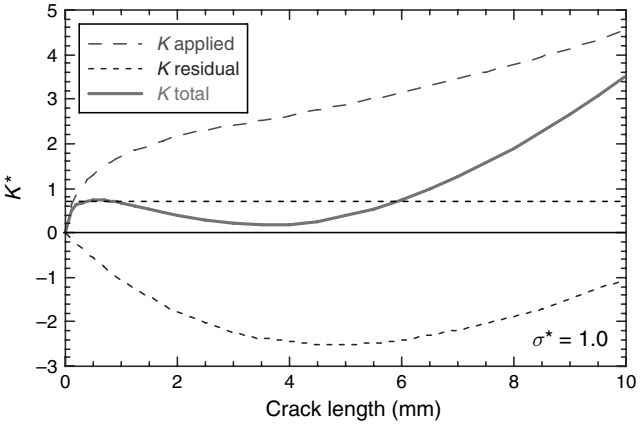


Figure 8.69. Dimensionless K for airfoil specimen for applied stress $\sigma^* = 1$.

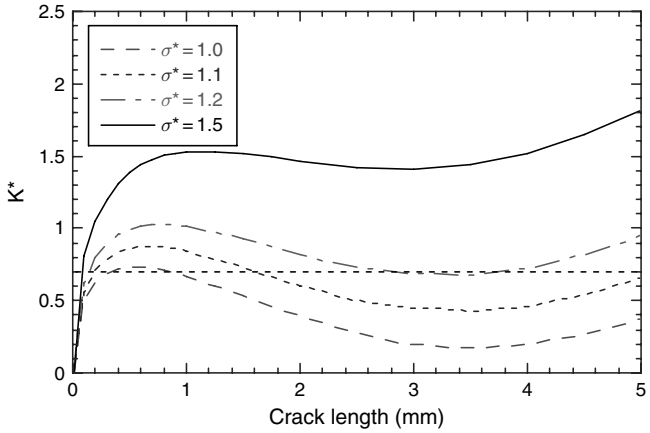


Figure 8.70. K values for several applied load levels in airfoil geometry.

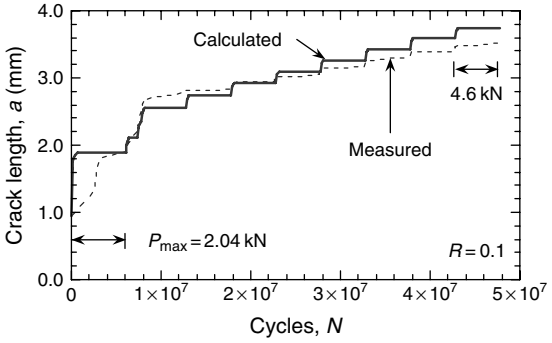


Figure 8.71. Crack growth behavior in airfoil geometry with LSP.

value of K_{res} was computed at that threshold condition. From this, a curve of K_{res} against crack length was deduced and subsequently used to predict the growth rate behavior using a da/dN curve having the appropriate threshold value. The approach taken and the numerical results are shown in Figure 8.72 which utilizes a value of K_{th} from other experiments. The curve indicated as "calculated K_{res}" is a visual best fit to the computed values of K_{res} over the range in crack lengths for which data were obtained. Using this curve and a fit to da/dN data, the growth rate/arrest behavior, shown in Figure 8.71, was well predicted.

Using a very crude approximation to the shape of the K_{res} profile from [67] and the K solution for the airfoil, Equations (8.12) and (8.13), some numerical simulations are presented to illustrate the growth/arrest behavior that can occur within a compressive residual stress field. In Figure 8.69 the shape of the applied, residual, and total stress

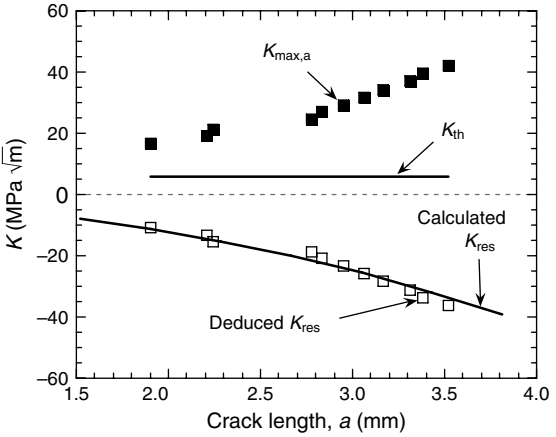


Figure 8.72. Maximum applied and residual K versus crack length.

intensity are shown. The values of stress and K are presented in a dimensionless form and no attempt is made to use real numbers in this illustrative example. Additionally, a dimensionless value of the threshold stress intensity is shown as a dashed line corresponding to an arbitrarily chosen value of $K^* = 0.7$. For the numbers chosen, the total stress intensity barely exceeds the threshold at a crack length in the vicinity of $a = 1$ mm. At a slightly longer crack length, if the crack could have been started at that crack length with a precrack or starter notch, the crack would be expected to arrest since the applied stress intensity then dips below the threshold. The same scenario is depicted in Figure 8.70 in a slightly expanded scale. Here, in addition to the total stress intensity at a dimensionless stress (or applied load) of $\sigma^* = 1$, the total K is shown for values of $\sigma^* = 1.1$, 1.2, and 1.5. At $\sigma^* = 1$, crack arrest is expected at a length of approximately 0.8 mm. If the load is increased to $\sigma^* = 1.1$, the crack should resume propagation until it reaches a length "a" approximately 1.6 mm. Further increase in load to $\sigma^* = 1.2$ should produce continued crack propagation until a length of about 3 mm where the crack barely arrests. If the applied load is $\sigma^* = 1.5$, no crack arrest should occur once the crack has been started. This is equivalent to the case cited above where crack growth data were obtained throughout a test on an LSP sample.

8.6.3.3. Crack growth retardation

Another example of the use of compressive residual stresses to retard crack growth is found in the work of Kang et al. [68] who used residual stresses from welding to retard crack growth in edge cracked specimens of a structural steel. They evaluated two methods for evaluating ΔK_{eff} in the presence of a residual stress field. The first, defined as the R' method, considers ΔK and R to be determined from the applied K values and the

computed K_{res} as shown in Equations (8.15) and (8.16). The value of K_{res} as a function of crack length, a, is found from the conventional weight function method as

$$K_{res}(a) = \int_0^a \sigma_{res}(x) p(x, a)\, dx \tag{8.24}$$

where $p(x, a)$ is the weight function for the specific geometry used and $\sigma_{res}(x)$ is the initial residual stress field in an unflawed specimen. It is important to point out that the computations are valid only when the entire crack is open under the total loading, that is the stress field due to the applied load plus the residual stress field.

The second method used in [68] involved the use of experimental closure (or crack opening) measurements to determine the effective value of K. The two methods, based on calculations of K_{res} and K_{op}, were used to compare experimental crack growth rate measurements. It was found that, in the region where the residual stresses changed sign from compression to tension, the R' method gave non-conservative results in comparing experimental crack growth rates to predicted values. The predictions, based on measured values of K_{op}, were also not very good unless the load-displacement traces, used to determine K_{op}, were interpreted to distinguish between the opening and the closing portion of the cycle. The authors concluded that the behavior of the crack, in the region where the residual stress field went from compression to tension, involved a partial opening of the crack. This would violate the assumption of a fully open crack in the calculations of the value of K_{res} as indicated above. Their speculation centers around the correct determination of the opening load when the load-up and unload traces are slightly different in the compliance measurements.

In determining thresholds for high cycle fatigue, it is important to recognize the limitations of the approaches for determining the effective value of K in crack growth analysis. This, in turn, creates concerns in applying these approaches to the threshold condition for long life (crack arrest) based on experimental measurements on a specimen or component that has been subjected to a residual compressive stress field.

8.6.3.4. A numerical example

We conclude the discussion of the use of compressive residual stresses in retarding or arresting cracks with some simple numerical examples of a two-dimensional body with a crack growing from the edge from applied far-field loads. In addition to the applied K, a residual K will reduce the total K depending on the residual compression induced in the specimen. We specifically examine the effects of the depth of the residual stress field and the shape. For this purpose, we take two depths, 0.1 and 1 mm, and two shapes, uniform and triangular, as depicted in Figure 8.73. The shallow depth is representative of a typical magnitude imparted by conventional shot peening while the deeper residual stresses are representative of methods such as LSP or LPB or deep roller burnishing. The triangular profile is a more realistic representation of what has been measured for the

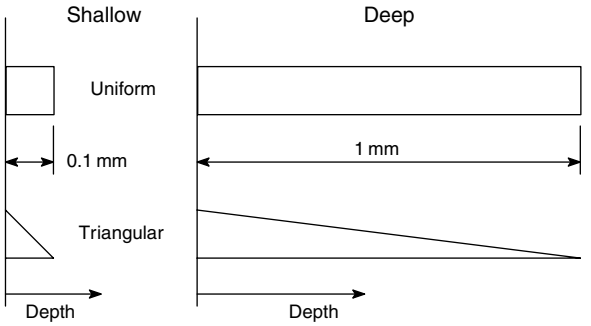


Figure 8.73. Profiles of residual stress fields used in numerical examples.

residual stress field rather than the uniform stress which is a mathematical approximation in some analyses.

The residual K values for the stress profiles of Figure 8.73 are shown in Figures 8.74 and 8.75 for a residual stress amplitude (maximum) of 100 MPa for the shallow and deep profiles, respectively. Both stress and K are shown here as positive values but for residual compressive stresses, the stresses are negative as are the values of K. These are only mathematical values of K and although they are negative, they are to be subtracted from the values of K for the applied stresses. Figure 8.74, for the shallow residual stresses, shows that the residual K peaks at about the depth of the stress profile (0.1 mm) for the uniform stress while K peaks at a value of about half of that for the triangular profile. For the deep stress profile, the identical trends are observed. In fact, if the depth is made dimensionless by using a/t, where t is the total thickness, or by using a/d where d is

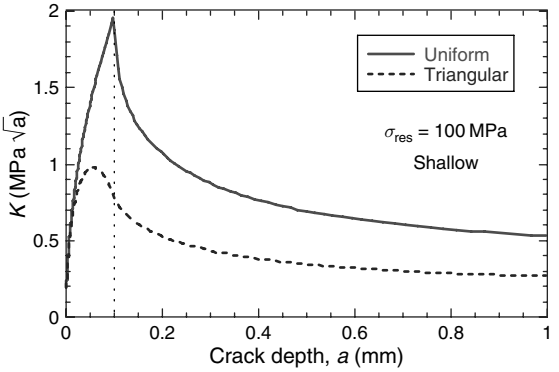


Figure 8.74. Residual K from the residual stress fields of Figure 8.73 for shallow residual stress profile, $\sigma_{res} = 100$ MPa.

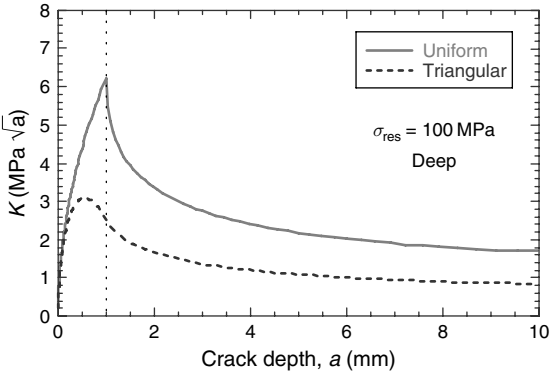


Figure 8.75. Residual K from the residual stress fields of Figure 8.73 for deep residual stress profile, $\sigma_{res} = 100\,\text{MPa}$.

the depth of the residual stresses, then the plots are identical. For K, the numerical values are proportional to $\sqrt{a}$. Figures 8.74 and 8.75 are identical, then, if K values are reduced by $\sqrt{10}$ and "a" is normalized to a/d. In both cases, the residual stresses continue to have an effect on the residual K for depths far beyond the depth of the stress profile. It is often (mistakenly) assumed in the literature that the crack is retarded only when it is in the residual stress field. These computations illustrate that it is the value of K, not the stress field at the crack tip, that retards crack growth. As noted previously, the K calculations are valid only for a fully open crack and become invalid when the residual K (compression) exceeds the applied K (tension).

8.6.4. Autofrettage

We conclude the discussion of residual stresses with some comments and observations on autofrettage, a metal fabrication technique in which the stock is momentarily subjected to enormous pressure. Also known as strain hardening, the goal of autofrettage is to increase the resistance to fatigue, either crack initiation, or crack propagation, of the part. The technique is commonly used in the manufacture of high pressure pump cylinders, battleship cannon barrels, and fuel injection systems for diesel engines. Autofrettage became an important consideration during World War II when it was first used in the production of large numbers of cannon by the US Army.

The pressurization of a cylinder can provide beneficial effects in fatigue by either inducing residual compressive stresses at the inner diameter or through the process of strain hardening the material in the same region. In both cases, the material has to be deformed beyond the elastic limit. The stresses in a cylinder due to internal pressure are easily computed for the elastic case from well-known equations in the theory of elasticity

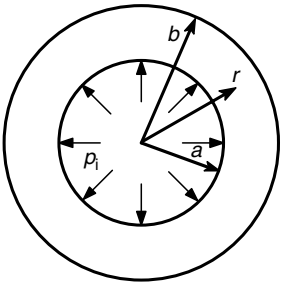


Figure 8.76. Schematic diagram of hollow cylinder with nomenclature.

such as found in [69]. Denoting the internal pressure by p_i, the radial position by r, and the dimensions of the cylinder as shown in Figure 8.76, the hoop stresses are

$$\sigma_\theta = \frac{a^2 p_i}{b^2 - a^2}\left(1 + \frac{b^2}{r^2}\right) \tag{8.25}$$

Theses stresses are plotted in Figure 8.77 for several different ratios of b/a, the ratio of the outer to inner diameter of the cylinder. From both the plot as well as from the equation, it is readily seen that the maximum hoop stress is at the inner diameter. The magnitude of this maximum stress is

$$\sigma_{\theta,\max} = \frac{p_i(a^2 + b^2)}{(b^2 - a^2)} \quad \text{at} \quad r = a \tag{8.26}$$

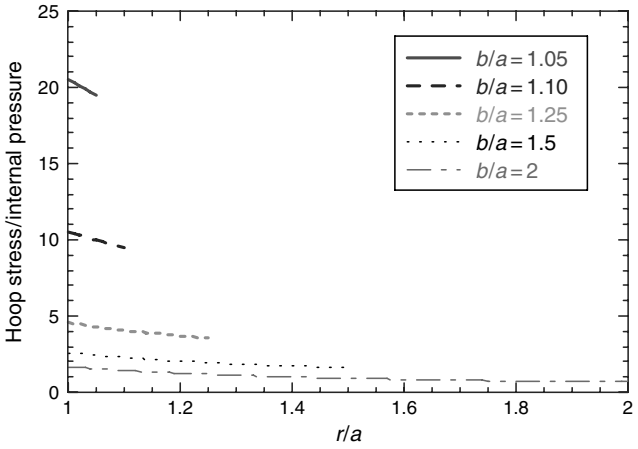


Figure 8.77. Normalized hoop stresses for cylinder with internal pressure.

It is clear, then, that if the pressure is sufficient to cause yielding of the cylinder due to hoop stresses beyond the elastic limit, this yielding will take place first at the inner diameter.

The residual stress state that results from plastic straining will depend on the cylinder geometry, material strain-hardening characteristics, unloading behavior of the material, and the level of strain hardening imposed. A typical circumferential stress state near the inner diameter (see [70] for example) is depicted schematically in Figure 8.78 where the tensile stresses due to loading are added to the residual stresses, the latter being compressive. The net stresses can then be used to calculate the resultant value of K, the stress intensity, using methods such as weight functions as done in [70]. In that article, the authors point out that the computed stress intensity is the sum of the contributions due to the internal pressure loading, the residual stresses, and the internal pressure acting on the crack faces. The resulting values of K can be as depicted schematically in Figure 8.79 where the value of K decreases with increase in crack length near the inner diameter. Thus, it is possible for a crack to initiate but arrest due to the decrease in K with crack length as depicted. As long as the stress intensity is below threshold, there should be no further crack extension.

In determining the threshold for crack propagation, two issues should be considered. First, it should be established whether the applied cyclic loading is in the LCF or HCF regimes. If it is in HCF, involving very large cycle counts, then the use of ΔK_{th} is warranted. On the other hand, if the loading is LCF involving a low number of cycles such as start up and shut down of a mechanical system, then the use of ΔK_{th} can be conservative because ΔK_{th} typically corresponds to a growth rate of 10^{-10} m/cycles (see Section 8.4). A value of ΔK corresponding to a higher growth rate would suffice, provided that the total crack extension during LCF was within acceptable limits. The second issue,

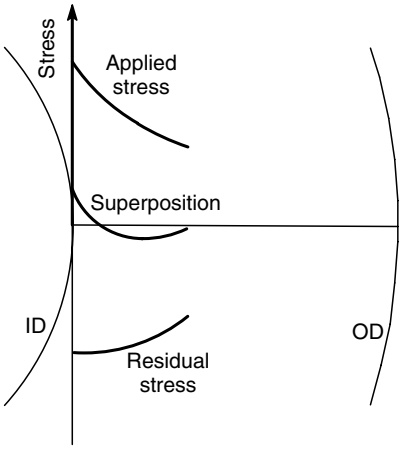


Figure 8.78. Schematic diagram of stresses near inner diameter of pressurized cylinder.

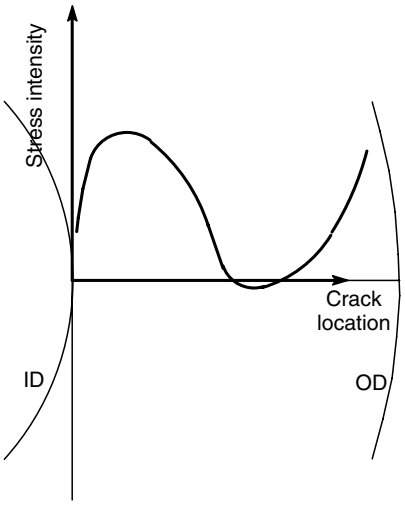


Figure 8.79. Schematic diagram of stress intensity in pre-stressed pressurized cylinder.

one that is normally neglected in design, is to use a value of ΔK_{th} that represents the threshold of the material that has been subjected to strain hardening. Since such data are rarely available, this procedure is normally not followed and the values of ΔK_{th} for the unstrained material are sufficient, if not conservative. From a technical point of view, the local strain hardening near the crack tip during crack growth far exceeds the strain hardening applied to the bulk material during the autofrettage process. Thus, the use of ΔK_{th} of the unstrained material is acceptable.

REFERENCES

1. Nicholas, T. and Maxwell, D.C., "Mean Stress Effects on the High Cycle Fatigue Limit Stress in Ti-6Al-4V", *Fatigue and Fracture Mechanics: 33rd Volume, ASTM STP 1417*, W.G. Reuter and R.S. Piascik, eds, American Society for Testing and Materials, West Conshohocken, PA, 2002, pp. 476–492.
2. Tabernig, B., Powell, P., and Pippan, R., "Resistance Curves for the Threshold of Fatigue Crack Propagation in Particle Reinforced Aluminium Alloys", *Fatigue Crack Growth Thresholds, Endurance Limits, and Design, ASTM STP 1372*, J.C. Newman, Jr., and R.S. Piascik, eds, American Society for Testing and Materials, West Conshohocken, PA, 2000, pp. 96–108.
3. Smith, S.W. and Piascik, R.S., "An Indirect Technique for Determining Closure-Free Fatigue Crack Growth Behavior", *Fatigue Crack Growth Thresholds, Endurance Limits, and Design, ASTM STP 1372*, J.C. Newman, Jr., and R.S. Piascik, eds, American Society for Testing and Materials, West Conshohocken, PA, 2000, pp. 109–122.

4. Haake, F.K., Salivar, G.C., Hindle, E.H., Fischer, J.W., and Annis, C.G., Jr., "Threshold Fatigue Crack Growth Behavior", WRDC-TR-89-4085, Wright-Patterson AFB, OH, October 1989 (ADA218063).
5. Larsen, J.M., Worth, B.D., Annis, C.G., Jr., and Haake, F.K., "An Assessment of the Role of Near-Threshold Crack Growth in High-Cycle-Fatigue Life Prediction of Aerospace Titanium Alloys under Turbine Engine Spectra", *Int. J. Fracture*, **80**, 1996, pp. 237–255.
6. Cowles, B.A., "High Cycle fatigue in Aircraft Gas Turbines – An Industry Perspective", *Int. J. Fracture*, **80**, 1996, pp. 147–163.
7. Nicholas, T. and Zuiker, J.R., "On the Use of the Goodman Diagram for High Cycle Fatigue Design", *Int. J. Fracture*, **80**, 1996, pp. 219–235.
8. Guedou, J.-Y. and Rongvaux, J.-M., "Effect of Superimposed Stresses at High Frequency on Low Cycle Fatigue", *Low Cycle Fatigue*, ASTM, Philadelphia, 1988, pp. 938–969.
9. Hawkyard, M., Powell, B.E., Husey, I., and Grabowski, L., "Fatigue Crack Growth under Conjoint Action of Major and Minor Stress", *Fatigue Fract. Eng. Mater. Struct.*, **19**, 1996, pp. 217–227.
10. Engine Structural Integrity Program (ENSIP), MIL-STD-1783 (USAF), 30 November 1984.
11. Morrissey, R.J., McDowell, D.L., and Nicholas, T., "Frequency and Stress Ratio Effects in High Cycle Fatigue of Ti-6Al-4V", *Int. J. Fatigue*, **21**, 1999, pp. 679–685.
12. Paris, P.C. and Tada, H., "Near Threshold Fatigue Crack Growth versus Long Finite Life", *Fatigue Fract. Eng. Mater. Struct.*, **25**, 2002, pp. 727–733.
13. Skorupa, M., "Load Interaction Effects during Fatigue Crack Growth under Variable Amplitude Loading – A Literature Review. Part I: Empirical Trends", *Fatigue Fract. Eng. Mater. Struct.*, **21**, 1998, pp. 987–1006.
14. Skorupa, M., "Load Interaction Effects during Fatigue Crack Growth under Variable Amplitude Loading – A Literature Review. Part II: Qualitative Interpretation", *Fatigue Fract. Eng. Mater. Struct.*, **22**, 1999, pp. 905–926.
15. Schütz, W., "A History of Fatigue", *Engng. Fract. Mech.*, **54**, 1996, pp. 263–300.
16. "Standard Test Method for Measurement of Fatigue Crack Growth Rates", *Annual Book of ASTM Standards*, E 647-91, 1991, pp. 654–681.
17. Döker, H., Bachmann, V., and Marci, G., "A Comparison of Different Methods of Determination of the Threshold for Fatigue Crack Propagation", *Fatigue Thresholds*, J. Backlund, A.F. Blom, and C.J. Beevers, eds, EMAS, Warley, UK, 1982, p. 45.
18. Castro, D.E., Marci, G., and Munz, D., "A Generalized Concept of a Fatigue Threshold", *Fatigue Fract. Engng. Mater. Struct.*, **10**, 1987, pp. 305–314.
19. Lenets, Y.N. and Nicholas, T., "Load History Dependence of Fatigue Crack Growth Thresholds for a Ti-Alloy", *Engineering Fracture Mechanics*, **60**, 1998, pp. 187–203.
20. Mall, S., Perez, J.A., and Nicholas, T., "Influence of Loading History on Fatigue Threshold Behavior in a Titanium Alloy", *Engineering Fracture Mechanics*, **37**, 1990, pp. 15–26.
21. Döker, H. and Bachmann, V., "Determination of Crack Opening Load by use of Threshold Behavior", *Mechanics of Fatigue Crack Closure, ASTM STP 982*, J.C. Newman, Jr., and W. Elber, eds, ASTM, Philadelphia, 1988, pp. 247–259.
22. Suresh, S. and Ritchie, R.O., "On the Influence of Fatigue Underloads on Cyclic Crack Growth at Low Stress Intensities", *Mater. Sci. and Engng*, **51**, 1981, pp. 61–69.
23. Ritchie, R.O., Boyce, B.L., Campbell, J.P., Roder, O., Thompson, A.W., and Milligan, W.W., "Thresholds for High-Cycle Fatigue in a Turbine Engine Ti-6Al-4V Alloy", *Int. J. Fatigue*, **21**, 1999, pp. 653–662.
24. Forth, S.C., Newman, J.C., Jr., and Forman, R.G., "On Generating Fatigue Crack Growth Thresholds", *Int. J. Fatigue*, **25**, 2003, pp. 9–15.

25. Forth, S.C., Newman, J.C., Jr., and Forman, R.C., "Evaluation of Fatigue Crack Thresholds using Various Experimental Methods", *J. ASTM International*, American Society for Testing and Materials, **2**, No. 6, Paper ID JAI12847, June 2005, pp. 1–16.
26. Bain, K.R. and Miller, D.S., "Fatigue Crack Growth Threshold Stress Intensity Determination via Surface Flaw (Kb Bar) Specimen Geometry", *Fatigue and Fracture Mechanics: 31st Volume, ASTM STP 1389*, G.R. Halford, and J.P. Gallagher, eds, American Society for Testing and Materials, West Conshohocken, PA, 2000, pp. 445–456.
27. Sheldon, J., Bain, K.R., and Donald, J.K., "Investigation of the Effects of Shed-rate, Initial K_{max}, and Geometric Constraint on ΔK_{th} in Ti-6Al-4V at Room Temperature", *Int. J. Fatigue*, **21**, 1999, pp. 733–741.
28. VanStone, R.H. and Lawless, B.H., "Modeling of Threshold Crack Growth in Ti-6Al-4V at Room Temperature", Proceedings, Fifth National Turbine Engine High Cycle fatigue Conference, Chandler, AZ, March 2000.
29. VanStone, R.H., "Residual Life Prediction Methods for Gas Turbine Components", *Mat. Sci. Eng.*, **A103**, 1988, pp. 49–61.
30. Lawson, L., Chen, E.Y., and Meshii, M., "Near-Threshold Fatigue: A Review", *Int. J. Fatigue*, **21**, 1999, pp. S15–S34.
31. Elber, W., "Fatigue Crack Closure under Cyclic Tension", *Eng. Fract. Mech*., **2**, 1970, pp. 37–45.
32. Elber, W., "The Significance of Fatigue Crack Closure", *Damage Tolerance in Aircraft Structures, ASTM STP 486*, American Society for Testing and Materials, Philadelphia, 1971, pp. 230–242.
33. Suresh, S., Zaminski, G.F., and Ritchie, R.O., "Oxide Induced Crack Closure: An Explanation for Near-Threshold Corrosion Fatigue Crack Growth Behavior", *Metallurgical Transactions*, **12A**, 1981, pp. 1435–1443.
34. Walker, N. and Beevers, C.J., "A Fatigue Crack Closure Mechanism in Titanium", *Fatigue Engng. Mater. Struct.*, **1**, 1979, pp. 135–148.
35. Ritchie, R.O., "Mechanisms of Fatigue Crack Propagation in Metals, Ceramics and Composites: Role of Crack-Tip Shielding", *Materials Science and Engineering*, **103**, 1988, pp. 15–28.
36. Ritchie, R.O., "Mechanisms of Fatigue-Crack Propagation in Ductile and Brittle Solids", *International Journal of Fracture*, **100**, 1999, pp. 55–83.
37. Sadananda, K. and Vasudevan, A.K., "Short Crack Growth Behavior", *Fatigue and Fracture Mechanics: 27th Volume, ASTM STP 1296*, R.S. Piascik, J.C. Newman, and N.E. Dowling, eds, American Society for Testing and Materials, 1997, pp. 301–316.
38. Vasudevan, A.K., Sadananda, K., and Glinka, G. "Critical Parameters for Fatigue Damage", *Int. J. Fatigue*, **23**, 2001, pp. S39–S53.
39. Schmidt, R.A. and Paris, P.C., "Threshold for Fatigue Crack Propagation and Effects of Load Ratio and Frequency", *Progress in Fatigue Crack Growth and Fracture Testing, ASTM STP 536*, American Society for Testing and Materials, Philadelphia, 1973, pp. 79–94.
40. Vasudevan, A.K. and Sadananda, K., "A Review of Crack Closure, Fatigue Crack Threshold and Related Phenomena", *Mater. Sci. Eng.,* **A188**, 1994, pp. 1–22.
41. Boyce, B.L. and Ritchie, R.O., "Effect of Load Ratio and Maximum Stress Intensity on the Fatigue Threshold in Ti-6Al-4V", *Eng. Fract. Mech*., **68**, 2001, pp. 129–147.
42. Vasudevan, A.K. and Sadananda, K., "Application of Unified Fatigue Damage Approach to Compression-Tension Region", *Int. J. Fatigue*, **21**, 1999, pp. S263–S273.
43. Lang, M., "A Model for Fatigue Crack Growth, Part I: Phenomenology", *Fatigue Fract. Eng. Mater. Struct.*, **23**, 2000, pp. 587–601.

44. Heywood, R.B., "The Effect of High Loads on Fatigue", *I.U.T.A.M. Colloquium on Fatigue*, W. Weibull, and F. Odqvist, eds, Springer-Verlag, Berlin, 1956, pp. 92–102.
45. Gerber, T.L. and Fuchs, H.O., "Improvement in the Fracture Strength of Notched Bars by Compressive Self-Stresses", *Achievement of High Fatigue Resistance in Metals and Alloys, ASTM STP 467*, American Society for Testing and Materials, Philadelphia, 1970, pp. 276–295.
46. Gadd, E.R., "Fatigue in Aero-Engines", *Proceedings of the International Conference on Fatigue of Metals*, Institution of Mechanical Engineers, London, 1956, pp. 658–671.
47. Prevey, P.S., Jayaraman, N., and Ravindranath, R., "Incorporation of Residual Stresses in the Fatigue Performance Design of Ti-6Al-4V", presented at *International Conference on Fatigue Damage of Structural Materials V*, Hyannis, MA, 19–24 September 2004 (to be published in *Int. J. Fatigue*).
48. Murakami, Y., *Metal Fatigue: Effects of Small Defects and Nonmetallic Inclusions*, Elsevier Science, Ltd, Kidlington, Oxford, 2002.
49. Neuber, H., *Theory of Notch Stresses: Principle for Exact Stress Calculations*, Edwards, Ann Arbor, Mich, 1946.
50. Almen, J.O. and Black, P.H., *Residual Stresses and Fatigue in Metals*, McGraw-Hill, New York, 1963.
51. Hanyuda, T., Nakamura, S., Endo, T., and Shimizu, H., "Effect of Shot Peening on fatigue Strength of Titanium Alloy", *Proceedings of the ICSP5, 5th International Conference on Shot Peening*, Oxford, 1993, pp. 139–148.
52. Wagner, L., Gerdes, C., and Lutjering, G., "Influence of Surface Treatment on Fatigue Strength of Ti-6Al-4V", *Titanium 84 Sci. and Technol*, Proc. 5th Int. Conf., 1985, pp. 2147–2154.
53. Hasegawa, N., Watanabe, Y., and Kato, Y., "Effect of Shot Peening on Fatigue Strength of Carbon Steel at Elevated Temperature", *Proceedings of the ICSP5, 5th International Conference on Shot Peening*, Oxford, 1993, pp. 157–162.
54. Dorr, T. and Wagner, L., "Influence of Stress Gradient on Fatigue Behavior of Shot Peened Timetal 1100", *Proceedings of the ICSP6, 6th International Conference on Shot Peening*, San Francisco, 1996, pp. 223–232.
55. Shao, P.-G., Yao, M., Li, X.-B., Ru, J.-L., and Wang, R.-Z., "Qualitative Analysis About Effect of Shot Peening on Fatigue Limit of a 300M Steel under the Rotating Bending Condition", *Proceedings of the ICSP6, 6th International Conference on Shot Peening*, San Francisco, 1996, pp. 290–295.
56. Li, J., Yao, M., and Wang, R.-Z., "A New Concept for Fatigue Strength Evaluation of Shot Peened Specimens", *Proceedings of the ICSP4, 4th International Conference on Shot Peening*, Tokyo, 1990, pp. 255–262.
57. Song, P.S. and Wen, C.C., "Crack Closure and Crack Growth Behaviour in Shot Peened Fatigued Specimen", *Engineering Fracture Mechanics*, **63**, 1999, pp. 295–304.
58. Drechsler, A., Kiese, J., and Wagner, L., "Effects of Shot Peening and Roller-Burnishing on Fatigue Performance of Various Titanium Alloys", *Proceedings of the ICSP7, 7th International Conference on Shot Peening*, Warsaw, 1999, pp. 145–152.
59. Guagliano, M. and Vergani, L., "An Approach for Prediction of Fatigue Strength of Shot Peened Components", *Engineering Fracture Mechanics*, **71**, 2004, pp. 5015–5512.
60. Rodopoulos, C.A., Curtis, S.A., de los Rios, E.R., and SolisRomero, J., "Optimisation of the Fatigue Resistance of 2024-T351 Aluminium Alloys by Controlled Shot Peening – Methodology, Results and Analysis", *Int. J. Fatigue*, **26**, 2004, pp. 849–856.
61. Curtis, S., de los Rios, E.R., Rodopoulos, C.A., and Levers, A., "Analysis of the Effects of Controlled Shot Peening on Fatigue Damage of High Strength Aluminium Alloys", *Int. J. Fatigue*, **25**, 2003, pp. 59–66.

62. Nalla, R.K., Altenberger, I., Noster, U., Liu, G.Y., Scholtes, B., and Ritchie, R.O., "On the Influence of Mechanical Surface Treatments – Deep Rolling and Laser Shock Peening – on the Fatigue Behavior of Ti-6Al-4V at Ambient and Elevated Temperatures", *Mat. Sci. Eng.*, **A355**, 2003, pp. 216–230.
63. Clauer, A.H. and Fairand, B.P., *Interactions of Laser-Induced Stress Waves with Metals*, ASM International, Materials Park, OH, 1979.
64. Ruschau, J.J., John, R., Thompson, S.R., and Nicholas, T., "Fatigue Crack Growth Rate Characteristics of Laser Shock Peened Titanium", *Jour. Eng. Mat. Tech.*, **121**, 1999, pp. 321–329.
65. Ruschau, J.J., John, R., Thompson, S.R., and Nicholas, T., "Fatigue Crack Nucleation and Growth Rate Behavior of Laser Shock Peened Titanium", *Int. J. Fatigue*, **21**, Supp. 1, 1999, pp. S199–S209.
66. Clauer, A.H. and Holbrook, J.H., "Effects of Laser Induced Shock Waves on Metals", *Shock Waves and High-Strain-Rate Phenomena in Metals*, M.A. Meyers, and L.E. Murr, eds, Plenum Press, New York, 1981, pp. 675–702.
67. Lykins, C. and John, R., "Prediction of Crack Growth in a Laser Shock Peened Zone", *Proceedings of International Symposium on Inelastic Deformation, Damage and Life Analysis*, V.K. Arya, ed., Springer-Verlag, May 1997.
68. Kang, K.J., Song, J.H., and Earmme, Y.Y., "Fatigue Crack Growth and Closure Behaviour Through a Compressive Residual Stress Field," *Fatigue Fract. Engng. Mater. Struct.*, **13**, 1990, pp. 1–13.
69. Timoshenko, S.P. and Goodier, J.N., *Theory of Elasticity*, 3rd edn, McGraw-Hill, New York, 1970, p. 71.
70. Thumser, R., Bergmann, J.W., and Vormwald, M., "Residual Stress Fields and Fatigue Analysis of Autofrettaged Parts", *Int. J. Pressure Vessels and Piping*, **79**, 2002, pp. 113–117.

Appendix A*
Early Railroad Accidents and the Origins of Research on Fatigue of Metals

George P. Sendeckyj

ABSTRACT

The origins of research on fatigue of metals are reviewed. It is shown that early railroad axle failures and railroad bridge collapses were the driving forces behind the development of the field of fatigue of metals. The early work on failure of railroad axles led to the correct description of the fatigue crack growth process and engineering solutions of the axle fatigue failure problem. The work on developing design criteria for iron bridge structures led to the first fatigue design criterion. All of this occurred before Wöhler's systematic fatigue experiments.

INTRODUCTION

The beginning of systematic research in fatigue of metals is linked to the numerous axle failures on the early railroads and especially to the deadly accident on the Paris-Versailles railroad on 11 May 1842 [1]. The extent of the early axle failures is poorly documented in the literature [2–11], since axle failures were seldom involved in deadly railroad accidents. Moreover, proof testing of axles and daily inspections were instituted by the Belgian government in 1843 [8] as a means of preventing accidents due to axle failures. As is shown in the next section, limits on the service life of axles were also instituted. Nevertheless, axle failures were common affecting the economics of railroad operations. As the trains became faster and larger, railroad bridge failures became rather common. This led to the investigation of iron structures subjected to impact and vibratory loading.

As is show herein, many research efforts were performed before Wöhler's systematic fatigue experiments during the 1856–1870 time period [12–18]. The initial experiments were on railroad axles and consisted of low cycle fatigue (actually repetitive impact) tests,

* This document is an unpublished manuscript contributed by Dr. George Sendeckyj. This research was performed in the Materials and Manufacturing Directorate, Air Force Research Laboratory, Wright-Patterson Air Force Base, Ohio. The author would like to thank Ms. Jeannie Stewart, the inter-library loan librarian, for obtaining copies of most of the references.

which led to engineering solutions to the fatigue failure problem. These early experiments cannot be considered to be true fatigue experiments. True fatigue research activities started with the systematic testing performed as part of the work to develop design criteria for railroad bridge structures. This work included design of the first fatigue test machines and systematic fatigue testing of iron beams manufactured by various suppliers. The tests were of relatively short duration (less than 100,000 cycles). Longer duration tests (some lasting over 10^8 cycles) were also performed before Wöhler's systematic experiments.

EARLY RAILROAD ACCIDENTS

The first documented railroad passenger fatality occurred on 15 September 1830, the day upon which the Manchester and Liverpool railroad was formally opened [2]. The first American railroad accident to kill a passenger happened on 11 November 1833 and was caused by a broken axle on one of the cars [11]. Besides these historical firsts, there were many accidents during the development of the early railroads that led to various engineering and safety innovations. These included numerous locomotive and carriage axle failures that caused derailments [11], with serious economic consequences but not many passenger fatalities. This is apparent from the following railroad safety statistics.

Gillespie [4] stated that

> On the English railroads, according to the parliamentary returns, between 1840 and 1845, both inclusive, more than 120,000,000 of passengers were carried, and of these only 66 were killed, or one in nearly two millions; and only 324 others were in any way injured, or one in nearly four hundred thousand. On the Belgian railroads, 6,609,215 persons travelled between 1835 and 1839, and of these 15 were killed and 16 wounded. But of these, 26 were persons employed on the railroads, and only 3 passengers were killed and 2 wounded. In 1842, of 2,716,755 passengers, only three were killed, and of these one was a suicide, and the other two met their deaths by crossing the line. On French railroads, 212 miles in length, of 1,889,718 passengers who travelled over 316,945 miles, in the first half of 1843, not one was either killed or wounded, and only three servants of the railroad suffered. Comparing with this the travelling by horse-coaches in the same region, we find that in seven years, from 1834 to 1840, 74 persons were killed, and 2073 wounded!

Lardner [5] provided the actual statistics for horse-coach travel in Paris and its environs for the years 1834 through 1840, which are reproduced in Table A.1. Moreover, he analyzed 100 randomly selected railroad accidents and found that 18 were due to broken wheels or axles and 14 were due to defective rails.

The Versailles to Paris railroad accident of 11 May 1842 is considered by some as the crucial event in the development of fatigue of materials [1] because it was caused by an axle failure and there were many fatalities. According to Adams [2], the train that went from Versailles to Paris

Table A.1. Ordinary horse-drawn coach accidents in Paris and its environs

Year	*Killed*	*Wounded*
1834	4	134
1835	12	214
1836	5	220
1837	11	361
1838	19	366
1839	9	384
1840	14	394

was densely crowded, and so long that two locomotives were required to draw it. As it was moving at a high rate of speed between Bellevue and Meudon, the axle of the foremost of these two locomotives broke, letting the body of the engine drop to the ground. It instantly stopped, and the second locomotive was then driven by its impetus on top of the first, crushing its engineer and fireman, while the contents of both the fire-boxes were scattered over the roadway and among *débris*. Three carriages crowded with passengers were then piled on top of this burning mass and there crushed together into each other. The doors of these carriages were locked, as was then and indeed is still the custom in Europe, and it so chanced that they had all been newly painted. They blazed up like pine kindlings. Some of the carriages were so shattered that a portion of those in them were enabled to extricate themselves, but the very much larger number were held fast; and of these such as were not so fortunate as to be crushed to death in the first shock perished hopelessly in the flames before the eyes of a throng of lookers-on impotent to aid. Fifty-two or fifty-three persons were supposed to have lost their lives in this disaster, and more than forty others were injured; the exact number of the killed, however, could never be ascertained, as the pile-up of the cars on top of the two locomotives had made of the destroyed portion of the train a veritable holocaust of the most hideous description.

The apparent inconsistency between the early railroad fatality statistics and the large number of accidents due to axle failures can be readily reconciled. Huish [19] indicated that

> The carriage stock of railway Companies is generally of so superior a kind, both as to design and construction, that accidents arising from their failure are very rare. The wheels and axle-boxes are the most severely tested parts of the vehicle, but if originally of a proper construction, give very little trouble in their maintenance and repair.... During the last four years, only six wheels have failed, in the very large stock of the London and North Western Company.... If, however, there is no part of the railway machinery which so little danger may be apprehended as the passenger carriage, the same cannot be claimed on the part of the merchandise wagon. Whether the absence of direct danger to human life, or an injudicious economy, has been the cause, the fact is, that in no portion of the system has so little improvement been exhibited, and in which, as the present moment, there is so great a necessity for a complete modification. In this respect England is far behind the

> Continent. The axles of wagon stock have, in many instances, been of the most faulty model and material. The accidents to the trains, from the fracture of these parts, have been very numerous, while the destruction of property has been sufficient to have paid for the very superior vehicle. In one recent instance, several hundred axles, of a peculiar form, were removed from a leading railway, after a short experience of their working.

The New York State Senate report [6] indicated that

> To guard more effectually against the accidents arising from the alleged deterioration of the iron . . . , it has been the practice, on some roads, to run the wheels and axles one year only under passenger cars, and then transfer them to freight cars. The safety beams have been introduced on the cars of many of our roads, by means of which the axle is upheld when broken. This has undoubtedly been the means of safety, by keeping the fractured ends of the axle suspended until the motion of the train could be arrested; but, in many cases, it is not calculated to hold them with sufficient steadiness to prevent the wheels from leaving the rail.

This is an early example of fail-safe design practice.

Twenty accidents occurred during the first year of operation of the Great Western Railway in Canada [7]. Of these accidents, only one was due to an axle failure. According to the report, Mr. William Scott, formerly one the Engineers to the Company, in his evidence, states "that on examination the iron of the axle appeared to be very bad – the worst that he had ever seen, and that he believes, but is not positive, that there must have been a visible flaw before the occurrence." If such had really been the case, it ought to have been detected in the daily and close examination of all the rolling stock in use enjoined by the regulations of the Company; but on the other hand, the usual examination is declared to have taken place, and no flaw to have been discovered, and as to the pre-existence of the flaw, Mr. Scott is himself doubtful.

As this quotation indicates, by 1854 it was common practice to daily inspect the rolling stock as a safety measure.

Simon [20] summarized results from an official paper issued by the Association of German Railways on broken axles in 1865. He indicated that 153 axles broke and 40 were discovered before complete breakage occurred. The probable cause of breakage was: 17 cases of bad workmanship of axle, 32 cases of bad material, 21 cases of bad design, 6 cases of overloading, 10 cases of want of grease or oil, 46 cases of too long use, and 3 cases due to breakage of another axle. Thus, 30% of the failures were due to fatigue.

Stretton [9] summarized railroad accidents during 1889 as reported to the Board of Trade. There were 106 collisions, 44 cases of passenger train derailments 13 cases of trade goods train derailments, 8 cases of trains travelling in the wrong direction through facing points, 30 cases of trains running into stations at too high a speed, 135 cases of trains running over cattle, 44 instances of trains running through gates at level crossings, 239 failures of axles, 9 failures of couplings, 668 failures of tires, 2 failures of wheels,

3 failures of ropes used in working inclines, 4 failures of bridges, 262 broken rails, 12 cases of flooding of permanent way, 10 slips in cuttings or embankments, and 8 fires in trains. These results indicate that 15.1% of the accidents were due to axle failures. This is consistent with the results quoted by Lardner [5], who indicated that 18% of the accidents were due to axle failures at a much earlier date.

Stretton [9] compiled the total number of axles of all descriptions which broke when running during 1878 through 1885. These results are given in Table A.2. He also summarized data for 1883 on the total number of axles in use, the number of axles broken when running, and the number taken out in shops as flawed. These results are reproduced in Table A.3.

Wilson [10] compiled the causes of accidents on British railroads for the period of 1872 through 1875. He indicated that there were 162, 133, 229 and 478 axles failures during 1872, 1873, 1874 and 1875, respectively.

FATIGUE OF RAILROAD AXLES

Apparently, the earliest documented research on fatigue of materials was conducted by Albert [21], who performed repetitive tension tests on hoist chains in the mines in the Harz mountains as early as 1828. Poncelet [22] first used the term fatigue in his book

Table A.2. Axles broken in eight years, 1878–1885 [9]

Year	*Engine axles*		*Tender axles*	*Carriage axles*	*Wagon axles*	*Salt van axles*	*Total*
	Crank or driving	*Leading or trailing*					
1878	266	21	19	3	221	10	540
1879	248	24	23	3	190	8	496
1880	251	27	25	1	192	18	514
1881	262	21	37	3	200	17	540
1882	242	22	32	2	140	13	451
1883	247	28	21	2	141	11	450
1884	200	23	24	6	113	19	385
1885	190	31	17	4	130	5	377

Table A.3. Engine axles broken or defective, 1883 [9]

	Number in use	*Broken in running with passenger trains*	*Broken in running with goods trains*	*Taken out in shops flawed*
Crank axles	12 943	70	108	680
Straight axles	1 905	10	19	24
	14 848	80	127	704

in 1839. According to Smith [23], "The spectacular growth of the railroads in the 1830s was accompanied by an equally spectacular growth in the number of failures of wrought-iron axles, and the failure of some of the iron bridges that were being built in large numbers." As a result, considerable research and discussion took place in the engineering communities on axle failures.

According to Haigh [24],

> Mechanical fatigue was first recognized as a mode of fracture differing from that produced by loads acting steadily, in the course of an investigation from 1840 to 1842, carried out by the engineers of the London and Birmingham Railway. Crankshafts, of tough irons that showed high ductility in bending tests, were found to fail in service by the gradual development of a crack in a brittle manner, without any considerable preliminary local distortion. The immediate difficulty was overcome by limitation of piston speed; and, as a precaution, axles were periodically examined for cracks in the early stages of development.

Observations of axle failure processes

Apparently, the first published observations of axle failure processes were due to Arnoux in France [25]. Edwards [25] described Arnoux's observations as follows:

> The fracture commences at the lower angle of the axle on the side of the traction, which is evidently in fixed axles the point of greatest fatigue, and in those axles which have given way under the weight of the load, the fissure has in some instances nearly traversed the axle before it broke entirely, and it is then easy to trace the accident from its engine. I will endeavour to describe its usual appearance by the following diagram (Figure A.1a); the arrow shows the direction in which the carriage moves. The fracture invariably originates at the angle *a*, and appears to progress at intervals by zones as shown by the lines in the diagrams, the first, at the point *a* becoming perfectly black, the colour of each being lighter as they

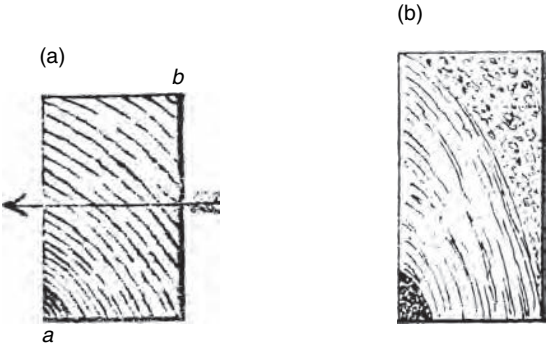


Figure A.1. Arnoux observations of axle failures; (a) Edwards; (b) Morin.

> gradually extend form this point, and as the contact of the two sides of the fracture becomes more intimate, the grain of the iron towards the angle *a* is coarse, and has a large crystalline texture, which diminishes in size as the fracture approaches the angle *b*, at which point the metal remains slightly fibrous, having evidently undergone a more rapid deterioration at its point of greatest strain.

A similar description of Arnoux's observations was given by Morin [26], as can been seen by comparing Figures A.1a and 1b.

At about the same time, Rankine [27]* showed that a gradual deterioration takes place in axles. He presented drawing of five specimens,

> representing the exact appearance of the metal at the point of fracture, which in each case occurred at the re-entering angle, where the journal joined the body. The fractures appear to have commenced with a smooth, regularly-formed, minute fissure, extending all round the neck of the journal, and penetrating on an average to a depth of half an inch. They would appear to have gradually penetrated from the surface towards the centre, in such a manner that the broken end of the journal was convex, and necessarily the body of the axle was concave, until the thickness of sound iron in the centre became insufficient to support the shocks to which it was exposed. In all the specimens the iron remained fibrous; proving that no material change had taken place in its structure."

Rankine published the figures in a discussion of a paper by Kirkaldy [28].

Glynn [29], who personally experienced two axle failure incidents in 1843, presented similar observations on the fracture of tender axles. He stated that

> Both the fractures presented the same appearance (Figure A.2); for about 1/2 inch in depth all round, there was a perfectly smooth cleft of a blue and purple colour; this annular cleaving appeared to have been produced by a constant process; the central crystallized part being gradually reduces in diameter, until it was barely able to sustain the weight, and it broke on being exposed to a sudden strain. . . . It is observed, that the fracture commences at the end of the key groove, which is about 1/4 inch from the shoulder, against which the wheel is fixed. The author is of opinion, that the breaking action commences with the first journey of the tender, and that the axles continually receive such injury as they would, if they were laid over the edge of an anvil at A, and received a constant succession of smart blows from a hammer upon the point B, the axle being constantly turned round.

McConnell [30] made similar observations in 1849 and stated that "a gradual breaking up of the fibre at the back of the wheel goes on, which is shown by an annular space, varying from 3/8 to 3/4 inch in breadth; the strength is completely destroyed of this

* During the early 19th century, engineers did not publish their research results, but presented them at various society meetings. Reporters that were present at the meetings documented the presentations and discussions in various publications. As a result, the research work was described in many publications.

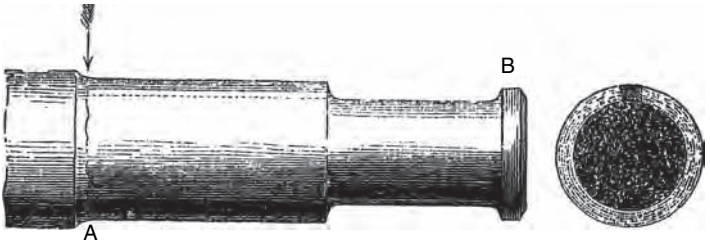


Figure A.2. Fracture of railway carriage axle.

portion, and a sudden shock of the wheel upon some point of the road competes the fracture of the axle."

Stopfl [31] made a significant, but little noticed, contribution to the understanding of the fatigue of railroad axles. He indicated that 18 locomotive axles failed in one year on the north Austrian railroad and, as a result, the Austrian government initiated a test program to investigate and find ways to prevent such failures. These tests were performed to explore factors influencing the axle failure process. He did not accept the prevalent explanation of the failure process based on the then prevalent crystallization theory of fatigue. He tested specimens with different geometries and showed that the appearance of the fracture surface is a function of the way the axles are loaded, disproving the crystallization theory of fatigue. He stated that abrupt shape changes affected the failure process. Moreover, he observed that failed axles had developed either circumferential or part through cracks, which showed evidence of a color change (rusting) on the fracture surfaces. Based on these observations, he concluded that the cracks developed gradually during service, prior to the final failure.

Marcoux [26] noticed that axles, made with good quality iron, broke because small cracks that are difficult to recognize are formed at the axle shoulders. If these cracks (which are shallow when first formed) remain unobserved, the axles break at that location when they penetrate 10–15 mm in the axle. He thought that these cracks are caused by vibration of the axles, and that effect is produced in an analogous manner to what happens when one breaks a wire while bending it several times in different directions. Figure A.3

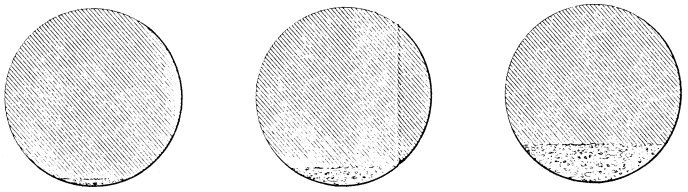


Figure A.3. Marcoux observations on crack growth in axles.

reproduces his sketch indicating the gradual growth of cracks observed on axles on mail coaches.

Finally, in a continuation of a discussion on axles, McConnell [32] indicated that

> The axle . . . broke in ordinary working close at the back of the wheel as is usually found, and the fractured ends . . . afford the most distinct proof of the annular space, which was . . . observable all round the surface of the fracture; and this is not only short grained and crystalline, but there is also . . . evident distinct separation to the extent of the annular space which it would appear takes place some time before the final fracture, as if each successive blow, heavy or light, lateral or vertical, received or transmitted through the wheels, had each tended to destroy its proportion of cohesion of the previously crystallized substance of the axle at that particular place where the fracture occurs.

McConnell tested the center section of the axle and found that it was not damaged.

Consequences of axle failure observations

The aforementioned observations on axle failures during service had a number of important consequences. First of all, they led to an engineering solution to the axle failure problem. This was done by Rankine [27] and, independently, by Stopfl [31]. Rankine [27] "proposed, in manufacturing axles, to form the journals with a large curve in the shoulder, before going to the lathe, so that the fibres shall be continuous throughout, . . . Several axles having one end manufactured in this manner, and the other by the ordinary method, were broken; the former resisted from five to eight blows of a hammer, while the latter were invariably broken by one blow." This extract from the paper indicates that Rankine correctly realized the importance of the stress concentration at a re-entrant corner and presented an engineering solution for improving the performance of railroad axles. Similarly, Stopfl [31] recommended the use of gradual thickness transitions and made specific recommendations for the manufacturing of railroad axles.

Another engineering consequence of the observed failures of railroad axles was the practice to limit the service life of axles on passenger carriages. Arnoux [25, 26] indicated that it was the practice not to touch axles before they saw 60,000 to 70,000 kilometers of service. Marcoux [26] recommended the axles be "renewed" after having provided 60,000 kilometers of service. In a sense, the endurance limit for the service loading on the axles was 60,000 kilometers. At the end of this service life, the axles were either replaced or repaired. If repaired, their service life was further limited. Moreover, the French government appointed a commission to investigate means of avoiding railroad accidents [33] as a result of the Versailles to Paris railroad accident. The report of the commission [34, 35] recommended monitoring the usage of axles to establish their useful life, before being reworked and/or replaced.

Finally, Haigh [36] stated in 1925

> And it is interesting to note that several of the conclusions reached before 1842 are still of practical value in comparable circumstances. It was found that the safe mileage decreased rapidly with speed; and that piston speed afforded a serviceable basis of comparison for different designs and different metals. A piston speed of 1,000 feet per minute soon came to have a recognized significance as a standard for the purpose. Periodic inspection was instituted at this same period, with the result that fatigue cracks were often detected before they extended far enough to cause breakdown.

Beginning of systematic fatigue testing of axles

The French commission report [8, 34, 35] described

> an apparatus for submitting axles of locomotives and cars to all the movements and resistances, to which they may be exposed in use. By this method, we shall evidently arrive at the same results as by observations of axles which have seen much service. This apparatus being kept in constant operation, enables us to arrive more speedily at an estimate of the course of crystallization, taking into account, at the same time, the changes occasioned in the nature of iron by variations of temperature.

According to With [8], "The Austrian government has had the same idea, and it has the merit of having put in operation some time since, in consequence of the almost daily breaking of axles, upon the State railroad, after having been kept in perfectly good order for five years."

With [8] presented results of experiments that were published in *Journal des Chemins de Fer*. The experimental

> apparatus consisted of a bent axle, which was firmly fixed up to the elbow in timber, and which was subjected to torsion by means of a cog-wheel connected with the end of the horizontal part. At each turn the angle of torsion was 24°. A shock was produced each time that the bar left one tooth to be raised by the next. An index adapted to the apparatus indicated the number of revolutions and shocks.

The test results and observations are summarized in Table A.4. These results are also presented by Wood [37], who indicated that the experiments were performed in France.

Engerth [38], von Burg [39] and Schrötter [40] indicated that Kohn performed the first controlled tests to find the effect of alternating torsion on wrought iron, the crank-shaped samples being subsequently broken in a hydraulic press, after as many as 128,309,000 reversed torsion cycles. Schrötter, analyzing Kohn's results, concluded that repeated torsion can change the fracture of a bar from fibrous to crystalline and then lamellae. It should be noted that the Kohn data is identical with the results presented by With [8]. Hence, the question remains whether the results given by With are actually those of Kohn.

Table A.4. Experiments and observations on axles (With [8])

No. of Torsions	*Observations*
32,400	No failure and no change in texture upon being fractured in hydraulic press
129,000	Broken after the test. "No alteration of the iron could be discovered, by the naked eye, on the surface of rupture; but tried with a microscope, the fibres appeared without adhesion, like a bundle of needles."
388,000	Broken in two. "A change in its texture, and an increased size in the grain of the iron, was observed by the naked eye.
3,888,000	". . . the axle was broken in many places; a considerable change in its texture was apparent, which was more striking towards the centre; the size of the grains diminished towards the extremities."
23,328,000	". . . completely changed in its texture; the fracture in the middle was crystalline, but not very scaly."
78,732,000	". . . fracture, produced by an hydraulic press, showed clearly an absolute transformation of the structure of the iron: the surface of rupture was scaly like pewter."
128,304,000	". . . presented a surface of rupture like that in the preceding experiment. The crystals were perfectly well defined, the iron lost every appearance of wrought iron."

Discussions of the causes of fatigue failures

The fatigue failures were characterized by an apparent change from *fibrous* to *crystalline* structure of the wrought iron. This failure mode classification seems to have been introduced in 1724 by Réaumur [23] and in the early 1820's by Tredgold [41]. We now know that the crystalline appearance of the failure surfaces was actually evidence of brittle fracture, but this was contrary to the knowledge available to the then practicing engineers.

The prevalent explanation of the failures was that the wrought iron crystallized as a result of the repetitive loading and various explanations were sought for the phenomenon [42, 43]. Vignoles [43] stated that François and Aubert attributed fractures of broken axles to the magnetic or electric changes in the molecular structure of iron, caused by friction on the bearings and great velocities. Moreover, Vignoles believed that it was probable that the continual strains and percussions to which the cranked axle is subjected will account for the changes in the molecular constitution of the iron. Nasmyth [44] was of the opinion that the alternate strains in opposite directions, which the axles were exposed to, rendered the iron brittle, from the sliding of the particles over each other. York [45] attributed fracture in railway axles to the sudden strains and injury produced by concussions and vibration.

In a discussion on the strength of railway axles, McConnell [30] expressed the opinion that the iron in the axles crystallized during usage. *R*. Stephenson [Ref. [30], p. 22] disagreed with McConnell and mentioned cases of "vibration going on from year to year without any sensible change occurring in wrought or cast-iron." Finally, Slate [Ref. [30], p. 26] stated that he "did not think that any change from a fibrous to a crystalline texture was produced in iron unless it were strained beyond the limit of its elasticity." He further stated that

he had made a machine in which he put an inch square bar subjected to a constant strain of 5 tons, and an additional varying strain of 2 1/2 tons, alternately raised and lowered by an eccentric 80 or 90 times per minute, and this motion was continued for so long a time that he considered it equal to the effect of 90 years' railway working, but no change whatever was perceptible; and therefor he was one of those who did not believe in a change from a fibrous to a crystalline structure in iron.

McConnell [32] also presented

some instances of tough fibrous wrought-iron being rendered brittle and breaking off quite square with a close-grained fracture from the effect of the concussion of very small blows rapidly repeated for a long period; the blows being very small in force compared to the strength of the iron. These specimens are from the machines for making shanks . . . The hammer in these machines is about 2 1/2 lb. weight, and is lifted by a rod 3/8 inch square, which has a pull upon it of about 12 lbs. from the difference of leverage; the hammer strikes 120 blows per minute, . . . The lifting rods always break with a close-grained short fracture, although made of the toughest and most fibrous iron that can be obtained, and they sometimes last only a few months; the rods break near to the end, which is fixed with a coupling, and the deterioration of the iron appears to be confined within a small portion, the iron remaining quite tough and fibrous within an inch of the fracture, . . .

Another specimen from the same machines is the lever for pushing off the work from the machine when stamped; the lever is about 1/2 inch square, made of the toughest wrought-iron, it is 9 inches long, and falls back against a stop at one-third of its length from the centre of motion at the bottom, being thrown back sharply by a spring, the total strain upon the lever varying from about 1 lb. to about 12 lbs., according to the accidental circumstances in the working of the machine. These levers all break off quite short and close-grained within an inch of the part that strikes against the stop, but the iron continues quite fibrous and unchanged to within an inch of the point of fracture, as shown in the specimen. They were driven at the same speed . . . ; but they broke so frequently, lasting sometimes only a few weeks, that it was determined at last to reduce the speed of the machines from 120 to about 100 blows per minute, and in consequence of this reduction in speed the levers are much less frequently broken, and last on the average about four times as long as before.

In a subsequent discussion, R. Stephenson [46] indicated that

since their last meeting he had turned his attention to ascertain, if possible, whether any real difference exists in the molecular arrangement of the material or structure of a piece of iron called crystalline, and a piece of iron called fibrous; and for this purpose he had examined them under a powerful microscope, and it would, probably, surprise the members to know that no real difference could be perceived, and that if he had not previously seen with the naked eye the specimens called fibrous and crystalline, he should not have been able to distinguish the one from the other in the microscope. The best specimen he could select of the kind called fibrous, exhibited to the naked eye an arrangement of dark and light lines, but the light lines composing the apparent fibre were, in point of fact, as crystalline as the other kind of iron, and, therefore, however fibrous it might appear, it was essentially a crystalline

> mass. Even in a piece of iron, with large facets, which appeared extremely crystalline, when one of the crystals was examined, it gave much the same appearance under the microscopy as a fibrous surface gives to the naked eye; in fact, it would appear to consist of bundles of fibres broken through at certain angles, just as slate was observed in the quarries to break in particular rhomboidal forms. Now, in the instance of slate, there was nothing fibrous or crystalline, but owing to the large scale something resembling the appearances to the observed in iron-like fibres being broken through in particular planes.

Mr. Adams "Opined that the appearance called crystalline was caused by nothing more or less than a bundle of fibres, consisting of many small crystals being sheared off square, forming one facet."

G. B. Thorneycroft [47, 48] discussed the quality of iron, manufactured in different ways, and stated "that the compression of iron, when cold, is certain to change fibrous, into granular iron, and that vibration or bending, even to a slight extent, if continued for any length of time, has the effect of compressing all the particles consecutively." He also presented some experimental results to justify the use of straight axles. He [48] further stated that "If a shoulder was left on an axle, it should be curved, for if it was left square, it would induce fracture at that part. It would appear that there was a constant progressive tendency to fracture whenever opportunity was afforded for commencing."

In a discussion of the form of shafts and axles, T. Thorneycroft [49] stated

> To determine what these elements of self-destruction are, and to what extent they are in operation, has lately occupied the highest mathematical and practical talent of this kingdom; and they have recorded as the result of their experiments and investigation, that to resist the effects of reiterated flexure, iron should scarcely be allowed to suffer a deflection equal to one-third of its ultimate deflection, for should the deflection reach one half of its ultimate deflection, fracture will sooner or later take place.

Braithwaite [50], in 1854, was apparently the first to use the term fatigue in the title of a paper. He stated "that the term 'fatigue' as applied to . . . deterioration of metal, was suggested by Mr. Field; . . . " He gave numerous examples of the occurrence of fatigue failures in practice and stated that

> There have been many instances of the sudden, and unexpected fracture of axles, cranks, crank-pins, levers, cranes, crane-chains, hooks, &c., and almost of all parts of various kinds of machinery, when subjected to continuous, and repeated strains, jerks, or concussions, and it is very remarkable, that in all cases, the destructive effect of this fatigue, was evident, in the metal at the fractures being altered in its structure. . . . the Author has arrived at the conclusion, that many of the railway accidents, to bridges, ash-pans, parts of locomotive engine, carriages, or the chains connecting them, hitherto deemed unaccountable, are to be attributed to the fatigue of the metal, and he is of opinion, that a rigid examination, and subsequent strengthening, or changing of the parts, where necessary, of all bridges, machinery, and engines, will greatly tend to the prevention of such accidents, which, unhappily, must, on railways, always be of a very serious kind.

During the discussion of this paper, Fairbairn said that

> his experience led him to believe, that fractures in iron and other metals, subjected to severe strain, were, in many cases, due to some original imperfection in the manufacture; it was then only a question of time, how soon fracture would occur. In all cases of bodies subjected to intermittent strain, a progressive deterioration appeared to take place in the resisting powers of the material, in consequence of which, they would ultimately give way, under a load which they were at first fully equal to sustain, and this deterioration of strength appeared to proceed rapidly, or slowly, as the strains bore a greater, or less ratio to the ultimate resistance. Thus crank-axles were frequently subjected to a succession of jerks which could not be resisted for any length of time, even by iron of the best quality. He believed that wrought iron exposed to constant variations of strain, frequently underwent a complete change in molecular structure, assuming a crystalline, instead of a fibrous arrangement.

In concluding the discussion, Braithwaite stated

> that most of the . . . remarks confirmed his views on the subject. When shafts had not been unduly loaded, they lasted well; but when called upon to perform increased duty, they incurred fatigue, and consequently, broke. The vibrating action upon a wheel, however, was not exactly analogues to that upon a shaft; still, increased duty would produce the same effect upon the former as upon the latter. So also with bridge girders; if they were originally constructed of proper dimensions, and of good metal, they would last; but that strength would no longer suffice, if the weight of the engines was increased, and they were impelled at a greater velocity. It was the excess of duty to which rails and bridge girders were now exposed, that was the main cause of their deterioration.

McConnell [51, 52] described a process for manufacturing sound hollow axles and experimentally showed that the hollow axles were superior to solid ones. In the discussion of the paper [52], Mr. Slate

> remarked, that in reference to the crystallization produced in iron by concussion, he thought the effect did not take place unless the strain was beyond the elastic limit more than five or six tons per inch, so as to cause a permanent change in the arrangement of the particles of the iron. He had tried an experiment in connexion with Mr. Wild, in which a weight was suspended by a bar an inch square, and was lifted up and down eighty times per minute by an eccentric worked by a steam engine constantly, night and day. This was continued for a length of time that was supposed equivalent to the effect of twenty-five years' work, but no change or crystallization in the iron was perceived.

FATIGUE OF RAILROAD STRUCTURES

On 27 August 1847, a commission was appointed by the British government to inquire

> into the conditions to be observed by Engineers in the application of Iron in Structures exposed to violent concussions and vibration; . . . to ascertain such principles and form such

> rules as may enable the Engineer and Mechanic, in their respective spheres, to apply the Metal with confidence, and shall illustrate by theory and experiment the action which takes place under varying circumstances in Iron Railway Bridges which have been constructed; . . .

A report [53] summarizing the results of the investigations was published in 1849. This report was widely publicized and reprinted without the complete appendices [6, 54, 55]. The report contains the first systematic investigation of the effect of moving loads on railroad bridge structures and fatigue of rails. The pertinent experiments were performed by E. Hodgkinson, Captain H. James and Lt. D. Galton.

The commissioners [53] stated their research goals as follows: The questions to be examined may be arranged under two heads, namely—

1. Whether the substance of metal which has been exposed for a long period to percussion and vibrations, undergoes any change in the arrangement of its particles, by which it becomes weakened?
2. What are the mechanical effects of percussions, and of the passage of heavy bodies, in deflecting and fracturing the bars and beams upon which they are made to act?

The report [53] describes the following fatigue experiments, performed by Hodgkinson, on cast and wrought iron:

> A bar of cast iron 3 inches square, was placed on supports about 14 feet asunder. A heavy ball was suspended by a wire 18 feet long, from the roof, so as to touch the centre of the side of the bar. By drawing this bar out of the vertical position at right angles to the length of the bar, in the manner of a pendulum, to any required distance, and suddenly releasing it, it could be made to strike a horizontal blow upon the bar, the magnitude of which could be adjusted at pleasure, either by varying the size of the ball or the distance from which it was released. Various bars, (some of smaller size than the above) were subjected by means of this apparatus to successions of blows, numbering in most cases as many as 4,000. The magnitude of the blow, in each set of experiments being made, greater or smaller, as occasion required. The general result obtained, was that when the blow was powerful to bend the bars, through one half of their ultimate deflection (that is to say, the deflection which corresponds to their fracture by dead pressure) no bar was able to stand 4,000 of such blows in succession; but all the bars (when sound) resisted the effects of 4,000 blows, each bending them through one third of their ultimate deflection.

The report [53] describes the following fatigue experiments, performed by James and Galton:

> Other cast iron bars, of similar dimensions, were subjected to the action of a revolving cam, driven by a steam engine. By this they were quietly depressed in the centre, and allowed to restore themselves, the process being continued to the extent, even in some cases, of a hundred thousand successive periodic depressions for each bar, and at a rate of about

> four per minute. Another contrivance was tried, by which the whole bar was also, during the depression, thrown into a violent tremor. The results of these experiments were, that when the depression was equal to one-third of the ultimate deflection, the bars were not weakened. This was ascertained by breaking them, in the usual manner, with stationary loads in the centre. When, however, the depressions produced by the machine were made equal to one-half of the ultimate deflection, the bars were actually broken by less than nine hundred depressions. This result corresponds with and confirms the former.

The experimental setup used by James and Galton was illustrated in the discussion by Timoshenko of a paper by Peterson [56].

The report [53] describes the following fatigue experiments, performed by Willis, James and Galton: "By other machinery, a weight equal to half of the breaking weight, was slowly and continually dragged backwards and forwards from one end to the other of a bar of similar dimensions to the above. A sound bar was not apparently weakened by ninety-six thousand transits of the weight."

The report [53] concluded that

> It may, on the whole, therefore be said, that as far as the effects of reiterated flexure are concerned, cast iron beams should be so proportioned, as scarcely to suffer a deflection of one-third of their ultimate deflection. And, as it will presently appear, that the deflection produced by a given load, if laid on the beam at rest, is liable to be considerably increased by the effect of percussion, as well as by motion imparted to the load, it follows, that to allow the greatest load to be one-sixth of the breaking weight, is hardly a sufficient limit for safety, even upon the supposition that the beam is perfectly sound.
>
> In wrought iron bars, no very perceptible effect was produced by 10,000 successive deflections by means of a revolving cam, each deflection being due to half the weight, which, when applied statically, produced a large permanent flexure.

The report [53] also summarizes the experimental and analytical studies performed by Willis on the effect of moving loads on the deflection of bridge bars and beams. Willis [57] studied the effect of a moving load on a beam, in an attempt to understand the "action which takes place under varying circumstances in iron railway bridges." This study used the experiments performed by James and Galton on full scale bridge type of structures and small scale tests on model systems performed by himself. The experimental results were compared with theoretical analyses by Stokes. The main conclusions of these studies were that the deflections experienced by the bridge structures due to moving loads are higher than those due to static loads. They could be over twice those produced by static loads of the same magnitude.

The report [53] recommended that

> . . . , as it has been shown that to resist the effects of reiterated flexure, iron should scarcely be allowed to suffer a deflexion equal to one-third of its ultimate deflexion, and since the deflexion produced by a given load is increased by the effects of percussion, it is advisable

that the greatest load in railway bridges should, in no case, exceed one-sixth of the weight which would break the beam when laid on at rest in the centre.

The commissioners conclude their report with the statement that they "lament that the limited means which have been placed at our disposal, and the great time required for such investigations, have compelled us to leave in an imperfect state, or even to neglect altogether, many interesting and important branches of experimental inquiry . . . " This conclusion [58] was further reinforced as follows: "we understand that the labors of this important Commission were prematurely stopped by cutting off the necessary funds for carrying on the experiments. Surely, seeing the important uses to which, on land and sea, iron is now employed, it was not a wise economy to put an end to an inquiry which promised to be of such great national importance." These comments are reminiscent of the laments of present day researchers, who quite often bemoan the lack of adequate funding and time to accomplish their research, and the premature termination of promising research activities.

DISCUSSION AND CONCLUSION

As can be seen from the research efforts discussed in the previous section, the practicing engineers correctly described the fatigue crack growth process during the early 1840s. While Edwards [25] and Rankine [27] were apparently the first ones to publish a description of the fatigue process, others [26, 29–31] arrived independently at similar descriptions of the fatigue failure process. Rankine developed and experimentally verified an engineering solution for preventing failure of railway axles with reentrant corners. This solution was adopted and Rankine went on to other research, which established his reputation.

While the correct qualitative description of the crack growth process was developed, no attempt was apparently made to quantify it. The scientific and engineering communities were misled by the observation that the failure surfaces of axles that failed in service had a crystalline appearance, while axles that were failed when new had a fibrous appearance. Various explanations for the change in the appearance of the failure surfaces were offered based on the prevalent theories. These included magnetism, electrical charging, and the caloric theory of materials. Even thought convincing proof that materials do not exhibit a change from fibrous to crystalline fracture was presented by Stopfl [31] and Kirkaldy [59], who showed that the change can be caused by changing the loading rate and by the presence of notches in the specimens, the crystallization theory of fatigue persisted into the early 1900s.

Besides railroad axle failures, early railroad bridge failures were common. These were due to the increase in railroad engine and car weight, and train speed. The numerous bridge failures led to the creation of the royal commission to inquire into the application of iron to railway structures. Its report [53] includes the first systematic fatigue experiments

in England and the development of the first fatigue design criterion. Unfortunately, this significant fatigue research has been overlooked because the fatigue results were only published in the report of the commission and not in the scientific literature. Also, it should be noted that funding for this significant research effort was terminated before it could be properly completed [53, 58].

Other significant fatigue research was performed before Wöhler's systematic fatigue test program and the formulation of the so-called Wöhler's laws of fatigue.

REFERENCES

1. Smith, R. A., "The Versailles Railway Accident of 1842 and the First Research into Metal Fatigue". in *Fatigue 90*, H. Kitagawa and T. Tanaka, eds, **4**, Birmingham: Materials and Component Engineering Publications Ltd, 1990, 2033–2041.
2. Adams, C. H., *Notes on Railroad Accidents*. New York: G. P. Putman's Sons. 1879.
3. Howland, S. A., *Steamboat Disasters and Railroad Accidents*. Worcester: Warren Lazell. 1846.
4. Gillespie, W. M., *A Manual of the Principles and Practice of Road-Making: Comprising the Location, Construction, and Improvement of Roads (Common, Macadam, Paved, Plank, etc.) and Rail-Roads.* New York: A. S. Barnes & Co. 1850.
5. Lardner, D., *Railway Economy: A Treatise on the New Art of Transport, Its Management, Prospects, and Relations, Commercial, Financial and Social, with an Exposition of the Practical Results of the Railways in Operation in the United Kingdom, on the Continent, and in America*. London: Taylor, Walton and Maberly, 1850.
6. New York State Senate, *Report of the Committee Appointed to Examine and Report the Causes of Railroad Accidents, the Means of Preventing Their Recurrence, &c*. Albany: C. van Benthuysen, 1853.
7. Anon, *Report of the Commissioners Appointed to Inquire Into a Series of Accidents and Detentions on the Great Western Railway, Canada West*. Quebec: S. Derbishire and G. Desbarats. 1855.
8. With, E., *Railroad Accidents: Their Causes and the Means of Preventing Them*, translated from the French by G. F. Barstow. Boston: Little, Brown and Company. 1856.
9. Stretton, C. E., *Safe Railway Working. A Treatise on Railway Accidents: Their Cause and Prevention, etc.*, 2nd Edition. London: Crosby Lockwood and Son, 1891.
10. Wilson, H. R., *The Safety of British Railways*. Westminster: P. S. King and Son, 1909.
11. Reed, R. C., *Train Wrecks. A Pictorial History of Accidents on the Main Line*. Atglen PA: Schiffer Publishing, 1996.
12. Wöhler, A., "Bericht über die Versuche, welche auf der Königl. Niederschlesisch-Märkischen Eisenbahn mit Apparaten zum Messen der Biegung und Verdrehung von Eisenbahn-wagen-Achsen während der Fahrt, angestellt wurden", *Zeitschrift für Bauwesen*, 1858, 8, 642–651.
13. Wöhler, A., "Versuche über Biegung und Torsion der Eisenbahnwagen-Achsen", *Dingler's Polytechnischen Journal*. 1859, **151**, 233–236.
14. Wöhler, A., "Versuche zur Ermittelung der auf die Eisenbahnwagenachsen einwirkenden Kräfte und der Widerstandsfähigkeit der Wagen-Achsen", *Zeitschrift für Bauwesen*, 1860, **10**, 583–616.
15. Wöhler, A., "Über die Versuche zur Ermittelung der Festigkeit von Achsen, welche in den Werkstätten der Niederschlesisch-Märkischen Eisenbahn zu Frankfurt a.d.O. angestellt sind", *Zeitschrift für Bauwesen*, 1863, **13**, 233–258.

16. Wöhler, A., "Resultate der in der Central-Werkstatt der Niederschlesisch-Märkischen Eisenbahn zu Frankfurt a.d.O. angestellten Versuche über die relative Festigkeit von Eisen, Stahl und Kupfer", *Zeitschrift für Bauwesen*, 1866, **16**, 67–83.
17. Wöhler, A., "Über die Festigkeits-Versuche mit Eisen und Stahl", [On strength tests of iron and steel]", *Zeitschrift für Bauwesen*. 1870, **20**, 73–106.
18. Anon. Wöhler's Experiments on the "Fatigue" of Metals. *Engineering (London)*, 1871, **11**, 199–200, 221, 243–244, 261, 299–300, 326–327, 349–350, 397, 439–441.
19. Huish, M., "Railway Accidents; Their Cause, and Means of Prevention", *J. the Franklin Institute*. 1853, **25**, 96–103,145–149.
20. Simon, H., "The Breaking of Railway Axles", *J. of the Franklin Institute*, 1866, **52**, 399.
21. Albert, W. A. J., "Über Treibseile am Harz [Driving ropes in the Harz]", *Archiv für Mineralogie, Geognosie, Bergbau und Hüttenkunde*, 1838, **10**, 215–234.
22. Poncelet, J. V., *Introduction à la Mécanique Industrielle, Physique ou Expérimentale [Introduction to Industrial, Physical or Experimental Mechanics]*, 1st Edition, 1839.
23. Smith, C. S., *A History of Metallography*, Cambridge MA: MIT Press, 1988.
24. Haigh, B. P., Theory of Rupture in Fatigue. in *Proceedings of the First International Congress for Applied Mechanics, Delft, 1924*, C. B. Biezeno and J. M. Burgers, eds, Delft:Technische Boekhandel en Drukkerij J. Wlatman Jr. 1925, 326–332.
25. Edwards, H. H., "Wrought Iron Axles", *The Civil Engineer and Architect's Journal*, 1843;6;48.
26. Morin, A., *Leçons de Mécanique Practique - Résistance des Matériaux* [Studies in Practical Mechanics - Strength of Materials], Paris: Librairie de L. Hachette et Cie, 1853.
27. Rankine, W. J. M., "On the Causes of the Unexpected Breakage of the Journals of Railway Axles, and on the Means of Preventing Such Accidents by Observing the Law of Continuity in Their Construction", *Minutes of Proceedings of the Institution of Civil Engineers.* 1843, 2, 105–108, *J. of the Franklin Institute*, 1843, **6**, 178–180.
28. Kirkaldy, D., "Results of an Experimental Inquiry into the Comparative Tensile Strength and other Properties of Various Kinds of Wrought Iron and Steel", *Transactions of the Institution of Engineers in Scotland*, 1863, **6**, 27–51.
29. Glynn, J., "On the Causes of Fracture of the Axles of Railway Carriages", *Minutes of Proceedings of the Institution of Civil Engineers.* 1844, **3**, 202–203; *The Civil Engineer and Architect's Journal*, 1845, **8**, 109.
30. McConnell, J. E., "On Railway Axles", *Proceedings of the Institution of Mechanical Engineers, London*, 1849, October, 13–27; *The Civil Engineer and Architect's Journal*, 1849, **12**, 375–378.
31. Stopfl, P., "Achsenbrüche an Lokomotiven, Tender und Wagen, ihre Erklärung und Beseitigung" [Axle Failures in Locomotives, Tenders and Wagons – Their Causes and Methods of Avoiding], *Organ für die Fortschritte des Eisenbahnwesens in technischer Beziehung*, 1848, **3**(2), 55–67.
32. McConnell, J. E., "On the Deterioration of Railway Axles", *Proceedings of the Institution of Mechanical Engineers, London*, January 1850;5–19; *The Civil Engineer and Architect's Journal*, 1850, **13**, 120–123.
33. Anon, "Chemins de Fer – Formation d'une Commission de Statistique", *nnales des Ponts et Chaussées*, 1842, **2**, 308–310.
34. de Boureuille, _. Adressé à M. le Ministre des Travaux Publics par la Commission Speciale Chargée de Rechercher les Mesures de Sûrité Applicables aux Chemins de Fer,. *Annales des Ponts et Chaussées*, 1846, **12**, 261–315.
35. de Boureuille, _. "Safety of Railways", *The Civil Engineer and Architect's Journal*, 1847;10:41–45.

36. Haigh, B. P., "Fatigue in Non-Ferrous Alloys", *Bulletin of the British Non-Ferrous Metals Association*, 1925, **15** July, 11–16.
37. Wood, De Volson. *A Treatise on the Resistance of Materials and an Appendix on the Preservation of Timber*, 6th Edition, New York:John Wiley and Sons. 1888.
38. Engerth, W., "Ueber die Veränderung der Textur des Eisens, welches bei stattfindender Torsion zugleich StöBen ausgesetzt ist", *Zeitschrift und das als besondere Beilage herausgegebene Notizen- und Intelligenzblatt des österreichischen Ingenieur-Vereines für das Jahr 1851*. 1851, **3**, 34–36.
39. von Burg, Ritter., "Ueber die von dem Civil-Ingenieur Hrn. Kohn, angestellten Versuche, um den Einfluss oft wiederholter Torsionen auf den Molekularzustand des Schmiedeisen auszumitteln", *Sitzungsberichte der Kaiserlichen Akademie der Wissenschaften, Wien*, 1851, **6**, 149–152.
40. Schrötter, A., "Ist die krystallinische Textur des Eisens von Einfluss auf sein Vermögen magnetisch zu Werden?", *Sitzungsberichte der Kaiserlichen Ajademie der Wissenschaften, Wien*, 1857, **23**, 472–481.
41. Tredgold, T., *Practical Essay on the Strength of Cast Iron and Other Metals*, 4th Edition with Notes by Eaton Hodgkinson, London:John Weale. 1842.
42. Hood, C., "On Some Peculiar Changes in the Internal Structure of Iron, Independent of, and Subsequent to, the Several Processes of Its Manufacture", *Philosophical Magazine*, 1842, **21**(136), 130–137, *Minutes of Proceedings of the Institution of Civil Engineers*, 1842, **2**, 180–184, *The Civil Engineer and Architect's Journal*, 1842, **5**, 418.
43. Vignoles, C., "On Straight Axles for Locomotives", *Reports of the British Association for the Advancement of Science*, 1842, **12**, 104–105.
44. Nasmyth, J., "On the Strength of Hammered and Annealed Bars of Iron and Railway Axles", *Reports of the British Association for the Advancement of Science*, 1842, **12**, 105–106.
45. York, J. O., "Account of a Series of Experiments on the Comparative Strength of Solid and Hollow Axles", *Minutes of Proceedings of the Institution of Civil Engineers*, 1843, **2**, 89–94.
46. McConnell, J. E., "On the Deterioration of Railway Axles", *Proceedings of the Institution of Mechanical Engineers, London*, 1850, April, 13–14.
47. Thorneycroft, G. B., "On the Manufacture of Malleable Iron; with the Results of Experiments on the Strength of Railway Axles", *Minutes of Proceedings of the Institution of Civil Engineers*, 1850, **9**, 294–302.
48. Thorneycroft, G. B., "On the Manufacture of Malleable Iron, and Railway Axles", *The Civil Engineer and Architect's Journal*, 1850, **13**, 259–261; *J. the Franklin Institute*. 1852, 24, 330–335.
49. Thorneycroft, T., "On the Form of Shafts and Axles", *Proceedings of the Institution of Mechanical Engineers, London,* 1850, July, 35–41, (October):4–15.
50. Braithwaite, F., "On the Fatigue and Consequent Fracture of Metals", *Minutes of Proceedings of the Institution of Civil Engineers*, 1853, **13**, 463–475, *The Civil Engineer and Architect's Journal*, 1854, **17**, 237.
51. McConnell, J. E., "On Hollow Railway Axles", *J. the Franklin Institute*, 1853, **26**, 361–366, *The Civil Engineer and Architect's Journal*, 1853, **16**, 387–389.
52. McConnell, J. E., "On Hollow Railway Axles", *J. the Franklin Institute*, 1854, **27**, 82–85.
53. Wrottesley, J. Willis, R., James, H., Rennie, G., Cubitt, W., and Hodgkinson, E., *Report of the Commissioners Appointed to Inquire into the Application of Iron to Railway Structures*. London: Wm. Clowes and Sons, for Her Majesty's Stationery Office. 1849;XX + 453 pages.
54. Wrottesley, J. Willis, R., James, H., Rennie, G., Cubitt, W., and Hodgkinson, E., "Report of the Commissioners Appointed to Inquire into the Application of Iron to railway Structures",

The Civil Engineer and Architect's Journal, London, 1850;13:49–64,84–94,181–183; *J. the Franklin Institute*, 1850, **19**, 289–302, 360–371.

55. Dempsey, G. D., *Iron Applied to Railway Structures: Comprising an Abstract of Results of Experiments Conducted Under the Authority of the Commissioners Appointed by Her Majesty to Inquire Into the Application of Iron to Railway Structures, with Practical Notes and Illustrated by Plates and Descriptions of Some of the Principal Railway Bridges*. London: Atchley & Co. 1850.
56. Peterson, R. E., "Discussions of a century ago concerning the nature of fatigue and review of some of the subsequent researches concerning the mechanism of fatigue", *Bull. ASTM*, 1950, **164**, 50–56.
57. Willis, P., "Essay on the Effects Produced by Causing Weights to Travel Over Elastic Bars", Appendix C in Barlow, P., *A Treatise on the Strength of Materials*, revised by P. W. Barlow and W. H. Barlow. London: Lockwood & Co. 1867, 326–386.
58. Anon, "Report of the Commissioners Appointed to Inquire into the Application of Iron to Railway Structures" *J. the Franklin Institute*, 3rd Series, 1850, **20**, 361–364.
59. Kirkaldy, D., *Results of an Experimental Inquiry into the Tensile Strength and Other Properties of Various Kinds of Wrought-Iron and Steel*, 2nd Edition. 1863.

Appendix B*
Final Report for the USAF High Cycle Fatigue Program

Otha Davenport

INTRODUCTION

In the mid 1980s, high performance gas turbine engines with relatively high thrust to weight ratios were beginning to reach the boundaries of the empirically based design systems for the phenomena that was to become High Cycle Fatigue (HCF). Simply stated, HCF is the formation and propagation of cracks in a structure that results for many millions (or billions) of cycles at stresses well below the yield strength of the material. The relatively small stresses can be the result of any or all of a myriad of stimuli that can be extraordinarily complex.

As jet engines provided higher performance at lower weights, difficulties in unexplored areas developed. In the 1960s, the challenge was compressor stall when the throttle was abruptly moved, or the aircraft maneuvered. Tools and methods for stall prediction, avoidance, and recovery were developed and became the standard for the engine manufacturers

In the 1970s, unexpected and unpredicted structural failures were the next major technical challenge for engine designers. Extensive testing and analysis, along with characterization of a new generation of materials, showed that the large mechanical and thermal strain associated with the full range of throttle movements from starting through maximum power was developing and propagating cracks in the major rotating components. This was characterized as Low Cycle Fatigue (LCF) and the USAF developed and promulgated the Engine Structural Integrity Program as a development and sustainment process to manage the application of the LCF tools and methods throughout the life cycle and preclude unexpected structural failures.

As HCF field failures continued to occur through the late 1980s and early 1990s, the effects of these failures became more and more onerous on the war fighting commands. It became imperative for the engineering staffs within the government and the engine manufacturers to better understand the many dimensions of this phenomenon. The first study of HCF was conducted by ASC/EN in 1989, followed by a USAF Scientific Advisory Board review in 1991. The issue was recognized as a major issue by the

* This document was prepared by Otha Davenport, Director of Engineering, Propulsion Product Group, Wright-Patterson AFB, retired.

then Assistant Secretary of Defense, Dr. John Deutch in 1994 who said **"Engines are *the* major readiness issue for USAF."** Further, the Secretary of the Air Force, the Honorable F. Whitten Peters stated, "**This is not only a readiness issue, it is a retention issue.** . . . " Meanwhile, the Air Force Chief of Staff, Gen Fogleman, stated in 1995:

> Part of the problem is the workload that our flightline troops and our engine shops are experiencing due to new inspection requirements to combat *high cycle fatigue*.

A further emphasis was added as new configurations of higher thrust to weight engines were being developed with higher aerodynamic loading with little or no inherent mechanical damping as integrally bladed rotors were chosen as the preferred configurations. The USAF Air Force Research Laboratory responded to this imperative in 1995 with the National High Cycle Fatigue Initiative which grew into the International High Cycle Fatigue Program with the participation of the United Kingdom Ministry of Defense (MoD).

The program began with and has preserved the objective of the development of a physics-based design system that encompasses the underlying but necessarily complex interactions of the steady and the unsteady aerodynamic forces, the damped mechanical response of the structure, the capability of the material to withstand the stresses that are applied and the experimental tools to measure these characteristics and to verify the physics-based analytical tools as they are developed. The HCF failures have generally been experienced in only a very small percentage of a population of engines. This implies that these failures occur in the extremes of a probabilistic distribution of the contributing factors and are difficult, if not impossible, to precisely replicate in a laboratory or test facility.

The program has accomplished many of the objectives initially outlined and many physics-based design tools have been transitioned to routine use in company design systems, however these tools have yet to be integrated into a comprehensive design process for HCF. New instrumentation concepts and products have greatly expanded the understanding of the excitation forces and mechanical responses. New and innovative material test methods have greatly shortened the time required to characterize the HCF properties of materials. New damping approaches are yielding products to reduce the vibratory responses of lightly damped components. New processes for surface treatments to impart large compressive surface stresses have largely matured as a result of this program and are in production on several engines.

The most elusive objective that has yet to be reached is the ability to integrate the inherent probabilistic nature of HCF. A characterization protocol has been developed to better understand the nature of these statistical distributions of significance but a method to demonstrate a desired level of resistance to HCF has yet to emerge.

Even at the current stages of maturity of the various HCF tools and methods, the impact of the HCF program on current and development engines has been enormous. The field

engine inspection workload for HCF has been reduced by over 90% and the proportion of engine mishaps resulting from HCF has been reduced from 54 to 7%, far exceeding the HCF program goal of a 50% reduction in mishaps.

Further, these same tools are enabling technologies for the next generation of high performance jet engines and for the foundation of the F135 and F136 engines for the F-35 Joint Strike Fighter that is intended for use by the USAF, USMC, USN, and many allied and friendly countries. Without these tools and methods, the development programs would likely encounter many unexpected development difficulties with the accompanying delays and cost growth.

BACKGROUND

Emergence of HCF as critical issue

In the mid 1980s HCF began to emerge as a critical issue for the USAF. The designs of engines prior to the F100 and F110 used primarily steel compressor blades and rotors while solid nickel blades and rotors were used in the turbines. The introduction of titanium blades and rotors in the fans and compressors allowed higher blade loading, greater rotor speeds, all in a material with less inherent material damping than the traditional steel materials. Relatively early in the fielding of the F-16 aircraft, HCF issues began to appear with no indication of the existence of these problems in the engine development and qualification programs. The F-16, being the most prevalent aircraft in the USAF inventory and being a single engine fighter, accentuated the issue because an engine failure caused loss of the aircraft in about 80–90 % of the cases.

In one engine model, the first stage compressor blades and disk posts failed and the fleet was impacted with blade change outs. This was followed by the development of ultrasonic inspection techniques to find the cracking before it led to failures. One characteristic of HCF also began to emerge at this time, namely the probabilistic nature of the failure mode. In all, only about 1 in 1000 blades ever indicated cracking. The underlying cause of these cracks was not well understood but the traditional methods of reducing or eliminating HCF were all applied. These included reduction of the net section stresses and reduction of fretting in the blade/disk interface. While these redesigns served to reduce the incidence of cracking they were not adequate to eliminate the problem and ultrasonic inspections continued for many years.

In another engine model, the HCF cracking occurred in the last stage of a three-stage fan. Engine failures were caused by the loss of fan blades and disk segments. Much attention was focused on this issue as it only began to appear after the fleet had accumulated slightly over 1,000,000 flying hours with no indication of the issues being present. This particular issue caused great disruption of the fleet maintenance process as fan removal was required frequently for an effective inspection. Again the traditional

tools were again applied for redesigns and proved totally inadequate as the frequency of failure actually increased as the redesigns were incorporated. Only after the initial stages of the HCF Program were underway did it become known that the aerodynamic driver was the downstream stationary airfoils and an effective redesign occurred.

By the late 1980s Headquarters Tactical Air Command became concerned enough with HCF failures and fleet impacts, that the Director of Logistics sent a letter to the Air Force Systems Command's Aeronautical Systems Division (ASD) requesting a thorough review of the design, development, and qualification process that was not catching these issues before they occurred in the field. The ASD/EN conducted a study that noted the issue and made modest recommendations for improvements.

As the decade of the 90s opened, HCF became a more notable problem as the B-1 engine experienced two spectacular failures, one of which led to the engine separating from the aircraft. These failures demonstrated a high susceptibility of the fan to Foreign Object Damage (FOD) with stimulation by the inlet characteristics that had never been tested. The Assistant Secretary of the Air Force directed an Air Force Scientific Advisory Board (SAB) study of the issue which focused on the issue of the use of titanium alloys in jet engine compression systems (fans and compressors). The 1992 SAB report entitled "Air Force Jet Engine Manufacturing and Production Processes" presciently made five recommendations that later would form the backbone of the HCF program and the technical partitioning of the program. These included: extension of the application of fracture mechanics to HCF; establishing a substantial research program to increase understanding of HCF; and determining a procedure to demonstrate resonant frequencies and vibratory stress levels in qualification engine testing.

HCF becomes a crisis

By the mid 1990s HCF issues had become the dominant failure mode for fighter engines in the USAF. With tensions high on the Korean peninsula, specially equipped F-16s with the mission to suppress enemy air defenses were grounded due to an HCF issue in a rotating air seal while the deep strike F-15Es were restricted due to an HCF issue with a low pressure turbine blade. This placed a constriction on the forces the theater commander could rely on should hostilities arise. Further HCF issues were becoming apparent in fans while inspections were continuing to limit safety concerns in compressors. All of these issues arising over a fairly short time period evoked a high level of interest across the USAF and the DOD. Studies of the rates of USAF mishaps over a period of 15 years showed over 50% resulted from HCF. Similar data for the USN showed over 40% of mishaps resulted from HCF. Also during this time HCF began to appear in commercial engines to a lesser extent than in military engines but with severe consequences to the manufacturer's development programs and revenue service for airlines.

HCF initiative

With all of this interest, it fell to the AFRL and AFMC to develop a comprehensive set of programs to bring the situation under control. The AFRL began the development of the HCF Initiative while the USAF Propulsion Product Group Manager began the planning for the Robust Engine Initiative.

The HCF Initiative consisted of a broad strategy to develop the tools and techniques to change the basis of HCF design from empirically based to physics based and then to demonstrate and transition these tools to the industry design systems. The HCF Initiative was further broken down into an S&T Initiative under the leadership of the AFRL Propulsion Directorate with major support from the Materials and Manufacturing Directorate and a T&E initiative under the leadership of Arnold Engineering and Development Center. The S&T Initiative funding changed fairly dramatically over the first couple of years. It was originally planned to be about a $140M program over a 5-year period (~$100 M government and ~$40 M industry), it then rose to ~$230 M as other organizational funding (US Navy, NASA and AFOSR) was included and the program was extended to FY01. It then was reduced to a low of about $120 M to fit budget allocations and all flight and altitude demonstrations were eliminated. A Quality Functional Deployment process was implemented to determine where these limited funds should be allocated. The highest payoff areas were identified and some funding restored to ~$110 M government. The T&E Initiative was envisioned as a more modest program of about $10 M over the same period. The Robust Engine Initiative (REI) was a more expensive program of as much as $600 M depending on the extent of changes found to be needed on fleet and developmental engines and the cost of making these changes.

The S&T Initiative originally consisted of seven segments assigned to seven action teams. These were: Materials Damage Tolerance, Component Surface Treatment, Passive Damping Technology, Forced Response Prediction, Component Analysis, Aeromechanical Characterization, and Instrumentation. Engine demonstrations were an eighth action team but as the engine demonstrators supported the overall IHPTET program, they were eventually not counted in the HCF Initiative.

The T&E Initiative was focused on better tools for gathering and processing strain gage data and improvements in non-contact stress measuring systems (NSMS, tip timing, light probes, etc.)

The Robust Engine Initiative was never funded. The USAF decision makers determined that the return on finding the issues before they surfaced in the field did not counter the costs of testing and application of the emerging HCF tools. It should be noted that about 85–90% of the suspect areas identified in the program plan later surfaced as field issues and were corrected through the AF Component Improvement Program with costs similar to those projected for the REI but with the field impacts that REI sought to avoid.

As the HCF Program matured, it became clear the program was clearly supporting the overall objectives of the central propulsion S&T program, the Integrated High

Performance Turbine Engine Technology Program – IHPTET; therefore the HCF Program became a part of the IHPTET program with the goal-oriented structure that had become the hallmark of technical excellence. The HCF Program adopted the architecture of a steering committee made up of all of the stakeholders who were investing institutional resources in the program.

The HCF program goals were established as follows:

Goal	*Fans*	*Compressors*	*Turbines*
Determine alternating stress within . . .	20%	25%	25%
Damp resonant stress by . . .	60%	20%	25%
Reduce uncertainty in capability of damaged components by . . .	50%	50%	50%
Increase leading edge defect tolerance . . .	15×(5–75 mils)	n/a	n/a

By the late 1990s with the British participation in the Joint Strike Fighter (F-35) Program, it became apparent that the UK MoD and Rolls-Royce plc should be a part of the HCF Program as the British elements of the program were likely to be vulnerable to HCF. After years of working the government to government agreements, the UK MoD joined the HCF steering committee in 2000.

The HCF steering committee was augmented by an industry advisory panel (IAP) made up of representatives of all of the US turbine engine manufacturers and later included Rolls-Royce plc and Rolls-Royce Corp. The steering committee with the advice of the IAP provided guidance to the seven action teams on technical progress, resource allocations, and priorities.

As the program progressed, an Executive Independent Review Team was formed with graybeards from the academic, industrial, and government sectors, which provided additional oversight and guidance to the action teams and the steering committee.

During the fall of 1999, the HCF National Action Team completed a Project "Relook" study defining the efforts necessary to mitigate critical risk issues—both current program "shortfalls" and "new requirements." Reprogramming plans were extensively reviewed and approved by both the HCF Industry Advisory Panel and a special committee. This reprogramming action extended the HCF program through 2006, with increased focus on Joint Strike Fighter (JSF) technology transition and greater attention to UAV/small engine issues. This was to be the last major restructuring of the HCF Program although funding issues in 2004 and 2005 limited some of the demonstrations of the HCF tools.

Appendix C*
HCF in ENSIP

MIL-HDBK-1783B
15 February 2002

DEPARTMENT OF DEFENSE HANDBOOK

ENGINE STRUCTURAL INTEGRITY PROGRAM (ENSIP)

The purpose of this handbook is to establish structural performance, design development, and verification guidance to ensure structural integrity for engine systems. The guidance contained herein includes the experience and lessons learned and achieved during development of US Air Force engine systems since the mid-1940s. Recent experience indicates superior structural safety and durability, including minimum structural maintenance, can be achieved on an engine system if the guidance contained herein is included and successfully executed during system development.

4.6. Material characterization

The materials used in the engine should have such adequate structural properties as strength, creep, low cycle fatigue, high cycle fatigue, fracture toughness, crack growth rate, stress corrosion cracking, thermomechanical fatigue, oxidation/erosion, wear, ductility, elongation, and corrosion resistance so that component design can meet the operational requirements for the design service life and design usage of the engine specified in 4.3 and 4.4.

4.13.3. High cycle fatigue

The probability of failure due to high cycle fatigue (HCF) for any component within or mounted to the engine should be below 1×10^{-7} per EFH on a per-stage basis, provided the system-level safety requirements are met.

* The sections in this Appendix from this version of ENSIP are those that deal with material behavior under HCF conditions and the associated design guidelines. They are extracted verbatim from the ENSIP document reference in the title.

5.13.3.2. Component vibrations

Verification of model validity, model characteristics, vibration amplitudes, steady stresses, and all other aspects of the HCF problem should be performed at each step of the design and verification process. An integrated approach where each stage of the design/verification process builds upon the previous one should be utilized. Verification should include numerical verification (sensitivities to key parameters) and data generated in component bench testing, rig testing, engine testing, and, ultimately, operational use. Established methods to compare experimental and analytical results should be employed where possible. Probabilistic design margins and predictions should be validated with bench, rig, and engine test experience in addition to statistical comparisons to operating fleet databases. Assurance is to be provided by verifying that the probability levels for each contributing random variable used to compute probabilistic design margins or probability of failure are within the experimental data range for that variable.

VERIFICATION GUIDANCE (A.5.3.2)

Failure modes (e.g., LCF, HCF, creep, etc.) analyses should be conducted by the contractor to establish design stress levels and lives for engine cold parts based on the design usage.

A.4.6. Material characterization

The materials used in the engine should have adequate structural properties, such as strength, creep, low cycle fatigue, high cycle fatigue, fracture toughness, crack growth rate, stress corrosion cracking, thermomechanical fatigue, oxidation/erosion, wear, ductility, elongation, and corrosion resistance, so that component design can meet the operational requirements for the design service life and design usage of the engine specified in 4.3 and 4.4.

REQUIREMENT RATIONALE (A.4.6)

Material structural properties should be quantified in advance of detail design so that materials selection and design operating stress levels can be established which provide a high degree of confidence that operational requirements will be met. Early generation of sufficient data for use in preliminary and detail design is emphasized since later surprises relative to structural properties will have a significant impact on redesign, substantiation, and replacement needs, and weapon system availability.

REQUIREMENT GUIDANCE (A.4.6)

Structural properties used in design (design allowables) should be based on minimum material capability unless otherwise stated in this document. The intent is to base all material properties except fracture toughness and crack growth on minus three Sigma (-3σ) values with a 50% confidence level or minus two Sigma (-2σ) values with a 95% confidence level. Another option is to state that material properties will be based on B0.1 probability values. The confidence level for B0.1 is 50%. Another alternative is "A Basis" from MIL-HDBK-5, which uses properties for 99% exceedance with 95% confidence. Typically, B50 properties may be used to characterize fracture toughness and crack growth rate. In addition, design allowables should be justified by the contractor's experience base design methodology, and design criteria. Specimens fabricated from "as produced" parts should be tested to verify properties relative to different locations within the part (i.e., locations that receive different amounts of work during manufacture such as the bore, web, and rim regions of disks). If "as produced" parts are unavailable, the use of parts produced by equivalent practices, or parts sufficiently similar, should be considered, if available.

High Cycle Fatigue

The material properties should be established at stresses (steady and vibratory), frequencies, temperatures, and other parameters representative of the operating environment of the engine. Loading conditions for which stresses in materials are established for HCF should be determined from stress and vibration analysis based on a probabilistic formulation of static and dynamic forcing functions. The probability of failure due to these forcing functions should be maintained below 1×10^{-7} per EFH on a per-stage basis, provided the system-level safety requirements are met. Material allowables for high cycle fatigue should be based on basic building block specimen and sub-element laboratory tests, and validated against sub-element and component laboratory bench tests. In the establishment of these allowables, the methodology for transferability of laboratory data to components should be identified. The statistical basis and significance of material allowables should be defined. In the establishment of material allowables, consideration should be given to the combination of applied vibratory stress levels, mean stresses, multiaxial stress state, vibratory frequency, maximum number of applied cycles (see Section A.4.13.3), and state of material damage. Material damage should include, but not be limited to, variation in initial material quality due to manufacturing, fabrication, or inherent material defect population; in-service damage such as that produced by low cycle fatigue loading, fretting or fretting fatigue, wear, or foreign object damage; any other anticipated damage including, but not limited to, corrosion or other environmentally induced degradation of material

capability, thermal or thermal–mechanical cycling, static or cyclic creep, and break-in or green run engine cycles.

Material damage states which should be addressed in the design process include all conditions which are considered by design, analysis, or field experience to limit the durability of the material or component or produce conditions which require either periodic inspection or replacement at set intervals. The damage accumulated immediately prior to the inspection or periodic maintenance interval should be considered with respect to its effect on the HCF behavior of the material or component. Allowable HCF vibratory loading should be less than that which would cause such damage to worsen or propagate due to HCF loading.

In addition to the above damage states, any combinations of these which are deemed likely to occur during the lifetime of the component and may produce a degradation of the HCF capability of the material should be considered in the establishment of the material design allowables.

REQUIREMENT LESSONS LEARNED (A.4.6)

Premature structural failures have occurred prior to design service life (based on average material properties) and have been attributable to components with material capabilities as low as minimum, unforeseen vibratory stresses or damage modes, or errors in analysis.

A.5.6 Material characterization

Material structural properties should be established by test and modeling. Anticipated properties under damage states (e.g., fretting, etc.) should be verified through combinations of laboratory specimen, sub-element and component testing, material damage models which have been validated against databases and supplemented with historical data which cover the range of potential damage states, or databases which cover the properties under damage states.

VERIFICATION RATIONALE (A.5.6)

Material properties should be established by test and should be based on specimens fabricated from “as produced” parts, from parts produced by equivalent practices, or from parts sufficiently similar in processing and size, since critical structural properties are dependent upon the manufacturing processes. Damage states in the parts which may occur during field usage should be verified for their potential impact on HCF life.

VERIFICATION GUIDANCE (A.5.6)

General

A material characterization plan should be prepared and existing data should be presented. Final definition of structural capability should be based on the testing of specimens fabricated from "as produced" parts, from parts produced by equivalent practices, or from parts sufficiently similar in processing and size. The contractor should review existing data on proposed materials and processes and develop a material characterization plan that identifies and schedules each of the tasks and interfaces in design, material selection, and testing. The tasks to be identified in the plan should include:

(a) correlation of the operating envelope conditions to which each material will be subjected (i.e., temperature, loading frequency, max and min cyclic stresses, steady and vibratory stresses, etc.) through the test environment and usage;
(b) a parts listing with the corresponding materials and manufacturing processes;
(c) identification of mechanical properties that should be generated for each material/part;
(d) test specimen configuration;
(e) the source of material data;
(f) number of tests to be conducted for each material property curve needed for each part;
(g) quality control actions or vendor substantiation test requirements that will be utilized to ensure at least minimum mechanical properties will be attained in finished parts through the production run; and
(h) risk assessment and abatement plan for use of any advanced materials and processes.

Existing data obtained through earlier tests can be used during initial design only when the manufacturing processes are similar (i.e., same methods of producing billets, forgings, heat-treat processes, machining, surface treatment, etc.). Final definition of structural capability should be based on the material property curves generated by testing specimens fabricated from the "as produced" parts, from parts produced by equivalent practices, or from parts sufficiently similar in processing and size to verify material properties relative to different locations on the part, as appropriate, based on screening tests or historical data. Material properties should be defined for each material/part source (i.e., material and manufacturing vendor).

The number of tests conducted for each curve or condition should be adequate to establish minimum material properties used in design or to establish the correlation between the data obtained from specimens cut from parts and the database within the calibrated design methodology.

High cycle fatigue

Material allowables should be based on the combination of mean and vibratory stress amplitude, or equivalent quantities for multiaxial stress conditions. Material allowables for a uniaxial stress state, presented in the form of a constant life Haigh diagram (commonly referred to as "a Goodman diagram"), should be based on actual data. Straight line extrapolations from fully reversed ($R = -1$) loading data to the quasi-static yield or ultimate stress are not acceptable for engine full production release status. Further, for high values of mean stress greater than one-half the static yield stress, maximum stress (= mean stress + alternating stress) should be used as the material allowable in addition to vibratory stress to establish a factor of safety. For materials that exhibit time-dependent deformation (e.g., titanium at room temperature), strain accumulation should be considered in the establishment of material allowables. Time-dependent deformation should include effects due to: (a) static creep – deformation accumulated on the basis of time spent at stress levels above which static creep can occur and (b) cyclic creep or creep ratcheting – deformation accumulated on a cycle by-cycle basis due to hysteresis in the stress–strain response of the material. Cyclic-dependent creep or creep ratcheting should be considered when plasticity effects are more pronounced, specifically for larger stress ratios, R, above 0.7. At high stress ratios, the use of $K_{\max}$ as well as ΔK should be considered for damage tolerance.

Material capability in the presence of a damage state as described in section A.4.6 should be verified. The following damage states should be verified as follows:

Low cycle fatigue

Cracks which might form due to LCF loading and grow to an inspectable size should be considered in HCF analysis. It should be demonstrated that the largest crack which might be present just before inspection should not propagate due to HCF loading if present, based on a threshold stress intensity applicable to the specific crack size considered. For cracking below the inspection limit, it should be shown that HCF would not lead to failure within twice the inspection interval.

In regions of contact (i.e., blade to disk), it should be assumed that a crack of depth $2a_0$, normal to the contact surface, can develop during service. It should be demonstrated that such a crack will not grow to a catastrophic size during a time corresponding to twice the inspection interval in regions where inspections are performed to detect cracks of depth $2a_0$, or for twice the design service life for regions where such an inspection cannot be (is not) performed. Crack detection is defined as the ability to find a crack with a reliability of 50% and a confidence limit of 90%. When the growth rate is established, the bulk stresses in the component – including both LCF and vibratory stresses – should be considered, in addition to contributions from the local stress field due to the contact loads. Where vibratory stresses are present, the threshold stress intensity should be used to insure HCF propagation will not occur (see HCF section, above) unless it can be shown that crack arrest will occur after further crack growth.

Note: a_0 is determined from the El Haddad formulation (see A.2.3) which relates threshold ΔK to • endurance and ensures growth behavior is outside the "short crack" regime, so anomalous short crack behavior does not have to be considered.

$$a_0 = \frac{1}{\pi}\left(\frac{\Delta K_{\text{th}}}{F\Delta\sigma_{\text{end}}}\right)^2$$

where ΔK_{th} is the threshold stress intensity range, σ_{end} is the endurance limit stress range, and F is the geometry factor for the specific crack being considered. For a through edge crack, $F = 1.12$, while for a thumbnail crack in a smooth bar, $F = 1.12(2/\pi) = 0.713$. In general, F is defined from the stress intensity solution for any crack as

$$K = \sigma F\sqrt{\pi a}$$

Fretting fatigue

a. Stress states which result from combined steady and vibratory loading should be shown to be below that which would produce HCF failure in a region which may be subjected to fretting fatigue damage. The fretting fatigue damage state and the resultant degradation of the fatigue limit should be determined from the predicted vibratory loads and interfacial conditions where fretting fatigue may occur. The reduced fatigue limit should be determined under conditions representative of the fretted region, including consideration of contact and friction stress interaction with applied mechanical stresses.
b. A reduction in design allowables is not required for HCF if it can be shown that the stresses and other conditions in the interface region produce damage values sufficiently low as to have a negligible effect on the high cycle fatigue limit of the undamaged material.

***Foreign object damage* (*FOD*)**

High cycle fatigue material allowables should be determined based on the probability of the type and severity of FOD damage determined from combinations of prior field experience, analysis, and testing, as well as a probabilistic assessment of the size and occurrence of foreign object damage. A fatigue notch factor (K_{f} = fatigue strength in smooth bar/fatigue strength in notched bar) criterion may be used in preliminary design for guidance to assess FOD capability; however, a fatigue notch factor applicable to each specific component should be used for final design. In the establishment of the fatigue notch factor, consideration should be given to the geometry and severity of the FOD on which the design is based. Foreign object damage capability should be established based on analysis and testing of specific component and FOD geometry including effects of associated residual stress fields. For components which cannot be inspected, it should be demonstrated that combined steady and vibratory stress levels, whether from axial, bending, or torsional loads, or any combination thereof, are: (a) below the threshold for fatigue crack growth and continued propagation when cracks, including microcracks, are present and (b) below the fatigue limit stress in the absence of cracks from FOD. Threshold can be defined from fracture mechanics using ΔK or from fatigue limit stress. If this requirement cannot be met in the manner specified above, a FOD/DOD detection system may be installed as a means

to reduce the risk of failure to an acceptable level. Blend limits for FOD and criteria for removal or repair should be based on the FOD analysis required in the preceding paragraph. Material allowables for material which has been repaired, such as by blending or welding, should be adjusted as necessary to account for any degradation of the fatigue limit due to the blend or repair operation. The effect of any redistribution of internal stress, whether induced by FOD or by prior processing, should be considered in the development of safe blending limits.

Other Damage States

Material allowables should be established based on any other damage state as described in section A.4.6 under the "High Cycle Fatigue" heading.

Analytical studies have shown that not every part location will be limited by a crack growing to a calculated critical stress intensity equal to the material's fracture toughness. Some part locations will in fact be life-limited by cracks growing to a predicted vibratory threshold ΔK_{th} HCF, where

$$K_{\max,\text{allowable}}\,\text{LCF} = \Delta K_{th}\text{HCF}/(1-R)$$

and

$$R = \frac{(\sigma_{\text{steady}} - \sigma_{\text{vibratory}})}{(\sigma_{\text{steady}} + \sigma_{\text{vibratory}})}$$

$$\sigma_{\text{steady}} = \text{maximum operating stress neglecting vibratory stress}$$

$$\sigma_{\text{vibratory}} = 1/2(\text{peak to peak vibratory stress})$$

and

$$\Delta K_{th}\ \text{HCF} = f(R, \text{temp.})$$

Overspeed residual strength requirements need not be considered for those part locations limited by cracks reaching a calculated vibratory threshold. One overspeed cycle occurring at a crack size equal to the vibratory threshold creates less damage (change in crack size) than additional LCF–HCF crack growth from the vibratory threshold to a maximum stress intensity (K_{CRIT}) defined by the material fracture toughness.

For those locations not limited by vibratory stress concerns, the part's maximum allowable crack size should be limited to a size that will survive the maximum design stress that occurs on the last cycle of the calculated safety limit.

REQUIREMENT GUIDANCE (A.4.8.5)

The flaw growth interval is also known as the *safety limit*. It is recommended that the flaw growth intervals be twice the inspection intervals specified in A.4.8.4. Flaw growth interval margins, other than two, can be used when individual assessments of variables (i.e., initial flaw size, da/dN, KIC, etc.) that affect flaw growth can be made (e.g., to account

for observed scatter in crack growth during testing). The following should be considered in treatment of variables which can affect the calculation of the flaw growth interval:

(a) No life credit should be taken of any beneficial effects of residual stresses or surface treatments such as shot peening or coatings, except when the following conditions are met:

(1) The beneficial effect of residual stresses or a surface treatment can be verified through analysis and testing for the duration of the service interval and under the actual anticipated usage and maintenance conditions such as polishing for eddy current inspection.
(2) Quality control procedures for application and in-service integrity are demonstrated to a satisfactory level of reliability.

These beneficial effects should be verified and the extent of life "crediting" should be approved by the Procuring Activity.

(b) Damage in a primary structure may result in load increases in the secondary structure. The analysis of such secondary structures should account for this.

(c) Continuing damage should be assumed at critical locations where the initial damage assumption does not result in failure of the part (e.g., the case of a free surface at a bolthole). The following assumptions of initial damage and location should be considered with the limiting condition used to establish safety limits and inspection intervals:

(1) When the primary crack and subsequent growth terminates prior to component failure, an initial flaw equal to or greater than that which is demonstrated to be inspectable in 4.8.3 should be assumed to exist at the opposite side of the feature after the primary crack has terminated. The stress gradient assumed at the opposite location should be based on the boundary conditions that exist when crack growth has terminated at the primary location. The safety limit for this condition should be the sum of the crack growth at the primary location and at the opposite location.
(2) Growth of an assumed initial flaw at the location opposite the primary location should be verified as an initial condition.

(d) The effects of vibratory stress on unstable crack growth should be accounted for when the safety limit is established. Threshold crack size should be established at each individual sustained power condition (Idle, Cruise, Intermediate) using the appropriate values of steady stress and vibratory stress. The largest threshold crack size should be used as a limiting value in calculation of the safety limit if it is

less than the critical crack size associated with the material fracture toughness. An analytical approach to defining the effects of vibratory stress is based on a maximum stress intensity allowable, $K_{\text{max,allowable}}$ LCF (as a function of stress ratio, R), which is predicted from appropriate material HCF vibratory threshold ΔK_{th} HCF (as a function of stress ratio, R) properties at steady-state operating conditions. This relationship is as follows:

$$\text{Assume, } K_{\text{max,allowable}}\ \text{LCF} = \Delta K_{\text{th}}\text{HCF}/(1-R)$$

$$\text{where} \qquad R = \frac{(\sigma_{\text{steady}} - \sigma_{\text{vibratory}})}{(\sigma_{\text{steady}} + \sigma_{\text{vibratory}})}$$

$$\sigma_{\text{steady}} = \text{max operating stress neglecting vibratory stress}$$

$$\sigma_{\text{vibratory}} = 1/2(\text{peak to peak vibratory stress})$$

$$\text{and} \qquad \Delta K_{\text{th}}\ \text{HCF} = f(R, \text{temp})$$

ΔK_{th} HCF versus R-ratio material property curves used in this verification at various temperatures should be developed during material characterization, as necessary.

(e) The ΔK allowable for threshold crack growth rate should be based on the crack length under consideration; the maximum allowable crack extension which will not produce failure, instability, or measurable change in dynamic response characteristics; and number of HCF cycles between inspections for damage-tolerant components, or full fatigue life (per section A.4.13.3) for durability-limited components.

It should be demonstrated, through analysis or testing, that the limit in the number of allowable HCF cycles should not be exceeded as specified above for the values of $\mathrm{d}a/\mathrm{d}N_{\text{th}}$ and ΔK_{th} chosen for the definition of the threshold condition.

For conditions where $\mathrm{d}a/\mathrm{d}N$ versus ΔK is not known (for example, in the small crack regime or where a crack has not formed to a measurable or deterministic size), then the threshold condition should be based on a fatigue limit (as specified in section A.4.13.3) for the required number of cycles. In general, the threshold crack growth rate condition, $\mathrm{d}a/\mathrm{d}N_{\text{th}}$, *and* the fatigue limit that corresponds to both the appropriate number of HCF cycles required by the design condition and to the maximum allowable crack size or damage state should be met.

(f) Galling/fretting limits (i.e., permissible depth of surface damage) for all contact surfaces should be defined based on $K_{\text{max,allowable}}$ LCF (as a function of stress ratio, R) or stress analysis that demonstrates that the fatigue limit is not exceeded for the specific part under the applied steady and vibratory stresses.

(g) Calculation of hold time crack growth. Assessments of material/design acceptability do not typically account for the flaw growth under constant load conditions. The duty cycle is compressed such that only the cyclic content is preserved. If the constant load duty cycle content is neglected, the rate of growth of cracks can

be underestimated. Early assessments of material/design candidates should include the effects of hold time crack growth under representative load and temperature conditions. Initial screening and subsequent re-screening as the duty cycle matures should be performed to pre-empt service failures.

REQUIREMENT LESSONS LEARNED (A.4.8.5)

Since average fracture properties have been used in analysis, parts made from materials with scatter factors greater than two have failed prior to their inspection interval. Thus, for materials with large scatter factors (i.e., greater than two), factors of safety greater than two, on residual life, should be considered. In addition, the USAF has experienced several disk post (lug) failures attributed to high stress gradients arising at the Edge of Contact (EoC) between the blade and disk. Conventional lifing assessment practices did not address the susceptibility of the material/design to prevent the cracks from propagating under hold time crack growth conditions.

A.5.8.5. Flaw growth.

The requirements of 4.8.5 should be verified by analyses and tests.

VERIFICATION RATIONALE (A.5.8.5)

Verification of flaw growth is necessary to ensure initial flaws will not grow to critical size and cause failure due to the application of the required residual strength load.

VERIFICATION GUIDANCE (A.5.8.5)

The test should be conducted in accordance with A.4.8.

Analyses should demonstrate that the assumed initial flaws will not grow to critical size for the usage, environment, and required damage tolerance operational period. The analyses should account for repeated and sustained stresses, environments, and temperatures, and should include the effects of load interactions. Analysis methods should be verified by test, utilizing engine and rig testing.

VERIFICATION LESSONS LEARNED (A.5.8.5)

None.

A.4.13.3. High cycle fatigue.

The probability of failure due to HCF for any component within or mounted to the engine should be below 1×10^{-7} per EFH on a per-stage basis, provided the system-level safety requirements are met.

REQUIREMENT RATIONALE (A.4.13.3)

High cycle fatigue has been a major safety and maintenance problem in jet engines. Proper attention is required to minimize these failures. A requirement based upon probability of failure is most consistent with HCF experience, given the inherent variability of the many factors involved.

REQUIREMENT GUIDANCE (A.4.13.3)

General guidance for HCF design is provided here. Specific guidance for HCF design is provided in A.4.13.3.1 through A.4.13.3.3.

Variations in the endurance capability of the material, determination of dynamic stresses, determination of steady-state stresses (or pseudo-steady-state stresses), the sequence in which combinations of stresses occur, and other factors all affect the determination of HCF probability of failure. Indeed, this observation has led to the establishment of the probability of failure requirement. The HCF design will be a function of probabilistic design margins on frequency, predictions on the variation on alternating stress, and the current threshold-based approach for material capability.

The probabilistic design margin on frequency will give the probability of resonance for a mode at a given operational condition and should be compared to the system-level reliability requirement. It is conservatively assumed the probability of resonance equals the probability of failure for modes determined to have significant modal excitation (i.e., low order modes and adjacent upstream engine order excitations). Probabilistic design margins on frequency should be computed on the basis of steady-state operation at low order crossings and all known drivers within two stages either upstream or downstream of the subject component. Variations in resonance conditions should be accounted for through probabilistic analysis or appropriate engine test data distributions for the system design condition. Probabilistic design margins lead to a Probabilistic Campbell Diagram, which follows. Deterministic design margins of 10% may be used for preliminary design or when there is insufficient confidence in probabilistic solutions.

In the event an insufficient probabilistic design margin on frequency exists to meet the probability of failure requirement, the next level of probabilistic design analysis is required to predict the variation in resonant stress response. Such probabilistic design

analysis includes physical models of forced response, damping, and mistuning, along with the appropriate probability models for each random variable and correlations between those variables, as appropriate. It should be shown that at the resonant condition that was not avoided with the probabilistic design margin on frequency, the vibratory stress distribution is at a level that meets system reliability requirements when the stress is integrated with material capacity to predict failure. A deterministic design margin may be used when there is insufficient confidence in the probabilistic solution.

Refer to the Figure C.1 below for margins on the material capacity and the current threshold-based approach, and to section A.4.6 for definition of margin-related terminology.

Root mean square component vibratory stresses should not be within 60% of the minimum material endurance capability (i.e., limited to a maximum of 40% of the minimum material endurance capability). If instantaneous peak component vibratory stresses are used, they should not be within 40% of the material endurance capability (i.e., limited to a maximum of 60% of the minimum material allowance capability). Minimum material endurance capability is defined by S/N fatigue tests of a statistically significant population of fatigue specimens at various combinations of steady and alternating loads, or *R*-ratios, representing various levels of local component steady-state or pseudo-steady-state stress.

All engine parts should have a minimum HCF life of 10^9 cycles. This number is based on the observation that an endurance limit does not exist for most materials. If it can be shown through analysis or test that a given part will not experience 10^9 cycles during its design life, a number lower than 10^9 may be used. Such a condition may be established through analysis of vibrating frequencies and probabilities of a given part being subjected to steady-state or transient vibrations. It should be shown that the total time of exposure to any frequency and amplitude is less than 10^9 cycles or that the amplitude is less than the material allowable at 10^9 cycles. An alternate approach is to use a life of 10^9 cycles based on data obtained at shorter lives, but not less than 10^7 cycles, and a demonstrated valid method to extrapolate to 10^9 cycles to establish an endurance

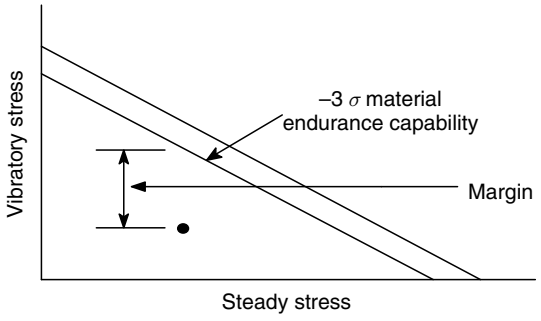


Figure C.1. Material capacity margins.

limit. Cycles which have vibratory stress amplitudes less than the endurance limit at 10^9 cycles can be considered to have no detrimental effect on pristine material and can be ignored in damage accumulation evaluation, provided no other damage is present (see section A.4.6).

For airfoils with FOD/DOD damage tolerance requirements of $K_f = 3$, for instantaneous peak values of component vibratory stress, the alternating stress should be limited to 40% (for RMS values −27%) of the minimum unnotched HCF material allowable or 100% of the $K_f = 3$ minimum notched HCF material allowable. Further guidance to establish damaged material capability is provided in section A.5.6.

One-hundred percent of the Goodman allowable may be used for components with surface enhancements, such as laser shock peening (LSP). When this is done, a threshold analysis and a B.1 life must be established based on data measurements from aeromechanical testing. The minimum life must be based on 1 per the anticipated number of engines in the fleet or no less than 1 per 1000 engines, as a minimum. In other words, there can be no more than 1 engine with 1 blade having an HCF life occurring at one times (1×) the number of blades in the stage for the entire fleet or 1000 engines, whichever is more.

REQUIREMENT LESSONS LEARNED (A.4.13.3)

Complications exist with the concept of specifying all parts be designed to some discrete specified endurance limit. Some of these are:

(a) Prior stressing at a higher stress can cause a lowering of the endurance limit.
(b) Stress cycling at gradually increased cyclic stress can result in an increased endurance limit (this is known as "coaxing").
(c) Interactions between LCF and HCF can result in either increased or decreased lives depending upon the magnitude of the loads, the order of the loading, and the material. This is referred to as "load sequencing." This phenomenon is evidence that HCF margin determination cannot be defined accurately without consideration of the overall stress-state over time.
(d) Installation, handling, and environmental sensitivities can result in significantly higher steady-state and vibratory stresses which will reduce or even have negative margins for HCF capability. Such an example would be external parts which may be sensitive to all of the above. Realistic levels of stress due to these sensitivities should be included when HCF capability is assessed.

Because these complications exist, future efforts should be aimed at components designed to the HCF probability of failure requirement. Future efforts should also strive to integrate

HCF-related damage with other forms of damage (e.g. LCF, creep, etc.) by full consideration of the load sequence and the response of the material to that load sequence.

A.5.13.3 High cycle fatigue.

Verification of the engine's ability to withstand HCF should be through analysis and test. Probabilistic design margins and predictions should be validated with bench, rig, and engine test experience in addition to statistical comparisons to operating fleet databases. Assurance is to be provided by verifying that the probability levels for each contributing random variable are within the experimental data range for that variable.

VERIFICATION RATIONALE (A.5.13.3)

High cycle fatigue is a very complex problem. A great deal of testing and analysis is necessary to avoid HCF problems in the field.

VERIFICATION GUIDANCE (A.5.13.3)

When a validated design system is not in place, a method to extrapolate empirical data should be used to demonstrate compliance with 4.13.3 (e.g., integrally bladed rotors [IBR's] validated with F100 data). Specific guidance for HCF is provided in sections A.5.13.1 through A.5.13.3.

Because of the complex nature of HCF, maximum effort should be expended to insure that all information gathered at all steps of the design and verification process are leveraged. This approach is referred to as "an holistic approach." Models developed during the earliest stages of the design process can be used to assess the sensitivity of mode shapes and frequencies to geometric variations and variations in boundary conditions or operational conditions (referred to as "influence parameters"). Efforts should be aimed at maintenance of consistent modal characteristics over the range of geometric tolerances and influence parameters the part may experience.

Design models should be carried forward to the verification process. The verification process should include accepted practices for validation of the models such as the modal assurance criteria (MAC) and others. (For more information on MAC, see *Shock and Vibration Handbook*, Cyril M. Harris, 4th edition, McGraw Hill, New York, 1995 and its cited references.) Once models are verified, they should be used to establish optimal instrumentation locations for subsequent tests. Criteria to define optimum locations include mode sensitivity (the ability of the sensor to detect maximum mode amplitude), mode identification (the ability to distinguish between modes of similar frequency), and

other physical criteria such as lead routing, proximity of sensors, and the like. Variations in part geometry can be addressed using sensitivity-based approaches applied to a nominal-geometry model.

After verification, models can be used to define vibratory and steady stress fields for all component locations and at engine operating conditions. These normalized stress fields can be scaled to results derived during experimental test to establish the stress time history (load sequence). Should the component fail to meet HCF design requirements, the verified models can be used to direct redesign efforts.

Verification tests in a lab environment (shaker table), in rigs, and in full-up engines generate large volumes of strain data. All these data should be archived to establish a database of responses that can be used to assess variabilities and be used in the validation of probabilistic predictions. Further, examination of all relevant data is useful to define the robustness of a given design over the range of variables tested. Part-to-part variability and the variation of responses to influence parameters—like local pressure, temperature, or flow angularity—can be assessed using these data to define statistically what the maximum expected response may be during operational deployment.

One-hundred percent of the Goodman allowable may be used for components with surface enhancements, such as LSP. When this is done, a threshold analysis and a B.1 life must be established based on data measurements from aeromechanical testing. The minimum life must be based on 1 per the anticipated number of engines in the fleet or no less than 1 per 1000 engines as a minimum. In other words, there can be no more than 1 engine with 1 blade having an HCF life occurring at one times (1×) the number of blades in the stage for the entire fleet or 1000 engines, whichever is more.

VERIFICATION LESSONS LEARNED (A.5.13.3)

Historical approaches to HCF verification have relied almost entirely on experimental results. Design models were generally used only to establish whether the design should be fabricated and to define the steady stress field at some assumed critical operating condition. Once fabricated, the locations of maximum vibratory stress, determination of critical locations, and HCF margin were done almost exclusively using experimental methods.

Newer designs have features that have made an entirely experimental verification approach less reliable. Low aspect ratio blades tend to have a large number of modes closely spaced in frequency within the operating range of the engine. This makes mode avoidance difficult. It also makes identification of modes using response frequency alone more difficult. Mode shapes and frequencies of low aspect ratio blades tend to be more sensitive to small variations in geometry. This leads to greater variability in blade-to-blade stresses and HCF margin—a non-robust characteristic.

Newer designs have also tended to employ integrally bladed rotors; i.e., conventional dovetail or firtree attachments have been eliminated. This has led to reductions in damping for rotor systems and increased complexity system dynamics. Such newer designs also tend to admit a higher degree of disk-blade coupling than earlier, heavier designs. Such coupling is known to increase the probability of HCF failure events with significant potential for uncontained failure modes.

All of these factors have necessitated an evolution in the verification process to integrate analytical techniques and experimental approaches. It also shows the importance of using probabilistic approaches to predict the variation response that need to be validated with test and historical databases.

A.4.13.3.2. Component vibrations.

Engine components should be free of detrimental resonance at all speeds in the operating range. This can be accomplished by intentionally designing modes out of the engine operating speed range or by providing sufficient damping, a probabilistic design margin on frequency and a probabilistic prediction of vibratory stress with respect to steady-state operating speeds, or excitation control to ensure that modes which remain in the running range do not respond detrimentally. A detrimental response is one that exceeds criteria outlined in A.4.13.3.

REQUIREMENT RATIONALE (A.4.13.3.2)

Resonance conditions should be avoided or controlled so that amplified response and structural failure does not occur. Margin, as defined in A.4.13.3, is required due to frequency variations that can occur among a population of engines; or because of changes in operational conditions, deterioration, distortion, or combinations thereof; and other important random design variables. Experience has shown that engine structural components operating under combined steady and vibratory stress conditions should be designed to ensure resistance to HCF cracking.

REQUIREMENT GUIDANCE (A.4.13.3.2)

Resonances in the engine-operating speed range should not occur at steady-state operating speeds such as, but not limited to, idle, carrier approach, hover, cruise, or maximum. Sufficient frequency margin, as defined in the A.4.13.3, and established during normal operation of a nominal engine at sea-level conditions, should be provided to insure resonances at steady-state operating conditions do not occur elsewhere in the flight

envelope or within a larger population of engines. Frequency margin can be provided above or below the steady-state speed. Engine components should not fail due to HCF or a combination of HCF and LCF when subject to the maximum attainable combined steady-state and vibratory stresses at a rate above that stated in A.4.13.3.

Low-order crossings and all known drivers within two stages either upstream or downstream of the subject component should have probabilistic design margins for final design that account for the variation in speeds for different operating conditions. A deterministic 10% frequency margin on component modes is acceptable for preliminary design or when there is insufficient confidence in probabilistic methods.

In the event that insufficient margin exists to meet the probability of failure requirement, the next level of probabilistic design analysis is required. Such probabilistic design analysis includes physical models of forced response, damping, and mistuning, along with the appropriate probability models for each random variable and correlations between those variables, as appropriate. Analyses on blades, vanes, disks, and integrally bladed rotors (IBRs or blisks) should include the effects of response to unsteady aerodynamic pressures, damping, and mistuning. Probabilistic methods should be applied to predict the probability distribution of the dynamic responses. Without these analyses, HCF response of the component may be seriously underestimated.

Appendix D*
Evaluation of the Staircase Test Method using Numerical Simulation

Major Randall Pollak

INTRODUCTION

Numerical simulation was used to model the staircase test method for determining the fatigue strength at a given number of cycles. The simulation allows the user to specify the true fatigue strength distribution (modeled as normally distributed in all cases) by specifying the mean and standard deviation of the fatigue strength at the number of cycles of interest. Individual simulated test sequences for the staircase test procedure, described in Chapter 3, are chosen randomly consistent with the assumed normal distribution function and values of the parameters chosen for that function. Numerical simulation was used to model the staircase test in order to determine the effects of starting stress, step size, and number of specimens on parameter estimates using Dixon–Mood statistics as presented in Chapter 3.

The objective of these simulations was to evaluate the feasibility of using the staircase test to estimate a material's fatigue strength distribution using small sample sizes. There were two primary considerations when evaluating the staircase methodology. The first was to assess how accurate the test is, on average. In this sense, the goal was to demonstrate that the test method estimates the mean of fatigue strength distribution parameters as closely to true values as possible—i.e., a test with little bias in results. The second consideration involved the ability to estimate the scatter in results. Because a designer or researcher must make conclusions based on a limited set of data, it is important that a test should not be subject to a wide dispersion in results due to statistical scatter alone. In other words, one would prefer a test method with results as tightly grouped as possible around the true parameter values.

These two considerations led to recommending the use of two different techniques to improve the fatigue strength analysis using a small-sample staircase test strategy. The first technique involved the use of a non-linear correction term to the Dixon–Mood standard deviation estimate in order to mitigate the bias inherent in this equation with small sample

* This document was prepared by Major Randall Pollak from the work that is part of his PhD dissertation at the Department of Aeronautics and Astronautics, Air Force Institute of Technology. Much of the work in this Appendix was presented at the 10th National Turbine Engine High Cycle Fatigue Conference in New Orleans, LA, 8–11 March 2005.

sizes. The second technique was the incorporation of a simple bootstrapping algorithm to help mitigate scatter in results. Through a combination of these techniques, a modified staircase strategy emerged which is generally more accurate (less bias) and more precise (less scatter) than traditional Dixon–Mood analysis alone.

THE STAIRCASE METHOD

The staircase method, first analyzed by Dixon and Mood [1] for explosives testing, and later popularized by Little [2–3] for fatigue strength testing, utilizes a very simple protocol in which a specimen is tested at a given starting stress for a specified number of cycles or until failure, whichever occurs first. If the specimen survives, the stress level is increased for the next specimen; likewise the stress is decreased if the specimen fails. This protocol is continued for a batch of specimens with statistical equations applied to provide an estimate for the mean fatigue strength and its standard deviation at the specified number of cycles. Unfortunately, it is difficult in practice to provide accurate estimates of the standard deviation using this method for small-sample test programs typical of high-cycle or ultra high-cycle fatigue testing.

Typically, the step size between adjacent stress levels is held constant (approximately equal to the standard deviation of fatigue strength), in which case the statistics of Dixon and Mood may be applied directly to estimate mean and standard deviation of the fatigue strength at a given number of cycles. Even though the true standard deviation in fatigue strength is one of the unknowns, Dixon notes that it is not too important if the interval is actually incorrect with respect to the true standard deviation by as much as 50% [4]. However, Little notes that arbitrary spacing between stress levels may be used when accompanied by a probit-type analysis [2]. In fact, tests conducted with non-uniform spacing may be more statistically efficient than uniform spacing; however, the analysis becomes much more tedious and the equations and tables derived for uniformly spaced tests are no longer useful [5].

The equations for the mean, μ, and standard deviation, σ, from the staircase method (denoted by subscript "sc") are (see Chapter 3):

$$\mu_{\mathrm{SC}} = S_{i=0} + s\left(\frac{\sum_{i=0}^{i_{\max}} i m_i}{\sum_{i=0}^{i_{\max}} m_i} \pm 0.5\right) \tag{D.1}$$

$$\sigma_{\mathrm{SC}} = 1.62s\left(\frac{\sum_{i=0}^{i_{\max}} m_i \sum_{i=0}^{i_{\max}} i^2 m_i - \left(\sum_{i=0}^{i_{\max}} i m_i\right)^2}{\left(\sum_{i=0}^{i_{\max}} m_i\right)} + 0.029\right) \tag{D.2}$$

In these equations, s denotes the step size and the parameter "i" is an integer denoting the stress level, with $i_{\max}$ corresponding to the highest stress level in the staircase. If the majority of specimens failed, then the lowest stress level at which a survival occurs (i.e., run-out) corresponds to the $i = 0$ level and m_i corresponds to the number of specimens which survived each stress level. The next highest stress level would be the $i = 1$ level, and the stress level one above that would be $i = 2$, etc. If the majority of specimens survived the given number of cycles, then the lowest stress level at which a failure was observed is denoted as the $i = 0$ level and m_i corresponds to the number of specimens which failed at each stress level. The standard deviation equation above, Equation (D.2), should only be used if the quotient term in this equation is greater than or equal to 0.3, otherwise the standard deviation is estimated as $0.53s$.

The primary condition of the analysis on which these equations is based is that the variate under consideration must be normally distributed. In the case of fatigue testing, this would imply that the fatigue strength distribution must be normally distributed. This condition would seem to be very restrictive and rule out staircase testing for many materials; however, a transformation of the stress values may be applied. For example, the fatigue strength distribution of some materials may be reasonably represented using a lognormal distribution, in which case the logarithm of stress values would be normally distributed. The staircase test would then be conducted using steps of equal intervals with respect to the natural logarithm of stress. Depending on the skewness of the distribution, other transformations may be applied to make the distribution reasonably normal, although there is no guarantee that every distribution can be transformed to approach normality. In addition to logarithmic transformations, power transformations are often applied for such a purpose. Squared and cubic transformations (as well as other powers greater than one) are used to reduce negative skewness, while logarithmic and powers less than 1 (such as a square-root transformation) as well as negative reciprocals ($-1/x$) are often used to reduce positive skewness [6]. Thus, the normality condition is not as restrictive as it first appears. However, it is often likely to be the case where there are not enough data to actually estimate the distribution shape prior to conducting a staircase test. Thus, one must either make a guess as to the shape based on data from a similar material and apply an appropriate transformation if non-normal, or simply accept the initial assumption of normality and conduct the test without a stress transformation and then use the data from the experiment itself to estimate the distribution.

STAIRCASE SIMULATION

A computer simulation was designed to analyze the effects of staircase parameter settings. The simulation allows the user to specify the true fatigue strength distribution (mean and standard deviation). The underlying distribution was modeled as Gaussian in all cases.

The staircase test parameters (starting stress, step size, and number of specimens) were then specified. For each specimen, the simulation calculated a random fatigue strength based on the specified underlying distribution and compared this value to the current stress level to determine if the specimen failed or survived. The stress level was then increased or decreased for the next specimen according to the staircase protocol. This procedure was repeated 1000 times in order to provide a distribution of calculated means and standard deviations according to the Dixon–Mood equations. Comparison of runs made with 1000 replications versus 10,000 replications showed that 1000 replications provided more than adequate statistical significance. The simulation was later expanded to allow the use of bootstrapping and various iterative test schemes.

STAIRCASE PARAMETER ANALYSIS

The first set of simulations focused on the effects of starting stress on parameter estimates using the Dixon–Mood equations. Figure D.1a shows the effect of starting stress on estimates of mean fatigue strength. Figure D.1b shows the starting stress impact on standard deviation estimates.

As one would expect, starting higher than the true mean leads to an estimate for mean fatigue strength that is slightly too high on average, and starting lower leads to lower estimates. As the number of specimens increases, the importance of starting stress on calculations of mean fatigue strength is diminished. This analysis reaffirms a fact that is generally already accepted—namely, that one should start the staircase test as closely to the true mean as possible. However, there are techniques already developed in the literature to account for staircase results which begin with a string of failures (when starting at stresses higher than the mean) or survivals (when starting too low). Brownlee et al. first investigated this problem in 1953 and proposed a modified equation for the mean [7]. Dixon later proposed a set of lookup tables for the mean in 1965 [4], and Little expanded these tables in 1972 [5]. In short, there are adequate methods to estimate the mean fatigue strength using small-sample data quite accurately.

For standard deviation estimation, Figure D.1b shows that even for small samples, the effect of starting stress is rather small. However, use of offset starting stresses does have some beneficial effect for small sample sizes by alleviating some of the standard deviation bias. This result is due to the fact that when one starts above or below the mean, it is statistically more likely that a failure will be observed below the mean (if starting below) or a survival will be encountered above the mean (if starting above), simply because one is conducting more testing above or below the mean, on average. In a small-sample test, just one of these outcomes can lead to a higher estimate of standard deviation, and therefore, on average, there is a slight reduction of the standard deviation underestimating bias for small-sample tests. This effect is not overwhelming enough to

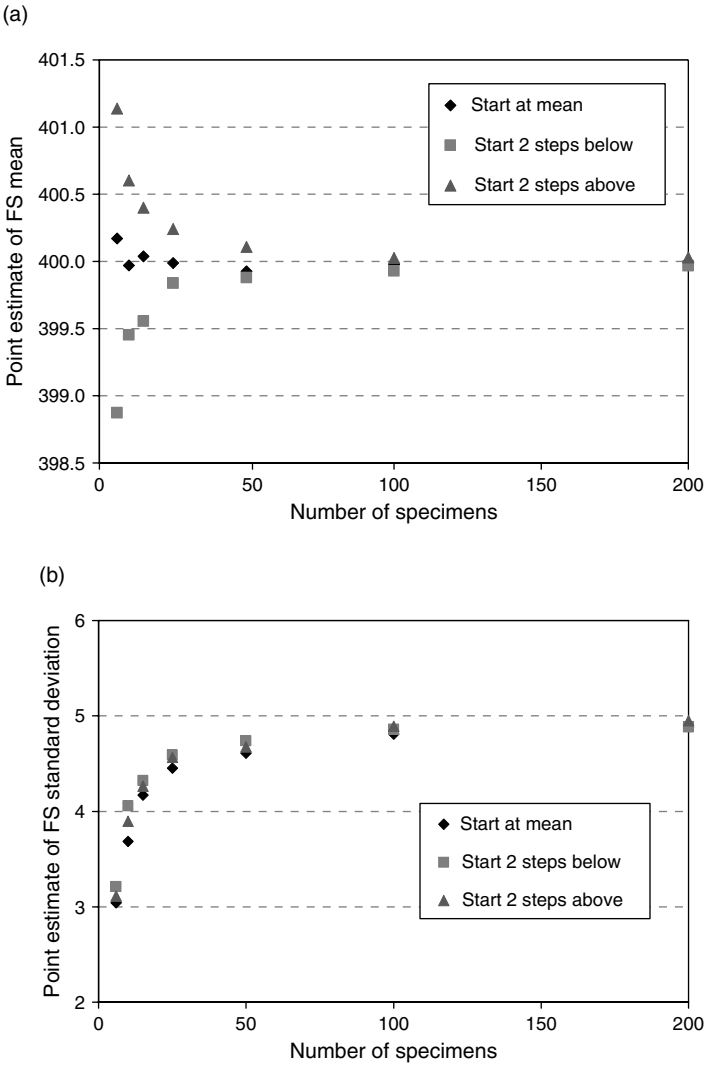


Figure D.1. Effect of starting stress on (a) mean and (b) standard deviation estimates for true underlying distribution Normal ($\mu = 400, \sigma = 5$) and step size 1σ.

eliminate the bias altogether, but does provide some means of softening it. For the data in Figure D.1b, the mean standard deviation for $N = 10$ samples is 3.68 (26.3% error) when starting at the mean, but 4.06 (18.9% error) when starting two steps below the mean. The traditional approach of starting the staircase at the mean in order to maximize accuracy of the estimate for mean fatigue strength may be modified in order to improve standard

deviation estimation, especially since adequate means of handling offset starting stresses exist for mean fatigue strength estimation.

Next, the effect of step size was analyzed. The choice of step size had little effect on the calculated fatigue strength mean in an average sense, although Figure D.2 shows that as step size increases, there is more scatter in fatigue strength mean estimates. This result is rather intuitive since one would expect a tighter grouping around the mean for small steps. Thus, a single staircase test is more likely to have error in calculated mean fatigue strength for larger steps versus smaller steps.

Figure D.3 shows the calculated standard deviation as a function of step size and number of specimens. This figure represents the expected value of standard deviation for any combination of step size and number of specimens. When normalized by the true standard deviation, these expected values are independent of the true standard deviation. Note that in the limit (simulated using 1000 specimens), the calculated standard deviation is close to the true standard deviation for all step sizes ranging from 0.1σ to 1.7σ. However, for small-sample tests, the standard deviation is significantly underestimated. Braam and van der Zwaag [8], along with Svensson and de Maré [9], also noted this underestimating bias for small-sample tests. Note that existing guidance stemming from Dixon and Mood's original work suggests a step size in the $2\sigma/3$ to $3\sigma/2$ range. To remove standard deviation bias, however, Figure D.3 shows that step sizes must be larger, on the order of 1.6σ to 1.75σ. Beyond this region, the standard deviation estimates converge to the $0.53s$ line. It is clear from Figure D.3 that standard deviation bias is magnified as either step size or sample size are reduced.

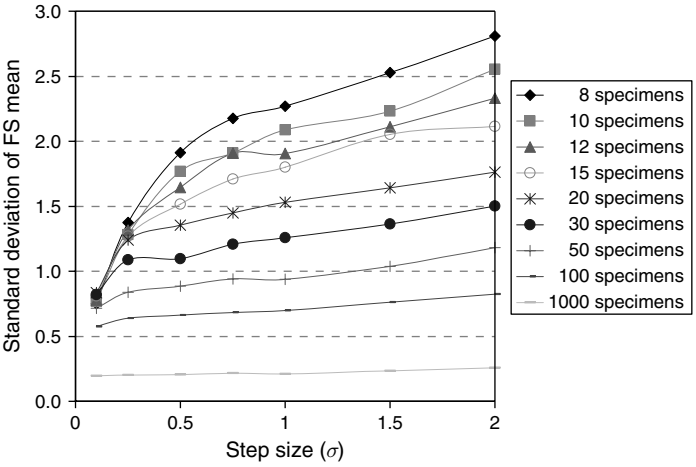


Figure D.2. Effect of step size on scatter of fatigue strength mean estimates for true underlying distribution Normal ($\mu = 400, \sigma = 5$).

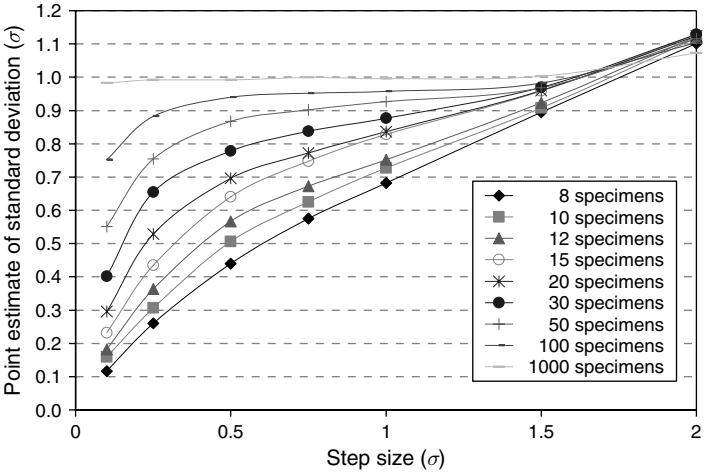


Figure D.3. Effect of step size on estimated fatigue strength standard deviation.

In addition to being more accurate on average, use of a higher step size reduces the variance in standard deviation estimates compared to the estimates obtained using a step of $2\sigma/3$ to $3\sigma/2$, as illustrated by Figure D.4. This effect is due in part to the larger steps producing more results using the $0.53s$ standard deviation estimate, which is constant for a given step size. In general, it appears that use of steps in the 1.6σ to 1.75σ range will result in both less bias and less scatter than smaller step sizes.

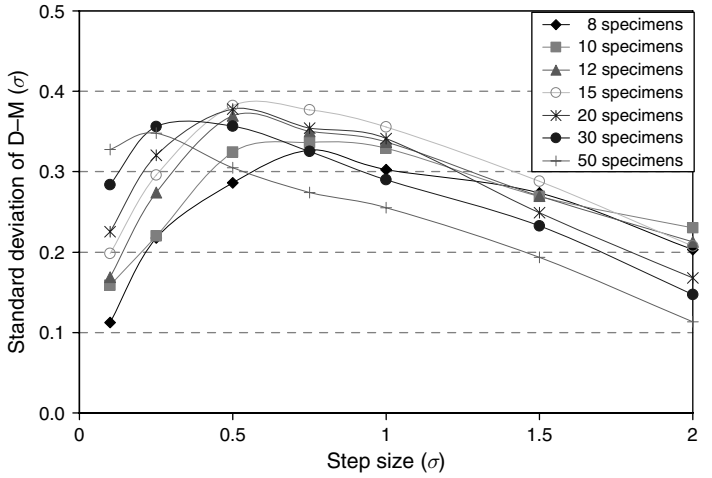


Figure D.4. Effect of step size on scatter of fatigue strength standard deviation estimates.

Thus, there is a bit of a tradeoff here. Larger step sizes on the order of 1.7σ provide generally more accurate estimates of standard deviation with less scatter, but result in slightly more scatter in fatigue strength mean. Remedies to this tradeoff will be presented in the next section.

CORRECTION FOR STANDARD DEVIATION

Due to the bias in standard deviation estimates for small sample sizes, a correction term was investigated to allow the use of Dixon–Mood equations at smaller steps to avoid the increased scatter in fatigue strength estimates inherent in the use of higher step sizes. A starting point for such a correction was the linear correction factor presented by Svensson et al. [10]. This work addressed the problem of standard deviation bias, noting that no theoretical solution to this bias was apparent. A correction factor for the standard deviation was proposed based on the number of tested specimens, given as:

$$\sigma_{\text{corr}} = \sigma_{\text{DM}} \left(\frac{N}{N-3} \right) \tag{D.3}$$

where σ_{corr} is the modified (corrected) standard deviation, σ_{DM} is the standard deviation calculated using the Dixon–Mood equation, and N is the number of specimens.

This linear correction (which will be called the "Svensson–Lorén correction" herein) was applied to the standard deviation estimates from the simulation results from Figure D.3, with corrected standard deviations shown in Figure D.5. Notice that the step

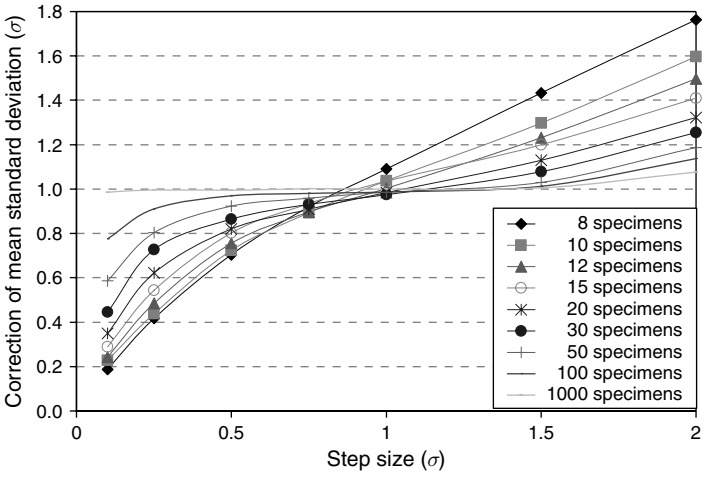


Figure D.5. Svensson–Lorén correction for fatigue strength standard deviation estimates.

size for unbiased standard deviation estimates has shifted from 1.7σ to approximately 1σ. This result is significant since it allows the use of smaller step sizes without standard deviation bias. However, since the true standard deviation is unknown, it is not possible to plan a test at precisely this unbiased step size. If one tests at too low a step size, standard deviation is still underestimated (on average). Likewise, the standard deviation is overestimated at higher step sizes. One would prefer a correction which allowed a greater range of unbiased step sizes.

A more elaborate correction factor was developed based on analysis of simulation results and is proposed for small-sample staircase tests. This correction factor accounts for both sample size and step size, and has the form:

$$\sigma_{\text{corr}} = A\sigma_{\text{DM}}\left(\frac{N}{N-3}\right)\left(B\frac{\sigma_{\text{DM}}}{s}\right)^{m} \tag{D.4}$$

In this equation, A, B, and m are constants based on the number of specimens, with other variables as previously defined. Table D.1 shows the values for these constants based on simulation results for selected numbers of specimens. Since standard deviation bias is independent of both the true mean and true standard deviation of the underlying fatigue strength distribution, these constants are not specific to a particular simulation case. These constants were determined in order to calibrate the mean standard deviation estimate from Dixon–Mood analysis to be as unbiased as possible. Figure D.6 shows the corrected mean estimates for standard deviation using this non-linear correction, with Figure D.7 comparing the standard deviation estimates for Dixon–Mood, the Svensson–Lorén correction, and this non-linear correction for $N = 20$ specimens.

These figures suggest that the proposed correction allows a greater range of unbiased (or only slightly biased) step sizes. Thus, when using this correction, one is less reliant on the initial guess of true standard deviation in order to get meaningful results. However, it should be noted that it is only the mean standard deviation from Dixon–Mood that is

Table D.1. Non-linear correction constants based on number of specimens

Number of specimens	*A*	*B*	*m*
8	1.30	1.2	1.72
10	1.08	1.2	1.10
12	1.04	1.2	0.78
15	0.97	1.2	0.55
20	1.00	1.2	0.45
30	1.00	1.2	0.22
50	1.00	1.2	0.15
>50	Use Svensson–Lorén.		

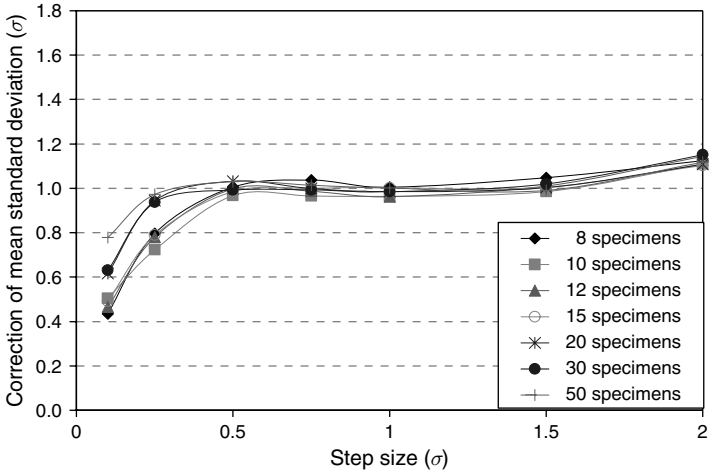


Figure D.6. Proposed correction applied to mean of fatigue strength standard deviations.

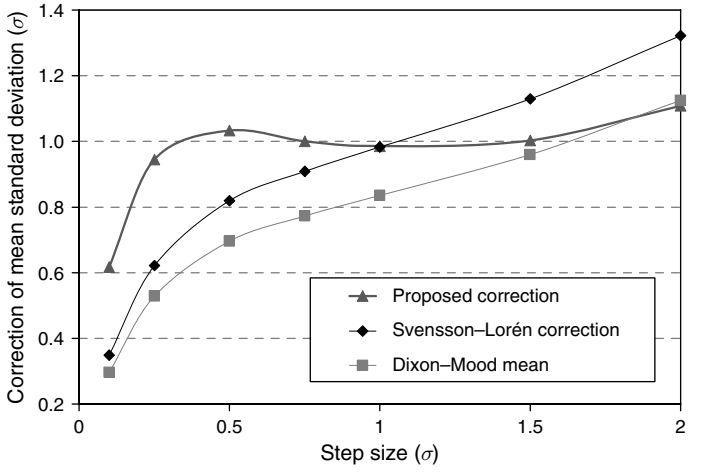


Figure D.7. Comparison of Dixon–Mood, Svensson–Lorén correction, and proposed correction for $N = 20$ specimens.

unbiased. Of course, there will be estimates for standard deviation which are both higher and lower than the mean, and these estimates will not be corrected to the true value using this correction. Compared to both Dixon–Mood and Svensson–Lorén, the proposed correction tends to have more scatter (though less than Braam-van der Zwaag's correction [8]). Thus, in an average sense, bias is reduced, but for any individual test the results may

not be improved compared to either Dixon–Mood or Svensson–Lorén. The next section will address the means of reducing this scatter.

THE USE OF BOOTSTRAPPING

Obviously, one of the biggest problems inherent in small-sample testing is that statistical scatter can greatly impact results. Use of both the Svensson–Lorén correction and the proposed correction increases the already significant scatter inherent in the Dixon–Mood standard deviation estimate. The bootstrapping method was investigated as a possible means to reduce this variance. The bootstrap is a data-based simulation which utilizes multiple random draws from real test data to improve statistical inferences about the underlying population [11]. Essentially, the bootstrap method can be summed up by the following conjecture: Assuming the test data collected accurately represents the true distribution, what other results could have been obtained if the test were repeated?

The bootstrap algorithm for the staircase application is based on the associated probabilities of failure computed using the number of survivals and failures at each stress level (i.e., P–S data). Using these data, simulated staircase tests can be generated numerically using the same starting stress, step size, and number of specimens. For the first specimen, a random number is drawn and compared to the probability of failure associated with the initial stress level. The stress level is increased or decreased depending on the result of this draw (if the random number is less than the probability of failure, the result is considered a failure, otherwise it is a survival). Another random number is then drawn for the second specimen and compared to the probability of failure for its associated stress level, with the stress level increased or decreased based on this comparison, and the process is repeated until all specimens are used. Note that test data must be bounded by both $P(\text{failure}) = 0$ and $P(\text{failure}) = 1$ stress levels or the staircase may walk to a stress level where no data exists. Through this algorithm, a set of "virtual" staircase tests is generated for the one "real" staircase test. For each virtual staircase, the Dixon–Mood method can be applied to provide a standard deviation estimate. The result is a distribution of standard deviation estimates. Lastly, the revised point estimate can be taken as the mean of this distribution, or another statistic such as the median or other percentile point.

The staircase simulation was modified to accommodate this bootstrapping algorithm by simulating a "real" staircase using an assumed underlying fatigue strength distribution, and then using the P–S data from this simulated staircase to bootstrap additional staircases from which a distribution of standard deviation estimates can be analyzed. Figure D.8 shows a comparison of mean bootstrap results to Dixon–Mood statistics for the case of a 12-specimen test conducted at a step size of 1σ. From Figure D.3, the expected value for standard deviation is approximately 3.7. Fifty staircases were conducted with

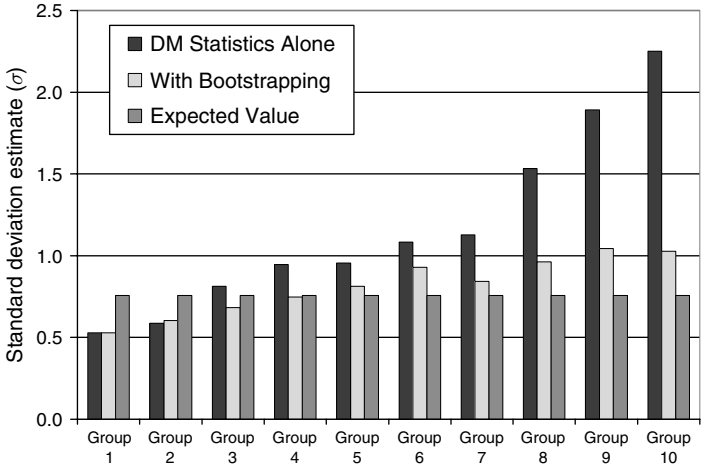


Figure D.8. Comparison of bootstrapped results to Dixon–Mood statistics for 12-specimen test with step size 1σ.

5000 bootstrap replications each, with the results sorted in groups as the staircase test produces discretized results (in this case, there were 10 different values for standard deviation based on the 50 "real" staircase tests). One can see how the standard deviation estimate is closer to the expected value using bootstrapping. Figure D.9 presents this same data through a different means, showing how the distribution of calculated standard deviations is narrowed using bootstrapping. In fact, for this case the standard deviation of the estimates was reduced from 0.35σ to 0.14σ using the bootstrap.

The bootstrap provides a measure of protection against large errors associated with small-sample tests due to statistical variance. The bootstrap thus provides the first real tool to reduce the scatter inherent in the Dixon–Mood standard deviation method. The algorithm adjusts the estimate for standard deviation to be closer to the expected value given the test parameters. It has been shown to adjust Dixon–Mood estimates towards their expected value. Thus, if one tests in an unbiased region, such as the $s = 1.7\sigma$ region, then the bootstrap should drive Dixon–Mood estimates towards the true standard deviation. However, when combined with a correction for bias, the expected value should be closer to the true standard deviation, and therefore the bootstrap will drive the results towards the true standard deviation value. One important note, however, is that the bootstrap tends to have little influence on staircase tests resulting in just two or three stress levels as these tests result in standard deviation estimates which are based almost solely on the $0.53s$ rule. Investigation of the bootstrap in conjunction with both Svensson–Lorén and the proposed bias corrections shows that for test results with at least four stress levels, use of the average of the 60th and 65th percentiles of the bootstrapped standard deviation distribution provides a better estimate than use of the mean of bootstrapped distribution.

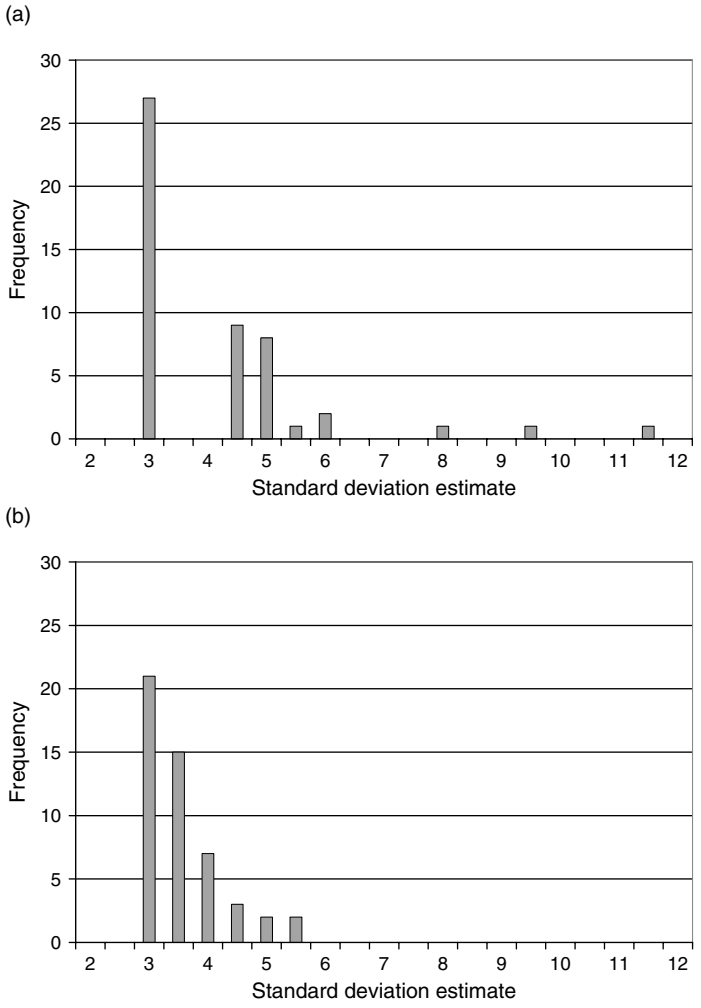


Figure D.9. Histogram of Dixon–Mood ((a) top) and bootstrap ((b) bottom) standard deviation estimates for same conditions as Figure D.8.

CONCLUSIONS

The results of the analysis presented here are summarized as follows:

1. The Dixon–Mood equation using small-sample data generally underestimates standard deviation using traditional $2\sigma/3$ to $3\sigma/2$ step sizes.
2. Step sizes on the order of 1.7σ reduce both standard deviation bias and scatter, but larger step sizes increase scatter in fatigue strength mean.

3. Use of a non-linear correction factor was shown to allow a larger range of unbiased standard deviation estimation (in an average sense) in the $2\sigma/3$ to $3\sigma/2$ range. This correction factor generally increases scatter in results, however.
4. Use of a bootstrapping algorithm was shown to significantly reduce scatter in standard deviation estimates. This simple numerical procedure therefore provides a measure of protection against large errors when conducting small-sample staircase tests. The bootstrap requires test results with at least 4 stress levels to be effective.
5. Combination of bias correction and bootstrapping provides a generally more reliable and robust means of calculating standard deviation using Dixon–Mood staircase analysis by improving expected values and reducing scatter.

REFERENCES

1. Dixon, W.J. and Mood, A.M., "A Method for Obtaining and Analyzing Sensitivity Data", *Journal of the American Statistical Association*, **43**, 1948, pp. 109–126.
2. Little, R.E., *Manual on Statistical Planning and Analysis*, American Society for Testing and Materials, STP 588, 1975.
3. Little, R.E. and Jebe, E.H., *Statistical Design of Fatigue Experiments*, John Wiley & Sons, New York, 1975.
4. Dixon, W.J., "The Up-and-Down Method for Small Samples", *Journal of the American Statistical Association*, **60**, 1965, pp. 967–978.
5. Little, R.E., "Estimating the Median Fatigue Limit for Very Small Up-and-Down Quantal Response Tests and for S–N Data with Runouts", *Probabilistic Aspects of Fatigue*, American Society for Testing and Materials, STP 511, 1972.
6. Neter, J., Kutner, M.H., Nachtsheim, C.J., and Wasserman, W., *Applied Linear Statistical Models*, 4th Ed., Irwin, Chicago, 1996.
7. Brownlee, K.A., Hodges, J.L., Jr., and Rosenblatt, M., "The Up-and-Down Method with Small Samples", *Journal of the American Statistical Association*, **48**, 1953, pp. 262–277.
8. Braam, J.J. and van der Zwaag, S., "A Statistical Evaluation of the Staircase and the ArcSin$\sqrt{P}$ Methods for Determining the Fatigue Limit", *Journal of Testing and Evaluation*, **26**, 1998, pp. 125–131.
9. Svensson, T. and de Maré, J., "Random Features of the Fatigue Limit", *Extremes*, **2**, 1999, pp. 165–176.
10. Svensson, T., de Maré, J., Wadman, B., and Lorén, S., "Statistical Models of the Fatigue Limit", Project paper, www.sp.se/mechanics/Engelska/FoU/ModFatigue.htm, 2000.
11. Efron, B. and Tibshirani, R.J., *An Introduction to the Bootstrap*, Chapman & Hall, New York, 1993.

Appendix E*
Estimation of HCF Threshold Stress Levels in Notched Components

Alan Kallmeyer

INTRODUCTION

The determination of the allowable threshold stress level, or fatigue limit stress, for notched components is an important consideration in an HCF design methodology. It has long been recognized that the use of the peak notch-root stress, calculated using the theoretical stress concentration factor k_t, results in overly conservative life-predictions. Even when localized plasticity at the notch root (resulting in shakedown) is taken into account, the peak stress alone is still insufficient to predict the fatigue life or limiting stress from smooth specimen data. Although there are a number of contributing factors, it is generally acknowledged that the stress gradients in the vicinity of the notch play a significant role. Evidence has shown that the steeper the stress gradient, the more non-conservative the prediction using k_t. This phenomenon can be explained by recognizing that, under equivalent peak stress conditions, a steeper stress gradient results in a smaller volume of material subjected to a high stress level. Utilizing a stochastic viewpoint of the fatigue process, cracks would be less likely to initiate from a smaller highly stressed volume of material than in a larger highly stressed volume such as found in smooth, axially loaded specimens.

A common design methodology that has been used to account for the observed behavior defines a "fatigue notch factor," k_f, where $k_f \leq k_t$. k_f is often defined in terms of a "notch sensitivity factor," q, which is dependent on the material and the notch-root radius (which affects the stress gradients). As the notch radius decreases, q decreases, reflecting a greater deviation between k_t and k_f. Although this approach has been successfully applied to some common notch geometries under uniaxial loading conditions, the definitions of q and k_f are ambiguous for more complex notch/component geometries or under multiaxial loading conditions.

More recent approaches for estimating notch threshold stress levels have attempted to account for the complexities associated with the steep stress gradients on crack initiation

* This appendix was prepared by Dr. Alan Kallmeyer, Department of Mechanical Engineering, North Dakota State University. Much of the material is extracted from the final report of the National Turbine Engine High Cycle Fatigue program [1]. Very special thanks to Dr. Stephen J. Hudak, Jr. and his collaborative researchers at Southwest Research Institute, San Antonio, TX, for their contributions to the research on very sharp notches, both experimental and analytical, particularly the development of the Worst Case Notch concept.

and propagation in a more systematic manner. Two such models are described below. The Stressed Surface Area approach, relying on a feature-stress (Fs) weighting term, is a crack initiation model that incorporates a modification to the peak notch-root stress based on the stress gradients around the notch. The Worst Case Notch (WCN) model is a fracture mechanics approach that assumes that microcracks initiate early in the life of notched components, and considers the unique behavior of small cracks in the crack growth analysis. The two methods are compared to experimental data from fatigue tests on specimens containing small, sharp notches with severe stress gradients, as may be typically observed in turbine blades subjected to foreign object damage (FOD) or near edge-of-contact conditions.

STRESSED SURFACE AREA (Fs) APPROACH

The Stressed Surface Area, or Fs approach, accounts for the stress gradient effect through consideration of the stress distribution on the surface of a component in the vicinity of a notch. This approach is based on the "weakest-link" concept, which assumes that fatigue failure will initiate at the weakest grain or defect in a material and, therefore, will be dependent on the volume of material that is exposed to the highest stresses. Since crack initiation normally takes place on the surface of a material, particularly in titanium, the Fs approach was developed recognizing that there is a higher probability of finding a weak grain on the surface of a large notch or smooth component than on the surface of a small notch [2]. Thus, the stressed surface area was evaluated as compared to volume in the Fs approach.

As explained by Murthy et al. [2], in using the weakest link approach the probability of survival, R, of a small surface area ΔA_i, subjected to a stress of σ_i, is assumed to be

$$(R_0(\sigma_i))^{\Delta A_i} = \left(\exp\left[-\left(\frac{\sigma_i}{\beta}\right)^{\alpha}\right]\right)^{\Delta A_i} \tag{E.1}$$

This formulation adopts a two-parameter Weibull distribution for the fatigue strength with α as the shape factor (a measure of dispersion) and β as the scale parameter (a measure of the mean stress value). The probability of survival of all the stressed areas (a total of n areas) would then be given by

$$\ln(R) = \sum_{i=1}^{n} [\ln R_0(\sigma_i)]\, \Delta A_i \tag{E.2}$$

If two specimens have the same fatigue life, then their probability of survival is the same. By equating the two probabilities, we get

$$\left(\frac{\sigma_{\max,1}}{\beta}\right)^{\alpha} F\mathrm{s}_1 = \left(\frac{\sigma_{\max,2}}{\beta}\right)^{\alpha} F\mathrm{s}_2 \tag{E.3}$$

where the parameter Fs is given by

$$Fs_j = \sum_{i=1}^{n} \left[- \left(\frac{\sigma_{i,j}}{\sigma_{\max,j}} \right)^{\alpha} \right] \Delta A_{i,j} \tag{E.4}$$

and $\sigma_{\max}$ is the maximum stress on the surface of the specimen (e.g., the peak notch-root stress in a notched specimen). From Equations (E.3) and (E.4), an equivalent stress corresponding to smooth bar data is obtained as

$$\Delta\sigma_{\text{eq},1} = \left(\frac{Fs_2}{Fs_1} \right)^{\frac{1}{\alpha}} \Delta\sigma_{\text{eq},2} \tag{E.5}$$

where $\sigma_{\text{eq},2}$ is the equivalent peak stress in the notched component and $\sigma_{\text{eq},1}$ is the equivalent stress in a smooth bar specimen that has the same life as that of the notched component. The equivalent stresses in Equation (E.5) can be defined in terms of any equivalent-stress-based fatigue parameter, allowing for the inclusion of mean stress effects or multiaxial loadings. In addition, note that the negative sign in Equation (E.4) can be dropped in the computation since a ratio of Fs terms is computed in Equation (E.5).

The Fs approach has been successfully applied to describe the fatigue behavior of specimens containing both large and small blunt notches [1]. To evaluate the capabilities of the Fs method in the analysis of components containing severe stress gradients, such as may occur near FOD impact sites or edge-of-contact conditions, the method was used to estimate the HCF threshold stress levels for Ti-6AL-4V specimens containing very small, sharp notches. The double-edge-notched specimens had a rectangular cross-section with gross-section dimensions of $0.235" \times 0.125"$ ($6.0\,\text{mm} \times 3.2\,\text{mm}$). The specimens contained small notches produced by EDM, followed by a stress relief and chem mil to leave a smooth surface free of residual stresses [1]. The effective stress concentration factors and stress gradients in the specimens were varied by adjusting the notch depth, b, and notch root radius, ρ, as illustrated in Figure E.1. The specimens were tested in load control at $R = 0.5$ to experimentally determine the threshold stress levels, defined as the 10^7 cycle notch fatigue strength, using a step-test procedure.

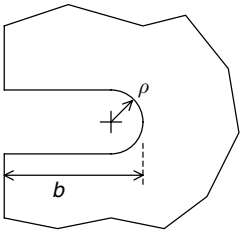


Figure E.1. Small, sharp notch details.

In the application of the Fs approach to these specimens, the equivalent stresses in Equation (E.5) were calculated using the Modified Manson-McKnight (MMM) multiaxial fatigue model, which allowed for the multiaxial stress state at the notch root and mean stress effects to be accounted for. Using this model, the equivalent stress parameter is calculated as [3]

$$\sigma_{\text{eqv}} = 0.5(\Delta\sigma_{\text{psu}})^{w}(\sigma_{\max})^{(1-w)} \tag{E.6}$$

where $\Delta\sigma_{\text{psu}}$ is a "pseudo-stress range" defined as

$$\Delta\sigma_{\text{psu}} = \frac{1}{\sqrt{2}}\sqrt{\begin{array}{c}\left(\Delta\sigma_{xx}-\Delta\sigma_{yy}\right)^2+\left(\Delta\sigma_{yy}-\Delta\sigma_{zz}\right)^2+\left(\Delta\sigma_{zz}-\Delta\sigma_{xx}\right)^2\\ +6\left(\Delta\sigma_{xy}^2+\Delta\sigma_{yz}^2+\Delta\sigma_{zx}^2\right)\end{array}} \tag{E.7}$$

and $\sigma_{\max}$ is calculated as $\sigma_{\max} = \sigma_{\text{mean}} + 0.5\Delta\sigma_{\text{psu}}$, where

$$\sigma_{\text{mean}} = \frac{\beta}{2\sqrt{2}}\sqrt{\begin{array}{c}\left(\Sigma\sigma_{xx}-\Sigma\sigma_{yy}\right)^2+\left(\Sigma\sigma_{yy}-\Sigma\sigma_{zz}\right)^2+\left(\Sigma\sigma_{zz}-\Sigma\sigma_{xx}\right)^2\\ +6\left(\Sigma\sigma_{xy}^2+\Sigma\sigma_{yz}^2+\Sigma\sigma_{zx}^2\right)\end{array}} \tag{E.8}$$

In these equations, $\Delta\sigma_{\text{ij}}$ and $\Sigma\sigma_{\text{ij}}$ define the stress range and summed stress, respectively, for each stress component based on the maximum and minimum points in the fatigue cycle, and the Manson-McKnight coefficient, β, is defined as [2]

$$\beta = \frac{(\Sigma\sigma_1 + \Sigma\sigma_3)}{(\Sigma\sigma_1 - \Sigma\sigma_3)} \tag{E.9}$$

where, $\Sigma\sigma_1$ and $\Sigma\sigma_3$ are the sums of the first and third principal stresses, respectively, at the maximum and minimum stress points in the fatigue cycle. The exponent w is a material- and temperature-dependent constant that collapses variable mean stress data into a single curve.

The value of Fs for each notched specimen was calculated using Equation (E.4). An elastic finite element analysis was first performed to obtain the peak notch root stress $\sigma_{\max}$ and the surface stress distribution across each specimen. The summation in Equation (E.4) was performed over all the elements in the model adjacent to a free surface of the specimen, with σ_i taken as the first principal stress associated with the nodes on the free surface of element i, and A_i the free-surface area of that element. Since the value of Fs is calculated from a ratio of stresses, it does not change appreciably with load level, provided notch-root yielding is small; thus, the use of an elastic finite element analysis is appropriate for this calculation. However, in Equation (E.5), the calculation of the equivalent peak stress in the notched component, $\sigma_{\text{eq},2}$, must take into account localized yielding. Therefore, an elastic-plastic finite element analysis was performed to determine

this value, using Equations (E.6)–(E.9) for cyclic loading. Finally, Equation (E.5) was used to determine the adjusted equivalent stress for the notched component, $\sigma_{eq,1}$, which was then compared to smooth specimen results using the following relationship between the MMM parameter and fatigue life for Ti-6Al-4V (stresses in ksi):

$$0.5(\Delta\sigma_{psu})^{w}(\sigma_{max})^{(1-w)} = 3501.8\ N^{-0.5164} + 36.74N^{0.00068} \tag{E.10}$$

In these computations, a value of $\alpha = 35$ was used, which was previously obtained by correlating smooth and notched test data for Ti-6Al-4V [1], and $Fs_1 = 0.161$ was used as the reference value for a smooth, axial specimen.

The notch dimensions (ρ and b) used in this study were selected to correspond to the average measured notch dimensions of the specimens tested. Due to the difficulty in machining the very small notches, in many cases the measured notch dimensions deviated substantially from the target values, and there were significant deviations from the average for certain specimens within a group. Consequently, only a limited number of direct comparisons could be made between the experimental and predicted threshold stress levels.

The notch dimensions and associated elastic stress concentration factors for the samples considered in this study are shown in Table E.1. The stress concentration factors were calculated from the elastic FEA solution. Two values of k_t are included in the table for each specimen, one based on the net-section area through the notch (the traditional definition of k_t), and the other based on the cross-section area ($0.235" \times 0.1257"$). The net-section k_t values range from approximately 3.2 to 5.

The comparison of the predicted and experimental threshold stress levels, based on the gross cross-section dimensions, is shown in Table E.2. Although limited in number, these

Table E.1. Small notch dimensions and elastic stress concentration factors

Notch	ρ (in.)	b (in.)	k_t (*net section*)	k_t (*gross section*)
1	0.0064	0.0080	3.24	3.48
2	0.0062	0.0230	4.56	5.67
3	0.0064	0.0490	4.99	8.55

Table E.2. Threshold Stress Estimates for Small Notched Specimens using the Fs Approach

	Predicted				*Experimental*		
Notch	ρ (in.)	b (in.)	σ_{max} (ksi)	$\Delta\sigma_{th}$ (ksi)	ρ (in.)	b (in.)	$\Delta\sigma_{th}$ (ksi)
1	0.0064	0.0080	43.2	21.6	0.0064	0.0089	16.3
2	0.0062	0.0230	26.2	13.1	0.0060	0.0236	11.1
3	0.0064	0.0490	17.5	8.75	0.0064	0.0495	6.0
					0.0064	0.0484	7.9

comparisons provide some useful information concerning the capabilities and accuracy of the *F*s approach. In all cases, the predicted threshold stress levels exceeded the experimental values. However, the differences between the actual and modeled notch dimensions may have contributed to the discrepancies to some degree. For example, in notch 1, the actual notch depth was approximately 10% greater than the modeled value. This would increase the effective stress concentration factor, thereby reducing the nominal threshold stress level. The differences in notch dimensions were less severe in the other cases. Nevertheless, it is apparent the *F*s method tends to underestimate the notch strength reduction in components containing very small, sharp notches with severe stress gradients. However, the accuracy of the method improves in cases of more blunt notches [1].

FRACTURE MECHANICS (WORST CASE NOTCH) APPROACH

The fracture mechanics approach employed to predict the nominal HCF threshold stress, $\Delta\sigma_{th}$, assumes that microcracks can initiate relatively early in the life of a notched component due to a variety of reasons, such as the damage imparted by an initial FOD impact, the highly concentrated HCF stresses associated with either an FOD notch or edge-of-contact zone, or the intermittent occurrence of low cycle fatigue (LCF). Moreover, since the stress gradients at sharp notches and edge-of-contact zones are steep and die out at relatively short distances from the notch surface, it is necessary to consider the unique behavior of small fatigue cracks when performing a fracture mechanics analysis.

The method used, termed the "Worst Case Notch" (WCN) model, enables the boundaries between crack initiation, crack growth followed by arrest, and crack growth to failure to be delineated. In this model, "true" crack initiation is assumed to actually occur as predicted by the classical *S–N* approach when the applied stress range is equal to the endurance limit divided by the elastic stress concentration factor ($\Delta\sigma_e/k_t$). However, for sharper notches, the initiated cracks can subsequently arrest due to the unique behavior of small cracks, which cause $\Delta\sigma_{th}$ to initially increase, achieve a maximum, and finally decrease as crack size increases. The growth/arrest boundary is determined by equating the applied stress intensity factor (SIF) range to the threshold SIF for fatigue crack propagation. The unique behavior of small fatigue cracks is modeled in the WCN approach by a crack-size-dependent threshold SIF. The remainder of this section summarizes several enhancements to the WCN model, and compares the model predictions with several small, sharp notch experimental results [1].

Incorporation of notch plasticity and surface cracks in the WCN model

The WCN model was originally developed for through-thickness cracks and surface cracks with one degree of freedom (DOF) emanating from notches [4]. Consequently, in analyses

involving thumbnail cracks, the cracks were restricted in shape so that they remained semi-circular, and crack growth was characterized only by the SIF at the deepest point on the flaw. These restrictions resulted in certain predicted crack growth behaviors that were not entirely consistent with observations. To overcome these limitations, the WCN model has been extended to semi-elliptical surface cracks whose growth is characterized by two DOF, namely, the SIFs at both the surface and deepest points on the crack front. In these cases, crack growth and arrest is determined by the manner in which the crack shapes evolve from the initially specified shapes, and this evolution is governed by the stress gradient ahead of a notch and the crack growth rate equation. Therefore, implementation of the WCN model for two DOF cracks requires HCF crack growth calculations to be performed. To facilitate these calculations the crack growth rate behavior was described using the Walker crack growth rate equation based on an effective stress intensity factor, ΔK_{eff}. This general equation describes crack growth rate behavior from initiation at threshold to failure from the onset of static failure modes.

To incorporate notch plasticity and associated shakedown of the mean stresses at the notch, an approximate elastic-plastic stress analysis was used to determine the local notch-tip stress state. The methodology used here was based on the isotropic shakedown module for univariant stressing developed for the computer code, DARWIN™[5]. The shakedown module requires as input the elastic stress field ahead of a notch, which was obtained using a modification of the method of Amstutz and Seeger [6], as described in [7].

Figure E.2 compares predictions of the WCN model for a 2-D through-thickness crack both with and without plastic shakedown for a notch of 0.025" (0.635 mm) depth and

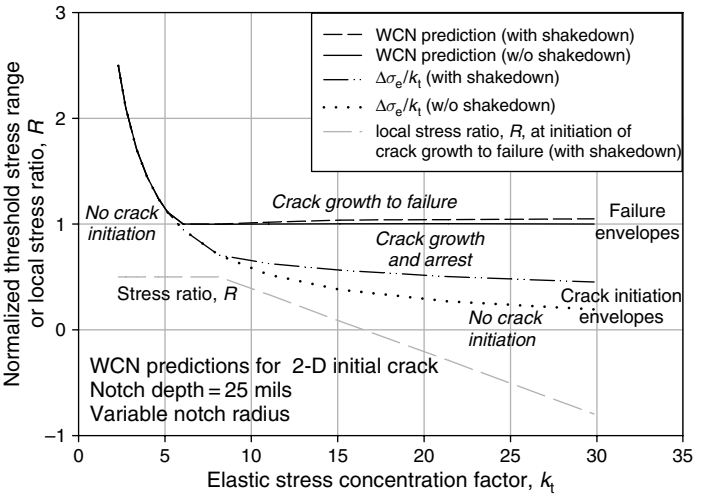


Figure E.2. Comparison of WCN model predictions with and without plastic shakedown of notch-tip stresses. The local *R*-value is also shown to decrease with increasing notch severity as the result of plastic shakedown.

varying notch radii to give the range of k_t values (based on the gross cross-sectional area) shown. In this figure, the threshold stress is normalized by the limiting threshold value obtained for a notch with a high k_t. As indicated, the threshold values determined with and without shakedown differ significantly at the initiation of cracking, but the two sets of values differ only slightly at the threshold stress corresponding to failure. The reason for this can be seen from the plot of the local stress ratio (R) that is also presented in Figure E.2. At the higher cyclic stresses needed to initiate and propagate cracks to failure, shakedown has occurred at the notch tip and changed the local stress ratio at initiation so that it is no longer simply related to the remote stress ratio, specified as being $R = 0.5$ in this example. Indeed, at high k_t values, the local stress ratio becomes negative. Although these negative stress ratios will increase the cyclic threshold stress needed to initiate cracking, they clearly do not significantly influence the threshold needed to cause propagation to failure. This is a consequence of the fact that the residual stress field due to shakedown is very localized at the notch tip, and cracks can readily propagate to depths where the localized stress has little influence on the applied SIF. Threshold stresses that fall between the initiation and failure envelopes shown in Figure E.2 will initiate cracks either on the initiation envelope or at cyclic stress values above this envelope if shakedown occurs, but these cracks are predicted to eventually arrest.

Figure E.3 compares WCN model predictions for 2-D and 3-D surface cracks. Although the trends in threshold behaviors for the two cases are similar, the 3-D crack model for notches with high k_t values predicts that failure will occur at threshold stresses less than

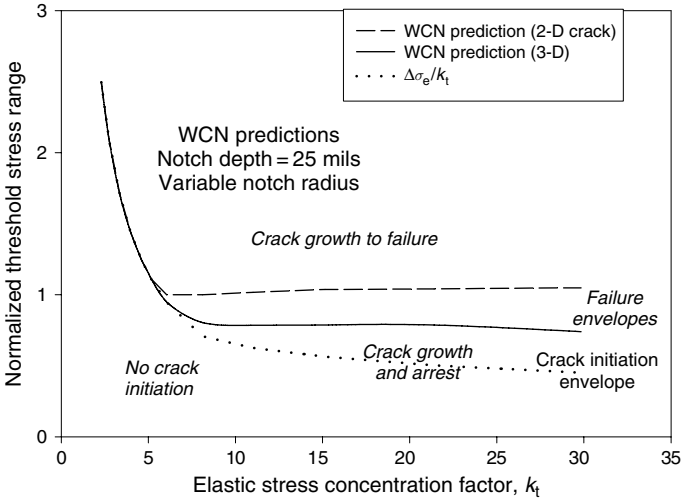


Figure E.3. Comparison of WCN model predictions for 2-D versus 3-D cracks. All results include the effects of plastic shakedown of notch mean stresses.

those predicted for the 2-D crack. It should be noted that in the fatigue crack growth calculations the 3-D crack was allowed to grow at both the deepest and surface locations of the crack front, so that situations could occur during growth where one location was propagating when the other crack tip location was not, and vice versa. This is the reason why the crack with the additional DOF associated with the 3-D crack gives lower threshold stresses.

Comparison of WCN predictions with experimental results

Threshold stress estimates from the 3-D WCN model are compared in Figure E.4 to experimental results from the small, sharp notch tests described in the previous section. In discussing these results, it is useful to separately consider blunt ($k_t < 6.5$) and sharp ($k_t > 6.5$) notches. For the case of blunt notches, the data tend to lie above the curve defined by the assumed initiation curve ($\Delta\sigma_e/k_t$), regardless of notch depth. However, for the sharp notches, the data tend to be layered with respect to notch depth as predicted by the WCN model. This is most clearly illustrated for the case of the notch depth of 24 mils where the data point is considerably above the initiation curve but in excellent agreement with the WCN prediction for $b = 24$ mils. A similar trend can be seen for the case of $b = 48$ mils; however, in this case the distinction between the predicted initiation and failure curves is less distinct because the two curves are relatively close together.

Ideally, one would like to generate additional small sharp notch data at higher k_t values for all notch depths to verify the predicted limiting values for the various notch depths.

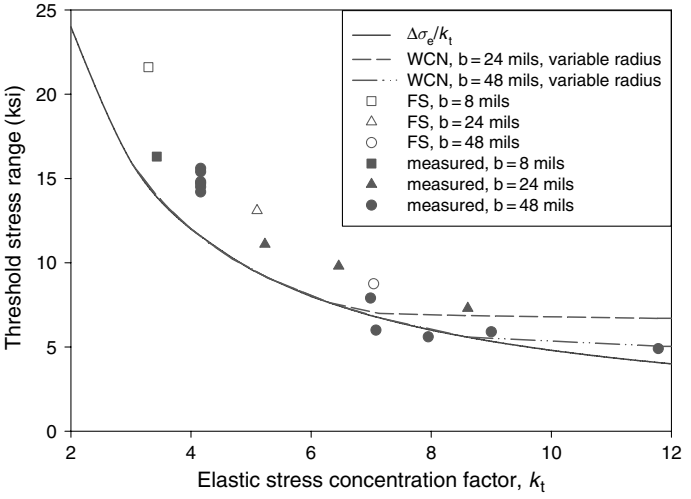


Figure E.4. Comparison of WCN and *F*s model predictions with small, sharp notch data for varying notch depths.

However, generating such data is limited by the sharpest notches that can be machined. In this set of experiments, the sharpest notch radii ($\rho = 2$ mils) could only be produced by EDM, since the final chem milling used for all other notches significantly reduced the notch sharpness to about $\rho = 4$ mils. Although the use of EDM without subsequent chem milling raised the possibility of producing notches that would initiate cracks prematurely, this does not appear to have been the case since the threshold stresses for small sharp EDM notches were significantly above the initiation curve, as well as above data on blunter notches produced by EDM plus chem milling. Moreover, this trend is consistent with the WCN theory that predicts a limiting threshold stress that depends on notch depth and corresponds to the growth and arrest of microcracks in the steep stress gradient ahead of the sharp notches.

The fact that blunt notches ($k_t < 6.5$) also resulted in measured threshold stresses that were above the initiation curve, corresponding to $\Delta\sigma_e/k_t$, could be due to a number of factors. First, this simple initiation criterion may be inaccurate for the biaxial stresses that exist at the notch surface. Thus, it may be necessary to include a more accurate multiaxial crack initiation criterion such as that employed in the Fs approach described in the previous section. To assess this hypothesis, the Fs predictions from Table E.2 are included in Figure 4 for comparison. These predictions, which use the multiaxial criterion, shift the predictions in the correct direction; i.e., they predict higher threshold stresses than those given by $\Delta\sigma_e/k_t$. However, the predicted results are now greater than the measured results, as previously discussed. This is an undesirable prediction for use in HCF design since the predictions are non-conservative with respect to the measured results. It may be that the multiaxial initiation criterion is accurate for blunt notches, but the surface area correction term in Fs is overcompensating for notch size effects.

An alternative explanation for the deviation between the measured blunt notch data in Figure E.4 and the simple initiation prediction given by $\Delta\sigma_e/k_t$ is that crack growth is contributing to the specimen's life, which would effectively increase the threshold stress in the step test. It may be possible to differentiate between the above two interpretations by carefully monitoring experiments for the presence of crack initiation, growth, or arrest. This could be achieved either by interrupting multiple specimens and performing metallographic sectioning or by obtaining crack size measurements on a single specimen using either crack replication or direct observation in a cyclic loading stage of a scanning electron microscope.

REFERENCES

1. Gallagher, J. et al., "Advanced High Cycle Fatigue (HLF) Life Assurance Methodologies", Report # AFRL-ML-WP-TR-2005-4102, Air Force Research Laboratory, Wright-Patterson AFB, OH, July 2004.

2. Murthy, H., Rajeev, P.T., Farris, T.N., and Slavik, D.C., "Fretting Fatigue of Ti-6A1-4V Subjected to Blade/Disk Contact Loading", *Developments in Fracture Mechanics for the New Century*, 50th Anniversary of Japan Society of Materials Science, Osaka, Japan, May 2001, pp. 41–48.
3. Doner, M., Bain, K.R., and Adams, J.H., "Evaluation of Methods for the Treatment of Mean Stress Effects on Low-Cycle Fatigue", *Journal of Engineering for Power*, 1981, pp. 1–9.
4. Hudak, S.J., Jr., Chan, K.S., Chell, G.G., Lee, Y.-D., and McClung, R.C., "A Damage Tolerance Approach for Predicting the Threshold Stresses for High Cycle fatigue in the Presence of Supplemental Damage", *Fatigue – David L. Davidson Symposium*, K.S. Chan, P.K. Liaw, R.S. Bellows, T.C. Zogas, and W.O. Soboyejo, eds, TMS (The Minerals, Metals & Materials Society), Warrendale, PA, 2002, pp. 107–120.
5. Southwest Research Institute, DARWIN User's Guide, Version 3.5, Appendix : *Shakedown Residual Stress Methodology and Validation of SHAKEDOWN Module*, 2002.
6. Amstutz and Seeger, T., *Accurate and Approximate Elastic Stress Distribution in the Vicinity of Notches in Plates Under Tension*. Unpublished results (referenced in G. Savaidis, M. Dankert, and T. Seeger, "An Analytical Procedure for Predicting Opening Loads of Cracks at Notches", *Fatigue Fract. Engng Mater. Struct.*, **18**, 1995, pp. 425–442).
7. Gallagher, J.P. et al. "Improved High Cycle Fatigue Life Prediction", Report # AFRL-ML-WP-TR-2001-4159, University of Dayton Research Institute, Dayton, OH, January 2001 (on CD ROM).

Appendix F*
Analytical Modeling of Contact Stresses

Bence B. Bartha, Narayan K. Sundaram and Thomas N. Farris

INTRODUCTION

Closed-form analytical solutions exist for a body having an arbitrary contact geometry contacting either an infinite half space or a finite thickness plate. The equations for the stress and displacement fields in the normal and tangential directions have been formulated and put into computer codes that provide numerical methods of solution of the contact problems. This appendix provides the equations and the solution methods that have been incorporated into two computer codes developed at Purdue University. The first code CAPRI (Contact Analysis for Profiles of Random Indenters) provides a solution method for contact of a finite body of arbitrary contact profile on a half-space when the two materials are identical. The second code CARTEL (Contact Analysis of Relatively Thin Elastic Layers) provides the contact solution for an indenter on a finite thickness plate. The latter problem is one that is encountered when a thin specimen is tested between two pads (indenters) in a fretting fatigue experiment. Both codes are available through Purdue University, School of Aeronautics and Astronautics, West Lafayette, IN.

CONTACT STRESSES IN A HALF-SPACE, THE CAPRI CODE

The Cauchy Singular Integral Equations (henceforth referred to as SIE) governing the contacts of two similar, isotropic elastic bodies are derived from Flamant's solution for a point load on a half-space [1]. The contact geometry before deformation is illustrated in Figure F.1. If $\bar{v}_A(x)$ and $\bar{v}_B(x)$ are the normal displacements of the two bodies, it can be shown that within the contact

$$h(x) - \bar{v}_A(x) + \bar{v}_B(x) - C_0 - C_1 x = 0 \tag{F.1}$$

$h(x)$ is the gap function (profile) in the local (symmetric) coordinate system, C_1 is the term associated with rigid-body rotation, and C_0 with rigid-body translation. Similar to the gap in the y direction, $h(x)$, the gap or relative initial displacements in the x direction are defined as $g(x)$.

*This document was prepared by students under the supervision of Prof. Thomas Farris at Purdue University, West Lafayette, IN as part of a major fretting fatigue research program headed by Prof. Farris. Dr. B. Bartha is currently at the Air Force Research Laboratory at Wright-Patterson AFB, OH.

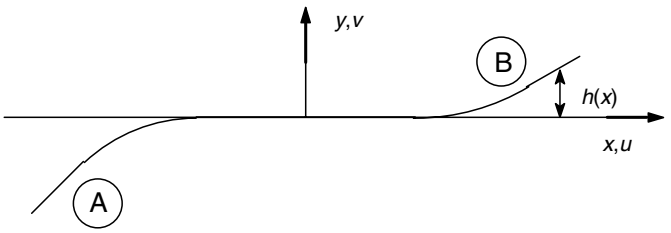


Figure F.1. Schematic of contact region showing coordinate system and gap function.

The following equations [2] govern the pressure traction $p(x)$ and the shear traction $q(x)$

$$\frac{\mathrm{d}[h(x)]}{\mathrm{d}x} - C_1 = \frac{\mathrm{d}}{\mathrm{d}x}(\bar{v}_\mathrm{A} - \bar{v}_\mathrm{B}) = \frac{4(1-\nu^2)}{\pi \mathrm{E}} \int_{-a}^{+a} \frac{p(s)}{(x-s)} \mathrm{d}s \tag{F.2}$$

$$\frac{\mathrm{d}}{\mathrm{d}x}(\bar{u}_\mathrm{A} - \bar{u}_\mathrm{B}) = -\frac{\mathrm{d}g(x)}{\mathrm{d}x} = -\frac{4(1-\nu^2)}{\pi E} \int_{-a}^{+a} \frac{q(s)}{(x-s)} \mathrm{d}s + \frac{\sigma_0(1-\nu^2)}{E} \tag{F.3}$$

where $\bar{u}_\mathrm{A}$ and $\bar{u}_\mathrm{B}$ are the tangential displacements of the bodies and σ_0 is a remotely applied bulk-stress. Note that the unknown tractions occur inside the integral in both equations and "a," the contact half-width, is unknown *a priori*. In this two-dimensional formulation, plane strain conditions are assumed.

It is important to note that the maximum value of shear traction is limited by the coefficient of friction, μ. Further, the problems of most interest are the so-called partial slip problems (mixed boundary-value problems), in which the contact is divided into outer "slip" regions, where $|q(x)| = \mu p(x)$ and a central "stick" region, in which

$$\frac{\partial \mathrm{g}(x)}{\partial x} = \mathrm{g}'(x) \tag{F.4}$$

where $g'(x)$ is the value of the derivative when the particles first enter the stick zone [1]. The partial derivative is present because of the quasi-static formulation of the problem. In the most general case, this is load-history dependent and has to be obtained incrementally. Again, the size of this stick zone, denoted by c, is not known *a priori*.

The Equations (F.2) and (F.3) are subject to the following equilibrium boundary conditions:

$$\int_{-a}^{+a} p(x)\mathrm{d}x = \mathrm{P} \tag{F.5}$$

$$\int_{-a}^{+a} xp(x)\mathrm{d}x = \mathrm{M} \tag{F.6}$$

$$\int_{-a}^{+a} q(x)\mathrm{d}x = \mathrm{Q} \tag{F.7}$$

where P, M, and Q are the applied normal force, moment, and shear, respectively.

It is also known that for incomplete contacts, the pressure traction must vanish at the extremities, that is

$$p(-a) = p(a) = 0 \tag{F.8}$$

In the above SIEs, the pressure equation can be solved independently of the shear equation and we proceed to do this first.

Apart from the unknowns already mentioned in the problem, there are two more: the contact eccentricity "e" and the stick-zone eccentricity "e_{c}," which do not explicitly occur in the above equations. The contact eccentricity "e" is defined as the separation between the local (x) and global (X) coordinate systems

$$X = x + e \tag{F.9}$$

Thus, in the global coordinate system, the contact is from $(-\mathrm{a} + \mathrm{e})$ to $(\mathrm{a} + \mathrm{e})$ and the stick zone is from $(-\mathrm{c} + \mathrm{e_c})$ to $(\mathrm{c} + \mathrm{e_c})$.

Pressure solution

For arbitrary smooth profiles $h(x)$, it is not generally possible to invert the integral Equation (F.2) to obtain a closed-form solution for $p(x)$. (A limited number of profiles have analytical solutions [3, 4, 5].) However, it is possible to use a trigonometric variable transformation [6] to obtain an analytical solution. Murthy et al. [2] develop this as follows. Using the substitutions $x = \mathrm{a}\cos\phi$ and $s = \mathrm{a}\cos\theta$

$$\frac{\mathrm{d}h}{\mathrm{d}\phi} = \frac{\mathrm{d}h}{\mathrm{d}x}\frac{\mathrm{d}x}{\mathrm{d}\phi} = -a\frac{\mathrm{d}h}{\mathrm{d}x}\sin\phi \tag{F.10}$$

the pressure SIE becomes

$$\frac{1}{a\sin\phi}\frac{\mathrm{d}h}{\mathrm{d}\phi} + \mathrm{C}_1 = -\frac{4(1-\nu^2)}{\pi E}\int_0^{\pi}\frac{p(\theta)\sin\theta\mathrm{d}\theta}{\cos\phi - \cos\theta} \tag{F.11}$$

Next, the pressure traction function is expressed as an infinite cosine series

$$p(\theta) = \sum_{n=0}^{\infty}\frac{p_n\cos n\theta}{\sin\theta} \tag{F.12}$$

Further, from tables of integrals, the following definite integral is known

$$\int_0^{\pi}\frac{\cos n\theta\mathrm{d}\theta}{\cos\phi - \cos\theta} = \frac{\pi\sin n\phi}{\sin\phi} \tag{F.13}$$

Substituting Equations (F.12) and (F.13) into Equation (F.11),

$$\frac{\mathrm{d}h}{\mathrm{d}\phi} + \mathrm{C}_1 a \sin\phi = a \sin\phi \frac{4(1-\nu^2)}{E} \sum_{n=1}^{\infty} \frac{p_n \sin n\phi}{\sin\phi} \tag{F.14}$$

Note that the summation starts at $n = 1$, not $n = 0$.

The last step in the exercise is to express $\mathrm{d}h/\mathrm{d}\phi$ in such a form that a term-by-term comparison can be made between the left- and right-hand sides of the equation. This is achieved by expressing the slope as a Fourier sine series

$$\frac{\mathrm{d}h}{\mathrm{d}\phi} = \sum_{n=1}^{\infty} h_n \sin n\phi \tag{F.15}$$

Finally,

$$p_n = \frac{E h_n}{4a(1-\nu^2)} \quad n > 1 \tag{F.16}$$

$$p_1 = \frac{E(h_n + \mathrm{C}_1 a)}{4a(1-\nu^2)} \quad n = 1 \tag{F.17}$$

where p_1 is still not determined, because C_1 is also unknown. However, using the force equilibrium condition, Equation (F.5), we find

$$p_0 = \frac{P}{\pi a} \tag{F.18}$$

Similarly, from the moment equilibrium condition, Equation (F.6), we find

$$p_1 = \frac{2\mathrm{M}}{\pi a^2} \tag{F.19}$$

Also, $p(0) = 0$ implies

$$\lim_{\theta \to 0} \frac{p_0 + p_1 \cos\theta + p_2 \cos 2\theta + \cdots}{\sin\theta} = 0 \tag{F.20}$$

For this limit to exist, the numerator has to vanish, hence

$$p_0 = -\sum_{k=0}^{\infty} p_k \tag{F.21}$$

Similarly, using $p(\pi) = 0$

$$p_1 = -\sum_{k=1}^{\infty} p_{2k+1} \tag{F.22}$$

Solving for pressure in CAPRI (the solver developed for similar materials in Purdue) involves finding the correct (a, e) pair corresponding to the applied force and moment. This is typically an iterative or search-type process. Guess values of "a" smaller than the actual value, for example, will lead to a pressure traction whose resultant is smaller than the applied force P. Fourier decompositions like the one in Equation (F.15) can be done very rapidly using the discrete sine-transform.

Shear solution

The case of full-sliding is trivially solved ($q(x) = \mu p(x)$). However, different possibilities occur while computing shear tractions in partial sliding. The assumption is that there is a central stick zone with two slip zones, one at either end; the size and eccentricity of the stick zone is unknown *a priori*. Depending on the value of applied bulk-stress, the signs of shear in the slip-zones may be the same or opposing, positive or negative, which makes four possibilities in all.

Positive shear stresses in both slip zones

As described in [7], the shear traction is expressed as a superposition of two tractions

$$q(\mathrm{X}) = q'(\mathrm{X}) - q''(\mathrm{X}) = \mu p(\mathrm{X}) - q''(\mathrm{X}) \tag{F.23}$$

Clearly, $q''(\mathrm{X})$ must be zero in the slip zones. The term "$\mathrm{d}g/\mathrm{d}x$," as described earlier is a history dependent term. In the very first shear loading step, it will be zero. In [2], a detailed analysis is carried out, considering shear-loading, unloading and re-loading, while keeping normal load constant. It is pointed out that after loading, relative slip is measured from the displacement state at Q and σ_0 for unloading. Here only the simple case when there is no prior history is considered. Substituting Equation (F.23) into Equation (F.3) and setting $\mathrm{d}g/\mathrm{d}x = 0$, the stick-zone equation becomes

$$0 = \frac{4\mu(1-\nu^2)}{\pi E}\int_{-a}^{+a}\frac{p(s)}{(x-s)}\mathrm{d}s - \frac{4(1-\nu^2)}{\pi E}\int_{-a}^{+a}\frac{q''(s)}{(x-s)}\mathrm{d}s - \frac{\sigma_0(1-\nu^2)}{E} \tag{F.24}$$

Substituting for the pressure term and re-arranging,

$$\mu\left(\frac{\mathrm{d}h}{\mathrm{d}x} - \mathrm{C}_1\right) - \left(\frac{\sigma_0(1-\nu^2)}{E}\right) = \frac{4(1-\nu^2)}{\pi E}\int_{-a}^{+a}\frac{q''(s)}{(x-s)}\,\mathrm{d}s \tag{F.25}$$

which is similar in form to the original pressure equation, but with C_1 and $\mathrm{d}h/\mathrm{d}x$ modified. Additionally, the equilibrium boundary condition for this equation is

$$\int_{-a}^{+a}\mathrm{q}''(x)\,\mathrm{d}x = \mu P - Q \tag{F.26}$$

Also, $q''(x)$ has to vanish at both stick-slip boundaries; global coordinates are to be assumed in the following expression

$$q''(-c+e_c) = q''(c+e_c) = 0 \tag{F.27}$$

The solution procedure consists of finding c and e_c such that all the prescribed conditions are satisfied.

Different signs of shear in the two-slip zones

This occurs when the bulk-stress exceeds a certain critical value in either direction; in this case, again $q(x)$ is split into two parts as follows [2, 8]:

$$q'(\mathrm{X}) = \mu p(\mathrm{X}), \mathrm{X} \in [-a+e, -c+e_c] \tag{F.28a}$$

$$q'(\mathrm{X}) = \mu p(-c+e_c) - (\mathrm{X}+c-e_c) \times \frac{\mu p(c+e_c) + \mu p(-c+e_c)}{2c}, \quad \mathrm{X} \in [\text{stick zone}] \tag{F.28b}$$

$$q'(\mathrm{X}) = -\mu p(\mathrm{X}), \mathrm{X} \in [c+e_c, a+e] \tag{F.28c}$$

The term in the middle, Equation (F.28b), simply represents a linear interpolation of the shear stress in the stick zone. Of course, the other possibility of different signs of shear is negative in the left slip-zone and positive in the right slip-zone.

The corrective shear traction can be found again by using the principle that in the stick zone, no relative sliding can occur. The assumed shear function $q'(x)$, however, produces a slope of displacement $\mathrm{d}g'(x)/\mathrm{d}x$; for the case with no history,

$$\frac{\mathrm{d}g'(x)}{\mathrm{d}x} - \frac{\sigma_0(1-\nu^2)}{E} = \frac{4(1-\nu^2)}{\pi E} \int_{-a}^{+a} \frac{q''(s)}{(x-s)}\,\mathrm{d}s \tag{F.29}$$

subject to the equilibrium boundary condition

$$\int_{-a}^{+a} q''(x)\,\mathrm{d}x = Q' - Q \tag{F.30}$$

Again, the conditions in Equation (F.27) apply as boundary conditions for the corrective shear. This equation can also be solved using the sine-series technique described for pressure. For further details see [2].

History effects and general loading cases

In most general loading case, it is possible there may be slip on only one end or no slip at all. An example loading case is when P and Q are applied together [9]. The "history"

or path-dependence comes about due to growth of the stick zone into areas that were previously slipping ("slip-lock"). In such cases, a direct solution as outlined above cannot be used; the load step has to be broken into increments and the slope of slip $\mathrm{d}g/\mathrm{d}x$ has to be updated at the end of every increment.

CONTACT STRESSES IN A FINITE THICKNESS BODY, THE CARTEL CODE

The analytical solution of the surface tractions produced by an indenter on a half space can be solved using SIEs [10] as outlined in the first section of this Appendix. Bodies that are dissimilar but still isotropic can still be solved analytically even with the coupling effects between P and Q [9]. The corresponding subsurface stress field can be obtained from the elasticity solution of any arbitrary traction on a half-space. The complete stress field due to any traction applied to the surface of a half-space can be solved using Fast Fourier Transforms (FFTs). SIE cannot be used when the elastic half-space is replaced by an infinite length sheet with finite thickness [11, 12]. SIEs have been derived to account for this finite thickness by [16] assuming a rigid pad indenting a finite thickness infinite layer. The derivation of the elasticity solution for the stress field of a half space due to any traction will be used in order to develop a numerical solution of the tractions on any finite thickness body [6, 13].

Previous researchers have studied the stress field of an infinite half-space using many techniques such as complex analysis [14] and Fourier transform technique [4] among others. For the FFT technique, the solution has been derived by satisfying the two-dimensional biharmonic equation, also known as the Airy stress function by using the compatibility relation in the absence of body forces and Fourier techniques [15].

The two-dimensional biharmonic equation $\nabla_1^4 \chi = 0$, can be rewritten in the frequency domain by taking the Fourier transform.

$$\begin{aligned} \int_{-\infty}^{\infty} \nabla_1^4 \chi \mathrm{e}^{-\mathrm{i}\alpha x}\,\mathrm{d}x &= \left(\frac{\mathrm{d}^2}{\mathrm{d}y^2} - \alpha^2\right)^2 \int_{-\infty}^{\infty} \chi e^{-\mathrm{i}\alpha x}\,\mathrm{d}x = 0 \\ \chi(x, y) &= \frac{1}{2\pi} \int_{-\infty}^{\infty} G(y, \alpha) e^{-\mathrm{i}\alpha x}\,\mathrm{d}\alpha \end{aligned} \tag{F.31}$$

Using the substitution of variables, the biharmonic equation can be rewritten as a second-order partial differential equation with a general solution,

$$\begin{aligned} G &= \int_{-\infty}^{\infty} \chi e^{\mathrm{i}\alpha x}\,\mathrm{d}x \left(\frac{\mathrm{d}^2}{\mathrm{d}y^2} - \alpha^2\right)^2 G = 0 \\ G &= (\mathrm{A} + \mathrm{B}y) e^{-\alpha y} + (\mathrm{C} + \mathrm{D}y) e^{\alpha y} \end{aligned} \tag{F.32}$$

where A, B, C, and D are constants to be determined from boundary conditions. From the Fourier inversion theorem, the Airy stress function can be written as

$$\chi(x, y) = \frac{1}{2\pi} \int_{-\infty}^{\infty} G(y, \alpha) e^{-i\alpha x} \, \mathrm{d}\alpha \tag{F.33}$$

The stresses in rectangular coordinates can be written in terms of the Airy stress function using the equations of equilibrium. The stresses can then be rewritten in terms of G from the above Fourier technique.

$$\begin{aligned}
\sigma_{\mathrm{x}} &= \frac{\mathrm{d}^2\chi}{\mathrm{d}y^2} \quad \int_{-\infty}^{\infty} \sigma_{\mathrm{x}} e^{i\alpha x} \, \mathrm{d}x = \frac{\mathrm{d}^2 G}{\mathrm{d}y^2} \quad \sigma_{\mathrm{x}} = \frac{1}{2\pi} \int_{-\infty}^{\infty} \frac{\mathrm{d}^2 G}{\mathrm{d}y^2} e^{-i\alpha x} \, \mathrm{d}\alpha \\
\sigma_{\mathrm{y}} &= \frac{\mathrm{d}^2\chi}{\mathrm{d}x^2} \quad \int_{-\infty}^{\infty} \sigma_{\mathrm{y}} e^{i\alpha x} \, \mathrm{d}x = -\alpha^2 G \quad \sigma_{\mathrm{y}} = -\frac{1}{2\pi} \int_{-\infty}^{\infty} \alpha^2 G e^{-i\alpha x} \, \mathrm{d}\alpha \\
\tau_{\mathrm{xy}} &= \frac{\mathrm{d}^2\chi}{\mathrm{d}x\mathrm{d}y} \quad \int_{-\infty}^{\infty} \tau_{\mathrm{xy}} e^{i\alpha x} \, \mathrm{d}x = i\alpha \frac{\mathrm{d}G}{\mathrm{d}y} \quad \tau_{\mathrm{xy}} = \frac{1}{2\pi} \int_{-\infty}^{\infty} i\alpha \frac{\mathrm{d}G}{\mathrm{d}y} e^{-i\alpha x} \, \mathrm{d}\alpha
\end{aligned} \tag{F.34}$$

In a similar manner, the displacement field can be derived from the stress–strain relations.

$$\begin{aligned}
\frac{E}{(1+\nu)} \frac{\delta \mathrm{u}}{\delta \mathrm{x}} &= (1-\nu)\sigma_{\mathrm{x}} - \sigma_{\mathrm{y}} \\
\frac{E}{2(1+\nu)} \left[\frac{\delta \mathrm{u}}{\delta \mathrm{y}} + \frac{\delta \mathrm{v}}{\delta \mathrm{x}} \right] &= \tau_{\mathrm{xy}}
\end{aligned} \tag{F.35}$$

The displacements can also be rewritten in terms of G by substituting the general solution of the stress field found:

$$\begin{aligned}
u &= \frac{1+\nu}{2\pi E} \int_{-\infty}^{\infty} \left[(1-\nu) \frac{\mathrm{d}^2 G}{\mathrm{d}y^2} + \nu\alpha^2 G \right] \mathrm{i} \mathrm{e}^{-i\alpha x} \frac{\mathrm{d}\alpha}{\alpha} \\
v &= \frac{1+\nu}{2\pi E} \int_{-\infty}^{\infty} \left[(1-\nu) \frac{\mathrm{d}^3 G}{\mathrm{d}y^3} + (2+\nu)\alpha^2 \frac{\mathrm{d}G}{\mathrm{d}y} \right] \mathrm{e}^{-i\alpha x} \frac{\mathrm{d}\alpha}{\alpha^2}
\end{aligned} \tag{F.36}$$

The above general stress- and displacement-traction relationships can be used to solve for the subsurface stresses and the surface tractions of two bodies in contact.

Half-space solution

The particular solution of the subsurface stress field can be evaluated by obtaining the correct boundary conditions (Figure F.2). These boundary conditions can then be applied to the stress and displacement field equations to solve for A, B, C, and D. For example, if the semi-infinite plate has a normal traction $-p(x)$ applied to the surface, then the

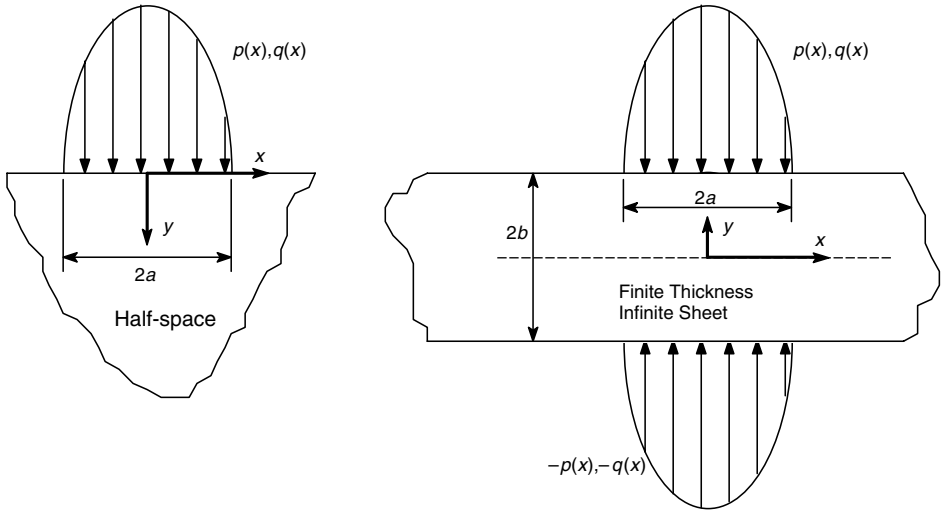


Figure F.2. The coordinate system and applied boundary conditions for the half-space and finite thickness problem.

boundary conditions in Equation (F.38) can be used to solve for G. The results can then be used in order to solve for the corresponding stress field.

$$\begin{aligned} \sigma_y &= -p(x) \quad \text{at } y = 0 \\ \tau_{xy} &= 0 \quad \text{at } y = 0 \\ \sigma_x &= \sigma_y = \tau_{xy} \to 0 \text{ when } y \to \infty \end{aligned} \tag{F.37}$$

From the conditions at infinity, $C = 0$ and $D = 0$ is obtained. From the conditions at $y = 0$ the other two constants can be found:

$$A = \frac{\bar{p}(\alpha)}{\alpha^2}, \qquad B = \frac{\bar{p}(\alpha)}{\alpha} \tag{F.38}$$

The particular solution of a normal traction on a half-space can now be obtained from the particular solution of G.

$$\begin{aligned} \sigma_x &= \frac{1}{2\pi}\int_{-\infty}^{\infty} -\bar{p}(\alpha)\,[1-\alpha y]\,e^{-\alpha y}e^{-i\alpha x}\,\mathrm{d}\alpha \\ \sigma_y &= -\frac{1}{2\pi}\int_{-\infty}^{\infty} \bar{p}(\alpha)\,[1-\alpha y]\,e^{-\alpha y}e^{-i\alpha x}\,\mathrm{d}\alpha \\ \tau_{xy} &= \frac{1}{2\pi}\int_{-\infty}^{\infty} -i\alpha\bar{p}(\alpha)\,y e^{-\alpha y}e^{-i\alpha x}\,\mathrm{d}\alpha \end{aligned} \tag{F.39}$$

The stresses due to a shear traction $q(x)$ can be obtained by applying the boundary conditions in a similar manner.

$$\begin{aligned} &\sigma_x = 0 \quad \text{at } y = 0 \\ &\tau_{xy} = q(x) \quad \text{at } y = 0 \\ &\sigma_x = \sigma_y = \tau_{xy} \to 0 \text{ when } y \to \infty \end{aligned} \tag{F.40}$$

The constants C and D are again zero, however, A and B are different in this case.

$$\mathrm{A} = 0, \qquad \mathrm{B} = \frac{\bar{q}(\alpha)}{i\alpha} \tag{F.41}$$

The particular solution of a shear traction on a half-space can now be obtained from the particular solution of G.

$$\begin{aligned} \sigma_x &= \frac{1}{2\pi}\int_{-\infty}^{\infty} \frac{\bar{q}(\alpha)}{i\alpha}\left[-2\alpha + \alpha^2 y\right] e^{-\alpha y} e^{-i\alpha x}\,\mathrm{d}\alpha \\ \sigma_y &= -\frac{1}{2\pi}\int_{-\infty}^{\infty} \alpha^2 \frac{\bar{q}(\alpha)}{i\alpha} y e^{-\alpha y} e^{-i\alpha x}\,\mathrm{d}\alpha \\ \tau_{xy} &= \frac{1}{2\pi}\int_{-\infty}^{\infty} i\alpha \frac{\bar{q}(\alpha)}{i\alpha}\left[1 - \alpha y\right] e^{-\alpha y} e^{-i\alpha x}\,\mathrm{d}\alpha \end{aligned} \tag{F.42}$$

Similarly, the solution for the displacement field of the body can be obtained.

$$\begin{aligned} v_p(x) &= \frac{1+\nu}{2\pi E}\int_{-\infty}^{\infty} \frac{\bar{p}(\alpha)}{\alpha}\left[2(1-\nu)\right] e^{-i\alpha x}\,\mathrm{d}\alpha \\ v_q(x) &= \frac{1+\nu}{2\pi E}\int_{-\infty}^{\infty} \frac{-i\bar{q}(\alpha)}{\alpha}[5-2\nu] e^{-i\alpha x}\,\mathrm{d}\alpha \\ u_p(x) &= \frac{1+\nu}{2\pi E}\int_{-\infty}^{\infty} \frac{-i\bar{q}(\alpha)}{\alpha}[1-2\nu] e^{-i\alpha x}\,\mathrm{d}\alpha \\ u_q(x) &= \frac{1+\nu}{2\pi E}\int_{-\infty}^{\infty} \frac{-\bar{q}(\alpha)}{\alpha}[2(1-\nu)] e^{-i\alpha x}\,\mathrm{d}\alpha \end{aligned} \tag{F.43}$$

Finite thickness solution

In order to apply a similar methodology for solving the analytical solution of a layered body subjected to a normal and shear traction, the correct boundary values to the general solution must be chosen (Figure F.3). The boundary conditions stay the same on the

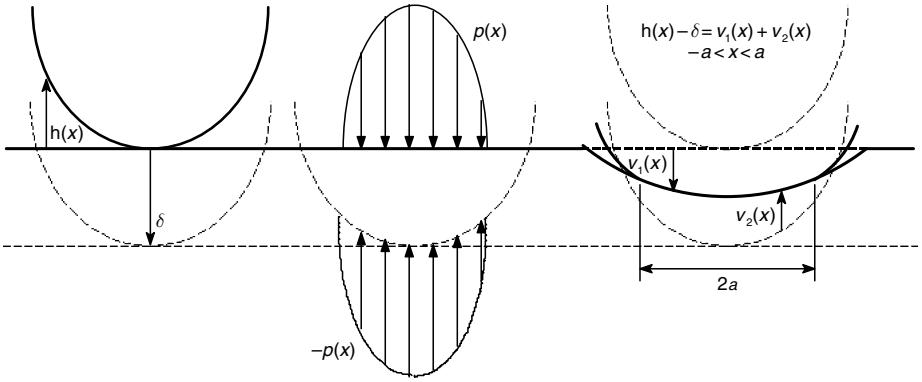


Figure F.3. Relationship between gap function h*(x)* and vertical displacements, $v_1(x)$, due to normal traction p(x).

surface and symmetry is used at the half thickness. First, the subsurface stresses due to a normal traction give the boundary conditions

$$\begin{aligned} \sigma_y &= -p(x) \quad \text{at} \quad y = b \\ \tau_{xy} &= -p(x) \quad \text{at} \quad y = b \\ v(x) &= 0 \quad \text{at} \quad y = 0 \\ \tau_{xy} &= 0 \quad \text{at} \quad y = 0 \end{aligned} \tag{F.44}$$

From the symmetry boundary conditions, $B = -D$ and $A = C$ can be obtained. Similarly, from the surface boundary conditions the other two constants are obtained:

$$\begin{aligned} A &= \left[\frac{1}{\alpha} + b\frac{\cosh(\alpha b)}{\sinh(\alpha b)}\right] B \\ B &= \frac{\bar{p}(\alpha)}{2\alpha^2} \; \frac{\alpha \sinh(\alpha b)}{\alpha b + \cosh(\alpha b)\sinh(\alpha b)} \end{aligned} \tag{F.45}$$

The constants for a shear traction on the surface can be obtained in a similar manner.

$$\begin{aligned} \sigma_y &= 0 \quad \text{at } y = b \\ \tau_{xy} &= q(x) \quad \text{at } y = b \\ v(x) &= 0 \quad \text{at } y = 0 \\ \tau_{xy} &= 0 \quad \text{at } y = 0 \end{aligned} \tag{F.46}$$

From the symmetry boundary conditions, $B = -D$ and $A = C$ are obtained again. However, from the surface boundary conditions, A and B are obtained in terms of the shear traction $\bar{q}(\alpha)$, α and the thickness b.

$$\begin{aligned} B &= \frac{\cosh(\alpha b)}{b\sinh(\alpha b)} A \\ A &= \frac{i\bar{q}(\alpha)}{2\alpha^2} \frac{\alpha b \sinh(\alpha b)}{\alpha b + \cosh(\alpha b)\sinh(\alpha b)} \end{aligned} \tag{F.47}$$

The equations in this form can be used to solved for the subsurface stress field, Equation (F.34), of any finite thickness infinite sheet subjected to a given shear and normal traction without iterating. However, a different approach must be implemented from the above relationships in order to obtain the particular surface tractions.

Surface tractions

The surface tractions can be obtained by applying a different set of boundary conditions and by deriving a different set of relations between the surface displacements and the corresponding tractions. The equations in this form can be used to solved for the subsurface stress field of any finite thickness infinite sheet subjected to a given shear and normal traction [16].

The relationship between the displacements and the surface tractions can be used to obtain a solution for the surface tractions, Equation (F.36). At the surface where $y = b$, the total displacement u and v due to each traction can be written as a function of the two forms of G from the normal and shear tractions with the constants corresponding to Equations (F.45) and (F.47).

$$\begin{aligned} v(x) = {} & \frac{1+\nu}{2\pi E} \int_{-\infty}^{\infty} \frac{-\bar{p}(\alpha)}{\alpha} \left[\frac{2(1-\nu)\sinh^2(\alpha b)}{\alpha b + \cosh(\alpha b)\sinh(\alpha b)} \right] e^{-i\alpha x} d\alpha \\ & + \frac{1+\nu}{2\pi E} \int_{-\infty}^{\infty} \frac{-i\bar{q}(\alpha)}{\alpha} \left[(5-2\nu) - \frac{2(1-\nu)\alpha b}{\alpha b + \cosh(\alpha b)\sinh(\alpha b)} \right] e^{-i\alpha x} d\alpha \\ u(x) = {} & \frac{1+\nu}{2\pi E} \int_{-\infty}^{\infty} \frac{-i\bar{p}(\alpha)}{\alpha} \left[(1-2\nu) - \frac{2(1-\nu)\alpha b}{\alpha b + \cosh(\alpha b)\sinh(\alpha b)} \right] e^{-i\alpha x} d\alpha \\ & + \frac{1+\nu}{2\pi E} \int_{-\infty}^{\infty} \frac{\bar{q}(\alpha)}{\alpha} \left[\frac{2(1-\nu)\cosh^2(\alpha b)}{\alpha b + \cosh(\alpha b)\sinh(\alpha b)} \right] e^{-i\alpha x} d\alpha \end{aligned} \tag{F.48}$$

The above displacement-traction relationships may be used for deriving the solution for the tractions inside the contact zone. It must be noted that Equation (F.48) differs slightly from previous results [9, 17]. The vertical displacement $v(x)$ due to $q(x)$ has a $(5-2\nu)$ term instead of $(1-2\nu)$. This result can be first compared to the half-space solution in

Equation (F.43). The solution for $v(x)$ in Equation (F.48) must be equal to the solution in Equation (F.43) for a large thickness b for any given shear stress $q(x)$. This is true since the hyperbolic sine and cosine terms for $v(x)$ go to zero for $b \to \infty$ in Equation (F.48). This result was also validated with the same procedure using the finite thickness constants from Equation (F.47). This difference is shown for completeness if the correct vertical displacement must be calculated correctly for a half-space or a finite thickness infinite length plate. The shear traction $q(x)$ acts equal and opposite on each body in contact, therefore, the $(5-2\nu)$ half-space term must disappear when the gap function $h_0(x)$ is calculated from the relative displacement $v_1 - v_2$ of the two bodies, otherwise, the shear traction $q(x)$ would influence the normal traction $p(x)$ even for a half-space

As previous work has shown [10], the displacement field can be used to derive the tractions. When two bodies come in contact with one another, there is a gap function, h(x), which describes the distance the two bodies are away from each other at each point before deformation (Figure F.3). If one body is allowed to inter-penetrate the other by a rigid body displacement dv, then there is a normal traction, $p(x)$, which can be applied equal and opposite to each body which would produce no inter-penetration inside the contact zone, and one which integrates to the total load P, Equation (F.49).

$$
\begin{aligned}
|x| \le \mathrm{a}\ \mathrm{h}(x) &= v_1(x) + v_2(x) + \delta_{\mathrm{v}1} + \delta_{\mathrm{v}2} \\
&= v_{\mathrm{p}1}(\alpha)p(x) + v_{\mathrm{q}1}(\alpha)\mathrm{q}(x) \\
&\quad + v_{\mathrm{p}2}(\alpha)p(x) + v_{\mathrm{q}2}(\alpha)q(x) + \delta_{\mathrm{v}} \\
|x| \ge \mathrm{a}\ p(x) &= 0 \quad q(x) = 0 \\
\mathrm{P} &= \int_{-a}^{+a} p(x)\mathrm{d}x
\end{aligned}
\tag{F.49}
$$

The boundary condition to obtain the shear traction is slightly different (Figure F.4). The shear traction is defined to be $q(x) = \mu p(x)$ in the slip zone. The relative horizontal slip can next be assumed to be $u(x) = \delta_{\mathrm{u}}$ in the stick-zone, where δ_{u} is the amount of relative

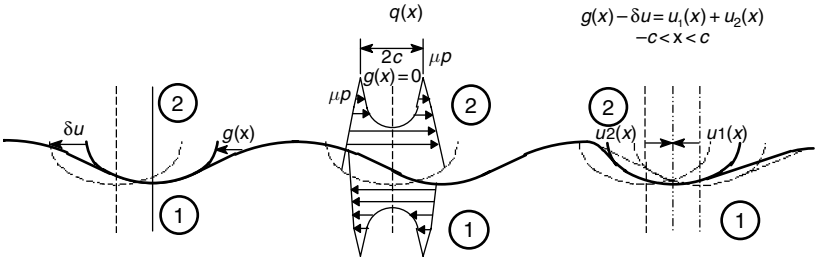


Figure F.4. Relationship between slip function $g(x)$ and horizontal displacements $u_{\mathrm{i}}(x)$ due to a shear traction $q(x)$.

tangential displacement between the pad and specimen before the shear traction is applied. By specifying the stick-zone size $2c$ and knowing the total shear load Q applied, the shear traction can be iterated for simultaneously with the normal traction in such a way that an equal and opposite shear traction on each body causes there to be no inter-penetration, and the shear traction is continuous throughout the contact zone, Equation (F.50).

$$\begin{aligned} |x| \le \mathrm{c}\ g(x) &= u_1(x) + u_2(x) + \delta_{\mathrm{u1}} + \delta_{\mathrm{u2}} \\ &= u_{\mathrm{p1}}(\alpha)p(x) + u_{\mathrm{q1}}(\alpha)q(x) \\ &\quad + u_{\mathrm{p2}}(\alpha)p(x) + u_{\mathrm{q2}}(\alpha)q(x) + \delta_{\mathrm{u}} \\ a \ge |x| > c &\quad q(x) = \mu \mathrm{p}(x) \\ |x| \ge c\ p(x) = 0 &\quad q(x) = 0 \\ Q = \int_{-a}^{+a} q(x)\mathrm{d}x & \end{aligned} \tag{F.50}$$

When there is a moment M present, then the pad profile $h_0(x)$ is rotated by an angle θ_{m} such that the resulting normal traction satisfies the moment boundary condition M for a particular pad rotation angle, Equation (F.51).

$$\mathrm{M} = \int_{-a}^{+a} xp(x)\mathrm{d}x \tag{F.51}$$

Note that the equilibrium conditions for contact on a finite thickness plate, given in Equations (F.49), (F.50) and (F.51), are identical to the equilibrium conditions for the half-space given earlier as Equations (F.5), (F.6), and (F.7).

Bulk stress effect can be accounted for by assuming that there is a constant strain in the stick zone due to the remote bulk stress that causes each point to displace by an amount based on the property of the material, Equation (F.52).

$$\begin{aligned} \varepsilon_{\mathrm{XX}} &= \frac{\sigma_{\mathrm{bulk}}\left(1-\nu^2\right)}{E} \\ u_1(x) &= \frac{\sigma_{\mathrm{bulk}}\left(1-\nu^2\right)}{E}x + \delta_{\mathrm{u1}} \end{aligned} \tag{F.52}$$

Unlike the half-space solution, however, this solution methodology is similar to that of the traction solution for dissimilar materials and anisotropic materials because the shear and normal tractions must be calculated simultaneously [12]. There is no need to account for singularities, however, because SIEs are not used here. Unfortunately, there are many other convergence issues to be resolved when working within the frequency domain. By knowing the profile, ($\mathrm{h}_0(x)$), material properties, (E, ν), and the total load applied, (P, Q, M, σ_{bulk}), the normal and shear tractions, ($p(x)$, $q(x)$) can be iterated for by assuming

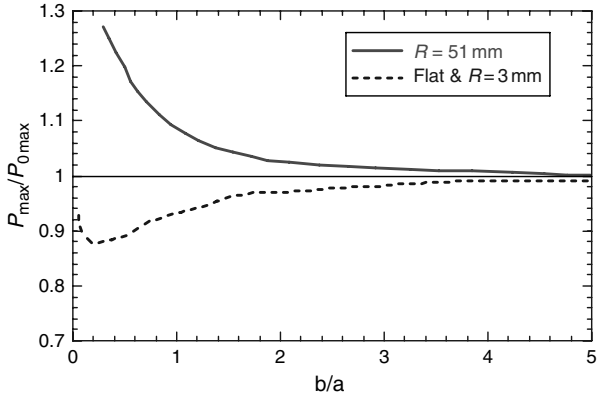


Figure F.5. Ratio of peak pressure $P_{\max}$ to peak pressure $P_{0\max}$ for increasing thickness to contact length ratio for two pad geometries.

the correct contact length, (a), stick zone size, (c), pressure eccentricity, (e), stick zone eccentricity, (e_c), the normal rigid-body displacement, (δ_v), the tangential rigid body displacement, (δ_u), and the pad profile rotation angle (θ_m).

The peak pressure $P_{\max}$ was also calculated for increasing specimen thickness to study the thickness effect on the pressure distribution. A normal load of 1.2×10^6 N/m was applied to a pad geometry of 51 mm radius pad as well as a 3-mm flat and edge radius pad for increasing thickness. The peak pressure was obtained for each specimen thickness and pad geometry and normalized with the peak pressure $P_{0\max}$ obtained from the half-space solution. Figure F.5 shows that the CARTEL solution (finite thickness) approaches the CAPRI solution (half-space) for a thickness where the thickness to contact length ratio b/a is greater than 5. The half-contact length that was used for the two pad geometries was $a = 1.1$ mm for the cylindrical pad and $a = 1.7$ mm for the flat pad.

REFERENCES

1. Hills, D.A., Nowell, D., and Sackfield A., *Mechanics of Elastic Contacts*, Kluwer Academic Publishers, 1992.
2. Murthy, H., Harish, G., and Farris, T.N., "Efficient Modeling of Fretting of Blade/Disk Contacts Including Load History Effects", *ASME Journal of Tribology*, **126**, 2004, pp. 56–64.
3. Ciavarella, M., Hills, D.A., and Monno, G., "The Influence of Rounded Edges on Indentation by a Flat Punch", Proc. Inst. Mech. Eng., Part C: *J. Mech. Eng. Sci.*, **212**(4), 1998, pp. 319–328.
4. Jager, J., "Half-planes Without Coupling Under Contact Loading", *Archive of Applied Mechanics*, **67**, 1997, pp. 247–259.
5. Goryacheva, I.G., Murthy, H., and Farris T.N., "Contact Problem with Partial Slip for the Inclined Punch with Rounded Edges", *Int. J. Fatigue*, **24**, 2002, pp. 1191–1201.

6. Barber, J.R., *Elasticity*, Kluwer Academic Publishers, Netherlands, 1992.
7. Mindlin, R.D., "Compliance of Elastic Bodies in Contact", *J. Appl. Mech.*, **16**(3), 1949, pp. 259–268.
8. Farris, T.N., "Mechanics of Fretting Fatigue Tests of Contacting Dissimilar Elastic Bodies", *STLE Tribol. Trans.*, **35**, 1992, pp. 346–352.
9. Hills, D.A. and Nowell, D., *Mechanics of Fretting Fatigue*, Kluwer Academic Publishers, 1994.
10. Johnson, K.L., *Contact Mechanics*, Cambridge University Press, Cambridge, 1985.
11. Nowell, D.A. and Sackfield, A., *Mechanics of Elastic Contacts*, Butterworth-Heinemann, Oxford, 1993.
12. Rajeev, P. and Farris, T., "Numerical Analysis of Fretting Contacts of Dissimilar Isotropic and Anisotropic Materials", *J. Strain Analysis*, **37**(6), 2002, pp. 503–517.
13. Szolwinski, M.P. and Farris, T.N., "Mechanics of Fretting Fatigue Crack Formation", *Wear*, **198**, 1996, pp. 193–107.
14. Westergaard, H.M., "Bearing Pressures and Cracks", *Journal of Applied Mechanics*, June, 1939, pp. A49–A53.
15. Filon, L.N.G., "On an Approximate Solution for the Bending of a Beam of Rectangular Cross-Section under any System of Load, with Special Reference to Points of Concentrated or Discontinuous Loading", *Philosophical Transactions*, **201**, 1903, pp. 63–155.
16. Sneddon, I.N. (1951), *Fourier Transforms*, McGraw-Hill, New York, 1951.
17. Bentall, R.H. and Johnson, K.L., "An Elastic Strip in Plane Rolling Contact", *Int J. Mech. Sci.*, **10**, 1968, pp. 637–663.

Appendix G*
Experimental and Analytical Simulation of FOD*

Jeffrey Calcaterra

INTRODUCTION

Foreign Object Damage (FOD), as described in Chapter 7, is one of the most difficult problems facing designers and maintainers of modern gas turbine engines. One of the main reasons for the difficulty is the uncertainty associated with FOD events. To simulate and model, an FOD event and the resulting damage requires replicating, analytically or numerically, the results of impacts of objects onto structural components or specimens that represent structural component materials and geometries. This, in turn, requires detailed knowledge of the event that actually took place. In most cases, the evidence after an FOD field event is the damaged component. The event itself is surmised from the inspection of the damage and comparing it with damage produced under controlled simulated conditions, even though what is being simulated is not completely known. The uncertainties about FOD events center around the wide variety of hard-body FOD sources, ranging from very small impactors such as sand and small rocks, up to large impactors such as tools and bolts. Further, similar types of impactors can cause a wide range of damage. They can impact the leading edge, trailing edge, or somewhere on the body of the blade. They can also dent, crater, nick, or tear the blade. Not only does FOD cause a wide range of damage sizes, but even similarly shaped damage can cause significantly different post-impact responses. An example of this is shown in Figure G.1. In this figure, laboratory specimens are shown that were damaged under carefully controlled conditions. The specimens had the same geometry, both were impacted at the same location using 1 mm glass spheres at a velocity of 300 m/s and the resulting damage was geometrically similar.

Even more disparate results can be seen in Figure G.2 where nominally identical impacts under laboratory conditions resulted in different damage mechanisms. Both of these specimens were impacted with 1.0-mm-diameter glass spheres. In one case (Figure G.2a), the material was deformed while in the second case (Figure G.2b), the impact caused chipping and what the authors [2] designate as “loss of material” for obvious reasons.

Despite attempts to make the damage on both of these sets of specimens identical, the residual fatigue strengths of these specimens were widely disparate. The uncertainty in

* This document was prepared by Dr. Jeffrey Calcaterra of the US Air Force Research Laboratory, Materials Directorate and is based primarily on a document originally prepared for NATO RTO [1].

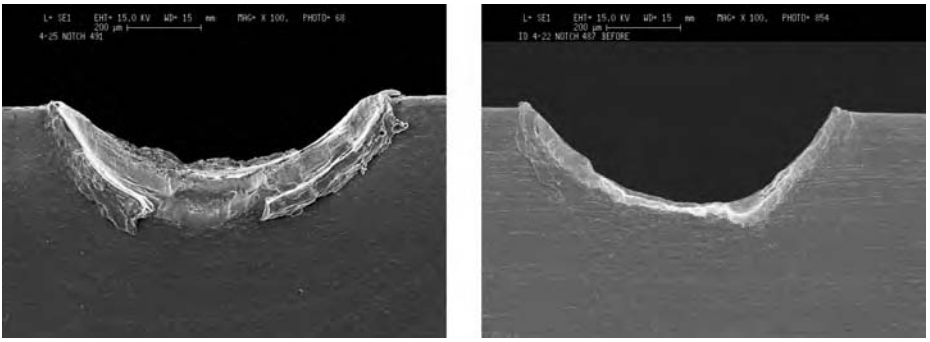


Figure G.1. Comparison of impact surfaces on simulated airfoil leading edges from 1 mm glass spheres at a velocity of 300 m/s.

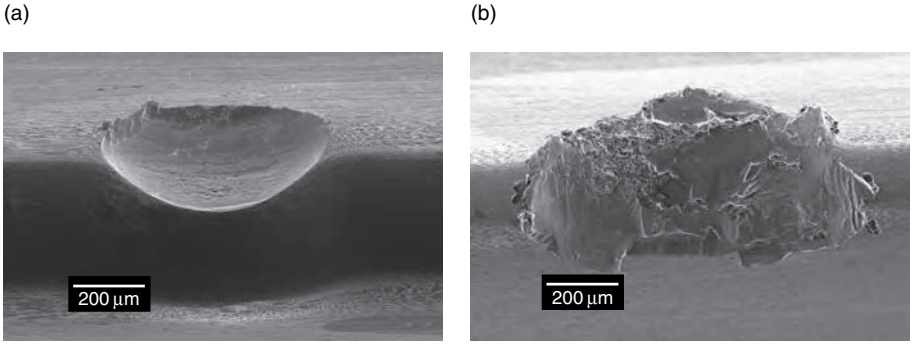


Figure G.2. Head-on view of a 30° ballistic impact FOD site for a 0.38-mm leading edge radius sample exhibiting (a) little or no loss of material and (b) a larger loss of materials.

the laboratory is only magnified in service, where the FOD impactor can be sand, rocks, pieces of a carrier deck, etc., and can strike the blade at a wide range of impact angles and velocities. In short, there is not one typical type of FOD.

The purpose of this appendix is to describe experimental and analytical simulation methods for the prediction and modeling of FOD. It sets out to describe the procedures that can be used to measure and predict the effects of FOD and gives current state-of-the-art examples of techniques and methodologies that are in use and/or are being developed.

Because of the uncertainty associated with FOD, simulating typical cases in order to develop design methodologies poses a significant challenge. The first step necessary to develop an FOD simulation method is to survey field experience and determine which types of impacts account for the most FOD occurrences. The second step is to determine how to best simulate these impacts. This step includes both numerical and experimental methods. The final step is to develop life prediction methodologies that account for

the relevant impact parameters and provide the most accurate prediction of post-impact capability. The sections of this appendix mirror these steps.

CHARACTERIZATION OF FIELD EXPERIENCE

Previous studies conducted by the United States Air Force [3] have indicated that there were very few pertinent data available from engine companies concerning the distribution of FOD sizes, shapes, and occurrence rates. As a result, the USAF initiated a field inspection campaign in order to collect such data. The first phase of the study involved inspecting complete fan and compressor modules from a number of engines. The study looked at over 75 stages and included data from approximately 5000 blades [3]. The FOD location relative to the blade span is summarized in Figure G.3.

As an example of the information presented in Figure G.3, approximately 12% of the damage to Stage 14 blades took place between 45 and 55% of the distance from root to tip. For each stage, the majority of the FOD occurs beyond 80% span. As the blade steady stresses are low towards the tip, the effects of centripetal stiffening are expected

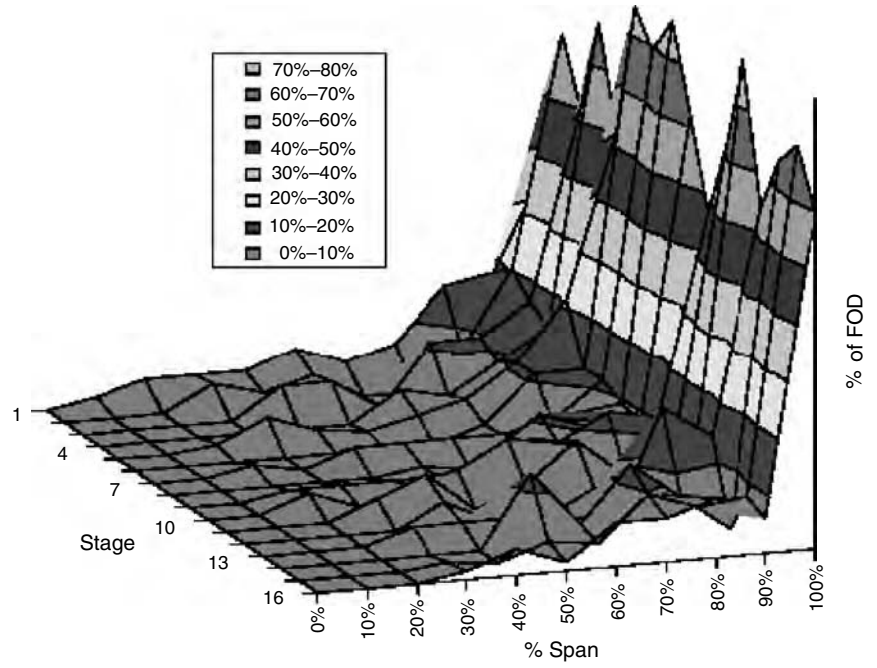


Figure G.3. Percentage of FOD located along the span relative to the blade tip.

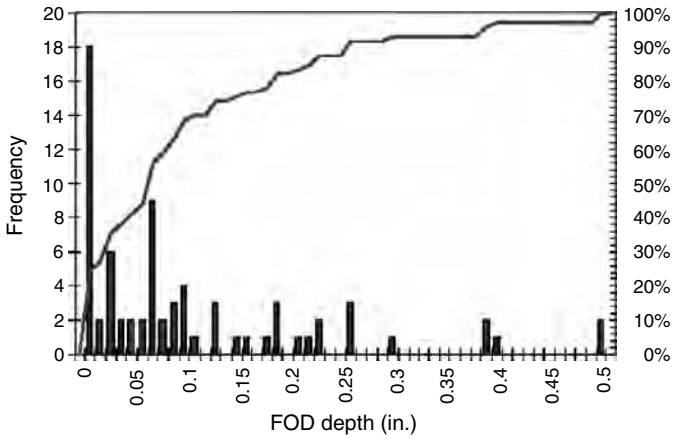


Figure G.4. Histogram and cumulative distribution function for FOD depth. The data shown are measured on a line normal to the leading edge to the deepest part of the damage along the chord of the blade. Viewing angle was not recorded.

to be low, as well as is the ratio of minimum to maximum stress (R) in the vicinity of most FOD events. The cumulative distribution of FOD depths is displayed in Figure G.4. The measured FOD depth ranged from 0.002 in. to 0.5 in. (0.05 to 13 mm) with an average depth of approximately 0.060 in. (1.5 mm). Although this study provided a wealth of information concerning average and extreme FOD values, it collected little data concerning the geometry and damage characterization of in-service FOD.

Due to this shortfall, the USAF initiated a second FOD study. The objective of this effort was to define the range of FOD geometries that could occur in service. To meet this objective, the USAF provided examples of "typical" FOD based on their experience in inspecting and overhauling turbine engines. A total of 51 Ti-8-1-1 blades from either 1st, 2nd or 3rd stage fans from turbojet fighter engines were provided for evaluation. These 51 blades had been identified as having FOD during a previous inspection; of these blades 31 contained a total of 42 discrete FOD sites. The remaining blades were severely damaged (e.g., see Figure G.5) and therefore were not further characterized.

The USAF study found the discrete FOD consisted of dents, tears, and notches, as can be seen by the examples in Figures G.6 through G.9. Damage was primarily to the leading edge of the blades – specifically, 40 leading edge FOD and two trailing edge FOD sites were observed. In two cases, the leading edge damage consisted of FOD that had been previously blended and returned to service. Additional details on the FOD geometry can be found in [3].

In addition to the USAF study, the information from a UK Ministry of Defence (MOD) study on FOD is included here. Examination of several Pegasus fan blades from Harrier aircraft indicates that FOD is only found on the pressure surface (except in the case of



Figure G.5. Examples of severely damaged blades (excluded from study).

stall). Common damage seen on all blades consists of small impact sites mostly smaller than 1 mm diameter. The density and severity of these impact sites increases noticeably from root to tip, which corresponds to the USAF study [3], Figure G.3. Figure G.10 is an example of pressure surface FOD damage. The leading edge is to the right and hence the object would be traveling from right to left and has impacted at an acute angle. It appears that the impact has completely stopped the progress of the particle, although glancing impact craters are also frequently found.

Figure G.11 shows FOD sites observed on a set of fan blades from a Tornado RB199 engine that had experienced major surge due to the FOD. The whole set of blades in the fan each displayed severe damage to the leading edge corner and several have tears and notches further down the blades.

FOD geometry distributions

In order to determine a typical FOD geometry measurements of depth and root radius were made from photographic enlargements (4X to 10X). The distribution of measured FOD depths is shown in Figure G.12. These data are shown along with a larger data set

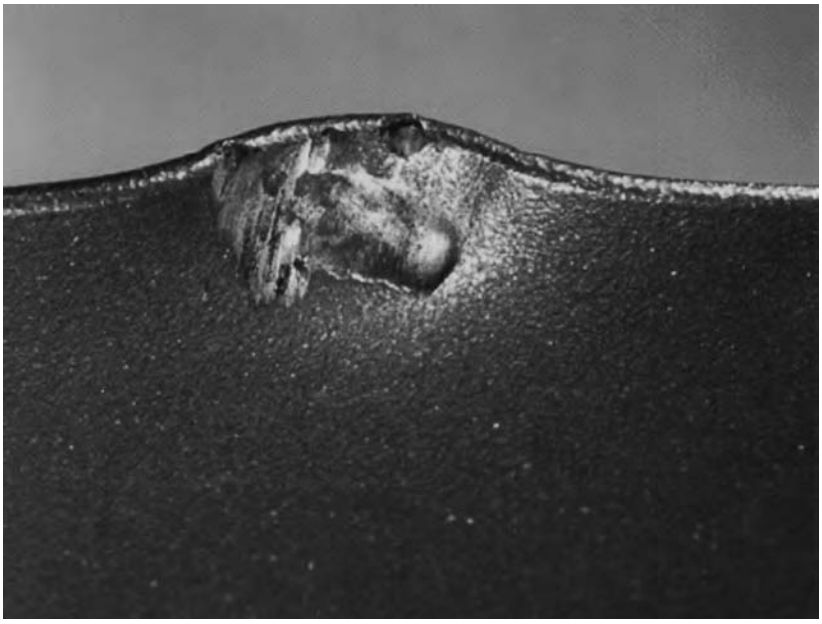


Figure G.6. 0.059 in. dent with no cracking in leading edge of 2nd stage fan blade.

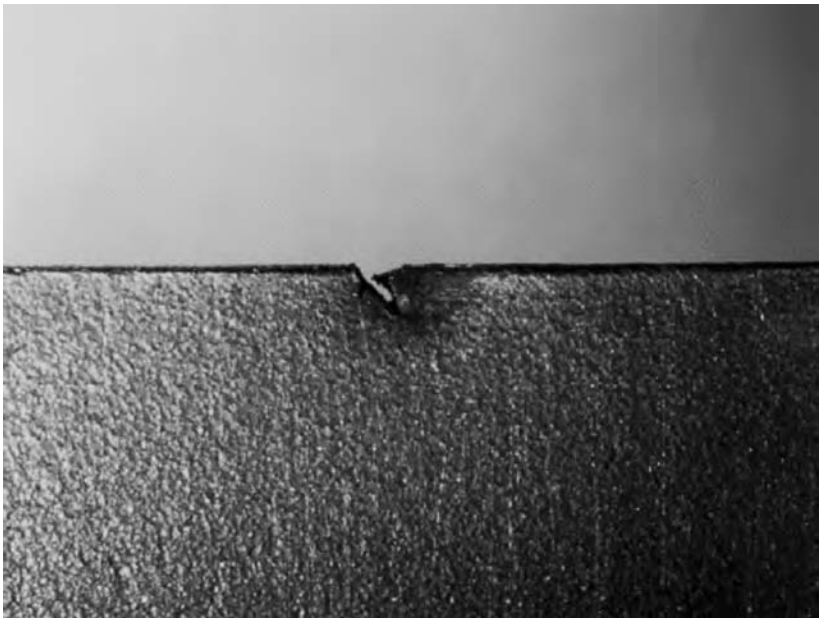


Figure G.7. 0.028 in. tear in 2nd stage fan blade.

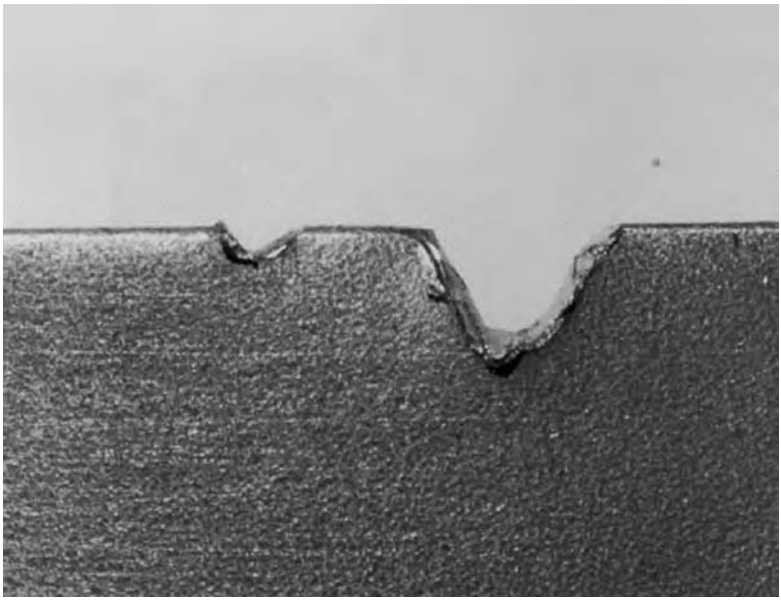


Figure G.8. Two notches in leading edge of 2nd stage fan blade. The smaller notch is 0.015 in. deep while the second is 0.059 in. deep. Microscopic examination of the deformation ridge indicates that impact occurred at an oblique angle.

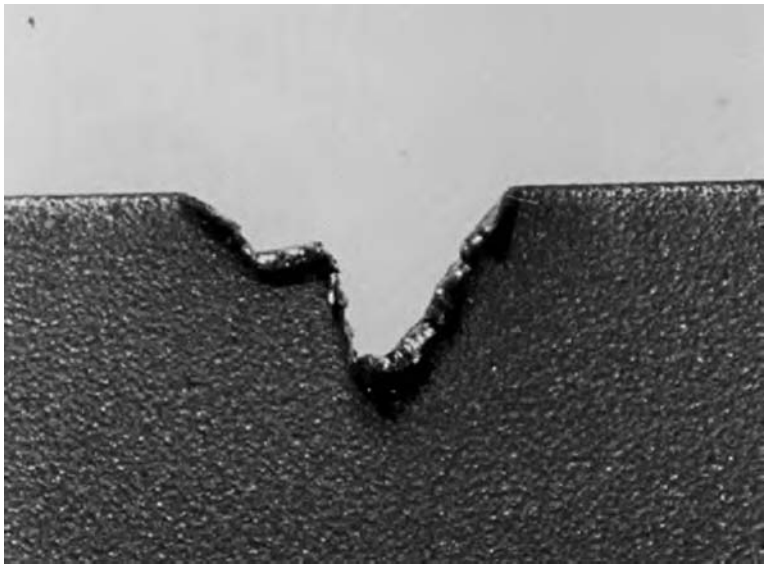


Figure G.9. 0.090 in. deep notch in leading edge of 2nd stage blade. Again microscopic examination of the deformation ridge provides clues about the impact angle.

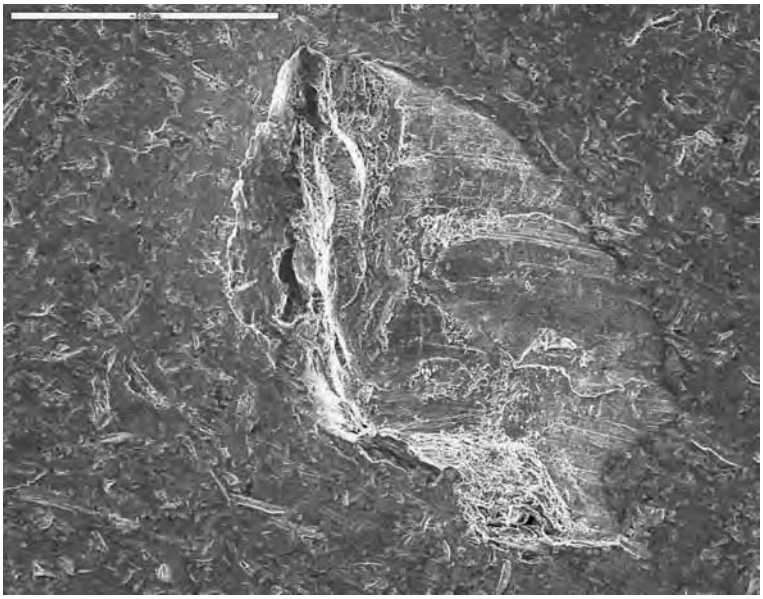


Figure G.10. FOD impact site on Pegasus fan blade.

previously obtained by Pratt and Whitney and the USAF in an extensive field survey of FOD damage [4]. All data in Figure G.12 are from 1st, 2nd, and 3rd stage fan blades of the same engine. As can be seen in Figure G.12 the two distributions are of very similar form, resembling either typical log normal or Weibull probability density functions. These results indicate that the sample population of this small study is representative of the FOD likely to be found in service for low-bypass engine fan blades.

It is important to recognize that FOD depth distributions are fundamentally different from crack size distributions used in classical damage tolerance analyses. The difference is due to the fact that cracks progress in a slow stable fashion throughout the life of the component, whereas FOD of any given depth can be introduced at any time in the component life, regardless of when the last inspection occurred. Thus, in developing an improved HCF design methodology, it appears that FOD depths beyond the blend limits also need to be evaluated to ensure that a blade will survive in operation until the next inspection.

The distribution of measured FOD root radii is shown in Figure G.13. As can be seen, this distribution is relatively uniform in comparison to the FOD depth distribution in Figure G.12. This difference in distribution shape indicates that there is minimal correlation between notch depth and root radius. An overall index of the severity of the FOD can be obtained by combining the measured FOD root radii of Figure G.13 with the FOD depths of Figure G.12 to determine the distribution of elastic stress

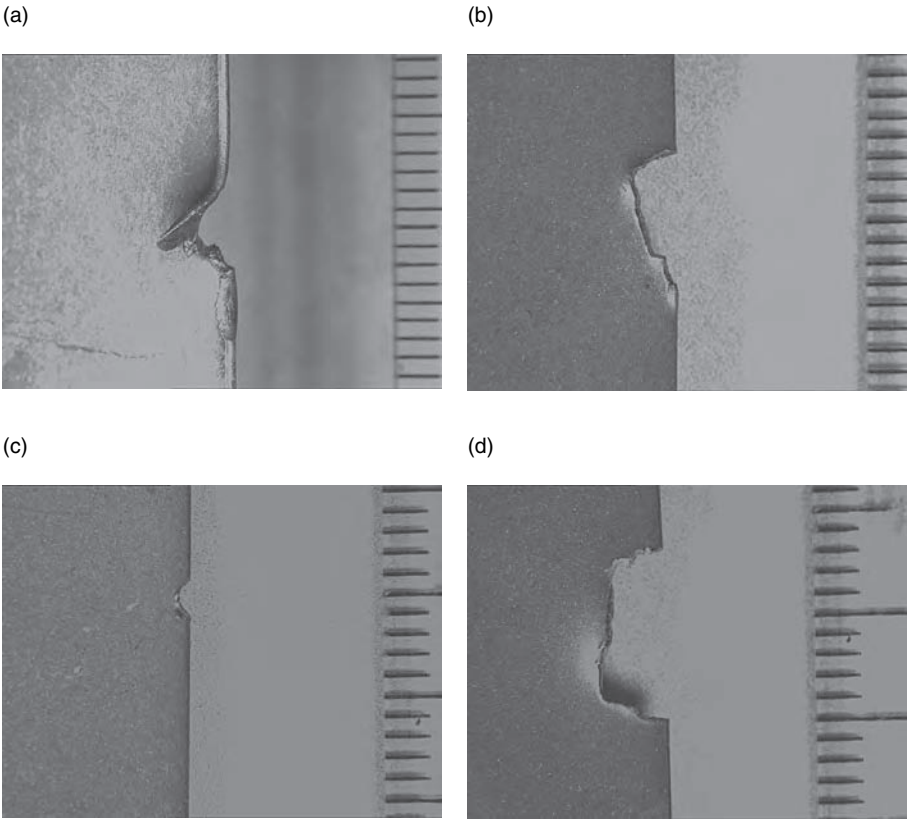


Figure G.11. Damage to RB199 fan blades.

concentration factors, k_t. The distribution of k_t is given in Figure G.14 [5]. The average k_t is about 4; however, values of up to 10 can occur for the more severe FOD notches.

Microscopic features of FOD

Metallographic and fractographic examinations were performed on selected samples to determine the extent of local deformation and the possible existence of cracking. It was found that FOD notches encompass a wide range of microscopic features. The impact event leading to the damage site often resulted in non-propagating cracks, as shown in Figure G.15. Non-propagating cracks have been found in laboratory experiments and can have surprisingly little effect on the path of final failure [2, 6].

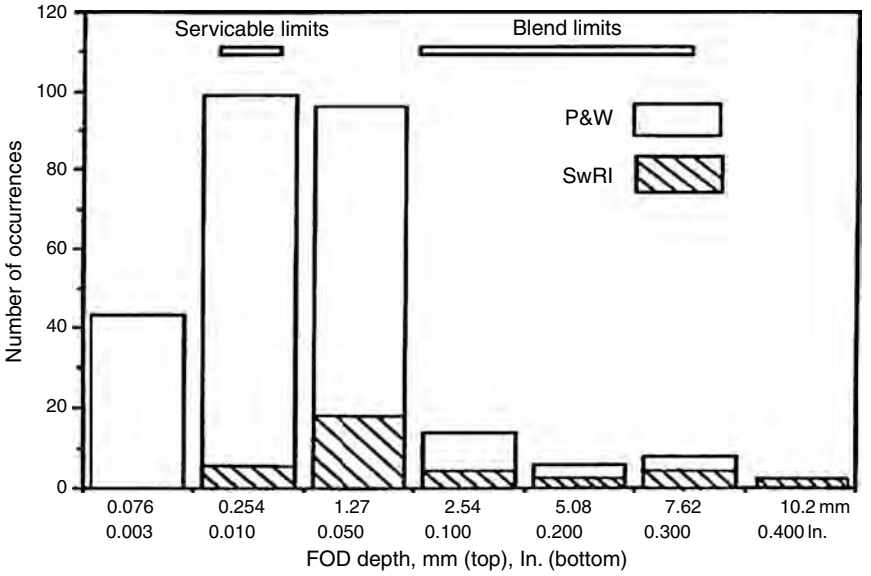


Figure G.12. Distribution of service-induced FOD from two different surveys. Southwest Research Institute (SwRI) conducted study under a USAF contract.

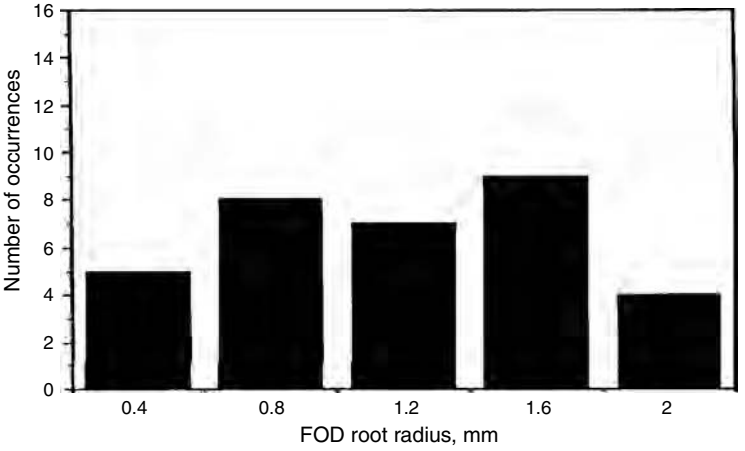


Figure G.13. Distribution of FOD notch root radii.

In addition to non-propagating cracks, several notches were found with extensive local deformation but no cracking. Several damage sites were found with little localized damage and some were impacted with enough energy to cause brittle failure and generate debris. In short, post-event inspection revealed that there had been a wide range of impact energies.

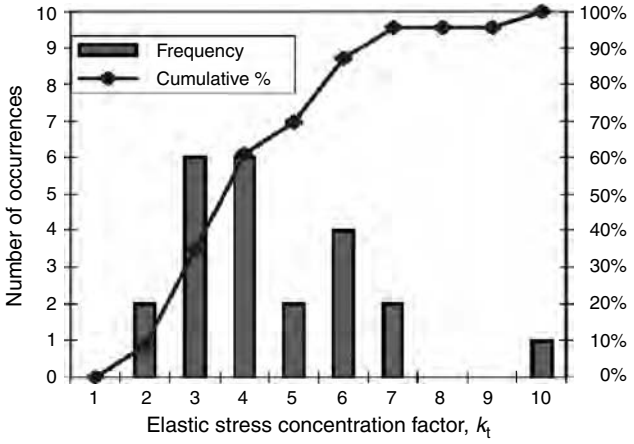


Figure G.14. Histogram and cumulative distribution function for FOD notch k_t.

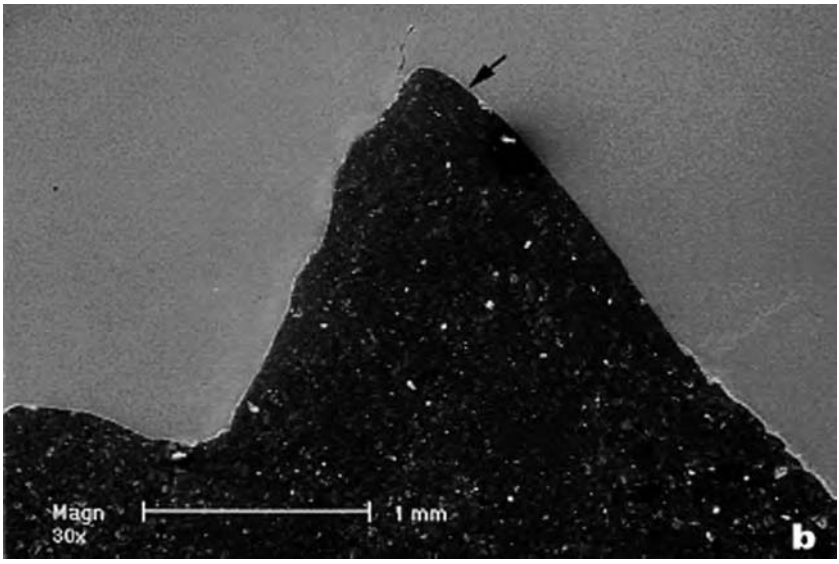


Figure G.15. Micrograph showing FOD site with non-propagating crack.

The biggest benefit of the microscopic investigation was the identification of impact surface details that indicated the angle of incidence. These features indicated that the impactor tended to strike the blade at angles of 30° to 60° relative to the blade leading edge centerline, which correlates well with airflow and blade dynamics, as shown in Figure G.16.

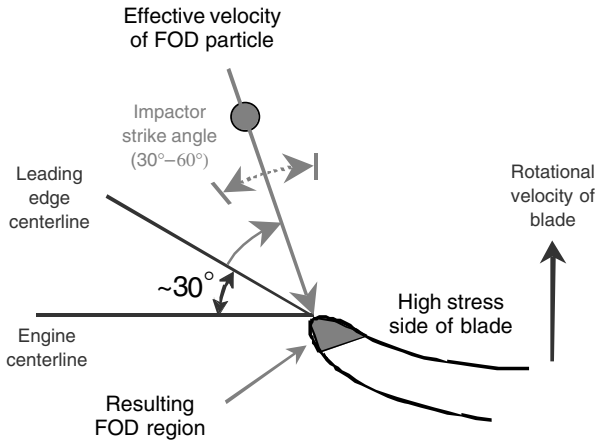


Figure G.16. Illustration of typical FOD impact angles in modern gas turbine engines.

Complex airfoil shapes and irregular impactors make it difficult to define accurately the point at which the damage begins. In controlled testing at Qineti$Q$, it was originally observed that the actual damage size was significantly smaller than was expected. Initially, this was attributed to the deflection of the impactor on striking the blade, thus creating a smaller notch than expected. However, it was observed that the basic method of measuring the notch depth did not always give an accurate representation of the notch depth; large notches need to be viewed from different angles than small notches to measure through the deepest part of the notch. To illustrate this, damage sites on titanium alloy specimens were measured by viewing at a range of angles. Figure G.17 shows the path that the impactor takes in relation to the viewing angles and shows the apparent depth at these angles; the zero degree datum is perpendicular to the engine centerline.

It can be seen that the small notches appear largest when viewed at an angle of between $-10°$ and $0°$ from the datum. This indicates that the notch is in almost the same direction as the incident projectile. However, as the damage gets larger, the angle of the notch changes, reflecting the fact that the projectile has been deflected through a larger angle.

The conclusion to be drawn from this graph is that there is no single viewing angle that would give a representative depth for all damage sizes. Indeed, it may be that trying to take a measurement of the silhouette is too simple a method to accurately characterize the notch. It has been suggested that measurements of damage should be made on both sides of the blade. This would enable more consistent measurements for the occasions where material has scabbed off the back.

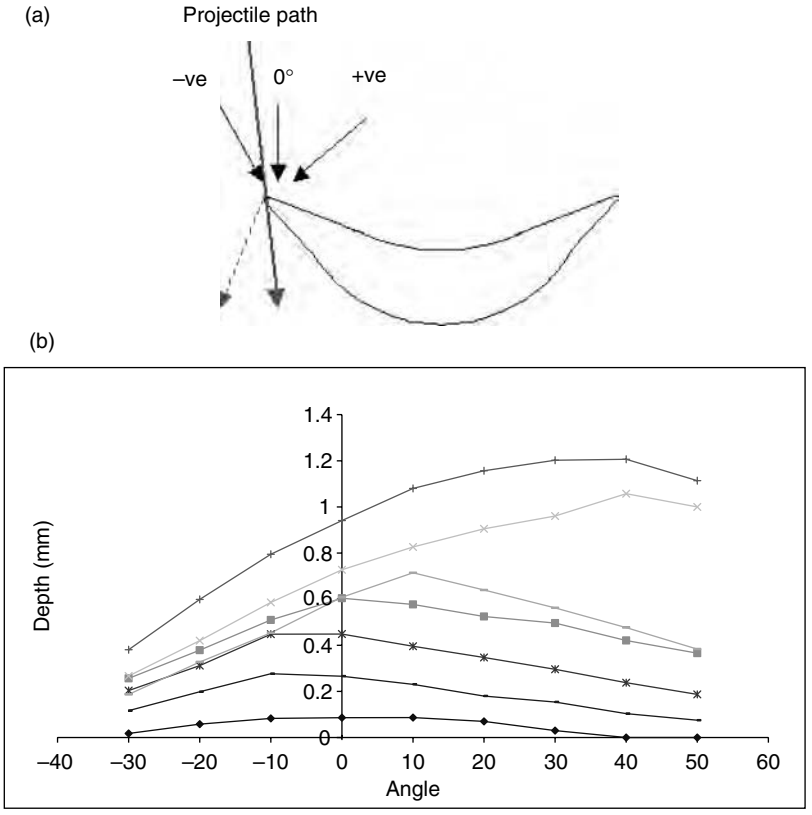


Figure G.17. Path of projectile and viewing angles.

EXPERIMENTAL FOD SIMULATION

The FOD problem is extremely complex due to a large number of factors including the random nature of ingested foreign objects, the complex geometries of turbine engine components and the complicated stress states in gas turbine airfoils, particularly with respect to vibratory loading. The typical blade in a large gas turbine engine is a complex airfoil with variable camber and twist. The stresses at the leading edge are the result of complex loads and moments that vary along the length of the blade due to inertial forces, pressure loads and, geometry variations. Centrifugal and gas loads are the dominant LCF loads that control the mean stresses, while vibratory loads produce the HCF alternating stresses. The mean stresses are significantly larger than the alternating stresses in the root and mid-section regions, whereas the tip regions may contain relatively higher vibratory stresses and lower mean stresses. Therefore, the stress ratio, R, may range from $R = 0.8$

(tension–tension) to $R = -\infty$ (fully reversed tension-compression or compression only) at various regions throughout the blade. The accurate simulation of FOD on blades and vanes is also very difficult due to compromises between effectiveness and cost of data. The type and quality of information that is required for analysis, as described in the following sections, determine this cost.

Impact simulation

Two concerns must be addressed in order to simulate FOD events as accurately as possible. These are specimen design and the process of inducing the FOD damage. During the development of the USAF's HCF program, six different methods for imparting damage were identified. These are:

- notch machining
- shear chisel application
- quasi-static indentation
- solenoid gun usage
- light gas gun impact
- engine debris ingestion.

These methods are nominally listed in perceived order of increasing difficultly.

Notch machining

One of the most common methods for simulating damage is simply machining a notch into the specimen. The machining process typically results in a notch with a very controlled geometry, such as that shown in Figure G.18.

Repeatability, control, and low cost are the primary benefits of this process. However, machining a notch does not produce damage that is representative of FOD. The difference is primarily caused by differences in residual stresses between the machining process and the impact event. Secondary differences include a lack of changes in the microstructure of the material and a lack of impact-induced cracking. Therefore, if a study of notch geometry variance or comparison of the relative merits of different blade designs is desired, machining can be used, provided that the above limitations are taken into account in the final analysis. Studies performed by the USAF indicate that there is little correlation between notch sizes and FOD sizes. Therefore, blade geometry cannot be evaluated by simply machining a notch that is bigger or smaller than an FOD notch size by some factor. Finally, machined notches offer no insight into the impact resistance of a given blade design.

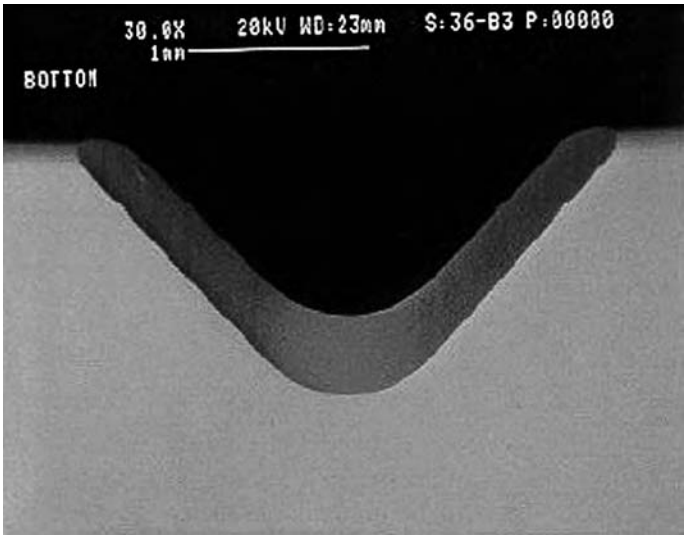


Figure G.18. Micrograph of a machined notch in a simulated airfoil.

Shear chisel, quasi-static impact and solenoid gun

Shear chisel, quasi-static impact and solenoid gun impact methods all have similar benefits and drawbacks to each other. Imparting damage via a shear chisel involves attaching an impactor to a pendulum, raising the arm to a predetermined height, and letting gravity accelerate the impactor until it contacts the specimen. A solenoid gun uses a similar method except that an electric coil is used to accelerate the impactor which is attached to the end of a rod. The impactor can be accelerated with a given energy or pushed into the specimen until the notch reaches a predetermined depth.

A quasi-static impact typically involves placing the specimen in front of the impactor and driving the impactor into a predetermined depth using hydraulic, mechanical, or both electrical actuation. The speed of the impact in this case is much smaller than both the solenoid gun and the shear chisel. In each of these methods, the shape of the impactor can be selected to deliver a notch shape of a given configuration. The energy or depth of the impact can be accurately controlled and the location of the impact is known beforehand. Finally, once machining has been set up to handle a specimen of a given geometry, several specimens can be damaged in quick succession, resulting in an affordable process. Unlike machining a notch, significant residual stresses can be imparted with any of these three methods. Additionally, material removal can be caused by the dynamics of the impact. These characteristics are much more like actual FOD than the notch produced by machining. An example of a notch caused by solenoid gun impact is shown in Figure G.19.

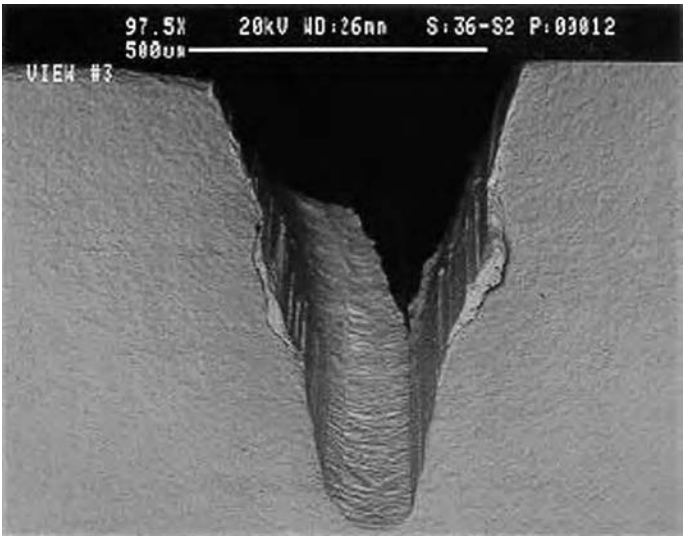


Figure G.19. Indentation from solenoid gun. Leading edge radius = 0.005 in. (0.13 mm), indentor radius = 0.005 in. (0.13 mm), impact angle 30°, high damage level.

The solenoid gun has good control and repeatability although it is not as good as notch machining. Since the process can be used to generate damage in a large number of specimens very rapidly, it has the additional benefits of quick turnaround time and low cost. The combination of good control, low cost and rapid turnarounds make the solenoid gun ideal for generating large amounts of data. However, like a machined notch, the damage produced by solenoid gun is not an accurate simulation of ballistic FOD damage. The solenoid gun produces some residual stress due to impact, but the amount of stress and cold work are much different than those created by typical FOD. Despite these shortcomings, the solenoid gun can be used to impart a given amount of energy into a blade and can, therefore, be used to evaluate the relative benefits of different blade designs.

Light gas gun

Ballistic impact from a light gas gun is the most accurate laboratory method for simulating the damage caused to an engine blade from foreign object ingestion. A standard light gas gun uses a compressed gas to accelerate the projectile to a speed that replicates the assumed speed of foreign objects in the gas path. Varying the pressure of the compressed gas regulates the velocity of the projectile. The caliber of the projectile launched by a light gas gun is not governed by the caliber of the gun barrel. Instead, most gas guns use a sabot to hold the projectile. This sabot allows the use of different projectile geometries,

such as spheres and cubes, and materials, such as glass or steel. In addition, the seating of the impactor in the sabot in a keyed barrel can be used to orient the impact event, such as when using a cube impacting along its side. The velocity of the impact is easily determined experimentally using photodiodes or other optical instrumentation close to the target end of the barrel. The target is held in a vice, which can be rotated to achieve the desired orientation.

The repeatability of gas gun shots is illustrated in Figures G.20 and G.21, with quantified results in Tables G.1 and G.2. The targets used were mild steel with a cross section that tapered towards each edge, and the projectiles were hardened steel cubes. The targets were oriented such that the path of the projectile was at 135° to the front face of the target. Two types of shots are illustrated; one type has the cube oriented point first, while



Figure G.20. Level 1 repeat shots.

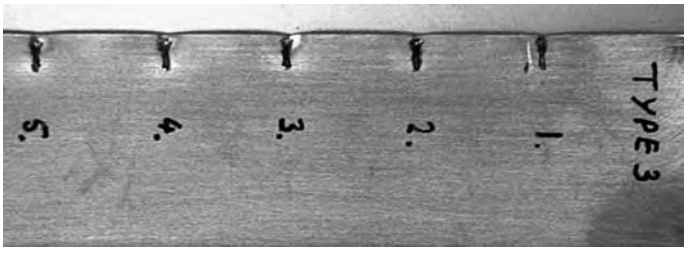


Figure G.21. Level 3 repeat shots.

Table G.1. Level 1 summary of shots

Shot	*Velocity* (m/s)	*Damage depth* (mm)
1	189	0.98
2	186	0.60
3	189	0.69
4	186	0.79
5	190	0.69

Table G.2. Level 2 summary of shots

Shot	*Velocity* (m/s)	*Distance from edge to* (mm)		
		Start of damage	*Deepest point*	*Furthest damage*
1	187	0.20	0.63	3.93
2	190	0.40	0.94	4.18
3	186	0.22	0.72	3.70
4	187	0.46	1.00	3.96
5	185	0.60	1.22	4.38

the other is oriented edge first. Five impacts were done at each damage level and the size of each measured. The use of cubes has been found to be one of the better ways of reproducing damage that is typical of that observed in the field for certain engines and operating conditions. For this reason, extensive FOD simulations have been carried out with a cube projectile to produce different levels of damage. A 3-mm-size cube has been found to be the one that produces typical damage.

Damage Level 1

This type of damage nominally produces a triangular notch 0.75 mm deep by firing the cube corner first. Figure G.20 shows the target with the five shots. The details of the five shots are summarized in Table G.1. The damage depth was measured to the base of the notch silhouette with the specimen in a horizontal position.

Damage level 2

As can be seen from Figure G.21, edge-on impact creates a dent that is entirely on the surface of the target. The cube is fired with an edge facing forward, but because the target is positioned at an angle, the cube hits point first and rotates to impact along its edge. This is why one end of the dent appears deeper than the other. Figure G.21 shows the five shots performed at this damage level. Figure G.22 shows the front of an impact and highlights the details of damage summarized in Table G.2.

Light gas guns require a significant amount of expertise to obtain repeatability and control of the damage. There may be enough variation in nominally identical damage sites to affect post-damage mechanical properties significantly. This is illustrated by the data in Tables G.1 and G.2. In some of these shots, the location of damage may vary by up to 0.6 mm, despite the careful controls on test parameters. A micrograph of a typical light gas gun impact site on a simulated airfoil is shown in Figure G.23.

The accuracy of the light gas gun impact method has been confirmed using extensive material analysis. Five impact sites in a Ti-6Al-4V leading edge test sample were metallographically investigated. Various diameter steel balls shot against the leading edge at



Figure G.22. Level 2 front surface.

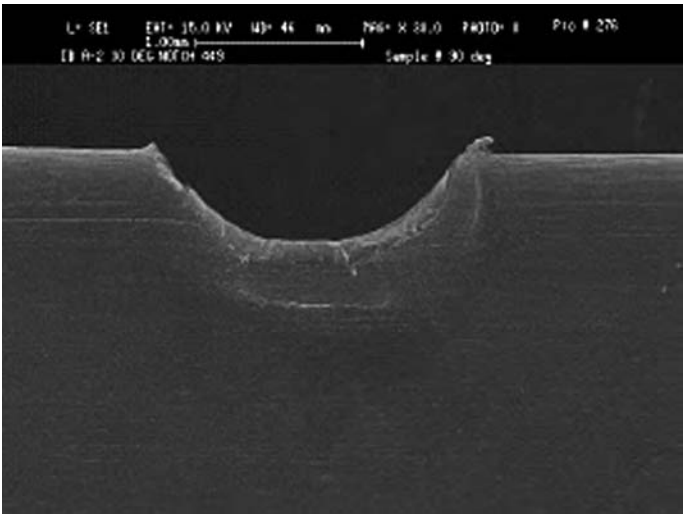


Figure G.23. Simulated FOD using light gas gun impact.

several velocities created the impact sites. The microstructural changes, aside from the scale of damage, were consistent for all specimens. The primary microstructural features due to impact damage were a compressed microstructural zone and the formation of adiabatic shear bands. The presence of adiabatic shear bands is an important indication that ballistic FOD simulation accurately represents the high rate deformation process seen during actual FOD. Adiabatic shear bands form only during high rate deformation by effectively melting and re-solidifying the metal, resulting in a different grain structure.

The presence of shear bands around the impact of a spherical projectile has been noted by some studies [7, 8]. Roder et al. [8] examined the damage caused by the impact of hardened steel spheres fired at 309 m/s at a flat plate and mapped the distribution of shear

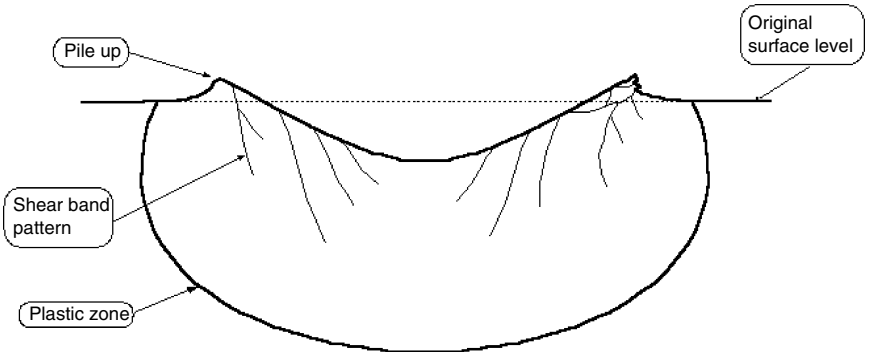


Figure G.24. Shear band pattern beneath impact crater [8].

bands. As can be seen from Figure G.24, their orientation is such that they could increase the susceptibility to fatigue crack growth.

Figure G.25 is a back-scattered electron image showing an area of the edge of a V-notch produced by firing a cube projectile at Ti-6AL-4V plate. The damage strongly resembles that seen on RB199 fan blades displaying shear bands with evidence of

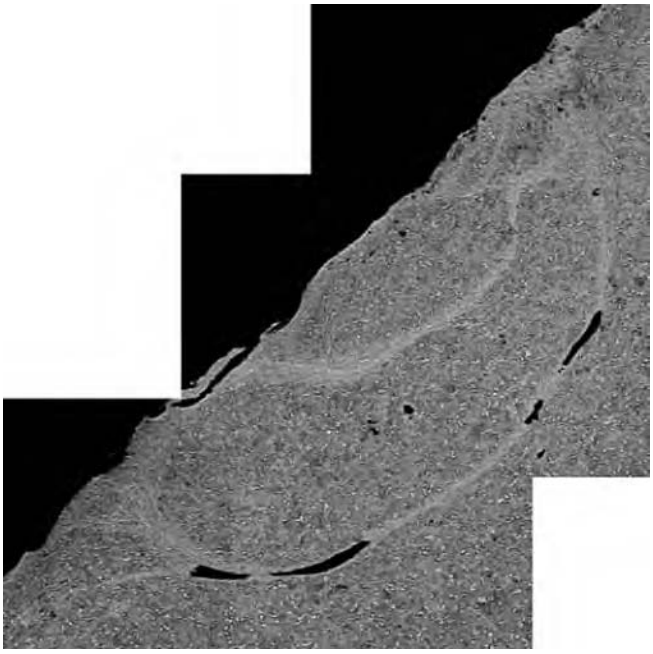


Figure G.25. Edge of ballistic damage on plate.

void opening. The microstructure is similar to the schematic representation shown on Figure G.24.

The final type of simulation is engine debris ingestion. This method is mentioned here only for the sake of completeness. Engine debris ingestion is prohibitively expensive and of little scientific value. However, it is the only method that accurately simulates the effect of FOD on an entire engine.

Specimen design

Once the appropriate impact procedure is selected, the next step is to determine which specimen geometry will be used. In the process of specimen design, it is necessary to determine what level of refinement is necessary in order to best capture the behavior of interest. For example, in the case of High Cycle Fatigue (HCF) design, it may only be of interest to know whether or not a crack will initiate from the FOD damage site. This is based on the philosophy that cycles accumulate so quickly under HCF loading conditions that cycle counting is impractical. In this case, the specimen must be designed so that stresses at the specimen notch tip are similar to those on the leading edge area of interest. As mentioned previously, these stresses are dominated by centripetal forces and can therefore be adequately simulated by standard uniaxial testing with any number of specimen geometries.

In order to capture experimentally the effect of FOD on a specific airfoil design, it is necessary to damage and test that particular configuration. Airfoil-based FOD evaluation involves shaker table or siren tests with simulated FOD. Shaker tables involve attaching a simulated blade specimen using to a high frequency actuator ($\sim$400 to 2000 Hz) in a cantilever arrangement. Siren tests rigidly fix the base of the blade and a "siren" blasts air over the free end. This allows the blade to resonate at many of its natural frequencies, which can enable testing up to 20 kHz. However, these tests are limited to fully reversed loadings ($R = -1$) and require full-scale blades in order to capture the effect of blade stress distributions. Additionally, these tables are unable to simulate the centrifugal force present in rotating turbo machinery. The obvious benefit of this type of test is the inherent applicability to the geometry that is being tested. Unfortunately, this type of testing is typically very costly, requires specialized equipment, and may not be applicable to arbitrary geometries.

Recent work sponsored by the USAF has developed improved test methods to investigate the behavior and life of FOD'd fan blades. These test methods are intended to supplement the siren tests and provide a more rigorous evaluation of FOD effects. In addition, these test methods will enable the designer to evaluate FOD effects over the full range of loading and leading edge geometries without fabricating full-scale blades. A cornerstone of this effort is the ability to accurately simulate blade stresses and FOD damage in the laboratory.

The typical fan blade in a large gas turbine engine is a complex airfoil with variable camber and twist as shown in Figure G.26.

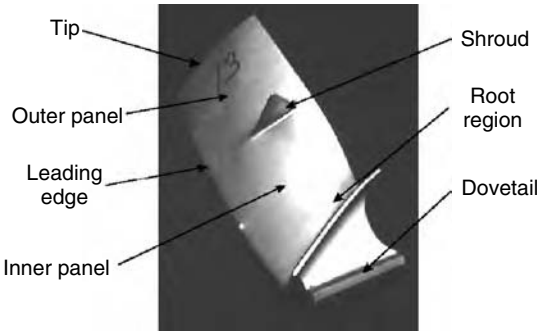


Figure G.26. Typical fan blade.

In many cases, larger blades contain mid-span shrouds, as shown in Figure G.26, to enhance the stability of the blade. The stresses at the leading edge during engine operation are the result of complex loads and moments that vary along the length of the blade due to inertial forces, pressure loads and geometry variations. The dominant LCF loads that control the mean stresses are those derived from the centrifugal and gas loads on the blade. The dominant HCF loading is typically caused by the vibration mode near or in the engine running range. As we move along the length of the blade from the root region to the tip region, the ratio of the LCF loadings and HCF loadings varies. In the root and mid-section regions, the leading edges are subject to relatively large mean stresses that significantly decrease towards the tip regions. Therefore, stress-ratio (R) effects ranging from $R = 0.8$ (tension–tension) to $R = -1$ (fully reversed tension – compression) need to be considered. The leading edge regions also see stress gradients due to the camber of the blade, and these gradients may be critical to accurately simulating blade stresses in a test specimen.

Figure G.27 presents a normalized stress distribution from a vibratory analysis of a typical fan blade. Due to the change in camber along the length of this blade, the critical stresses are located in the mid-section or lower panel of the blade. Figure G.28 contains a detailed contour plot of the stresses through the highest intensity cross section. Notice the relatively large stress gradient within the first 6.4 mm (0.25 in.) of the leading edge.

In recent years, a test specimen that can simulate leading edge stresses has been designed under a USAF contract and is shown in Figure G.29. The specimen and its use are discussed in detail in Chapter 7.

The artificial leading edges are far from the neutral axis so the leading edges will be highly stressed. This geometry was selected because (a) it could be easily cut from flat forgings, (b) it could have variable leading edge geometries, (c) it could be rather easily loaded to various stress ratios or with LCF–HCF mission cycles, and (d) the stress gradient in the leading edge could be adjusted by varying the overall height of the specimen. The

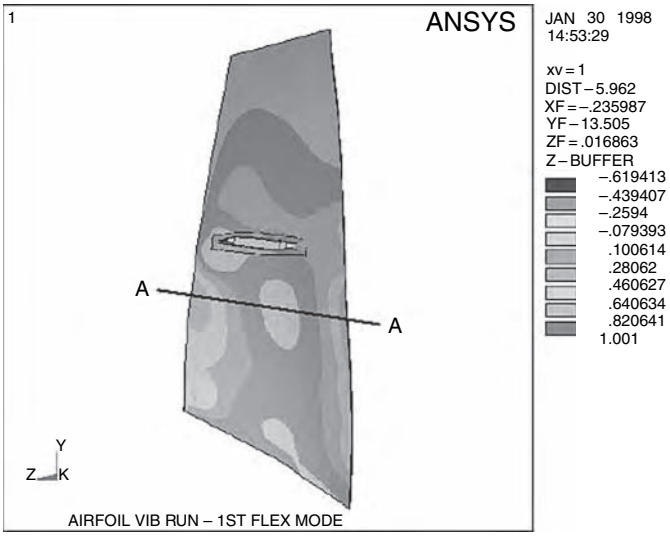


Figure G.27. Normalized stress distribution across typical fan blade.

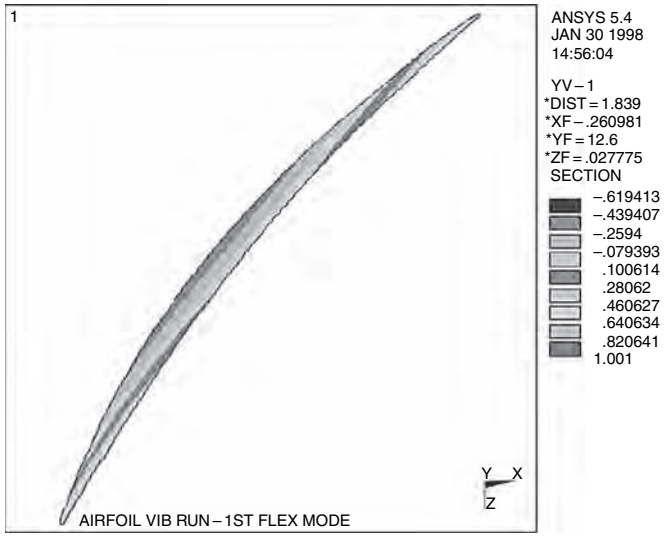


Figure G.28. Stress distribution across Section A-A.

specimen is loaded in four-point bending which enables uniform bending stresses in the loading span section.

An elastic stress analysis of this specimen was performed to compare the leading edge stresses of the blade to the specimen. Figure G.30 contains contour plots comparing these

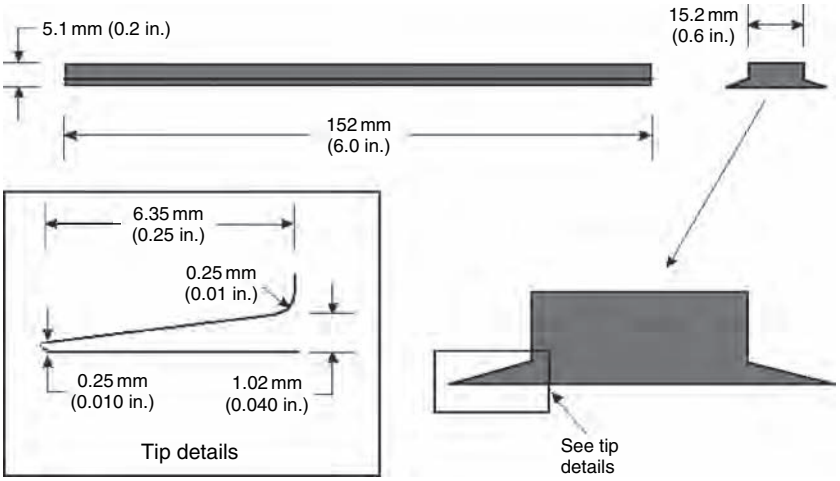


Figure G.29. Diagram of simulated leading edge specimen.

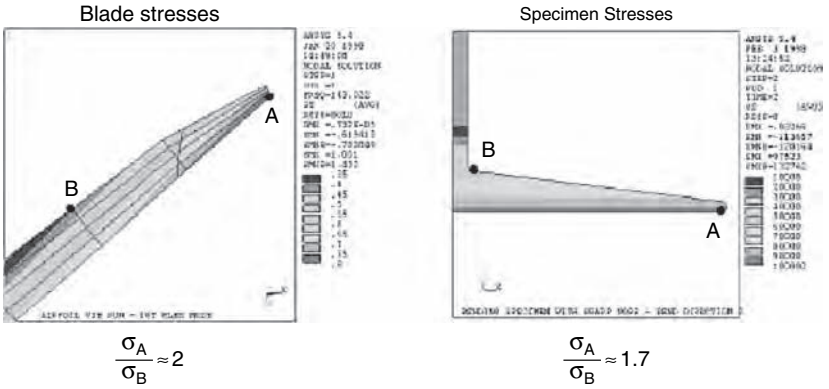


Figure G.30. Comparison of calculated blade and specimen stresses.

stresses. Notice the stress gradients from points A to B are very similar. If desired, the gradients could have matched exactly by reducing the overall 5.1 mm (0.2 in.) height of the specimen.

Due to the geometry of the specimen, the location of the neutral axis is shifted toward the bottom of specimen that contains the simulated leading edge. As a result, the highest magnitude stress actually occurs on the top of the specimen since it is farther from the neutral axis; however, the stresses on the top of the specimen are compressive which are not as damaging in fatigue as tension. Peak tensile stresses are located at the simulated

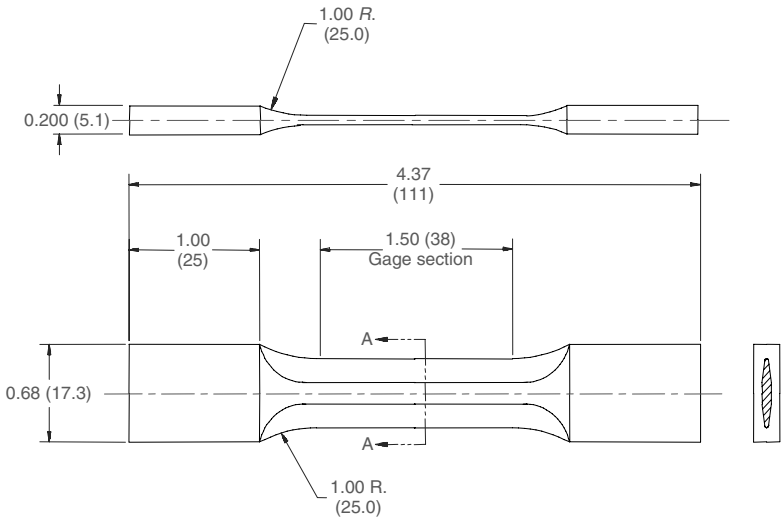


Figure G.31. Overview of diamond cross-section tension (DCT) specimen.

leading edge and the stress concentration associated with the FOD damage should ensure failures in the FOD location.

Having gone down in complexity from full airfoils to laboratory specimens in four point bending, the last specimen type to discuss is a simple uniaxial specimen. This category of specimens is inclusive of all geometries where the application of a load along the major axis does not result in bending or equivalent stress gradients. For applicability to airfoil geometries, FOD testing has been performed on specimens with a diamond cross section as shown in Figure G.31. The use of this geometry is discussed in Chapter 7.

NUMERICAL FOD SIMULATION

This section describes the basic methodology that is required in order to develop a method for predicting the damage to a blade or vane from the impact of a foreign object. The examples used are based on work that has been carried out by the USAF. While the basic methodology for numerical simulation should remain the same, new tools and methods will inevitably be developed, as better technology, such as improved material models, becomes available. The flaws inherent in the selected examples are to be viewed by the reader as pitfalls that should be avoided and not as unchanging shortcomings of the analysis method.

Researchers worldwide have studied numerous variables related to FOD impact damage and residual stress distribution [2, 6–10]. In order to model damage accurately, it

is necessary to use an explicit finite element code or a particle-in-cell code that can capture the peculiarities of dynamic material behavior and response. All of the examples used in this appendix were computed using the explicit finite element (hydrocode) code MSC/DYTRAN [11], though there are several other codes that will also model dynamic impact behavior.

Characteristic materials, airfoil leading edge geometries and impact conditions representing gas turbine compressor blades were selected for this study. Titanium (Ti-6Al-4V) specimens with representative leading edge radii were impacted with steel balls at angles and velocities seen by typical compressor airfoils. A parametric analysis with varying impactor size, speed, angle, and specimen leading edge radii was conducted.

Finite element models were generated using an eight-noded reduced integration-explicit Lagrangian brick element throughout the mesh for both the specimen and impacting ball. Tetrahedral and Penta elements were avoided in the mesh by utilization of an interface in the transition region that acts as a contact surface and is used to transfer loads across surfaces with dissimilar meshes. Because the reduced integration element has only one integration point at the centroid of the element, hourglass controls were used to eliminate zero energy modes or "hourglassing." The density of the mesh was weighted towards the impact site to better catch the contact between the ball and the specimen and to better predict the stress field. Figure G.32 shows a representative finite element mesh for a sharp-edged specimen being impacted at 30° with a 0.079 in. (2 mm) diameter ball. Different specimen model meshes were utilized near the impact site for each diameter ball to keep the number of elements across the length in the impact region identical for each diameter ball.

Ballistic events introduce high strain rates and titanium has been shown to be highly rate sensitive. Therefore, a strain-rate–dependent constitutive material model must be used for accurate analysis. Selected models should allow for the modeling of nonlinear material behavior with appropriate allowances for plasticity, material flow, and hardening. For ballistic impact simulation, appropriate strain rates can vary from $10^{-4}\,\text{sec}^{-1}$ to $10^{6}\,\text{sec}^{-1}$. This creates attendant problems such as how can material properties at these strain rates be measured accurately.

One shortcoming of most explicit finite element model is their material failure criteria. For example, DYTRAN allows material failure, but the failure routines are not sophisticated and cannot accurately model crack propagation or the generation of new free surfaces. The lack of surface creation features in this package means that caveats must be placed on predictions of failure. For the example in this document, a basic material failure model based on the von Mises yield function was selected for evaluation. This chosen material model allows for failure of the element by definition of an effective plastic strain at failure. Once the failure limit is reached, the element loses all its strength. The single effective plastic strain variable utilized does not distinguish between different modes, and once the limit is reached regardless if it is tension, compression, shear, or

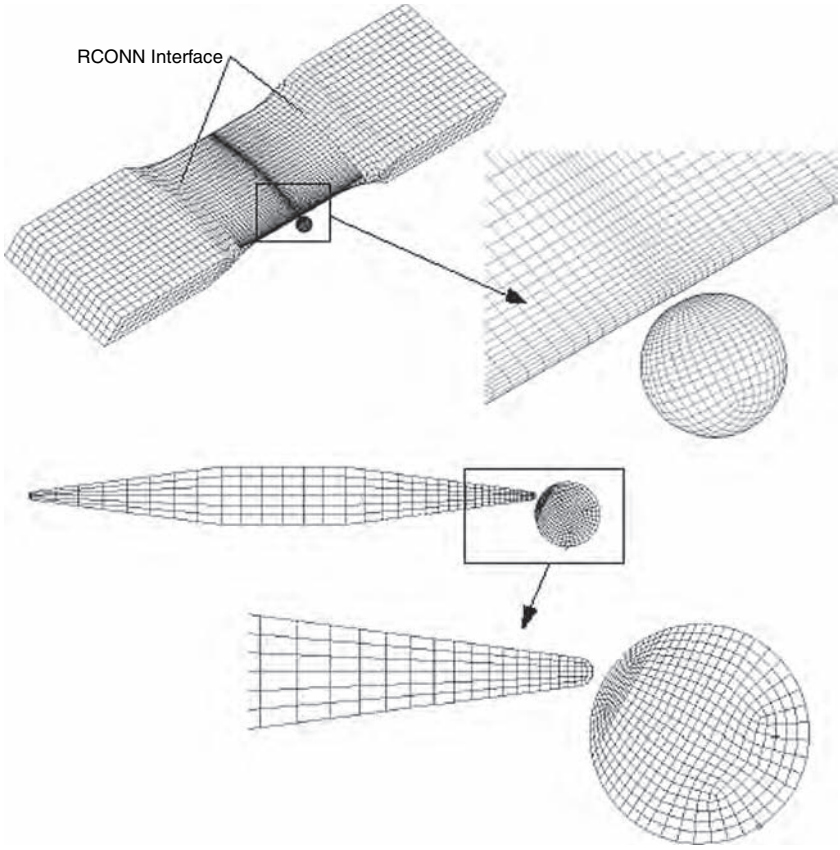


Figure G.32. Representative mesh for sharp-edged specimen impact.

mixed, it fails. The failure criterion does not have sufficient accuracy to model material dependent critical failure modes. The steel balls were modeled as linear elastic with a modulus of 29.6 Msi (204 GPa) and a density of 0.283 lb/in.^{3} (7832 kg/m^3).

As with all finite element analyses, whether they are explicit or implicit, the density of the mesh plays a role in the stress predictions and a mesh refinement study was conducted. However, explicit codes are much more sensitive to this refinement. In implicit codes, it is necessary to converge the mesh based on the area the analyst is interested in. In explicit codes, it is necessary to have a totally converged mesh so that all areas of stress and displacement are modeled correctly. This is necessary due to the fact that stress waves pass through nearly every point on the component during an impact event and that problems with mesh refinement away from the point of interest may affect the traveling wave speed and magnitude. The specimen mesh refinement study was conducted with

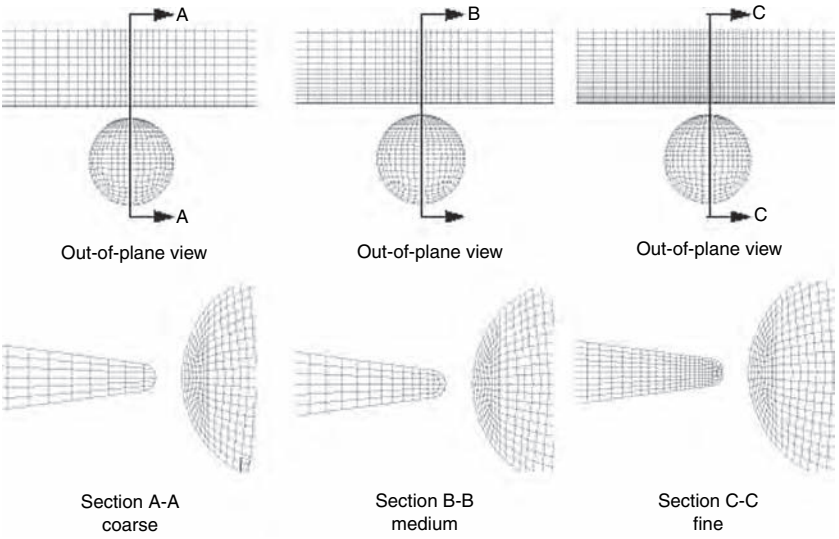


Figure G.33. Mesh geometries used in mesh refinement study.

the ball mesh density kept constant. Figure G.33 shows three successively finer meshes used in this analysis to determine the relative effect and efficiency of mesh refinement.

In typical mesh refinement studies, the output of the finite element model, such as stress, is compared to the previous iteration of element size. When the output changes by a very small value, the mesh is deemed to be refined. Unfortunately, the prediction of damage size did not reach an asymptote with the mesh options shown in Figure G.33. Instead, the size of predicted damage grew, and then decreased, so that the medium mesh predicted the largest damage. The results of the refinement were then compared to actual damage. This is shown in Figure G.34.

As can be seen from the analytical predictions, the medium mesh predicts the experimental results with the most accuracy. Both the coarse and fine meshes underpredict the depth and height for the test condition. Although the failure model is not very sophisticated, it predicts the general shape of failure remarkably well. The failure routine is based on a full element failure and partial element failure is not allowed; therefore, the mesh density (element size) will affect the failure predictions. A comparison of the smoothness of the predicted shapes with the abruptness of the corners seen in the experiment indicates that the deformation/failure model is not predicting the shearing deformation sufficiently accurately and that the deformation in the predicted shapes is not sufficiently local. It should be noted that penetration depth is relatively easy to predict, regardless of the material model used. It is suggested that predicted shape would be a better indicator of accuracy.

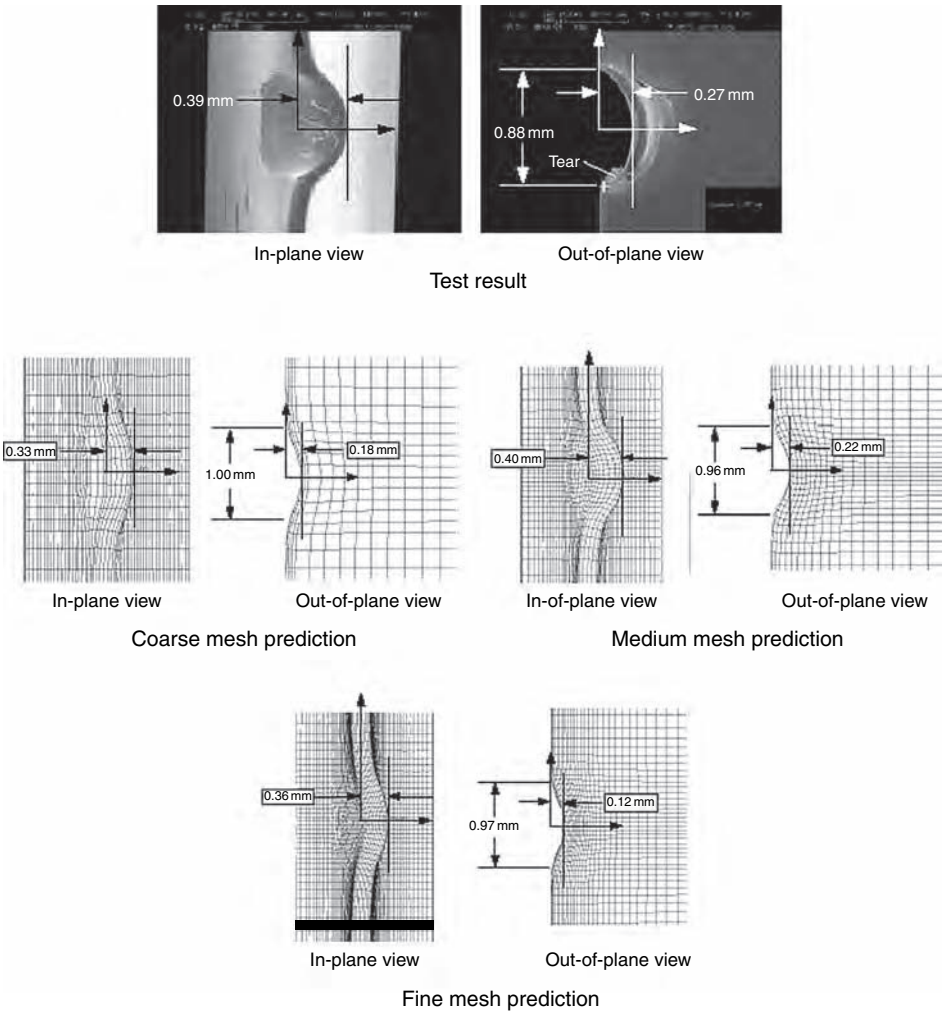


Figure G.34. Comparison of various mesh refinements to experimental damage.

The failure of the fine mesh to better predict material failure indicates that advanced codes such as hydrocodes and Particle-In-Cell (PIC) methods require significant expertise in order to be used correctly. In this case, the poor predictions may be due to mesh size, or they may well be due to the shortcomings in the deformation/failure constitutive model. In fact, the failure to arrive at a converged solution indicates that there may be competing shortcomings in various features of the model that may be offsetting each other. Because of this, these tools require expert users in order to predict damage prior to the impact event. Even without expert users, hydrocodes and PIC methods can be

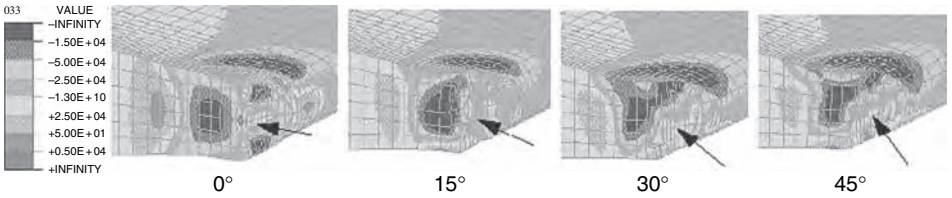


Figure G.35. Comparison of residual stress fields for different impact angles.

used to parametrically evaluate different facets of blade design. In this role, they can be useful design tools that can supplement experimental data in order to eliminate designs that are FOD intolerant. An additional benefit of hydrocode modeling is that the output of these models can be used to determine the relative magnitudes of residual stresses due to impact. For example, if a mesh refinement is chosen based on its correlation with impact damage size, that mesh could be used to predict residual stresses. An example of a parametric residual stress study based on an experimentally correlated mesh and a varying impact angle is shown in Figure G.35. Once the residual stresses are calculated, they can be superimposed over cyclic stresses in order to predict life with greater accuracy.

Numerical modeling of FOD is similar to modeling of all other ballistic impact events. Accurate predictions require physically realistic deformation and failure models within the code used. These need to be validated against experimental data to give trust in the results. A recent study carried out in the UK by QinetiQ to investigate the effects of FOD on a titanium alloy fan blade illustrates the state-of-the-art capability in ballistic modeling [12].

Detailed numerical FOD simulation

The study included determination of damage mechanisms and identification of the threshold perforation velocity of a hard steel sphere. The DYNA suite of Lagrangian hydrocodes [13] was used in the numerical simulations. The code features sophisticated contact algorithms and interface treatments. Deformation and failure models were constructed for steel and Ti-6Al-4V. These models were validated against both low rate mechanical tests and against relevant high rate tests such as plugging of a thin sheet by a projectile.

In the numerical simulation of an FOD event, each of the elements needs to translate the input energies and velocities into stresses and strains. There also needs to be a physically based means of determining when the material represented in each element fails. This is generally carried out by using a constitutive model to determine stresses and strains and a separate failure model. The failure model is applied to each element at each time step to determine if the failure criterion has been exceeded for that volume of material. The

accuracy of the overall prediction is dependent upon the accuracy of the constitutive and failure models.

The material models used by QinetiQ for the blade and the impactor materials are based on the modified Armstrong–Zerilli model shown in Equation (G.1).

$$\sigma = (C_1 + C_5\varepsilon^n)\,\frac{\mu_T}{\mu_{293}} + C_2 \exp\left[(C_3 + C_4 \ln \dot{\varepsilon})\,T\right] \tag{G.1}$$

where C_1 to C_5 and n are empirical constants and σ, ε, $\dot{\varepsilon}$ and T are respectively stress, strain, strain rate and temperature in °K; μ_{293} is the shear modulus at 293 °K and μ_T is the shear modulus at the current temperature.

The constants for the deformation model are taken from mechanical tests carried out at different strain rates and at different temperatures. For each test the effect of stress state on the measured flow stress is understood and this allows an effective uniaxial von Mises flow stress to be calculated for each separate condition. The variation of von Mises stress with strain allows the constants for the material to be calculated. Once these constants are calculated from simple mechanical tests, there is no need for them to be further changed, if the deformation model is accurate. Inaccurate predictions indicate that the model must be modified.

The fracture model used in the simulations was the Goldthorpe Path-Dependent Fracture Model [14, 15] where the accumulated damage is given in Equation (G.2)

$$\mathrm{d}S = 0.67^* \exp\left(1.5^*\sigma_n - 0.04^*\sigma_n^{-1.5}\right)^* \mathrm{d}\varepsilon + A^*\varepsilon_s \tag{G.2}$$

where σ_n is the stress triaxiality (pressure/flow stress or P/Y), $\mathrm{d}\varepsilon$ is the effective plastic strain, and ε_s is the maximum principle shear strain; A is a constant determined from torsion tests and S is the damage parameter.

The damage is then incremented in each time step and fracture occurs when the damage reaches a critical value S_c. The critical damage value is derived from tensile tests and has been shown to be a material parameter rather than a fitting constant. The damage essentially comprises a tensile component due to void growth and a shear failure component due to shear localization.

For the current illustration, constants for the titanium alloy were obtained from interrupted tensile tests on a standard untreated batch of Ti-6Al-4V. The values for the spherical ball were not available and were taken as a standard UK rolled homogeneous armour (RHA) for simplicity. The Mie-Gruniesen equation of state parameters used were standard values for this steel.

Initial modeling runs were used to confirm that the mesh used for the study produced a converged result in terms of hole size, stress state, etc. It should be noted that when an element reaches the critical failure condition, the element including its mass and energy is deleted from the calculation, thereby opening up a gap in the mesh. This is considered to be the best that the hydrocode can achieve in terms of crack formation.

A key issue in the simulation of the impact process is the degree to which the projectile deforms, particularly if it is spherical. This is crucial since the contact area on the blade will change dynamically during the impact and therefore influence the damage and fracture within the blade. To investigate this effect, the spherical projectile was simulated assuming a rigid body and also assuming a standard modified Armstrong-Zerilli model for RHA since these represent two extremes of behavior. It was found that the deformation of the spherical projectile was quite pronounced when the softer (deformable) material model was used. In reality, the ball is harder than RHA but will exhibit a small deformation.

For the case used in this illustration, the numerical modeling with a deformable projectile gave a predicted threshold speed for perforation of about 300 m/s which is in good agreement with the experimental data. As was expected, the majority of the damage is shear and a shear crack was observed running ahead of the projectile. It is worth noting that this crack took several time steps in the microsecond range to cross the thickness of the blade. In carrying out the study, the importance of the constitutive model was illustrated because the predicted threshold speed for the spherical projectile described using the RHA model was significantly higher than for the rigid material model. In addition, changing the damage parameters also affects the threshold perforation speed. This emphasizes the crucial need to characterize the actual materials being used since the results are sensitive to both the deformation and the failure models.

It is also interesting to note that in all the impact cases, the von Mises stress field, which can be related to the residual stress, becomes constant very quickly (about 100 μs) after the impact event. This is important when attempting to link the impact information to the much longer time cycling response of the blade.

An advantage of these simulations, and the trust that can be placed in them, is that a great deal of the information obtained can be used for quantitative analysis. Therefore, it is useful to compare bulge dimensions, plug velocities, spallation, and masses with experimental data. Although this may demand additional experiments, the techniques are available to accurately measure these phenomena. This is important since the general plug sizes and shape will influence the damage around the hole and may even indicate initial cracking around the hole. This may influence the subsequent life cycle of the blade due to fatigue cracking.

The capability of quantitatively observing the damage progression due to stress triaxiality is a major advance in understanding the blade response. The models used in this study are considered superior to previous failure models, which were largely based on effective plastic strain, since the latter cannot differentiate between tensile, shear, and compressive failures. In particular, understanding the time-scale of these mechanisms might allow better design of the blade to withstand the impact process by better material processing or geometrical changes.

A remaining issue is that the information generated from these simulations needs to be used as input into the simulation tool used to predict the fatigue life reduction incurred as the result of service incurred FOD.

The simulation of a real impact event, as opposed to a laboratory simulation using a spherical ball, was carried out under the Air Force HCF program [16]. There, a sphere impactor of equal mass to a cube were compared in a simulated leading edge impact event. The cube has been found to produce damage in laboratory experiments that looks much like that found in blades that have suffered FOD in the field. A sharp-edge blade specimen with a 0.127-mm leading edge radius (Figure G.32) was used for this study. The impact angle was fixed at 45°, and the simulation used a 1.33-mm steel ball as the reference mass. Figure G.36 compares the two local model mesh geometries. The cube is oriented such that a sharp cube edge impacts the blade specimen leading edge. This produces the characteristic V-notch FOD which is considered to be a worst case impactor orientation. Here, the impact velocity was 1000 ft/sec.

It was found that the sphere impact produces more local bending distortion around the FOD site, while the cube impact creates a deeper notch effect. The local bending distortion is produced by an interaction of blade edge radius, impactor radius, and impactor velocity. Slower and larger impactors produce more local bending distortion around the FOD site. As velocity increases, less local bending distortion is observed. It was also found that the exit side (top) compressive stress distributions are different for the two impactors. The sphere impact produced compressive stress all around the surface of the exit side while the cube impact created a very slight tensile stress at the exit side surface notch location with compressive stresses produced deeper into the blade specimen.

The calculations also compared the two models loaded to a nominal 20 ksi stress level. Both models showed tensile stresses on the projectile entrance side. The cube model produced localized tensile stress at the exit-side notch location. The results showed that

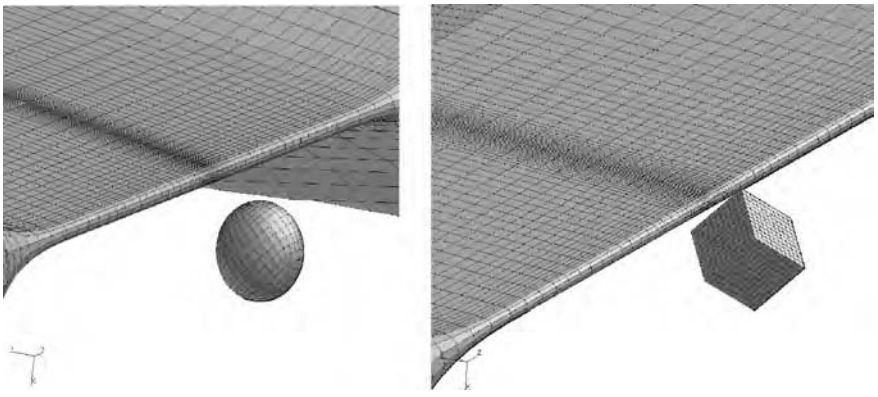


Figure G.36. Local sphere and cube impact models.

the 40 ksi nominal stress significantly reduces the compressive stress field on the exit-side of the cube impact, and a very localized tensile stress at the exit side notch root was clearly observed. The sphere impact still showed a large zone of compressive stress at the exit side.

Fatigue life to failure was investigated comparing the sphere impact to the cube impact. Velocity cases of 600, 800, 1000, and 1200 ft/sec were investigated for the 45° impact angle. Figure G.37 shows the effect of the cube and the sphere on fatigue life to failure.

Figure G.37 plots calculated fatigue life for the 0–20-ksi cycle and the 0–40 ksi-cycle. The effect of "with and without residual stress" is also shown. Figure G.37 clearly shows that the cube impact is more damaging to fatigue life than the sphere impact. Figure G.37 shows that fatigue life decreases for the increasing velocity, but the curves also appear to be converging as velocity increases. This suggests a possible upper limit on velocity for a minimum fatigue life point. For all cases, including residual stress reduced the predicted fatigue life to failure. The difference in fatigue life between "with and without residual stress" decreases as the cyclic stress range increases. This is observed by comparing the cube 0–40 ksi "with and without residual stress" curves.

This cube versus sphere study illustrated that FOD geometry has a significant effect on fatigue life, local residual stress distribution, and FOD site geometry. This points out the important fact that in simulating real FOD in the laboratory, the geometry and properties of the impactor play important roles in determining the type (geometry) of impact damage, the residual stress distribution, and the subsequent fatigue life.

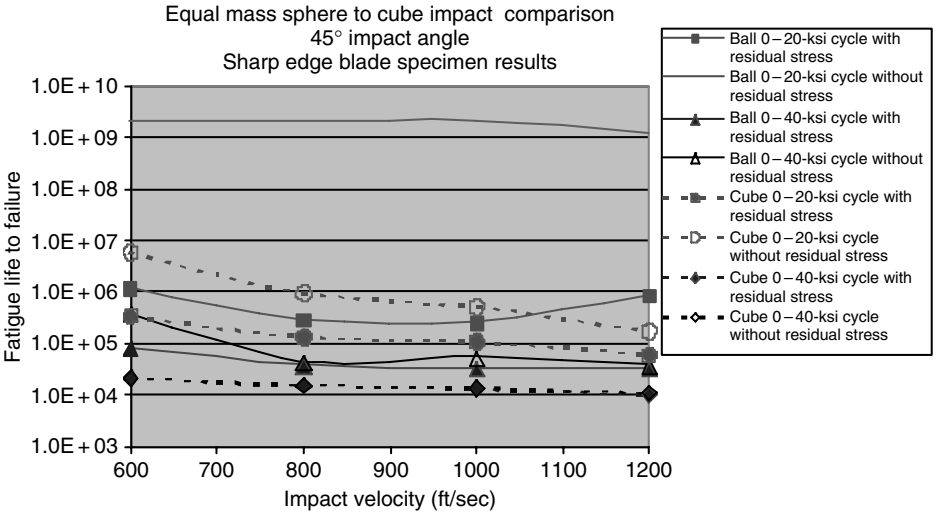


Figure G.37. Fatigue life comparison of cube impact to sphere impact.

Post-impact life prediction

The study of fatigue life prediction from damage sites has been examined for the past century using fracture mechanics concepts to describe crack growth. Unfortunately, a best life prediction method has not been agreed upon. This section attempts to describe several recently developed life prediction methods for FOD'd airfoils. Advantages and disadvantages of each methodology will be briefly discussed. In general, the methodologies fall into two different categories: total life and fracture mechanics.

Crack initiation

In the case of FOD, for HCF, total life prediction can be thought of as a crack initiation prediction. This type of model, described in Chapter 2, assumes that once a crack is initiated, the airfoil in question has effectively failed. The crack initiation method used to evaluate FOD in this section uses an equivalent stress life prediction parameter (σ_{equiv}) that is defined in Equation (G.3)

$$\sigma_{\text{equiv}} = 0.5\,(E\Delta\varepsilon)^{w}\,(\sigma_{\max})^{1-w} \tag{G.3}$$

where σ_{equiv} is the alternating Walker equivalent stress, E is the elastic modulus, $\Delta\varepsilon$ is the total strain range, and $\sigma_{\max}$ is the maximum stress. The Walker equivalent stress exponent w is a material and temperature-dependent parameter that collapses variable mean stress data into a single life curve. Given the focus of FOD life prediction for aircraft engine components is in the intermediate and long life (HCF) regime, elastic cycling conditions typically dominate so that $E\Delta\varepsilon = \Delta\sigma_{\text{psu}} \sim \Delta\sigma$. Parameter $\Delta\sigma_{\text{psu}}$ is the elastic equivalent stress or pseudostress used for the Walker model. This quantity basically assumes the plastic stress and strain are small and approximates the total stress range as the elastic stress range. This can be used to establish Equation (G.4) as:

$$\sigma_{\text{equiv}} = 0.5\,(\sigma_{\text{psu}})^{w}\,(\sigma_{\max})^{1-w} \tag{G.4}$$

This approach is essentially identical to the equivalent strain parameter that has been shown in the literature to collapse R_{ε} data for a number of different materials. This approach requires an elastic–plastic stress analysis, but does not require a plastic strain range term that is typically extremely small in the HCF life regime of interest to aircraft engine components. This approach also predicts a decrease in the importance of R_{ε} on life in the short life regime. An additional advantage of this approach is that a single curve collapses test data over the entire life regime (Figure G.38).

In order to arrive at an accurate life prediction, the stress analysis includes the effects of local plasticity at the notch root. This can be done using any number of available

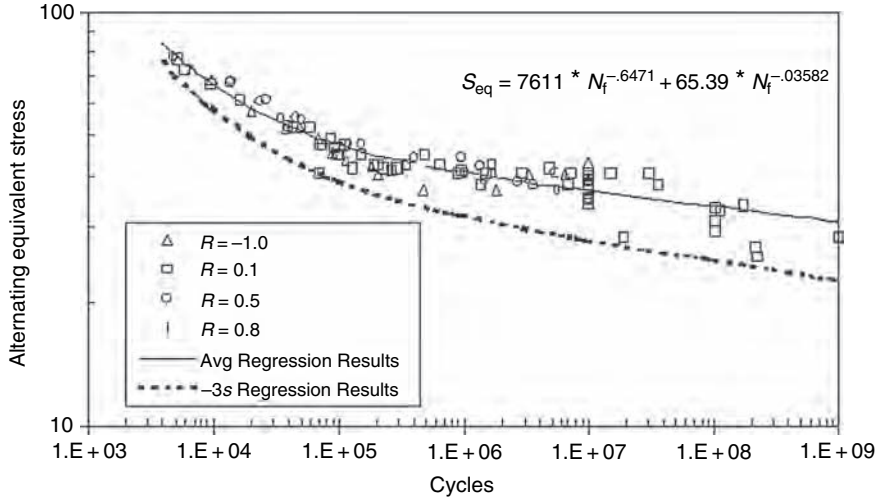


Figure G.38. Application of equivalent stress parameter to data with different stress ratios.

numerical stress analysis programs. Application of the elastic–plastic stress analysis, in conjunction with the life prediction parameter described above, results in good correlation with experimental data. An example of the correlation for the winged specimens described above is shown in Figure G.39. Once the equivalent stress is determined for the appropriate notch geometry and residual stress, the life of the notched specimen can be predicted by correlating the stress to life using a curve like that shown in Figure G.38.

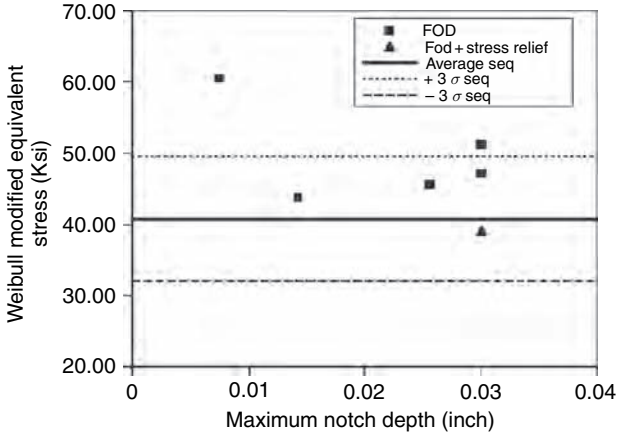


Figure G.39. Equivalent stress for a given notch depth on ballistically impacted winged specimens.

Crack growth

Unlike crack initiation, crack growth methodologies do not assume that failure occurs when cracks initiate. Crack growth methodologies allow the cracks to grow until they reach a critical size or arrest. The first question that must be answered is how can methodologies developed for smooth notches, often without residual stresses, be applied to FOD damage that does not conform to those assumptions. The USAF conducted a study to determine whether or not fracture mechanics methods could be applied to FOD [17]. The results from this study clearly indicate that fracture mechanics can be applied to FOD and that an increase in the crack tip stress intensity factor (K) is necessary to account for increased FOD depths. This conclusion was reached even in the presence of significant residual stresses.

The analysis of fatigue cracks emanating from notches is discussed in Chapter 5 in the notch fatigue section. The introduction and use of small crack theories is a vital part of the analysis since many cracks at FOD-induced notches are truly in the small crack regime. Faster crack growth rates than predicted by long crack LEFM are found under these conditions when stress levels are too high and small-scale yielding conditions are exceeded or the crack is so small that it is affected by microstructural conditions [18]. The Kitagawa diagram becomes an important tool under such conditions.

In order to apply fracture mechanics to FOD, there are essentially six steps to determine an endurance limit stress. These steps are (1) calculate normalized elastic K (initial crack dimensions must be assumed) for airfoil/notch geometry, (2) calculate elastic $K_{\max}$ and $K_{\min}$, (3) calculate residual K for airfoil/notch geometry, (4) calculate K and R-ratio with residual K, (5) compare K and R-ratio to K_{th} material capability, and (6) iterate on stress to converge on solution. The following paragraphs describe each of these steps in more detail.

Calculate normalized elastic K for LE (Leading Edge)/Notch geometry

Stress intensity analysis must be conducted on LE and notch geometries which cover the configurations of interest. Interpolation/extrapolation on notch depth is used to determine the normalized elastic K for the given airfoil/notch geometry. Obviously, this approach will result in some error in K predictions, but should be adequate to capture the behavior of FOD in the non-catastrophic regime, especially considering the amount of scatter in experimental data.

Calculate elastic K_{max} and K_{min}

Calculation of the elastic K_{max} and K_{min} is simply the normalized elastic K times the applied stress. To predict the endurance limit stress, an initial value of stress must be selected and iterated to a solution through the remaining steps.

Calculate residual K for airfoil/notch geometry

Residual K can be assumed to be solely a function of notch depth. This is a very simplistic approach to capturing the effects of residual stress local to the FOD notch. This approach

does not distinguish between the probable causes of the residual stress, FOD projectile impact, and local notch yielding. A more accurate representation would be to calculate the residual K trends with detailed impact and notch yielding FEA analysis. This will not only increase confidence in the methods, but also make them more robust by defining K residual as a function of airfoil, and notch parameters. Since notch residual stresses have a significant affect on crack growth from FOD damage, it is suggested to use the most accurate representation of residual stresses possible.

Calculate K and stress-ratio with residual K

The final calculations for the modeling are to determine the local K and stress-ratio, including the effects of the residual K. This is simply determined by subtracting the residual K from the maximum and minimum K, and recalculating R-ratio. Since residual K will reduce the elastic K_σ, the local R-ratio will always be less than the applied R-ratio.

Compare K and R-ratio to K_{th} material capability

Finally, the predicted K and R-ratio are compared to the K_{th} material capability. If the predicted K is above the material capability, cracks would be predicted to initiate.

Iterate on Stress to Converge on Solution

To determine the stress at which the onset of crack initiation will occur, the applied stress must be iterated until the predicted K and R-ratio match the material capability.

Like crack initiation models, many crack growth models assume material failure once the nucleated crack has begun to grow (initiate). However, in the case of FOD damage, residual stress plays a significant role in crack initiation. It is possible in certain cases of FOD to grow a crack through the residual stress region or the vibratory stress field to a point where the crack will arrest. In order to capture this behavior, the following model has been proposed.

Worst case notch (WCN)

The WCN model is described in Chapter 5. It assumes that the lowest threshold stress for onset of HCF is controlled by whether or not microcracks can continue to grow after having been initiated early in life by FOD and/or LCF. It makes use of a crack-size–dependent threshold stress intensity. The WCN model predicts the conditions for onset of crack initiation, as well as regimes of crack growth and arrest, or crack growth to failure.

The WCN model can use simple parametric notch-stress equations or finite element analysis to predict ΔS_{th} as a function of FOD-notch depth and sharpness, including residual stress effects. Since it explicitly treats the growth and arrest of microcracks, the WCN model is also applicable to cases where beneficial surface treatments are employed to enhance component life. An example of predictions of ΔS_{th} made using the WCN

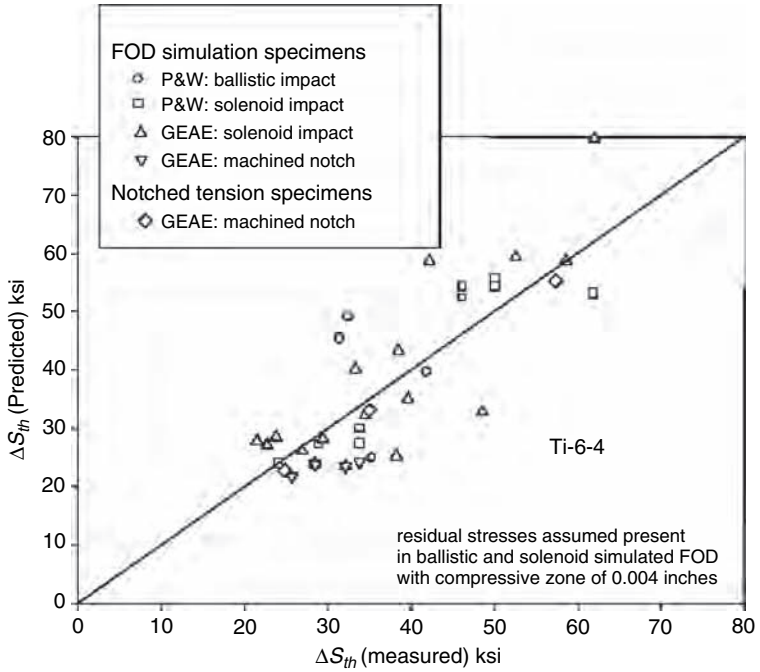


Figure G.40. Prediction of experimental versus predicted threshold stress using the WCN model.

model applied to various sources of specimen data involving both FOD and notched specimens is shown in Figure G.40. This figure shows the good correlation of experiment and prediction.

WCN Example

In order to apply the WCN method, an example of its use should prove beneficial. First, assume an FOD event has occurred on the leading edge of a blade resulting in a notch with a depth of 0.3 mm (0.012 in). The notch has a root radius of 0.06 mm (0.0024 in.) and does not have a crack emanating from it. General formulas for k_t can be looked up in handbooks, for example [19]. The k_t for this particular notch is given in Equation (G.5):

$$k_t(\rho/b) = (1 + 2b/\rho)\, f(\rho/b) \tag{G.5}$$

where $f(\rho/\mathrm{b})$ is given by Equation (G.6).

$$f(\rho/b) \cong 1 + 0.122\left(\frac{1}{1+\rho/b}\right)^{5/2} \tag{G.6}$$

For the notch in this example, k_t is approximately 11.85. This is a very sharp notch but k_ts of this size have been seen in field damage. If this blade material has an endurance limit at 10^7 cycles of 650 MPa for $R = 0.5$, then the use of k_t would predict that the maximum allowable stress should be 54.85 MPa.

Using the WCN method, it is necessary to compute the threshold stress intensity factor for small cracks and correlate that to the threshold applied stress that can be applied to the blade and still remain in the limit of safe operation. The first step is to calculate the small crack parameter, a_o.* Equation (G.7) defines a_o as a function of applied stress ratio:

$$a_o(R) = \frac{1}{\pi}\left[\frac{\Delta K_{th}(R)}{F\Delta\sigma_e(R)}\right]^2 \tag{G.7}$$

where $F = 1.122$ for a crack that goes through the thickness in a straight line (through crack) and 0.73 for a semi-elliptical crack that does not go through the thickness (thumbnail crack), ΔK_{th} is the crack growth threshold for a given R, and $\Delta\sigma_e$ is the smooth bar endurance stress range for the cyclic life in question. For this example, we will assume an endurance limit of 10^7 cycles, an endurance stress of 650 MPa, a through crack, and a ΔK_{th} of 3 MPa$\sqrt{m}$ all at a stress ratio of 0.5. Based on these assumptions, a_o (0.5) is 21.54 μm. The next step is to obtain the threshold stress that corresponds to the endurance limit based on these quantities. Hudak et al. [20], uses Equation (G.8) to determine $\Delta S_{th,L}$:

$$\Delta S_{th,L} = \frac{\Delta K_{th}}{(\pi)^{\sqrt{2}} g_n\left(\frac{\sqrt{ba_o}+b}{t}\right)\left(\sqrt{a_o}+\sqrt{b}\right)} \tag{G.8}$$

In this equation, g_n is a finite-thickness correction function that approaches 1.12 if the crack depth is much smaller than its length. Since the most interesting cases of FOD are those where cracks are small, it is conceivable that this approximation will be good in most cases. However, the function for g_n can be found in various stress handbooks such as [19]. If g_n is assumed to be 1.12, the equation above simplifies to (G.9):

$$\Delta S_{th,L} = \frac{\Delta K_{th}}{1.12\,(\pi)^{1/2}\left(\sqrt{a_o}+\sqrt{b}\right)} \tag{G.9}$$

Since b and a_o are independent of crack growth, the equation (G.9) results in a value of 68.8 MPa for $\Delta S_{th,L}$. The changes in the value of threshold stress for blade failure due to crack growth is due to the inclusion of small crack effects through the inclusion of notch size and to the incorporation of fracture mechanics crack growth thresholds into the stress prediction. A smaller notch with a sharper radius could have the same k_t and thus

* See Chapter 4 for a discussion of the effective small crack threshold and the Kitagawa diagram.

the same predicted fatigue endurance stress using the non-fracture mechanics approach. However, the change in notch size would further reduce the value of b from the example and the predicted endurance stress would increase accordingly if the WCN model were used. This makes physical sense because a very small notch with a k_t of 40 should be less detrimental to blade life than a notch with the same k_t that is three times as deep. In summary, it is suggested that FOD evaluation account for notch depth and fracture toughness of the material, rather than just fatigue strength and notch geometry.

SUMMARY

This appendix has presented the current state of the art in FOD simulation, modeling and life prediction. The most important part of experimental FOD simulation is the type of impact method and the stress state in the specimen. There are appropriate uses for each impact type and each specimen design. However, the most realistic and practical impact method is ballistic and the most accurate specimen design is one that captures the stress gradient in the airfoil of interest.

In the area of analytical modeling, models have been developed to predict impact damage and residual stress due to impact. These models typically require very experienced users and can easily be abused to get the wrong answer. However, correlation with experimental data can be used to avoid these errors. Once residual stresses and damage are predicted, elastic–plastic finite element simulations can be completed and life prediction routines can be implemented. Life prediction routines typically result in a trade-off between accuracy and complexity, so the appropriate life prediction method should be chosen to meet the resolution needed by the analysis.

REFERENCES

1. Best Practices for the Mitigation and Control of Foreign Object Damage–Induced High Cycle Fatigue in Gas Turbine Engine Compression System Airfoils, NATO AVT-094/RTG-027 Final Report, 2004. (http://www.rta.nato.int/Reports.asp)
2. Thompson, S.R., Ruschau, J.J., and Nicholas, T., "Influence of Residual Stresses on High Cycle Fatigue Strength of Ti-6Al-4V Subjected to Foreign Object Damage", *International Journal of Fatigue,* **23**, Supplement 1, 2001, pp. S405–S412.
3. Hudak, S.J. and Davidson, D.L., "Characterization of Service Induced FOD", United States Air Force Technical Report, Improved High Cycle Fatigue Life Prediction, Appendix 5A, AFRL-ML-WP-TR-2001-4159, Wright-Patterson AFB, OH, January 2002.
4. Haake, F.K., Salivar, G.C., Hindle, E.H., Fischer, J.W., and Annis, C.G., "Threshold Fatigue Crack Growth Behaviour", *United States Air Force Technical Report, WRDC-TR-89-4085,* Wright-Patterson AFB, OH, 1989.

5. Chell, G;G., and Hudak, S.J., "Development and Application of Worst Case Notch (WCN) to FOD", *United States Air Force Technical Report, Improved High Cycle Fatigue Life Prediction, Appendix 5I, AFRL-ML-WP-TR-2001-4159*, Wright-Patterson AFB, OH, January 2002.
6. Hamrick, J.L., "Effects of Foreign Object Damage from Small Hard Particles on the High-Cycle Fatigue Life of Ti-6Al-4V", Ph.D. Dissertation, *AFIT/DS/ENY/99-02,* Air Force Institute of Technology, Wright-Patterson AFB, OH, September 1999.
7. Birkbeck, J.C., "Effects of FOD on the Fatigue Crack Initiation of Ballistically Impacted Ti-6Al-4V Simulated Engine Blades", Ph.D. Thesis, School of Engineering, University of Dayton, Dayton, OH, August 2002.
8. Roder, O., Thompson, A.W., and Ritchie, R.O., "Simulation of Foreign Object Damage of Ti-6Al-4V Gas-Turbine Blades", in *Proceedings of the Third National Turbine Engine High Cycle Fatigue Conference*, W.A. Stange and J. Henderson, eds, Universal Technology Corp., Dayton, OH, 1998, CD-ROM, Session 10, pp. 6–12.
9. Williams, D.P., Nowell, D., and Stewart, I.F., "The Effect and Assessment of Foreign Object Damage to Aero Engine Blades and Vanes", *Proceedings of the 5th National Turbine Fatigue High Cycle Fatigue Conference,* Phoenix, AZ, 7–9 March 2000.
10. Weeks, C., Bastnagel, P., Cook, T., Daiuto, R., and Delp, J., "FOD Analytical Modeling – FOD Event Modeling", *United States Air Force Technical Report, Improved High Cycle Fatigue Life Prediction, Appendix 5E, AFRL-ML-WP-TR-2001-4159*, Wright-Patterson AFB, OH, January 2002.
11. *MSC/DYTRAN Version 4.0 User's Manual,* The MacNeal-Schwendler Corporation, 1997.
12. Tranter, P.H., Gould, P.J., and Harrison, G.F., "Laboratory Simulation and Finite Element Modeling of Aerofoil Impact Damage", *Proceedings of the 8th National Turbine Fatigue High Cycle Fatigue Conference,* Monterey, CA, 14–16 April 2003.
13. *LS-DYNA Users Manual*, Livermore Software Technology Corporation, 2002.
14. Butler, A., Church, P., and Goldthorpe, B., "A Wide Ranging Constitutive Model for bcc Steels", *Jnl de Physique 4*, C8-471, 1994.
15. Goldthorpe, B., "A Path Dependent Model for Ductile Fracture", Jnl de Physique 7, C3-705, 1997.
16. Gallagher, J. et al., "Advanced High Cycle Fatigue (HCF) Life Assurance Methodologies", *Report # AFRL-ML-WP-TR-2005-4102*, Air Force Research Laboratory, Wright-Patterson AFB, OH, July 2004.
17. Gallagher, J.P. et al., "Improved High Cycle Fatigue Life Prediction", *United States Air Force Technical Report, AFRL-ML-WP-TR-2001-4159*, Wright-Patterson AFB, OH, January 2001.
18. The Behaviour of Short Fatigue Cracks, ed. K.J. Miller and E.R. de los Rios, Mechanical Engineering Publications Limited, London, 1986.
19. Tada, H., Paris, P., and Irwin, G., "The Stress Analysis of Cracks Handbook, 2nd Edition", Del Research Corporation, 1985.
20. Hudak, S.J., Chell, G.G., Slavik, D., Nagy, A., and Feiger, J.H., "Influence of Notch Geometry on High Cycle Fatigue Threshold Stresses in Ti-6Al-4V", *Proceedings of the 6th National Turbine Fatigue High Cycle Fatigue Conference,* Jacksonville, FL, 5–8 March 2001.

Appendix H*
FOD in JSSG

JSSG-2007
30 October 1998

DEPARTMENT OF DEFENSE

JOINT SERVICE SPECIFICATION GUIDE (JSSG)

ENGINES, AIRCRAFT, TURBINE

3.3.2 Ingestion capability (hazard resistance)

3.3.2.1 Bird ingestion

The engine shall continue to operate and perform during and after the ingestion of birds as specified in Table VIII.

3.3.2.2 Foreign object damage (FOD)

The engine shall meet the requirements of the specification for the design service life of 3.4.1.1 without repair after ingestion of foreign objects which produce damage equivalent to a stress concentration factor (K_t) of _____ at the most critical locations of flow path components.

3.3.2.3 Ice ingestion

The engine shall operate and perform in accordance with table IX, during and after ingestion of hailstones and sheet ice at the takeoff, cruise, and descent aircraft speeds. The engine shall not be damaged beyond field repair capability after ingesting the hailstones and ice.

The excerpts in this Appendix are extracted from JSSG and are those that deal with tolerance of aircraft turbine engines to ingestion of foreign objects such as birds, sand, dust, ice, and other debris. They are extracted from JSSG document referenced in the title.

3.3.2.4 Sand and dust ingestion

The engine shall meet all requirements of the specification during and after the sand and dust ingestion event specified herein. The engine shall ingest air containing sand and dust particles in a concentration of (a) mg sand/m^3. The engine shall ingest the specified course and fine contaminant distribution for (b) and (c) hours, respectively. The engine shall operate at intermediate thrust for TJ/TFs or maximum continuous power for TP/TSs with the specified concentration of sand and dust particles, with no greater than (d) percent loss in thrust or power, and (e) % gain in specific fuel consumption. Helicopter engines shall ingest the 0–80 micron (0–3.15 $\times 10^{-3}$ in.) sand and dust of section 4.11.2.1.3 in a concentration of 53 mg/m^3 (3.3×10^{-6} lb/ft^3) air for 54 hours and inspection shall reveal no impending failure.

A.3.3.2 Ingestion capability (hazard resistance).

A.3.3.2.1 Bird ingestion.

The engine shall continue to operate and perform during and after the ingestion of birds as specified in Table VIII.

REQUIREMENT RATIONALE (A.3.3.2.1)

Engines must be capable of ingesting birds encountered during missions without significant power loss, deterioration, or safety implications. The total weapon system mission environment must be studied to examine the probability of bird strike occurrence, bird sizing criteria, flocking densities, mission routing, training, etc., to determine the design criteria for bird ingestion capability requirements for an engine.

REQUIREMENT GUIDANCE (A.3.3.2.1)

The following should be used to tailor Table VIII:

In the event of specific air system bird strike criterion has not been established for the engine, the following birds vs. inlet area criteria should be used.

The inlet area to be used should be the aircraft inlet or engine inlet whichever is smaller.

The number of birds to be ingested should be based on inlet area as follows: one 100 gm (3.5 oz) bird per 300 cm^2 (46.5 $in.^2$) of inlet area plus any fraction larger than 50% thereof, up to a maximum of 16 birds; one 1 kg (2.2 lb.) bird per 1500 cm^2 (232.5 $in.^2$) of inlet

area plus any fraction larger than 50% thereof; one 2 kg (4.4 lb.) bird, regardless of the size of the inlet, provided the inlet is large enough to admit a 2 kg (4.4 lb.) bird.

The 100 gm (3.5 oz) birds should be ingested at random intervals and be randomly dispersed over the inlet area. Birds weighing 1 kg (2.2 lb.) and larger should be directed at critical areas of the engine face.

The bird velocity and engine power setting for each condition should be as described below:

Birds weighing 100 gm (3.5 oz) (a maximum of 16 at a time) and birds weighing 1 kg (2.2 lb.) (one at a time) ingested at a bird velocity equal to the takeoff flight speed, with the engine at intermediate thrust for TJ/TFs or maximum power for TP/TSs.

Birds weighing 100 gm (3.5 oz) (a maximum of 16 at a time) and birds weighing 1 kg (2.2 lb.) (one at a time) ingested at a bird velocity equal to the cruise flight speed with the engine at cruise power setting.

Birds weighing 100 gm (3.5 oz) (a maximum of 16 at a time) and birds weighing 1 kg (2.2 lb.) (one at a time) ingested at a bird velocity equal to the descent flight speed with the engine at descent power.

For aircraft that have a low level, high speed mission requirement: birds weighing 100 gm (3.5 oz) (a maximum of 16 at a time) and birds weighing 1 kg (2.2 lb.) (one at a time) ingested at a bird velocity equal to the aircraft maximum sea-level speed and the engine power setting required to achieve that speed.

Birds weighing 2 kg (4.4 lb.) ingested at a bird velocity equal to the aircraft takeoff speed or low level operational airspeed, whichever is more severe, with engine power equal to that required for the flight condition.

For 100 gm (3.5 oz) birds, the engine should sustain a performance of 95% or greater of the initial thrust or power, and all damage to the blades and vanes should be blendable (within repair limits) with flight line-type tooling. The 1 kg (2.2 lb.) bird ingestion may cause some damage; however, it should not result in immediate engine shutdown, and post-ingestion thrust or power levels should be 75% or greater of the initial thrust or power at the operating condition. Under condition e. above, no engine failure should occur which would result in damage to the aircraft or adjacent engines. No bird ingestion should prevent the engine from being safely shutdown.

Performance recovery times will vary as a function of the bird size, number of birds, and size of the engine. The performance recovery time after ingestion of the 100 gm (3.5 oz) bird(s) should occur in 5 seconds or less after the final volley of birds has been ingested. The performance recovery time after ingestion of the 1 kg (2.2 lb.) bird(s) should occur in 5 seconds or less for small engines, 5–10 seconds for moderate-sized turbofans or turbojets, and up to 5–15 seconds for large by-pass turbofans.

Turboshaft engines should recover within 5 seconds after an ingestion event with no less than 95% of the power prior to the ingestion event, and without exceeding any engine control limits.

Background:

Bird strike durability is a necessary safety design criteria to be used in all engines. Analyses should be conducted to determine the sensitivities to blade design, blade to stator spacing design, control system operation, and stator design for structure performance, and engine control. Bird strike tolerance can be enhanced by providing large axial clearances between blade and stators at the front of the engine.

REQUIREMENT LESSONS LEARNED (A.3.3.2.1)

Since helicopter takeoff flight speed differs from fixed wing, the following was used for the T800:

A bird of 50–100 grams (0.11–0.22 lb.) ingested at a bird velocity equal to Mach number of 0.1 and with the engine at maximum rated power set by rated Measured Gas Temperature (MGT).

A bird of 50–100 grams (0.11–0.22 lb.) ingested at a bird velocity equal to Mach number of 0.3 with the engine at maximum continuous power set by rated MGT.

A bird of 50–100 grams (0.11–0.22 lb.) ingested at a bird velocity equal to a Mach number of 0.2 with the engine at 25% of the maximum continuous rated power obtained in paragraph b.

Results of findings for bird ingestion experience assembled by Aerospace Industry Association, "Bird Ingestion Experience for Aircraft Turbine Engines," 1979, generally supports the FAA part 33.77 criteria. Similar military studies have indicated that the engine may receive over 60% of the total aircraft strikes, and most strikes occur below 1.8 km (6000 feet) at takeoff, landing, and low-level penetration speeds.

A GAO/NSIAD-89-127 report, dated July 1989, states that from 1983 to 1987, military aircraft have collided with birds over 16,000 times. Many of these collisions caused only minor damage; however, the services lost six crew members, incurred $318 million in damages, and lost nine aircraft. During this period, the Air Force lost six aircraft, the Navy lost two aircraft, and the Army lost one aircraft. A review of nine military jet engines developed since the early 1970s showed that the Services lessened the military specification requirements in engine model specifications for the sizes and the numbers of medium birds used in testing engines.

Recent studies (USAF/ASC & AIA) of bird ingestion data indicate that older specifications did not accurately reflect the sizes and the number of birds actually ingested. Prior to the publication of this specification, engine military specifications required medium birds sizes for ingestion tests of 1.5 pounds for the Air Force and 2 pounds for the Navy.

DOT Report DOT/FAA/CT-84/13 by Gary Frings, dated 9/84, states that bird ingestion is a rare but probable event. For every one million aircraft operating hours, 230 bird

ingestions (of all weights) will occur, on average. An average bird weighs 26 ounces. Most likely weight of birds in the areas of runways is 11 ounces. A small percentage ($< 3\%$) of ingestion events involved birds weighing 61 ounces. Ten percent of events involved ingestion of multiple birds into a single engine; 0.5% of events involved multiple engine ingestions; 5% of all bird ingestions resulted in engine failure.

A.4.3.2.1 Bird ingestion

The requirements of 3.3.2.1 shall be verified by:

VERIFICATION RATIONALE (A.4.3.2.1)

A test with a complete engine is necessary to ensure all interactive effects of a bird strike are properly accounted for in the engine design. Analysis and component test (fan and compressor rigs) have been successfully used to predict loading and deflection criteria leading up to full-scale engine tests.

VERIFICATION GUIDANCE (A.4.3.2.1)

Past verification methods have included analyses, demonstrations, and tests.

The contractor should specify in the pretest data the critical target area for bird ingestion. Test target area is subject to approval by the Using Service.

Background:

A development test program consisting of analysis and component test should be established to provide confidence in the design prior to formal engine ingestion tests. The number of birds, bird sizes, engine RPMs, bird velocities, performance criteria, and amount of damage for the test engine should be based on the parameters of 3.3.2.1. Analysis should indicate the location for critical bird strikes at the front face of the engine and pass/fail criteria should be included in the test plan. The birds should be ingested in a random sequence and dispersed over the inlet area to simulate an encounter with a flock. Synthetic "birds" have not been used by the military services to date, but their use should not be precluded in future programs if sufficient information and justification is presented to the Using Service.

VERIFICATION LESSONS LEARNED (A.4.3.2.1)

Severe out-of-balance conditions creating high vibrations, along with rotating to static structural contact, have been encountered following bird ingestion events.

Table VIII. Bird ingestion

Bird Size	*Number of Birds*	*Bird Velocity*	*Thrust/Power Setting*	*Percent Thrust/ Power Retention*	*Thrust/ Power Recovery Time*	*Damage*
100 gm (3.5 oz)		Takeoff =				Blendable
100 gm (3.5 oz)		Cruise =				Blendable
100 gm (3.5 oz)		Low Level Hi-Speed =				Blendable
100 gm (3.5 oz)		Descent =				Blendable
1 kg (2.2 lbs)		Takeoff =				Minor
1 kg (2.2 lbs)		Cruise =				Minor
1 kg (2.2 lbs)		Low Level Hi-Speed =				Minor
1 kg (2.2 lbs)		Descent =				Minor
2 kg (4.4 lbs)		Takeoff or Low Level Hi-Speed =				Contain Failure

Each line of the table must be satisfied to comply with the requirements of 3.3.2.1.

A.3.3.2.2 Foreign object damage (FOD).

The engine shall meet the requirements of the specification for the design service life of 3.4.1.1 without repair after ingestion of foreign objects which produce damage equivalent to a stress concentration factor (K_t) of _____ at the most critical locations of flow path components.

REQUIREMENT RATIONALE (A.3.3.2.2)

The engine inlet airflow velocities create conditions where loose foreign objects may be ingested into the engine resulting in gas path damage. The engine must tolerate the ingested objects up to a specified level.

REQUIREMENT GUIDANCE (A.3.3.2.2)

The following should be used to tailor the specification paragraph:
A value of at least 3.
Background:
The stress concentration factor of 3 is similar to a notch in the fan or compressor blade or stator caused by impact damage from a small object.

Typical foreign objects to be considered are nuts, bolts, rivets, rocks, aircraft parts, shell casings, and tools. Therefore, structures subject to this type of damage must be

capable of operating to the next subsequent depot interval to avoid immediate teardown when damage is detected and determined to be within acceptable limits.

REQUIREMENT LESSONS LEARNED (A.3.3.2.2)

Blades insufficiently designed for FOD considerations have caused In-Flight Shut Downs (IFSDs) and costly damage to the engine. FOD tolerance can be enhanced by use of more damage tolerant materials and a redistribution of the blade mass.

Foreign object damage costs the Navy over $15M each fiscal year based on a conservative estimate in one source reference. Common culprits are "housekeeping" items, such as nuts, bolts, safety wire, screwdrivers, etc. This paragraph is aimed at this type of FOD problem (environmental factors such as ice, sand, water, and birds are covered in other specification paragraphs).

A.4.3.2.2 Foreign object damage (FOD).

The requirements of 3.3.2.2 shall be verified by:

VERIFICATION RATIONALE (A.4.3.2.2)

Analysis, demonstration, and test are required to ensure that the fan and compressor airfoils can meet the operational requirement of 3.3.2.2 and to establish accept or reject criteria for damage that is detected during flight line inspections.

VERIFICATION GUIDANCE (A.4.3.2.2)

Past verification methods have included analysis, demonstration, and test.

The following verification procedure may be used for guidance.

"Simulated foreign object damage shall be applied to the (a) critical stage blades at one or more sections of the (b) of the airfoil. The damage applied shall produce at least the stress concentration factor (K_t) of 3.3.2.2. Following the foreign object damage application, the damaged blades shall be tested to the life required in 3.4.1.1. At the completion of the test, there shall be no evidence of blade failure or flaw sizes beyond values allowed by the in-service inspection flaw size of 3.4.1.7.3 as the result of the foreign object damage. Sufficient instrumentation for monitoring the structure of the engine shall be included in the test engine."

The following should be used to tailor the preceding guidance paragraph:

(a) The first three stages of the compression system are usually considered the critical stages for FOD damage.
(b) The leading edge, or at stage(s) and blade location(s) where the highest stresses of 3.3.2.2 occur.

Since notched blades are an HCF concern, they should be tested for the HCF life requirements per 4.4.1.5.2.
Background:
The locations selected for simulated FOD should be those most sensitive to FOD. Typically, the critical location is where a combination of steady state and vibratory stresses combine, and results in the lowest fatigue life. The addition of a stress riser, resulting from FOD, at this critical location further degrades the life of the airfoil. The engine test cycle should be in accordance with the endurance test. A successful engine test will demonstrate that the engine design is robust enough to safely meet the test requirements.

It is recommended that LCF and residual life analysis of 4.4.1.5.2 and 4.4.1.7.1, respectively, be reviewed to ensure proper blade and stage locations are used in the test.

VERIFICATION LESSONS LEARNED (A.4.3.2.2)

Past engine programs have shown that FOD ingestion and subsequent engine repair are a problem aboard aircraft carriers, because it requires engine module rework or extra maintenance to blend out damage.

A.3.3.2.3 Ice ingestion.

The engine shall operate and perform in accordance with Table IX, during and after ingestion of hailstones and sheet ice at the takeoff, cruise, and descent aircraft speeds. The engine shall not be damaged beyond field repair capability after ingesting the hailstones and ice.

REQUIREMENT RATIONALE (A.3.3.2.3)

Sufficient structural capability is needed to tolerate ingestion of environmentally generated ice (hailstones), ice shed from the air vehicle, and engine inlet generated ice.

Particles or chunks of ice can be dislodged or break off of inlet duct components such as cowl lips, boundary layer bleed wedges, inlet accessory covers, and variable inlet spikes, and cause compressor damage.

REQUIREMENT GUIDANCE (A.3.3.2.3)

The following should be used to tailor table IX:

For inlet capture area of 0.065 m^2 (100 $in.^2$) the engine should be capable of ingesting one 25 mm (1.0 in.) diameter hailstone. For each additional 0.065 m^2 (100 $in.^2$) increase of the initial capture area (0.065 m^2 [100 $in.^2$]), supplement the first hailstone with one 25 mm (1.0 in.) and one 50 mm (2.0 in.) diameter hailstone. The engine should be capable of ingesting pieces of ice of various sizes and shapes including spears, slabs and sheets. Past engine programs have used 5–8 and 7–9 pieces with one piece weighing at least 0.34 kg (0.75 pounds). For turbofan engines the amount of ice has ranged from 2.3 to 4.1 kg (5 to 9 pounds) of total ingested weight.

Within 5 seconds after an ice ingestion event, the engine thrust or power should be at least 95% of the thrust or power immediately prior to the event. The hailstones and sheet ice should be between 0.80 g/cm^3 (50 $lb./ft^3$) and 0.90 g/cm^3 (56 $lb./ft^3$) specific gravity. Hailstones should be ingested at typical takeoff, cruise, and descent conditions. Sheet ice should be ingested at typical takeoff and cruise condition.

Background:

All-weather aircraft engines should be designed to withstand potential hail conditions. An engine should also have some capability to ingest, without major damage, chunks or sheets of ice which may dislodge or break off of inlet duct components, such as cowl lips, inlet ramps or doors, inlet accessory covers, and air vehicle surfaces.

REQUIREMENT LESSONS LEARNED (A.3.3.2.3)

Past engine programs have used these ice ingestion requirements:

Airflow kg/s (pps)	*No. of Pieces*	*Weight* Kg (lb.)	*Velocity* km/hr (ft/sec)	*Miscellaneous Information*
112 (246)	7–9	2.3 (5)	54 (50)	no piece weighing greater than 0.34 kg (0.75) lb.
118 (260)	7–9	2.3 (5)	54 (50)	no piece weighing greater than 0.34 kg (0.75 lb.)
161 (355)	5–8	4.1 (9)	not specified	no piece less than 0.4 kg (1 lb.), one 0.9 kg (2 lb.) spear 114 cm (45 in.) long

Engines that have inlet guide vanes and lack adequate anti-icing or deicing provisions have had operational restrictions and increased maintenance workloads when exposed to

icing conditions. The problems were eliminated by providing adequate anti-icing systems that reduced inlet case ice accumulation and resultant fan blade damage. Whereas the damage from inlet case ice shedding is a maintenance problem (blending and replacement of fan blades), ice shed from the air vehicle or environmentally generated ice can be a safety of flight concern if sufficient structural capability in the engine design is not provided.

Numerous incidents of axial-flow compressor damage caused by ice ingestion are on record. Some of these resulted in complete engine failure and disintegration of the engine.

The Engine L, on the Navy's Aircraft B, passed its Full Scale Development (FSD) icing condition requirement by similarity. However, during fleet operations, engines experienced damage from ice ingestion events. The damage occurred when ice, formed on the inlet lip and duct walls during flight, was dislodged and ingested during descent in warm weather and during hard carrier landings.

Naval Research Laboratory Report 9025, dated 30 December 1986, states that about 525 mishaps related to ice ingestion have occurred on U.S. Navy aircraft from 1964 through 1984. It mentions that the Engine J (Aircraft I) often sustained compressor blade damage that was substantial or required an overhaul. Engine J had not been tested for ice ingestion during qualification tests so the effects of ice ingestion were unknown when the engine entered service. It became apparent in field deployment that ice ingestion was a concern and this may have been determined earlier if an ice ingestion test had been conducted during development of the engine.

A.4.3.2.3 Ice ingestion.

The requirements of 3.3.2.3 shall be verified by:

VERIFICATION RATIONALE (A.4.3.2.3)

Engine ice ingestion verification is needed to ensure satisfactory engine performance is maintained in icing conditions throughout the aircraft flight envelope.

VERIFICATION GUIDANCE (A.4.3.2.3)

Past verification methods have included analysis, demonstration, and test.

The test procedure should require the engine to run for at least 5 minutes following ice ingestion, before it is shut down for inspection. During the ingestion test, high speed photographic coverage should be taken. Sufficient instrumentation for monitoring the structure of the engine should be included in the test engine.

The procedures to be used for introduction of the hailstones and sheet ice at the engine inlet and the engine power settings and speed at which the hailstones and sheet ice are to be ingested should be specified in the pretest data. The temperature of the ice should be between −2.2 and 0 °C (28−32 °F). The test procedure for sheet ice ingestion should require the most severe ice velocities representing ice shedding off the aircraft inlet lip.

VERIFICATION LESSONS LEARNED (A.4.3.2.3)

After undergoing icing tests behind a tanker, Aircraft I with Engine J sustained severe damage from ice when the aircraft descended to a warmer altitude and inlet ice was ingested by the engine.

For turboshaft engines the most severe ice ingestion velocities may occur at low velocities reflecting the ingestion of ice shed from the inlet.

A.3.3.2.4 Sand and dust ingestion.

The engine shall meet all requirements of the specification during and after the sand and dust ingestion event specified herein. The engine shall ingest air-containing sand and dust particles in a concentration of (a) mg sand/m^3. The engine shall ingest the specified course and fine contaminant distribution for (b) and (c) hours, respectively. The engine shall operate at intermediate thrust for TJ/TFs or maximum continuous power for TP/TSs with the specified concentration of sand and dust particles, with no greater than (d) percent loss in thrust or power, and (e) percent gain in specific fuel consumption. Helicopter engines shall ingest the 0–80 micron (0–3.15×10^{-3} in.) sand and dust of 4.11.2.1.3 in a concentration of 53 mg/m^3 (3.3×10^{-6} lb/ft^3) air for 54 hours and inspection shall reveal no impending failure.

REQUIREMENT RATIONALE (A.3.3.2.4)

The operation of aircraft in sand and dust environments can result in serious erosion damage to engine parts. Sand and dust particles are highly abrasive and tend to erode the thin metal tips and trailing edges of gas turbine engine compressor blades and vanes.

Sand and dust ingestion is also needed to determine the effect on surface coatings.

Engine power loss, surge margin loss, and specific fuel consumption gain may adversely affect system safety.

REQUIREMENT GUIDANCE (A.3.3.2.4)

Table XXXV should be used to tailor the specification paragraph.
Background:
This requirement is based upon a severe but realistic potential service ground environment. It is recognized, however, that the time the engine is subjected to the concentration of sand and dust particles is quite dependent upon the particular engine and air vehicle contribution.

The coarse and fine sand and dust particle size is representative of field deployment where pilots will train in the United States desert areas and be sent to the Middle East desert as in Operation Desert Shield and Desert Storm.

Large particles are more likely to cause erosion on airfoils (blades and stators) while small particles are more likely to block cooling holes in the turbine and cause corrosion. The SiO_2 in both particle size distributions are likely to melt in the combustor discharge gases and be deposited on first stage turbine nozzle vanes. A verification should be made to determine the effect of different sand compositions on the combustor and HPT at elevated temperatures.

Notes on sand and dust concentration in guidance:

The thrust or power loss above should be verified at constant turbine temperature for all engine classes. If verifying at constant commanded power setting, the engine thrust or power loss will be less. This is because engines commanding constant fan speed tend to increase thrust as components deteriorate rather than decrease. SFC loss should be verified at constant thrust or power output.

The ratio of thrust or power loss to SFC loss varies with engine cycle. The ratio of shaft power loss to SFC loss is as high as 3:1 for typical helicopter engines. The relative losses can be verified by calculating performance with changes in compressor efficiency.

The Air Force ATF sand and dust requirement is the MIL-E-87231 and MIL-E-5007D and MIL-E-8593A sand and dust contaminant requirement at a "$53\,mg/m^3$ (3.3×10^{-6} lb./ft^3) of air concentration" with a 2 hour test allowing a 10% loss of thrust and a 10% increase in SFC. Recent Army helicopter engine specifications since 1971 have all used "C-Spec" (MIL-E-5007C) sand with a concentration of $53\,mg/m^3$ (3.3×10^{-6} lb./ft^3). The Engine D specification added an additional 54 hour sand test with 0–80 micron ($0–3.12 \times 10^{-3}$ in.) AC Fine air cleaner test dust. The Engine H specification uses a 0–200 micron ($0–7.87 \times 10^{-3}$ in.) sand (AZ Road Dust Coarse) at a "$53\,mg/m^3$ (3.3×10^{-6} lb./ft^3) of air" concentration with a 20 hour test allowing a 10% loss of power and a 10% increase in SFC.

The deterioration factors for power and SFC loss may be approximately the same for higher pressure ratio engines. Helicopter engines, with lower pressure ratios, experience power loss more rapidly than SFC loss (at constant T41). The factors may be more equal for higher pressure ratio engines.

Coarse sand produces blade erosion and a near term loss of compressor efficiency. Fine sand causes plugging of cooling holes, deposits, and long-term engine distress. Fine sand tests should be conducted to determine the engine's vulnerability to airhole plugging and nature of deposits. Deposits formed also depend upon the composition of the sand.

Most of the arid regions of the world correspond to "C-Spec" sand in size except regions in the Middle East. Saudi sand, in general, is close to "C-Spec" in size, very sharp particle shape, with high alumina content. When mixed with water (i.e., waterwash), Saudi sand may form cement, which when heated may form porcelain. Saudi fine sand has been encountered at as high as 4572 m (15,000 feet). Very fine sand is found in parts of Israel and some other nearby regions.

The performance loss due to coarse sand ingestion depends upon the total quantity of sand ingested, particle size, and engine power setting. Total quantity of sand depends upon engine airflow rate, sand concentration in the air, and duration of the test ($53\,mg/m^3[3.3 \times 10^{-6}\,lb/ft^3]$ for 50 hour may be equivalent to $530\,mg/m^3[3.3 \times 10^{-5}\,lb/ft^3]$ for 5 hour). Particle size ingested varies rapidly with hover height, for clouds created by rotor downwash. Particle size is largest near the surface and decreases rapidly with height. Power setting affects the effectiveness of the IPS. The IPS is most effective at high power settings where high airflows result in high velocities. Filtration is needed to be effective at all power settings or with the finer particles. A helicopter on the ground at low engine power settings could conceivably experience more sand damage than when hovering a few feet above the ground at high power. A comprehensive sand test should, therefore, consider sand concentration level, composition, particle size in the bed, particle size in the cloud, hover height, time duration, and power setting. The present sand test (constant concentration, time, and power setting regime) forms a good benchmark for engine vulnerability to sand erosion, but may not be indicative of actual field experience.

USAF bases and commercial airports are permitted to sand icy taxiways and runways with sand particles of up to 0.475 cm (0.187″). If prolonged operation in these environments is anticipated, the FOD potentials of this size sand need to be considered. AFI 32-1045 and FAA Circular 150/5200-30A should be consulted for specific information on allowable sand dimensions and quantities.

While this requirement paragraph is oriented around thrust or power and SFC performance, it is stated that the engine has to meet all requirements of the specification. This includes life and performance effectiveness of special technology materials and features on the engine inlet or front face which may be vulnerable to sand erosion and FOD.

REQUIREMENT LESSONS LEARNED (A.3.3.2.4)

The operation of aircraft in sand and dust environments has resulted in serious erosion damage to engine parts. Sand and dust particles are highly abrasive and tend to erode the thin metal tips and trailing edges of gas turbine engine compressor blades and vanes.

Helicopter operations are most significantly impacted by the sand and dust problem, although fan blade leading edge damage has been experienced on Engine L in Aircraft B as a result of operation "near sandy, dry desert-like areas such as NAS Miramar." One source pointed out that the "accelerated replacement of erosion damaged helicopter turbines in Southeast Asia was estimated to cost the U.S. Government about $150 million a year" (during the Vietnam war period). The finer particles of sand and dust have been known to clog turbine cooling passages and cause engine failures. Sand and dust has been encountered several hundred miles out at sea as well as over land masses.

Sand has been determined to be more detrimental during foreign operation due to the differences found in the sand composition. A lower melting point has been observed in foreign sand test samples which allows the sand to melt and form a glaze coating on the turbine airfoils. Spalling of the coating and base metal then occurs.

Due to the unexpected turbine blade failure and short life encountered in engines with gas temperatures in excess of 1093 °C (2000 °F), special consideration in blade design should be taken into account. The soil analysis of Saudi Arabia and other middle eastern countries reveals that very high amounts of sulfur, calcium, and magnesium exist. A study has shown that an HPT blade failure occurred because of excessive sulphidation. At high temperatures, a flux or coating of calcium sulfate and magnesium sulfate attaches to the blade, attacks the base metal, and corrodes it, leading to failure.

USAF Aircraft A bases have raised questions about operating on taxiways and runways with sand particle sizes specified in FAA and Air Force Instructions. Subsequent analysis revealed that Aircraft A engines are vulnerable to stage 1 fan FOD when operating on sanded areas. Sand and dust ingestion and subsequent performance is a primary cause of engine removal on helicopters.

References:

Particle distribution: "Development of the Lycoming Inertial Particle Separator", H.D. Conners, presented at the Gas Turbine Conference & Products Show, Washington DC, 17–21 March 1968.

Particle densities: ASME 70-GT-96, J.C. Arribat, ASME Gas Turbine Conference, Brussels, Belgium, 24–28 May 1970.

Particle distribution: SEA AIR 947, Issue 1, 2/71.

Blade damage including blade and vane erosion, secondary airflow deposits resulting in power reduction and stall margin loss. ASME 68-GT-37, G.C. Rapp and S.H. Rosenthal, presented at Gas Turbine Conference & Products Show, Washington DC, 17–21 March 1968.

Particle distribution: "Evaluation of the Dust Cloud Generated by Helicopter Blade Downwash," Sheridan Rogers, MSA Research, Proceedings of the 7th Annual National Conference on Environmental Effects on Aircraft and Propulsion Systems, 25–27 September 67. Single helicopter dust concentration reached 16.2 mg/cu ft [572 mg/m^3

(35.7×10^{-6} lb./ft^3)] takeoff and approach reach 40 mg/cu ft (1413 mg/m^3 [88.2×10^{-6} lb/ft^3]). Two helicopter levels of 64 mg/ft^3 (2260.1 mg/m^3 [141.1×10^{-6} lb/ft^3]) were reached.

Particle distribution: Kaman Report No. R-169, "Amount of Dust Recirculated by a Hovering Helicopter," dated 26 December 1969. Densities ranged from 0.29 gm/cu ft to 26 gm/cu ft.

A.4.3.2.4 Sand and dust ingestion.

The requirements of 3.3.2.4 shall be verified by:

VERIFICATION RATIONALE (A.4.3.2.4)

The effect of sand ingestion on the performance, bleed air quality, and internal air cooling system must be verified.

VERIFICATION GUIDANCE (A.4.3.2.4)

Past verification methods have included analysis, inspection, and test. ISO/FDIS 12103-1 can be used for guidance on Arizona test dust.

The contractor should propose a sand ingestion test to verify the operation and performance of the engine at worst case power levels derived from the mission profile.

This test could be combined with the AMT. If combined, the sand test should occur after post-AMT recalibration and endurance test completion, due to performance degradations of the engine.

The following procedure may be used as a verification method.

For fixed wing and VSTOL engines:

"During the engine test, the coarse sand and dust shall be ingested first, with the fine particle sand and dust ingested afterward. An engine disassembly and inspection shall be conducted between the coarse and fine sand tests as specified by the Using Service.

The engine shall be tested at Intermediate thrust, with sand and dust ingested at the concentration levels and for the length of time specified in 3.3.2.4. During each hour of operation, at least one deceleration to idle and acceleration to maximum augmentation shall be made, with power lever movements of 0.5 seconds or less. If an anti-icing system is provided, ten periods of one minute operation of the anti-icing system shall be performed during the first test hour. During the entire test, maximum customer bleed air shall be extracted from the engine. The customer bleed air shall be continually filtered and the total deposits measured and recorded. Following the post-test performance check,

the engine shall be disassembled to determine the extent of erosion, and the degree to which the contaminant may have entered critical areas in the engine. The test will be considered satisfactorily completed when the criteria of 3.3.2.4 have been met and the teardown inspection reveals no failure or evidence of impending failure."

For helicopter engines:

"The engine shall be tested with a 0–80 micron (0-3.15×10^{-3} in.) sand and dust ingested at the concentration levels specified in 3.3.2.4. The engine shall be tested for 9 hours at maximum, 27 hours at intermediate, and 18 hours at maximum continuous, for a total of 54 hours with not less than 27 starts. The test cycle shall be 10 minutes at maximum, 20 minutes at maximum continuous and 30 minutes at intermediate. All ratings shall be initially set to measured gas temperature associated with rated rotor inlet temperature. After test initiation, the engine shall be run at a constant gas generator speed unless the measured gas temperature associated with the T4.1 deterioration limit is reached in which case the measured gas temperature will be held constant. This test shall be terminated and the engine shall be removed and disassembled if power deterioration based on measured gas temperature is excessive or if engine failure or impending failure is evident. The engine shall be tested with the IPS if it is an integral part of the engine design. During each hour of operation, at least two deceleration to idle and acceleration to maximum continuous speed shall be made, with power lever movements of 0.5 seconds or less. A calibration test shall be performed at the beginning, at 25 hours and end of the test run. The engine shall be inspected at 25 hours by borescope and other visual techniques that do not require disassembly of the engine. Upon completion of the test run the engine shall be disassembled in such a way that the contamination displacement is minimized. The engine shall be disassembled to determine the extent of sand erosion, and the degree to which sand may have entered critical areas in the engine. Each major rotating and stationary component subject to the effects of sand ingestion shall be weighed at engine build, disassembly and after cleaning. The test will be considered satisfactorily completed when 54 hours of testing have been completed and the teardown inspection reveals no failure or evidence of impending failure."

"The engine shall be tested with the coarse sand at maximum continuous rated measured temperature with sand and dust ingested at the concentration levels and the length of time specified in 3.3.2.4. The engine shall be tested with the IPS if it is an integral part of the engine design. During each hour of operation, at least one deceleration to idle and acceleration to maximum continuous rated measured temperature shall be made, with power lever movements of 0.5 seconds or less. If an anti-icing system is provided, ten periods of one minute operation of the anti-icing system shall be performed during the first hour of each five hour cycle. The engine shall be shut down and cooled at least 12 hours following each five hours of sand ingestion. During the entire test, maximum customer bleed air shall be extracted from the engine. The customer bleed air shall be continually filtered, and the total deposits measured and recorded. If an engine internal washing system

is provided, it shall be demonstrated once during each shut down. Components such as air-oil coolers with exposure to inlet sand and dust conditions shall be considered inlets for this test but a rig test may be performed to satisfy the requirements herein. Following the post-test performance check, the engine shall be disassembled to determine the extent of sand erosion, and the degree to which sand may have entered critical areas in the engine. The test will be considered satisfactorily completed when the criteria of 3.3.2.4 have been met and the teardown inspection reveals no failure or evidence of impending failure."
Background:
The recommended text decreases the operational time in the extreme sand and dust environment from ten hours to two hours for turbofan and turbojet engines. Engine contractors have been unwilling in the past to guarantee their engines for ten hours (helicopter subjected to the severe Vietnam sand and dust environment typically used inlet filtration systems). The time requirement will have to be negotiated with each engine contractor in specific future specification negotiations based upon the intended usage in regions of the world where sand will be a concern.

The sand concentration should be calculated with customer bleed air extraction. The anti-icing switch should be activated five times during each hour of sand ingestion at equally spaced intervals. The test should be conducted with a thrust bed and load cell measurement of thrust in lieu of calculating thrust by EPR. Disassembly and inspection between the coarse and fine sand tests should be conducted for 45.4 kg/s (100 lb./sec) airflow or smaller engines.

VERIFICATION LESSONS LEARNED (A.4.3.2.4)

The Engine V sand and dust test did not use the recommended sand and dust mixture due to commercial unavailability of the mixture. The specification for fine sand calls for a particle size distribution which cannot be obtained commercially. Specifically, calcite and gypsum could not be obtained with a particle size distribution to match the specified particle size distribution. Table XXXVIa and b shows the closest particle size distributions which the Engine V sand and dust test team could find along with the required size distribution.

Appendix I*
Computation of High Cycle Fatigue Design Limits under Combined High and Low Cycle Fatigue

Joseph R. Zuiker

ABSTRACT

Applications in rotating machinery often result in stress states that produce both low cycle fatigue (LCF) damage in addition to the damage produced from the high frequency or high cycle fatigue (HCF) vibratory loading. While the Haigh diagram takes into account the vibratory as well as the steady stress amplitudes for a fatigue limit corresponding to a (large) given number of cycles, it does not consider the combined effects of LCF and HCF. To account for the combined effects analytically, an initiation model for combined cyclic fatigue (CCF) is coupled with a threshold fracture mechanics crack propagation model to predict fatigue thresholds for CCF. The results are contrasted with the HCF allowable stresses represented in a constant-life Haigh diagram. Experimental data from the literature for a Ti-6Al-4V alloy are used to demonstrate the viability of the analysis and the limitations of the use of the Haigh diagram in design. Comments on the limitations on the use of a Haigh diagram for combined HCF–LCF loading are presented.

NOMENCLATURE

C	Paris-Walker law constant
CCF	combined cycle fatigue
d	Paris-Walker law constant
d	damage parameter
d_i	initiation phase damage parameter
D	diameter of rod
HCF	high cycle fatigue
K_t	stress concentration factor
LCF	low cycle fatigue
LEFM	linear elastic fracture mechanics

* This document was contributed by Dr. Joseph Zuiker, a former employee of the Air Force Research Laboratory. It is based on unpublished work conducted by him while with the Air Force. Dr. Zuiker is currently with General Electric Company Power Systems Division.

m	Paris-Walker law constant
n	number of HCF cycles per LCF cycle
N	number of CCF cycles
$N_{i,CCF}$	number of cycles to crack initiation in CCF loading
$N_{i,HCF}$	number of cycles to crack initiation in HCF-only loading
$N_{i,LCF}$	number of cycles to crack initiation in LCF-only loading
Q	stress intensity range ratio $= \Delta K_{HCF}/\Delta K_{LCF}$
r	exponent for initiation life equation
R	stress ratio $= \sigma_{min}/\sigma_{max}$
γ	crack growth rate acceleration factor
ΔK_{HCF}	stress intensity factor range of HCF cycles
ΔK_{LCF}	stress intensity factor range of LCF cycles
ΔK_{th}	threshold stress intensity factor range
ΔK_{onset}	ΔK_{LCF} value at which HCF crack growth becomes active in CCF
$\Delta K_{th,o}$	ΔK_{th} at $R = 0$ (in CTOD-based model)
$\Delta\varepsilon_{HCF}$	strain range of HCF cycle
$\Delta\sigma$	stress range
$\Delta\sigma_{end}$	endurance limit stress range below which no initiation damage is caused
$\Delta\sigma_{HCF}$	stress range of HCF cycle
$\Delta\sigma_{LCF}$	stress range of LCF cycle
σ^*	constant for initiation life equation
σ_a	alternating stress
$\sigma_{a.eq}$	equivalent alternating stress at $R = 0$ for a stress state at $R \neq 0$.
$\sigma_{a,HCF}$	alternating stress of HCF cycle to be converted to equivalent $R = 0$ cycle
σ_{fs}	alternating stress causing failure in a specified number of cycles at $R = -1$
σ_m	mean stress
$\sigma_{m,HCF}$	mean stress of HCF cycle to be converted to equivalent $R = 0$ cycle
σ_{ult}	ultimate strength
σ_y	yield strength

INTRODUCTION

Design of components for HCF must generally account for the detrimental effects of a superimposed mean stress. This accounting is often in the form of an alternating versus mean stress (Haigh) diagram that shows allowable vibratory stress amplitude as a function of applied mean stress for a specified life. In many cases little or no data are available for conditions other than fully reversed loading where the stress ratio $R = \sigma_{min}/\sigma_{max} = -1$, and tensile overload ($R = 1$) or ultimate stress, and assumptions such as a straight line fit must be made in order to interpolate between these limiting cases.

A more general Haigh diagram can be produced using data at various values of mean stress and a specified number of cycles to failure, e.g. 10^7, as obtained from *S–N* curves and plotting the locus of points. For any of these plots, the number of cycles is typically taken to be those corresponding to a "runout" condition, perhaps 10^8 or even 10^9, but there are few data available to demonstrate that a true runout condition ever exists for a material. This has been shown to be the case in several studies on titanium (cf. [1, 2]). For convenience and practicality, the number of cycles chosen is taken to correspond to the region where the *S–N* curve becomes nearly flat with increasing number of cycles, or is selected such that the number of cycles exceeds that which might be encountered in service. In some cases, neither condition may be satisfied. For design purposes, because of the statistical variability of fatigue data, particularly in the long-life regime where *S–N* curves tend to be close to horizontal, Haigh diagrams commonly represent a statistical minimum. For the purposes of the present discussion, only average material property data will be discussed.

The straight line Goodman assumption and corresponding Haigh diagram are widely used in design for HCF. Henceforth, we shall consider only the Goodman assumption, but it is understood that any discussion of the Haigh diagram is equally valid for any other assumptions regarding the shape of the diagram. A critical issue in the use (or misuse) of the Haigh diagram in design is the degree of initial or service induced damage that may be present in a component, but may not be present in the material used for generation of the Haigh diagram. In the present study, we deal with damage induced by superimposed LCF. If such damage is present, the Haigh diagram is not valid for the material because it represents "good" or undamaged material. Therefore, a design methodology which considers the development of damage from sources other than the constant amplitude HCF loading must be used to account for the different state of the material. Turbine engine components, for example, which are subjected to HCF, are typically subjected to LCF in addition because the non-zero mean stress is achieved through the centrifugal loading typical of operation. Each startup and shutdown constitutes an LCF cycle. Thus, the component experiences combined HCF and LCF or CCF and, for design purposes, the effect of LCF loading on the HCF life should be considered.

In this appendix, we present a simple model for the CCF of a typical turbine engine alloy and use data from the literature to predict the effect of superimposed LCF on the HCF capability of the material. Here, LCF refers to large amplitude, low frequency cycles whose total number is typically less than 10^3–10^4, while HCF refers to small amplitude, high frequency cycles at high mean stress, whose number generally exceeds 10^6–10^7. In the following sections, a prediction methodology is described including descriptions of the initiation life model, the propagation life model, the experimental data used to calibrate the model, and the assumptions concerning the interaction of the HCF and LCF cycles. Then, numerical predictions are presented to confirm the model accuracy and

show its sensitivity to a variety of factors. Finally, we close with a discussion of the results, conclusions, and possible future efforts.

It is important to note a principal difference between this work and the majority of the previous studies on CCF. While most of the literature has been concerned with the effect of superimposed HCF on the LCF life of materials and structures, this appendix deals with the effect of superimposed LCF on the HCF capability of the material and further and, further, addresses total life as a sum of initiation and propagation phases, the latter of which uses fracture mechanics analysis.

LIFE PREDICTION METHODOLOGY

In order to illustrate HCF–LCF interactions, analytical predictions are made of the total fatigue life and presented as a Haigh diagram for a material experiencing 10^7 HCF cycles divided equally over N LCF loading blocks. It is assumed that total life can be divided into two distinct phases: a crack initiation phase, and a crack propagation phase. Each CCF loading block consists of a low frequency cycle over which the material is loaded from zero stress to a given mean stress and held while $n = 10^7/N$ high frequency cycles are superimposed about the mean stress as shown schematically in Figure I.1. The details of the analysis follow.

Initiation life

During initiation the material is assumed to be uncracked. Initiation damage, d_i, is accumulated over each HCF and LCF cycle until $d_i = 1$ at which point it is assumed that a crack of depth a_i has initiated. The number of LCF cycles required to reach $d_i = 1$ is

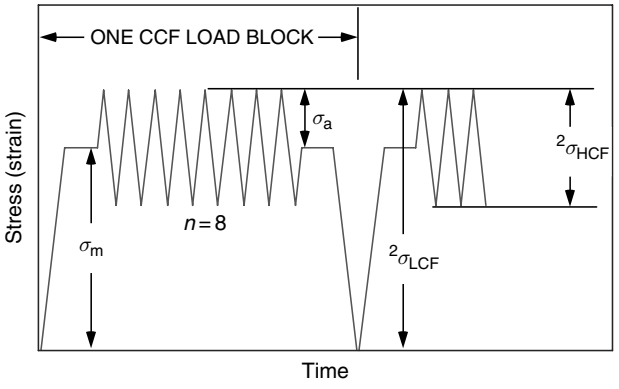


Figure I.1. Idealized combined cycle fatigue load block.

defined as $N_{i,LCF}$. For LCF-only cycling applied at $R = 0$ ($\Delta\sigma = 2\sigma_a = 2\sigma_m$), a power law function of the applied stress range using a form similar to the Basquin equation is used such that

$$N_{i,LCF} = \sigma^*(2\sigma_a)^r \tag{I.1}$$

where σ_a is the alternating stress amplitude and σ^* and r are constants. In fitting the response of actual materials, multiple sets of constants are used over specific ranges of σ_a such that Equation (I.1) forms a piece-wise linear approximation to the actual material response when plotted on a log-log scale. Equation (I.1), which is written for LCF-only loading ($R = 0$), can also be used for HCF cycles at $R \neq 0$ by substituting an equivalent alternating stress amplitude, $\sigma_{a,eq}$. The equivalent alternating stress is obtained by moving along a line of constant life on a Haigh diagram from the point defining the HCF cycle (σ_m, σ_a) at $R \neq 0$ to a point at $R = 0$. The form of the constant life line must be assumed. Here, we postulate that the straight-line Goodman assumption governs mean stress effects on initiation life in the same manner as it governs mean stress effects on total life. That is, straight lines passing through ($\sigma_{ult}, 0$) exhibit constant initiation life. The fully reversed stress to initiation, $\sigma_{fs,i}$ is defined as the y-axis intercept of a line passing through points defining the HCF load cycle at $R \neq 0$ ($\sigma_{m,HCF}$, $\sigma_{a,HCF}$) and ($\sigma_{ult}, 0$). Fully reversed initiation stress, $\sigma_{fs,i}$ can be defined in terms of $\sigma_{a,HCF}$, $\sigma_{m,HCF}$, and σ_{ult}; and substituted into the modified Goodman equation for σ_{fs}, the fully reversed alternating stress amplitude. The equivalent alternating stress is then obtained by setting $\sigma_a = \sigma_m = \sigma_{a,eq}$ and solving for $\sigma_{a,eq}$, as

$$\sigma_{a,eq} = \frac{1}{\left(\dfrac{1}{\sigma_{ult}} + \dfrac{1}{\sigma_{a,HCF}} - \dfrac{\sigma_{m,HCF}}{\sigma_{a,HCF}\sigma_{ult}}\right)} \tag{I.2}$$

Thus, the initiation life due to HCF cycles, $N_{i,HCF}$, is obtained via Equation (I.1) by replacing σ_a with $\sigma_{a,eq}$ from Equation (I.2).

To determine the initiation life under combined HCF–LCF loading, the linear damage summation model [3, 4] is used such that the initiation life, in CCF blocks, is

$$N_{i,CCF} = \frac{1}{\left(\frac{1}{N_{i,LCF}} + \frac{n}{N_{i,HCF}}\right)} \tag{I.3}$$

where $N_{i,CCF}$ is the initiation life under CCF in terms of CCF load blocks. The linear damage summation model has been criticized for its inability to account for load sequencing affects. However, it is noted that when different cycles are mixed evenly over the life of a component, the Palmgren–Miner rule gives acceptable results (cf. [5, 6]). More advanced nonlinear damage summation models have been proposed. While many give

better results than the linear damage summation model, they are often limited to specific materials or conditions and require experience to be used with confidence [7].

After $N_{i,CCF}$ loading blocks, a crack, which is amenable to fracture mechanics techniques for predicting crack growth, is assumed to have formed in the component and grows according to LEFM to failure. The size, shape, and location of the crack must be assumed and, here, will be taken from experimental data in the literature.

For cases in which $N_{i,CCF} \gg 1$, it may be sufficiently accurate to round $N_{i,CCF}$ to the nearest integer and begin crack propagation with the next load block. In other cases this may not be accurate and it is important to determine at what point in the load block the crack initiates and crack propagation begins. As a first approximation, it is assumed that all initiation damage in each cycle occurs during the loading portion of the cycle. Thus, if $N_{i,CCF}$ is fractional, the first portion of the fractional cycle is attributed to the LCF cycle; the remainder of the fractional initiation damage is attributed to HCF cycles, and during the remaining portion of the load block the crack is assumed to have initiated and begins to grow in HCF.

Initiation example

Consider the case of a specified loading sequence consisting of $n = 8000$ HCF cycles per CCF load block. For a specified maximum stress and HCF stress range, the initiation lives are found as $N_{i,LCF} = 1.6 \times 10^4$ and $N_{i,HCF} = 3 \times 10^7$. In this case, the initiation damage per CCF load block due to LCF is $d_{i,LCF} = 1/N_{i,LCF} = 6.250 \times 10^{-5}$, the initiation damage per CCF load block due to HCF is $d_{i,HCF} = n/N_{i,HCF} = 2.667 \times 10^{-4}$, the total initiation damage per CCF load block is $d_{i,CCF} = d_{i,LCF} + d_{i,HCF} = 3.292 \times 10^{-4}$, and $N_{i,CCF} = 1/d_{i,CCF} = 3037.975$. Thus, after 3037 CCF load blocks, $d_i = 0.999679$. During the loading portion of the LCF cycle in load block 3038, d_i increases by 6.250×10^{-5} to 0.999742×10^{-n}. Each HCF cycle then increases the damage by 3.333×10^{-8} until the crack initiates after 7740 HCF cycles in load block 3038. Thus, during HCF cycle 7741 in CCF load block 3038, the crack is considered to have initiated and begins to grow under the assumptions of fracture mechanics.

Propagation life

During the crack propagation phase, the crack grows under the assumptions of linear elastic fracture mechanics. Short crack behavior is neglected. During LCF and HCF cycles, the crack is assumed to grow in mode I following the Paris law as modified by Walker [8] to account for stress ratio effects as

$$\frac{da}{dN^*} = C\frac{(\Delta K)^m}{(1-R)^d} \tag{I.4}$$

Here, C and m are material constants describing the crack growth rate at $R = 0$, and d is a material constant accounting for the higher crack growth rate at higher R for the same

ΔK, an effect attributed to K_{max} or mean stress effects. For LCF cycles, N^* corresponds to a single LCF cycle, ΔK_{LCF} replaces ΔK, and $R=0$. For HCF cycles, N^* corresponds to a single HCF cycle, ΔK is replaced by ΔK_{HCF}, and in general $R > 0$. Equation (I.4) holds for $\Delta K > \Delta K_{th}$ for individual LCF cycles as well as individual HCF cycles provided that the appropriate stress range and value of R are used in each case. In accordance with experimental observations, ΔK_{th} is assumed to be a decreasing function with increasing R. The values of ΔK_{LCF} and ΔK_{HCF} are calculated from $\Delta\sigma_{LCF}$ and $\Delta\sigma_{HCF}$ which are shown in Figure I.1. It can be deduced from the figure that ΔK_{HCF} is typically less than ΔK_{LCF} for a given crack length and, therefore, the threshold in LCF should be reached before that in HCF. However, when considering growth rate per block of cycles, the number of cycles per block, n, if large, could dominate the growth rate if both values of ΔK for HCF and LCF are above threshold.

In the case of tension–compression cycling ($R < 0$), the crack tip is assumed to be open, and the crack growing, only when the applied stress is positive. Thus, the minimum effective stress is always positive or zero, and R never drops below zero in Equation (I.4). This is, however, a minor point as we are most interested in loading typical of turbine engine components in which the mean stress is high, the vibratory stress is relatively low, and $R_{HCF} > 0$.

The specimen is assumed to fail when K_{max} surpasses K_{IC}, or when the crack depth exceeds an appropriate length scale indicative of tensile overload in the specimen, whichever occurs first. Crack growth is calculated for each HCF and LCF cycle, and is assumed to occur during the loading portion of each cycle. Thus, growth increments are determined sequentially for an LCF cycle, n HCF cycles, another LCF cycle, and so on.

Under these assumptions, several failure sequences are possible. The particular sequence encountered is a function of four characteristic crack depths that, in turn, are a function of the material properties and LCF and HCF stress ranges. They are

- a_i – the crack depth at initiation, which is defined by experimental data
- a_{crit} – the crack depth at which K_{IC} is exceeded at the crack tip (or a depth appropriate to the specimen size if a_{crit} exceeds characteristic specimen dimensions), which is a function of $\Delta\sigma_{HCF}$, $\Delta\sigma_{LCF}$, and K_{IC}
- $a_{g,LCF}$ – the crack depth beyond which the crack grows during LCF cycles, which is a function of $\Delta\sigma_{LCF}$ and ΔK_{th} (at $R=0$ for LCF cycles) and
- $a_{g,HCF}$ – the crack depth beyond which the crack grows during HCF cycles, which is a function of $\Delta\sigma_{HCF}$ and ΔK_{th} (at R for HCF cycles).

There are 24 possible permutations of these four crack depths, any of which will produce one of seven failure sequences which are shown in Figure I.2. Path 1 is not likely if reasonable initiation data are available. Path 2 is unlikely for load levels of interest. Paths 4 and 7 produce HCF-only crack propagation, which is a possible failure mode if ΔK_{th} in HCF (at high R) is sufficiently small in comparison with ΔK_{th} in LCF (at $R=0$),

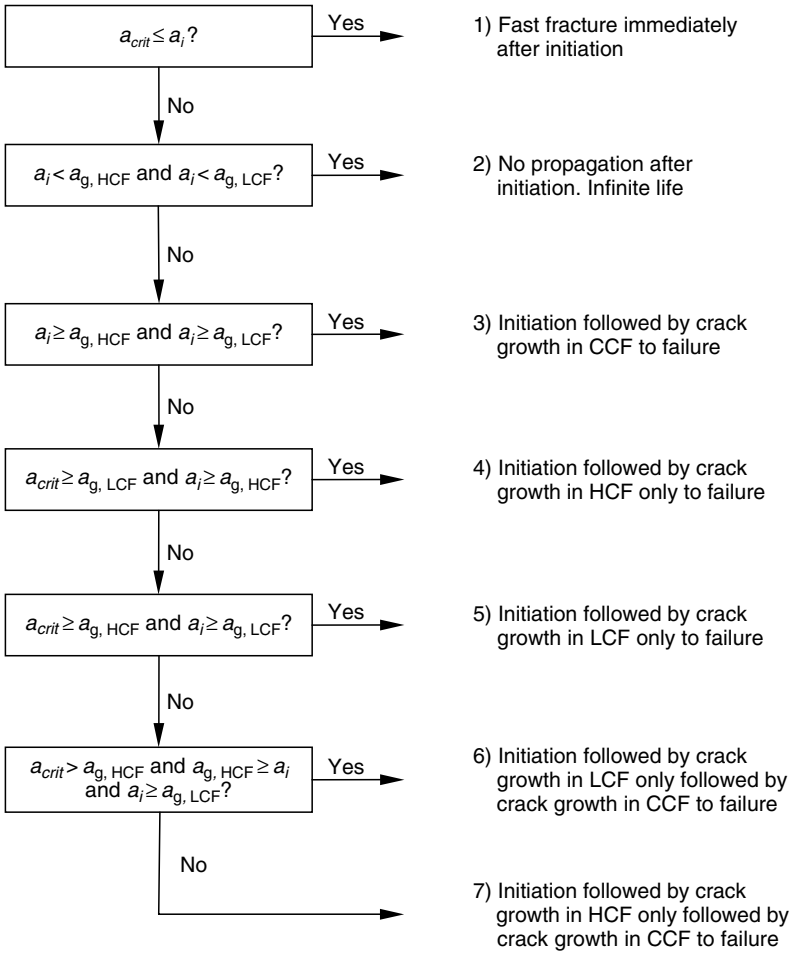


Figure I.2. Flow chart of possible failure sequences under CCF.

and $\Delta\sigma_{HCF}$ is sufficiently large to grow the crack. While this situation depends on the assumed relation of ΔK_{th} with R, neither of these HCF-only crack propagation modes has been observed in any of the numerical calculations reported here. Paths 3, 5, and 6, then, are of the most practical interest.

Model Calibration

In order to calibrate and exercise the model, crack initiation and propagation data on surface-cracked round bars [9] are used. In this study, electropotential drop techniques were used to determine the number of cycles required to produce 50 μm deep surface

cracks in mildly notched ($K_T = 2$) Ti-6Al-4V round bars with an α/β microstructure. Total life was measured in both mildly notched and smooth bars. Chesnutt et al. [10] and Grover [11] reported total life measurements on Ti-6Al-4V materials with a similar microstructure at lower stress levels (and longer lives) at various values of K_T. Using these data, total life estimates for long life tests at $K_T = 2$ were interpolated and are shown, along with the short life data by Guedou and Rongvaux [9], in Figure I.3. A multi-part power law fit to the initiation life curve was generated by connecting the ultimate stress at $N = 1$ to the LCF data from Guedou and Rongvaux [9]. A power law fit to the experimental data was extrapolated to lower stress values. Two scenarios were considered for low stresses. In the first, alternating stress ranges below 300 MPa ($R = 0$) cause no damage. Thus the life is infinite for lower stresses and the final portion of the *S–N* curve is a horizontal line. This stress range was chosen to agree approximately with the observed runout behavior in the long life tests [10, 11]. The contrasting scenario assumes that no endurance limit exists. Any alternating stress causes a finite amount of damage. In this scenario, the *S–N* curve extends downward continuously. Both cases are shown in Figure I.3. The corresponding total life curve was generated by adding the analytical estimate of the propagation life to the initiation life measurement and correlated well with the experimentally measured total life values shown in Figure I.3.

Crack propagation data at $R = 0.05$ and 0.85 [9] were used to determine parameters C, m, and d for the Paris–Walker relation in Equation (I.3). The values used here are $C = 5.376 \times 10^{-12}$, $m = 3.409$, and $d = 1.3$. The values of ΔK_{th} for Ti-6A1-4V are taken

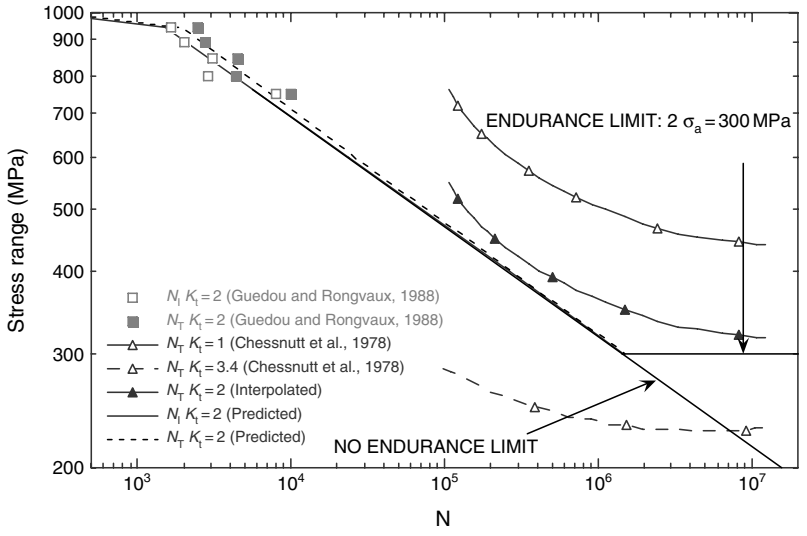


Figure I.3. Predicted and measured values of N_i and total life (N_T) as a function of applied stress range at $R = 0$.

from Hawkyard et al. [12] and are assumed to decrease linearly from $5\,\mathrm{MPa}\sqrt{\mathrm{m}}$ to $2.25\,\mathrm{MPa}\sqrt{\mathrm{m}}$ at $R=0.7$ and maintain values of 5 and $2.25\,\mathrm{MPa}\sqrt{\mathrm{m}}$ at $R<0$ and $R>0.7$, respectively. The stress intensity factor solution of Raju and Newman [13] for surface cracked smooth bars is utilized, and assumptions are made concerning the geometry of the crack such that the stress intensity factor may be approximated as

$$K=\sigma\sqrt{\frac{\pi a}{1.63}}\left(1+\frac{a}{D}\right) \tag{I.5}$$

where a is the crack depth and D is the diameter of the bar. Due to the presence of the notch, the applied stress is multiplied by a K_{T} of 2 in order to determine ΔK_{HCF}, ΔK_{LCF}, a_{crit}, $a_{g,\mathrm{HCF}}$, and $a_{g,\mathrm{LCF}}$. This is an appropriate assumption when the crack is very short. However, as the crack extends out of the notch, it has been shown that the crack growth rate will approach that for $K_{\mathrm{T}}=1$ and a crack depth equaling the total depth of the crack and notch [14]. These assumptions using K_{T} are conservative and will cause the model to underestimate the crack propagation life. However, under the conditions of interest, the propagation life is a small percentage of the total life.

NUMERICAL RESULTS

The numerical algorithm has been implemented on a personal computer and operates in one of two modes. In the first mode, the user specifies σ_{a}, σ_{m}, and n, and the total life corresponding to 10^7 HCF cycles is calculated in terms of CCF load blocks, N. In the second mode, the user specifies σ_{m}, N, and n, and an iterative algorithm is invoked to determine σ_{a} such that the calculated value of N is within a specified tolerance of the requested value of N. Solution time increases with increasing N and increasing fraction of total life spent in crack propagation, especially when the crack is actively growing in both HCF and LCF cycles. For the most computationally intensive cases considered, the solution took no more than one to two minutes on a 100-MHz personal computer.

Correlation with experiment

A limited number of HCF–LCF tests on notched bars were conducted by Guedou and Rongvaux [9]. Ti-6Al-4V bars were cycled at room temperature with $n=1800$ HCF cycles per CCF load block and $R_{\mathrm{HCF}}=0.85$. The resulting initiation lives are shown along with those for LCF-only tests in Figure I.4. All results are plotted as a function of maximum stress $(\sigma_{\mathrm{m}}+\sigma_{\mathrm{a}})$. A power law fit to the LCF-only initiation data is also shown. This fit was used to define the S–N curve shown in Figure I.3 which, in turn, defines the constants for use in the modified Goodman equation over intermediate values of alternating stress range. Predictions for the HCF–LCF initiation life using Equation (I.2) are also shown

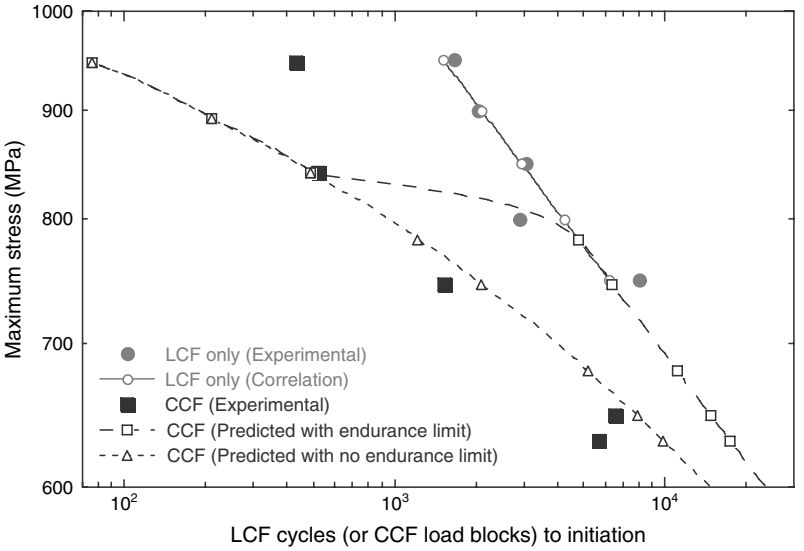


Figure I.4. Comparison of predicted and measured LCF and CCF initiation life for Ti-6-4 [9] with $R_{HCF}=0.85$ and $n=1800$.

for both scenarios: $\Delta\sigma_{end}=300\,\text{MPa}$ and $\Delta\sigma_{end}=0$. As expected, the predictions are identical for cases in which $\Delta\sigma_{HCF} > 300\,\text{MPa}$. At high values of maximum stress, both assumptions overestimate the detrimental effect of HCF cycles on the initiation life. At lower maximum stress levels, the best correlation is found when $\Delta\sigma_{end}=0$.

Figure I.5 shows a similar comparison of experimentally inferred and numerically predicted crack propagation lives for the LCF-only and HCF–LCF tests of Guedou and Rongvaux [9]. The numerical predictions underestimate the propagation lives of the LCF-only tests. This is expected, since K_T at the crack tip has been taken as two over the entire life of the crack. As discussed earlier, this is a conservative assumption which is expected to underestimate the propagation life. Predicted values for the HCF–LCF tests are, of course, the same under either endurance limit assumption. The drastic change in slope is unrelated to that of the finite endurance limit assumption shown in Figure I.4. In Figure I.5, it is a function of ΔK_{th}. The number next to each predicted point corresponds to the fraction of propagation life over which the crack does not grow in HCF. (The crack grows in CCF during the remainder of the propagation life.) The four highest stress predictions begin growing in CCF immediately upon crack initiation (Path 3 in Figure I.2). In these cases, crack propagation life is underestimated by approximately an order of magnitude. At lower values of maximum stress (and constant R_{HCF}), ΔK_{HCF} is initially below ΔK_{th} at crack initiation and the crack must propagate for a period in LCF-only before CCF crack growth can occur (Path 6 in Figure I.2.). Better correlation with experiment is obtained at lower stresses, possibly indicating that the values of ΔK_{th}

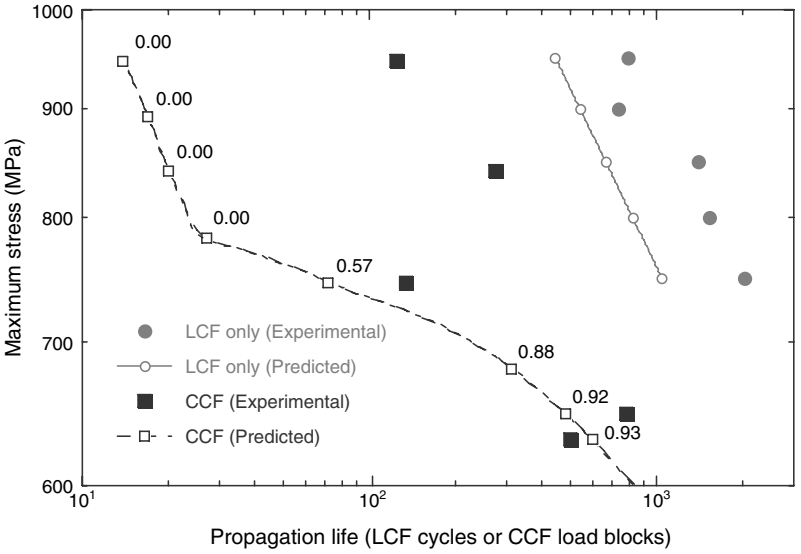


Figure I.5. Comparison of predicted and measured LCF and CCF crack propagation life for Ti-6-4 [9] with $R_{HCF} = 0.85$ and $n = 1800$.

as a function of R used here are lower than those in the material tested. Guedou and Rongvaux [9] estimate $\Delta K_{th} = 3\,\text{MPa}\sqrt{\text{m}}$ at $R = 0.85$, whereas $\Delta K_{th} = 2.25$ at $R = 0.85$ has been used here.

Finally, Figure I.6 shows the correlation between the experimentally measured and predicted vales of total life. The total life is dominated by the initiation life. Thus, the assumption of no endurance limit gives better correlation with the total life. The assumptions concerning the K_T at the crack tip during crack propagation have little effect on the correlation with total life. Unless otherwise noted, subsequent results are calculated under the assumption of no endurance limit.

Effect of LCF on HCF capability

Figure I.7 shows the computed values of allowable σ_a as a function of σ_m for failure in 10^7 HCF cycles (plus one LCF cycle representing the initial loading to a peak stress of $\sigma_a + \sigma_m$.) Line 1 indicates the alternating and mean stress combinations which will cause initiation in 10^7 HCF cycles with no superimposed LCF cycles ($N = 1$). If the number of cycles to initiation is increased from 10^7 to 10^8, the line moves down as shown. Another curve (line 2) is drawn to indicate the stress states above which a crack will propagate under HCF based on an initiation crack size (50 μm here) and the assumed value of ΔK_{th} as a function of R. At low values of mean stress, this line has a slope which increases significantly and follows a line along which $\sigma_a + \sigma_m = \text{constant}$. This value of maximum

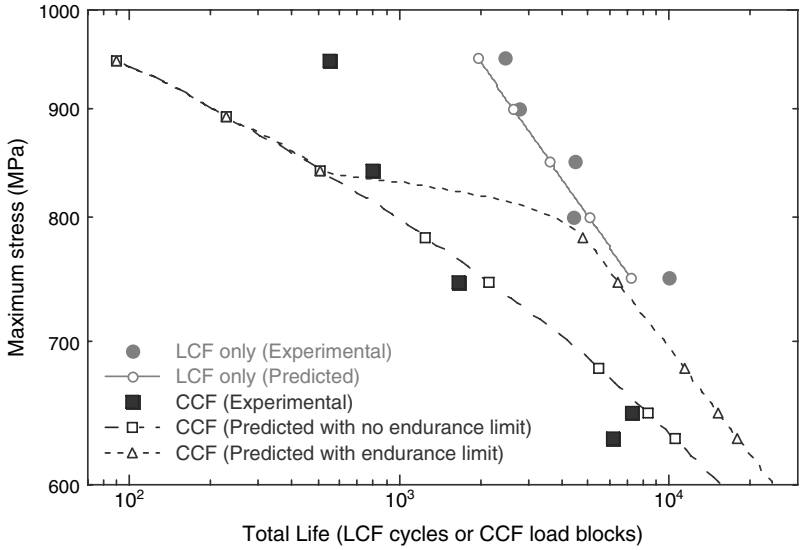


Figure I.6. Comparison of predicted and measured LCF and CCF total life for Ti-6-4 [9] with $R_{HCF}=0.85$ and $n=1800$.

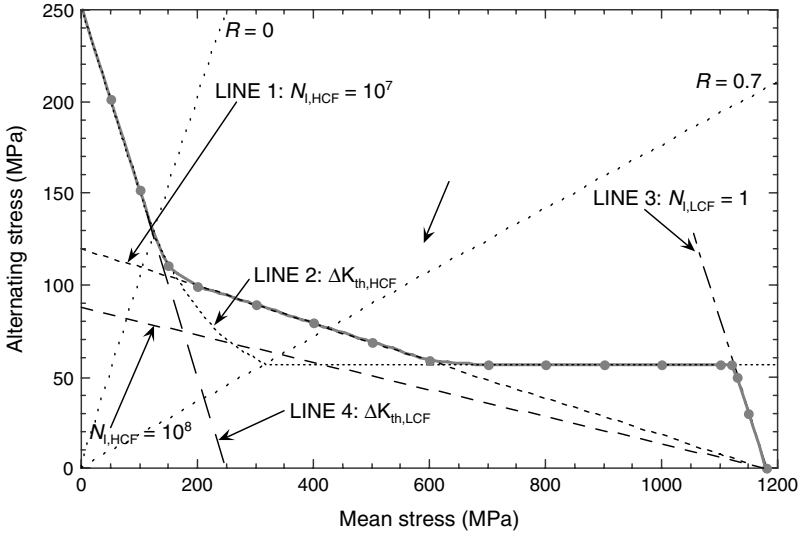


Figure I.7. Haigh diagram as predicted by analysis showing underlying mechanisms which govern the shape of the solution curve.

stress corresponds to $\Delta K_{HCF} = \Delta K_{th}$ at the initiating crack length. Note that in this low mean stress region, corresponding to negative R, the crack can initiate in less than 10^7 HCF cycles at stress states above line 1 but will never propagate if the stress state is below line 2. Conversely, there is a region bounded by $200 < \sigma_m < 600$ MPa where the crack will not initiate (below line 1), yet a 50-μm crack could propagate (above line 2) based on the assumptions in this analysis. If the numerical assumptions are correct, this would imply that within this range of mean stresses, which is in a "safe" design space for initiation based on an initiation criterion represented in a Haigh diagram, the material is intolerant to small amounts of damage. For initial defects or service induced damage such as FOD equivalent to a crack of 50 μm or greater, that damage would grow and eventually cause failure under HCF loading. This could occur, even though the stress states in this region indicate that cracks would not initiate under either LCF or HCF.

Following the same series of assumptions, additional curves can be drawn for the boundaries below which LCF cycles will not cause initiation in a specified number, N, of cycles, or below which a 50-μm crack will not propagate. The initiation curve for $N = 1$ LCF cycle is shown as line 3 in Figure I.7 and represents $\sigma_a + \sigma_m = \sigma_{ult}$. Any stress state above or to the right of this line will cause tensile failure on the first cycle. Finally, above and to the right of line 4, crack growth will occur under LCF loading once a crack initiates. Note that line 4 coincides with line 2 at low values of σ_m, above which HCF crack growth will occur (for a 50-μm crack). This is due to the assumption that the crack is closed at $\sigma = 0$ so that for $R_{HCF} < 0$, $\Delta K_{LCF} = \Delta K_{HCF}$. Under the assumptions of this analysis, the region where failure can occur due to either HCF or LCF is above the heavy line in Figure I.7.

The safe design space defined for $N = 1$ in Figure I.7 can be determined for other values of N. Figure I.8 shows solutions for various values of N and n where $Nn = 10^7$. As N increases, the allowable alternating stress decreases at higher values of mean stress. As expected, a finite number of LCF cycles reduces the maximum mean stress that may safely be applied to the structure. Comparison of Figures I.3 and I.8 indicates that the limiting value of mean stress for a given value of N corresponds to the allowable stress range for a specified value of N in Figure I.3.

Parametric studies

Inherent in the previous analyses were several assumptions concerning the behavior of the material. Among these were the variation in ΔK_{th} with R and the form of the initiation damage relationship. In each case, alternate assumptions can be used and lead to different results. Here, we consider the sensitivity of the results to such changes.

First, consider the form of the ΔK_{th} versus R behavior. Experimentally measured values of ΔK_{th} as a function of R are shown in Figure I.9 [12] for Ti-6-4. Two fits to the experimental data are also shown. A piecewise linear fit is shown which can be

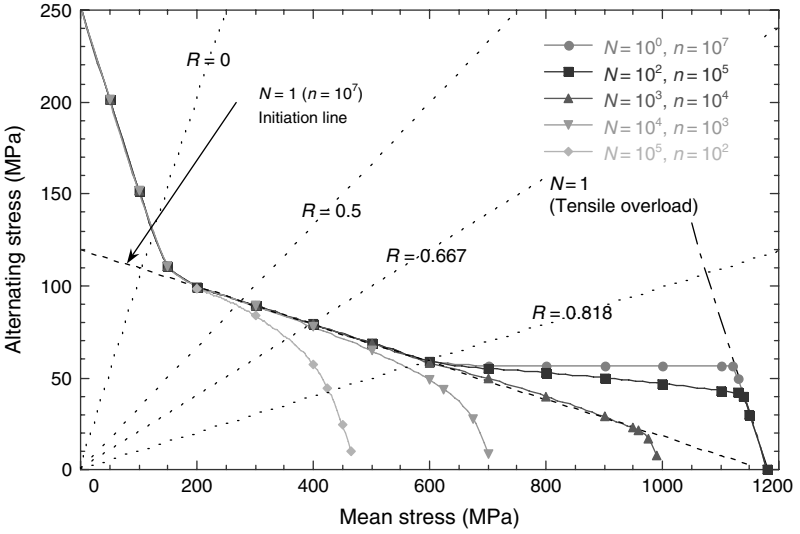


Figure I.8. Effect of number of superimposed LCF cycles on the HCF capability of Ti-6-4 as estimated by analysis.

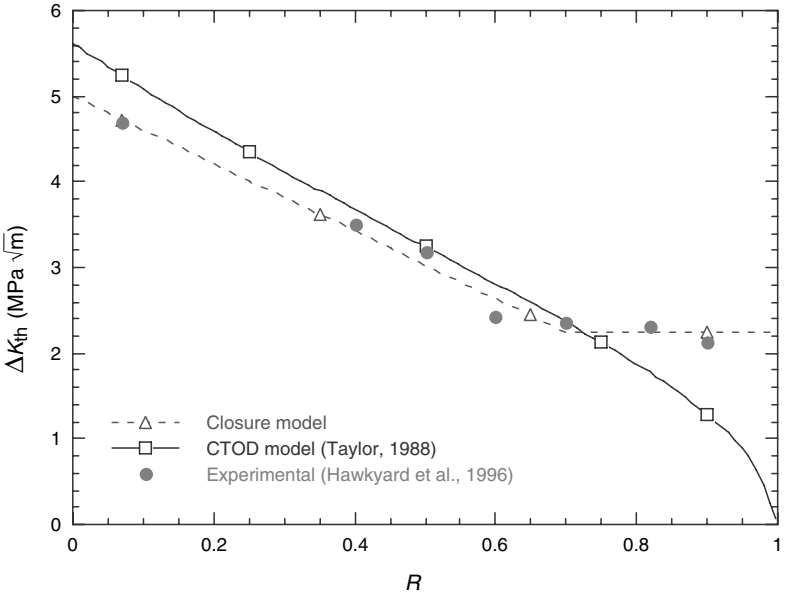


Figure I.9. Comparison of CTOD-based and closure-based ΔK_{th} vs R models with experimental data on Ti-6-4 [12].

rationalized through closure arguments and is incorporated into the previous analyses. As an alternative, ΔK_{th} may be defined as

$$\Delta K_{th} = \Delta K_{th,o} \left(\frac{1-R}{1+R} \right)^{0.5} \tag{I.6}$$

which is based on cyclic crack-tip opening displacement (CTOD) arguments [15]. In each case, a least squares approach has been used to obtain an optimal fit to the experimental data. Although in this material, the closure-based approach clearly correlates better with experiment, data obtained on other materials have been shown to correlate well with the CTOD approach [15, 16].

Figure I.10 indicates how the different variations in ΔK_{th} with R affect the form of the solution. The dashed lines indicate the magnitude of alternating stress required to cause crack propagation in a 50-μm-deep crack using ΔK_{th} variation based on both closure and CTOD models. Differences in the solution for allowable σ_a versus σ_m are significant and are particularly noticeable at high R. Thus, the variation in ΔK_{th} at high R appears to be important in predicting HCF life as a function of mean stress. Figure I.11 repeats the results shown in Figure I.8 which show the allowable σ_a versus σ_m for various combinations of HCF and superimposed LCF. Here, however, predictions are made using both CTOD and closure-based $\Delta K_{th}(R)$ values. Note that while the differences between the methods are significant for small values of N at high mean stress, when N becomes sufficient to cause reductions in the allowable alternating stress (versus pure HCF), the results become relatively insensitive to the ΔK_{th} model in use.

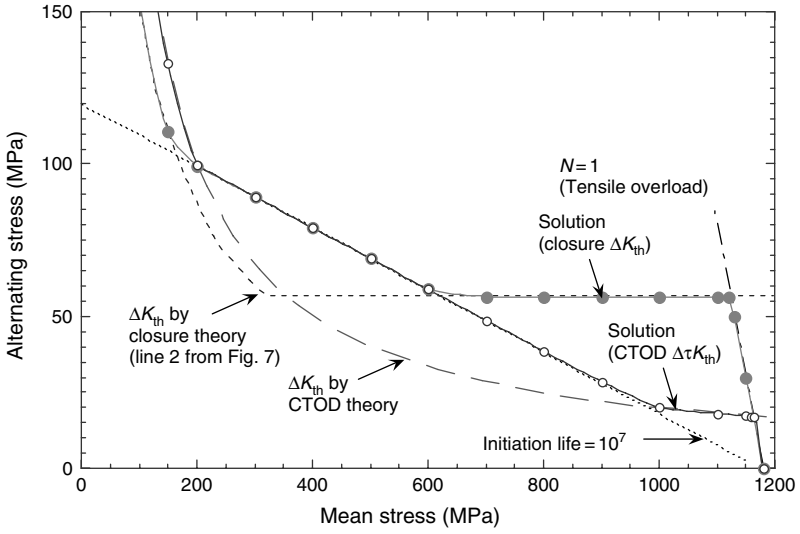


Figure I.10. Effect of ΔK_{th} vs R model on the HCF-only Haigh diagram as predicted by analysis.

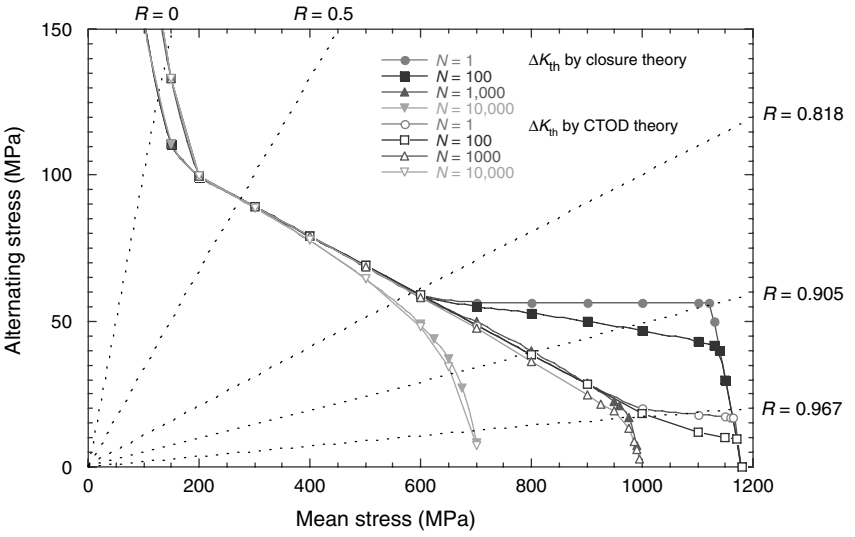


Figure I.11. Effect of ΔK_{th} vs R model on the CCF Haigh diagram as predicted by analysis.

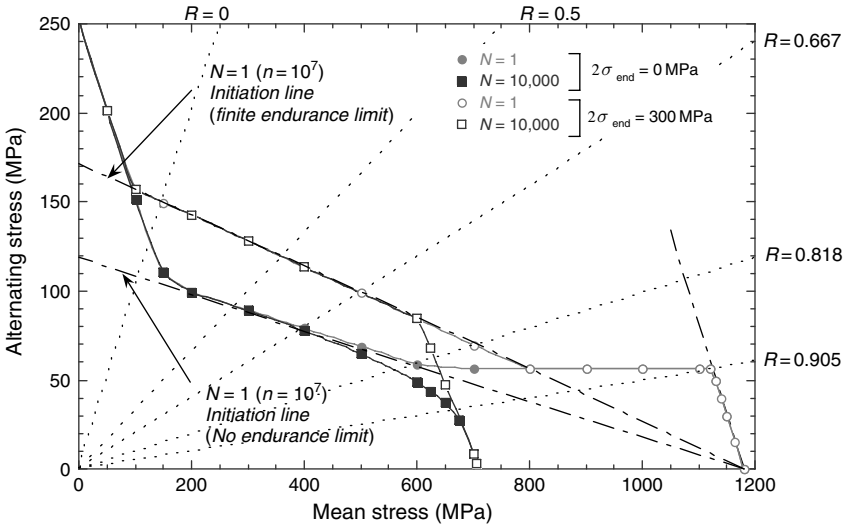


Figure I.12. Effect of endurance limit assumption on the HCF-only and CCF ($N = 10{,}000$) Haigh diagrams as predicted by analysis.

In Figure I.12, Haigh diagrams are shown for two different initiation phase assumptions: (a) the case of "no endurance limit" such that HCF cycles of infinitesimal stress amplitude cause finite damage (as incorporated in the previous analyses) and (b) the

case of $\Delta\sigma_{end} = 300\,\text{MPa}$. Results are shown for $N = 1$ and 10,000. The presence of an endurance limit effectively raises the initiation line (line 1 in Figure I.7). Note that the intersection of the solution for $\Delta\sigma_{end} = 300\,\text{MPa}$ and the $R = 0$ line corresponds to half the endurance limit stress range which again matches the 10^7 initiation life point in Figure I.3.

CLOSURE

Discussion

The numerical results presented here are based on simple models of crack initiation and propagation. Many potentially important phenomena are neglected such as the possible non-linear accumulation of initiation damage, the effect of previous cycling on the instantaneous endurance limit, acceleration in the HCF crack growth rate due to periodic underloads (LCF cycles), reduction in ΔK_{th} as a function of the number of LCF cycles, small crack effects, hold time effects on LCF cycles, and many more. Therefore, these results must be viewed as preliminary, giving only a qualitative indication of how LCF and HCF cycling interact to reduce overall life. Although simple, the method satisfactorily predicts the effects of combined HCF–LCF loading (see, e.g. Figure I.5) despite the limited amount of experimental data available for calibration. Additional experimental results should allow for better calibration and will pave the way for incorporation and assessment of many of the above phenomena.

Although the Goodman assumption is used in accounting for mean stress effects in crack initiation, the resulting Haigh diagram obtained differs from the Goodman assumption for total life in two regions as shown, for example, in Figure I.7. At very low mean stress, the predicted response curve follows lines 2 and 4, and is significantly steeper than that displayed by the Haigh diagram. At high mean stress, the allowable alternating stress follows line 2 and remains constant up to very high mean stress. In both high and low mean stress cases, the differences between the predicted response and the expected Goodman-type response (i.e. a straight line) are due to regions in the Haigh diagram in which a crack is predicted to initiate but not grow. For the experimental data considered here, this phenomenon may be due to the small crack size considered ($a_i = 50\,\mu\text{m}$) which may exhibit increased crack growth rates due to small crack effects. Such effects are not considered in this analysis. If a longer initial crack size were considered, both lines 2 and 4 in Figure I.5 would move down and to the left resulting in a solution curve which looks more like the Haigh diagram. Note also that considering a ΔK_{th} versus R curve for which $\Delta K_{th} \Rightarrow 0$ as $R \Rightarrow 1$ also results in a solution curve which approaches the Goodman assumption as shown in Figure I.10. Interestingly, the solution curve shown in Figure I.7 is similar in form to the experimental results reported by Bell and Benham [17] for stainless steel sheet (see, also, [18]). In that work notched ($K_t = 2.44$)

and unnotched stainless steel sheets (18Cr-9Ni) were fatigued under loads leading to lives of 10^1–10^7 cycles and over the range $-1.0 < R \leq 0.91$ at frequencies of 0.1 to 50 Hz. The resulting Haigh diagrams for the notched specimens exhibited a steep decline in allowable alternating stress as R increased from -1 to 0.33 followed by a region of relatively constant allowable alternating stress until the allowable stress began to quickly fall along a line approximating $\sigma_a + \sigma_m = \sigma_{ult}$. In any case, the resulting Haigh diagram diverges significantly from the Goodman assumption, especially at high values of mean stress.

It is interesting to note that this behavior of the model can qualitatively predict the experimental observations of Suhr [6]. In this work, a 12% CrNiMo blading alloy was cycled at a mean strain of 0.01 and variable alternating strain amplitude of 0–600 microstrain. Tests were conducted in HCF-only; HCF with superimposed periodic underloads to zero strain every 10^5 HCF cycles (combined HCF–LCF loading); and with a fixed number of LCF cycles preceding HCF-only cycling to failure (or runout). The results indicate that at high values of alternating strain, the number of cycles to failure is independent of whether LCF cycles are distributed throughout the HCF loading or all applied prior to HCF loading. As the alternating strain amplitude is reduced, a transition in behavior occurs such that specimens with all LCF cycling applied prior to HCF cycling exhibit significantly longer lives than specimens subjected to the same number of LCF cycles distributed periodically between blocks of HCF cycles. The explanation for this behavior is as follows. At high $\Delta\varepsilon_{HCF}$, ΔK_{HCF} is above ΔK_{th} and once a crack initiates, it grows in both HCF and LCF. As all HCF and LCF cycles cause finite damage in both the crack initiation and propagation phases, there is little dependence on the order of the cycles. At lower $\Delta\varepsilon_{HCF}$, when all LCF cycles are applied prior to HCF cycles, most or all LCF cycles act to initiate the crack. After the last LCF cycle has been completed, the crack is still sufficiently small such that $\Delta K_{HCF} < \Delta K_{th}$. Therefore, the crack will not grow and the specimen will exhibit very long life, as shown by the runouts in Suhr's data. At lower $\Delta\varepsilon_{HCF}$, when LCF cycles are distributed periodically between HCF cycles, HCF cycles play an active role in initiating the crack, and at the point of crack initiation there are sufficient LCF cycles remaining to grow the crack to a length sufficient for crack growth to occur in HCF cycles.

Despite any shortcomings, the analysis provides insight into designing for HCF–LCF loading. It has been common practice to use a form of the Haigh diagram to design for allowable vibratory stress in the presence of a mean stress in metal components. For high frequency, low-amplitude fatigue, the crack propagation life is generally observed to be a small fraction of the total life. (In the numerical simulations presented above, crack propagation life was generally less than 1% of total life.) Thus, the $N = 1$, $n = 10^7$ initiation line is a good approximation to the Haigh diagram for the Ti-6Al-4V material under investigation. This is shown in Figure I.13 along with the numerical predictions from Figure I.8 for $N = 10^4$. The allowable mean stress at $\sigma_a = 0$ is, by definition, the

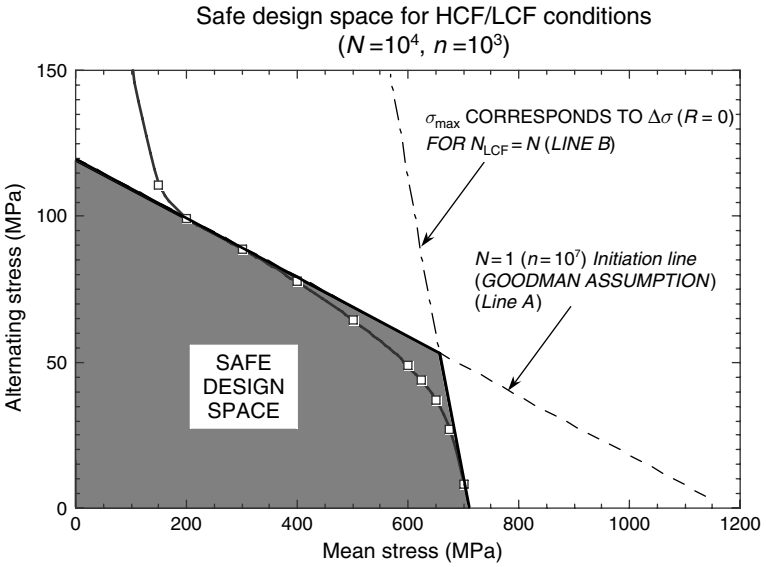


Figure I.13. Proposed safe design space for CCF.

stress range for an LCF life of N cycles (10^4 in this case) as plotted in Figure I.3. The data for $N = 10^4$ appears to follow a line of constant maximum stress as the allowable alternating stress increases. That is, for a given value of N

$$\sigma_a + \sigma_m = \Delta\sigma_{LCF} \tag{I.7}$$

where $\Delta\sigma_{LCF}$ is the stress range causing failure in N cycles at $R = 0$. This same relationship was found to hold in both Ti-6Al-4V and Inconel 718 smooth bar specimens at low values of alternating stress [9]. Thus, it is hypothesized that the safe design space for combined HCF–LCF loading is below the Goodman line, and to the left of the line of constant maximum stress corresponding to the appropriate number of LCF cycles. For a significant number of LCF cycles, this removes a sizable region at high values of R from the safe design space.

Note that near the intersection of the Goodman line (line A) and the $\Delta\sigma_{LCF}$ line (line B), the safe design space proposed here is somewhat larger than the safe design space predicted numerically. The discrepancy is greatest at the intersection of the two lines and its magnitude is dependent upon the details of the numerical analysis. For example, if we consider the existence of an endurance limit for initiation damage, then, as shown in Figure I.12, the "knee" of the curve (at $\sigma_m \approx 600$ MPa) has much less curvature and the safe design space proposed here is more accurate. That there is less curvature in the knee for the case of an endurance limit is easily explained. For such a case, any stress point

on the Haigh diagram below the Goodman initiation line (line A in Figure I.13), HCF cycles will cause no damage of any form. Thus below this line initiation is brought about only through LCF cycling. To the left of the line defined by $\sigma_a + \sigma_m = \Delta\sigma_{LCF}$ (line B in Figure I.13), initiation in LCF requires in excess of 10^4 cycles and the part is safe for the required life. However, if there is initiation damage attributable to HCF cycles below the endurance limit, then the actual safe design space will lie within the proposed safe design space, as the numerical solution does in Figure I.13. Prediction of the exact form of the safe design space will require further refinement of the numerical model.

Conclusions

Predictions have been made for the safe design space under combined HCF–LCF loading in terms of allowable values of mean and alternating stress using data from the literature on Ti-6Al-4V. The numerical procedure provides satisfactory correlation with limited experimental data on HCF–LCF loading. The predicted safe design space is a subset of the safe design space for pure HCF with the size of the safe design space decreasing with increasing number of LCF cycles. The region removed from the safe design space as defined by the Haigh diagram corresponds to the region of high mean stress in the design space where the greatest concern for HCF failures exists.

Further detailed experimental studies will help us to understand the behavior of ΔK_{th} at high R; understand the accumulation of initiation damage; understand and quantify the synergistic interactions in CCF such as reduction in ΔK_{th} and crack growth acceleration; and confirm the findings presented here. Many of these activities were conducted as part of the USAF initiative on HCF and are reported on elsewhere.

REFERENCES

1. Atrens, A., Hoffelner, W., Duerig, T.W., and Allison, J.E., "Subsurface Crack Initiation in High Cycle Fatigue in Ti-6Al-4V and in a Typical Martensitic Stainless Steel", *Scripta Metallurgica*, **17**, 1983, pp. 601–606.
2. Nishida, S., Urashima, C., and Suzuki, H.G., "Fatigue Strength and Crack Initiation of Ti-6Al-4V", *Fatigue 90*, Materials and Component Engineering Publications Ltd, Birmingham UK, 1990, pp. 197–202.
3. Palmgren, A., "Die Lebensdauer von Kugellagern", *Zeitschrift des Vereins Deutscher Ingenieure*, **68**, 1924, pp. 339–341.
4. Miner, M.A., "Cumulative Damage in Fatigue," *Jour. Appl. Mech.*, **12**, 1945, pp. 159–164.
5. Collins, J.A., *Failure of Materials in Mechanical Design: Analysis, Prediction, Prevention*, John Wiley & Sons, New York, 1981.
6. Suhr, R.W., "Interaction of High-Strain and High-Cycle Fatigue in Turbine Materials", *Fatigue Fract. Engng. Mater. Struct.*, **15**, 1992, pp. 399–415.
7. Frost, N.E., Marsh, K.J., and Pook, L.P., *Metal Fatigue*, Clarendon Press, Oxford, 1974.

8. Walker, K., "The Effect of Stress Ratio During Crack Propagation and Fatigue for 2024-T3 and 7075-T6 Aluminum", *Effects of Environment and Complex Load History for Fatigue Life, ASTM STP 462*, American Society for Testing and Materials, Philadelphia, 1970, pp. 1–14.
9. Guedou, J.-Y. and Rongvaux, J.-M., "Effect of Superimposed Stresses at High Frequency on Low Cycle Fatigue", *Low Cycle Fatigue*, ASTM, Philadelphia, 1988, pp. 938–969.
10. Chesnutt, J.C., Thompson, A.W., and Williams, J.C., "Influence of Metallurgical Factors on the Fatigue Crack Growth Rate in Alpha-Beta Titanium Alloys", AFML-TR-78-68, Wright-Patterson AFB, OH, May 1978 (ADA063404).
11. Grover, H.J., *Fatigue of Aircraft Structures*, Government Printing Office, Washington, DC, 1966.
12. Hawkyard, M., Powell, B.E., Husey, I., and Grabowski, L., "Fatigue Crack Growth under Conjoint Action of Major and Minor Stress", *Fatigue Fract. Eng. Mater. Struct.*, 1996, pp. 217–227.
13. Raju, I.S. and Newman, J.C., "Stress-Intensity Factors for Circumferential Surface Cracks in Pipes and Rods Under Tension and Bending Loads", *Fracture Mechanics: Seventeenth Volume*, *ASTM STP 905*, J.H. Underwood, R. Chait, C.W. Smith, D.P. Wilhem, W.A. Andrews, and J.C. Newman, eds, American Society for Testing and Materials, Philadelphia, 1986, pp. 789–805.
14. Dowling, N.E., "Notched Member Fatigue Life Predictions Combining Crack Initiation and Propagation", *Fatigue of Engineering Materials and Structures*, **2**, 1979, pp. 129–138.
15. Taylor, D., *Fatigue Thresholds*, Butterworths, London, 1989.
16. Taylor, D., *A Compendium of Fatigue Thresholds and Crack Growth Rates*, EMAS, Warley, UK, 1985.
17. Bell, W.J. and Benham, P.P., "The Effect of Mean Stress on Fatigue Strength of Plain and Notched Stainless Steel Sheet in the Range From 10 to 10^7 Cycles", *Symposium on Fatigue Tests of Aircraft Structures: Low-cycle, Full-scale, and Helicopters, ASTM STP 338*, ASTM, Philadelphia, 1963, pp. 25–46.
18. Madayag, A.F., *Metal Fatigue: Theory and Design*, John Wiley and Sons, Inc., New York, 1969.

Index

AMT (Accelerated mission test), 5
Applications, 377–471
Autofrettage, 464–71

Biaxial tests, 130–4

Coaxing, 70–4, 89–90
Component Improvement Program (CIP), 6
Constant-life diagrams, 27–47
  equations, 41–7
    Gerber, 42–3, 388
    Goodman, 42, 254, 388
    Heywood, 55
    Jasper, 56–65, 386–7, 439–40
    Launhardt–Weyrauch (L–W), 42–3
    Smith–Watson–Topper (SWT), 53, 118–19, 121, 296, 381, 405, 436–9
    Soderberg, 42
    Walker, 48, 54, 369, 405–7, 417
  Goodman diagram *see* Haigh diagram
  Haigh diagram, 36, 47–56, 379–81, 384, 396–8, 401–23, 436, 618–19
  Nicholas–Haigh diagram, 62, 386
Contact fatigue *see* Fretting fatigue
Creep rupture, 254–9, 401

Damage tolerance, 10, 16–23, 143–376, 398–400
  Retirement for Cause (RFC), 19
Defects, effects of, 251–4, 390–6

El Haddad short crack correction, 145–51, 224, 240, 249–51, 303
Elevated temperature:
  Haigh diagram for, 47–51
  notch fatigue at, 254–9
Endurance limit, 27, 123
  notches, 241–2
  see also Constant-life diagrams, Jasper
Energy considerations:
  in FOD, 345–7
ENSIP (Engine Structural Integrity Program):
  HCF issues in, 5, 10, 17, 21, 499–516
  see also JSSG (Joint Service Specification Guide)

Factor of safety, 379–81
Fatigue notch factor, 216–22, 347–52, 531
  relations with SCF, 217–22, 441
Field experience, 13–16, 25–6, 204–12, 324–9, 336–8, 424, 493–6
  see also Foreign object damage (FOD)
Findley parameter, 244, 296
Foreign object damage (FOD), 12, 322–75, 558–99, 600–16
  analytical/numerical modeling, 368–71, 582–91
    life prediction, 592–8
    perturbation study, 371–4
  JSSG requirements, 323, 600–16
    bird ingestion, 600–7
    ice ingestion, 607–10
    sand and dust ingestion, 610–16
  laboratory simulation, 338–44, 570–82
  residual stress, 344–5
  types of damage, 329–36, 560–70
Frequency effects, 134–43
Fretting fatigue, 11, 261–321, 542–57
  combined stress and K approach, 306–9
  contact stresses in half-space, 542–8
  critical plane parameters:
    Fatemi-Socie parameter, 298
    modified shear-stress-range (MSSR), 297
    shear stress range (SSR), 296
    see also Constant-life diagrams, Smith–Watson–Topper (SWT); Findley parameter
  finite thickness solutions, 548–56
  fracture mechanics approaches, 300–6

Fretting fatigue (*Continued*)
role of coefficient of friction, 312–17
test fixtures, 305, 309–12

Gigacycle fatigue, 27–34, 70

Haigh, B.P., 54, 59, 477, 481
Haigh diagram, 36, 47
High cycle fatigue:
definition, 4, 476
design issues, 5–11, 379–402, 510–15
design requirements, 9–11, 499–516, 600–17
history, 3, 70–5, 472–92
root causes, 11–13

JSSG (Joint Service Specification Guide), 600–16

Kitagawa diagram, 145–8, 159, 163–5, 223, 248–51, 253, 303, 423

Low Cycle Fatigue, interactions with, 11, 145–212, 396–8, 504–5, 617–38
combined cycle fatigue, 204–12, 619–37
erroneous behavior, 197–207
nomenclature, 196–7
notched specimens, 166–7

Material quality, 40, 384
Modeling errors, 381–4

Notch fatigue, 213–60, 531–41
crack-like behavior, 222–8
mean stress effects, 228–38
stress gradients, 242–51, 532–6
critical distance approaches, 242–6
see also Stressed surface area (FS)
Worst Case Notch (WCN) approach, 536–40, 595–8

Probabilities and statistics, 6–7, 76–80, 91–105, 120–2, 517–30
application to FOD design, 425–30
bootstrapping, 527–30
Dixon and Mood method, 95–9, 120, 518–27
material quality considerations, 384–5
SEV distribution, 110–12

Random fatigue limit (RFL) model, 109–22, 362
Ratcheting, 83–5
Residual stress in design, 430–6
crack growth retardation, 461–2
deep residual stresses, 447–64
notch fatigue, 436–40
shot peening, 441–7
see also Autofrettage; Foreign object damage (FOD)
Run-outs, 126–9

S–N curve *see* Wöhler diagram
Stress:
alternating, 34, 43
amplitude ratio, 35
equivalent, 48–51, 121, 298, 592–3
mean, 22, 29, 34, 39, 51–6
range, 34
Stress concentration factor (SCF), 213–16, 322, 531
Stress ratio, 34, 47, 302, 389, 391, 417, 420–2
negative, 65–70, 238
Stress relief annealing, 179–80, 184, 189–90, 353–9
Stressed surface area (FS), 307, 363–8, 532–6

Testing techniques, 70–109, 123–42, 481
constant stress tests, 123–8
other methods, 106–9
Prot method, 73–5
resonance testing, 129–33, 137
staircase testing, 90–105, 517–41
"artificial staircase", 105–6
step testing, 65–70, 75–89, 355
last loading block, 85–8
Thresholds for HCF:
engineering approach for determination, 423
experimental considerations, 409–23
compression precracking, 416
"jump-in" method, 409–12
load-shed method, 411, 414–16

fatigue limit strength, 9, 27, 35–41, 405–7
  effects of defects on *see* Defects, effects of
  role of residual stresses, 63–4, 344, 430–62
fracture mechanics approach, 66, 170–83, 386–90, 403–4, 508
  crack closure, 418–22, 454–8, 630–4
  K_{max}–ΔK concept, 419–22
  K_{PR} concept, 422
  overloads and load-history effect, 12, 170–82, 190–3, 414
  mechanisms, 412–14

Wöhler, A., 3, 472–3
  Wöhler diagram (S–N curve), 4, 7, 18, 47, 382–4, 405–7
Wöhler diagram, 4, 7

This page intentionally left blank